

IMPACT FACTOR
10.057

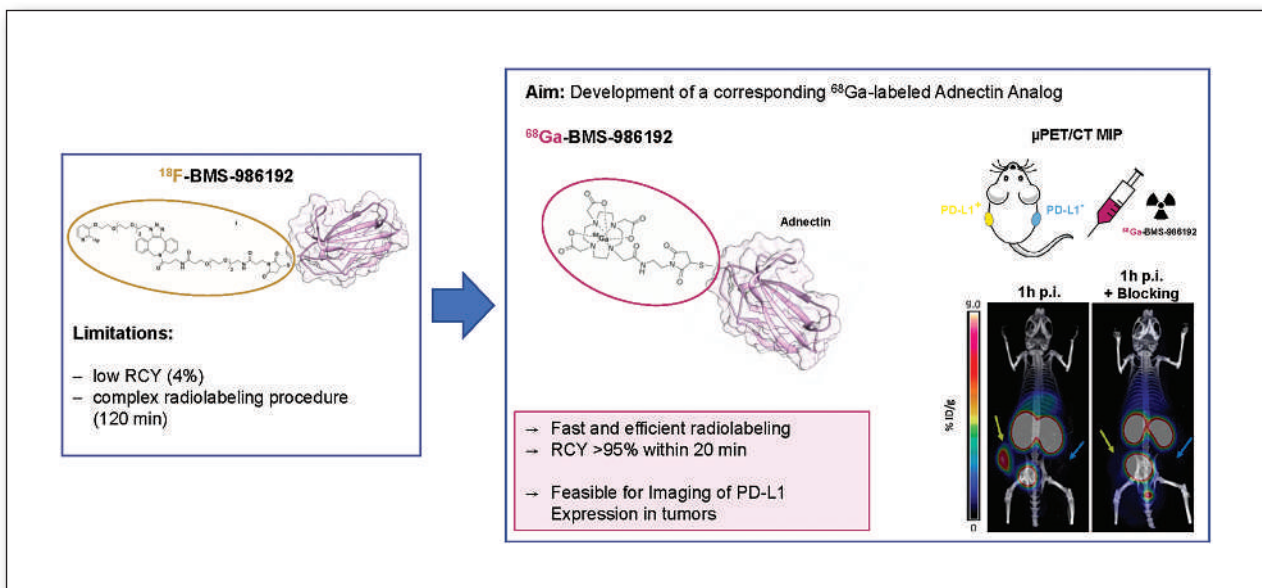
#1 NUCLEAR MEDICINE,
MOLECULAR IMAGING AND
MOLECULAR RADIOTHERAPY
JOURNAL

JNM

The Journal of Nuclear Medicine

FEATURED ARTICLE

Synthesis and Preclinical Evaluation of a ^{68}Ga -Labeled Adnectin, ^{68}Ga -BMS-986192, as a PET Agent for Imaging PD-L1 Expression. Stephanie Robu et al. See page 1228.



Pretargeted immuno-PET: improving detection of metastatic medullary thyroid carcinoma lesions. Caroline Bodet-Milin et al. See page 1221.



Achieve the True Mark of **Quality & Safety** for Your Facility with IAC

A leader in accreditation for 30 years and counting, **IAC accreditation clearly indicates a 'seal of approval'** to current and prospective patients — proof that the facility has undergone a rigorous evaluation, by clinical experts, of all aspects of the operations deemed relevant to providing quality patient care.

IAC's quality solutions and resources provide facilities with a foundation to create and achieve realistic patient care goals:



The **IAC Quality Improvement (QI) Tool** allows facilities to assess their case studies and final reports, receive a quantitative report targeting opportunities for continuous improvement and satisfy a component of the MIPS Improvement Activity score.



Free access to the IAC **Online Accreditation** application including the capability to upload cases to a HIPAA-compliant, secure medical image sharing service. Trained, clinical staff are dedicated to guiding you through the process via phone, live chat or e-mail.



The IAC website offers **helpful resources** including a robust calendar of CE courses and free access to live special topic webinars, accreditation webinars and webcasts offering CE credit. Plus sample and guidance documents, accreditation checklist and more!

What can **IAC accreditation** do for **your** facility?

VASCULAR TESTING
ECHOCARDIOGRAPHY
NUCLEAR/PET
MRI . CT . DENTAL CT



CAROTID STENTING
VEIN CENTER
CARDIAC ELECTROPHYSIOLOGY
CARDIOVASCULAR CATHETERIZATION

Improving health care through accreditation® | intersocietal.org | 800.838.2110

Submission Window Opens: September 2021

CALL FOR ABSTRACTS

If you are a young professional in the field, we invite you to submit a clinical or scientific abstract for the 2022 ACNM Annual Meeting on one of the following topics:

- ✔ Aspects of Clinical and Basic Science in Nuclear Medicine
- ✔ Correlative Imaging in Nuclear Medicine and Radiology
- ✔ Nuclear Pharmacy and Physics
- ✔ Nuclear Cardiology
- ✔ Theranostics
- ✔ Quality and Safety in Nuclear Medicine

2022 ACNM Annual Meeting Abstract AWARDS

Learn more about award opportunities available when you submit your abstract for the 2022 ACNM Annual Meeting.



www.snmimi.org/MWM2022

January 27-29
2022
**SNMMI MID-WINTER &
ACNM ANNUAL MEETING**

SNMMI

2022 Mid-Winter Meeting

ACNM
ANNUAL MEETING

**HILTON ORLANDO
LAKE BUENA VISTA
ORLANDO, FLORIDA**



Large Screen Interface Fully Integrated DICOM

CAPTUS® 4000e THYROID UPTAKE SYSTEM

- Thyroid uptake and well counting system including automated QC, bioassay, wipe tests, lab tests, with fully functional 1024 channel MCA, including timed activity
- Twenty inch, all-in-one touch-screen computer
- Improved graphical touch-screen user interface
- Fully integrated DICOM interface
- Ergonomically designed stand
- Fully articulating collimator arm for easy positioning
- Medical grade Corian countertop with convenient shelf for document storage
- Custom protocol program included

Absorbed Dose ALERT Software

Captus 4000e ALERT Software provides an initial field screening to rapidly triage and identify individuals with significant amounts of internal contamination, allowing for dual functionality for both routine thyroid uptakes and emergency screening requirements. The Alert Program records patient demographic data, selects appropriate body type, measures and quantifies internal organ burden and generates results in μCi -intake.



Call 1-800-631-3826
for more information



SNMMI NEWSLINE

- 9N** *JNM* 2020 Impact Factor Rises Sharply
- 9N** FDA Encourages Inclusion of Incurable Cancers in Trials
- 10N** ABNM Celebrating 50 Years
George M. Segall
- 11N** SNMMI Leadership Update: Progress in Prostate Cancer
Theranostics
Richard L. Wahl
- 12N** Newsbriefs

EDITOR'S PAGE

- 1177** The Annual Journal Impact Factor Saga
Johannes Czernin

DISCUSSIONS WITH LEADERS

- 1178** Leadership Focus on Advancing Cancer Research and
Treatment
Johannes Czernin, Caius Radu, and Antoni Ribas

STATE OF THE ART

- 1181** Image-Guided High-Intensity Focused Ultrasound, A Novel
Application for Interventional Nuclear Medicine?
Xinrui Zhang, Lisa Landgraf, Nikolaos Bailis, Michael Unger,
Thies H. Jochimsen, and Andreas Melzer

HOT TOPICS

- 1189** Why Will PET Be the Future of Nuclear Cardiology?
Marcelo F. Di Carli

CONTINUING EDUCATION

- 1192** Systemic Radiopharmaceutical Therapy of
Pheochromocytoma and Paraganglioma
Jorge A. Carrasquillo, Clara C. Chen, Abhishek Jha, Karel Pacak,
Daniel A. Pryma, and Frank I. Lin

FOCUS ON MOLECULAR IMAGING

- 1200** Current Landscape in Clinical Pretargeted
Radioimmunotherapy and Therapy
Vilma I.J. Jallinoja and Jacob L. Houghton

ISSUES AND CONTROVERSIES

- 1207** Diversity, Equity, and Inclusion in Academic Nuclear
Medicine: National Survey of Nuclear Medicine Residency
Program Directors
Jocelyn L. Cheng, Elizabeth H. Dibble, Grayson L. Baird,
Leonie L. Gordon, and Hyewon Hyun

ONCOLOGY

Clinical

- 1214** Value of ¹⁸F-FES PET in Solving Clinical Dilemmas in Breast
Cancer Patients: A Retrospective Study
Jorianne Boers, Naila Loudini, Celina L. Brunsch, Sylvia A. Koza,
Erik F.J. de Vries, Andor W.J.M. Glaudemans, Geke A.P. Hospers,
and Carolina P. Schröder
- 1221** ■ **FEATURED CLINICAL INVESTIGATION ARTICLE.** Anti-CEA
Pretargeted Immuno-PET Shows Higher Sensitivity Than
DOPA PET/CT in Detecting Relapsing Metastatic Medullary
Thyroid Carcinoma: Post Hoc Analysis of the iPET-MTC Study
Caroline Bodet-Milin, Alain Faivre-Chauvet, Thomas Carlier,
Catherine Ansquer, Aurore Rauscher, Eric Frampas,
Frederique Toulgoat, Damien Masson, Mickael Bourgeois,
Evelyne Cerato, et al.

Basic

- 1228** ■ **FEATURED ARTICLE OF THE MONTH.** Synthesis and
Preclinical Evaluation of a ⁶⁸Ga-Labeled Adnectin,
⁶⁸Ga-BMS-986192, as a PET Agent for Imaging PD-L1
Expression
Stephanie Robu, Antonia Richter, Dario Gosmann, Christof Seidl,
David Leung, Wendy Hayes, Daniel Cohen, Paul Morin, David J. Donnelly,
Daša Lipovšek, et al.

THERANOSTICS

Clinical

- 1235** ⁶⁸Ga-PSMA-11 PET/CT Improves Tumor Detection and
Impacts Management in Patients with Hepatocellular
Carcinoma
Nader Hirmas, Catherine Leyh, Miriam Sraieb, Francesco Barbato,
Benedikt M. Schaarschmidt, Lale Umutlu, Michael Nader,
Heiner Wedemeyer, Justin Ferdinandus, Christoph Rischpler, et al.
- 1242** ■ **EDITORIAL.** PSMA Theranostics: Is the Time Ripe to Pave
the Way to Further Tumor Entities?
Winfried Brenner, Joachim Strobel, and Vikas Prasad
- 1244** The Impact of Monosodium Glutamate on ⁶⁸Ga-PSMA-11
Biodistribution in Men with Prostate Cancer: A Prospective
Randomized, Controlled Imaging Study
Wesley R. Armstrong, Andrei Gafita, Shaojun Zhu, Pan Thin,
Kathleen Nguyen, Rejah Alano, Stephanie Lira, Kiara Booker,
Linda Gardner, Tristan Grogan, et al.
- 1252** Combination of Forced Diuresis with Additional Late
Imaging in ⁶⁸Ga-PSMA-11 PET/CT: Effects on Lesion
Visibility and Radiotracer Uptake
Ian Alberts, Jan Niklas-Hünemund, Christos Sachpekidis,
Helle Damgaard Zacho, Clemens Mingels, Lotte Dijkstra,
Karl Peter Bohn, Tilman Läppchen, Eleni Gourni, Axel Rominger, et al.
- 1258** Head-to-Head Comparison of ⁶⁸Ga-Prostate-Specific
Membrane Antigen PET/CT and Ferumoxtran-10-Enhanced
MRI for the Diagnosis of Lymph Node Metastases in
Prostate Cancer Patients
Melline G.M. Schilham, Patrik Zamecnik, Bastiaan M. Privé, Bas Israël,
Mark Rijpkema, Tom Scheenen, Jelle O. Barentsz, James Nagarajah, and
Martin Gotthardt

1264 SUVs Are Adequate Measures of Lesional ¹⁸F-DCFPyL Uptake in Patients with Low Prostate Cancer Disease Burden

Yves J.L. Bodar, Berend P.F. Koene, Bernard H.E. Jansen, Matthijs C.F. Cysouw, Dennie Meijer, N. Harry Hendrikse, André N. Vis, Ronald Boellaard, and Daniela E. Oprea-Lager

1270 ■ BRIEF COMMUNICATION. Detection of Early Progression with ¹⁸F-DCFPyL PET/CT in Men with Metastatic Castration-Resistant Prostate Cancer Receiving Bipolar Androgen Therapy

Mark C. Markowski, Pedro Isaacsson Velho, Mario A. Eisenberger, Martin G. Pomper, Kenneth J. Pienta, Michael A. Gorin, Emmanuel S. Antonarakis, Samuel R. Denmeade, and Steven P. Rowe

1274 ■ BRIEF COMMUNICATION. Addition of ¹³¹I-MIBG to PRRT (⁹⁰Y-DOTATOC) for Personalized Treatment of Selected Patients with Neuroendocrine Tumors

David L. Bushnell, Kellie L. Bodeker, Thomas M. O'Doriso, Mark T. Madsen, Yusuf Menda, Stephen Graves, Gideon K.D. Zamba, and M. Sue O'Doriso

1278 Dual PET Imaging in Bronchial Neuroendocrine Neoplasms: The NETPET Score as a Prognostic Biomarker

David L. Chan, Gary A. Ulaner, David Pattison, David Wyld, Rahul Ladwa, Julian Kirchner, Bob T. Li, W. Victoria Lai, Nick Pavlakis, Paul J. Roach, et al.

ENDOCRINOLOGY

1285 Assessment and Comparison of ¹⁸F-Fluorocholine PET and ^{99m}Tc-Sestamibi Scans in Identifying Parathyroid Adenomas: A Metaanalysis

Julia Whitman, Isabel E. Allen, Emily K. Bergsland, Insoo Suh, and Thomas A. Hope

NEUROLOGY

Clinical

1292 Tau^{IQ}: A Canonical Image Based Algorithm to Quantify Tau PET Scans

Alex Whittington and Roger N. Gunn, for the Alzheimer's Disease Neuroimaging Initiative

1301 ■ SPECIAL CONTRIBUTION. Hypermetabolism on Pediatric PET Scans of Brain Glucose Metabolism: What Does It Signify?

Harry T. Chugani

Basic

1307 Dopamine D₁ Receptor Agonist PET Tracer Development: Assessment in Nonhuman Primates

Olivier Barret, Lei Zhang, David Alagille, Cristian C. Constantinescu, Christine Sandiego, Caroline Papin, Jenna M. Sullivan, Thomas Morley, Vincent M. Carroll, John Seibyl, et al.

MOLECULAR IMAGING

Basic

1314 ■ BRIEF COMMUNICATION. Optical Navigation of the Drop-In γ -Probe as a Means to Strengthen the Connection Between Robot-Assisted and Radioguided Surgery

Samaneh Azargoshasb, Krijn H.M. Houwing, Paul R. Roos, Sven I. van Leeuwen, Michael Boonekamp, Elio Mazzone, Kevin Bauwens, Paolo Dell'Oglio, Fijs W.B. van Leeuwen, and Matthias N. van Oosterom

CHALLENGING CASE STUDIES

1318 Distinguishing Primary Lateral Sclerosis from Parkinsonian Syndromes with the Help of Advanced Imaging

Pegah Masrori, Donatienne Van Weehaeghe, Koen Van Laere, and Philip Van Damme

LETTERS TO THE EDITOR

1320 Bowel Obstruction as a Complication of Peptide Receptor Radionuclide Therapy

Christopher E. Wee, Ayca Dundar, Rachel A. Eiring, Mohamed Badawy, Timothy J. Hobday, A. Tuba Kendi, Annie T. Packard, and Thorvardur R. Halfdanarson

1320 Reply: Bowel Obstruction as a Complication of Peptide Receptor Radionuclide Therapy

Jonathan R. Strosberg, Taymeh Al-Toubah, and Ghassan El-Haddad

DEPARTMENTS

8A This Month in JNM

The Official Publication of **SNMMI**

Publications Committee

TODD E. PETERSON, PhD, FSNMMI
Chair

CAROLYN ANDERSON, PhD, FSNMMI
PAIGE B. BENNETT, MD
JOYITA DUTTA, PhD
MICHAEL M. GRAHAM, PhD, MD, FSNMMI
HOSSEIN JADVAR, MD, PhD, FACNM,
FSNMMI
STEVEN M. LARSON, MD, FACNM
HEINRICH R. SCHELBERT, MD, PhD, FSNMMI
HEIKO SCHÖDER, MD, MBA
DAVID M. SCHUSTER, MD
JESSICA WILLIAMS, CNMT, RT(N),
FSNMMI-TS
HARVEY A. ZIESSMAN, MD, FSNMMI

Ex officio

JOHANNES CZERNIN, MD
KATHY S. THOMAS, MHA, CNMT,
PET, FSNMMI-TS
HENRY F. VANBROCKLIN, PhD, FSNMMI
RICHARD L. WAHL, MD, FACNM

Associate Director of Communications

SUSAN ALEXANDER

Senior Copyeditor

SUSAN NATH

Senior Publications & Marketing Service Manager

STEVEN KLEIN

Editorial Production Manager

PAULETTE MCGEE

Editorial Project Manager

MARK SUMIMOTO

Director of Communications

REBECCA MAXEY

CEO

VIRGINIA PAPPAS

MISSION STATEMENT: *The Journal of Nuclear Medicine* advances the knowledge and practice of molecular imaging and therapy and nuclear medicine to improve patient care through publication of original basic science and clinical research.

JNM (ISSN 0161-5505 [print]; ISSN 2159-662X [online]) is published monthly by SNMMI, 1850 Samuel Morse Drive, Reston, VA 20190-5316. Periodicals postage is paid at Herndon, VA, and additional mailing offices. Postmaster, send address changes to *The Journal of Nuclear Medicine*, 1850 Samuel Morse Drive, Reston, VA 20190-5316. The costs of publication of all nonsolicited articles in *JNM* were defrayed in part by the payment of page charges. Therefore, and solely to indicate this fact, these articles are hereby designated "advertisements" in accordance with 18 USC section 1734.

DISCLOSURE OF COMMERCIAL INTEREST: Johannes Czernin, MD, editor-in-chief of *The Journal of Nuclear Medicine*, has indicated that he is a founder of Sofie Biosciences and holds equity in the company and in intellectual property invented by him, patented by the University of California, and licensed to Sofie Biosciences. He is also a founder and board member of Trethera Therapeutics and holds equity in the company and in intellectual property invented by him, patented by the University of California, and licensed to Triangle. He also serves on the medical advisory board of Actinium Pharmaceuticals and on the scientific advisory boards of POINT Biopharma, RayzeBio, and Jubilant Pharma and is a consultant for Amgen. No other potential conflicts of interest were reported. Manuscripts submitted to *JNM* with potential conflicts are handled by a guest editor.

EDITORIAL COMMUNICATIONS should be sent to: Editor-in-Chief, Johannes Czernin, MD, *JNM* Office, SNMMI, 1850 Samuel Morse Drive, Reston, VA 20190-5316. Phone: (703) 326-1185; Fax: (703) 708-9018. To submit a manuscript, go to <https://submit-jnm.snmjournals.org>.

BUSINESS COMMUNICATIONS concerning permission requests should be sent to the publisher, SNMMI, 1850 Samuel Morse Drive, Reston, VA 20190-5316; (703) 708-9000; home page address: jnm.snmjournals.org. Subscription requests and address changes should be sent to Membership Department, SNMMI at the address above. Notify the Society of change of address and telephone number at least 30 days before date of issue by sending both the old and new addresses. Claims for copies lost in the mail are allowed within 90 days of the date of issue. Claims are not allowed for issues lost as a result of insufficient notice of change of address. For information on advertising, contact Team SNMMI (Kevin Dunn, Rich Devanna, and Charlie Meitner; (201) 767-4170; fax: (201) 767-8065; TeamSNMMI@cunasso.com). Advertisements are subject to editorial approval and are restricted to products or services pertinent to nuclear medicine. Closing date is the first of the month preceding the date of issue.

INDIVIDUAL SUBSCRIPTION RATES for the 2021 calendar year are \$574 within the United States and Canada; \$617 elsewhere. Make checks payable to the SNMMI. CPC IPM Sales Agreement No. 1415158. Sales of individual back copies from 1999 through the current issue are available for \$60 at <http://www.snmml.org/subscribe> (subscriptions@snmml.org; fax: (703) 667-5134). Individual articles are available for sale online at <http://jnm.snmjournals.org>.

COPYRIGHT © 2021 by the Society of Nuclear Medicine and Molecular Imaging. All rights reserved. No part of this work may be reproduced or translated without permission from the copyright owner. Individuals with inquiries regarding permission requests, please visit <http://jnm.snmjournals.org/site/misc/permission.xhtml>. Because the copyright on articles published in *The Journal of Nuclear Medicine* is held by the Society, each author of accepted manuscripts must sign a statement transferring copyright (available for downloading at <http://jnm.snmjournals.org/site/misc/ifora.xhtml>). See Information for Authors for further explanation (available for downloading at <http://www.snmjournals.org/site/misc/ifora.xhtml>).

The ideas and opinions expressed in *JNM* do not necessarily reflect those of the SNMMI or the Editors of *JNM* unless so stated. Publication of an advertisement or other product mentioned in *JNM* should not be construed as an endorsement of the product or the manufacturer's claims. Readers are encouraged to contact the manufacturer with any questions about the features or limitations of the products mentioned. The SNMMI does not assume any responsibility for any injury or damage to persons or property arising from or related to any use of the material contained in this journal. The reader is advised to check the appropriate medical literature and the product information currently provided by the manufacturer of each drug to be administered to verify the dosage, the method and duration of administration, and contraindications.

Editor-in-Chief

Johannes Czernin, MD
*University of California at Los Angeles
Los Angeles, California*

Immediate Past Editor

Dominique Delbeke, MD, PhD
*Vanderbilt University Medical Center
Nashville, Tennessee*

Newsline Editor

Harvey A. Ziessman, MD
Takoma Park, Maryland

Associate Editors, Continuing Education

Heiko Schöder, MD
*Memorial Sloan Kettering Cancer Center
New York, New York*
H. William Strauss, MD
*Memorial Sloan Kettering Cancer Center
New York, New York*

Associate Editors

Ramsey Derek Badawi, PhD
*UC Davis Medical Center
Sacramento, California*
Henryk Barthel, MD, PhD
*Leipzig University
Leipzig, Germany*
Frank M. Bengel, MD
*Hannover Medical School
Hannover, Germany*
Lisa Bodei, MD, PhD
*Memorial Sloan Kettering Cancer Center
New York, New York*
Irene Buvat, PhD
*Université Paris Sud
Orsay, France*
Jérémy Calais, MD
*University of California at Los Angeles
Los Angeles, California*
Marcelo F. Di Carli, MD
*Brigham and Women's Hospital
Boston, Massachusetts*
Alexander E. Drzezga
*University Hospital of Cologne
Cologne, Germany*
Jan Grimm, MD, PhD
*Memorial Sloan Kettering Cancer Center
New York, New York*
Ken Herrmann, MD, MBA
*Universitätsklinikum Essen
Essen, Germany*
Lale Kostakoglu, MD, MPH
*University of Virginia Health System
Charlottesville, Virginia*
Jason S. Lewis, PhD
*Memorial Sloan Kettering Cancer Center
New York, New York*
David A. Mankoff, MD, PhD
*University of Pennsylvania
Philadelphia, Pennsylvania*
Wolfgang Weber, MD
*Technical University of Munich
München, Germany*

Series Editor, Focus on MI

Carolyn J. Anderson, PhD
*University of Missouri
Columbia, Missouri*

Series Editor, Hot Topics

Heinrich R. Schelbert, MD, PhD
*University of California at Los Angeles
Los Angeles, California*

Consulting Editors

Nancy Knight, PhD
*University of Maryland School of Medicine
Baltimore, Maryland*
Barry A. Siegel, MD
*Mallinckrodt Institute of Radiology
St. Louis, Missouri*
Arnold M. Strashun, MD
*SUNY Downstate Medical Center
Scarsdale, New York*

Associate Editors (International)

Gerald Antoch, MD
Düsseldorf, Germany

Richard P. Baum, MD, PhD
Bad Berka, Germany
Ambros J. Beer, MD
Ulm, Germany
Francois Benard, MD
Vancouver, Canada
Thomas Beyer, PhD
Vienna, Austria
Andreas K. Buck, MD
Würzburg, Germany
Ignasi Carrió, MD
Barcelona, Spain
June-Key Chung, MD
Seoul, Korea
Stefano Fanti, MD
Bologna, Italy
Markus Hacker, MD
Wien, Austria
Rodney J. Hicks, MD
Melbourne, Australia
Michael S. Hofman, MBBS
Melbourne, Australia
Ora Israel, MD
Haifa, Israel
Andreas Kjaer, MD, PhD, DMSc
Copenhagen, Denmark
Adriaan A. Lammertsma, PhD
Amsterdam, The Netherlands
Michael Lassman, PhD
Würzburg, Germany
Helmut R. Mäcke, PhD
Freiburg, Germany
Wim J.G. Oyen, MD, PhD
Milan, Italy
John O. Prior, MD, PhD
Lausanne, Switzerland
Osman Ratib, MD, PhD
Geneva, Switzerland
Mike Sathekge, MBChB, MMed, PhD
Pretoria, South Africa
Markus Schwaiger, MD
München, Germany
Andrew M. Scott, MD
Heidelberg, Australia
Nagara Tamaki, MD, PhD
Kyoto, Japan
Jia-He Tian, PhD
Beijing, China
Mei Tian, MD, PhD
Hangzhou, China
Hans-Jürgen Wester, PhD
Garching, Germany

Editorial Consultants

Martin S. Allen-Auerbach, MD
Los Angeles, California
Magnus Dahlbom, PhD
Los Angeles, California
Andrew Quon, MD
Los Angeles, California
Christiaan Schiepers, MD, PhD
Los Angeles, California
Daniel H. Silverman, MD, PhD
Los Angeles, California
Roger Slavik, PhD
Winterthur, Switzerland

Editorial Board

Diane S. Abou, PhD
St. Louis, Missouri
Valentina Ambrosini, MD, PhD
Bologna, Italy
Norbert Avril, MD
Cleveland, Ohio
Shadfar Bahri
Los Angeles, California
Jacques Barbet, PhD
Saint-Herbalin, France
Bradley Jay Beattie, PhD
New York, New York
Matthias Richard Benz, MD
Los Angeles, California
Pradeep Bhambhani, MD
Birmingham, Alabama
Angelika Bischof-Delaloye, MD
Lausanne, Switzerland

Christina Bluemel, MD
Würzburg, Germany
Ronald Boellaard, PhD
Groningen, The Netherlands
Nicolaas Bohnen, MD
Ann Arbor, Michigan
Wesley E. Bolch, PhD
Gainesville, Florida
Elias H. Botvinick, MD
San Francisco, California
Winfried Brenner, MD, PhD
Berlin, Germany
Richard C. Brunken, MD
Cleveland, Ohio
Ralph Buchert, PhD
Hamburg, Germany
Alfred Buck, MD
Menzingen, Switzerland
Denis B. Buxton, PhD
Bethesda, Maryland
Weibo Cai, PhD
Madison, Wisconsin
Federico Caobelli, MD
Basel, Switzerland
Giuseppe Carlucci, PhD
Los Angeles, California
Richard E. Carson, PhD
New Haven, Connecticut
Paolo Castellucci, MD
Bologna, Italy
Francesco Ceci, MD, PhD
Turin, Italy
Juliano J. Cerci
Curitiba, Brazil
Delphine Chen, MD
Seattle, Washington
Xiaoyuan Chen, PhD
Singapore
Simon R. Cherry
Davis, California
Arturo Chiti, MD
Rozzano, Italy
Peter M. Clark, PhD
Los Angeles, California
Christian Cohade, MD
Montreal, Canada
Ekaterina (Kate) Dadachova, PhD
Saskatoon, Canada
Issa J. Dahabreh, MD
Boston, Massachusetts
Heike Elisabeth Daldrop-Link, MD, PhD
Stanford, California
Farrokh Dehdashti, MD
St. Louis, Missouri
Robert C. Delgado-Bolton, MD, PhD
Logroño, Spain
Thorsten Derlin, MD
Hannover, Germany
Elisabeth G.E. de Vries, PhD
Groningen, The Netherlands
David W. Dick, PhD
Iowa City, Iowa
Vasken Dilisizian, MD
Baltimore, Maryland
Sharmila Dorbala, MBBS
Lexington, Massachusetts
Jacob Dubroff, MD, PhD
Philadelphia, Pennsylvania
Janet F. Eary, MD
Bethesda, Maryland
W. Barry Edwards, PhD
Columbia, Missouri
Matthias Eiber, MD
Munich, Germany
David Eidelberg, MD
Manhasset, New York
Georges El Fakhri, PhD
Boston, Massachusetts
Peter J. Ell, MD
London, United Kingdom
Keigo Endo, MD
Nantan, Japan
Einat Even-Sapir, MD, PhD
Tel Aviv, Israel
Frederic H. Fahey, DSc
Boston, Massachusetts

Editorial Board, continued

- Melpomeni Fani, PhD, MSc
Basel, Switzerland
- Wolfgang Peter Fendler, MD
Essen, Germany
- James W. Fletcher, MD
Indianapolis, Indiana
- Amy M. Fowler, MD, PhD
Madison, Wisconsin
- Kirk A. Frey, MD, PhD
Ann Arbor, Michigan
- Andrei Gafita
Los Angeles, California
- Victor H. Gerbaudo, PhD, MSHCA
Boston, Massachusetts
- Frederik L. Giesel, MD, PhD, MBA
Heidelberg, Germany
- Serge Goldman, MD, PhD
Brussels, Belgium
- Stanley J. Goldsmith, MD
New York, New York
- Martin Gotthardt, MD, PhD
Nijmegen, The Netherlands
- Michael Graham, MD, PhD
Iowa City, Iowa
- David Groheux, MD, PhD
Paris, France
- Uwe A. Haberkorn, MD
Heidelberg, Germany
- Mathieu Hatt, PhD, HDR
Brest, France
- Wolf-Dieter Heiss, MD
Cologne, Germany
- Karl Herholz, MD
Manchester, United Kingdom
- Thomas F. Heston, MD
Las Vegas, Nevada
- John M. Hoffman, MD
Salt Lake City, Utah
- Carl K. Hoh, MD
San Diego, California
- Jason P. Holland, DPhil
Zurich, Switzerland
- Thomas A. Hope, MD
San Francisco, California
- Roland Hustinx, MD, PhD
Liege, Belgium
- Andrei H. Iagaru, MD
Stanford, California
- Masanori Ichise, MD
Chiba, Japan
- Heather A. Jacene, MD
Boston, Massachusetts
- Hossein Javvar, MD, PhD, MPH, MBA
Los Angeles, California
- Francois Jamar, MD, PhD
Brussels, Belgium
- Jae Min Jeong, PhD
Seoul, Korea
- John A. Katzenellenbogen, PhD
Urbana, Illinois
- Kimberly A. Kelly, PhD
Charlottesville, Virginia
- Laura M. Kenny, MD, PhD
London, United Kingdom
- Fabian Kiessling, MD
Aachen, Germany
- E. Edmund Kim, MD, MS
Orange, California
- Francoise Kraeber-Bodéré, MD, PhD
Nantes, France
- Clemens Kratochwil, MD
Heidelberg, Germany
- Kenneth A. Krohn, PhD
Portland, Oregon
- Brenda F. Kurland, PhD
Pittsburgh, Pennsylvania
- Constantin Lapa, MD
Augsburg, Germany
- Suzanne E. Lapi, PhD
Birmingham, Alabama
- Steven M. Larson, MD
New York, New York
- Dong Soo Lee, MD, PhD
Seoul, Korea
- Jeffrey Leyton, PhD
Sherbrooke, Canada
- Hannah M. Linden, MD
Seattle, Washington
- Martin A. Lodge, PhD
Baltimore, Maryland
- Egesta Lopci, MD, PhD
Milan, Italy
- Katharina Lückerath, PhD
Los Angeles, California
- Susanne Lütje, MD, PhD
Bonn, Germany
- Umar Mahmood, MD, PhD
Boston, Massachusetts
- H. Charles Manning, PhD
Nashville, Tennessee
- Giuliano Mariani, MD
Pisa, Italy
- Chester A. Mathis, PhD
Pittsburgh, Pennsylvania
- Alan H. Maurer, MD
Philadelphia, Pennsylvania
- Jonathan McConathy, MD, PhD
Birmingham, Alabama
- Alexander J.B. McEwan, MD
Edmonton, Canada
- Yusuf Menda, MD
Iowa City, Iowa
- Philipp T. Meyer, MD, PhD
Freiburg, Germany
- Matthias Miederer, MD
Mainz, Germany
- Erik Mittra, MD, PhD
Portland, Oregon
- Christine E. Mona, PhD
Los Angeles, California
- Dae Hyuk Moon, MD
Seoul, Korea
- Jennifer Murphy, PhD
Los Angeles, California
- Helen Nadel, MD, FRCPC
Stanford, California
- Matthias Nahrendorf, MD, PhD
Boston, Massachusetts
- Yuji Nakamoto, MD, PhD
Kyoto, Japan
- David A. Nathanson, PhD
Los Angeles, California
- Sridhar Nimmagadda, PhD
Baltimore, Maryland
- Egbert U. Nitzsche, MD
Aarau, Switzerland
- Medhat M. Osman, MD, PhD
Saint Louis, Missouri
- Christopher J. Palestro, MD
New Hyde Park, New York
- Miguel Hernandez Pampaloni, MD, PhD
San Francisco, California
- Neeta Pandit-Taskar, MD
New York, New York
- Michael E. Phelps, PhD
Los Angeles, California
- Gerold Porenta, MD, PhD
Vienna, Austria
- Sophie Poty, PhD
Montpellier, France
- Edwin (Chuck) Pratt, PhD, MS Eng
New York, New York
- Daniel A. Pryma, MD
Philadelphia, Pennsylvania
- Valery Radchenko, PhD
Vancouver, Canada
- Caius G. Radu, MD
Los Angeles, California
- Isabel Rauscher, MD
Munich, Germany
- Nick S. Reed, MBBS
Glasgow, United Kingdom
- Mark Rijpkema, PhD
Nijmegen, The Netherlands
- Steven P. Rowe, MD, PhD
Baltimore, Maryland
- Mehran Sadeghi, MD
West Haven, Connecticut
- Orazio Schillaci, MD
Rome, Italy
- Charles Ross Schmidlein, PhD
New York, New York
- David M. Schuster, MD
Atlanta, Georgia
- Travis Shaffer, PhD
Stanford, California
- Sai Kiran Sharma, PhD
New York, New York
- Anthony F. Shields, MD, PhD
Detroit, Michigan
- Barry L. Shulkin, MD, MBA
Memphis, Tennessee
- Yu Shyr, PhD
Nashville, Tennessee
- Albert J. Sinusas, MD
New Haven, Connecticut
- Riemer H.J.A. Slart, MD, PhD
Groningen, The Netherlands
- Piotr Slomka, PhD, FACC
Los Angeles, California
- Ida Sonni, MD
Los Angeles, California
- Michael G. Stabin, PhD
Richland, Washington
- Lisa J. States, MD
Philadelphia, Pennsylvania
- Sven-Erik Strand, PhD
Lund, Sweden
- Rathan M. Subramaniam, MD, PhD, MPH
Dunedin, New Zealand
- John Sunderland, PhD
Iowa City, Iowa
- Suleman Surti, PhD
Philadelphia, Pennsylvania
- Julie Sutcliffe, PhD
Sacramento, California
- Laura H. Tang, MD, PhD
New York, New York
- Ukihide Tateishi, MD, PhD
Tokyo, Japan
- James T. Thackeray, PhD
Hannover, Germany
- Mathew L. Thakur, PhD
Philadelphia, Pennsylvania
- Alexander Thiel, MD
Montreal, Canada
- Daniel L.J. Thorek, PhD
St. Louis, Missouri
- David W. Townsend, PhD
Singapore
- Timothy Turkington, PhD
Durham, North Carolina
- Gary A. Ulaner, MD, PhD
Irvine, California
- David Ulmert, MD, PhD
Los Angeles, California
- Christopher H. van Dyck, MD
New Haven, Connecticut
- Douglas Van Nostrand, MD
Washington, District of Columbia
- Patrick Veit-Haibach, MD
Toronto, Canada
- Nerissa Viola-Villegas, PhD
Detroit, Michigan
- John R. Votaw, PhD
Atlanta, Georgia
- Richard L. Wahl, MD
St. Louis, Missouri
- Anne Marie Wallace, MD
La Jolla, California
- Martin A. Walter, MD
Geneva, Switzerland
- Rudolf A. Werner, MD
Wuerzburg, Germany
- Andreas G. Wibmer, MD
New York, New York
- Anna M. Wu, PhD
Duarte, California
- Randy Yeh, MD
New York, New York
- Hyewon (Helen) Youn, PhD
Seoul, Korea
- Pat B. Zanzonico, PhD
New York, New York
- Brian M. Zeglis, PhD
New York, New York
- Robert Zeiser, MD
Freiburg, Germany
- Hong Zhang, MD, PhD
Hangzhou, China
- Hongming Zhuang, MD, PhD
Philadelphia, Pennsylvania
- Sibylle I. Ziegler, PhD
Munich, Germany

Assistant to the Editor

Joshua N. Wachtel
Los Angeles, California

Discussions with leaders: *JNM* editor-in-chief Johannes Czernin, with Caius Radu, continues a series of interviews with leaders in nuclear and molecular imaging and therapy with a conversation with Antoni Ribas, MD, PhD, about advancing cancer research and treatment. **Page 1178**

Image-guided HIFU in nuclear medicine: Zhang and colleagues present a state-of-the-art review of the principles and clinical applications of image-guided high-intensity focused ultrasound, including examples of future potential development. **Page 1181**

Cardiac PET and the future: Di Carli offers perspective on the changing epidemiology and pathobiology of coronary artery disease, the efficacy of conventional imaging tools, and the advantages of quantitative PET as a transformative modality in nuclear cardiology. **Page 1189**

Pheochromocytoma and paraganglioma: Carrasquillo and colleagues provide an educational overview of the clinical features of pheochromocytoma and paraganglioma, as well as therapeutic strategies with ^{131}I -MIBG and ^{90}Y - or ^{177}Lu -DOTA-somatostatin analogs. **Page 1192**

Current clinical pretargeting: Jallinoja and Houghton survey the recent history of pretargeting radioimmunotherapy and therapy studies, challenges faced in human studies and regulatory approval, and future avenues for clinical translation. **Page 1200**

Diversity in nuclear medicine: Cheng and colleagues report on the results of a study designed to characterize the status in nuclear medicine of women and racial/ethnic groups underrepresented in medicine in the United States. **Page 1207**

^{18}F -FES PET for clinical dilemmas: Boers and colleagues present findings from a retrospective study of the utility of ^{18}F -FES PET imaging in resolving questions in breast cancer after standard workups. **Page 1214**

Pretargeted immuno-PET in MTC: Bodet-Milin and colleagues describe the results of analyses to determine the sensitivity of anti-carcinoembryonic antigen immuno-PET in relapsing medullary thyroid carcinoma

and compare these with conventional imaging and ^{18}F -DOPA PET/CT. **Page 1221**

^{68}Ga -BMS-986192 for PD-L1 PET: Robu and colleagues detail the development and pre-clinical evaluation of a ^{68}Ga -labeled adnectin protein to facilitate imaging of PD-L1 expression in tumors. **Page 1228**

PSMA PET for HCC: Hirnas and colleagues assess the effects of ^{68}Ga -prostate-specific membrane antigen-11 PET/CT neovasculature imaging on disease staging, prognostics, and management of patients with hepatocellular carcinoma. **Page 1235**

Expanding PSMA theranostics: Brenner and colleagues offer perspective on the potential for nonprostatic applications of prostate-specific membrane antigen-based theranostics, particularly in tumors with high need for therapy improvement. **Page 1242**

MSG and ^{68}Ga -PSMA PET/CT: Armstrong and colleagues use ^{68}Ga -PSMA-11 PET to determine the effect of monosodium glutamate administration on prostate-specific membrane antigen-radioligand biodistribution in healthy organs and tumor lesions in men with prostate cancer. **Page 1244**

Diuresis and dual-time-point PSMA PET: Alberts and colleagues investigate a modified prostate-specific membrane antigen PET/CT protocol combining late additional imaging with hydration and forced diuresis in assessment for uncertain findings. **Page 1252**

^{68}Ga -PSMA PET/CT versus nano-MRI: Schilham and colleagues compare characteristics of prostate-specific membrane antigen PET/CT and ferumoxtran-10 nanoparticle-enhanced MRI to determine the feasibility of their complementary use for prostate cancer imaging. **Page 1258**

SUV and TBR in ^{18}F -DCFpYL PET/CT: Bodar and colleagues explore whether SUV on PET/CT, as compared with tumor-to-blood ratio, can provide adequate quantification of uptake of this ligand in a patient cohort with low prostate cancer burden. **Page 1264**

PSMA PET and bipolar androgen therapy: Markowski and colleagues analyze the utility of ^{18}F -DCFpYL PET/CT in determining

clinical response to this emerging treatment for metastatic castration-resistant prostate cancer. **Page 1270**

PRRT plus ^{131}I -MIBG: Bushnell and colleagues report on preliminary results of a study on the addition of ^{131}I -MIBG to ^{90}Y -DOTA-TOC peptide-receptor radionuclide therapy for progressive metastatic neuroendocrine tumors. **Page 1274**

NETPET score in lung NENs: Chan and colleagues describe evaluation of this prognostic score, combining ^{18}F -FDG and somatostatin receptor imaging agent uptake data, in bronchial neuroendocrine neoplasms. **Page 1278**

^{18}F -FCH PET metaanalysis: Whitman and colleagues summarize data on the sensitivities and specificities of ^{18}F -FCH PET in localizing hyperparathyroidism and compare these results with those from comparable $^{99\text{m}}\text{Tc}$ -sestamibi scans. **Page 1285**

Tau^{1Q} algorithm: Whittington and Gunn report on development of a PET data quantification algorithm for the complex spatial distribution of tau radiotracers, with specific promise in longitudinal analyses and early detection of tau deposition. **Page 1292**

Hypermetabolism on brain ^{18}F -FDG PET: Chugani discusses and provides examples of the multiple causes of hypermetabolism on ^{18}F -FDG PET studies that should not be interpreted as seizure activity. **Page 1301**

DIR PET tracers: Barret and colleagues characterize in nonhuman primates 2 novel D_1 receptor agonist PET radiotracers, racemic ^{18}F -MNI-800 and its more active atropisomeric (–)-enantiomer, ^{18}F -MNI-968. **Page 1307**

Enhancing robot-assisted radioguided surgery: Azargoshasb and colleagues describe development of a real-time fluorescence-video-based tracking method that integrates the DROP-IN γ -probe with navigated robotic surgery. **Page 1314**

Advanced imaging for primary lateral sclerosis: Masrori and colleagues present results from work-up imaging with MRI, ^{123}I -FP-CIT PET, ^{18}F -PE2I PET, and ^{18}F -FDG PET in a patient with unilateral mild paresis, slowing of the upper limb, and parkinsonism. **Page 1318**

JNM 2020 Impact Factor Rises Sharply

The SNMMI and editors of *The Journal of Nuclear Medicine* announced on July 1 that the publication had achieved the highest impact factor in its history, now ranking third among all medical imaging journals, according to new data released in the *2020 Journal Citation Reports*. “This is a tribute to the great contributions of diverse scientists from all areas of the field,” said *JNM* editor-in-chief Johannes Czernin, MD. “I am grateful for the support of SNMMI and its Publications Committee, the invaluable contributions of our staff, the critical input from our editorial board members, and the hard work and creativity of the team of national and international associate editors who made this success possible.”

JNM's impact factor increased more than 27% from that in the previous year, from 7.887 (2019) to 10.057 (2020). With 32,949 total citations, the journal moved up to third in impact factor among all 134 journals in the medical imaging category. The journal's total citations increased by 23%, its immediacy index increased by 68%, and its article influence score and 5-year impact factor increased by 26%. Among nuclear medicine journals, *JNM* continues to have the highest impact

factor, total citations, 5-year impact factor, Eigenfactor score, and article influence score. “The high journal impact with the associated high visibility of *JNM* will continue to attract pre-clinical and clinical contributors from oncology, neurology, cardiology, endocrinology, infectious diseases, and other fields,” Czernin said.

The impact factor is a quantitative measure of the frequency with which an article in a journal is cited. It is used as a measure of the overall influence of a journal within scientific, professional, and academic communities. The immediacy index is an indicator of the speed with which citations to a specific journal appear in published literature. “Three of our top 10 articles contributing to the impact factor calculation describe advances in imaging instrumentation, with the remaining 7 introducing various important aspects of theranostics,” said Czernin. “It is thus evident that theranostics and the search for novel and relevant targets remain at the forefront of nuclear medicine research. Revolutionary advances in instrumentation will open new and exciting research opportunities. Similarly, artificial intelligence will find its way into the clinic based on solidly designed clinical studies.”

FDA Encourages Inclusion of Incurable Cancers in Trials

On June 24 the U.S. Food and Drug Administration (FDA) issued draft guidance encouraging inclusion of patients with incurable cancers in oncology clinical trials, regardless of prior therapies. “Historically, many clinical trials have required that participating patients previously received multiple therapies,” said Richard Pazdur, MD, director of the FDA Oncology Center of Excellence and acting director of the Office of Oncologic Diseases in the Center for Drug Evaluation and Research. “The FDA believes patients with incurable cancers, if provided adequate information to make an informed decision, should be eligible to participate in oncology clinical trials. If there is no scientific rationale for excluding these patients, then clinical trial eligibility criteria should be broadened to include these patients, with appropriate informed consent.”

The draft guidance, titled “Cancer clinical trial eligibility criteria: Available therapy in noncurative settings,” is part of the FDA's broader initiative to encourage “rational expanded patient eligibility” for oncology clinical trials. When finalized, the guidance will provide recommendations to sponsors designing clinical trials of drug and biologic products for expanding eligibility to patients with incurable cancers as well as inclusion of patients who have not received available therapy/therapies (e.g., evaluating these patients in separate cohorts from patients who have received available therapies). The draft guidance is available at: <https://www.federalregister.gov/documents/2021/06/25/2021-13585/cancer-clinical-trial-eligibility-criteria-approach-to-available-therapy-in-non-curative-settings>.

ABNM Celebrating 50 Years

George M. Segall, MD, Executive Director, American Board of Nuclear Medicine

The American Board of Nuclear Medicine (ABNM) is celebrating its first 50 years as a certification board for nuclear medicine physicians. The ABNM was the first conjoint board established under provisions of the “Essentials for Approval of Examining Boards in Medical Specialties” of the American Board of Medical Specialties (ABMS). It was sponsored by the American Board of Internal Medicine, the American Board of Pathology, the American Board of Radiology, and the Society of Nuclear Medicine. The ABNM was incorporated on July 28, 1971, and had its first meeting on October 23 of the same year. The ABNM became a primary certifying board in 1985 and is currently 1 of 24 member boards of the ABMS.

The ABNM has certified 5,917 physicians since the first certification examination was given in 1972. Certificates issued between 1972 and 1991 were valid for life. There are currently 1,681 active physicians (not retired or deceased) with lifetime certificates. The ABNM began issuing time-limited certificates in 1992. Diplomates initially certified between 1992 to 2017 were required to pass the Maintenance of Certification (MOC) examination every 10 years to maintain certification. There are currently 1,996 active physicians with time-limited certificates. The ABNM introduced CertLink® in 2018, a longitudinal assessment pilot program, as an alternative to the MOC examination. Currently 1,172 diplomates are participating in CertLink, most with certificates expiring prior to 2027. The number of participating diplomates is expected to significantly increase next year, because the ABMS approved CertLink in 2021 as a regular part of the ABNM’s MOC program, and the board will require all ABNM diplomates who do not wish to take the MOC examination for recertification to begin participating in CertLink by January 2022.

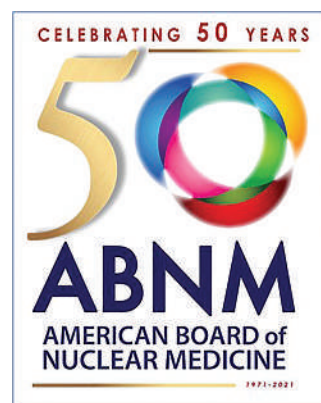
CertLink is only a part of the ABNM MOC program. Other parts are professionalism, lifelong learning and self-assessment, and practice improvement. The ABNM has taken several steps to make MOC easier and more valuable for physicians. Diplomates should log onto their profiles on the ABNM website at least once each year to update their information and see the latest news. All 24 ABMS member boards are reevaluating their MOC programs following the report issued by the ABMS *Commission on Continuing Certification: Vision for the Future* (<https://visioninitiative.org/>). The far-reaching report made several recommendations to make

certification a “meaningful, contemporary, and relevant professional development activity for diplomates that ensures they remain up-to-date in their specialty.” The ABMS and member boards have begun a process to implement the recommendations, starting with a revision of the standards that all member boards must follow. The

ABMS board of directors will vote on the final standards in October. The ABNM has already made changes to comply with the recommendations of the ABMS commission and the draft standards, which include adoption of CertLink. One of the potentially most significant impacts of the new standards, if approved, is the adoption of a uniform assessment cycle of 5 years for diplomates of all 24 member boards.

The practice of medicine and health care economics have dramatically changed over the past 50 years, and nuclear medicine has grown to include hybrid imaging, molecular imaging, and theranostics. The ABNM has made significant changes in certification standards to keep up with these and other changes, including support for training leading to dual certification in Nuclear Medicine and Diagnostic Radiology because of the importance of hybrid imaging and revision of the requirements for radionuclide therapy following the approval of several new radiopharmaceuticals for targeted radionuclide therapy. The ABNM has also made significant changes to keep up with society at large, including a process to select new board members that supports diversity, equity, and inclusion, and revision of the leave policy during training to support trainees who need to take medical/parental/caregiver leave. Other challenges remain to be addressed, such as attracting more young professionals into the specialty and maintaining high standards for certification that differentiate a nuclear medicine physician from other specialists doing the same work.

Nuclear medicine has a bright future, and the ABNM is prepared to meet the opportunities and challenges of the next 50 years.



Progress in Prostate Cancer Theranostics

Richard L. Wahl, MD, SNMMI President

The past few months have been very exciting for the field of nuclear medicine and molecular imaging, specifically the advances made in the diagnosis and treatment of prostate cancer. New agents are changing the course of treatment for prostate cancer patients and will ultimately help to improve outcomes.

According to the Surveillance, Epidemiology, and End Results (SEER) program, an estimated 248,500 new prostate cancer cases will be diagnosed in 2021, and more than 34,000 men will die from the disease. About 30% of prostate cancer patients will have a recurrence, including those who will develop castration-resistant prostate cancer. With the latest advances in imaging and theranostics, nuclear medicine and molecular imaging professionals hope to help many of these men.

In May, the U.S. Food and Drug Administration (FDA) approved a new imaging agent for detection of prostate cancer, providing a more effective imaging approach to detect metastases. ^{18}F -piflufolastat injection is the first fluorinated prostate-specific membrane antigen (PSMA) agent approved by the FDA and also the first widely commercially available PSMA PET imaging agent in the United States.

Recently published results from the phase III VISION trial are also promising for patients with metastatic castration-resistant prostate cancer. The study reported a 38% reduced risk of death and a 60% reduced risk of progression for those treated with the targeted radiopharmaceutical ^{177}Lu -PSMA-617 vs. standard of care controls.

Given the number of patients who would benefit from these diagnostic and therapeutic radiopharmaceuticals, prostate cancer is an area of high interest and growth for SNMMI. SNMMI's Value Initiative—the society's strategic vision and roadmap for advancing the field—includes many programs that support the progress being made in nuclear theranostics for prostate cancer.

To gather research on targeted radiopharmaceutical therapies (RPT), the SNMMI Board of Directors approved the development of the Radiopharmaceutical Therapy Registry. This registry will monitor anonymized data from patients who received radiopharmaceutical therapies. Work will soon begin to identify pilot sites and partners to collect these important data.

A Coding and Reimbursement Workgroup has been created to evaluate existing radiation oncology codes that could be used for nuclear medicine, identify common therapy pathways with applicable codes for RPT, and develop standardized billing criteria for medical physicists. The workgroup will also provide education for members on coding and reimbursement for RPT through webinars and educational articles.

SNMMI has also launched a Radiopharmaceutical Therapy Centers of Excellence (RPTCOE) program. Sites utilizing radiopharmaceutical therapies can apply to earn

designation as a clinical or comprehensive RPTCOE, which confirms that the site meets strict regulatory, training, qualification, experience, and performance criteria.

The RPTCOE is also working to standardize how and when dosimetry should be implemented when treating patients with RPT. A ^{177}Lu Dosimetry Challenge was launched in early 2021 to assess variability in methodology, equipment, personnel, time requirements, and results in calculating personalized dosimetry. The response to the challenge has been overwhelmingly positive and will result in a valuable dataset to identify areas for standardization. Early results from the challenge are expected to be published in a supplement to *The Journal of Nuclear Medicine (JNM)* in December.

SNMMI's RPTCOE and R&D Domain have developed a Cancer Cooperative Group Junior Faculty Mentorship Program to enhance the presence of nuclear medicine and molecular imaging professionals in the NCI National Clinical Trial Network cooperative groups. Six awards will be granted in 2021 to individuals in an effort to help influence, design, and lead these trials.

To ensure that these new radiopharmaceuticals are accessible to patients, SNMMI is collaborating with regulatory agencies. The society is working with the FDA to streamline approval processes and with the Centers for Medicare and Medicaid Services to approve and streamline reimbursement. Appropriate use criteria for PET PSMA are near completion.

SNMMI is also focused on promoting innovative and impactful research as it relates to prostate cancer. *JNM* articles are now available online immediately following acceptance, and articles are published online up to a month ahead of print release. A targeted public relations campaign has also been launched to share this research on a broader level.

With all of these great advances, the nuclear medicine and molecular imaging workforce pipeline must be strong. SNMMI's Workforce Pipeline Domain has formed a subgroup to focus on outreach to medical, undergraduate, and high school students in an effort to expose them to nuclear medicine. The SNMMI Diversity, Equity, and Inclusion Task Force, Women in Nuclear Medicine Committee, Early Career Professionals Committee, and Resident/In-Training Committee are collaborating on this effort as well.

The field of nuclear medicine and molecular imaging is being transformed, as shown by advances in the treatment of prostate cancer. SNMMI is committed to being there every step of the way to ensure success.



Richard L. Wahl, MD

Humana Reverses Nononcologic PET/CT Noncoverage Policy

Humana, Inc. (Louisville, KY) convened a medical review board in late May to address its previous decision to deny coverage for PET/CT for cardiac indications and PET/CT and SPECT/CT for neurologic indications. This followed a decision earlier in the year to reverse previous denial of coverage for PET/CT imaging in gastric and esophageal oncologic indications. The result of the May meeting was a broad cardiac PET/CT coverage policy that is current with scientific evidence and the Centers for Medicare and Medicaid Services National Coverage Decision on ¹⁸F-FDG PET for infection and inflammation. The policy, which in July was still in draft form, included the following coverage areas: (1) myocardial viability assessment as indicated by 1 or more of the following: chronic secondary mitral regurgitation, and individual is candidate for revascularization if viable myocardium identified; known or suspected ischemic cardiomyopathy with left ventricular ejection fraction 35% or less; SPECT myocardial perfusion scan or stress echocardiogram findings inconclusive or no viable myocardium evident; OR (2) suspected prosthetic valve endocarditis as indicated by ALL of the following: clinical suspicion of endocarditis; AND nondiagnostic echocardiogram results; AND prosthetic valve implanted more than 3 months prior; OR (3) sarcoidosis with suspected cardiac involvement. The draft policy also made changes to SPECT/CT and PET/CT for neurologic indications, including that Humana members may be eligible for SPECT with concurrently acquired CT for preoperative localization of parathyroid adenomas and for PET with concurrently acquired CT for presurgical evaluation to localize the focus of refractory seizure activity.

Since November 2020, SNMMI has worked closely with several other

medical societies in communicating with Humana about expanding its coverage.

Humana, Inc.

CMS and Nononcologic ¹⁸F-FDG PET

In December 2020, the Centers for Medicare and Medicaid Services (CMS) retired the National Coverage Determination (NCD) for ¹⁸F-FDG PET for infection and inflammation, effective January 1, 2021. In the absence of an NCD, coverage determinations for PET for infection and inflammation were then to be made at the discretion of local Medicare Administrative Contractors (MACs). The CMS decision to retire the NCD for ¹⁸F-FDG PET in infection and inflammation opened a path to reimbursement and improved care in a range of disease settings.

On June 8, 2021, CMS published an updated transmittal with lists of nationally covered and noncovered ICD-10-CM indications for the various NCDs. To the surprise of the nuclear medicine community, the ICD-10-CM codes for some osteomyelitis and fever of unknown origin codes were listed as noncovered under the infection and inflammation NCD that was retired. Because the transmittal was binding on MACs, those indications would not be covered by local MACs.

On July 13, however, CMS published its CY 2022 Medicare Physician Fee Schedule Proposed Rule, which included a proposal to remove the “exclusionary language” from the NCD transmittal. This will leave nononcologic PET indications (unless noted by NCD 220.6.1-220.6.20) to the discretion of local MACs. CMS stated, “We believe that extending local contractor discretion for nononcologic indications of PET provides an immediate avenue to potential coverage in appropriate candidates and provides a framework that better serves the needs of the Medicare program and

its beneficiaries.” New U.S. Food and Drug Administration–approved nononcologic radiopharmaceuticals will be covered under MAC discretion.

In online commentary on the latest proposed rule, SNMMI noted: “Unfortunately, in this proposal, the national noncoverage determination for beta amyloid PET (NCD 220.6.20) remains. SNMMI and our partners are working to resolve this coverage discrepancy. Also, to our dismay, the proposed rule proposes to cut the conversion factor to \$33.58 in CY 2022, as compared to \$34.89 in CY 2021; this follows the expiration of the 3.75% payment increase, a 0.00% conversion factor update, and a budget neutrality adjustment. SNMMI will work with the medical community to prevent cuts to physician reimbursement.”

SNMMI

Centers for Medicare and Medicaid Services

SNMMI “Ones to Watch” in 2021

SNMMI announced on July 16 its annual list of 30 early-career professionals selected as “Ones to Watch” in 2021. Launched in 2018, the society’s Ones to Watch campaign aims to recognize those with the potential to shape the future of precision medicine across all areas of the field. Members can nominate themselves or others whose actions, work, or studies have set them apart as future thought leaders in nuclear medicine and molecular imaging. Recipients are selected with the help of the SNMMI Committee on Councils and Centers. The honorees included Olayinka Abiodun-Ojo, MD, MPH (Emory University School of Medicine); Eduardo Aluicio-Sarduy, PhD (University of Wisconsin–Madison); Benjamin Auer, PhD (University of Massachusetts Medical School); Eric Berg, PhD (University of California, Davis); Jessica J. Comstock, PharmD, BCNP (PharmaLogic Holdings); Matthew F. Covington, MD (University of Utah/Huntsman

Cancer Institute); Carolina de Aguiar Ferreira, PhD (University of Wisconsin–Madison); Shreya Goel, PhD (University of Texas MD Anderson Cancer Center); Junior Gonzales (Memorial Sloan Kettering Cancer Center); Javier Hernández-Gil, PhD (Memorial Sloan Kettering Cancer Center); Hyung-Jun Im, MD, PhD (Seoul National University); Amir Iravani, MD (Washington University in St. Louis); Simone Susanne Krebs, MD, MS (Memorial Sloan Kettering Cancer Center); Courtney Lawhn-Heath, MD (University of California, San Francisco); Zhibo Liu, PhD (Beijing University); Dominique S. Newallo, MD, RT(R)(CT) (Emory University); Thomas Ng, MD, PhD (Harvard Medical School/Massachusetts General Hospital); Negar Omidvari, PhD (EXPLORER Molecular Imaging Center, University of California, Davis); Alejandro D. Arroyo Pacheco, PhD (Memorial Sloan Kettering Cancer Center); Austin Patel, MD, MSTR (University of Pennsylvania); Sonya Youngju Park, MD (St. Mary’s Hospital, Seoul); Giacomo Pirovano, PhD (Memorial Sloan Kettering Cancer Center); Chaitanya Rojulpote, MD (The Wright Center for Graduate Medical Education); Brian Horacio Santich, PhD (Y-mABs Therapeutics, Inc.); Lino M. Sawicki, MD, PhD (Heinrich Heine University Dusseldorf); Jennifer Anne Schroeder, MD (Wake Forest University/Baptist Medical Center); Mark A. Sellmyer, MD, PhD (Perelman School of Medicine at the University of Pennsylvania); Senthil Selvaraj, MD (University of Pennsylvania); Hong Song, MD, PhD (Stanford Health Care/Stanford University); and Ning Zhao, PhD (University of California, San Francisco).

SNMMI

National Coverage Determination Analysis on AD Treatment Opens

The Centers for Medicare and Medicaid Services (CMS) announced on July 12 the opening of a National Coverage Determination (NCD) Analysis to provide data to determine whether Medicare will establish a national

coverage policy for monoclonal antibodies targeting amyloid in the treatment of Alzheimer disease (AD). This NCD analysis will be applicable to national coverage considerations for aducanumab, which was recently approved by the U.S. Food and Drug Administration, as well as any future monoclonal antibodies that target amyloid for treatment of AD. As part of the NCD process, a 30-day public comment period was opened from July 12 to August 11. CMS hosted 2 public listening sessions to provide an opportunity for public input.

“Alzheimer’s is a devastating illness that has touched the lives of millions of American families, and as CMS opens our NCD analysis, we invite interested stakeholders to participate,” said CMS Administrator Chiquita Brooks-LaSure. “We want to consider Medicare coverage of new treatments very carefully in light of the evidence available. That’s why our process will include opportunities to hear from many stakeholders, including patient advocacy groups, medical experts, states, issuers, industry professionals, and family members and caregivers of those living with this disease.”

The nuclear medicine and molecular imaging community is a key stakeholder, with projected uses of PET in AD diagnosis and monitoring of treatment. One of the 5 focal areas to be addressed in the analysis is “What health care providers should be included as part of the patient’s treatment team? Should medical specialists be included in the care team of patients receiving treatment? If so, which specialists should be included in the care?”

To determine whether a national policy is appropriate, CMS will follow a standard process that includes multiple opportunities for the public to participate and present comments through both listening sessions and the CMS Coverage website. The analysis will determine whether the evidence meets the Medicare law’s requirements that items or services be “reasonable and necessary for the diagnosis or treatment of illness or injury . . .” To make this determination, CMS uses a formal

process that includes an assessment of clinical evidence, such as published clinical studies, professional society guidelines, and public comments. Following this analysis, CMS will post a *proposed* NCD, which will be open to a second 30-day public comment period. After review, CMS will announce its *final* decision for a national policy, which could range from Medicare coverage of this product type, coverage with evidence development, noncoverage, or deference to local Medicare Administrative Contractors. A proposed decision is expected to be posted within 6 months and a final within 9 months.

NCDs are posted with additional developing information on the CMS Medicare Coverage Center website: <https://www.cms.gov/Center/Special-Topic/Medicare-Coverage-Center#skipNavTarget>.

To submit or view public comments, see: <https://www.cms.gov/medicare-coverage-database/details/nca-tracking-sheet.aspx?NCAId=305>.

Centers for Medicare and Medicaid Services

Annual Report on U.S. Cancer Status

Overall cancer death rates continue to decline for all racial and ethnic groups in the United States, according to the latest *Annual Report to the Nation on the Status of Cancer*. From 2001 to 2018, these declines accelerated for lung cancer death rates and, more recently, melanoma death rates, the latter reflecting advances in treatment for metastatic melanoma. Declines in prostate, colorectal, and female breast cancers, however, have slowed and in some disease settings disappeared. Overall incidence of cancer increased slightly for females, children, and adolescents and young adults but remained stable for males in this period.

The report was published on July 8 ahead of print in *JNCI: The Journal of the National Cancer Institute* and featured in a press release from the American Cancer Society (ACS) on the same day. All trends in the report covered the period before the COVID-

19 pandemic. The annual publication is a collaborative effort from the ACS, the Centers for Disease Control and Prevention, the National Cancer Institute (NCI), and the North American Association of Central Cancer Registries (NAACCR).

Death rates decreased for 11 of the 19 most common cancers among men and 14 of the 20 most common cancers among women. Death rates increased for a few cancers, including brain, other nervous system, and pancreas in both sexes; oral cavity and pharynx in males; and liver and uterus in females.

The report also found that overall cancer death rates decreased in every racial and ethnic group during the period from 2014 to 2018, despite significant disparities remaining. “When evaluating health disparities, it is critical to acknowledge the social factors that influence the health of the communities and access to health care,” said Betsy A. Kohler, MPH, NAACCR Executive Director. “Social and economic indicators, particularly based on small area assessments, are increasingly important to understanding the burden of cancer.”

Preventable disease was also addressed in detail in the report. “The continued decline in cancer death rates should be gratifying to the cancer research community, as evidence that scientific advances over several decades are making a real difference in outcomes at the population level,” said Norman E. “Ned” Sharpless, MD, director of

NCI. “I believe we could achieve even further improvements if we address obesity, which has the potential to overtake tobacco use to become the leading modifiable factor associated with cancer.”

American Cancer Society

JNCI: The Journal of the National Cancer Institute

Sharp Declines in Breast and Cervical Cancer Screening

The total number of cancer screening tests received by women through the Centers for Disease Control and Prevention (CDC) National Breast and Cervical Cancer Early Detection Program declined by 87% for breast cancer and 84% for cervical cancer in April 2020 compared with the previous 5-year averages for that month. These findings were published online on June 30 ahead of print in *Preventive Medicine* and accompanied on the same day by a press release from CDC. The authors concluded that prolonged delays in screening related to the COVID-19 pandemic may lead to delayed diagnoses, poor health consequences, and an increase in cancer disparities among women already experiencing health inequities.

“This study highlights a decline in cancer screening among women of racial and ethnic minority groups with low incomes when their access to medical services decreased at the beginning of the pandemic,” said Amy DeGross, PhD, MPH, CDC health scientist and

lead author of the study. “They reinforce the need to safely maintain routine health care services during the pandemic, especially when the health care environment meets COVID-19 safety guidelines.”

Effects on health equity were highlighted with specific data, noting, for example, that declines in breast cancer screening varied from 84% percent among Hispanic women to 98% among American Indian/Alaskan Native women and that declines in cervical cancer screening varied from 82% among Black women to 92% among Asian Pacific Islander women. Screening volumes had begun to recover in all groups by June 2020, the end of the observation period.

“CDC encourages health care professionals to help minimize delays in testing by continuing routine cancer screening for women having symptoms or at high risk for breast or cervical cancer,” said DeGross. “The Early Detection Program can help women overcome barriers to health equity by educating them about the importance of routine screening, addressing their concerns about COVID-19 transmission, and helping them to safely access screening through interventions like patient navigation.” For more information about CDC’s work on breast and cervical cancer, see <https://www.youtube.com/watch?v=mDIYzBjgNHQ> and <https://www.cdc.gov/cancer/nbccedp/>.

The Annual Journal Impact Factor Saga

Johannes Czernin

David Geffen School of Medicine at UCLA, Los Angeles, California

The *Journal of Nuclear Medicine* Journal Impact Factor (JIF) has reached a new milestone at 10.057 and now ranks #3 among all imaging journals. This achievement should not be overhyped, but it does provide evidence for the high visibility of the published work. We are aware that the calculation of the JIF has changed. Clarivate Analytics announced that it was moving toward a future that calculated the JIF based on the date of electronic publication and not the date of print publication (1). Thus, citations of early content were included in the calculation of the JIF for 2020, and drops in JIF will invariably follow in 2021. However, the overall *JNM* ranking improved, and *JNM* is the #1 publication among all nuclear medicine and molecular imaging journals (Fig. 1).

This is a tribute to the great contributions of diverse scientists from all areas of the field. Three of the top 10 articles contributing to the JIF calculation describe advances in imaging instrumentation (2–4), with the remaining 7 introducing various important aspects of theranostics (standardization of image interpretation (5), new targets and probes (6–8), translational or clinical PSMA-targeting diagnostic studies (9,10), and therapeutic approaches (11)).

It is thus evident that theranostics and the search for novel and relevant targets remain at the forefront of nuclear medicine research. However, revolutionary advances in instrumentation will open new and exciting research opportunities. Similarly, artificial intelligence will find its way into the clinic through solidly designed clinical studies (12). The high JIF, with the associated high visibility of the journal, will continue to attract leading basic and clinical scientists from oncology, neurology, cardiology, endocrinology, infectious diseases, and other fields. Continuation of scientific growth and advances is a

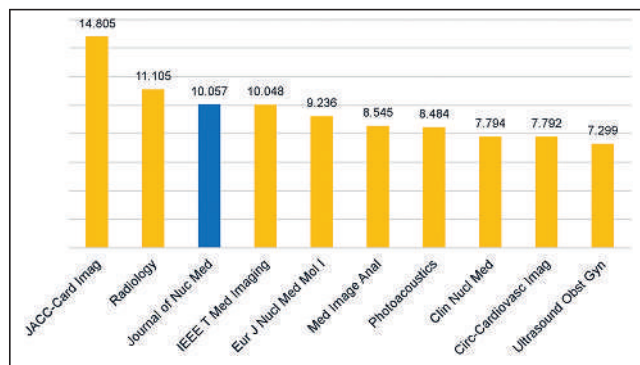


FIGURE 1. JIF: top 10 in medical imaging (June 30, 2021).

condition for the sustainable success of nuclear medicine, molecular imaging, and theranostics (13). With significant industry buy-in (14), we expect further clinical translation into powerful therapeutic approaches that we will publish in our flagship journal.

I am grateful for the support of SNMMI and its publications committee, the invaluable contributions of our staff, the critical input from our editorial board members, and the hard work and creativity of the team of national and international associate editors who made this success possible.



Johannes Czernin

REFERENCES

1. Quaderi N. The JCR reload and a look ahead to the introduction of early access content in 2021. Clarivate website. <https://clarivate.com/blog/the-jcr-reload-and-a-look-ahead-to-the-introduction-of-early-access-content-in-2021/>. Published October 26, 2020. Accessed July 2, 2021.
2. Cherry SR, Jones T, Karp JS, Qi J, Moses WW, Badawi RD. Total-body PET: maximizing sensitivity to create new opportunities for clinical research and patient care. *J Nucl Med*. 2018;59:3–12.
3. Badawi RD, Shi H, Hu P, et al. First human imaging studies with the EXPLORER total-body PET scanner. *J Nucl Med*. 2019;60:299–303.
4. van Sluis J, de Jong J, Schaar J, et al. Performance characteristics of the digital Biograph Vision PET/CT system. *J Nucl Med*. 2019;60:1031–1036.
5. Eiber M, Herrmann K, Calais J, et al. Prostate Cancer Molecular Imaging Standardized Evaluation (PROMISE): proposed mITNM classification for the interpretation of PSMA-ligand PET/CT. *J Nucl Med*. 2018;59:469–478.
6. Kratochwil C, Flechsig P, Lindner T, et al. ⁶⁸Ga-FAPI PET/CT: tracer uptake in 28 different kinds of cancer. *J Nucl Med*. 2019;60:801–805.
7. Lindner T, Loktev A, Altmann A, et al. Development of quinoline-based theranostic ligands for the targeting of fibroblast activation protein. *J Nucl Med*. 2018;59:1415–1422.
8. Loktev A, Lindner T, Mier W, et al. A tumor-imaging method targeting cancer-associated fibroblasts. *J Nucl Med*. 2018;59:1423–1429.
9. Roach PJ, Francis R, Emmett L, et al. The impact of ⁶⁸Ga-PSMA PET/CT on management intent in prostate cancer: results of an Australian prospective multicenter study. *J Nucl Med*. 2018;59:82–88.
10. Giesel FL, Knorr K, Spohn F, et al. Detection efficacy of ¹⁸F-PSMA-1007 PET/CT in 251 patients with biochemical recurrence of prostate cancer after radical prostatectomy. *J Nucl Med*. 2019;60:362–368.
11. Giesel FL, Kratochwil C, Lindner T, et al. ⁶⁸Ga-FAPI PET/CT: biodistribution and preliminary dosimetry estimate of 2 DOTA-containing FAP-targeting agents in patients with various cancers. *J Nucl Med*. 2019;60:386–392.
12. Buvat I, Orlhac F. The T.R.U.E. checklist for identifying impactful artificial intelligence-based findings in nuclear medicine: is it true? Is it reproducible? Is it useful? Is it explainable? *J Nucl Med*. 2021;62:752–754.
13. Weber WA, Czernin J, Anderson CJ, et al. The future of nuclear medicine, molecular imaging, and theranostics. *J Nucl Med*. 2020;61(suppl 2):263S–272S.
14. Calais J. FAP: The next billion dollar nuclear theranostics target? *J Nucl Med*. 2020; 61:163–165.

Leadership Focus on Advancing Cancer Research and Treatment

A Conversation Between Johannes Czernin, Caius Radu, and Antoni Ribas

Johannes Czernin¹, Caius Radu¹, and Antoni Ribas²

¹Department of Molecular and Medical Pharmacology, University of California Los Angeles, Los Angeles, California; and ²Department of Medicine, Department of Surgery, University of California Los Angeles, Los Angeles, California

Johannes Czernin, MD, editor-in-chief of *The Journal of Nuclear Medicine*, and Caius Radu, MD, PhD, a professor of Molecular and Medical Pharmacology at the University of California Los Angeles (UCLA), talked with Antoni Ribas, MD, PhD. Dr. Ribas is a professor of Medicine, Surgery, and Molecular and Medical Pharmacology and director of the Parker Institute for Cancer Immunotherapy Center at UCLA. He is also director of the UCLA Jonsson Comprehensive Cancer Center Tumor Immunology Program. He is the president of the American Association for Cancer Research.

He earned his medical and doctoral degrees from the University of Barcelona (Spain). He completed internship and residency at the Hospital Vall d'Hebron (Barcelona) and postdoctoral fellowships in surgical oncology and a clinical fellowship in hematology/oncology at the UCLA David Geffen School of Medicine. From 2001 to 2010, Dr. Ribas was the assistant director for Clinical Programs at the UCLA Human Gene Medicine Program and led the Jonsson Cancer Center's Cell and Gene Therapy Core Facility from 2004 to 2010. He also co-led the Stand Up to Cancer Cancer Research Institute–AACR Immunotherapy Dream Team with Nobel Laureate James Allison, PhD.

His research has focused on the use of immunotherapy to treat melanoma. He led the clinical program that demonstrated the effectiveness of the immunotherapeutic pembrolizumab (Keytruda), a significant advance in treatment of melanoma and other malignancies. Recent work includes laboratory and clinical translational research in adoptive cell transfer therapy with T-cell receptor engineered lymphocytes; examining the antitumor activity of PD1-blocking antibodies; testing novel targeted therapies blocking oncogenic events in melanoma; and studying primary and acquired resistance to melanoma therapies. Dr. Ribas and his laboratory team use molecular imaging technologies to investigate the mechanisms of novel immunotherapies.

Dr. Czernin: Thank you for taking the time to talk to us. What inspired you to become a translational cancer researcher?

Dr. Ribas: I finished my clinical training as a medical oncologist in Spain in the mid-1990s. At that time, all we could do was to give chemotherapy. This worked in some patients but not in many others, and it was toxic. I did not think it was a good idea to spend the next years giving these drugs to patients without deeper knowledge. I wrote letters to various labs in the United States that pursued gene therapy and immunotherapy for cancer. My colleagues in Barcelona told me I was crazy

and that this had no future. How could the immune system treat cancer? When I joined UCLA, I worked with Jim Economou, MD, PhD, who tried exactly that. I interacted with Michael Phelps, PhD, Owen Witte, MD, and Harvey Herschman, PhD, who taught me to understand the process and turn it into a therapeutic. To me, the term “translational medicine” makes a lot of sense, because if you want to treat cancer successfully you have to understand the cause and what is happening.



Antoni Ribas, MD, PhD

Dr. Radu: What was a defining moment in your career when you reached a crossroads and made a decision that brought you to where you are right now?

Dr. Ribas: After 2 years as a postdoc with Jim Economou the easy thing would have been to return to Spain. However, we were doing these interesting things, like making dendritic cells and giving them to mice where there was benefit. There was also anecdotal evidence of benefit in humans. The potential of doing something that was completely academic in a clinical trial was exciting. This helped me later to understand how things could be translated into the clinic. I decided to become a melanoma expert, understand the disease, and then apply approaches that were science based, including immunotherapy. There was a real clinical need, because radiation and chemotherapy had limited-to-no benefit in this cancer. Surgery was the only option for a cure but only for early-stage disease. It was a wide-open field where anything new that made sense could be used. That is when the BRAF mutation was discovered, and I had the benefit of seeing first-hand the work of Charles Sawyers, MD, in translating the concept of inhibiting driver mutations with drugs like Gleevec. I thought that when people made drugs targeting BRAF I wanted to be there to give them to patients. I have always focused on things that I thought had a good chance to work in patients. I have little patience for continuing with treatments that are not working. For example, when I concluded that dendritic cells were not working for the majority of patients, that was it. Even if I had grants, I would not do more experiments.

Dr. Radu: You already mentioned people with whom you interacted and by whom you were influenced. Are there other people who inspired you?

Dr. Ribas: I would go back to the names I mentioned already and would add John Glaspy, MD, my clinical mentor. These are inspirational people with whom I was lucky to be associated. Fifteen years

ago, David Baltimore, PhD, put T-cell receptor genes into hematopoietic stem cells, and he wanted to work with someone who could do this in humans. This project also gave us the opportunity to do what Sam Gambhir, MD, PhD, had pioneered with Dr. Herschman, putting reporter genes into cells and then tracking them in people with a PET scanner. We did that and acquired these incredible images that helped us develop new therapies and understand how they work.

Dr. Czernin: Tell us a little bit about the history of chimeric T-cell receptor studies.

Dr. Ribas: The early clinical trials with engineered T cells demonstrated that if we gave enough T cells that have a receptor that recognizes a cancer antigen, we could get regressions of melanoma and synovial sarcomas. These cancers are now considered treatable. At that time, they were not treatable. In parallel, Arie Belldegrun, MD, set up a company to develop immunotherapies. I thought that redirecting T cells to a surface marker would empower T cells, for example, to treat incurable lymphoma that progressed after prior therapies. We were creating these modified T cells in our GMP facility, which helped with translation. Then we talked about commercialization, and this was the start of Kite Pharma, which became a great success story.

Dr. Czernin: What is your vision of the most appropriate and efficient industry-academia relationships? Do you have a model in mind or is it just simplifying the processes? What is the future there?

“The biggest difference in the last few years has been that we no longer look at 1 gene at a time when we do an experiment; many times we look at all the genes. Every time we do something, we tend to allocate less time for the actual experiment and a lot longer for analyzing and interpreting the data.”

Dr. Ribas: Our job is to develop things that work. Financial investments are needed to change medical practice and improve patients' lives. There is no way this can be done with academic grants alone. If the idea is good, people are willing to invest in it. This then becomes what we call a company. However, it is also an extension of our work. I think the academic field must embrace entrepreneurship. It is something we should not be ashamed of. Let us make things clear: we are trying to develop things that work, and someone must invest enough money to help develop that clinically. There is nothing wrong with that. We need to be open. We disclose and are honest about the goals. I think this is a process that should be celebrated, cherished, and supported as opposed to being hidden or talked down.

Dr. Czernin: Do you think that the current academic environment nationally and internationally is supportive of that concept?

Dr. Ribas: There must be checks and balances. But I do not think these interactions and collaborations should be discouraged. When there is a success, everyone jumps on it, yet you have people who frown on these relationships or talk behind others' backs. Success should mean that we develop effective therapies that help people. The NIH has always had a policy that its funds should create new knowledge. You disclose the funds that make it happen, and this becomes a patent. Then the investigator can develop the intellectual property with no strings attached. This concept has been perhaps the biggest source of new ideas and drugs that help people—more than any other funding. It has amplified and leveraged the money invested by the NIH in a logarithmic scale with benefit to many people.

Dr. Radu: Back to molecular imaging. You were one of the early adopters. What do you think about the status and future of molecular imaging? Where do you see it going?

Dr. Ribas: I think molecular imaging has much to give that we have not yet realized. We do not need to image every treatment, every time. We just need to understand what the treatments do. Where does the drug go? Visualizing CD8+ T cells together with Anna Wu, PhD, using immuno-PET imaging has been among the most exciting things I have done in my career. It is a key to understanding all immunotherapy for cancer. It took her several years, and now we see the images in humans and can track T cells as they invade the tumor.

Dr. Radu: As I think back to many meetings and discussions, you have always emphasized that one must understand not only what the immune system does but also what happens in tumor cells. Sometimes we focus too much on one part or the other and lose sight of how immunotherapies impact the dynamic interplay between cancer cells and immune cells. What made you think along these lines in the first place?

Dr. Ribas: So much knowledge about how cancers grow and how they interact with their microenvironment has been generated, and we learned how one could use molecular biology to understand how cancers change and adapt to therapies. In addition, when we started seeing acquired resistance to immunotherapy, we knew we had to study cancer cells themselves. We knew we had to study what genes and which signal transduction networks had changed to allow the cancer to become resistant to immunotherapy.

Dr. Czernin: This leads to the question of combination therapies. What is your view of accelerating the application of rational combination therapies in cancer?

Dr. Ribas: It is rather naïve to think that in complex processes like cancer a single drug could treat a significant number of cancers successfully. We have to start somewhere, and then we need to understand how the cancers respond or escape from the treatment. We need to develop combination treatments. Cancer tries to escape in many ways. Our best options are upfront combination therapies. The cancers that are not being treated successfully with current therapies need to be tested for the effects of 3 or 4 drug combinations if this can be done safely at therapeutic levels. Our goal is to cure cancer.

Dr. Radu: I take it you don't buy into the view that one can convert the remaining most challenging types of solid tumors into some type of chronic disease that can be managed?

Dr. Ribas: When we did not have good treatments for melanoma, people were saying, “Oh, well, let us try to get people to live 2 or 3 months longer.” That changed when we started seeing that we can get these metastatic cancers to respond for years. I would not want to lower the bar to say that we will turn cancer into a chronic disease. My aim will continue to be to make metastatic cancer disappear, because we understand the vulnerabilities of the cancer and we really hit it hard. These standards have led to some people with diseases that were once a death sentence going on to live normal lives. This remains the unchanged goal.

Dr. Czernin: There is a lot of excitement about the new vaccination approaches, particularly in light of the COVID pandemic. Is there any potential translation into cancer therapies?

Dr. Ribas: Let us start with the opposite, which is the reason we had these mRNA vaccines available for COVID-19 so rapidly. They

were developed as mRNA vaccines for mutational antigens that differentiate cancer cells from normal cells to make a vaccine that would tell the immune system to target them. To do this, the developers needed a sufficiently versatile platform to move from the sequencing of the tumor to vaccinating a person in as little as 2 months. Within 2 months of having the sequence of the COVID-19 virus, 2 companies were already doing vaccine trials in humans. That's because the platform existed. The process of sequencing and making that RNA vaccine was not that different for a virus for cancer. For cancer, the problem is that it keeps growing and establishes metastases that have a whole different set of issues. We will have to see whether those vaccines are powerful enough to treat them.

Dr. Radu: In your lab, what has changed over the last decade in how people are approaching research? What would be your advice to researchers in training? What should they focus on and why?

Dr. Ribas: The biggest difference in the last few years has been that we no longer look at 1 gene at a time when we do an experiment; many times we look at all the genes. Every time we do something, we tend to allocate less time for the actual experiment and a lot longer for analyzing and interpreting the data. The number of people in my lab who are experts in bioinformatics keeps increasing, and the ones who are not admit that these skills are needed. With CRISPR screens, we are now doing experiments genome wide, which was unthinkable not that long ago. And we are learning a lot because now we can study multiple targets in a single experiment.

Dr. Radu: Are there any downsides in generating massive datasets with so many potential correlations or emerging hypotheses? What advice would you give a young scientist about dealing with and managing big data?

Dr. Ribas: The NIH grants review dogma of focusing on a system that you control completely and then interrogate only 1 thing is no longer the goal. On the other hand, fishing expeditions leading to uninterpretable data are also a bad idea. There is an approach between these, however, where you develop and incorporate new techniques that give high-throughput data but you know what you are looking for. You know why you did the experiment and then are interpreting the results based on your understanding of that biologic system.

Dr. Czernin: What are your goals as president of the AACR, and what is its current mission?

Dr. Ribas: The AACR is the oldest and largest cancer research association in the world, and it is an honor to serve as its president. The goal is to improve the life of all people with cancer. I assumed this leadership position when we were in the pandemic lockdown, when I was chair of the organizing committee of an annual meeting with close to 30,000 people registered. We converted the meeting to a virtual format at a time when there was no existing platform for large virtual meetings. We owed it to scientists who had sent their best work for oral and poster presentations. So, in an incredibly short time, the professionals at the AACR got it done and we held 2 virtual meetings. We had close to 100,000 people who attended remotely. It became the most attended medical conference ever.

Then we had the tragic deaths of George Floyd, Breonna Taylor, Ahmaud Arbery, and others. It shocked us to see that there can be so much ongoing racism in society—that our colleagues who are Black Americans struggled because they know that racism is part of their lives and that many people see them as Black before they see them as cancer researchers, clinicians, entrepreneurs, nurses, or health care workers. We had to speak up. It does not matter that some people do not agree that a cancer organization should speak up against racism. It's the right thing to do. All disparities, including health care disparities, need to be addressed. We are developing therapies that work but are very expensive. Our job is to make them available to everyone.

Dr. Radu: Can you comment on what the focus of young people who embark on a career in translational science should be?

Dr. Ribas: My father was a professor and chair of Medicine in Barcelona. He had trained in Germany and Switzerland and in the United States when he was young. He always went back to Spain because he wanted to build his department there. When I was growing up and became a physician, he taught me that it was most important to understand why things happen. When I was a full-time clinician, it was hard to focus on why things were happening. There was perhaps time to open *Harrison's Principles of Internal Medicine* to identify the best drug to use for a specific problem, but not always to completely understand the processes at work. However, we can only change and improve things when we understand why things happen. Only then can we intervene and change the outcomes.

Dr. Czernin: This is the perfect closing statement! Thank you for taking the time to talk with our readers and us.

Dr. Ribas: Thank you for the great questions and to both of you for doing this. It's an honor.

Image-Guided High-Intensity Focused Ultrasound, A Novel Application for Interventional Nuclear Medicine?

Xinrui Zhang¹, Lisa Landgraf¹, Nikolaos Bailis², Michael Unger¹, Thies H. Jochimsen³, and Andreas Melzer^{1,4}

¹Innovation Center Computer Assisted Surgery (ICCAS), University of Leipzig, Leipzig, Germany; ²Department of Diagnostic and Interventional Radiology, University of Leipzig, Leipzig, Germany; ³Department of Nuclear Medicine, Leipzig University Hospital, Leipzig, Germany; and ⁴Institute of Medical Science and Technology (IMSaT), University of Dundee, Dundee, Scotland

Image-guided high-intensity focused ultrasound (HIFU) has been increasingly used in medicine over the past few decades, and several systems for such have become commercially available. HIFU has passed regulatory approval around the world for the ablation of various solid tumors, the treatment of neurologic diseases, and the palliative management of bone metastases. The mechanical and thermal effects of focused ultrasound provide a possibility for histotripsy, supportive radiation therapy, and targeted drug delivery. The integration of imaging modalities into HIFU systems allows for precise temperature monitoring and accurate treatment planning, increasing the safety and efficiency of treatment. Preclinical and clinical results have demonstrated the potential of image-guided HIFU to reduce adverse effects and increase the quality of life postoperatively. Interventional nuclear image-guided HIFU is an attractive noninvasive option for the future.

Key Words: image-guided HIFU; targeted drug delivery; tumor ablation; hyperthermia; PET/MR image guidance

J Nucl Med 2021; 62:1181–1188
DOI: 10.2967/jnumed.120.256230

High-intensity focused ultrasound (HIFU) has gained clinical acceptance for therapeutic applications, especially as a thermal ablative treatment modality for benign uterine fibroids, bone metastases, and prostate carcinoma, as well as for essential and Parkinson tremors (1). HIFU ablation at temperatures above 55°C is considered noninvasive surgery without physical access to the target region, and clinical HIFU systems have received regulatory approval in Europe, America, and Asia (2). Additionally, HIFU-induced hyperthermia in a temperature range of 40°C–45°C for up to 60 min was reported as a sensitizer for ionizing radiation and a mediator of thermal-sensitive drug delivery in the treatment of solid tumors (3).

Compared with other clinically used techniques for thermal therapy (ablation) such as laser, radiofrequency, and microwaves, which generate heat through probes by electromagnetic waves, causing the rotation of water molecules and thus inducing heating, ultrasound is a mechanical-wave-based technique. Although it is possible to generate focused heat through microwaves or radiofrequencies, electromagnetic waves cannot be focused as precisely as ultrasound waves, and the penetration depth of electromagnetic waves is limited. HIFU

provides adequate tissue penetration, ranging from 1 to 20 cm, with specific focal spot. Therefore, it overcomes the limitation of electromagnetic wave-based techniques. Moreover, HIFU is a promising alternative and the only noninvasive technique for clinical ablation and hyperthermia (4).

In recent years, image-guided therapeutic interventions have become an increasingly important area in the oncology field, integrating radiologic imaging methods such as MRI, ultrasound imaging, CT, radiography, and PET with surgery and therapies (2). Evaluation of treatment with an adequate imaging protocol is essential as a clinical prognostic readout. The broad clinical applications of HIFU were reviewed by Izadifar et al. (5). In addition to that review, we provide clinical details of some of the most prevalent and important clinical HIFU applications, describing the relative systems for these clinical cases. An overview of the latest preclinical and clinical studies is given in this review.

PRINCIPLES OF HIFU

Regarding the application of HIFU, ultrasound waves are typically generated by piezoelectric material, and focusing is enabled either by a single focused transducer that bundles sound waves with the bowl-shape transducer (Fig. 1A) or by phased-array transducers via beam forming (Fig. 1B).

Numerous parameters should be taken into consideration from the physical aspect. For example, the selected frequency, in the range of 0.25–3 MHz for medical applications, is related to penetration depth, indications, and the required acoustic intensity. For intraabdominal applications, a frequency of 1 MHz is typically used to produce sufficiently high intensities for deep-seated tissues. Another important parameter is the acoustic impedance, which comprises sound speed in the medium and the density of the medium, affecting the transport of sound waves. When ultrasound waves propagate through tissues, sound waves are reflected at the interface if the acoustic impedances of 2 tissues are different. The reflection of sound waves can increase the signal display and help to distinguish the tissue interface (e.g., muscle and bone interface) with diagnostic ultrasound; however, reflection of sound waves is unexpected and may cause injuries in HIFU applications. Thus, air bubble-free coupling of the patient to the HIFU system is required to avoid reflection-induced skin damage. In this context, image guidance is of high importance to prevent scattering or the reflection of sound waves and avoid potential safety issues, especially for applications close to specific regions such as the lungs, intestines, and bones (6).

HIFU generates acoustic waves at a high energy level; absorption of acoustic energy creates a thermal effect in the tissues via mechanical friction. Cavitation, acoustic radiation force, acoustic streaming,

Received Nov. 13, 2020; revision accepted May 5, 2021.
For correspondence or reprints, contact Andreas Melzer (andreas.melzer@uni-leipzig.de).
Published online June 4, 2021.
COPYRIGHT © 2021 by the Society of Nuclear Medicine and Molecular Imaging.

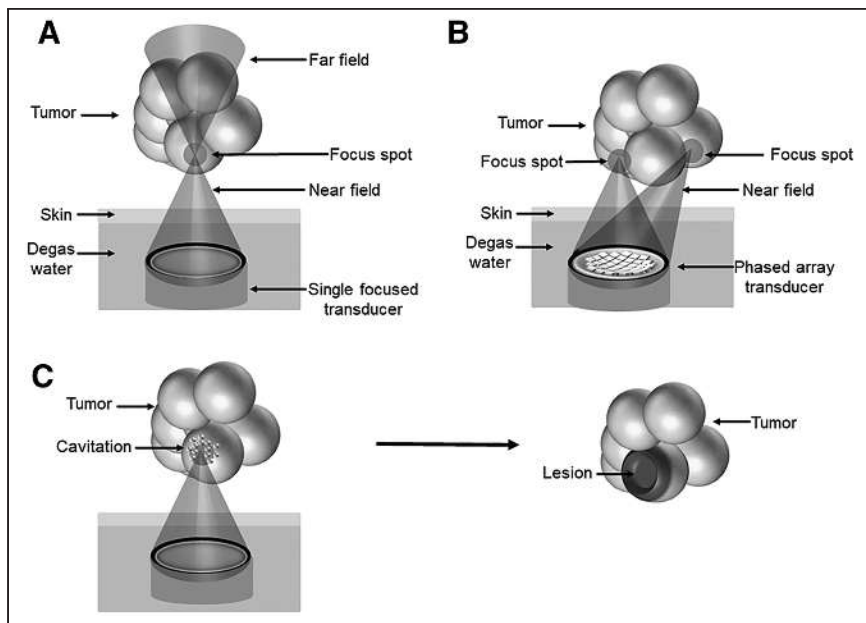


FIGURE 1. Schematic representation of HIFU ablation. (A) High level of sound energy in focal spot leads to heating of tissue to temperatures above 55°C, resulting in coagulation with subsequent necrosis in tissue. Sensitive structures in near and far fields can be spared. (B) Ablation of large-volume tumors is realized by scanning focal zone through entire tumor using phased-array transducer via beam forming. (C) Histotripsy destroys tissue by induction of cavitation events, generating lesions in target region.

and shock waves are considered nonthermal mechanisms of HIFU-induced biologic effects. Cavitation describes the oscillation and collapse of gas-filled cavities in the acoustic field. The process is divided into stable (noninertial) and inertial cavitation (7). Enhanced membrane permeability via the induction of stable cavitation is named sonoporation, and this is applied to open the blood–brain barrier and support drug delivery into the central nervous system. In contrast, inertial cavitation is typically used for tissue destruction (histotripsy) or in combination with chemotherapy, which is the so-called sonodynamic therapy (8). Histotripsy describes the disintegration or liquefaction of tissue by short ultrasound shots, showing that HIFU is capable of generating pure mechanical damage to tissues (Fig. 1C).

IMAGING GUIDANCE MODALITIES AND THERMOMETRY

To ensure the noninvasiveness of HIFU application, imaging guidance plays essential roles in treatment planning, temperature monitoring, and follow-up after therapy. Currently, only single-modality imaging guidance, either ultrasound imaging or MRI, is used in the clinic. Dual-modality imaging, such as PET/CT and PET/MRI, has drawn attention in recent years. Integration of the

NOTEWORTHY

- HIFU ablation has been used in the clinic for the noninvasive treatment of various diseases under ultrasound or MRI guidance.
- The combination of HIFU with other therapies showed promising advances in recent preclinical and clinical studies.
- Integration of the multifunctional imaging guidance modality into HIFU is required for precise treatment and accurate evaluation of treatment outcome.

HIFU system into PET/MRI provides additional information on metabolism in the targeted tissue and allows precise HIFU-triggered drug delivery, especially for the treatment of neurodegenerative diseases.

Ultrasound imaging enables real-time anatomic imaging during HIFU treatment, offering an advantage in the treatment of moving organs. For example, tumor in the liver moves together with respiration during treatment and may lead to noise in MR images, but ultrasound imaging can overcome such limitations (9). The main drawback of ultrasound imaging–guided HIFU (USgHIFU) is the lack of real-time temperature mapping; the temperature and the thermal dose inside the target region cannot be determined. Since temperature feedback to control ultrasound power is not available, USgHIFU is usually conducted using a short sonication duration (e.g., 3–4 s) to avoid overheating and may result in incomplete ablation (10). Moreover, the high absorption and reflection of ultrasound by the skull bone are the main limitations of transcranial ultrasound and restrict the treatment of neurologic diseases using USgHIFU.

In contrast, MRI-guided HIFU (MRgHIFU) provides spatial guidance in the targeted area for precise treatment planning. Nearly real-time temperature monitoring during treatment is feasible via MR thermometry using temperature-dependent proton resonance frequency shifting, T1 temperature mapping, or diffusion temperature mapping (11). However, MRgHIFU is more costly than USgHIFU, and the patient is required to be enclosed in a confined MRI scanner during treatment.

CLINICAL APPLICATIONS OF IMAGE-GUIDED HIFU

Image-guided HIFU systems have been developed and are used clinically for the treatment of various diseases. On the basis of physical parameters and available clinical systems with a focused spot of 1 mm–4 cm (5), HIFU treatment is typically conducted through several subsequential sonications (refers to the application of ultrasound energy) across the whole treated region. Here, we discuss some of the most commonly used clinical applications and relevant HIFU systems. Commercially available clinical HIFU systems are listed in Table 1.

Ablation of Uterine Fibroids

Uterine fibroids are the most common benign tumors in the uterus, showing great variability in shape, size, and localization. They occur in up to 80% of women during the reproductive period and are the leading indication for hysterectomy. Clinically relevant symptoms, including pelvic pain, dysmenorrhea, and dyspareunia, can be released with pharmacologic agents; however, adverse effects and a lack of adequate control are the main problems. Hospitalization and several weeks of recovery time are required after surgical resection (12).

The MRgHIFU system ExAblate 2000 (Insightec) was first approved by the U.S. Food and Drug Administration to treat uterine fibroids in 2004, and the Sonalleve system from Profound Medical was approved in Europe in 2011 (Fig. 2A). The Sonalleve system

TABLE 1
Clinically Used HIFU Systems

Device	Company	Location	Application field
MRgHIFU			
Low-intensity FUS pulsation	BrainSonix	Sherman Oaks, California	Neuromodulation
Sonallevé	Profound Medical	Mississauga, Canada	Myomas, bone metastasis
Tulsa-Pro			Prostate carcinoma
SonoCloud	CarThera	Paris, France	Brain
Targeted FUS	Image Guided Therapy	Pessac, France	Breast, uterus
ExAblate 2000	Insightec	Tirat Carmel, Israel	Uterus
ExAblate 4000			Essential tremor
ExAblate 2100 CBS			Bones
ExAblate Prostate			Prostate
ArcBlate	EpiSonica	Hsichu City, Taiwan	Uterus, pancreas
USgHIFU			
Edison	HistoSonics	Ann Arbor, Michigan	Prostate
HIFU Synthesizer	International Cardio Corp.	Minnetonka, Minnesota	Arteriosclerosis
Mirabilis	Mirabilis Medical	Bothell, Washington	Uterus fibroids
Sonablate	SonaCare Medical	Charlotte, North Carolina	Prostate
Valvopulse	Cardiawave	Paris, France	Aortic valve stenosis
EchoPulse	Theraclion	Malakoff, France	Fibroadema breast, thyroid
Alpius 900	Alpinion Medical Systems	Seoul, Korea	Uterus
FEP-BY02	Beijing Yuande Bio-Medical Engineering	Beijing, China	Pancreas
JC200	Chongqing Haifu Medical Technology Co.	Chongqing, China	Uterus, liver, bones, breast
HIFUNIT 9000	Shanghai A&S Science Technology Development Co.	Shanghai, China	Pancreas
PRO2008	Shenzhen PRO HITU Medical Co.	Shenzhen, China	Uterus
Ablatherm	EDAP-TMS	Lyon, France	Prostate
Focal One			

is introduced here as an example. The phased-array transducer consists of 256 elements that can be controlled independently, allowing beam forming. Formation of the ultrasound beam is established through electronic activation of each element separately at different phases, thereby creating a target zone with variable sizes and orientations. Treatment planning is based on the T2-weighted MR image, and the treatment volume within the target fibroids is determined in 3 orthogonal planes. Each sonication increases the temperature to 60°C–85°C in a matter of seconds and causes coagulative necrosis. The treatment outcome is evaluated with the nonperfused volume via contrast-medium-supported T1-weighted images (Fig. 2B). Nonperfused volume describes the tissue volume without blood flow and correlates with a fibroid volume reduction. In most cases, only a few hours of clinical monitoring are necessary, and the patients can continue with their daily activities after HIFU treatment.

Compared with traditional surgery, HIFU treatment is less invasive, avoids general anesthesia, and has the advantages of low morbidity, fewer complications, and a shorter recovery time. The symptoms subside either entirely or almost entirely 3–12 mo after successful therapy (nonperfused volume > 60%). Various studies have shown a reduction in fibroid-associated complaints and an improved quality of life. The most significant advantages of

image-guided HIFU over myomectomy are the higher pregnancy rate and the significantly reduced interval between pregnancy and treatment. The incidence of uterine rupture is rare in pregnant patients who have received HIFU ablation previously but should be considered to avoid serious adverse effects (13). The disadvantages are limited to the relatively long treatment duration of 2–4 h and the latency period until freedom from symptoms. Notably, the thick abdominal subcutaneous fat and the abdominal scar from previous surgery are associated with thermal injury and influence the risk of unsuccessful HIFU ablation of uterine fibroids (14). This complication can be avoided by careful preparation of the patients.

Ablation Treatment of Essential Tremors

Essential tremor is a neurologic disorder that causes rhythmic shaking, most often in the hands, and has a great impact on the quality of life. Some patients may not be able to work because of uncontrolled movements (15). Medications can be used at the early stage but are insufficient when the tremor progresses. Surgery is highly effective; however, open neurosurgical operation is associated with risks such as serious neurologic deficits and infections.

The ExAblate Neuro system from Insightec (Fig. 3A), compatible with both GE Healthcare and Siemens MRI scanners, has been

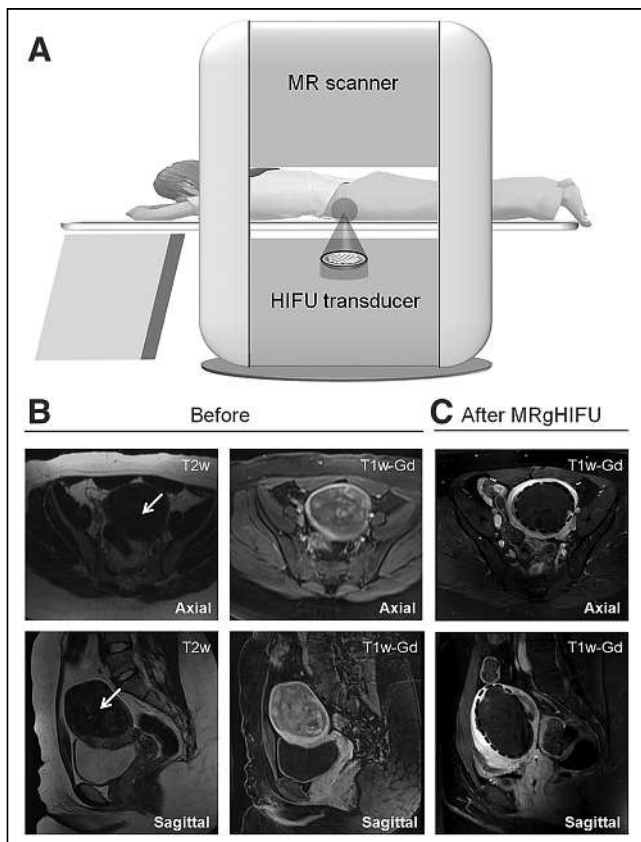


FIGURE 2. MRgHIFU for uterine fibroid treatment. (A) Schematic drawing of MRgHIFU treatment of uterine fibroids with Sonalleve or ExAblate 2000. Diagnostic T2- and T1-weighted contrast-enhanced (gadolinium) images are shown of patients with hyper- and dysmenorrhea and Funaki type 1 fibroid before (B, white arrow) and after (C, black circle) MRgHIFU. Fibroid volume is 184 mL; treatment duration is up to 4 h. w = weighted.

approved for the treatment of essential and Parkinson tremors and pain treatment. The helmet-shaped phased-array transducer contains 1,024 individual elements, enabling the focus of ultrasound beams in deep brain targets without a surgical incision. A sealed degassed water system is used for coupling and cooling during treatment. Clinical systems for the blood-brain barrier opening operate at 250 kHz, and systems for ablation while penetrating the skull operate at 720 kHz. The frequencies used for neurologic applications are lower than those used for body applications.

A pivotal clinical trial, conducted at 8 international centers for the treatment of essential tremors using the ExAblate transcranial MRgHIFU system (NCT01827904), is in the final phase of a 5-y follow-up. Improvement in the hand-tremor score was observed 3 mo after treatment (16), and continued beneficial effects in tremor control and the quality of life, with no progressive complications, were reported during follow-up for up to 4 y (17).

Ablation of Thyroid Nodules and Breast Fibroadenomas

Thyroid nodules are common and are mostly benign, although some become large and symptomatic (18). Surgical resection is the standard treatment but may cause bleeding, hematoma, and infection, and general anesthesia is required. HIFU allows nonsurgical ablation and offers an alternative treatment for benign thyroid nodules (19).

To date, the EchoPulse (Theraclion; Fig. 3B) is the only commercially available device for the treatment of thyroid nodules. It consists of an ultrasound imaging system and a HIFU delivery

system. The linear-array imaging probe uses frequencies of 7.5–12 MHz as guidance, and the treatment is performed with the HIFU probe at 3 MHz with an acoustic power of up to 125 W.

The first-in-humans trial of HIFU ablation of thyroid nodules was performed in France (20). The pathologic analysis showed significant nodule destruction, and histologic examination demonstrated that ablated lesions were confined to the target region, without damage to surrounding tissues. The safety and efficiency of the treatment were confirmed by Prakash et al. (21). The diameters of the thyroid nodules were reduced at 6 mo after treatment without complications (e.g., skin burns and hematoma), demonstrating the great potential of HIFU in the treatment of thyroid nodules.

In addition, breast fibroadenoma is another indication that can be treated using the EchoPulse system. A clinical trial was conducted in which patients were treated at an intensity of 40 W for 38 min under local anesthesia; a success rate of 89% was reported (22).

Ablation of Prostate Cancer

Prostate cancer is the second-most-common cancer in men worldwide (23). Conventional clinical therapies such as hormone therapy (chemical castration), radiation therapy (RT), and prostatectomy have side effects, including loss of sexual function, injury of the neurovascular bundle, and induction of urinary incontinence. Hence, local treatment options are gaining increasing interest. Laser ablation, cryoablation, and irreversible electroporation are used for prostate ablation (24), all of these applications require the insertion of probes, with associated side effects.

As the first approved MRgHIFU system for prostate cancer ablation, the TUSLA-Pro system (Fig. 3C) developed by Profound Medical combines real-time MRI and robotically driven transurethral ultrasound with temperature control. The individually controlled elements in the transurethral applicator generates directional thermal ultrasound, and an endorectal water-cooling device protects the rectum during treatment. The treated prostate tumor volume is limited to 40 cm³ for most transrectal HIFU systems; a total ablation of larger volumes is difficult because of the limited penetration depth. In contrast, the transurethral applicator has advantages for ablation of prostate lesions up to 200 cm³ by continuous rotation. The TUSLA-Pro system can be integrated into MRI scanners from various vendors; clinical feasibility and safety have been proven (25). The first integration with the PET/MRI scanner at OncoRay, University of Dresden, Germany, was realized within our SonoRay BMBF Project (<https://www.oncoray.de/research/sono-ray>), and a pilot clinical study is being conducted.

A multicenter phase I clinical trial of MRgHIFU whole-gland prostate ablation (NCT01686958) was conducted using the TUSLA-Pro system, and the radiologic findings were reported by Bonekamp et al. (26). Chin et al. (27) reported the oncologic outcomes and quality of life and stated that the erectile function of the patients was recovered after 12 mo. Klotz et al. (28) reported similar outcomes from a prospective trial (NCT02766543) with 115 patients in 2021, whereby the prostate-specific antigen decreased in 96% of the patients, and erections were maintained in 75% of the patients after 12 mo. The clinical data suggest that TUSLA-Pro is an effective tool for prostate cancer ablation, with minimal impact on the quality of life.

The novel HIFU hemiablation procedure targets only the cancerous tissue of the prostate, enabling the healthy tissue to be spared, which shows the potential to increase the effectiveness and safety of treatment compared with resection of the entire gland. Ganzer et al. (29) reported a multicenter phase II trial using the HIFU

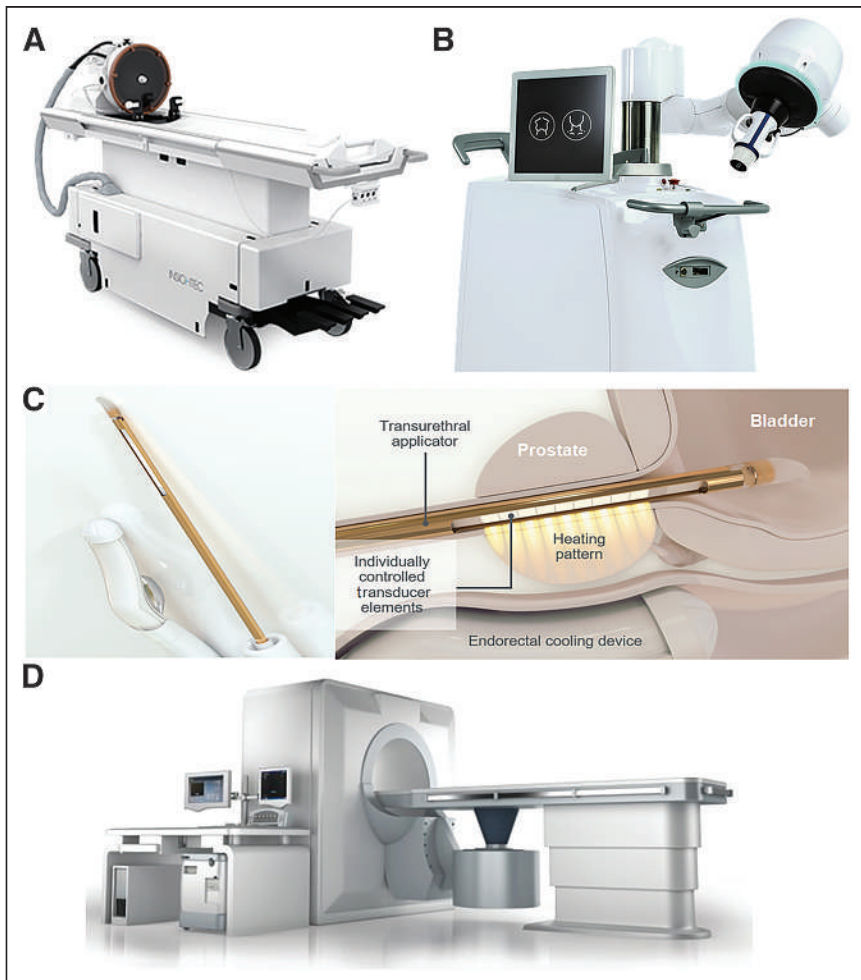


FIGURE 3. Clinically approved HIFU systems. (A) MRgHIFU system for neurologic application (ExA-plate Neuro). Patient table includes FUS transducer mounted on mechanical positioning unit with MRI-compatible head frame that can be docked to MRI scanner. (B) EchoPulse USgHIFU system for treatment of thyroid nodules and breast fibroadenomas. (C) Transurethral TUSLA-Pro MRgHIFU ablation system for prostate cancer. (D) JC USgHIFU system for solid tumor ablation of all types of soft tissue. (Images courtesy of Insightec, Theraclion, Profound Medical, and Chongqing Haifu.)

hemiblation approach. The 1-y follow-up indicated a significant reduction in prostate-specific antigen from 6.2 to 2.9 ng/mL. Patients had a preserved quality of life after treatment. The lack of long-term follow-up on oncologic control and functional outcomes is the main obstacle to encouraging patients to choose this approach.

Relief of Pain from Bone Metastases

Bone is a common site of solid tumor metastases. Symptoms, including localized pain, pathologic fractures, and functional deficits, may occur early in the metastatic course. The treatment of painful metastases requires an interdisciplinary approach. There are many procedures available for treatment. The most common is RT at a single fraction of 8 Gy or at 10 fractions of 3 Gy each; however, a high toxicity rate was reported (30).

In a phase III study (31), pain relief was observed in two thirds of the respondents within 3 d after MRgHIFU treatment. Similarly, 89% of the patients experienced pain reduction, 72% of whom were completely pain-free, as reported by Napoli et al. (32). These results highlight the capability of HIFU in pain management of bone metastases, with rapid, successful, and durable effects. A new multicenter, 3-armed, randomized controlled trial including more than 200 patients

started in 2020 to investigate the pain palliation effect of MRgHIFU as an alternative or addition to RT (NCT04307914).

For successful HIFU treatment, patient selection is critical. Lesions of the spinal column should be carefully assessed because of the adjacent critical nerve structures. Notably, blood perfusion in highly vascularized lesions will lead to a heat-sink effect, and embolization should be considered in these cases.

Ablation of Pancreatic Cancer

Pancreatic cancer is aggressive, with a poor 5-y survival rate of 8%. Symptoms include jaundice, malaise, weight loss, and loss of appetite, reducing patients' quality of life severely. Cancer-related abdominal or back pain is experienced in most patients, and established chemotherapy or radiochemotherapy has a limited antitumor effect and pain control duration (33).

The most frequently used clinical USgHIFU system, JC, was developed by Haifu (Chongqing; Fig. 3D) and has been approved for the treatment of uterine fibroids; pancreatic cancer; and liver, bone, and breast tumors. The system has a 0.8-MHz single transducer integrated into the patient table, and fronted acoustic lenses allow focus-length adjustment. An ultrasound-imaging device (1–8 MHz) is equipped for real-time guidance.

A clinical trial in 2018 showed a reduction in tumor volume of 58% after 6 mo and a longer median overall survival (16.2 mo) than for patients who received chemotherapy or radiochemotherapy (34). An improvement in quality of life was reported in 2021, with physical, emotional, and social functioning

increasing while the rate of side effects remained low, demonstrating that HIFU is a worthwhile supportive treatment for advanced pancreatic cancer (35).

INNOVATIVE APPLICATIONS OF IMAGE-GUIDED FOCUSED ULTRASOUND (FUS)

In addition to the image-guided HIFU ablation described above, FUS at various intensities offers advantages in many other potential applications. The following section presents selected preclinical and clinical studies of FUS as a single or adjuvant therapy.

Histotripsy

As mentioned previously, dense energetic bubble clouds can be produced at the focus point by very short, infrequent, high-amplitude bursts of acoustic waves that mechanically fractionate the tissue into subcellular components in histotripsy (36). Compared with thermal applications, histotripsy avoids overheating and the heat-sink effect in the targeted tissues, and tissue fragments are more easily absorbed after treatment.

Several recent studies showed the feasibility of using histotripsy to create precise lesions at the desired location, such as the liver,

prostate, or brain (36). Notably, lesions can be created through the ribs safely throughout the entire liver (37). The first-in-humans study using cavitation histotripsy for the treatment of prostate enlargement was reported in 2018. An improvement in lower-urinary-tract symptoms was observed, with no intraoperative side effects. However, the treatment outcome was not as significant as expected, because of the technical limitations of the FUS device (38). The development of a precisely controlled histotripsy FUS system is necessary.

Histotripsy is a neurosurgical option (39) in which lesions with a dimension of up to 1 cm are created in the porcine cortex without thermally induced damage to the surrounding neurons. Moreover, histotripsy carries the potential to overcome the limitations of current thrombolytic drugs and to shorten the treatment time. In vitro and in vivo experiments have shown that FUS histotripsy thrombolysis can cause a direct mechanical breakdown of clots and achieve blood flow restoration noninvasively (40).

FUS-Mediated Drug Delivery

The systemic toxicity of chemotherapy is the main challenge in clinical oncology and may induce adverse effects such as hair loss, anemia, nausea, and vomiting. The encapsulation of chemotherapeutic drugs in carriers or the triggering of drug delivery in the target tissue with external physical stimulation has been considered to improve treatment efficiency and reduce adverse effects. FUS-mediated targeted drug delivery based on mechanical and thermal mechanisms has become a topic of intensive research in the last 20 y. The drug carriers can be opened in situ and allow controlled drug release in specific regions with FUS exposure, and the permeability of the cell membrane and the drug uptake can be enhanced as well (41). A preclinical study reporting on the combination of the chemotherapeutic agent gemcitabine with FUS showed that the treatment led to a reduction in tumor growth compared with a single treatment in the xenograft pancreatic cancer model (42).

In addition to chemotherapeutic drugs, ultrasound-mediated gene delivery provides a new strategy for cancer treatment. The typical ultrasound parameters used for gene delivery are frequencies of 1–2 MHz, intensities of 0.1–3 W/cm², and short durations of 2–8 s, with ultrasound contrast agent microbubbles usually being added to enhance the sonoporation effect (43). Noroozian et al. (44) demonstrated the FUS-mediated recombinant adeno-associated viral vector across the blood–brain barrier into the brain parenchyma, which resulted in efficient gene transduction and expression in both mouse and rat models.

A single-center phase I trial (NCT02181075) was conducted in the United Kingdom to analyze the safety and feasibility of FUS hyperthermia–triggered doxorubicin delivery from thermosensitive liposomes (45). Thermosensitive liposomal doxorubicin was administered by intravenous infusion, followed by FUS exposure at a single target liver tumor. The concentration of doxorubicin inside the target tumor was increased by 3.7-fold immediately after FUS treatment, compared with the group without FUS.

FUS Supporting RT

RT is one of the most commonly used treatment modalities in the clinic. Various biologic mechanisms are involved in enhancing the antitumor effects of RT, including inhibition of DNA damage repair, induction of apoptosis, and changes in the tumor microenvironment (46). A few clinical studies have shown that FUS is a sensitizer of RT in different cancers, including those of the head and neck, breast, prostate, and central nervous system (3).

A phase I study by Chu et al. (47) reported combined treatment with MRgHIFU hyperthermia, RT, and chemotherapy for recurrent rectal cancer. Patients received daily fractionated RT (total dose, 30.6 Gy) and oral capecitabine. HIFU hyperthermia was performed at a mean temperature of 42.5°C for 30 min immediately before RT on days 1, 8, and 15. No intraoperative complications, serious adverse effects, or unexpected tissue damage attributed to HIFU hyperthermia were observed, showing the safety and feasibility of the treatment. Another phase II study reported a 7-y overall survival rate of 94% in advanced prostate cancer patients after combined treatment with transrectal ultrasound hyperthermia, RT, and androgen suppression (48).

A better understanding of ultrasound radiosensitization mechanisms is necessary, although benefits have been shown in several clinical studies. The significant radioadditive effect of FUS in prostate cancer was demonstrated in our in vitro study (49,50). It is critical to optimize the combination-treatment protocols to increase treatment efficiency in terms of treatment sequences, intervals, thermal doses, and radiation doses. The integration of FUS into RT and the administration of both treatments simultaneously may improve the radiosensitization effect further.

FUS-Mediated Immunotherapy

Immunotherapy has changed cancer treatment strategies, aiming to improve the antitumor immune response and directly kill cancer cells (51). The immune system is activated or the activation process is boosted by immunotherapeutic agents such as checkpoint inhibitors to attack cancer cells through natural mechanisms and avoid relative side effects.

FUS provides the possibility of delivering immunotherapy agents, and FUS administration, especially the mechanisms of cavitation, is considered a stimulator for the immune system (52). Eranki et al. (53) reported that the mechanical fractionation of neuroblastoma tumors using HIFU significantly increases cellular immunity, and the combination of HIFU and checkpoint inhibitors induces systemic immunity and dramatically enhances survival. More experimental and clinical evidence of FUS-induced immune effects was systematically reviewed by van den Bijgaart et al. (54). However, the safety of FUS-induced immune therapy is the main obstacle for clinical translation because of tumor heterogeneity. The underlying mechanisms of the interactions between ultrasound and cells are of vital importance, and a better understanding is needed before clinical trials.

Neuromodulation by Low-Intensity FUS

Transcranial FUS application in neurologic diseases is of particular interest. The potential indications include Alzheimer disease, depression, obsessive–compulsive disorder, epilepsy, and Huntington disease. FUS-mediated neuromodulation is performed at low intensities and for short durations (55). Mechanical effects are considered the main driver for neuron stimulation, since the temperature increase is limited at the target.

Storz Medical has introduced the CE (Conformité Européenne)-marked system Neurolith for single-pulse-wave treatment of Alzheimer disease, with promising initial clinical results (56). Low-intensity FUS with short bursts is a promising method for the safe stimulation or inhibition of neurons in future clinical neurologic applications and will not require that the patient's hair be shaved. A new clinical FUS system operating at diagnostic sound pressure for neuromodulation has been developed collaboratively by the Innovation Center Computer Assisted Surgery and the Fraunhofer IBMT and is currently being validated at the Max Planck Institute for

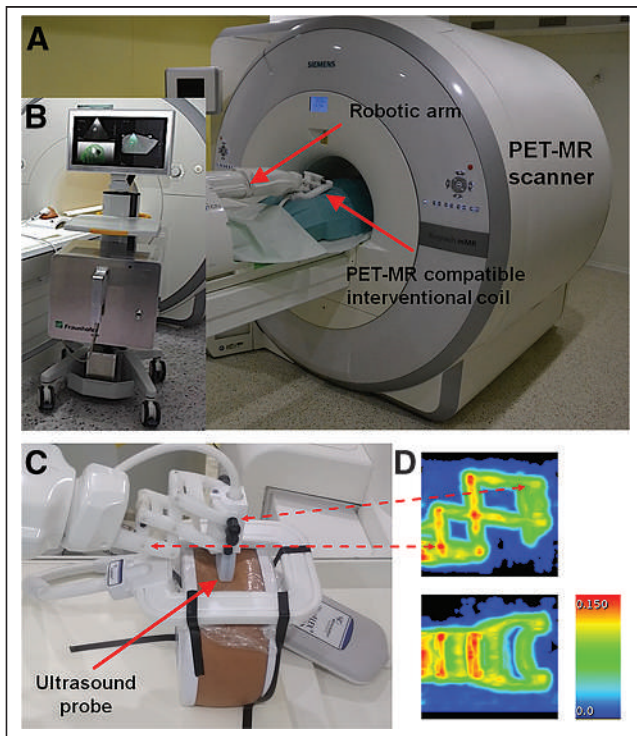


FIGURE 4. Integration of Innomotion robotic arm (InnoMedic GmbH) into Biograph mMR PET/MRI scanner (Siemens Healthineers). (A) Robotic arm was modified to fit into PET/MRI system holding ultrasound imaging probe. (B) MRI-compatible FUS system Diphas (Fraunhofer IBMT) can be integrated into PET/MRI scanner. (C) Three-dimensionally printed adaptor and fixation parts were manufactured to hold ultrasound transducer. (D) Attenuation map of robotic arm visualized by 2 perpendicular maximum-intensity projections of PET annihilation photons (in 1/cm) with linear attenuation coefficient of 511 keV, obtained by stand-alone PET scanner equipped with $^{68}\text{Ge}/^{68}\text{Ga}$ rod sources.

Cognitive and Neurosciences in Leipzig. The preliminary results were reported at the first Focused Ultrasound Neuromodulation Symposium in Oxford, England, on September 23–25, 2019. Further work is necessary to explore the ultrasound parameters and to develop targeted neuromodulation methods for different brain regions.

NOVEL TECHNIQUES FOR POTENTIAL IMAGE-GUIDED HIFU APPLICATIONS

Various studies have been conducted to integrate multifunctional imaging modalities into the FUS system to improve the safety, treatment efficiency, and accuracy of the outcome assessment. PET/MRI was also reported to detect the local recurrence of prostate cancer patients after HIFU ablation, which is not detectable by MRI. Moreover, PET/MR images could be used to optimize targeting of a secondary HIFU ablation and could improve patient survival (57). Novel tracers, such as those utilizing the prostate-specific membrane antigen, have shown promising results in patients for the detection of prostatic cancer using PET/MRI (58). In combination with HIFU, such tracers may allow for a 1-stop-shop focal treatment.

A robotic assistance system was previously integrated into an MRI scanner to provide precise and reproducible instrument positioning (59). To realize precise FUS positioning under PET/MRI guidance, we are working toward integrating a robotic arm system with an MRI-compatible FUS transducer into the clinical PET/MRI scanner (Fig. 4) (60). This new concept expands the application

field of image-guided FUS interventions, may provide clinical feasibility, and will soon allow precise treatment.

CONCLUSION

Imaged-guided HIFU is a promising noninvasive, nonaccess clinical method that has been proven to be efficient and safe in several studies. It has been approved in all major markets around the world for the treatment of uterine fibroids, bone metastases, liver tumors, brain cancer, and prostate cancer. The advantages of the method are its noninvasiveness, absence of ionizing radiation, comparatively low complication rate, and low side effect rate, with a correspondingly low impairment of quality of life. With a transcranial HIFU system, the treatment of essential tremors and Parkinson-induced tremors is clinically approved, and studies that are currently under way have had promising initial results in neurologic diseases. The potential of HIFU has been demonstrated for various medical applications to improve other treatment modalities such as chemotherapy and ER and to support drug delivery. Imaging innovation together with HIFU treatment may provide a new strategy for future clinical applications.

DISCLOSURE

The work described was supported by research grants funded by the German Ministry of Science and Technology BMBF project SONO-RAY (03ZIL511). No other potential conflict of interest relevant to this article was reported.

ACKNOWLEDGMENTS

We thank the Departments of Nuclear Medicine and Radiation Therapy of the Leipzig University Hospital for supporting some of the work mentioned (further results will be published elsewhere), and we thank the Saxon Incubator for Clinical Translation and the Fraunhofer Institute for Cell Therapy and Immunology for supporting the preclinical experiments.

REFERENCES

- Kennedy JE. High-intensity focused ultrasound in the treatment of solid tumours. *Nat Rev Cancer*. 2005;5:321–327.
- Siedek F, Yeo SY, Heijman E, et al. Magnetic resonance-guided high-intensity focused ultrasound (MR-HIFU): technical background and overview of current clinical applications (part 1). *Rofo*. 2019;191:522–530.
- Zhu L, Altman MB, Laszlo A, et al. Ultrasound hyperthermia technology for radio-sensitization. *Ultrasound Med Biol*. 2019;45:1025–1043.
- Jolesz FA. MRI-guided focused ultrasound surgery. *Annu Rev Med*. 2009;60:417–430.
- Izadifar Z, Izadifar Z, Chapman D, Babyn P. An introduction to high intensity focused ultrasound: systematic review on principles, devices, and clinical applications. *J Clin Med*. 2020;9:460.
- McWilliams JP, Lee EW, Yamamoto S, Loh CT, Kee ST. Image-guided tumor ablation: emerging technologies and future directions. *Semin Intervent Radiol*. 2010;27:302–313.
- Prentice P, Cuschierp A, Dholakia K, Prausnitz M, Campbell P. Membrane disruption by optically controlled microbubble cavitation. *Nat Phys*. 2005;1:107–110.
- Rosenthal I, Sostaric JZ, Riesz P. Sonodynamic therapy: a review of the synergistic effects of drugs and ultrasound. *Ultrasound Sonochem*. 2004;11:349–363.
- Orsi F, Amone P, Chen WZ, Zhang LA. High intensity focused ultrasound ablation: a new therapeutic option for solid tumors. *J Cancer Res Ther*. 2010;6:414–420.
- Orsi F, Monfardini L, Bonomo G, Krokidis M, Della Vigna P, Disalvatore D. Ultrasound guided high intensity focused ultrasound (USgHIFU) ablation for uterine fibroids: do we need the microbubbles? *Int J Hyperthermia*. 2015;31:233–239.
- Samset E. Temperature mapping of thermal ablation using MRI. *Minim Invasive Ther Allied Technol*. 2006;15:36–41.
- Stewart EA. Clinical practice. uterine fibroids. *N Engl J Med*. 2015;372:1646–1655.

13. Wu G, Li R, He M, et al. A comparison of the pregnancy outcomes between ultrasound-guided high-intensity focused ultrasound ablation and laparoscopic myomectomy for uterine fibroids: a comparative study. *Int J Hyperthermia*. 2020;37:617–623.
14. Duc NM, Keserci B. Review of influential clinical factors in reducing the risk of unsuccessful MRI-guided HIFU treatment outcome of uterine fibroids. *Diagn Interv Radiol*. 2018;24:283–291.
15. Hopfner F, Deuschl G. Managing essential tremor. *Neurotherapeutics*. 2020;17:1603–1621.
16. Elias WJ, Lipsman N, Ondo WG, et al. A randomized trial of focused ultrasound thalamotomy for essential tremor. *N Engl J Med*. 2016;375:730–739.
17. Park YS, Jung NY, Na YC, Chang JW. Four-year follow-up results of magnetic resonance-guided focused ultrasound thalamotomy for essential tremor. *Mov Disord*. 2019;34:727–734.
18. Durante C, Costante G, Lucisano G, et al. The natural history of benign thyroid nodules. *JAMA*. 2015;313:926–935.
19. Lang BHH, Wu ALH. High intensity focused ultrasound (HIFU) ablation of benign thyroid nodules: a systematic review. *J Ther Ultrasound*. 2017;5:11.
20. Esnault O, Franc B, Menegaux F, et al. High-intensity focused ultrasound ablation of thyroid nodules: first human feasibility study. *Thyroid*. 2011;21:965–973.
21. Prakash PS, Oh HB, Tan WB, Parameswaran R, Ngiam KY. The efficacy and safety of high-intensity focused ultrasound (HIFU) therapy for benign thyroid nodules: a single center experience from Singapore. *World J Surg*. 2019;43:1957–1963.
22. Hahn M, Fugunt R, Schoenfish B, et al. High intensity focused ultrasound (HIFU) for the treatment of symptomatic breast fibroadenoma. *Int J Hyperthermia*. 2018;35:463–470.
23. Barsouk A, Padala SA, Vakiti A, et al. Epidemiology, staging and management of prostate cancer. *Med Sci (Basel)*. 2020;8:28.
24. Valerio M, Cerantola Y, Eggener SE, et al. New and established technology in focal ablation of the prostate: a systematic review. *Eur Urol*. 2017;71:17–34.
25. Eggener S, Koch M, Penson D, et al. Pivotal trial of MRI-guided transurethral ultrasound ablation in men with localized prostate cancer: two-year follow-up [abstract]. *J Urol*. 2020;203(suppl):e369.
26. Bonekamp D, Wolf MB, Roethke MC, et al. Twelve-month prostate volume reduction after MRI-guided transurethral ultrasound ablation of the prostate. *Eur Radiol*. 2019;29:299–308.
27. Chin JL, Billia M, Relle J, et al. Magnetic resonance imaging-guided transurethral ultrasound ablation of prostate tissue in patients with localized prostate cancer: a prospective phase 1 clinical trial. *Eur Urol*. 2016;70:447–455.
28. Klotz L, Pavlovich CP, Chin J, et al. Magnetic resonance imaging-guided transurethral ultrasound ablation of prostate cancer. *J Urol*. 2021;205:769–779.
29. Ganzer R, Hadaschik B, Pahernik S, et al. Prospective multicenter phase II study on focal therapy (hemiblation) of the prostate with high intensity focused ultrasound. *J Urol*. 2018;199:983–989.
30. Loi M, Nuytens JJ, Desideri I, Greto D, Livi L. Single-fraction radiotherapy (SFRT) for bone metastases: patient selection and perspectives. *Cancer Manag Res*. 2019;11:9397–9408.
31. Hurwitz MD, Ghanouni P, Kanaev SV, et al. Magnetic resonance-guided focused ultrasound for patients with painful bone metastases: phase III trial results. *J Natl Cancer Inst*. 2014;106:dju082.
32. Napoli A, Anzidei M, Marincola BC, et al. Primary pain palliation and local tumor control in bone metastases treated with magnetic resonance-guided focused ultrasound. *Invest Radiol*. 2013;48:351–358.
33. Carrato A, Falcone A, Ducreux M, et al. A systematic review of the burden of pancreatic cancer in Europe: real-world impact on survival, quality of life and costs. *J Gastrointest Cancer*. 2015;46:201–211.
34. Marinova M, Huxold HC, Henseler J, et al. Clinical effectiveness and potential survival benefit of US-guided high-intensity focused ultrasound therapy in patients with advanced-stage pancreatic cancer. *Ultraschall Med*. 2019;40:625–637.
35. Marinova M, Feradova H, Gonzalez-Carmona MA, et al. Improving quality of life in pancreatic cancer patients following high-intensity focused ultrasound (HIFU) in two European centers. *Eur Radiol*. January 23, 2021 [Epub ahead of print].
36. Khokhlova VA, Fowlkes JB, Roberts WW, et al. Histotripsy methods in mechanical disintegration of tissue: towards clinical applications. *Int J Hyperthermia*. 2015;31:145–162.
37. Vlaisavljevich E, Owens G, Lundt J, et al. Non-invasive liver ablation using histotripsy: preclinical safety study in an in vivo porcine model. *Ultrasound Med Biol*. 2017;43:1237–1251.
38. Schuster TG, Wei JT, Hendlin K, Jahnke R, Roberts WW. Histotripsy treatment of benign prostatic enlargement using the Vortx Rx system: initial human safety and efficacy outcomes. *Urology*. 2018;114:184–187.
39. Sukovich JR, Cain CA, Pandey AS, et al. In vivo histotripsy brain treatment. *J Neurosurg*. October 1, 2018 [Epub ahead of print].
40. Shi A, Lundt J, Deng Z, et al. Integrated histotripsy and bubble coalescence transducer for thrombolysis. *Ultrasound Med Biol*. 2018;44:2697–2709.
41. Jain A, Tiwari A, Verma A, Jain SK. Ultrasound-based triggered drug delivery to tumors. *Drug Deliv Transl Res*. 2018;8:150–164.
42. Park EJ, Ahn YD, Lee JY. In vivo study of enhanced chemotherapy combined with ultrasound image-guided focused ultrasound (USgFUS) treatment for pancreatic cancer in a xenograft mouse model. *Eur Radiol*. 2018;28:3710–3718.
43. Yoon CS, Park JH. Ultrasound-mediated gene delivery. *Expert Opin Drug Deliv*. 2010;7:321–330.
44. Noroozian Z, Xhima K, Huang Y, et al. MRI-guided focused ultrasound for targeted delivery of rAAV to the brain. *Methods Mol Biol*. 2019;1950:177–197.
45. Lyon PC, Gray MD, Mannaris C, et al. Safety and feasibility of ultrasound-triggered targeted drug delivery of doxorubicin from thermosensitive liposomes in liver tumours (TARDOX): a single-centre, open-label, phase 1 trial. *Lancet Oncol*. 2018;19:1027–1039.
46. Rao W, Deng ZS, Liu J. A review of hyperthermia combined with radiotherapy/chemotherapy on malignant tumors. *Crit Rev Biomed Eng*. 2010;38:101–116.
47. Chu W, Huang Y, Pichardo S, et al. A phase I study of MR-hifu hyperthermia (HT) with radiation (RT) and chemotherapy (CT) for recurrent rectal cancer [abstract]. *J Glob Oncol*. 2019;5:78.
48. Hurwitz MD, Hansen JL, Prokopios-Davos S, et al. Hyperthermia combined with radiation for the treatment of locally advanced prostate cancer: long-term results from Dana-Farber Cancer Institute study 94-153. *Cancer*. 2011;117:510–516.
49. Hu S, Zhang X, Unger M, Patties I, Melzer A, Landgraf L. Focused ultrasound-induced cavitation sensitizes cancer cells to radiation therapy and hyperthermia. *Cells*. 2020;9:2595.
50. Zhang X, Bobeica M, Unger M, et al. Focused ultrasound radiosensitizes human cancer cells by enhancement of DNA damage. *Strahlenther Onkol*. April 22, 2021 [Epub ahead of print].
51. Riley RS, June CH, Langer R, Mitchell MJ. Delivery technologies for cancer immunotherapy. *Nat Rev Drug Discov*. 2019;18:175–196.
52. Mauri G, Nicolson L, Xu Z, et al. Focused ultrasound: tumour ablation and its potential to enhance immunological therapy to cancer. *Br J Radiol*. 2018;91:20170641.
53. Eranki A, Srinivasan P, Ries M, et al. High-intensity focused ultrasound (HIFU) triggers immune sensitization of refractory murine neuroblastoma to checkpoint inhibitor therapy. *Clin Cancer Res*. 2020;26:1152–1161.
54. van den Bijgaart RJ, Eikelenboom DC, Hoogenboom M, Futterer JJ, den Brok MH, Adema GJ. Thermal and mechanical high-intensity focused ultrasound: perspectives on tumor ablation, immune effects and combination strategies. *Cancer Immunol Immunother*. 2017;66:247–258.
55. Naor O, Krupa S, Shoham S. Ultrasonic neuromodulation. *J Neural Eng*. 2016;13:031003.
56. Beisteiner R, Matt E, Fan C, et al. Transcranial pulse stimulation with ultrasound in Alzheimer's disease: a new navigated focal brain therapy. *Adv Sci (Weinh)*. 2019;7:1902583.
57. Burger IA, Muller J, Donati OF, et al. ⁶⁸Ga-PSMA-11 PET/MR detects local recurrence occult on mpMRI in prostate cancer patients after HIFU. *J Nucl Med*. 2019;60:1118–1123.
58. Eiber M, Nekolla SG, Maurer T, Weirich G, Wester HJ, Schwaiger M. ⁶⁸Ga-PSMA PET/MR with multimodality image analysis for primary prostate cancer. *Abdom Imaging*. 2015;40:1769–1771.
59. Melzer A, Gutmann B, Remmele T, et al. Innomotion for percutaneous image-guided interventions: principles and evaluation of this MR- and CT-compatible robotic system. *IEEE Eng Med Biol Mag*. 2008;27:66–73.
60. Berger J, Unger M, Landgraf L, Melzer A. Evaluation of an IEEE 11073 SDC connection of two KUKA robots towards the application of focused ultrasound in radiation therapy. *Curr Dir Biomed Eng*. 2019;5:149.

Why Will PET Be the Future of Nuclear Cardiology?

Marcelo F. Di Carli

Cardiovascular Imaging Program, Departments of Radiology and Medicine; Division of Nuclear Medicine and Molecular Imaging, Department of Radiology; and Division of Cardiovascular Medicine, Department of Medicine, Brigham and Women's Hospital, Harvard Medical School, Boston, Massachusetts

Radionuclide myocardial perfusion imaging (MPI) has been an indispensable tool in the management of patients with suspected or known coronary artery disease (CAD) for almost half a century. Although radiopharmaceuticals and imaging technology for radionuclide MPI has evolved since its introduction by Zaret et al. in 1973 (1), the basic concepts of reversible and fixed perfusion defects as manifestations of ischemia and scarring remain to this day key information used for clinical decision making. Semi-quantitative evaluation of regional myocardial perfusion with SPECT imaging has been standard practice in nuclear cardiology for more than 3 decades. The enduring impact of SPECT MPI in patient management is based on the fact that the test is accurate, highly reproducible, and, most importantly, a powerful tool for risk stratification. However, there are powerful signs that the paradigm that served as the clinical rationale for radionuclide MPI for many decades may be insufficient to maintain a clinically relevant role for cardiovascular medicine in the future.

EVOLUTION OF DIAGNOSTIC TESTING FOR CAD EVALUATION

Over the last decade, we have witnessed an evolution in the diagnostic testing options available for patients with suspected CAD. These advances are leading to rapid changes in the way we use various testing options along the spectrum of CAD risk (2). There is little argument on what to do at the ends of the clinical risk spectrum—no testing necessary for patients at very low risk and consideration of coronary angiography for high-risk patients (2). However, testing options for patients with intermediate risk are changing. Coronary CT angiography with its high sensitivity and negative predictive value to exclude CAD makes it an attractive test for patients with a low to intermediate likelihood of obstructive CAD. This choice is now supported by clinical trial evidence and associated with improved outcomes, largely resulting from identification of patients in need of preventive therapies (3). The emergence of coronary CT angiography is shifting the use of radionuclide MPI toward higher-risk patients with a high prevalence of cardiometabolic risk factors (2).

CHANGING EPIDEMIOLOGY AND PRESENTATION OF CAD

In addition to the changing landscape of testing options, we are witnessing a dramatic change in the epidemiology of CAD,

especially with the exponential rise of cardiometabolic diseases. Over the last 20 y, there has been a steady rise in the prevalence of obesity, metabolic syndrome, and diabetes and their associated complications, including chronic kidney disease. Current statistics indicate that about 50% of the U.S. population is either overweight or obese and that this number is projected to increase to approximately 80% in the next decade (4). The obesity epidemic has led to a sharp rise in the prevalence of diabetes, which currently affects 10.5% of the U.S. population and 26.8% of those aged 65 y or older. Moreover, it is estimated that 1 in 3 individuals aged 65 y or older has prediabetes and 38% have chronic kidney disease.

There is also emerging evidence that the frequency of obstructive CAD as a key manifestation of the disease is declining. Over the last 2 decades, diagnostic yields have fallen, not only for invasive coronary angiography (5,6) but also for noninvasive stress testing (7,8). In one large registry from Denmark, the rate of non-obstructive atherosclerosis in patients with angina referred for invasive coronary angiography increased by 20%–40% over a 10-y period in women and men (5). This suggests that nonobstructive CAD now accounts for at least 33% and 65% of angiographic findings among symptomatic men and women, respectively. Moreover, recent data from Olmstead County, MN, also documented a steady decline in angiographically obstructive CAD over the last 2 decades (9). At the same time, the epidemic of cardiometabolic risk factors has been associated with an anatomic phenotype dominated by diffuse atherosclerosis and microvascular remodeling (10). The latter includes microvascular obstruction with luminal narrowing of the intramural arterioles and capillaries, and capillary rarefaction, often in the context of increased left ventricular mass (11). These changes help explain, at least in part, the significant temporal decline in the rate of abnormal SPECT MPI studies (8), with a marked reduction in the proportion of high-risk scans and a proportional increase in low-risk tests (7). Indeed, the presence of extensive structural abnormalities characterized by diffuse epicardial atherosclerosis and microvascular disease would be relatively invisible for our traditional radionuclide semiquantitative MPI approach designed to uncover focal obstructive CAD. Although the observations described above may be perceived as good news, the emerging evidence suggest that the rise in diffuse atherosclerosis and microvascular disease is also associated with significant adverse outcomes (4). Indeed, the incidence of acute presentations of atherothrombotic plaque rupture causing myocardial infarction (MI), particularly with ST-segment elevation, has decreased (12) whereas the rates of hospitalizations with a secondary MI diagnosis (13) and heart failure with preserved ejection fraction (14) have risen sharply. These secondary causes of MI have been

Received Jan. 19, 2021; revision accepted Jan. 27, 2021.
For correspondence contact, Marcelo F. Di Carli (mdicarli@bwh.harvard.edu).
Published online February 19, 2021.
© 2021 by the Society of Nuclear Medicine and Molecular Imaging.

associated with heart failure, atrial fibrillation, diabetes, and chronic kidney disease. Similar findings have been reported in patients experiencing an MI before 50 y of age (15).

THE NEED FOR NEW TOOLS: ADVANTAGES OF QUANTITATIVE PET IMAGING

The pioneering work of Schelbert and Gould (16,17) introducing the possibility of quantitative myocardial blood flow imaging noninvasively with PET in the early 1980s provided the field of nuclear cardiology with a powerful tool that now—nearly 40 y later—will prove to be indispensable in the evaluation of ischemic heart disease. As outlined below, the emerging evidence supports the notion that quantitative PET MPI is a superior approach to diagnosis and risk prediction, and to possibly to guide patient management.

A metaanalysis (18), a prospective European multicenter study (19), and a prospective comparative effectiveness study (20) support the notion that PET MPI is one of the most accurate noninvasive techniques for detecting flow-limiting CAD. These quantitative measures of myocardial perfusion improve the sensitivity and negative predictive value of PET for ruling out high-risk obstructive CAD. Equally important is the fact that quantitative measures of myocardial blood flow and flow reserve by PET are now recognized as the tests of choice for the evaluation of patients with angina or angina equivalents without obstructive CAD (2).

Radionuclide MPI provides robust prognostic assessments of patients with suspected stable CAD and forms the basis of its widespread use and clinical utility. Normal or low-risk radionuclide MPI results with SPECT or PET have been associated with an annual risk of major adverse cardiac events of less than 1% (21). However, the risk associated with normal results on semiquantitative radionuclide MPI has not necessarily been low (<1%) in higher-risk cohorts, including those with diabetes, chronic kidney impairment, and the elderly (22). The reasons for the observed increased adverse event rate in higher-risk cohorts despite a visually normal radionuclide MPI result are likely multifactorial. First, coexisting comorbidities including cardiometabolic risk factors increase clinical risk, even in the absence of obstructive CAD. Second, and notwithstanding the clinical utility of SPECT MPI, it is a somewhat insensitive test to uncover diffuse obstructive and nonobstructive atherosclerosis or coronary microvascular dysfunction associated with myocardial ischemia and increased risk of adverse events. Consequently, absolute quantification of myocardial blood flow and flow reserve by PET—an integrated marker of epicardial stenosis, diffuse atherosclerosis, and microvascular dysfunction—offers a definite advantage in higher-risk patients, which is precisely the group of patients who will become the primary target of radionuclide MPI. In such patients, a relatively preserved myocardial flow reserve (MFR) identifies truly low-risk individuals among high-risk patients (23–26). For example, patients with diabetes who have no known CAD but an abnormal MFR had a cardiac mortality risk similar to that of patients without diabetes who have known CAD (27). Conversely, patients with diabetes who have no overt CAD and have a relatively preserved MFR had an annual risk of less than 1%, which was comparable to subjects without diabetes or CAD. Similar findings have been shown in patients with chronic kidney disease (28).

Furthermore, the quantitative regional and global myocardial blood flow and flow reserve information obtained with PET MPI provides incremental risk stratification. Indeed, for any amount of ischemic or scarred myocardium, as assessed semiquantitatively,

having a severely reduced global MFR is associated with a higher risk of death or MI than is having a preserved MFR (23). The increased risk of adverse events in patients with a reduced MFR (<2.0) also applies to patients with visually normal radionuclide MPI findings, in whom the reduced MFR reflects a combination of diffuse nonobstructive atherosclerosis and coronary microvascular dysfunction and is found in half of symptomatic men and women without overt obstructive CAD (29). Importantly, the noninvasive PET measure of MFR has been able to improve risk reclassification, especially among high-risk cohorts (e.g., patients with diabetes, non-ST elevation MI, chronic renal impairment, or high coronary calcium scores). Thus, the ability to quantify MFR allows a level of risk assessment well beyond that achieved thus far using semiquantitative analysis of regional perfusion defects, by incorporating measures of endothelial function and vascular health status into routine patient evaluations.

OPENING NEW OPPORTUNITIES FOR NUCLEAR CARDIOLOGY IN DISEASE MANAGEMENT

Radionuclide MPI has been traditionally used to identify symptomatic patients for myocardial revascularization. Although this will likely continue to be one of its uses in the future, the ability to accurately quantify the extent and severity of coronary vascular dysfunction may offer an opportunity for identification of high-risk individuals who may benefit most from novel therapies. Such an approach may prove to be beneficial in clinical trials by identifying patients who have sufficient risk to benefit from these therapies, many of which are expensive and not without their own risk. In so doing, this test may be able to offer a cost-effective approach to patient selection for lifelong therapies and to assess response to treatment both in the clinical setting and in drug development.

CONCLUSION

CAD continues to be the leading cause of death and disability in the United States and worldwide. However, the epidemiology and pathobiology of the disease are changing with the rise of cardiometabolic disease. This poses significant challenges to the efficacy of our conventional imaging tools used in diagnosis, risk assessment, and patient management. Quantitative PET offers a powerful opportunity to tackle these challenges effectively, and we need to quickly embrace such changes to maintain the transformative role of nuclear cardiology in patient care and research.

DISCLOSURE

No potential conflict of interest relevant to this article was reported.

REFERENCES

1. Zaret BL, Strauss HW, Martin ND, Wells HP Jr, Flamm MD Jr. Noninvasive regional myocardial perfusion with radioactive potassium: study of patients at rest, with exercise and during angina pectoris. *N Engl J Med.* 1973;288:809–812.
2. Knuuti J, Wijns W, Saraste A, et al. 2019 ESC guidelines for the diagnosis and management of chronic coronary syndromes. *Eur Heart J.* 2020;41:407–477.
3. Williams MC, Adamson PD, Newby DE, Coronary CT. Angiography and subsequent risk of myocardial infarction. *N Engl J Med.* 2019;380:300.
4. Virani SS, Alonso A, Benjamin EJ, et al; American Heart Association Council on Epidemiology and Prevention Statistics Committee and Stroke Statistics Subcommittee. Heart disease and stroke statistics: 2020 update—a report from the American Heart Association. *Circulation.* 2020;141:e139–e596.

5. Jespersen L, Hvelplund A, Abildstrom SZ, et al. Stable angina pectoris with no obstructive coronary artery disease is associated with increased risks of major adverse cardiovascular events. *Eur Heart J*. 2012;33:734–744.
6. Maddox TM, Stanislawski MA, Grunwald GK, et al. Nonobstructive coronary artery disease and risk of myocardial infarction. *JAMA*. 2014;312:1754–1763.
7. Jouni H, Askew JW, Crusan DJ, Miller TD, Gibbons RJ. Temporal Trends of Single-Photon Emission Computed Tomography Myocardial Perfusion Imaging in Patients With Coronary Artery Disease: A 22-Year Experience From a Tertiary Academic Medical Center. *Circ Cardiovasc Imaging*. 2017;10:e005628.
8. Rozanski A, Gransar H, Hayes SW, et al. Temporal trends in the frequency of inducible myocardial ischemia during cardiac stress testing: 1991 to 2009. *J Am Coll Cardiol*. 2013;61:1054–1065.
9. Gerber Y, Gibbons RJ, Weston SA, et al. Coronary disease surveillance in the community: angiography and revascularization. *J Am Heart Assoc*. 2020;9:e015231.
10. Roberts WC. Quantitative extent of atherosclerotic plaque in the major epicardial coronary arteries in patients with fatal coronary heart disease, in coronary endarterectomy specimens, in aorta-coronary saphenous venous conduits, and means to prevent the plaques: a review after studying the coronary arteries for 50 years. *Am J Cardiol*. 2018;121:1413–1435.
11. Taqueti VR, Di Carli MF. Coronary microvascular disease pathogenic mechanisms and therapeutic options: JACC state-of-the-art review. *J Am Coll Cardiol*. 2018;72:2625–2641.
12. Yeh RW, Sidney S, Chandra M, Sorel M, Selby JV, Go AS. Population trends in the incidence and outcomes of acute myocardial infarction. *N Engl J Med*. 2010;362:2155–2165.
13. Sacks NC, Ash AS, Ghosh K, Rosen AK, Wong JB, Rosen AB. Trends in acute myocardial infarction hospitalizations: are we seeing the whole picture? *Am Heart J*. 2015;170:1211–1219.
14. Owan TE, Hodge DO, Herges RM, Jacobsen SJ, Roger VL, Redfield MM. Trends in prevalence and outcome of heart failure with preserved ejection fraction. *N Engl J Med*. 2006;355:251–259.
15. Singh A, Gupta A, DeFilippis EM, et al. Cardiovascular mortality after type 1 and type 2 myocardial infarction in young adults. *J Am Coll Cardiol*. 2020;75:1003–1013.
16. Schelbert HR, Wisenberg G, Phelps ME, et al. Noninvasive assessment of coronary stenoses by myocardial imaging during pharmacologic coronary vasodilation. VI. Detection of coronary artery disease in human beings with intravenous N-13 ammonia and positron computed tomography. *Am J Cardiol*. 1982;49:1197–207.
17. Gould KL, Schelbert HR, Phelps ME, Hoffman EJ. Noninvasive assessment of coronary stenoses with myocardial perfusion imaging during pharmacologic coronary vasodilatation. V. Detection of 47 percent diameter coronary stenosis with intravenous nitrogen-13 ammonia and emission-computed tomography in intact dogs. *Am J Cardiol*. 1979;43:200–208.
18. Takx RA, Blomberg BA, El Aidi H, et al. Diagnostic accuracy of stress myocardial perfusion imaging compared to invasive coronary angiography with fractional flow reserve meta-analysis. *Circ Cardiovasc Imaging*. 2015;8:e002666.
19. Neglia D, Rovai D, Caselli C, et al. Detection of significant coronary artery disease by noninvasive anatomical and functional imaging. *Circ Cardiovasc Imaging*. 2015;8:e002179.
20. Driessen RS, Danad I, Stuijzand WJ, et al. Comparison of coronary computed tomography angiography, fractional flow reserve, and perfusion imaging for ischemia diagnosis. *J Am Coll Cardiol*. 2019;73:161–173.
21. Shaw LJ, Hage FG, Berman DS, Hachamovitch R, Iskandrian A. Prognosis in the era of comparative effectiveness research: where is nuclear cardiology now and where should it be? *J Nucl Cardiol*. 2012;19:1026–43.
22. Shaw LJ, Iskandrian AE. Prognostic value of gated myocardial perfusion SPECT. *J Nucl Cardiol*. 2004;11:171–185.
23. Murthy VL, Naya M, Foster CR, et al. Improved cardiac risk assessment with non-invasive measures of coronary flow reserve. *Circulation*. 2011;124:2215–2224.
24. Gould KL, Johnson NP, Roby AE, et al. Regional, artery-specific thresholds of quantitative myocardial perfusion by PET associated with reduced myocardial infarction and death after revascularization in stable coronary artery disease. *J Nucl Med*. 2019;60:410–417.
25. Patel KK, Spertus JA, Chan PS, et al. Myocardial blood flow reserve assessed by positron emission tomography myocardial perfusion imaging identifies patients with a survival benefit from early revascularization. *Eur Heart J*. 2020;41:759–768.
26. Ziadi MC, Dekemp RA, Williams KA, et al. Impaired myocardial flow reserve on rubidium-82 positron emission tomography imaging predicts adverse outcomes in patients assessed for myocardial ischemia. *J Am Coll Cardiol*. 2011;58:740–748.
27. Murthy VL, Naya M, Foster CR, et al. Association between coronary vascular dysfunction and cardiac mortality in patients with and without diabetes mellitus. *Circulation*. 2012;126:1858–1868.
28. Charytan DM, Skali H, Shah NR, et al. Coronary flow reserve is predictive of the risk of cardiovascular death regardless of chronic kidney disease stage. *Kidney Int*. 2018;93:501–509.
29. Murthy VL, Naya M, Taqueti VR, et al. Effects of sex on coronary microvascular dysfunction and cardiac outcomes. *Circulation*. 2014;129:2518–2527.

Systemic Radiopharmaceutical Therapy of Pheochromocytoma and Paraganglioma

Jorge A. Carrasquillo^{1,2}, Clara C. Chen³, Abhishek Jha⁴, Karel Pacak⁴, Daniel A. Pryma^{*5}, and Frank I. Lin^{*2}

¹Molecular Imaging and Therapy Service, Memorial Sloan Kettering Cancer Center, New York, New York; ²Molecular Imaging Branch, National Cancer Institute, Bethesda, Maryland; ³Department of Radiology, Clinical Center, National Institutes of Health, Bethesda, Maryland; ⁴Section on Medical Neuroendocrinology, National Institute of Child Health and Human Development, National Institutes of Health, Bethesda, Maryland; and ⁵Department of Radiology, Hospital of University of Pennsylvania, Philadelphia, Pennsylvania

Learning Objectives: On successful completion of this activity, participants should be able to (1) describe the clinical features of pheochromocytoma and paraganglioma, including common symptoms and signs, management options, imaging findings, and the role of genetic and hormonal biomarkers; (2) identify and compare radiopharmaceutical agents available for treatment of metastatic or inoperable pheochromocytoma and paraganglioma; and (3) identify differences between low-specific-activity and high-specific-activity ¹³¹I-MIBG.

Financial Disclosure: This research was funded in part through the NIH/National Cancer Institute Cancer Center support grant P30 CA008748 and Eunice Kennedy Shriver National Institutes of Child Health and Human Development grant Z1AHD008735, NIH. Daniel Pryma receives research funding from Siemens and 511 Pharma and consulting fees from Siemens, 511 Pharma, and Bayer. The authors of this article have indicated no other relevant relationships that could be perceived as a real or apparent conflict of interest.

CME Credit: SNMMI is accredited by the Accreditation Council for Continuing Medical Education (ACCME) to sponsor continuing education for physicians. SNMMI designates each *JNM* continuing education article for a maximum of 2.0 AMA PRA Category 1 Credits. Physicians should claim only credit commensurate with the extent of their participation in the activity. For CE credit, SAM, and other credit types, participants can access this activity through the SNMMI website (<http://www.snmlearningcenter.org>) through September 2024.

Whereas benign pheochromocytomas and paragangliomas are often successfully cured by surgical resection, treatment of metastatic disease can be challenging in terms of both disease control and symptom control. Fortunately, several options are available, including chemotherapy, radiation therapy, and surgical debulking. Radiolabeled metaiodobenzylguanidine (MIBG) and somatostatin receptor imaging have laid the groundwork for use of these radiopharmaceuticals as theranostic agents. ¹³¹I-MIBG therapy of neuroendocrine tumors has a long history, and the recent approval of high-specific-activity ¹³¹I-MIBG for metastatic or inoperable pheochromocytoma or paraganglioma by the U.S. Food and Drug Administration has resulted in general availability of, and renewed interest in, this treatment. Although reports of peptide receptor radionuclide therapy of pheochromocytoma and paraganglioma with ⁹⁰Y- or ¹⁷⁷Lu-DOTA conjugated somatostatin analogs have appeared in the literature, the approval of ¹⁷⁷Lu-DOTATATE in the United States and Europe, together with National Comprehensive Cancer Network guidelines suggesting its use in patients with metastatic or inoperable pheochromocytoma and paraganglioma, has resulted in renewed interest. These agents have shown evidence of efficacy as palliative treatments in patients with metastatic or inoperable pheochromocytoma or paraganglioma. In this continuing medical education article, we discuss the therapy of pheochromocytoma and paraganglioma with ¹³¹I-MIBG and ⁹⁰Y- or ¹⁷⁷Lu-DOTA-somatostatin analogs.

Key Words: pheochromocytoma; paraganglioma; somatostatin; MIBG; DOTATATE; peptide receptor radionuclide therapy

J Nucl Med 2021; 62:1192–1199

DOI: 10.2967/jnumed.120.259697

Pheochromocytomas and paragangliomas are rare neuroendocrine tumors (NETs) typically arising in chromaffin tissue, with an overall incidence of 0.4–2.1 cases per million people (1), although higher incidences may be seen in pathology series. In accordance with World Health Organization guidelines, these tumors are classified as paragangliomas (2); we will refer to them as pheochromocytomas when they arise from the adrenal medulla and as paragangliomas when extraadrenal. Pheochromocytoma and paraganglioma most frequently arise from sympathetic tissues. Those arising from parasympathetic tissue are most often in the head and neck. In our previous article, we reviewed the genetics, phenotype, presentation, and imaging characteristics of pheochromocytoma and paraganglioma (3).

Patients with pheochromocytoma and paraganglioma often present with symptoms of elevated catecholamines, depending on the genotype. Tumors of sympathetic origin often secrete elevated levels of epinephrine or norepinephrine or of their metabolites metanephrine and normetanephrine. Tumors of parasympathetic origin may secrete elevated levels of dopamine or its metabolite 3-methoxy-tyramine but are often asymptomatic. A small percentage of pheochromocytoma and paraganglioma are biochemically silent.

Although only 2%–26% of pheochromocytomas and paragangliomas are metastatic (4), benign and malignant tumors cannot be differentiated histologically; thus, the term *metastatic* rather than *malignant* is used when tumor is found outside the normal sites of chromaffin or paraganglia tissues (2). Common sites of metastatic disease include the lymph nodes, bone, liver, and lung (4). Currently,

Received Nov. 2, 2020; revision accepted Feb. 16, 2021.

For correspondence or reprints, contact Jorge A. Carrasquillo (carrasj1@mskcc.org).

*Contributed equally to this work.

COPYRIGHT © 2021 by the Society of Nuclear Medicine and Molecular Imaging.

systemic radiopharmaceutical therapies (RPT) for pheochromocytoma and paraganglioma include ^{131}I -metaiodobenzylguanidine (iokebrogan, ^{131}I -MIBG) of low specific activity (LSA) or high specific activity (HSA) and peptide receptor radionuclide therapy (PRRT) with ^{90}Y - or ^{177}Lu -DOTA-somatostatin analogs.

GENERAL CONSIDERATIONS FOR SYSTEMIC RPT IN PHEOCHROMOCYTOMA AND PARAGANGLIOMA

Although most patients with benign pheochromocytoma and paraganglioma are cured with surgical resection, and local control of head and neck pheochromocytoma and paraganglioma is usually achieved with definitive external-beam radiotherapy, approximately one third are not cured and require long-term follow-up. Patients with benign disease have a survival rate similar to that of healthy individuals, whereas patients with metastatic disease have a 5-y survival rate of 55%–92% (4,5). The wide differences in survival of pheochromocytoma and paraganglioma patients are related to several variables, including genetic status, size of primary tumor, biochemical phenotype, and presence of metastatic disease at initial diagnosis (6,7). Long-term stability over 15 y is not uncommon. Since current treatments of metastatic disease are rarely curative, a watch-and-wait approach is often appropriate, reserving therapy for progressive or symptomatic disease that is not responsive to medical treatment or amenable to surgical resection (8). Systemic treatment is also an option for inoperable non-metastatic disease that is progressing or has refractory symptoms.

The goals of treatment are palliative, including prevention of progression and improvement of symptoms related to tumor burden or catecholamine release. For systemic treatment, the most common chemotherapy regimen is cisplatin, vinblastine, and dacarbazine, which may be preferred for rapidly progressing disease (9). Tyrosine kinase inhibitors that target the vascular endothelial growth factor pathway, such as sunitinib, may have efficacy (10). External radiation for localized symptomatic disease is generally successful for local control (11). For less urgent treatment, RPT with LSA or HSA ^{131}I -MIBG and PRRT are available. Except for HSA ^{131}I -MIBG, none of these approaches are currently approved by the U.S. Food and Drug Administration (FDA) for pheochromocytoma and paraganglioma.

PATIENT PREPARATION BEFORE RPT

When catecholamines or their metabolites (metanephrines) are elevated, experts recommend catecholamine blockade before invasive intervention or RPT; the target is blood pressure control, but often labile hypertension persists (12). Typically, first-line treatment consists of α -blockade (e.g., phenoxybenzamine or doxazosin). A concomitant β -blocker (e.g., atenolol or metoprolol) is often required but should never be used without adequate α -blockade, because unopposed α -adrenergic receptor stimulation could precipitate a hypertensive crisis. Occasionally, addition of metyrosine is needed to block catecholamine synthesis.

Catecholamine release symptoms (hypertension, tachycardia, palpitation, headache, chest pain, tachypnea, sweating, cutaneous flushing, anxiety, and the more severe or life-threatening symptoms of stroke and myocardial infarction) (13,14) are possible during PRRT and MIBG infusion or in the early posttreatment period (13,15). Gonias et al. (15) reported acute hypertension in approximately 14% of subjects and in 15% of high-radioactivity LSA ^{131}I -MIBG treatments, occurring approximately 30 min after initiation of infusion and requiring treatment. Sometimes hypertension

recurred on repeat treatment. Although it is difficult to predict who will develop a hypertensive response to RPT, patients who are biochemically silent will not. Although no acute hypertensive crises were observed with HSA ^{131}I -MIBG, the package insert indicates an 11% incidence of grade 3 or 4 hypertension within 24 h of infusion. Physicians administering RPT should be prepared to treat blood pressure elevation with oral or parenteral antihypertensives (e.g., phentolamine). Close coordination with other medical specialties, including intensive care, is prudent.

Because of the teratogenic effects of ionizing radiation, patients receiving RPT should avoid conception (7 mo for women and 4 mo for men) and must not be pregnant or breastfeeding during treatment. Patients must also be willing and able to follow radiation safety precautions.

POST-RPT RADIATION PROTECTION

In the United States, the Nuclear Regulatory Commission regulations allow for discharge of patients receiving RPT if exposure to others is not likely to exceed 0.5 cGy, and written instructions must be provided to outpatients if the dose is likely to be more than 0.1 cGy. Other countries require RPT to be administered as an inpatient procedure or use different activity levels as the cutoff. Even if release criteria for outpatient administration are met, inpatient treatment may be prudent for some patients. In the United States, outpatient therapies are often performed when LSA ^{131}I -MIBG therapy is less than 9.25 GBq or no more than 7.4 GBq of ^{177}Lu -DOTATATE, whereas with the recommended dose of approximately 18.5 GBq of HSA ^{131}I -MIBG, treatment must be inpatient.

^{131}I -MIBG THERAPY

^{131}I -MIBG was first described by Wieland et al. for imaging the adrenal medulla (16). At present, ^{123}I -MIBG is preferred for imaging and ^{131}I -MIBG for therapy. Currently, ^{131}I -MIBG is seldom used for imaging pheochromocytoma and paraganglioma except for performing dosimetry and for documenting posttreatment targeting. The physical properties of ^{131}I -MIBG make it a useful therapeutic agent, including a short-range 606-keV β -emission and a 364-keV γ -ray that allows imaging and dosimetry. Furthermore, its 8.02-d half-life allows flexibility for labeling and shipping.

MIBG is a derivative of guanethidine and a substrate for the norepinephrine (noradrenaline) transporter. Many pheochromocytomas and paragangliomas express norepinephrine (noradrenaline) transporter, as do other NETs (17). Most reports of ^{131}I -MIBG therapy in patients with pheochromocytoma and paraganglioma are retrospective, small, and use LSA ^{131}I -MIBG (Supplemental Table 1; supplemental materials are available at <http://jnm.snmjournals.org>). No direct therapeutic comparison studies of LSA ^{131}I -MIBG and HSA ^{131}I -MIBG have been performed.

^{131}I -MIBG Production

LSA ^{131}I -MIBG preparations (0.555–1.85 MBq/mg) typically contain approximately 1/2,000 MIBG molecules labeled with ^{131}I . Because uptake via norepinephrine (noradrenaline) transporter is saturable, a high administered mass of unlabeled MIBG could competitively inhibit uptake of the ^{131}I -MIBG, potentially reducing therapeutic efficacy, as has been demonstrated in vitro and in preclinical studies (18). Additionally, because MIBG is a competitive inhibitor of catecholamine reuptake, a high administered mass of MIBG can cause pharmacologic effects (19). This is rarely an

issue for diagnostic administrations (low mass) but occurs more frequently during therapeutic administration of LSA ^{131}I -MIBG (high mass).

In contrast, most MIBG molecules are labeled with ^{131}I in preparations of HSA ^{131}I -MIBG (92.5 GBq/mg). HSA ^{131}I -MIBG (Azedra; Progenics Pharmaceuticals, Inc.) was the first radiopharmaceutical the FDA approved to treat metastatic or inoperable pheochromocytoma or paraganglioma (20,21). Use of HSA ^{131}I -MIBG reduces the risk of infusion reactions and may enhance the therapeutic ratio (19,21,22), although the latter has not yet been proven in patients (23).

Patient Selection and Preparation for ^{131}I -MIBG RPT

Published procedure guidelines for ^{131}I -MIBG therapy preceded availability of HSA ^{131}I -MIBG. Nonetheless, these guidelines are broadly applicable to HSA ^{131}I -MIBG (24). When MIBG therapy is being considered, a positive ^{123}I -MIBG scan is required, as only patients with MIBG-avid disease are candidates for therapy. In our opinion, a ^{123}I -MIBG scan performed within 3–6 mo is adequate if there is no intervening therapy, especially if a ^{131}I -MIBG dosimetric scan will be performed. The amount of uptake required to allow therapy to be considered is poorly defined. Criteria have included visual assessment (uptake clearly visible above the background level), semiquantitative assessment (lesion-to-background uptake > 2), and estimates of tumor dose or more than 1% injected dose in tumor (17). Because tumors can lose MIBG avidity over time or after treatment, confirmation of avidity around the time of treatment is important, especially if the patient's symptoms have recently changed. Patients must be screened for marrow function (minimum platelets, 80,000/ μL ; minimum neutrophils, 1,200/ μL) and renal function (minimum creatinine clearance, 30 mL/min). To protect the thyroid by preventing uptake of free ^{131}I , stable iodine must be administered unless the thyroid is absent or previously ablated. Typically, 130 mg of an oral solution of potassium iodide (SSKI; Avondale Pharmaceuticals) is administered 24–48 h before therapy and continued for 10–15 d (24).

^{131}I -MIBG Administration

HSA ^{131}I -MIBG. Since the approval of HSA ^{131}I -MIBG by the FDA, there has been a surge of interest in MIBG therapy. The recommended dose is 296 MBq/kg in patients weighing no more than 62.5 kg or 18,500 GBq in those over 62.5 kg, given twice at least 90 d apart (20). With these doses, virtually all patients exceed Nuclear Regulatory Commission limits for outpatient treatment. Inpatients must be confined to rooms with appropriate shielding, and preparations must be made to limit exposure of other people to the radiation (in the United States, this is usually for 3 nights).

At dosimetric doses of less than 222 MBq, HSA ^{131}I -MIBG can be injected over 1 min, whereas therapeutic doses are administered over 30 min in adults and 60 min in children. Representative images for dosimetry and posttreatment HSA ^{131}I -MIBG are shown in Figure 1. Occasionally, there is a transient burning pain in the infusion vein, resolving almost immediately with saline flushing.

LSA ^{131}I -MIBG. In contrast to the 2-injection regimen recommended for HSA ^{131}I -MIBG, various approaches using different activities and cycles of LSA ^{131}I -MIBG have been reported (Supplemental Table 1) (17). Most inject approximately 7.4 GBq (25–28); 1 group injected approximately 18.5 GBq (29,30). The University of California San Francisco group has used a much higher activity, up to 666 MBq/kg, in conjunction with stem cell support. In the only direct comparison of a very low activity (5.55

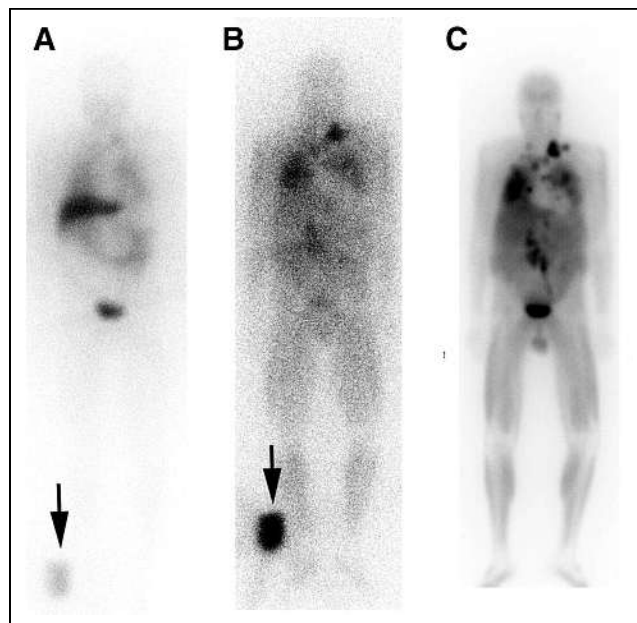


FIGURE 1. Anterior HSA ^{131}I -MIBG images in 60-y-old man with metastatic paraganglioma. (A and B) Dosimetric images were performed 1 h (A) and 96 h (B) after intravenous administration of 185 MBq of HSA ^{131}I -MIBG with standard in field of view (arrows) to allow calculation of organ dose limits. Images show multiple metastases that increase in contrast over time. (C) Three days after therapy with 18.4 GBq of HSA ^{131}I -MIBG, imaging revealed robust retention in sites of disease, including some not visible on dosimetric images. Patient exhibited markedly reduced hormonal symptoms, including decreased need for antihypertensive medications lasting over 2 y.

GBq) versus a low-to-intermediate activity (9.25–12.95 GBq), the low-to-intermediate activity had a more rapid onset of efficacy at the expense of increased acute and chronic toxicity (31). Representative diagnostic ^{123}I -MIBG images and post-LSA ^{131}I -MIBG images are shown in Figure 2. Others have suggested an improved response with higher single administered injections of more than 18.5 GBq versus less than 18.5 GBq (29).

Although high-activity therapies of up to 666 MBq/kg are common in children with neuroblastoma in conjunction with autologous stem cell support, an at least 444 MBq/kg activity of LSA ^{131}I -MIBG in adults with pheochromocytoma or paraganglioma appears to have high rates of toxicity, particularly pulmonary (15). Therefore, doses higher than 296 MBq/kg are not recommended.

In contrast to HSA ^{131}I -MIBG treatment (~ 18.5 GBq), low-activity treatments (≤ 9.25 GBq) can be administered to most patients as outpatients. Therefore, in patients who have relatively indolent disease or who are unwilling to undergo inpatient therapy, serial low-dose treatments can be considered. The most common approaches to low-dose therapy are 74–111 MBq/kg or 7.40 GBq/cycle administered 3 mo apart. Many practitioners give 3–4 cycles of therapy followed by reassessment and consideration of further therapy.

Because LSA ^{131}I -MIBG treatments contain a much higher mass of MIBG than do HSA ^{131}I -MIBG treatments, the former are usually administered over 1–2 h (15,17,25,27,32), although shorter infusions have been performed (26,30). Unlike HSA ^{131}I -MIBG, which is not associated with hypertension during infusion, hypertension occurs during 6%–14% of LSA ^{131}I -MIBG infusions, sometimes requiring pausing or decreasing the infusion rate and using antihypertensive treatment (15,21,33,34). Nonetheless,

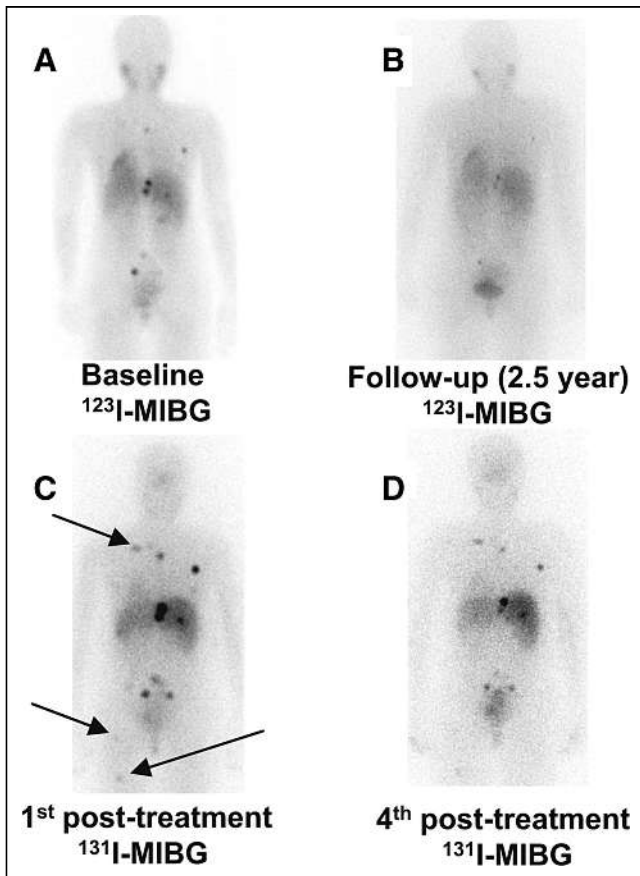


FIGURE 2. Patient with metastatic pheochromocytoma to bone with bone pain. Patient received 4 treatments of LSA ^{131}I -MIBG (111 MBq/kg; range, 5.74–6.18 GBq per treatment) totaling 24.01 GBq over 14 mo. Patient showed symptomatic improvement in bone pain. ^{123}I -MIBG scans were obtained at baseline (A) and at 2.5 y (B) after last ^{131}I -MIBG treatment. (C) ^{131}I -MIBG posttherapy scan a few days after first LSA ^{131}I -MIBG treatment shows better visualization of lesion, and more lesions are evident (arrows) than on baseline ^{123}I -MIBG scan (A). (D) ^{123}I -MIBG scan after all treatments (B) and last ^{131}I -MIBG posttreatment scan (D) shows decreased uptake in bone lesions, probably related to treatment. (Reprinted with permission of (66).)

significant worsening of preexisting hypertension in the first 24 h is reported in 11% of patients receiving HSA ^{131}I -MIBG and may also occur with LSA ^{131}I -MIBG.

Clinical Experience with ^{131}I -MIBG in Pheochromocytoma and Paraganglioma

There have been few controlled prospective trials and no phase III clinical trials of ^{131}I MIBG therapy. Loh et al. reviewed the experience of 21 centers using LSA ^{131}I -MIBG receiving an average of 3 (range, 1–11) single injections of 3.55–11.1 GBq and cumulative activities of 3.55–85.91 GBq (35). Thirty percent of patients had at least partial responses, and 4% had complete responses. Furthermore, there was at least a partial hormonal response in 45% of patients, 13% of whom had a complete response. A metaanalysis that included 243 patients with metastatic pheochromocytoma or paraganglioma receiving median cumulative activities ranging from 6.88–39.4 GBq with a median of 1–7 infusions revealed similar findings (36). Supplemental Table 1 shows therapeutic reports with 20 or more patients, including 2 reports using HSA ^{131}I -MIBG.

The pivotal prospective phase II trial supporting FDA approval of HSA ^{131}I -MIBG (21) enrolled 68 patients with advanced pheochromocytoma or paraganglioma and disease-related hypertension. For LSA ^{131}I -MIBG, the largest prospective trial on pheochromocytoma and paraganglioma enrolled 50 subjects treated with varying activities of LSA ^{131}I -MIBG, including some who received myeloablative doses and stem cell support (15). Using RECIST, both trials found a high rate of partial or durable stable disease in 92% of patients. However, an objective tumor shrinkage meeting RECIST for partial response was seen in only 22%–23% of patients. Furthermore, the peak anatomic response was often delayed, taking up to 12 mo from the first treatment. Other studies have shown somewhat higher objective response rates (34%–38%) using single administrations of approximately 14.467–18.5 GBq (29,30). At lower injected activities, objective response rates of 25%–47% were observed (26,27,31,37). In general, studies using lower single administered activities usually included a larger number of treatment cycles.

Biochemically, 31%–35% of the HSA ^{131}I -MIBG group had a response in norepinephrine and normetanephrine levels, and 68% of patients had a reduced chromogranin A level. In comparison, therapy with LSA ^{131}I -MIBG resulted in a complete or partial catecholamine or metanephrine response in 19%–100% of patients (Supplemental Table 1).

The endpoint of the HSA ^{131}I -MIBG study by Pryma et al. was blood pressure control; 68% of subjects had at least a 50% reduction in antihypertensive medication use lasting at least 6 mo (38). Although no studies of LSA ^{131}I -MIBG focused on hypertension control, a report by Thorpe et al. described improvement in 14% of hypertensive patients (30). Response in terms of overall survival and progression-free survival (Supplemental Table 1) has been variable, with some reporting progression-free survival of at least 2 y (25,30) and median overall survival of more than 3 y (21,29,30,39).

In patients with soft-tissue disease, the response to RPT is typically evaluated using anatomic imaging, most commonly CT scans. Other investigators have used functional imaging, including ^{123}I -MIBG, but given the quantitative nature of PET in patients with ^{18}F -FDG-avid disease, ^{18}F -FDG has also been used for response evaluation.

Dosimetric Scans

The HSA ^{131}I -MIBG regimen incorporates an initial dosimetric study using HSA ^{131}I -MIBG (3.7 MBq/kg, not to exceed 222 MBq), with whole-body imaging on the day of injection, 1–2 d afterward, and 2–5 d afterward, using the MIRD schema to ensure that delivered doses are within specified limits. Usually, the dose-limiting factor is renal exposure; any required activity reduction is split equally across the 2 planned treatments.

Side Effects and Toxicity Profile

Toxicity with ^{131}I -MIBG therapy is common; most patients recover with conservative care. The most common adverse reactions with HSA ^{131}I -MIBG are hematologic, with grade 3–4 hematologic toxicity in about 40% of patients treated with 296 MBq/kg, increasing to over 80% at higher doses (~444 MBq/kg). At the lower dose, 25% of patients required some hematologic support (most commonly packed red blood cells); careful monitoring of hematologic parameters after therapy is critical. Most patients reach nadir 4–6 wk after therapy, but monitoring should start no later than 2 wk after therapy. The risk of dose-limiting toxicity increases with retreatment, but because efficacy appears to remain

strong, particularly in those with favorable prior responses, patients with an adequate marrow reserve can safely be treated again. The incidence of myelodysplasia and leukemia after HSA ¹³¹I-MIBG is 6.8%, similar to the 3.9%–7% reported with LSA ¹³¹I-MIBG (15,31).

A 6.8% rate of hypothyroidism is noted with HSA ¹³¹I-MIBG, and 11%–20% with LSA ¹³¹I-MIBG (25,39,40), despite attempts at thyroid blockade. Gastrointestinal toxicity is common, with nausea and vomiting in 50%–75% of patients treated with a 296 MBq/kg dose of HSA ¹³¹I-MIBG; results are anecdotally similar with LSA ¹³¹I-MIBG. However, because grade 3 or greater gastrointestinal toxicity is extremely rare, conservative care with antiemetics and hydration is almost always adequate.

Most adverse effects were seen in heavily pretreated patients. The toxicity profile in less heavily pretreated patients remains to be seen.

In general, trials describing low-dose therapy (e.g., 74 MBq/kg) have similar but less severe toxicity, with lower (but nonzero) rates of grade 3–4 toxicity. However, hematologic toxicity remains common, particularly in later cycles of therapy, and careful monitoring is still indicated.

Summary

MIBG scintigraphy is the first step to determining eligibility for ¹³¹I-MIBG therapy. Given the overlapping therapeutic responses of LSA ¹³¹I-MIBG and HSA ¹³¹I-MIBG, and that only HSA ¹³¹I-MIBG is FDA-approved, HSA ¹³¹I-MIBG is recommended in the United States. Nonetheless, considering other factors such as the cost and whether the therapy will be inpatient or outpatient, low-activity treatment strategies may be preferred, especially outside the United States. Future studies are needed to guide clinicians on choosing the MIBG treatment regimen most suited to their patients' needs, including whether administration of a low activity and more frequent cycles of treatment with HSA ¹³¹I-MIBG would be useful. These trials should consider not only efficacy but also other parameters such as toxicity, side effects, and patient preferences.

PRRT WITH RADIOLABELED SOMATOSTATIN ANALOGS

Somatostatin receptors are highly expressed in NETs and have been targets for imaging and therapy, as reviewed recently in our continuing education article on imaging pheochromocytoma and paraganglioma (3). Somatostatin is a natural 14-amino-acid peptide hormone with regulatory effects in the endocrine system via binding to somatostatin receptors 1–5, which are highly expressed in NETs. Several somatostatin receptor agonists have been developed for imaging, and ¹⁷⁷Lu-DOTATATE is now available for therapeutic purposes. At present, this is the only PRRT agent approved by the FDA and the European Medicines Agency. The North American Neuroendocrine Tumor Society and Society of Nuclear Medicine and Molecular Imaging jointly published guidelines addressing screening, preparation, administration, radiation safety, adverse events monitoring, and follow-up for ¹⁷⁷Lu-DOTATATE treatment (41). Although pheochromocytoma or paraganglioma is not an approved indication for ¹⁷⁷Lu-DOTATATE, National Comprehensive Cancer Network guidelines provide a rationale for its off-label use (42).

Patient Selection and Preparation

A prerequisite for PRRT therapy of pheochromocytoma and paraganglioma is tumor avidity on somatostatin receptor imaging.

This avidity was initially determined with ¹¹¹In-pentetreotide using a qualitative visual measure of uptake known as the Krenning score (43). The Krenning score uses a 4-point scale in which grade 1 indicates uptake less than in the liver; grade 2, uptake equal to that in the liver; grade 3, uptake greater than in the liver; and grade 4, uptake greater than in the spleen or kidneys. Generally, tumors should have a score of grade 2 or higher to be eligible for PRRT. Almost universally, tumors appear more prominent on ⁶⁸Ga-DOTATATE PET (43); nonetheless, the same scoring concept is used, although significant differences from ¹¹¹In-pentetreotide scans can be present.

Because the dose-limiting organs in PRRT are the kidneys (44), it is desirable to have normal renal function (glomerular filtration rate > 50 mL/h) before treatment. Furthermore, adequate liver and bone marrow function should be documented, with the typical parameters being a hemoglobin level higher than 8 g/dL, a white blood cell count higher than 2.0 K/ μ L, a platelet count higher than 70 K/ μ L, and a total bilirubin level lower than 3 times the upper limit of normal (41).

Most guidelines recommend stopping short- and long-acting octreotide for at least 24 h and 3–4 wk, respectively, before ⁹⁰Y- or ¹⁷⁷Lu-DOTA-somatostatin analog administration because of the risk of competition for, or blocking of, uptake. However, recent studies indicate that octreotide administration does not decrease tumor accumulation of ⁶⁸Ga-DOTATATE, although decreases in normal spleen, liver, and thyroid uptake were observed (45,46).

PRRT Administration

Early ⁹⁰Y-DOTATOC studies showed cases of acute renal failure related to reabsorption and retention of the agent by the proximal renal tubules (44). However, administration of amino acid solutions containing lysine and arginine blocked renal uptake by approximately 40% (47,48). Although initial protocols used commercially available amino acid mixtures such as Clinisol (Baxter International Inc.) and Aminosyn II (Abbott Laboratories), solutions containing only lysine and arginine (18–25 g total of each, 1–2 L, osmolality \leq 1,050 mOsmol) minimize nausea and vomiting and are now preferred (41). Patients are pretreated with antiemetics followed by a continuous infusion of amino acids starting 30 min before ¹⁷⁷Lu-DOTATATE and continued during and after treatment for a total of approximately 4 h until the entire solution has been infused.

Measured exposure rates from patients treated with 7.4 GBq of ¹⁷⁷Lu-DOTATATE are low (under 4 mR/h at 1 min), resulting in doses to the public and caregivers of less than 0.5 cGy per year, thus allowing for outpatient treatment in the United States (49).

Clinical Experience with PRRT in Pheochromocytoma and Paraganglioma

⁹⁰Y-DOTATOC and ⁹⁰Y-DOTATATE are not commercially available, and their use is limited to certain academic centers. In contrast, ¹⁷⁷Lu-DOTATATE has been approved as safe and effective in gastroenteropancreatic NETs. In pheochromocytoma and paraganglioma, small studies have also shown benefit with limited toxicity.

Supplemental Table 2 shows studies containing 5 or more patients receiving a ⁹⁰Y- or ¹⁷⁷Lu-DOTA-somatostatin analog for metastatic or inoperable pheochromocytoma or paraganglioma. A metaanalysis found similar response rates between ⁹⁰Y-DOTATOC and ¹⁷⁷Lu-DOTATATE, with 25% of patients demonstrating an objective response; 61%, a clinical response; and 84%, biochemical

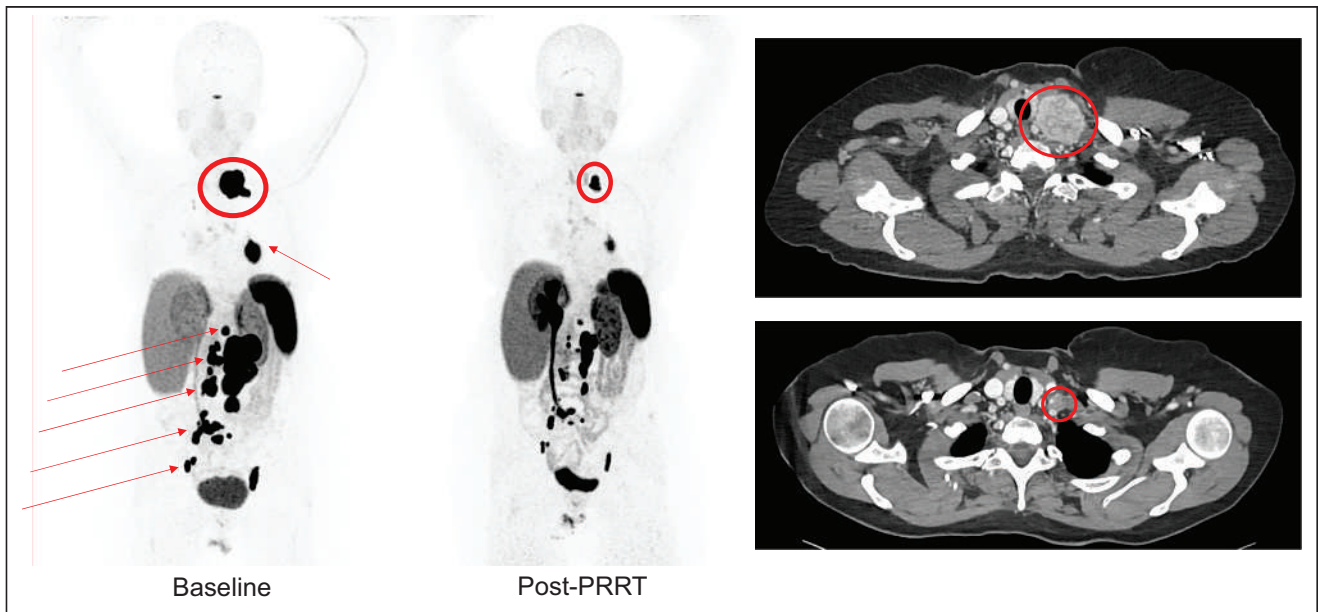


FIGURE 3. A 53-y-old woman with metastatic hormone-secreting *SDHB*-associated pheochromocytoma. Maximal-intensity-projection images of ^{68}Ga -DOTATATE at baseline (left) vs. 12 mo after PRRT with 7.4 GBq of ^{177}Lu -DOTATATE 4 times (middle) demonstrate significant decrease in tracer uptake in tumors in neck (encircled), left hilum, retroperitoneum, and pelvis (arrows). Baseline axial CT image (top right) through neck demonstrates large left supraclavicular mass at baseline (encircled), and post-PRRT axial CT image (bottom right) shows significant decrease in tumor size (encircled).

improvement. Estimated overall survival was 54.5 mo, and mean progression-free survival was 37.1 mo (50). Reports using ^{177}Lu -DOTATATE have demonstrated significant partial regressions and stable disease as determined by anatomic imaging, as well as significant biochemical and symptomatic responses (Supplemental Table 2). Representative examples of pre- and post-PRRT ^{68}Ga -DOTATATE and CT images are shown in Figure 3.

Dosimetry

The target organs for PRRT toxicity are the kidneys and bone marrow, as has been defined for nonpheochromocytoma and nonparaganglioma NETs. Bone marrow toxicity with a 50% drop in platelet counts is associated with a marrow dose of 2 Gy (51,52). Although a limit of 23-Gy cumulative absorbed dose can be used to avoid toxicity to the kidneys with biologically effective dose determinations, these limits could be better defined (52). Furthermore, other defined renal limits for patients with risk factors (28 Gy) may be lower than for those without risk factors (40 Gy) (53).

At present, we recommend that 7.4 GBq every 8 wk for 4 cycles, as approved by the FDA for gastroenteropancreatic NETs, also be used in patients with metastatic or inoperable pheochromocytoma or paraganglioma. Although there are no requirements for dosimetry, it should be considered if higher activities are administered. Groups that treat with more than 7.4 GBq/cycle or more than 4 cycles use dosimetry to limit the radiation dose to 23 Gy to the kidneys and less than 2 Gy to the bone marrow and have been able to administer up to 11 cycles with a maximum cumulative activity of 81.4 GBq versus the 29.6 GBq recommended in the package insert (54).

Response Evaluation with PRRT

Evaluating response to PRRT can be challenging. Morphologic criteria such as RECIST 1.1 are the most frequently used, but anatomic changes often lag behind functional changes in pheochromocytoma and paraganglioma and may be better detected using ^{68}Ga -DOTATATE, ^{18}F -FDG, or other functional PET

radiopharmaceuticals (55). Another issue is pseudoprogression, in which 9% of patients with RECIST-stable disease evidenced transient increases in tumor size by more than 10% at 6 wk after treatment (56). Three months appears to be the optimal time to determine treatment response. Changes in clinical status should guide the timing and interval of reevaluation.

Side Effects and Toxicity Profile

Although the toxicity profiles for ^{90}Y - and ^{177}Lu -PRRT have been characterized in patients with NETs, we feel that the toxicity profile in pheochromocytoma and paraganglioma is similar (57). Nonetheless, patients with pheochromocytoma or paraganglioma are at higher risk for certain side effects such as catecholamine release syndrome and tumor lysis syndrome (13,14).

A long-term follow-up study of patients receiving ^{90}Y -DOTATOC versus ^{177}Lu -DOTATATE with nephroprotection in NET found a slightly greater drop in renal function over time for ^{90}Y -DOTATOC than for ^{177}Lu -DOTATATE (58), although the overall incidence was low. In the pivotal NETTER-1 trial of ^{177}Lu -DOTATATE in gastroenteropancreatic NET, renal failure of all grades occurred in 12% of patients, with 3% having grade 3 or 4 toxicity. In pheochromocytoma and paraganglioma reports, approximately 9% had renal toxicity higher than grade 3 (59).

Hematologic side effects are usually mild. The incidence of anemia in the NETTER-1 trial was 81% overall, with no grade 3–4 events. Thrombocytopenia and neutropenia of any grade occurred in 53% and 26% of patients, with grade 3–4 events in 1% and 3%, respectively. Grade 3 and 4 decreases in lymphocytes are frequent but do not require dose modifications (60). However, myelodysplastic syndrome or acute leukemia was reported in 3.4% of patients with nonpheochromocytoma or nonparaganglioma (61). In patients with pheochromocytoma or paraganglioma treated with PRRT, the incidence of myelodysplasia is similarly low, ranging from 2.5% to 8.3% (14,62,63).

Summary

The available retrospective data considering PRRT in metastatic or inoperable pheochromocytoma and paraganglioma show promise. Although complete responses as defined by RECIST have not been reported, a significant number of patients are able to achieve partial responses, and many have stable disease. Side effects are generally mild and well tolerated. An ongoing prospective phase II clinical trial (NCT03206060) of patients with sporadic or *SDHx*-related metastatic or inoperable pheochromocytoma or paraganglioma with clear evidence of progression receiving 7.4 GBq of ¹⁷⁷Lu-DOTA-TATE every 8 wk (4 cycles) is ongoing. Preliminary evaluation after 2 cycles of treatment using functional imaging in 11 patients has shown promising results (64). Until final results are available, the National Comprehensive Cancer Network recommendations indicate that the use of ¹⁷⁷Lu-DOTA-TATE with the activity and schedule stated in the package insert may be beneficial to many patients with metastatic or inoperable pheochromocytoma or paraganglioma.

If tumor uptake of ¹⁷⁷Lu-DOTA-TATE and ¹³¹I-MIBG are equally good, the selection of radiopharmaceutical for RPT will rely on other considerations (65).

CONCLUSION

Currently, ¹³¹I-MIBG and PRRT are 2 RPT approaches that have shown efficacy in patients with metastatic or inoperable pheochromocytoma or paraganglioma, with acceptable toxicity profiles. Once the decision to use RPT is made, one must decide which of these 2 approaches to pursue. The first consideration is based on the degree of tumor localization of radiolabeled MIBG or DOTA-somatostatin analog. Given that disparate imaging results are not uncommon, this consideration will often inform the selection. However, if both tracers demonstrate good localization, other considerations, including cost, whether the treatment is inpatient or outpatient, and preexisting organ toxicities such as renal abnormalities or marrow toxicity, must be considered to pair each patient with the optimal radiopharmaceutical.

REFERENCES

1. Berends AMA, Buitenwerf E, de Krijger RR, et al. Incidence of pheochromocytoma and sympathetic paraganglioma in The Netherlands: a nationwide study and systematic review. *Eur J Intern Med.* 2018;51:68–73.
2. Lam AK. Update on adrenal tumours in 2017 World Health Organization (WHO) of endocrine tumours. *Endocr Pathol.* 2017;28:213–227.
3. Carrasquillo JA, Chen CC, Jha A, et al. Imaging of pheochromocytoma and paraganglioma. *J Nucl Med.* 2021;62:1033–1042.
4. Turkova H, Prodanov T, Maly M, et al. Characteristics and outcomes of metastatic SDHB and sporadic pheochromocytoma/paraganglioma: an National Institutes of Health study. *Endocr Pract.* 2016;22:302–314.
5. Sisson JC, Shulkin BL, Esfandiari NH. Courses of malignant pheochromocytoma: implications for therapy. *Ann N Y Acad Sci.* 2006;1073:505–511.
6. Hescot S, Curras-Freixes M, Deutschbein T, et al. Prognosis of malignant pheochromocytoma and paraganglioma (MAPP-Prone Study): A European Network for the Study of Adrenal Tumors retrospective study. *J Clin Endocrinol Metab.* 2019;104:2367–2374.
7. Crona J, Lamarca A, Ghosal S, Welin S, Skogseid B, Pacak K. Genotype-phenotype correlations in pheochromocytoma and paraganglioma: a systematic review and individual patient meta-analysis. *Endocr Relat Cancer.* 2019;26:539–550.
8. Hescot S, Leboulleux S, Amar L, et al. One-year progression-free survival of therapy-naive patients with malignant pheochromocytoma and paraganglioma. *J Clin Endocrinol Metab.* 2013;98:4006–4012.
9. Niemeijer ND, Alblas G, van Hulsteijn LT, Dekkers OM, Corssmit EP. Chemotherapy with cyclophosphamide, vincristine and dacarbazine for malignant paraganglioma and pheochromocytoma: systematic review and meta-analysis. *Clin Endocrinol (Oxf).* 2014;81:642–651.

10. O’Kane GM, Ezzat S, Joshua AM, et al. A phase 2 trial of sunitinib in patients with progressive paraganglioma or pheochromocytoma: the SNIPP trial. *Br J Cancer.* 2019;120:1113–1119.
11. Vogel J, Atanacio AS, Prodanov T, et al. External beam radiation therapy in treatment of malignant pheochromocytoma and paraganglioma. *Front Oncol.* 2014;4:166.
12. Pacak K. Preoperative management of the pheochromocytoma patient. *J Clin Endocrinol Metab.* 2007;92:4069–4079.
13. Makis W, McCann K, McEwan AJ. The challenges of treating paraganglioma patients with ¹⁷⁷Lu-DOTA-TATE PRRT: catecholamine crises, tumor lysis syndrome and the need for modification of treatment protocols. *Nucl Med Mol Imaging.* 2015;49:223–230.
14. Zandee WT, Feelders RA, Smit Duijzentkunst DA, et al. Treatment of inoperable or metastatic paragangliomas and pheochromocytomas with peptide receptor radionuclide therapy using ¹⁷⁷Lu-DOTA-TATE. *Eur J Endocrinol.* 2019;181:45–53.
15. Gonias S, Goldsby R, Matthay KK, et al. Phase II study of high-dose [¹³¹I]metaiodobenzylguanidine therapy for patients with metastatic pheochromocytoma and paraganglioma. *J Clin Oncol.* 2009;27:4162–4168.
16. Wieland DM, Wu JI, Brown LE, Mangner TJ, Swanson DP, Beierwaltes WH. Radiolabeled adrenergic neuron-blocking agents - adrenomedullary imaging with [¹³¹I]iodobenzylguanidine. *J Nucl Med.* 1980;21:349–353.
17. Carrasquillo JA, Pandit-Taskar N, Chen CC. Radionuclide therapy of adrenal tumors. *J Surg Oncol.* 2012;106:632–642.
18. Mairs RJ, Russell J, Cunningham S, et al. Enhanced tumor uptake and in-vitro radiotoxicity of no-carrier-added [¹³¹I] metaiodobenzylguanidine: implications for the targeted radiotherapy of neuroblastoma. *Eur J Cancer.* 1995;31A:576–581.
19. Barrett JA, Joyal JL, Hillier SM, et al. Comparison of high-specific-activity Ultratrace ¹²³/¹³¹I-MIBG and carrier-added ¹²³/¹³¹I-MIBG on efficacy, pharmacokinetics, and tissue distribution. *Cancer Biother Radiopharm.* 2010;25:299–308.
20. Noto RB, Pryma DA, Jensen J, et al. Phase 1 study of high-specific-activity I-131 MIBG for metastatic and/or recurrent pheochromocytoma or paraganglioma. *J Clin Endocrinol Metab.* 2018;103:213–220.
21. Pryma DA, Chin BB, Noto RB, et al. Efficacy and safety of high-specific-activity ¹³¹I-MIBG therapy in patients with advanced pheochromocytoma or paraganglioma. *J Nucl Med.* 2019;60:623–630.
22. Coleman RE, Stubbs JB, Barrett JA, de la Guardia M, Lafrance N, Babich JW. Radiation dosimetry, pharmacokinetics, and safety of Ultratrace iobenguane I-131 in patients with malignant pheochromocytoma/paraganglioma or metastatic carcinoma. *Cancer Biother Radiopharm.* 2009;24:469–475.
23. Owens J, Bolster AA, Prosser JE, et al. No-carrier-added ¹²³I-MIBG: an initial clinical study in patients with pheochromocytoma. *Nucl Med Commun.* 2000;21:437–440.
24. Giammarile F, Chiti A, Lassmann M, Brans B, Flux G. EANM. EANM procedure guidelines for ¹³¹I-meta-iodobenzylguanidine (¹³¹I-mIBG) therapy. *Eur J Nucl Med Mol Imaging.* 2008;35:1039–1047.
25. Shapiro B, Sisson IC, Wieland DM, et al. Radiopharmaceutical therapy of malignant pheochromocytoma with [¹³¹I]metaiodobenzylguanidine: results from ten years of experience. *J Nucl Biol Med.* 1991;35:269–276.
26. Mukherjee JJ, Kaltsas GA, Islam N, et al. Treatment of metastatic carcinoma tumours, pheochromocytoma, paraganglioma and medullary carcinoma of the thyroid with ¹³¹I-meta-iodobenzylguanidine [¹³¹I-mIBG]. *Clin Endocrinol (Oxf).* 2001;55:47–60.
27. Gedik GK, Hoefnagel CA, Bais E, Olmos RA. ¹³¹I-MIBG therapy in metastatic pheochromocytoma and paraganglioma. *Eur J Nucl Med Mol Imaging.* 2008;35:725–733.
28. Wakabayashi H, Taki J, Inaki A, et al. Prognostic values of initial responses to low-dose ¹³¹I-MIBG therapy in patients with malignant pheochromocytoma and paraganglioma. *Ann Nucl Med.* 2013;27:839–846.
29. Safford SD, Coleman RE, Gockerman JP, et al. Iodine-131 metaiodobenzylguanidine is an effective treatment for malignant pheochromocytoma and paraganglioma. *Surgery.* 2003;134:956–962.
30. Thorpe MP, Kane A, Zhu J, Morse MA, Wong T, Borges-Neto S. Long-term outcomes of 125 patients with metastatic pheochromocytoma or paraganglioma treated with ¹³¹I-MIBG. *J Clin Endocrinol Metab.* 2020;105:E494–E501.
31. Castellani MR, Seghezzi S, Chiesa C, et al. ¹³¹I-MIBG treatment of pheochromocytoma: low versus intermediate activity regimens of therapy. *Q J Nucl Med Mol Imaging.* 2010;54:100–113.
32. Schlumberger M, Gicquel C, Lumbroso J, et al. Malignant pheochromocytoma: clinical, biological, histologic and therapeutic data in a series of 20 patients with distant metastases. *J Endocrinol Invest.* 1992;15:631–642.
33. Kotecka-Blicharz A, Hasse-Lazar K, Handkiewicz-Junak D, et al. ¹³¹I MIBG therapy of malignant pheochromocytoma and paraganglioma tumours: a single-centre study. *Endokrynol Pol.* 2018;69:246–251.

34. Yoshinaga K, Oriuchi N, Wakabayashi H, et al. Effects and safety of ¹³¹I-metaiodobenzylguanidine (MIBG) radiotherapy in malignant neuroendocrine tumors: results from a multicenter observational registry. *Endocr J*. 2014;61:1171–1180.
35. Loh KC, Fitzgerald PA, Matthey KK, Yeo PP, Price DC. The treatment of malignant pheochromocytoma with iodine-131 metaiodobenzylguanidine (¹³¹I-MIBG): a comprehensive review of 116 reported patients. *J Endocrinol Invest*. 1997;20:648–658.
36. van Hulsteijn LT, Niemeijer ND, Dekkers OM, Corssmit EP. ¹³¹I-MIBG therapy for malignant paraganglioma and pheochromocytoma: systematic review and meta-analysis. *Clin Endocrinol (Oxf)*. 2014;80:487–501.
37. Krempf M, Lumbroso J, Mornex R, et al. Use of m-[¹³¹I]iodobenzylguanidine in the treatment of malignant pheochromocytoma. *J Clin Endocrinol Metab*. 1991;72:455–461.
38. Pryma D, Divigi C. Meta-iodobenzyl guanidine for detection and staging of neuroendocrine tumors. *Nucl Med Biol*. 2008;35(suppl 1):S3–S8.
39. Rutherford MA, Rankin AJ, Yates TM, et al. Management of metastatic pheochromocytoma and paraganglioma: use of iodine-131-meta-iodobenzylguanidine therapy in a tertiary referral centre. *QJM*. 2015;108:361–368.
40. Shilkrut M, Bar-Deroma R, Bar-Sela G, Berniger A, Kuten A. Low-dose iodine-131 metaiodobenzylguanidine therapy for patients with malignant pheochromocytoma and paraganglioma: single center experience. *Am J Clin Oncol*. 2010;33:79–82.
41. Hope TA, Abbott A, Colucci K, et al. NANETS/SNMMI procedure standard for somatostatin receptor-based peptide receptor radionuclide therapy with ¹⁷⁷Lu-DOTATATE. *J Nucl Med*. 2019;60:937–943.
42. Shah MH, Goldner WS, Halfdanarson TR, et al. NCCN guidelines insights: neuroendocrine and adrenal tumors, version 2.2018. *J Natl Compr Canc Netw*. 2018;16:693–702.
43. Hope TA, Calais J, Zhang L, Dieckmann W, Millo C. ¹¹¹In-pentetreotide scintigraphy versus ⁶⁸Ga-DOTATATE PET: impact on Krenning scores and effect of tumor burden. *J Nucl Med*. 2019;60:1266–1269.
44. Otte A, Herrmann R, Heppeler A, et al. Yttrium-90 DOTATOC: first clinical results. *Eur J Nucl Med*. 1999;26:1439–1447.
45. Aalbersberg EA, de Wit-van der Veen BJ, Versleijen MWJ, et al. Influence of lanreotide on uptake of ⁶⁸Ga-DOTATATE in patients with neuroendocrine tumours: a prospective intra-patient evaluation. *Eur J Nucl Med Mol Imaging*. 2019;46:696–703.
46. Ayati N, Lee ST, Zakavi R, et al. Long-acting somatostatin analog therapy differentially alters ⁶⁸Ga-DOTATATE uptake in normal tissues compared with primary tumors and metastatic lesions. *J Nucl Med*. 2018;59:223–227.
47. Hammond PJ, Wade AF, Gwilliam ME, et al. Amino acid infusion blocks renal tubular uptake of an indium-labelled somatostatin analogue. *Br J Cancer*. 1993;67:1437–1439.
48. Mogensen CE, Sølling K. Studies on renal tubular protein reabsorption: partial and near complete inhibition by certain amino acids. *Scand J Clin Lab Invest*. 1977;37:477–486.
49. Calais PJ, Turner JH. Radiation safety of outpatient ¹⁷⁷Lu-octreotate radiolabeled therapy of neuroendocrine tumors. *Ann Nucl Med*. 2014;28:531–539.
50. Satapathy S, Mittal BR, Bhansali A. Peptide receptor radionuclide therapy in the management of advanced pheochromocytoma and paraganglioma: a systematic review and meta-analysis. *Clin Endocrinol (Oxf)*. 2019;91:718–727.
51. Walrand S, Barone R, Pauwels S, Jamar F. Experimental facts supporting a red marrow uptake due to radiometal transchelation in ⁹⁰Y-DOTATOC therapy and relationship to the decrease of platelet counts. *Eur J Nucl Med Mol Imaging*. 2011;38:1270–1280.
52. Eberlein U, Cremonesi M, Lassmann M. Individualized dosimetry for theranostics: necessary, nice to have, or counterproductive? *J Nucl Med*. 2017;58(suppl 2):97S–103S.
53. Bodei L, Cremonesi M, Ferrari M, et al. Long-term evaluation of renal toxicity after peptide receptor radionuclide therapy with ⁹⁰Y-DOTATOC and ¹⁷⁷Lu-DOTATATE: the role of associated risk factors. *Eur J Nucl Med Mol Imaging*. 2008;35:1847–1856.
54. Vyakaranam AR, Crona J, Norlen O, et al. Favorable outcome in patients with pheochromocytoma and paraganglioma treated with ¹⁷⁷Lu-DOTATATE. *Cancers (Basel)*. 2019;11:909.
55. Nakazawa A, Higuchi T, Oriuchi N, Arisaka Y, Endo K. Clinical significance of 2-F-18 fluoro-2-deoxy-D-glucose positron emission tomography for the assessment of I-131-metaiodobenzylguanidine therapy in malignant pheochromocytoma. *Eur J Nucl Med Mol Imaging*. 2011;38:1869–1875.
56. Brabander T, van der Zwan WA, Teunissen JJM, et al. Long-term efficacy, survival, and safety of [¹⁷⁷Lu-DOTA⁰, Tyr³]octreotate in patients with gastroenteropancreatic and bronchial neuroendocrine tumors. *Clin Cancer Res*. 2017;23:4617–4624.
57. Strosberg J, El-Haddad G, Wolin E, et al. Phase 3 trial of ¹⁷⁷Lu-Dotatate for midgut neuroendocrine tumors. *N Engl J Med*. 2017;376:125–135.
58. Valkema R, Pauwels SA, Kvols LK, et al. Long-term follow-up of renal function after peptide receptor radiation therapy with ⁹⁰Y-DOTA⁰, Tyr³-octreotide and ¹⁷⁷Lu-DOTA⁰, Tyr³-octreotate. *J Nucl Med*. 2005;46(suppl 1):83S–91S.
59. Nastos K, Cheung VTF, Toumpanakis C, et al. Peptide receptor radionuclide treatment and ¹³¹I-MIBG in the management of patients with metastatic/progressive pheochromocytomas and paragangliomas. *J Surg Oncol*. 2017;115:425–434.
60. Kong G, Grozinsky-Glasberg S, Hofman MS, et al. Efficacy of peptide receptor radionuclide therapy for functional metastatic paraganglioma and pheochromocytoma. *J Clin Endocrinol Metab*. 2017;102:3278–3287.
61. Bodei L, Kidd M, Paganelli G, et al. Long-term tolerability of PRRT in 807 patients with neuroendocrine tumours: the value and limitations of clinical factors. *Eur J Nucl Med Mol Imaging*. 2015;42:5–19.
62. van Essen M, Krenning EP, Kooij PP, et al. Effects of therapy with ¹⁷⁷Lu-DOTA⁰, Tyr³ octreotate in patients with paraganglioma, meningioma, small cell lung carcinoma, and melanoma. *J Nucl Med*. 2006;47:1599–1606.
63. Imhof A, Brunner P, Marincek N, et al. Response, survival, and long-term toxicity after therapy with the radiolabeled somatostatin analogue [⁹⁰Y-DOTA]-TOC in metastasized neuroendocrine cancers. *J Clin Oncol*. 2011;29:2416–2423.
64. Lindenberg L, Carrasquillo J, del Rivero J, et al. Comparison of ¹⁸F-FDG and ⁶⁸Ga-DOTATATE before and after two cycles of PRRT [abstract]. *J Nucl Med*. 2019;60(suppl 1):1521.
65. Jha A, Taieb D, Carrasquillo JA, et al. High-specific-activity-¹³¹I-MIBG versus ¹⁷⁷Lu-DOTATATE targeted radionuclide therapy for metastatic pheochromocytoma and paraganglioma. *Clin Cancer Res*. 2021;27:2989–2995.
66. Carrasquillo JA, Pandit-Taskar N, Chen CC. I-131 metaiodobenzylguanidine therapy of pheochromocytoma and paraganglioma. *Semin Nucl Med*. 2016;46:203–214.

Current Landscape in Clinical Pretargeted Radioimmunoimaging and Therapy

Vilma I.J. Jallinoja^{1,2} and Jacob L. Houghton¹

¹Department of Radiology, Stony Brook University, Stony Brook, New York; and ²Chemical and Physical Biology Graduate Program, Vanderbilt University, Nashville, Tennessee

The principle of pretargeted radioimmunoimaging and therapy has been investigated over the past 30 y in preclinical and clinical settings with the aim of reducing the radiation burden of healthy tissue for antibody-based nuclear medicine techniques. In the past few decades, 4 pretargeting methodologies have been proposed, and 2 of them—the bispecific antibody–haptent and the streptavidin–biotin platforms—have been evaluated in humans in phase 1 and 2 studies. With this review article, we aim to survey clinical pretargeting studies in order to understand the challenges that these platforms have faced in human studies and to provide an overview of how the clinical approval of the pretargeting system has proceeded in the past several decades. Additionally, we will discuss the successes of the pretargeting human studies and compare and highlight the pretargeting approaches and conditions that will advance clinical translation of the pretargeting platform in the future.

Key Words: molecular imaging; PET; radioimmunoimaging; radionuclide therapy; radiopharmaceuticals; PET imaging; pretargeting; radioimmunotherapy

J Nucl Med 2021; 62:1200–1206

DOI: 10.2967/jnumed.120.260687

Pretargeted nuclear imaging and therapy is an alternative approach for conventional antibody-based nuclear medicine techniques (1). Pretargeting combines the specificity of a tumor-targeting antibody with the pharmacokinetic profile of a radiolabeled small molecule (radioligand) to reduce the overall radiation dose associated with directly radiolabeled antibody nuclear medicine agents. In 1985, Reardan et al. first introduced the concept of pretargeting in which a preadministered tumor-targeting antibody interacts in vivo with high specificity with a small molecule radioligand, commonly referred to as *bioorthogonal* reactivity (2). They reported a preclinical study of successful pretargeting using a bispecific antibody (bsAb) targeting a tumor antigen and an ethylenediaminetetraacetic acid chelate complex radioligand. Two years later, in 1987, Hnatowich et al. reported the use of another pretargeting approach in a preclinical model in which the pretargeting interaction between the tumor-bound antibody and the radioligand occurred via high-affinity avidin–biotin association (3). In total, 4 pretargeting mechanisms have been proposed and evaluated in vivo in preclinical studies (Fig. 1), and these have been reviewed by other groups previously (1,4).

To date, the streptavidin–biotin and the bsAb–haptent pretargeting platforms are the only systems that have been evaluated in humans. Since the first reported human studies of the streptavidin–biotin and bsAb–haptent approaches in 1990 and 1993, respectively (5,6), more than 30 reports describing original pretargeting studies in humans have been published (Fig. 2). Both approaches have proven capable of lowering the radiation burden to healthy tissue compared with conventional antibody-based nuclear medicine. In this review, we discuss the challenges and successes of both of the approaches in the clinic and what possible directions upcoming pretargeting strategies need to take to result in a first clinical application of the approach.

STREPTAVIDIN–BIOTIN PLATFORM IN THE CLINIC

The strong noncovalent interaction between streptavidin and biotin ($K \sim 10^{14} \text{ M}^{-1}$) has made the molecule pair desirable for many applications in biomedicine, and the pair has been applied to pretargeting as well. The streptavidin–biotin approach has been evaluated in humans for pretargeted scintigraphy (5,7) and radioimmunotherapy (Table 1) (8–13). Most of the pretargeted streptavidin–biotin human studies have been performed using full-length tumor-targeting antibodies conjugated with either biotin or streptavidin along with a clearing agent (CA) that is given before the biotin radioligand administration.

At the turn of the millennium, multiple human studies were performed evaluating pretargeted ⁹⁰Y radioimmunotherapy in patients with non-Hodgkin lymphoma, glioma, and gastrointestinal carcinoma. In 1999, Paganelli et al. produced the first set of promising results showing reduction of tumor burden in 25% of their high-grade glioma patients after 1 cycle of pretargeted ⁹⁰Y-biotin radioligand (8). Later, Paganelli et al. also reported an overall 25% response rate in recurrent grade II glioma and anaplastic astrocytoma patient cohorts (14). Around the same time, Grana et al. published a pretargeted ⁹⁰Y radioimmunotherapy study in high-grade glioma patients resulting in a median survival of 33.5 mo compared with the 8 mo of the control cohort (15). These promising results established the feasibility of the approach in human therapy and led to greater interest in the pretargeting concept, accelerating research in the field.

Almost all the clinical trials that have been performed using a 3-step method have included the use of a streptavidin or avidin or a biotin–galactose–based CA (10,12,16). The use of biotin–galactose derivatives as CAs before radioligand injection has been shown to dramatically decrease the presence of accessible antibody conjugate in the blood pool and to efficiently decrease the required lag time between the antibody and radioligand administrations (10,12). Interestingly, despite the use of the 3-step approach and

Received Dec. 31, 2020; revision accepted Mar. 26, 2021.
For correspondence or reprints, contact Jacob Houghton (jacob.houghton@stonybrookmedicine.edu).
Published online May 20, 2021.
COPYRIGHT © 2021 by the Society of Nuclear Medicine and Molecular Imaging.

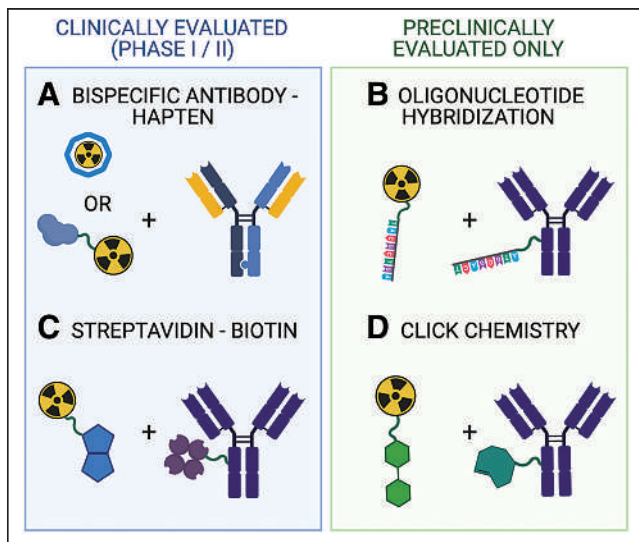


FIGURE 1. Pretargeting agents of the 4 main platforms that have been evaluated in clinical (A and C) or only in preclinical settings (B and D).

the evidence of its effect in reducing the antibody concentration in the blood pool, hematologic toxicity has appeared as a reoccurring difficulty in the streptavidin and biotin-based ^{90}Y pretargeted radioimmunotherapy studies (8,9,15). To address the issue, Breitz et al. reported the effects of different pretargeting parameters by adjusting the interval time and the dosing of the streptavidin-antibody conjugate, CA, and ^{90}Y -biotin (16). This optimization produced a pretargeting protocol that resulted in no hematologic toxicities in their patient population with various adenocarcinomas. However, the study did not report whether the optimized protocol resulted in a tumor uptake sufficient enough to show a clinical response.

In addition to the challenges with hematologic toxicity, the streptavidin-biotin platform has been marked by high incidence of immune response to the streptavidin- and avidin-based pretargeting agents. Development of anti-streptavidin or anti-avidin antibodies in patients has been observed in all of the clinical trials that reported an investigation of their immunogenicity studies (5,7-10,12-14,16). Despite several clinical evaluations of the platform's safety and efficacy, the immunogenicity of the pretargeting agents has not been addressed. Preclinical investigation of the platform is still ongoing, but its clinical evaluation has ceased with the last reported clinical trial in 2005.

bsAb-HAPTEN PLATFORM IN THE CLINIC

In addition to the streptavidin-biotin methodology, the bsAb-hapten platform has been widely studied in the clinical setting (Table 2). Two different strategies for bsAb-hapten pretargeting approaches have been studied clinically. Starting in 1993, with the first clinical trial of bsAb-hapten pretargeting approach, most clinical trials have used fragmented bispecific antibodies (Fab-Fab' along with a radiolabeled mono- or bivalent chelate complex serving as radioligand). This contrasts with the use of a CA as with the streptavidin-biotin system. The use of fragmented antibodies leads to a more rapid blood-pool clearance of the antibody construct because of the smaller size. Additionally, upon elimination of the Fc region, the antibody fragment negates the interaction with the neonatal Fc receptor, further reducing the circulating half-life of the constructs. The overall effect of this approach is reduced intervals between

administration of the targeting construct and radioligand, reduced potential for hematologic toxicity, and presumably an improvement in tumor-to-tissue uptake ratios.

In 2013, Schoffelen et al. reported the use of a bispecific trivalent antibody construct (Tri-Fab) in tandem with a histamine-succinylglycine (HSG) peptide-based hapten radioligand. Since then, all the reported bsAb-hapten clinical trials have used the Tri-Fab-HSG-hapten strategy. When the 2 approaches are compared, the Tri-Fab-HSG-hapten strategy has shown more promising results, providing excellent specificity and sensitivity for pretargeted PET imaging for patients with varying cancer profiles. Additionally, one of the major advantages of using peptide-based haptens, compared with the chelate complex haptens, is the ability to design a library of peptide haptens accompanied with different radionuclides with lowered risk of changing the haptens' binding to the antibody.

To date, the evaluation of the Tri-Fab-HSG-hapten approach in humans has included the use of only 1 antibody construct, a carcinoembryonic antigen (CEA) targeting humanized Tri-Fab bsAb called TF2 (NCT00860860) (17,18). This trivalent bsAb TF2 construct has been tested along with an HSG hapten called IMP288 for pretargeted PET imaging (^{68}Ga -IMP288) ((19-21); NCT01730638, NCT01730612) and radioimmunotherapy ($^{111}\text{In}/^{177}\text{Lu}$ -IMP288) ((17,18,22); NCT00860860, NCT01221675) in patients with colorectal cancer, medullary thyroid carcinoma, epidermal growth factor receptor 2-negative breast cancer and metastatic lung cancer. ^{90}Y - and ^{111}In -radiolabeled derivatives of IMP288 are being tested in a clinical setting as well ((20); NCT02587247, NCT02300922). The most recent work with the TF2- ^{68}Ga -IMP288 pretargeting pair has resulted in higher sensitivity and specificity in detecting tumor lesions in metastatic colorectal cancer patients compared with ^{18}F -FDG PET ((20); NCT02587247). The CEA-targeted pretargeting pair was also shown to be highly capable of detecting lesions in patients with human epidermal growth factor receptor 2-negative metastatic breast cancer ((21); NCT01730612). In that setting, the pretargeted immuno-PET showed higher overall sensitivity (94.7%) relative to ^{18}F -FDG PET (89.6%) (Fig. 3). The number of true-positive lesions detected in lymph nodes, bone, and liver was higher using immuno-PET than ^{18}F -FDG PET. Those exciting results have clearly exhibited the potential for pretargeted PET imaging in cancer.

As mentioned earlier, immunogenic response to the pretargeting agents has been a limitation of the streptavidin-biotin system. Immunogenicity of the bsAb constructs has been observed in the bsAb-hapten platform as well. Barbet et al. reported that a high percentage of their patients (61%) developed human antimouse antibodies (HAMA) when a fully murine anti-CEA \times anti-diethylenetriaminepentaacetic acid (DTPA) bsAb was administered as part of the pretargeting protocol (23). More recent trials have used mouse-human Fab-Fab' bsAbs, which has decreased the prevalence of HAMA development in patients ((24); NCT00467506). Yet, development of human antihuman antibodies (HAHA) against mouse-human pretargeting bsAb agents has been shown to occur as well ((24-26); NCT00467506). bsAb fragments tend to suffer from aggregation issues, which can induce an immunogenic response (27). However, Barbet et al. observed formation of high-molecular-weight aggregates and noticed a decrease in the HAMA induction after improving the production and purification process of the antibody fragment, indicating this problem can be overcome by appropriate formulation (23). Furthermore, premedication with an antihistamine and corticosteroid has been shown to reduce the prevalence of immunogenic response in patients. Using this

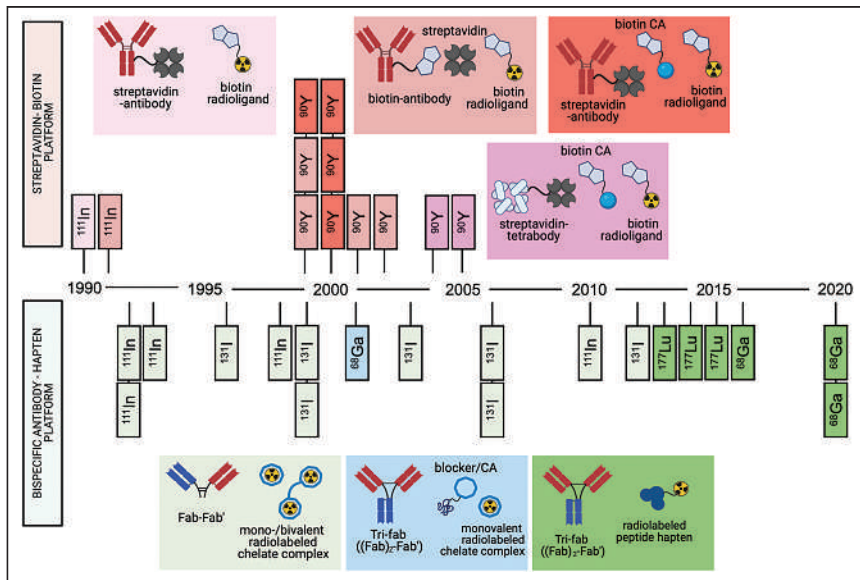


FIGURE 2. Timeline of clinical studies of bsAb and streptavidin–biotin pretargeting approaches. Each rectangle refers to a published report, with radionuclide note referring to primary radionuclide used in study. Pretargeting agents used in each report are color coded.

approach, Toucheffeu et al. reported that no patient ($n_{\text{total}} = 11$) developed HAHA in their TF2- ^{68}Ga -IMP288 pretargeted PET study ((20); NCT02587247). Rousseau et al. shared similar results, observing immunogenic response in only 16% of patients ($n_{\text{total}} = 23$) with the antihistamine and corticosteroid premedication ((21); NCT 01730612).

Many bsAb–hapten clinical trials have investigated the use of different pretargeting schedules and protocols to define the conditions that result in the highest tumor-to-background ratios and lowest radiation-induced toxicity ((17,19,22,25,28,29); NCT00860860, NCT01730638, NCT01221675). This is done by optimizing the amount of injected doses of each of the pretargeting components, the stoichiometric relation between these agents, and the interval time separating the administration of the doses. The interval time applied in the clinical pretargeting studies has varied between 1 and 7 d, and increasing the interval time has resulted in lower toxicity and better image quality to a certain extent. Schoffelen et al. showed that patients who received the ^{177}Lu -IMP288 hapten radioligand 1 d after TF2 antibody injection experienced significantly higher red marrow doses than patients who received the radioligand 5 d after antibody injection ((17); NCT00860860). Bodet-Milin et al. reported that increasing the interval time from 24 to 30 h decreased the mediastinum blood-pool values, whereas a 42-h delay time resulted in lower tumor SUV_{max} ($\text{T-SUV}_{\text{max}}$) and $\text{T-SUV}_{\text{max}}$ -to-mediastinum blood-pool ratios than the 30-h lag time ((19); NCT01730638).

From the point of view of adjusting both the interval time and the dosing, Kraeber-Bodéré et al. observed that a 5-d interval time resulted in a better tumor uptake of the hapten than the 7-d interval time. However, the tumor uptake increased and the tumor localization was visible even with the 7-d interval time when the bsAb dose was increased from 10 to 50 mg/m^2 (28). Certainly, one of the challenges for all of the pretargeting platforms is that each combination of target antigen, antibody construct, and radioligand requires its own pretargeting protocol, which will be a challenge when pretargeting is applied to a variety of different cancers for diagnostic and therapeutic purposes.

Surprisingly, direct comparison of pretargeted to the directly labeled approach using the same targeting molecule within the same patient population has not been performed extensively. Kraeber-Bodéré et al. have compared the dosimetry of a CEA-targeting ^{131}I -labeled bsAb with the pretargeted ^{131}I -hapten. The dosimetry of the ^{131}I -bsAb was determined first by scintigraphy over the several-day interval time, followed by an injection of the ^{131}I -hapten and study of its dosimetry (28). With 2 different pretargeting conditions (75 mg/m^2 ; 5-d interval or 100 mg/m^2 ; 7-d interval), the tumor-to-whole-body ratios were significantly higher for the pretargeted hapten compared with the directly labeled antibody. Additionally, the calculated tumor radiation doses were higher with the pretargeted ^{131}I -hapten than with the directly labeled ^{131}I -bsAb (3.9 and 2.0 Gy/GBq, respectively). The study showed that their pretargeting approach was superior to the directly labeled approach, with a tumor-to-whole-body ratio of 55:1 for pretargeting (75 mg/m^2 ; 5-d interval) and 16:1 for the conventional approach using just the ^{131}I -bsAb. Perhaps more importantly, the study was a good example of how to optimize a pretargeting platform to achieve success in patients.

Over the past 30 y, the bsAb–hapten platform has been studied consistently, and upcoming clinical trials using the TF2-IMP288 pretargeting strategy are planned (NCT02300922, NCT01730638). The recent work with the platform holds promise in solidifying the use of the pretargeting approach as an alternative to the use of directly radiolabeled antibodies.

DISCUSSION

Clinical investigations of pretargeted nuclear imaging and therapy have shown the utility of the pretargeting approach in overcoming the high overall radiation doses of conventional radioimmunodiagnosis and therapy. Both of the discussed pretargeting platforms are successful at lowering the overall radiation dose, but they both have hurdles to overcome if their full potential is to be realized. In the case of the streptavidin–biotin approach, the main challenge has been the immunogenicity of the streptavidin and avidin pretargeting constructs. During its 15-y period of separate clinical studies, the high prevalence of immunogenic response to the pretargeting agents was not addressed. Also, the addition of a third molecule (e.g., CA) to the pretargeting protocol makes it a more complicated approach, because of the need to optimize the CA dosing. These concerns compared with pretargeting platforms such as the bsAb–hapten system, which have been shown to work efficiently without a CA, put the streptavidin–biotin approach at a major disadvantage.

One major drawback of the bsAb–hapten approach is that it lacks modularity. The development of the HSG-haptens has been an improvement in this regard, but each bsAb agent targeting a different antigen of interest needs to be designed and engineered even if a clinical antibody already exists. The development of novel working

TABLE 1
Excerpts of Human Studies of Pretargeted Nuclear Medicine Using Streptavidin–Biotin System

Antibody radioligand pair and pretargeting timeline	Radioligand dose	Target antigen and study population	Main findings	Reference
<i>Hour 0:</i> Biotinylated antitenascin mAb BC4 <i>Hour 36:</i> (strept)avidin CA <i>Hour 54–60:</i> ⁹⁰ Y-DOTA-biotin	2.22–2.96 GBq/m ²	Tenascin and high-grade glioma patients	Reduction in tumor in 25% patients, all patients developed immune response.	(8)
<i>Hour 0:</i> SA-conjugated C2B8 mAb <i>Hour 34:</i> biotin CA <i>Hour 52:</i> ¹¹¹ In/ ⁹⁰ Y-DOTA-biotin	3–5 mCi (¹¹¹ In), 30–50 mCi/m ² (⁹⁰ Y)	CD20 and non-Hodgkin lymphoma patients	Good tumor-to-whole-body ratios (38:1), mild hematologic toxicity, 28% of patients with CR.	(12)
<i>Hour 0:</i> SA-conjugated NR-LU-10 mAb <i>Hour 24–72:</i> Biotin-galactose-HSA CA <i>Hour 28–96:</i> ¹¹¹ In/ ⁹⁰ Y-DOTA-biotin	185 MBq (¹¹¹ In), 370 MBq/m ² (⁹⁰ Y)	Ep-CAM and adenocarcinoma patients (majority colorectal and lung)	Good tumor-to-marrow absorbed dose ratio (63:1), all tested patients developed immune response.	(16)
<i>Hour 0:</i> Biotinylated antitenascin mAb BC4 <i>Hour 24:</i> avidin CA <i>Hour 42:</i> ⁹⁰ Y-DOTA-biotin (procedure repeated again 8–10 wk apart)	0.555–1.110 GBq	Tenascin and recurrent high-grade glioma, anaplastic astrocytoma patients	25% overall response to PRIT, no hematologic toxicity observed.	(14)
<i>Hour 0:</i> Biotinylated antitenascin mAb BC4 <i>Hour 24–36:</i> avidin CA <i>Hour 40–54:</i> ⁹⁰ Y-DOTA-biotin	2.2 GBq/m ²	Tenascin and high-grade glioma patients	Significantly higher OS in treated cohort than in control.	(15)
<i>Hour 0:</i> SA-conjugated CC49-(scFv) ₄ <i>Hour 48/72:</i> biotin CA <i>Hour 72/96:</i> ¹¹¹ In/ ⁹⁰ Y-DOTA-biotin	185 MBq (¹¹¹ In), 370 MBq/m ² (⁹⁰ Y)	TAG-72 and metastatic colorectal cancer	Tumor-to-normal-tissue dose ratio 54.5, immune response or toxicity not reported.	(11)

CR = complete response; SA = streptavidin; OS = overall survival.

bsAb agents is a time-consuming and costly process. Additionally, the bsAb constructs have faced a lot of challenges in their clinical translation, and currently only 2 bispecific antibodies are approved for clinical use (27). Because of the increasing need for antibody-based imaging and therapeutic nuclear agents, ideally the pretargeting agents need to be developed and manufactured efficiently and affordably in order to access a wide variety of different tumor antigens.

In addition to the 2 platforms discussed in this review, other promising pretargeting methodologies are moving toward clinical evaluation as well. In the last decade the inverse electron-demand Diels–Alder (IEDDA) click chemistry pretargeting approach has been shown to work well in preclinical models, delivering the radioligand to the target site with great specificity. As a result, the platform’s first clinical trials, which will notably not use a CA, are reported to start in 2021 (30). Compared with the bsAb-hapten approach, the click chemistry pretargeting components—a transcyclooctene-conjugated antibody and a tetrazene-based

radioligand—are highly modular, but the stability of the IEDDA pretargeting agents may prove a challenge for clinical translation (31,32). With the first clinical trials poised to begin within the year, the magnitude of this challenge will be revealed soon.

One of the main criticisms of all pretargeting approaches is the requisite use of noninternalizing or slowly internalizing antibodies, which limits the number of antibodies that can be used. Although the use of slowly internalizing antibodies such as CA19.9-targeting 5B1 and rapidly internalizing epidermal growth factor receptor–targeting cetuximab have been possible in a preclinical setting (33–35), it has yet to be reported in clinical studies. However, clinical translation will soon be attempted with the IEDDA-based approach and the slowly internalizing 5B1 antibody, which will help to determine more concretely what is possible in patients. It should also be noted that the process of antigen–antibody internalization is not always absolute. In preclinical studies, internalizing TF12 bsAb was shown to remain accessible for hapten binding because of the only partial internalization of the antibody construct

TABLE 2
Excerpts of Human Studies of Pretargeted Nuclear Medicine Using bsAb–Hapten System

Antibody radioligand pair and pretargeting timeline	Radioligand dose	Target antigen and study population	Main findings	Reference
<i>Hour 0:</i> anti-CEA × anti-DTPA indium bsAb <i>Hour 96–120:</i> ¹¹¹ In-bivalent DTPA hapten	100–200 MBq	CEA and medullary thyroid carcinoma	Immunogenic response in 61% of the patients. 80% true-positive tumor visualization.	(23)
<i>Hour 0:</i> hMN-14 × m734 bsAb <i>Hour 120/168:</i> ¹³¹ I-bivalent hapten	2.6–5.5 GBq	CEA and varied patient population with CEA-positive tumors	Tumor dose of ¹³¹ I-bsAb and pretargeted ¹³¹ I-hapten 2.0 Gy/GBq and 3.9 Gy/GBq, respectively. Tumor-to-whole-body ratio higher with ¹³¹ I-hapten.	(28)
<i>Hour 0:</i> TF2 bsAb <i>Hour 24–30:</i> ⁶⁸ Ga-IMP288 (premedicated with antihistamine and corticosteroid)	150 MBq	CEA and HER2-negative metastatic breast cancer	Immuno-PET showed higher total lesion sensitivity (94.7%) than ¹⁸ F-FDG PET (89.6%). Immunogenic response in 16% of the patients.	((21); NCT01730612)
<i>Hour 0:</i> TF2 bsAb <i>Hour 30:</i> ⁶⁸ Ga-IMP288 (premedicated with antihistamine and corticosteroid)	150 MBq	CEA and metastatic colorectal cancer	Immuno-PET showed higher sensitivity (88%) and specificity (100%) than ¹⁸ F-FDG PET (76% and 67%, respectively), no immunogenic response.	((20); NCT02587247)
<i>Hour 0:</i> TF2 bsAb <i>Hour 24/120:</i> ¹¹¹ In/ ¹⁷⁷ Lu-IMP288	185 MBq (¹¹¹ In) 2.5–7.4 GBq (¹⁷⁷ Lu)	CEA and advanced colorectal malignancy	10% patients experienced grade III–IV hematologic toxicity, no therapeutic effect detected.	((17,18); NCT00860860)

HER2 = human epidermal growth factor receptor 2.

(36). If those types of antibodies are successful in a clinical setting, it would increase the number of antibodies and molecular targets that can become part of the pretargeting tool kit, expanding the effectiveness of the approach.

In addition to imaging, pretargeting has immense potential to enhance radioimmunotherapy. Conventional radioimmunotherapy has shown good results in clinical response in patients with nonsolid tumors. However, solid tumors possess higher radio resistance and, relative to nonsolid tumors, 5- to 10-fold radiation doses are required to achieve a response (37). Because pretargeting produces faster delivery of the radiation source to the target site, larger doses could theoretically be administered with pretargeted radioimmunotherapy without inducing hematologic toxicities. It is exciting that a large portion of the clinical studies of pretargeting platforms have been for pretargeted radioimmunotherapy. However, phase 2 clinical trials have only shown modest efficacy for both platforms. In 2 different studies of bsAb–hapten pretargeting with a ¹³¹I-radiolabeled bivalent hapten radioligand in patients with CEA-positive cancer, Kraeber-Bodéré et al. reported no occurrence of complete or partial response (25,38). In another bsAb–hapten radioimmunotherapy study in patients with metastatic medullary thyroid carcinoma, a disease control rate of 76.2% (*n* = 32) was observed (24). Most of the patients enrolled in these pretargeted radioimmunotherapy studies

were late-stage cancer patients with high tumor burden and had already unsuccessfully undergone other forms of therapy. Also, in these studies only a single dose of therapeutic radioligand was administered as a standalone therapy. As clinical use of this approach expands, it may be useful to explore how pretargeted radioimmunotherapy would perform when joined with other therapies or when administered as multiple doses.

On average, more than 10 new cancer therapeutic antibodies enter late-stage clinical trials every year (39). As the role of antibodies in cancer therapeutics has increased, the potential for using antibody-based imaging agents in profiling patients' tumor antigen landscape to predict therapeutic response is consequential and significant. For the past 30 y, pretargeting has been proposed as an alternative approach to conventional antibody-based nuclear imaging and therapy. The approval rate of directly radiolabeled antibodies for clinical use has been low, with only 2 Food and Drug Administration–approved radioimmunoconjugates, ¹³¹I-tositumomab and ⁹⁰Y-ibritumomab, being approved in the early 2000s for non-Hodgkin lymphoma (37). According to a survey performed by Schaefer et al. in the United States, one of the bigger concerns for oncologists and hematologists in the use of ¹³¹I-tositumomab is the possible bone marrow damage that could preclude patients from further therapy (40). As our understanding of how to

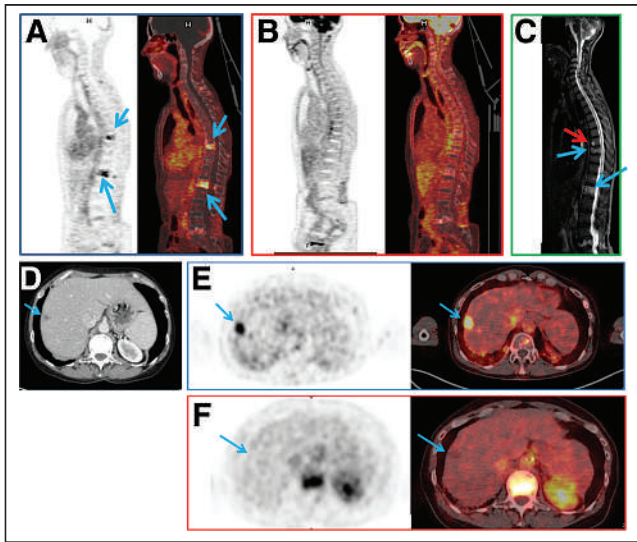


FIGURE 3. (A–C) In patient 1, pretargeted immuno-PET with TF2 and ^{68}Ga -IMP288 peptide images show 2 vertebral metastases (L1 and T9, arrows) (A), ^{18}F -FDG PET discloses no vertebral abnormalities (B), and vertebral MRI confirms both lesions (blue arrows) and discloses another lesion (red arrow) at T8 (C). (D–F) In patient 2, CT shows suspected liver lesion (D), and pretargeted immuno-PET with TF2 and ^{68}Ga -IMP288 peptide reveals high uptake by liver lesion (arrow) (E), which was not seen by ^{18}F -FDG PET (F). (Reprinted from (21).)

effectively implement pretargeted radioimmunotherapy expands, the preclinical data strongly suggest that these types of toxicities can be avoided, alleviating some of the concerns of physicians who want to use these strategies in the clinic.

Pretargeting is an approach that has shown significant promise in solving the challenge of relatively high radiation burden of the non-tumorous tissue that is associated in the use of radioimmunoconjugates such as ^{131}I -tositumomab and ^{90}Y -ibritumomab. Yet, the clinical data on the use of pretargeting have not been straightforward. The challenges with toxicity, immunogenicity, and modularity have not been fully addressed, but progress is gaining momentum and the outlook for pretargeted imaging and therapy remains promising.

DISCLOSURE

This work was financially supported by Finnish Academy of Science and Letters (Vilho, Yrjö and Kalle Väisälä fund) and NIH (1R21EB027982-01A1). No other potential conflict of interest relevant to this article was reported.

REFERENCES

- Bailly C, Bodet-Milin C, Rousseau C, Faivre-Chauvet A, Kraeber-Bodéré F, Barbet J. Pretargeting for imaging and therapy in oncological nuclear medicine. *EJNMMI Radiopharm Chem.* 2017;2:6.
- Reardan DT, Meares CF, Goodwin DA, et al. Antibodies against metal chelates. *Nature.* 1985;316:265–268.
- Hnatowich DJ, Virzi F, Ruscowski M. Investigations of avidin and biotin for imaging applications. *J Nucl Med.* 1987;28:1294–1302.
- Altai M, Membreno R, Cook B, Tolmachev V, Zeglis BM. Pretargeted imaging and therapy. *J Nucl Med.* 2017;58:1553–1559.
- Kalofonos HP, Ruscowski M, Siebecker DA, et al. Imaging of tumor in patients with indium-111-labeled biotin and streptavidin-conjugated antibodies: preliminary communication. *J Nucl Med.* 1990;31:1791–1796.
- Le Doussal JM, Chetanneau A, Gruaz-Guyon A, et al. Bispecific monoclonal antibody-mediated targeting of an indium-111-labeled DTPA dimer to primary

- colorectal tumors: pharmacokinetics, biodistribution, scintigraphy and immune response. *J Nucl Med.* 1993;34:1662–1671.
- Paganelli G, Magnani P, Zito F, et al. Three-step monoclonal antibody tumor targeting in carcinoembryonic antigen-positive patients. *Cancer Res.* 1991;51:5960–5966.
- Paganelli G, Grana C, Chinol M, et al. Antibody-guided three-step therapy for high grade glioma with yttrium-90 biotin. *Eur J Nucl Med.* 1999;26:348–357.
- Cremonesi M, Ferrari M, Chinol M, et al. Three-step radioimmunotherapy with yttrium-90 biotin: dosimetry and pharmacokinetics in cancer patients. *Eur J Nucl Med.* 1999;26:110–120.
- Knox SJ, Goris ML, Tempero M, et al. Phase II trial of yttrium-90-DOTA-biotin pretargeted by NR-LU-10 antibody/streptavidin in patients with metastatic colon cancer. *Clin Cancer Res.* 2000;6:406–414.
- Shen S, Forero A, LoBuglio AF, et al. Patient-specific dosimetry of pretargeted radioimmunotherapy using CC49 fusion protein in patients with gastrointestinal malignancies. *J Nucl Med.* 2005;46:642–651.
- Weiden PL, Breitz HB. Pretargeted radioimmunotherapy (PRIT) for treatment of non-Hodgkin's lymphoma (NHL). *Crit Rev Oncol Hematol.* 2001;40:37–51.
- Forero A, Weiden PL, Vose JM, et al. Phase I trial of a novel anti-CD20 fusion protein in pretargeted radioimmunotherapy for B-cell non-Hodgkin lymphoma. *Blood.* 2004;104:227–236.
- Paganelli G, Bartolomei M, Ferrari M, et al. Pre-targeted locoregional radioimmunotherapy with ^{90}Y -biotin in glioma patients: phase I study and preliminary therapeutic results. *Cancer Biother Radiopharm.* 2001;16:227–235.
- Grana C, Chinol M, Robertson C, et al. Pretargeted adjuvant radioimmunotherapy with yttrium-90-biotin in malignant glioma patients: a pilot study. *Br J Cancer.* 2002;86:207–212.
- Breitz HB, Weiden PL, Beaumier PL, et al. Clinical optimization of pretargeted radioimmunotherapy with antibody-streptavidin conjugate and ^{90}Y -DOTA-biotin. *J Nucl Med.* 2000;41:131–140.
- Schoffelen R, Woliner-van der Weg W, Visser EP, et al. Predictive patient-specific dosimetry and individualized dosing of pretargeted radioimmunotherapy in patients with advanced colorectal cancer. *Eur J Nucl Med Mol Imaging.* 2014;41:1593–1602.
- Schoffelen R, Boerman OC, Golderberg DM, et al. Development of an imaging-guided CEA-pretargeted radionuclide treatment of advanced colorectal cancer: first clinical results. *Br J Cancer.* 2013;109:934–942.
- Bodet-Milin C, Faivre-Chauvet A, Carlier T, et al. Immuno-PET using anticarcinoembryonic antigen bispecific antibody and ^{68}Ga -labeled peptide in metastatic medullary thyroid carcinoma: clinical optimization of the pretargeting parameters in a first-in-human trial. *J Nucl Med.* 2016;57:1505–1511.
- Toucheffeu Y, Bailly C, Frampas E, et al. Promising clinical performance of pretargeted immuno-PET with anti-CEA bispecific antibody and gallium-68-labelled IMP-288 peptide for imaging colorectal cancer metastases: a pilot study. *Eur J Nucl Med Mol Imaging.* 2021;48:874–882.
- Rousseau C, Goldenberg DM, Colombie M, et al. Initial clinical results of a novel immuno-PET theranostic probe in human epidermal growth factor receptor 2-negative breast cancer. *J Nucl Med.* 2020;61:1205–1211.
- Bodet-Milin C, Ferrer L, Rauscher A, et al. Pharmacokinetics and dosimetry studies for optimization of pretargeted radioimmunotherapy in CEA-expressing advanced lung cancer patients. *Front Med (Lausanne).* 2015;2:84.
- Barbet J, Peltier P, Bardet S, et al. Radioimmunodetection of medullary thyroid carcinoma using indium-111 bivalent hapten and anti-CEA x anti-DTPA-indium bispecific antibody. *J Nucl Med.* 1998;39:1172–1178.
- Salaun PY, Campion L, Bourmaud C, et al. Phase II trial of anticarcinoembryonic antigen pretargeted radioimmunotherapy in progressive metastatic medullary thyroid carcinoma: biomarker response and survival improvement. *J Nucl Med.* 2012;53:1185–1192.
- Kraeber-Bodéré F, Rousseau C, Bodet-Milin C, et al. Targeting, toxicity, and efficacy of 2-step, pretargeted radioimmunotherapy using a chimeric bispecific antibody and ^{131}I -labeled bivalent hapten in a phase I optimization clinical trial. *J Nucl Med.* 2006;47:247–255.
- Chatal JF, Campion L, Kraeber-Bodéré F, et al. Survival improvement in patients with medullary thyroid carcinoma who undergo pretargeted anti-carcinoembryonic-antigen radioimmunotherapy: a collaborative study with the French Endocrine Tumor Group. *J Clin Oncol.* 2006;24:1705–1711.
- Labrijn AF, Janmaat ML, Reichert JM, et al. Bispecific antibodies: a mechanistic review of the pipeline. *Nat Rev Drug Discov.* 2019;18:585–608.
- Kraeber-Bodéré F, Faivre-Chauvet A, Ferrer L, et al. Pharmacokinetics and dosimetry studies for optimization of anti-carcinoembryonic antigen x anti-hapten bispecific antibody-mediated pretargeting of Iodine-131-labeled hapten in a phase I radioimmunotherapy trial. *Clin Cancer Res.* 2003;9:3973S–3981S.
- Aarts F, Boerman OC, Sharkey RM, et al. Pretargeted radioimmunoscintigraphy in patients with primary colorectal cancer using a bispecific anticarcinoembryonic

- antigen CEA X anti-di-ethylenetriaminepentaacetic acid F(ab')₂ antibody. *Cancer*. 2010;116:1111–1117.
30. Peplow M. Click chemistry targets antibody-drug conjugates for the clinic. *Nat Biotechnol*. 2019;37:835–837.
 31. Rossin R, van den Bosch SM, Ten Hoeve W, et al. Highly reactive trans-cyclooctene tags with improved stability for Diels-Alder chemistry in living systems. *Bioconjug Chem*. 2013;24:1210–1217.
 32. Rossin R, van Duijnhoven SM, Lappchen T, van den Bosch SM, Robillard MS. Trans-cyclooctene tag with improved properties for tumor pretargeting with the Diels-Alder reaction. *Mol Pharm*. 2014;11:3090–3096.
 33. Houghton JL, Zeglis BM, Abdel-Atti D, Sawada R, Scholz WW, Lewis JS. Pretargeted immuno-PET of pancreatic cancer: overcoming circulating antigen and internalized antibody to reduce radiation doses. *J Nucl Med*. 2016;57:453–459.
 34. Keinänen O, Fung K, Pourat J, et al. Pretargeting of internalizing trastuzumab and cetuximab with a (18)F-tetrazine tracer in xenograft models. *EJNMMI Res*. 2017;7:95.
 35. Houghton JL, Membreno R, Abdel-Atti D, et al. Establishment of the in vivo efficacy of pretargeted radioimmunotherapy utilizing inverse electron demand Diels-Alder click chemistry. *Mol Cancer Ther*. 2017;16:124–133.
 36. Sharkey RM, van Rij CM, Karacay H, et al. A new tri-Fab bispecific antibody for pretargeting Trop-2–expressing epithelial cancers. *J Nucl Med*. 2012;53:1625–1632.
 37. Larson SM, Carrasquillo JA, Cheung NK, Press OW. Radioimmunotherapy of human tumors. *Nat Rev Cancer*. 2015;15:347–360.
 38. Kraeber-Bodéré F, Bardet S, Hoefnagel CA, et al. Radioimmunotherapy in medullary thyroid cancer using bispecific antibody and iodine 131-labeled bivalent hapten: preliminary results of a phase I/II clinical trial. *Clin Cancer Res*. 1999;5:3190s–3198s.
 39. Kaplon H, Muralidharan M, Schneider Z, Reichert JM. Antibodies to watch in 2020. *MAbs*. 2020;12:1703531.
 40. Schaefer NG, Ma J, Huang P, Buchanan J, Wahl RL. Radioimmunotherapy in non-Hodgkin lymphoma: opinions of U.S. medical oncologists and hematologists. *J Nucl Med*. 2010;51:987–994.

Diversity, Equity, and Inclusion in Academic Nuclear Medicine: National Survey of Nuclear Medicine Residency Program Directors

Jocelyn L. Cheng¹, Elizabeth H. Dibble¹, Grayson L. Baird², Leonie L. Gordon³, and Hyewon Hyun⁴

¹Department of Diagnostic Imaging, The Warren Alpert Medical School of Brown University/Rhode Island Hospital, Providence, Rhode Island; ²Lifespan Biostatistics Core, Providence, Rhode Island; ³Department of Radiology and Radiological Sciences, Medical University of South Carolina, Charleston, South Carolina; and ⁴Division of Nuclear Medicine and Molecular Imaging, Department of Radiology, Brigham and Women's Hospital, Harvard Medical School, Boston, Massachusetts

J Nucl Med 2021; 62:1207–1213

DOI: 10.2967/jnumed.120.260711

A diverse health-care workforce is a necessary component of equitable care delivery to an increasingly diverse U.S. population. In nuclear medicine (NM), there is a paucity of data on the numbers of women and members of racial and ethnic groups that are underrepresented in medicine in the United States (URiMs). This study sought to characterize the current state of women and URiMs in academic NM, describe the demographics of Accreditation Council for Graduate Medical Education (ACGME)-accredited NM residency program faculty and trainees, and assess the extent of NM exposure during medical school. **Methods:** This study was reviewed by the Institutional Review Board and deemed exempt. In this cross-sectional study, a link to an online 15-item survey was emailed to 41 ACGME-accredited NM residency program directors (PDs) in the United States. Data were collected between September 2018 and December 2018 using a secure web application that serves as an electronic data capture tool for research studies. **Results:** 23 of 41 (56.1%) PDs responded to the survey, 18 of 23 (78.3%) of whom were men and 5 of 23 (21.7%) women. Three of 23 (13.0%) PDs reported being URiMs. Of the 60 residents in the 23 NM residency programs whose PDs responded, 37 of 60 (61.7%) were men (7/37 [18.9%] URiMs) and 23 of 60 (38.3%) women (5/23 [21.7%] URiMs). Fourteen of 60 (23.3%) residents were U.S. medical school graduates (U.S. grads). PDs described demographics of 121 current NM faculty members: 86 of 121 (71.1%) were men (8/121 [6.6%] URiMs) and 35 of 121 (28.9%) women (7/121 [5.8%] URiMs). Sixty-five of 121 (53.7%) were U.S. grads. Sixteen of 23 (69.6%) divisional chiefs were men, and 7 of 23 (30.4%) were women. Four of 23 (17.4%) divisional chiefs were URiMs, and 7 of 20 (35.0%) NM PDs reported that NM was part of the medical school curriculum. **Conclusion:** Women and URiMs are underrepresented in NM training programs. This diversity gap is more pronounced among NM faculty and to an even greater extent in leadership positions. A greater proportion of NM trainees are international medical graduates compared with NM faculty members, suggesting declining NM recruitment among U.S. grads. NM is included in the medical school curriculum at fewer than one third of academic centers with NM residency programs, typically toward the end of medical school. Increased and earlier exposure to NM, especially for women and URiMs, may improve recruitment and mitigate diversity gaps.

Key Words: diversity; women; underrepresented in medicine; nuclear medicine; training

A diverse health-care workforce is one of the essential components to the provision of equitable and culturally competent care to an increasingly diverse U.S. patient population (1,2). Shared traits between patients and physicians including gender and race or ethnicity have been linked to better communication, adherence to medical recommendations, and overall health-care outcomes (3,4). Previous research indicates that improving patient-physician concordance of race, language, and social characteristics increases patients' trust of providers and satisfaction with care (5,6). The importance of a diverse workforce will only continue to increase in importance: U.S. Census projections indicate that racial and ethnic minorities will become the majority by the year 2050, with people of Hispanic ethnicity comprising 99.8 million people or 26% of the population (7), and people identifying as being of 2 or more races expected to become the fastest growing group over the next several decades (8).

Significant inequities in medical imaging have been documented, with individuals from racial and ethnic minority backgrounds disproportionately less likely to complete recommended imaging for both acute and chronic health conditions (9). For example, after adjusting for income, education, insurance, and health-care setting, Black people and people of Hispanic ethnicity in the Cancer Care Outcomes and Research Surveillance study population were less likely than non-Hispanic White people to receive guideline-recommended PET imaging during staging for non-small cell lung carcinoma, with potential adverse impacts on diagnosis accuracy and long-term survival (10). Other studies have reported that women are more likely to receive inappropriate SPECT myocardial perfusion imaging, suggesting a gender disparity in referral for this test (11).

Although women make up nearly half of U.S. medical school graduates, they remain underrepresented in numerous medical specialties and comprise a minority of faculty positions in academic medical centers, less than a third of division and section chiefs, and less than 20% of department chairs and medical school deans (12). Likewise, members of racial and ethnic groups that are underrepresented in medicine in the United States (URiMs), previously described as underrepresented minorities (13), are underrepresented as medical students (14), as medical school faculty members (15), and in medical school leadership positions (16).

Received Nov. 20, 2020; revision accepted Apr. 13, 2021.
For correspondence or reprints, contact Elizabeth H. Dibble (edibble@lifespan.org).

Published online April 23, 2021.

COPYRIGHT © 2021 by the Society of Nuclear Medicine and Molecular Imaging.

There is a paucity of data on the representation of women and URiMs in nuclear medicine (NM). Although we know that women are underrepresented in radiology in the United States, comprising 27.2% of radiologists (17), women are likely even more underrepresented in NM as they comprise less than 20% of physicians certified by the American Board of Nuclear Medicine. Although female residents comprised 44% of NM residents in 2018 based on Association of American Medical Colleges (AAMC) statistics (12), there are limited data available on the range of representation of women and URiM residents in NM training programs across the country, the representation of women and URiMs among NM faculty, the percentage of international medical graduates in NM training programs, and board certification pathways for faculty and current residents. There are also limited data on exposure to NM in medical school, with only 1 study recently reporting that 80% of current NM trainees first became interested in NM after medical school (18). The authors of this study also found significant differences in perception of NM exposure in the medical school curriculum between the faculty and NM trainees. To address these knowledge gaps, we sought to:

1. Characterize the current state of women and members of URiM racial and ethnic groups in Accreditation Council for Graduate Medical Education (ACGME)-accredited NM residency training programs,
2. Describe the demographics of ACGME-accredited NM residency program faculty and trainees including years in practice, country of medical school education, board certification status of faculty, and board certification plans for residents, and
3. Identify the extent of NM exposure during medical school.

We expect that insights gained could inform future strategies to address diversity gaps in NM.

MATERIALS AND METHODS

This study was deemed exempt by our institutional review board with a waiver of informed consent, and compliance with the U.S. Health Insurance Portability and Accountability Act was maintained.

In this descriptive cross-sectional study, a link to a 15-item online survey was sent via email to program directors (PDs) of the 41 ACGME-accredited NM residency programs in the United States. The anonymous survey included questions about divisional faculty, leadership and resident characteristics including gender, race and ethnicity, and country of medical school graduation as well as medical school exposure to radiology and NM (Supplemental Fig. 1; supplemental materials are available at <http://jnm.snmjournals.org>). Although URiM is an evolving concept, our survey defined URiM as Black/African American, American Indian/Alaska Native or Native Hawaiian/Pacific Islander, or Hispanic/Latinx based on U.S. Census Bureau race and ethnicity categories and historically underrepresented racial and ethnic groups in medicine (13). Respondents could opt out of any question they preferred not to answer; IP addresses were not collected, and no protected health information was obtained for this research project. Survey responses were collected between September and December 2018 and stored in REDCap (a secure web application that serves as an electronic data capture tool for research studies) until downloaded for analysis.

RESULTS

Twenty-three of the 41 (56.1%) PDs supervising 60 residents in ACGME-accredited NM residency programs in the United States

responded to the survey (Fig. 1). All survey responses were complete.

Resident Demographics

The percentage of NM residents who are women and the percentage of NM residents who are members of URiM racial and ethnic groups (Fig. 2 and Table 1) are lower than their respective percentages in the general population (Table 2).

Faculty Demographics

The percentage of current NM faculty members who are women and the percentage of NM faculty members who are members of URiM racial and ethnic groups (Fig. 2 and Table 1) are lower than their respective percentages in the general population (Table 2). This is also true at the leadership level (Fig. 2) where 5 of 23 (21.7%) PDs were women, 3 of 23 (13.0%) PDs reported being members of a racial or ethnic URiM group, 7 of 23 (30.4%) divisional chiefs were women, and 4 of 23 (17.4%) divisional chiefs were members of a racial or ethnic URiM group.

Figure 3 shows URiM representation in NM residents and faculty by gender.

Training and Certification of Faculty Versus Residents

PDs described board certification status of 113 clinical NM faculty members. Of 113 NM faculty members, 2 of 113 (1.8%) were certified by the American Board of Radiology (ABR); 1 of 113 (0.9%) ABR plus subspecialty certification (ABR + CAQ); 61 of 113 (54.0%) American Board of Nuclear Medicine (ABNM); 41 of 113 (36.3%) ABR + ABNM; and 4 of 113 (3.5%) other (2 American Board of Internal Medicine [ABIM] + ABNM, 3 ABIM, 2 Certification Board of Nuclear Cardiology [CBNC], 1 European). Results are illustrated in Figure 4.

PDs described country of graduation for 121 NM faculty members. The majority (65/121 [53.7%]) of NM faculty members graduated from medical school in the United States. PDs described experience of 137 clinical NM faculty members. Fifty-one of 137 (37.2%) had been out of training for more than 20 y, 33 of 137 (24.1%) 11–20 y, 31 of 137 (22.6%) 5–10 y, and 22 of 137 (16.1%) fewer than 5 y out of training.

By contrast, only 14 of 60 (23.3%) NM residents were graduates of U.S. medical schools. In addition, 1 of 60 (1.7%) planned to become board certified by ABR, 0 of 60 (0%) ABR + CAQ, 24 of 60 (40%) ABNM, and 35 of 60 (58.3%) ABR + ABNM.

Exposure to NM in Medical School

Only 7 of 20 (35.0%) NM PDs reported that NM is part of their medical school curriculum (3 PDs did not answer this question),

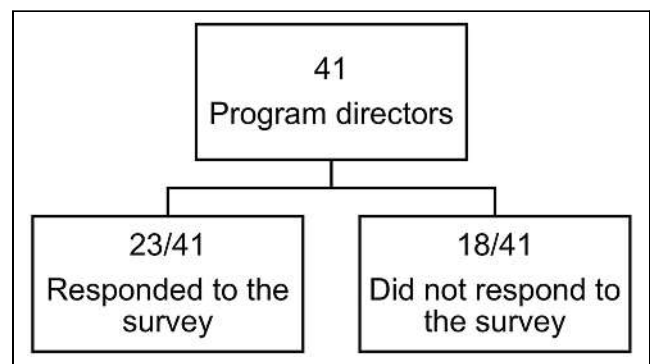


FIGURE 1. Flowchart of study participants.

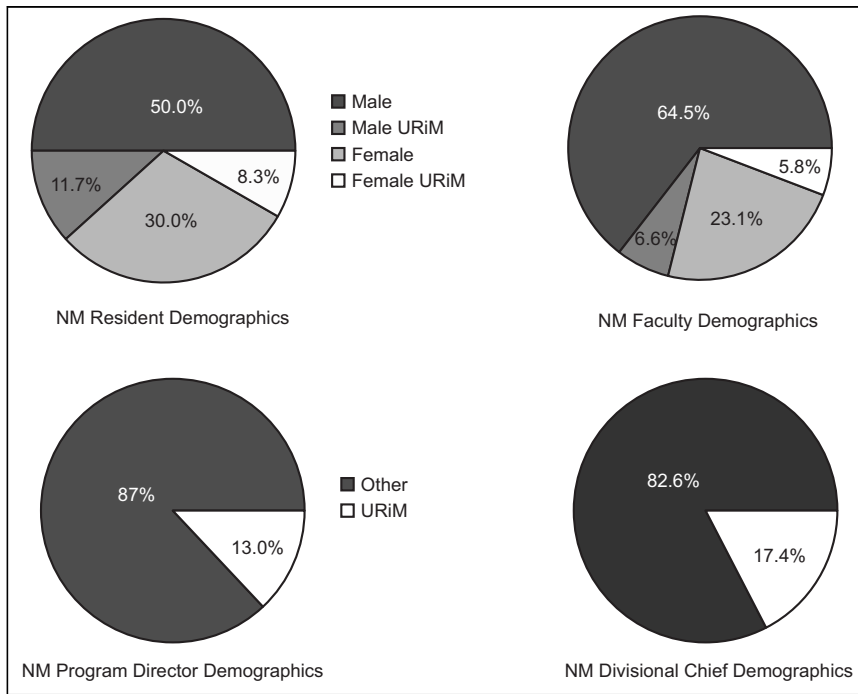


FIGURE 2. NM resident, faculty, program director, and divisional chief demographics.

with 5 of 7 (71.4%) institutions offering NM only as part of the radiology curriculum. Among schools where NM was offered as part of the radiology curriculum, it was mandatory in 4 of 5 (80%) programs. Most (6/7 [85.7%]) of the medical schools offering NM in the curriculum did so during years 3 and 4. Exposure to radiology and NM during medical school is detailed in Figures 5 and 6, respectively.

DISCUSSION

Our study results indicate that compared with the general population, women and members of URiM racial and ethnic groups are underrepresented in NM.

Among women, this diversity gap exists at the resident level, is greater at the NM faculty level, and is even more pronounced in

NM leadership positions. Our findings are consistent with other studies demonstrating underrepresentation of women in medical imaging both in the U.S. and globally, especially in higher rank positions. In a recent study of NM specialists in Canada and the United States, women comprised just 7.8% of first-in-command roles and 12.5% of second-in-command roles despite comparable academic performance in terms of number of publications, number of citations, years of active research, and h-index, which takes productivity and citation impact of the publications into account (19). Women in NM are also underrepresented compared with women in academic medicine at the resident, faculty, and PD level. The percentage of women division chiefs in our sample was slightly higher than the percentage of women department chairs in academic medicine (30.4% vs. 25.6%).

According to the AAMC, URiM is defined as “those racial and ethnic populations that are underrepresented in the medical profession relative to their numbers in the general population,” and historically underrepresented URiM groups include individuals who identify as Black, Mexican-American, Native American (i.e., American Indian, Alaska Native, and Native Hawaiian), and mainland Puerto Rican (13). As of 2014, 18% and 13% of the U.S. population identified as Hispanic or Black, respectively, but these URiM groups represented only 8.9% of the physician workforce (20). In our study, we found persistently low representation of URiMs in NM (defined as Black/African American, American Indian/Alaska Native or Native Hawaiian/Pacific Islander, or Hispanic/Latinx based on U.S. Census Bureau race and ethnicity categories and historically underrepresented racial/ethnic groups in medicine), particularly among faculty and leadership positions with just 6.6% of male faculty and 5.8% of female faculty belonging to a racial or ethnic URiM group. Although the percentage of NM residents who are members of URiM groups is slightly higher than the percentage of members of URiM groups in general

TABLE 1
Demographics of NM Residents and Faculty

Demographic	Residents (n = 60)		Faculty (n = 121)		Leadership			
	n	%	n	%	Division chiefs (n = 23)		Program directors (n = 23)	
					n	%	n	%
Male	37	61.7	86	71.1	16	69.6	18	78.3
Female	23	38.3	35	28.9	7	30.4	5	21.7
URiM	12	20.0	15	12.4	4	17.4	3	13.0
U.S. graduate	14	23.3	65	53.7				
IMG	46	76.7	56	46.3				

IMG = international medical graduate.

TABLE 2

Demographics of Residents, Faculty, and Department Chairs in Medicine and Demographics of U.S. General Population

Demographic	Residents (35)	Faculty (12)	Leadership		U.S. Population (37)
			Chairs (36)	Program Directors (12)	
Male	54.1	59.0	74.4	69.9	51.1
Female	45.8	41.0	25.6	31.1	48.9
URiM	13.8	12.5	7.5		34.4
US graduate	76.9	77.1			
IMG	23.1	22.9			

IMG = international medical graduate.
Data are percentages.

academic medicine, members of these racial and ethnic groups as a whole are underrepresented in medicine compared with the general

population. The percentage of NM faculty who are members of a URiM group is similar compared with the underrepresentation of these racial and ethnic groups in general academic medicine but underrepresented compared with the general population. The percentage of division chiefs in NM who are members of a URiM group is slightly higher than the percentage of general academic medicine department chairs who are members of a URiM group but remains grossly underrepresented compared with the general population.

Notably, we found a higher proportion of female and members of racial or ethnic URiM groups among current residents, with 38.3% being women and 20% members of URiM groups, compared with clinical NM faculty, suggesting a positive trend for future greater representation.

Our results demonstrate a lower percentage of U.S. medical school graduates among NM residents compared with faculty, supporting mounting evidence that fewer medical school graduates are entering the traditional NM training pathway in the United States. In the last decade, the number of ACGME-accredited NM residency programs has dropped by 23% and the number of NM residents has dropped by 48%; as of 2016 just 54% of NM residency slots and 35% of nuclear radiology fellowship spots were filled (21). In addition, the percentages of international medical graduate (IMG) residents and faculty in NM are much higher than the percentages of IMG residents and faculty in the general medical workforce.

Furthermore, whereas most NM clinical faculty members were U.S. medical school graduates certified by ABNM alone, current NM residents were predominantly international medical graduates planning to become board certified in ABR + ABNM. The increasing popularity of combining NM and radiology may be explained by job market forces. Physicians who are trained in both diagnostic radiology and NM/nuclear radiology (NR) have a competitive advantage over those trained solely in NM/NR because those with cross-training in diagnostic radiology can provide broader independent interpretations of imaging (21).

Although cross-trained diagnostic radiology and NM/NR physicians are well prepared to interpret imaging studies, the imaging-focused approach of dual NM/NR programs may not adequately train physicians to apply targeted NM therapies such as nuclear theranostics for optimally managing cancer and other medical conditions, for example, the use of peptide receptor radionuclide therapy to target somatostatin receptors diagnostically and therapeutically (22), radioiodine to forecast response to therapy among patients with advanced thyroid cancer and inform treatment pathways (23),

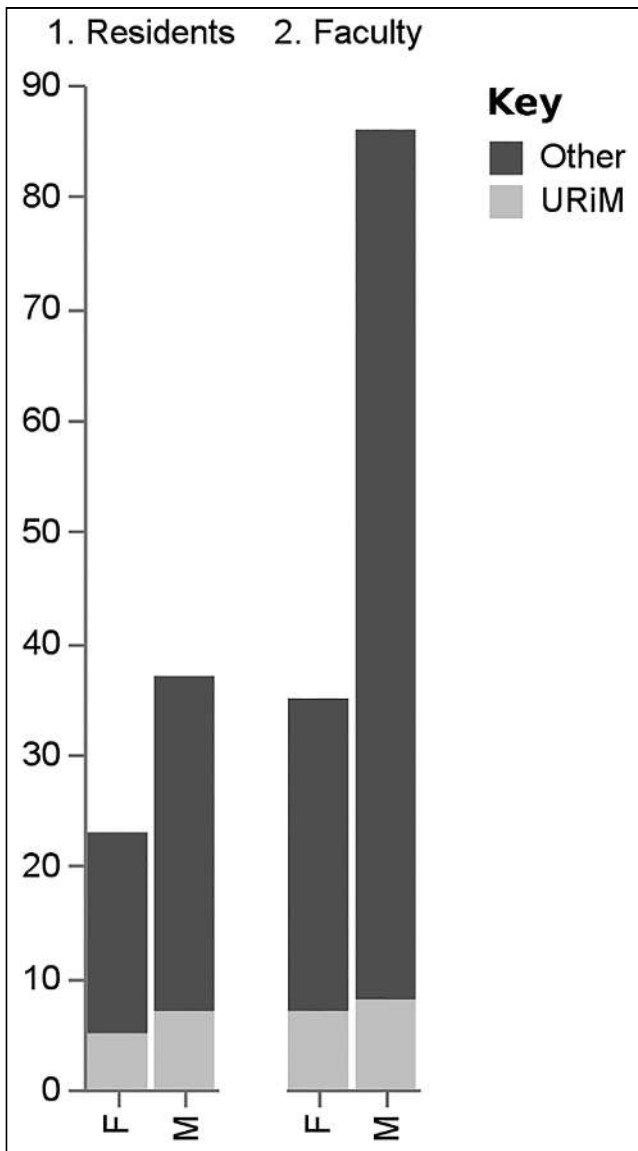


FIGURE 3. URiM representation in NM faculty by gender.

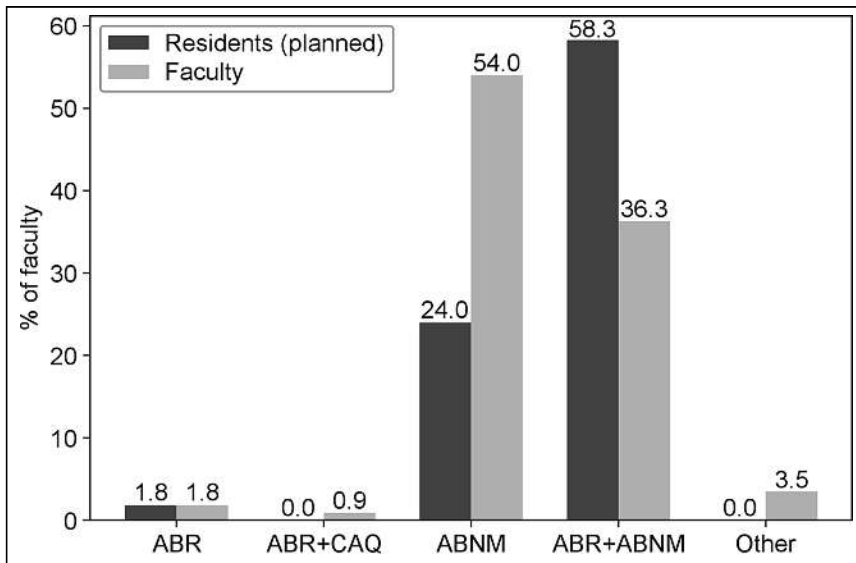


FIGURE 4. Board certification of 113 NM faculty at 23 training institutions.

and lutetium prostate-specific membrane antigen for metastatic prostate cancer (24). Beyond oncologic care, the use of theranostics is actively being pursued for the management of myriad conditions including pulmonary (25) and neurologic disorders (26). With increasing recognition of the potential of radiopharmaceutical therapy as a safe and effective targeted approach to treating numerous medical conditions, the clinical need for hospital-based radionuclide/radioligand therapy is expected to grow exponentially (27), making the training mismatch even more concerning, especially given the limited exposure to radionuclide/radioligand therapy topics in medical school curricula. Although our study shows insufficient NM exposure during medical school, our study did not examine specific medical student exposure to NM therapies, but we

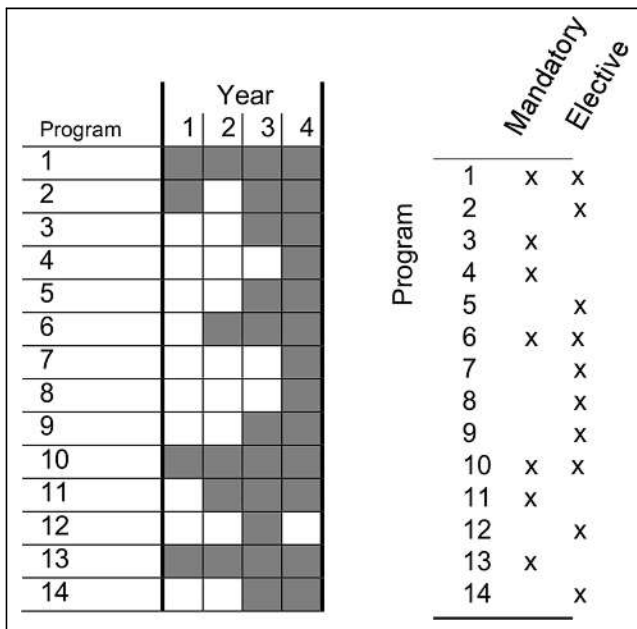


FIGURE 5. Exposure to radiology during medical school.

hypothesize that exposure to NM therapies is lacking similarly to general NM exposure in medical school curricula, if not more so, and future studies are warranted.

Our study identified low numbers of women and members of racial and ethnic URiM groups in NM, in addition to an overall decline in the percentage of U.S. medical school graduates pursuing NM. Physicians often cite exposure in medical school as a critical factor in specialty choice, and previous research has shown that women have less pre-clinical radiology exposure than do men (28). In our study, NM was included in the medical school curriculum at fewer than one third of academic centers with NM residency programs and was typically not offered until the third or fourth years of medical school. It is likely that students at medical schools without dedicated postgraduate NM training programs have even less NM exposure.

These findings are in line with a recent study that found that most NM experience came during radiology lectures or clinical clerkships. In this same study, there was a significant difference between the perception of NM exposure by NM trainees versus NM exposure reported by faculty. The NM trainee perception of exposure to NM in medical school was reported as 35% and 52% during preclinical and clinical medical school training, respectively, whereas that reported by faculty who teach NM was 76% and 91.7%, respectively (17). This difference of perception highlights the necessity for teaching NM in medical school, to do so early on, and for it to be a meaningful experience that allows students to imagine themselves becoming NM and molecular imaging physicians. Accordingly, incorporation of all facets of NM and molecular imaging into the medical school curriculum, from imaging interpretation to NM therapies, is warranted.

Female physicians have identified mentorship as an important factor in their career paths. Women with mentors have more publications and spend more time on research activity than those without mentors; in addition, women with a role model report higher overall career satisfaction (29). A lack of female role models in NM leadership and low exposure to NM in medical school may contribute to the underrepresentation of women in NM.

Possible barriers to members of racial and ethnic URiM groups and women choosing NM and reaching leadership positions in NM include lack of exposure to NM before medical school and in the first 2 y of medical school as well as lack of representation among NM faculty and leadership. As such, possible strategies to address diversity gaps in NM include increasing early exposure to NM, increasing NM mentorship and sponsorship, increasing awareness of structural racism and structural gender bias and how to combat them, and implementing leadership training, especially for women and members of racial and ethnic URiM groups.

Diversity gaps are not unique to medicine. They exist in many areas of society including in other fields requiring postgraduate training such as academia (in which the percentage of nonwhite professors at degree-granting postsecondary institutions is 22% and the percentage of women professors is 33% (30)) and law (in which the percentage of people of color who are partners is <10% and the percentage of women partners is <25% (31)) as well as in finance (in which the

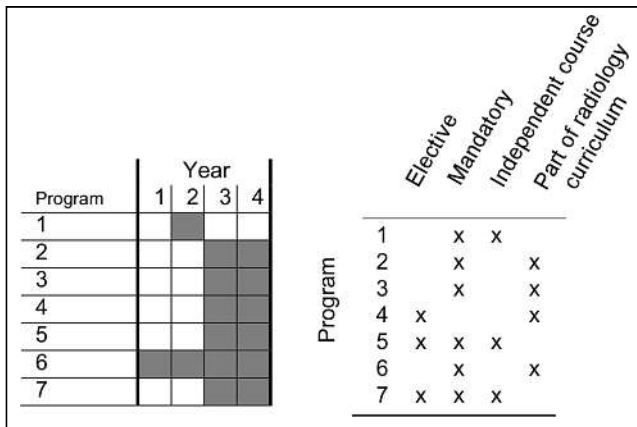


FIGURE 6. Exposure to NM during medical school.

percentage of African American officials and managers in the securities subsector is <5% and the percentage of women officials and managers in the securities subsector is <35% (32) and business (in which the percentage of Black chief executive officers of Fortune 500 companies is <1% (33) and the percentage of women Black chief executive officers of Fortune 500 companies is <8% (34)).

Our study had some limitations, most notably a small sample size of PDs answering on behalf of other faculty and residents. Responding to our survey was voluntary, and response bias is possible. However, PDs are well positioned to provide the type of factual programmatic information we sought in our research, so the information obtained is likely representative of respondents' institutions. In addition, our study focused on women and URiM racial and ethnic groups and did not assess representation of other URiM groups such as LGBTQ+ individuals or individuals with disabilities, who deserve further attention in future studies. In addition, and importantly, URiMs are a heterogeneous group of people of different races and ethnicities who are grouped together in this study. Future studies examining specific representation of members of each racial and ethnic group and of people with cross-sectional identities are warranted. We also surveyed only PDs of ACGME-accredited NM residency programs; we did not look at nuclear radiology fellowships, NM therapy fellowships, nonaccredited NM fellowships, or radiology residency programs with participants in the 16-mo combined diagnostic radiology/nuclear radiology dual-certification pathway. Nevertheless, the data we were able to gather enable a better understanding of representation of women and members of racial and ethnic URiM groups in a majority cross-section of ACGME-accredited NM residency programs in the United States.

CONCLUSION

Increasing early exposure to NM before and during medical school, with a special focus on women and members of racial and ethnic URiM groups, may improve recruitment of diverse trainees through both traditional and newer training pathways as 1 component of advancing diversity, equity, and inclusion in academic NM. We hope that this study encourages readers to evaluate the diversity of their workforce and assess whether it matches their community.

DISCLOSURE

No potential conflict of interest relevant to this article was reported.

KEY POINTS

QUESTION: In NM training programs, what percentage of trainees and faculty members are women or members of racial and ethnic groups that are underrepresented in medicine in the United States (URiM)?

PERTINENT FINDINGS: This survey study found that women and members of racial and ethnic URiM groups are underrepresented in NM training programs; this diversity gap is more pronounced among NM faculty and, to an even greater extent, in leadership positions. NM is included in the medical school curriculum at fewer than one third of academic centers with NM residency programs, typically toward the end of medical school.

IMPLICATIONS FOR PATIENT CARE: Increasing early exposure to NM in medical school with a special focus on women and members of racial and ethnic URiM groups may improve recruitment of diverse trainees, which can improve the provision of equitable and culturally competent patient care.

REFERENCES

- Jackson CS, Gracia JN. Addressing health and health-care disparities: the role of a diverse workforce and the social determinants of health. *Public Health Rep.* 2014; 129(suppl 2):57–61.
- Silver JK, Bean AC, Slocum C, et al. Physician workforce disparities and patient care: a narrative review. *Health Equity.* 2019;3:360–377.
- Cooper-Patrick L, Gallo JJ, Gonzales JJ, et al. Race, gender, and partnership in the patient-physician relationship. *JAMA.* 1999;282:583–589.
- Cooper LA, Powe NR. *Disparities in Patient Experiences, Health Care Processes, and Outcomes: The Role of Patient-Provider Racial, Ethnic and Language Concordance.* NEW YORK: The Commonwealth Fund; 2004.
- Thornton RL, Powe NR, Roter D, Cooper LA. Patient-physician social concordance, medical visit communication and patients' perceptions of health care quality. *Patient Educ Couns.* 2011;85:e201–e208.
- Street RL Jr, O'Malley KJ, Cooper LA, Haidet P. Understanding concordance in patient-physician relationships: personal and ethnic dimensions of shared identity. *Ann Fam Med.* 2008;6:198–205.
- U.S. Census Bureau. Population projections. U.S. Census Bureau website. <https://www.census.gov/programs-surveys/popproj.html>. Accessed July 21, 2021.
- Pew Institute. US population projections: 2005-2050. Pew Institute website. <https://www.pewresearch.org/hispanic/2008/02/11/us-population-projections-2005-2050/>. Accessed August 4, 2021.
- Betancourt JR, Tan-McGrory A, Flores E, Lopez D. Racial and ethnic disparities in radiology: a call to action. *J Am Coll Radiol.* 2019;16:547–553.
- Gould MK, Schultz EM, Wagner TH, et al. Disparities in lung cancer staging with positron emission tomography in the Cancer Care Outcomes Research and Surveillance (CanCORS) study. *J Thorac Oncol.* 2011;6:875–883.
- Doukky R, Hayes K, Frogge N. Appropriate use criteria for SPECT myocardial perfusion imaging: Are they appropriate for women? *J Nucl Cardiol.* 2016;23:695–705.
- Association of American Medical Colleges (AAMC). 2018-2019 The state of women in academic medicine: exploring pathways to equity. AAMC website. <https://www.aamc.org/data-reports/data/2018-2019-state-women-academic-medicine-exploring-pathways-equity>. Accessed July 21, 2021.
- Association of American Medical Colleges (AAMC). Underrepresented in medicine definition. AAMC website. www.aamc.org/initiatives/URM. Accessed July 21, 2021.
- Lett LA, Murdock HM, Orji WU, Aysola J, Sebros R. Trends in racial/ethnic representation among US medical students. *JAMA Netw Open.* 2019;2:e1910490.
- Guevara JP, Adanga E, Avakame E, Carthon MB. Minority faculty development programs and underrepresented minority faculty representation at US medical schools. *JAMA.* 2013;310:2297–2304.
- Pryor AD, Bader A, Talamini M. Minorities in leadership: are we moving the needle? *Surg Endosc.* 2019;33:3875–3879.
- Cater SW, Yoon SC, Lowell DA, et al. Bridging the gap: identifying global trends in gender disparity among the radiology physician workforce. *Acad Radiol.* 2018;25: 1052–1061.

18. Ng TSC, An BP, Cho SY, Hyun H. US trainee and faculty perspectives on exposure to nuclear medicine/molecular imaging during medical school. *Curr Probl Diagn Radiol*. 2021;50:585–591.
19. Moghimi S, Khurshid K, Jalal S, et al. Gender differences in leadership positions among academic nuclear medicine specialists in Canada and the United States. *AJR*. 2019;212:146–150.
20. Association of American Medical Colleges (AAMC). Diversity in the physician workforce: facts and figures. AAMC website. www.aamcdiversityfactsandfigures.org. Accessed July 21, 2021.
21. Harolds JA. Recruitment of new physicians, part I: preliminary steps. *Clin Nucl Med*. 2013;38:359–360.
22. Czernin J, Sonni I, Razmaria A, Calais J. The future of nuclear medicine as an independent specialty. *J Nucl Med*. 2019;60:3S–12S.
23. Ahn BC. Personalized medicine based on theranostic radioiodine molecular imaging for differentiated thyroid cancer. *BioMed Res Int*. 2016;2016:1680464.
24. Irvani A, Violet J, Azad A, Hofman MS. Lutetium-177 prostate-specific membrane antigen (PSMA) theranostics: practical nuances and intricacies. *Prostate Cancer Prostatic Dis*. 2020;23:38–52.
25. Suer H, Bayram H. Liposomes as potential nanocarriers for theranostic applications in chronic inflammatory lung diseases. *BBRJ*. 2017;1:1–8.
26. Kevadiya BD, Ottemann BM, Thomas MB, et al. Neurotheranostics as personalized medicines. *Adv Drug Deliv Rev*. 2019;148:252–289.
27. Sgouros G, Bodei L, McDevitt MR, Nedrow JR. Radiopharmaceutical therapy in cancer: clinical advances and challenges. *Nat Rev Drug Discov*. 2020;19:589–608.
28. Zener R, Lee SY, Visscher KL, Ricketts M, Speer S, Wiseman D. Women in radiology: exploring the gender disparity. *J Am Coll Radiol*. 2016;13:344–50.e1.
29. Levinson W, Kaufman K, Clark B, Tolle SW. Mentors and role models for women in academic medicine. *West J Med*. 1991;154:423–426.
30. National Center for Education Statistics (NCES). Digest of education statistics: 2019. NCES website. https://nces.ed.gov/programs/digest/2019menu_tables.asp. Accessed July 21, 2021.
31. National Association for Law Placement, Inc. (NALP). 2019 report of diversity in U.S. law firms. NALP website. https://www.nalp.org/uploads/2019_DiversityReport.pdf. Accessed July 21, 2021.
32. U.S. Equal Employment Opportunity Commission (EEOC). Diversity in the finance industry. EEOC website. <https://www.eeoc.gov/special-report/diversity-finance-industry>. Accessed July 21, 2021.
33. Wahba P. Only 19: The lack of black CEOs in the history of the Fortune 500. Fortune website. <https://fortune.com/longform/fortune-500-black-ceos-business-history/>. Accessed July 21, 2021.
34. Hinchliffe E. The number of female CEOs in the Fortune 500 hits an all-time record. Fortune website. <https://fortune.com/2020/05/18/women-ceos-fortune-500-2020/>. Accessed July 21, 2021.
35. Association of American Medical Colleges (AAMC). 2020 Report on Residents. AAMC website. <https://www.aamc.org/data-reports/students-residents/report-report-residents>. Accessed July 21, 2021.
36. Association of American Medical Colleges (AAMC). Department chairs by department, sex, and race/ethnicity, 2019. AAMC website. <https://www.aamc.org/data-reports/faculty-institutions/interactive-data/2019-us-medical-school-faculty>. Accessed July 21, 2021.
37. U.S. Census Bureau. Population estimates, July 1, 2019 (V2019). U.S. Census Bureau website. <https://www.census.gov/quickfacts/fact/table/US/PST045219>. Accessed July 21, 2021.

Value of ^{18}F -FES PET in Solving Clinical Dilemmas in Breast Cancer Patients: A Retrospective Study

Jorianne Boers¹, Naila Loudini¹, Celina L. Brunsch¹, Sylvia A. Koza¹, Erik F.J. de Vries², Andor W.J.M. Glaudemans², Geke A.P. Hospers¹, and Carolina P. Schröder¹

¹Department of Medical Oncology, University Medical Center Groningen, University of Groningen, Groningen, The Netherlands; and

²Department of Nuclear Medicine and Molecular Imaging, University Medical Center Groningen, University of Groningen, Groningen, The Netherlands

Breast cancer (BC) is a heterogeneous disease in which estrogen receptor (ER) expression plays an important role in most tumors. A clinical dilemma may arise when a metastasis biopsy to determine the ER status cannot be performed safely or when ER heterogeneity is suspected between tumor lesions. Whole-body ER imaging, such as 16α - ^{18}F -fluoro- 17β -estradiol (^{18}F -FES) PET, may have added value in these situations. However, the role of this imaging technique in routine clinical practice remains to be further determined. Therefore, we assessed whether the physician's remaining clinical dilemma after the standard workup was solved by the ^{18}F -FES PET scan. **Methods:** This retrospective study included ^{18}F -FES PET scans of patients who had (or were suspected to have) ER-positive metastatic BC and for whom a clinical dilemma remained after the standard workup. The scans were performed at the University Medical Center of Groningen between November 2009 and January 2019. We investigated whether the physician's clinical dilemma was solved, defined either as solving the clinical dilemma through the ^{18}F -FES PET results or as basing a treatment decision directly on the ^{18}F -FES PET results. In addition, the category of the clinical dilemma was reported, as well as the rate of ^{18}F -FES-positive or -negative PET scans, and any correlation to the frequency of solved dilemmas was determined. **Results:** One hundred ^{18}F -FES PET scans were performed on 83 patients. The clinical dilemma categories were inability to determine the extent of metastatic disease or suspected metastatic disease with the standard workup ($n = 52$), unclear ER status of the tumor ($n = 31$), and inability to determine which primary tumor caused the metastases ($n = 17$). The dilemmas were solved by ^{18}F -FES PET in 87 of 100 scans (87%). In 81 of 87 scans, a treatment decision was based directly on ^{18}F -FES PET results (treatment change, 51 scans; continuance, 30 scans). The frequency of solved dilemmas was not related to the clinical dilemma category ($P = 0.334$). However, the frequency of solved dilemmas was related to whether scans were ^{18}F -FES-positive ($n = 63$) or ^{18}F -FES-negative ($n = 37$; $P < 0.001$).

Conclusion: For various indications, the ^{18}F -FES PET scan can help to solve most clinical dilemmas that may remain after the standard workup. Therefore, the ^{18}F -FES PET scan has added value in BC patients who present the physician with a clinical dilemma.

Key Words: FES PET; breast cancer; clinical dilemma; conventional imaging

J Nucl Med 2021; 62:1214–1220

DOI: 10.2967/jnumed.120.256826

Breast cancer (BC) is the most common malignant disease among women worldwide (1). In The Netherlands, it is estimated that 1 of 7 women will be diagnosed with BC at some point in their life (2). Of all BC patients, roughly 10% develop distant metastases in the first 5 y after primary diagnosis (3). A clinically relevant characteristic of BC is the estrogen receptor (ER), which is expressed by most (79%) breast tumors (4). The ER is an important predictive and prognostic marker and used as a target for treatment. ER-positive breast tumors are likely to respond to hormonal therapy (5).

Currently, ER expression in BC is determined by immunohistochemistry (5,6). However, this gold standard has some limitations. A metastasis biopsy may lead to sampling errors and can be infeasible because of its invasive nature or the location of the lesion. Also, heterogeneity in ER expression between tumor lesions within patients can be a clinical challenge for clinicians (7,8). Discrepancies in ER expression between the primary tumor and the metastasis is observed in 16%–40% of patients (5,8). Furthermore, the ER expression of tumors may change over time. These factors may cause a clinical dilemma regarding both the correct diagnosis and the best choice of therapy, and regular evaluation of the ER status is therefore important. According to the guidelines of the European Society for Medical Oncology, repeated histologic biopsies are recommended to reevaluate the ER status of metastatic BC (9).

However, since it is impossible to evaluate the ER status of every lesion in the body by biopsy, a noninvasive imaging method to measure the ER expression of all tumor lesions in the body would be a useful and valuable tool. PET with 16α - ^{18}F -fluoro- 17β -estradiol (^{18}F -FES) could be such a tool (10). ^{18}F -FES PET has the potential to visualize the ER expression of all tumor lesions and to estimate the heterogeneity in ER expression in metastatic lesions across the body and can therefore be used for individualized therapy decision making (11,12). A high correlation has been found between ^{18}F -FES uptake and immunohistochemistry findings for determination of ER status (13–15).

^{18}F -FES PET, recently approved for human use in France and the United States, is an evolving imaging technique and may soon play an increasingly important role in clinical practice. Small studies have shown that ^{18}F -FES PET has added value for BC patients presenting a clinical dilemma (16–18). To confirm these initial findings, evaluation of the role of ^{18}F -FES PET in a larger patient sample size is needed, and the role of this imaging technique in routine clinical practice remains to be further determined. Therefore, the aim of this study was to assess the value of ^{18}F -FES PET in a large retrospective patient cohort by evaluating whether the physician's remaining clinical dilemma after the standard workup could be

Received Sep. 14, 2020; revision accepted Dec. 28, 2020.

For correspondence or reprints, contact Carolina P. Schröder (c.p.schroder@umcg.nl).

Published online May 14, 2021.

COPYRIGHT © 2021 by the Society of Nuclear Medicine and Molecular Imaging.

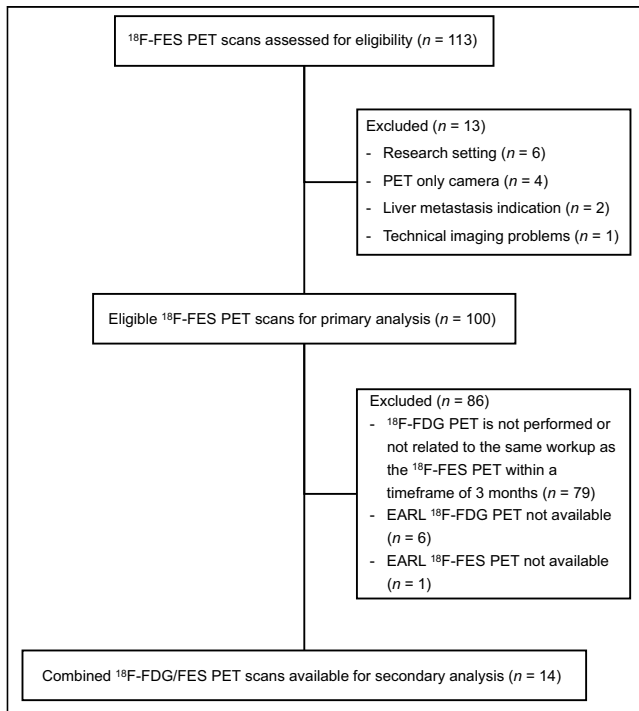


FIGURE 1. Consolidated Standards of Reporting Trials (CONSORT) diagram.

solved by the ^{18}F -FES PET findings and whether this imaging technique supported BC management.

MATERIALS AND METHODS

Study Design and Patients

This was a retrospective study of all consecutive patients who underwent clinical ^{18}F -FES PET at the University Medical Center of Groningen between November 2009 and January 2019. ^{18}F -FES PET scans were eligible for analysis if they were performed on patients who had, or were suspected to have, ER-positive metastatic BC and for whom pathologic assessment of the primary tumor or suspected metastasis was available but a clinical dilemma remained after the standard workup. For each patient, a ^{18}F -FES PET scan was requested by a medical oncologist in the context of the clinical dilemma, and the validity of the request was confirmed by a nuclear medicine physician. We used only scans that were acquired on a combined PET/CT scanner; scans that were acquired with a PET-only scanner were excluded. If there was a technical imaging problem, the scan was excluded, as were scans performed as part of a clinical trial. In addition, requests for ^{18}F -FES PET that related only to the detection of liver metastases were excluded because of unreliable image interpretation (19). All procedures were performed as part of routine care. The Medical Ethics Committee of the University Medical Center of Groningen reviewed the protocol and decided that this type of research was beyond the scope of the Medical Research Involving Human Subjects Act (METc 2018/418). All data were pseudonymized before data analysis.

^{18}F -FES PET Imaging

^{18}F -FES was produced as described previously (20). To prevent false-negative results, ER antagonists had to be discontinued at least 5 wk before ^{18}F -FES PET, whereas aromatase inhibitors could be continued (19). The tracer (~ 200 MBq) was intravenously injected 60 min before a whole-body ^{18}F -FES PET was performed, and the patients did not have to fast.

A 40- or 64-slice mCT PET/CT camera (Siemens CTI) was used with a 2-mm spatially reconstructed resolution and an acquisition time of 3 min per bed position. A low-dose CT scan was acquired for attenuation and scatter correction. Some patients underwent ^{18}F -FES PET in combination with a diagnostic CT scan. ^{18}F -FES PET scans were evaluated qualitatively by nuclear medicine physicians, and a standard clinical report was documented in the patient's file. The scans were divided into 2 categories: those showing ER-positive disease (i.e., at least 1 lesion showing visually increased ^{18}F -FES uptake above the background level) and those showing ER-negative disease (i.e., no lesion showing visually increased ^{18}F -FES uptake above the background level). In cases of ambiguous lesions on qualitative analysis of the ^{18}F -FES PET scan, tracer uptake in the lesion was quantified, using an SUV_{max} of 1.5 as the cutoff (19). In patients who had also undergone ^{18}F -FDG PET in the standard workup, a secondary (quantitative) analysis was performed. For both PET scans (^{18}F -FDG and ^{18}F -FES), patient preparation, tracer administration, and reconstruction were performed according to European Association of Nuclear Medicine (EANM) protocols. Quantitative analysis was performed on reconstructed images according to the method of EANM Research Ltd. (21).

Standard Workup

We used electronic patient records to assess the standard workup that had occurred before ^{18}F -FES PET was requested. We determined which conventional imaging methods were used, such as bone scintigraphy (with SPECT if necessary), CT, ^{18}F -FDG PET, or MRI, and whether a cytologic or histologic biopsy was performed and at which site. To ensure that the previous imaging techniques and the biopsy were used to solve the same dilemma as the ^{18}F -FES PET, a time frame of a maximum of 3 mo was set between the standard workup and the ^{18}F -FES PET scan.

Data Collection

The following patient data were retrieved from the electronic patient records: patient and tumor characteristics (including age, sex, BC stage, histology, and tumor receptor status), treatment before ^{18}F -FES PET (within a maximum of 4 wk) and after ^{18}F -FES PET (treatment decisions made within a maximum of 4 wk), previous standard workup, category of clinical dilemma, and visual interpretation of ^{18}F -FES PET results (positive or negative).

Outcomes

The primary endpoint was the percentage of cases in which the referring physician's clinical dilemma was solved on the basis of the ^{18}F -FES PET results. The dilemma was considered solved if the ^{18}F -FES PET provided a solution to the clinical dilemma or if a treatment decision (to change or continue) was based directly on the ^{18}F -FES PET result. If the physician had doubts about the diagnosis after the ^{18}F -FES PET examination, and additional workup was necessary for treatment decision making, the dilemma was considered not solved. Secondary endpoints were the type of clinical dilemma according to 3 categories (to determine the extent of suspected metastatic disease in cases of equivocal lesions on the standard workup or symptoms for which no abnormality could be found on conventional imaging, to determine the ER status of the disease, and to determine which primary tumor caused metastases and the frequency of solved dilemmas per category), the type of treatment before and after ^{18}F -FES PET, and the ^{18}F -FES PET scan results (ER-positive or ER-negative) in relation to how frequently the dilemma was solved.

Statistical Analysis

Descriptive statistics (categorical data) were used to report whether the physician's clinical dilemma was solved and are presented as percentages. Descriptive statistics were also used to depict the secondary outcomes. Continuous variables were expressed as mean \pm SD or median and range, depending on data distribution. A χ^2 test was performed to evaluate whether the number of ^{18}F -FES PET scans that solved the dilemma was dependent on the category of clinical dilemma and to

TABLE 1
Patients and Scan Characteristics ($n = 100$ ^{18}F -FES PET Scans in 83 Patients)

Characteristic	Data
Mean age \pm SD (y)	59 \pm 11
Female (n)	99 (99%)
BC stage at time of ^{18}F -FES PET	
Metastatic disease*	51 (51%)
Suspected metastatic disease	49 (49%)
Time from primary tumor diagnosis to ^{18}F -FES PET (y) [†]	
Median	6
Range	0–34
BC primary tumor ER expression ($n = 94^{\ddagger}$)	
Positive	92 (98%)
Negative [§]	2 (2%)
Histology of primary tumor ($n = 87$)	
Ductal	64 (74%)
Lobular	21 (24%)
Ductolobular	1 (1%)
Micropapillary	1 (1%)
ER expression in BC metastases [¶] ($n = 31$)	
Positive	28 (90%)
Negative [#]	3 (10%)
Standard workup before ^{18}F -FES PET	
At least 1 conventional technique**	90 (90%)
CT scan	59 (59%)
Bone scintigraphy	36 (36%)
MRI	23 (23%)
^{18}F -FDG PET	21 (21%)
Biopsy	29 (29%)
Breast lesion ^{††} ($n = 29$)	12 (41%)
Nonbreast lesion ($n = 29$)	17 (59%)

*Ultimately diagnosed with metastatic gastric carcinoma with breast metastases, instead of newly diagnosed metastatic BC ($n = 1$).

[†]If >1 primary BC, first diagnosis and histologic type of BC was included.

[‡]In 5/6 unknown cases, metastatic lesion or secondary primary BC ER-positive.

[§]One patient with ER-negative primary tumor presented with new palpable breast mass with metastases; it was unclear whether this new mass was secondary primary BC or recurrence, and biopsy was not possible. Another patient had mixed ER-negative and ER-positive primary tumor, which was treated as triple-negative BC.

^{||}If >1 primary BC, first diagnosis and histologic type of BC was included.

[¶]Metastasis biopsy was not always possible, was not performed, or was not representative; only cytology was available; or data were not available from medical records.

[#]Secondary (primary BC ER-positive).

**In 10 cases, standard workup could not or was not performed, for the following reasons: priority was to determine whole-body ER status for subsequent endocrine treatment ($n = 4$); previous tumor progression was detected only by ^{18}F -FES PET, not by conventional imaging, so conventional imaging was deemed noninformative in present setting ($n = 3$); there was clinical and biochemical suspicion of tumor progression and presence of 2 different tumor types ($n = 1$); biopsy was not possible to determine ER status ($n = 1$); and after completion of chemotherapy, further diagnostic workup was required to clarify origin of cancer metastases ($n = 1$).

^{††}With or without axillary dissection.

assess whether the result of the ^{18}F -FES PET scan (positive or negative) affected the success rate for solving the dilemma. Statistical analysis was performed for the qualitative assessment, and descriptive analysis was performed for the quantitative data. A P value of less than 0.05 was considered statistically significant. All statistical tests were done using SPSS, version 23.

RESULTS

Patients

In total, 100 consecutive ^{18}F -FES PET scans, performed on 83 patients, were included in the final database (Fig.1). Of the 12 patients with multiple ^{18}F -FES PET scans, 9 patients had 2 scans,

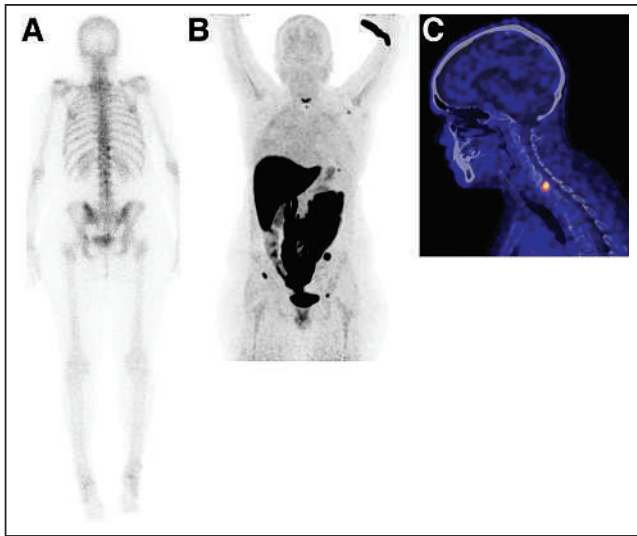


FIGURE 2. Equivocal lesions on standard workup. A 41-y-old woman known to have Bechterew disease was diagnosed with primary ER-positive BC 2 y previously. Conventional bone scanning was performed because of pain in neck region and showed heterogeneous uptake in spine and pelvis (A, static image posterior view). To differentiate between presence of bone metastases and lesions associated with Bechterew, ^{18}F -FES PET scan was performed. Increased ^{18}F -FES uptake was seen in multiple skeletal lesions: rib, left scapula, spine, and pelvis (B, maximum-intensity-projection view, and C, PET/CT sagittal view of cervical spine). On the basis of these findings, diagnosis was settled on metastatic BC, clinical dilemma was solved, and first-line endocrine treatment was started. In addition, patient received radiation to cervical spine.

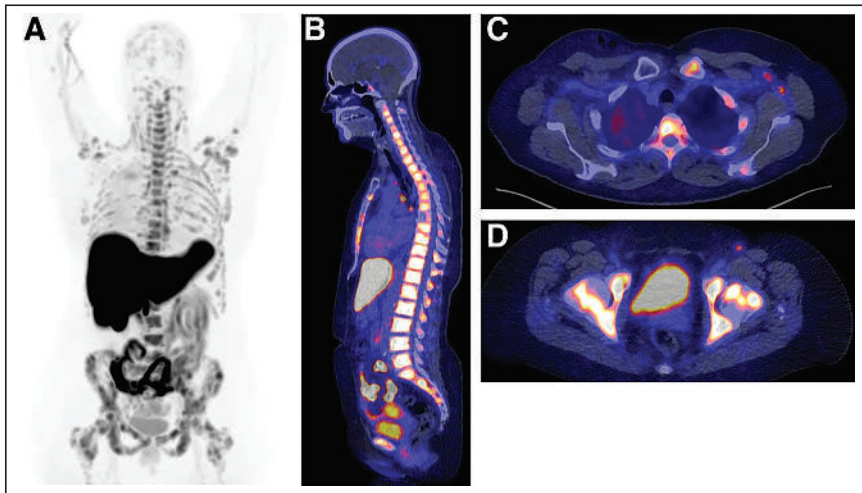


FIGURE 3. Determination of ER status of disease. In 59-y-old woman diagnosed with ER-positive lobular BC 2 y previously and treated with tamoxifen, ER-positive bone metastases were identified 1 y after initial diagnosis. She was treated with first-line endocrine therapy in palliative setting. Thereafter, disease became progressive and palbociclib was added. However, after 2 wk of treatment, she presented with pancytopenia. ^{18}F -FES PET was performed to determine whether bone metastases were still expressing ER and whether there was a rationale for another line of endocrine therapy. Increased ^{18}F -FES uptake could be seen in lymph nodes above and below diaphragm and in multiple bone lesions (e.g., spine, costae, scapulae, sternum, and pelvis) (A, maximum-intensity-projection image; B, PET/CT sagittal view; C, PET/CT transversal view of left axillary region; D, PET/CT transversal view of pelvic region with positive inguinal lymph node). In addition, bone marrow involvement was visible. Diagnosis was settled on ER-positive metastatic disease, clinical dilemma was solved, and another line of endocrine therapy could be considered. However, because of bone marrow involvement, chemotherapy was indicated to achieve therapeutic effect more rapidly.

and 3 patients had 3 or more scans. Scan characteristics are summarized in Table 1. All patients had ER-positive BC, based on primary-tumor or metastasis biopsy, except for 2 patients. One was a patient with an ER-negative primary breast tumor and a new palpable breast mass with metastases. A biopsy was not possible, and it was unclear whether this mass was a second primary breast tumor (and possibly ER-positive) or recurrence ($n = 1$). The other patient was one with suspected primary BC but for whom a histologic breast biopsy indicated a gastric carcinoma with breast metastases (instead of primary BC) ($n = 1$). In 10 cases, full standard workup before ^{18}F -FES PET was not feasible (Table 1). These cases were included in the analysis because they do present real-life dilemmas occurring in clinical practice.

Value of ^{18}F -FES PET

The physician's clinical dilemma was solved in 87% of the cases in which a ^{18}F -FES PET scan was performed (87/100). In most cases (81/87), a treatment decision was based directly on the ^{18}F -FES PET result. In 6 of 87 cases, ^{18}F -FES PET provided a solution to the clinical dilemma (an extra site to biopsy and additional imaging based on new ^{18}F -FES PET findings). In 13 of 100 cases, the dilemma was not solved, for the following reasons: there were still doubts about the diagnosis and an additional biopsy was considered ($n = 5$); the physician started treatment contradicting the ^{18}F -FES PET result ($n = 2$); the origin of the lesions remained unclear ($n = 2$); an additional biopsy to confirm a negative ^{18}F -FES PET scan in fact showed ER expression and thus treatment was based on ER-positive disease ($n = 2$; 1 patient had lack of response to endocrine treatment); there was doubt whether the metastatic disease was in remission or whether ER underwent

positive to negative conversion due to ^{18}F -FES-negative PET results, and therefore ^{18}F -FDG PET was performed to detect metabolically active bone metastases ($n = 1$); and there was discrepancy between conventional imaging results and ^{18}F -FES PET results ($n = 1$). Examples of cases in which the physician regarded the results of the ^{18}F -FES PET as conclusive, as well as an example of an inconclusive ^{18}F -FES PET scan, are shown in Figures 2–4.

In 14 patients, ^{18}F -FDG and ^{18}F -FES PET could be compared for secondary quantitative analysis (Fig. 1). As shown in Supplemental Table 1 (supplemental materials are available at <http://jnm.snmjournals.org>), we did not observe negative or minimally positive ^{18}F -FDG PET scans.

Category of Clinical Dilemma

Fifty-two of 100 ^{18}F -FES PET scans were requested because lesions were equivocal on standard workup. Thirty-one of 100 ^{18}F -FES PET scans were requested to investigate the ER status. Seventeen of 100 ^{18}F -FES PET scans were requested to determine the origin of metastases. Examples of an ^{18}F -FES PET scan for each indication are shown

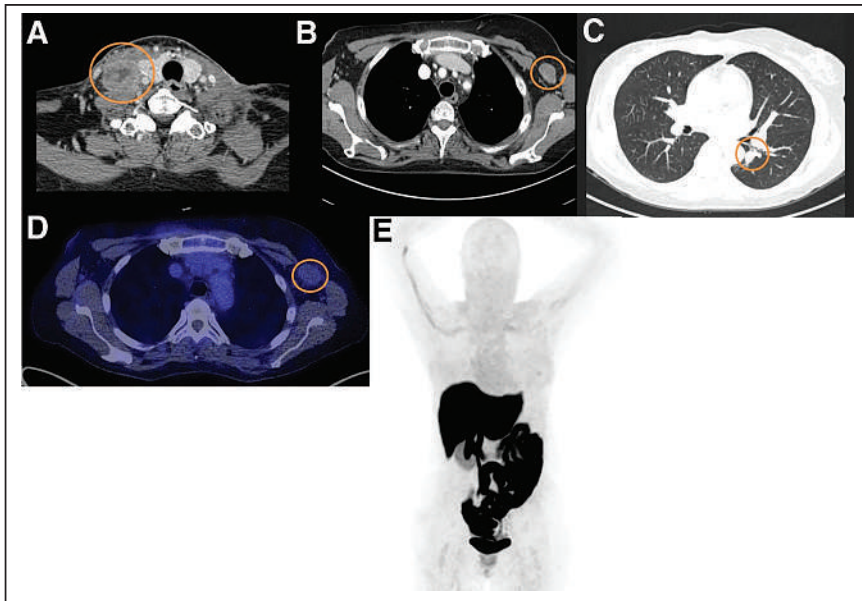


FIGURE 4. Inability to determine which primary tumor caused metastases. A 63-y-old woman known to have oral squamous cell carcinoma was recently diagnosed with ER-positive BC. At physical examination, a palpable mass was found in right neck region (level IV) and was also visible on CT (A). In addition, enlarged lymph node was visible in left axilla on CT (B), as well as abnormality in left lung (C). The dilemma was whether these metastases were associated with ER-positive BC or oral squamous cell carcinoma. ^{18}F -FES PET was performed to evaluate whether these lesions were metastasis from BC (in case of ^{18}F -FES-positive findings). However, ^{18}F -FES PET did not show any significant tracer uptake in metastatic lesions (D and E). ^{18}F -FES PET result did not solve dilemma, because there could be conversion from ER-positive to ER-negative status; therefore, biopsy of left axillary area was performed and confirmed presence of squamous cell carcinoma.

in Figures 2–4. The success rate of ^{18}F -FES PET in solving the physician’s clinical dilemma did not significantly differ between the different categories of clinical dilemmas ($P = 0.334$). Of the 52 ^{18}F -FES PET scans requested after an equivocal conventional workup, the clinical dilemma was solved in 47 cases (90%).

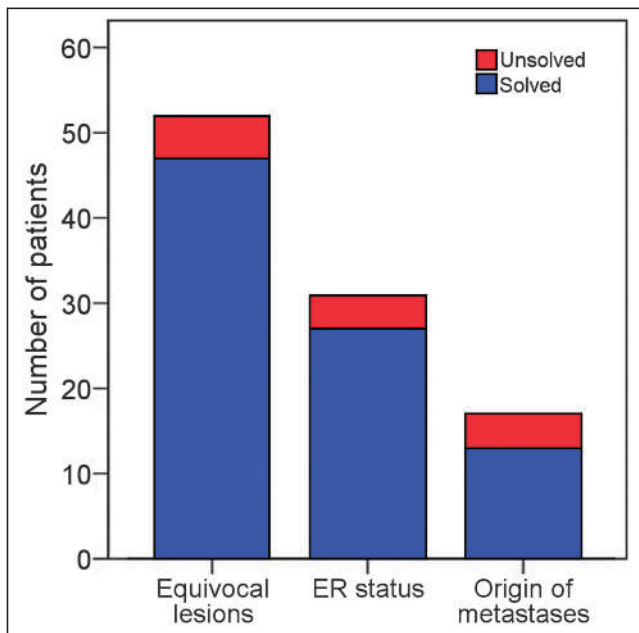


FIGURE 5. Value of ^{18}F -FES PET in solving clinical dilemmas, per category.

When ^{18}F -FES PET was requested to determine the ER status, the clinical dilemma of the physician was solved in 27 cases (87%). When ^{18}F -FES PET was requested to predict the origin of a metastasis, the dilemma was solved in 13 cases (76%; Fig.5).

Type of Treatment After ^{18}F -FES PET

Of the 81 cases for which a treatment decision was based directly on the ^{18}F -FES PET result, 51 received a new treatment (25/51 endocrine therapy with or without radiotherapy) and 30 continued their treatment. The type of treatment change is shown in Supplemental Table 2.

^{18}F -FES-Negative or ^{18}F -FES-Positive PET Results

Sixty-three of 100 ^{18}F -FES PET scans showed ER-positive disease, whereas 37 showed ER-negative disease. The physician’s clinical dilemma was solved in 61 (97%) of the 63 scans showing ER-positive disease and in 26 (70%) of the 37 scans showing ER-negative disease. As a result, the success rate for solving the dilemma differed significantly between the 2 groups ($P < 0.001$). Figure 4 provides an example of a ^{18}F -FES PET scan showing ER-negative disease in which the scan was not directly helpful for the clinician.

DISCUSSION

In this retrospective study, we aimed to investigate the value of ^{18}F -FES PET in the management of BC patients facing a clinical dilemma that could not be solved after the standard workup. Further investigation in such cases is of clinical importance since a persistent clinical dilemma might lead to decreased survival (22) and unnecessary therapy because of overtreatment or undertreatment (17).

To our knowledge, this was the largest study evaluating the value of ^{18}F -FES PET in this target group. We showed that ^{18}F -FES PET can be clinically meaningful and can support clinical decision making in most BC patients who present a persisting clinical dilemma despite standard workup. This study also provided more insight into the clinical indications for the examination and the physician’s diagnostic concerns. These findings can potentially support clinical implementation of ^{18}F -FES PET.

The percentage of clinical dilemmas solved by ^{18}F -FES PET (87%) is consistent with the findings of previous smaller studies (16,18). One study reported improved diagnostic understanding in 88% of cases based on the ^{18}F -FES PET scan (16). Another study found that ^{18}F -FES PET had added value (89%) in the diagnosis of newly diagnosed BC patients (18). By showing that ^{18}F -FES PET can support BC management with both a changed and a continued treatment plan, the present study adds value to the previous studies.

This study identified clinical dilemmas associated with BC in which ^{18}F -FES PET may play a role in guiding treatment

selection, including, but not limited to, determination of the ER status of the disease. An accurate request for ^{18}F -FES PET is necessary for clinical interpretation by the nuclear medicine physician and improves the ^{18}F -FES PET report (23). In the present study, the physician's clinical dilemma was equally solved for all 3 indication categories, as is in line with a previous study (16). One third of the ^{18}F -FES PET scans were requested to determine ER status in known or suspected metastatic lesions, in agreement with the results of van Kruchten et al. (16). The potential indications for ^{18}F -FES PET in the literature included assessment of ER status of disease, ER heterogeneity in metastatic disease, staging and restaging, therapeutic options for hormonal treatment, and prediction of response to hormonal therapy (13,15,19,24). However, the role of ^{18}F -FES PET is limited in detecting ER-positive lesions in the liver, because of high physiologic ^{18}F -FES uptake due to its metabolism.

The percentage of lobular tumors in the present study was slightly higher than in the general population (25,26). This finding supports the previously described hypothesis that metastatic lesions in lobular BC are difficult to detect with standard imaging (27,28) and that this disease presents the physician with a clinical dilemma relatively frequently. For this setting in the present study, we found that clinical dilemmas in lobular BC and clinical dilemmas in ductal BC were solved equally well by ^{18}F -FES PET (86% vs. 88%).

Recently, a high specificity of 98% and sensitivity of 78% for the assessment of ER status by ^{18}F -FES PET were reported, using biopsy as the gold standard (24). This means that there are few false-positive findings. Therefore, ^{18}F -FES PET can be a good alternative tool if a biopsy is not possible or does not solve the dilemma; both cases occurred in our study. In the present study, the clinical dilemma was solved more frequently if the ^{18}F -FES PET showed ER-positive disease than ER-negative disease—a finding that relates to its higher specificity than sensitivity. Our results are comparable to those of van Kruchten et al. (16). However, caution is necessary in scans showing ER-negative disease. In our study, 9 of 14 ^{18}F -FES PET scans of patients with known metastatic BC showed ER-negative disease despite an ER-positive primary tumor. This finding could be explained by the dynamics of BC over time (such as receptor status conversion), good response to endocrine treatment, or false-negative findings.

This study had limitations. It was retrospective, and data were retrieved from electronic patient charts. Therefore, interpretation bias may play a role. Furthermore, our retrospective design did not allow us to use questionnaires to grade how helpful the ^{18}F -FES PET was (16). Also, the intended therapy before ^{18}F -FES PET could not be compared with the therapy that was chosen after the scan. The strengths of this study were its large sample size, heterogeneous population, inclusion of all consecutive eligible patients over more than 9 y, and structured and detailed analysis of a real-life daily clinical practice setting.

CONCLUSION

We found that for various indications, the ^{18}F -FES PET scan can help to solve most clinical dilemmas that remain after standard workup. ^{18}F -FES PET improves the physician's understanding of the disease status in BC patients and provides information for personalized treatment decision making. Therefore, the ^{18}F -FES PET scan has added value in BC patients who present a clinical dilemma.

DISCLOSURE

No potential conflict of interest relevant to this article was reported.

KEY POINTS

QUESTION: Does ^{18}F -FES PET have added value for solving clinical dilemmas in BC patients?

PERTINENT FINDINGS: In this retrospective study in a real-life daily clinical practice setting, clinical dilemmas were solved by ^{18}F -FES PET in most BC patients.

IMPLICATIONS FOR PATIENT CARE: Our findings support the use of ^{18}F -FES PET as a clinically meaningful diagnostic tool that supports clinical decision making in BC patients who present a persisting clinical dilemma despite standard workup.

REFERENCES

1. Ferlay J, Colombet M, Soerjomataram I, et al. Cancer incidence and mortality patterns in Europe: estimates for 40 countries and 25 major cancers in 2018. *Eur J Cancer*. 2018;103:356–387.
2. van der Waal D, Verbeek ALM, den Heeten GJ, Ripping TM, Tjan-Heijnen VCG, Broeders MJM. Breast cancer diagnosis and death in the Netherlands: a changing burden. *Eur J Public Health*. 2015;25:320–324.
3. Lord SJ, Marinovich ML, Patterson JA, et al. Incidence of metastatic breast cancer in an Australian population-based cohort of women with non-metastatic breast cancer at diagnosis. *Med J Aust*. 2012;196:688–692.
4. DeSantis CE, Ma J, Gaudet MM, et al. Breast cancer statistics, 2019. *CA Cancer J Clin*. 2019;69:438–451.
5. Harbeck N, Gnant M. Breast cancer. *Lancet*. 2017;389:1134–1150.
6. Hammond MEH, Hayes DF, Dowsett M, et al. American Society of Clinical Oncology/College of American Pathologists guideline recommendations for immunohistochemical testing of estrogen and progesterone receptors in breast cancer. *J Clin Oncol*. 2010;28:2784–2795.
7. Haynes B, Sarma A, Nangia-Makker P, Shekhar MP. Breast cancer complexity: implications of intratumoral heterogeneity in clinical management. *Cancer Metastasis Rev*. 2017;36:547–555.
8. Zardavas D, Irrthum A, Swanton C, Piccart M. Clinical management of breast cancer heterogeneity. *Nat Rev Clin Oncol*. 2015;12:381–394.
9. Cardoso F, Senkus E, Costa A, et al. 4th ESO-ESMO international consensus guidelines for advanced breast cancer (ABC 4). *Ann Oncol*. 2018;29:1634–1657.
10. van Kruchten M, de Vries EGE, Brown M, et al. PET imaging of oestrogen receptors in patients with breast cancer. *Lancet Oncol*. 2013;14:e465–e475.
11. Boers J, Venema CM, de Vries EFJ, et al. Molecular imaging to identify patients with metastatic breast cancer who benefit from endocrine treatment combined with cyclin-dependent kinase inhibition. *Eur J Cancer*. 2020;126:11–20.
12. Nienhuis HH, van Kruchten M, Elias SG, et al. ^{18}F -fluoroestradiol tumor uptake is heterogeneous and influenced by site of metastasis in breast cancer patients. *J Nucl Med*. 2018;59:1212–1218.
13. Kumar M, Salem K, Tevaarwerk AJ, Strigel RM, Fowler AM. Recent advances in imaging steroid hormone receptors in breast cancer. *J Nucl Med*. 2020;61:172–176.
14. Chae SY, Ahn SH, Kim S-B, et al. Diagnostic accuracy and safety of ^{18}F -fluoro-17 β -oestradiol PET-CT for the assessment of oestrogen receptor status in recurrent or metastatic lesions in patients with breast cancer: a prospective cohort study. *Lancet Oncol*. 2019;20:546–555.
15. Evangelista L, Guameri V, Conte PF. ^{18}F -fluoroestradiol positron emission tomography in breast cancer patients: systematic review of the literature & meta-analysis. *Curr Radiopharm*. 2016;9:244–257.
16. van Kruchten M, Glaudemans AWJM, de Vries EFJ, et al. PET imaging of estrogen receptors as a diagnostic tool for breast cancer patients presenting with a clinical dilemma. *J Nucl Med*. 2012;53:182–190.
17. Sun Y, Yang Z, Zhang Y, et al. The preliminary study of ^{18}F -fluoroestradiol PET/CT in assisting the individualized treatment decisions of breast cancer patients. *PLoS One*. 2015;10:e0116341.
18. Liu C, Gong C, Liu S, et al. ^{18}F -FES PET/CT influences the staging and management of patients with newly diagnosed estrogen receptor-positive breast cancer: a retrospective comparative study with ^{18}F -FDG PET/CT. *Oncologist*. 2019;24:e1277–e1285.

19. Venema CM, Apollonio G, Hospers GAP, et al. Recommendations and technical aspects of 16α - ^{18}F fluoro- 17β -estradiol PET to image the estrogen receptor in vivo. *Clin Nucl Med*. 2016;41:844–851.
20. Venema CM, de Vries EFJ, van der Veen SJ, et al. Enhanced pulmonary uptake on ^{18}F -FES-PET/CT scans after irradiation of the thoracic area: related to fibrosis? *EJNMMI Res*. 2019;9:82.
21. Boellaard R, Delgado-Bolton R, Oyen WJG, et al. FDG PET/CT: EANM procedure guidelines for tumour imaging: version 2.0. *Eur J Nucl Med Mol Imaging*. 2015;42:328–354.
22. Bensch F, Brouwers AH, Lub-de Hooge MN, et al. ^{89}Zr -trastuzumab PET supports clinical decision making in breast cancer patients, when HER2 status cannot be determined by standard work up. *Eur J Nucl Med Mol Imaging*. 2018;45:2300–2306.
23. Finger A, Harris M, Nishimura E, Yoon HC. Inadequate clinical indications in computed tomography chest and abdomen/pelvis scans. *Perm J*. 2018;22:18-017.
24. Kurland BF, Wiggins JR, Coche A, et al. Whole-body characterization of estrogen receptor status in metastatic breast cancer with 16α - ^{18}F fluoro- 17β -estradiol positron emission tomography: meta-analysis and recommendations for integration into clinical applications. *Oncologist*. 2020;25:835–844.
25. Glass AG, Lacey JV, Carreon JD, Hoover RN. Breast cancer incidence, 1980-2006: combined roles of menopausal hormone therapy, screening mammography, and estrogen receptor status. *J Natl Cancer Inst*. 2007;99:1152–1161.
26. Li CI, Anderson BO, Daling JR, Moe RE. Trends in incidence rates of invasive lobular and ductal breast carcinoma. *JAMA*. 2003;289:1421–1424.
27. Venema C, de Vries E, Glaudemans A, Poppema B, Hospers G, Schröder C. ^{18}F -FES PET has added value in staging and therapy decision making in patients with disseminated lobular breast cancer. *Clin Nucl Med*. 2017;42:612–614.
28. Ulaner GA, Jhaveri K, Chandarlapaty S, et al. Head-to-head evaluation of ^{18}F -FES and ^{18}F -FDG PET/CT in metastatic invasive lobular breast cancer. *J Nucl Med*. 2021;62:326–331.

Anti-CEA Pretargeted Immuno-PET Shows Higher Sensitivity Than DOPA PET/CT in Detecting Relapsing Metastatic Medullary Thyroid Carcinoma: Post Hoc Analysis of the iPET-MTC Study

Caroline Bodet-Milin¹, Alain Faivre-Chauvet¹, Thomas Carlier¹, Catherine Ansquer¹, Aurore Rauscher², Eric Frampas¹⁻³, Frederique Toulgoat³, Damien Masson⁴, Mickael Bourgeois¹, Evelyne Cerato⁵, Vincent Rohmer⁶, Olivier Couturier⁷, Delphine Druil⁸, David M. Goldenberg⁹, Robert M. Sharkey¹⁰, Jacques Barbet¹¹, and Françoise Kraeber-Bodere¹

¹Université de Nantes, CHU Nantes, CNRS, INSERM, CRCINA, Nantes, France; ²Pharmacy Unit, ICO Cancer Center, Saint-Herblain, France; ³Radiology Department, University Hospital, Nantes, France; ⁴Biology Department, University Hospital, Nantes, France; ⁵Délégation à la Recherche Clinique et à l'Innovation, University Hospital, Nantes, France; ⁶Endocrinology Department, University Hospital, Angers, France; ⁷Nuclear Medicine Department, University Hospital, Angers, France; ⁸Endocrinology Department, University Hospital, Nantes, France; ⁹IBC Pharmaceuticals, Inc., Morris Plains, New Jersey; ¹⁰Immunomedics, Inc., Morris Plains, New Jersey; and ¹¹GIP Arronax, Saint-Herblain, France

J Nucl Med 2021; 62:1221–1227

DOI: 10.2967/jnumed.120.252791

Pretargeting parameters for the use of anti-carcinoembryonic antigen (CEA) bispecific monoclonal antibody TF2 and the ⁶⁸Ga-labeled IMP288 peptide for immuno-PET have been optimized in a first-in-humans study performed on medullary thyroid carcinoma (MTC) patients (the iPET-MTC study). The aim of this post hoc analysis was to determine the sensitivity of immuno-PET in relapsing MTC patients, in comparison with conventional imaging and ¹⁸F-L-dihydroxyphenylalanine (¹⁸F-DOPA) PET/CT. **Methods:** Twenty-five studies were analyzed in 22 patients. All patients underwent immuno-PET 1 and 2 h after ⁶⁸Ga-IMP288 injection pretargeted by TF2, in addition to neck, thoracic, abdominal, and pelvic CT; bone and liver MRI; and ¹⁸F-DOPA PET/CT. The gold standard was histology or confirmation by one other imaging method or by imaging follow-up. **Results:** In total, 190 lesions were confirmed by the gold standard: 89 in lymph nodes, 14 in lungs, 46 in liver, 37 in bone, and 4 in other sites (subcutaneous tissue, heart, brain, and pancreas). The number of abnormal foci detected by immuno-PET was 210. Among these, 174 (83%) were confirmed as true-positive by the gold standard. Immuno-PET showed a higher overall sensitivity (92%) than ¹⁸F-DOPA PET/CT (65%). Regarding metastatic sites, immuno-PET had a higher sensitivity than CT, ¹⁸F-DOPA PET/CT, or MRI for lymph nodes (98% vs. 83% for CT and 70% for ¹⁸F-DOPA PET/CT), liver (98% vs. 87% for CT, 65% for ¹⁸F-DOPA PET/CT, and 89% for MRI), and bone (92% vs. 64% for ¹⁸F-DOPA PET/CT and 86% for MRI), whereas sensitivity was lower for lung metastases (29% vs. 100% for CT and 14% for ¹⁸F-DOPA PET/CT). Tumor SUV_{max} at 60 min ranged from 1.2 to 59.0, with intra- and interpatient variability. **Conclusion:** This post hoc study demonstrates that anti-carcinoembryonic antigen immuno-PET is an effective procedure for detecting metastatic MTC lesions. Immuno-PET showed a higher overall sensitivity than ¹⁸F-DOPA PET/CT for disclosing metastases, except for the lung, where CT remains the most effective examination.

Key Words: immuno-PET; MTC; carcinoembryonic antigen; bispecific antibody; pretargeted radioimmunoimaging

Medullary thyroid carcinoma (MTC) arises from calcitonin-producing parafollicular C cells and represents 1%–2% of thyroid cancers (1). The tumor is frequently aggressive; on initial staging, 35% of MTC patients have tumor extending into the thyroid-surrounding tissues or regional lymph node involvement, and 13% have distant metastases, especially in the lung, liver, or bones (2,3). According to American Thyroid Association guidelines, when calcitonin is higher than 150 pg/mL, anatomic imaging-based staging is recommended, such as neck ultrasonography or CT, chest CT, liver CT or MRI, and spine and pelvis bone or bone marrow MRI (4,5). As indolent tumors, MTCs have a generally low avidity for ¹⁸F-FDG; therefore, PET with ¹⁸F-FDG is not recommended for initial staging but can be useful for assessing advanced disease characterized by dedifferentiation and rapid progression. ¹⁸F-L-dihydroxyphenylalanine (¹⁸F-DOPA) PET/CT has a higher sensitivity and specificity than ¹⁸F-FDG PET/CT in MTC and can reveal occult metastases or small lesions for initial staging and at relapse. These examinations also can play a crucial role in the management of relapsing MTC patients (6–12).

Carcinoembryonic antigen (CEA) is a cell-surface glycoprotein overexpressed in several solid tumors, including MTC, and functional imaging using radiolabeled anti-CEA monoclonal antibodies represents a potentially interesting method for detection of MTC metastases (13). TF2 is an engineered bispecific monoclonal antibody (BsMAb) comprising an antihapten Fab fragment derived from the murine 679 antibody recognizing the histamine-succinyl-glycine motif, as well as 2 humanized anti-CEA Fab fragments derived from the hMN-14 antibody (labetuzumab), formed into a trivalent 157-kD protein by the Dock-and-Lock (Immunomedics) procedure (14). IMP288 is a bivalent histamine-succinyl-glycine hapten that can be labeled with a variety of radionuclides for

Received Jul. 8, 2020; revision accepted Jan. 13, 2021.

For correspondence or reprints, contact Caroline Bodet-Milin (caroline.milin@chu-nantes.fr).

Published online February 5, 2021.

COPYRIGHT © 2021 by the Society of Nuclear Medicine and Molecular Imaging.

therapy (^{90}Y and ^{177}Lu), scintigraphy (^{111}In), or PET (^{124}I , ^{68}Ga , and ^{18}F) (15–17).

We previously reported the optimization of the pretargeting parameters (BsmAb and peptide molar doses and pretargeting delay) of pretargeted immuno-PET using TF2 and ^{68}Ga -IMP288 in the iPET-MTC first-in-humans study performed on MTC patients (18). The aim of this post hoc analysis was to determine the sensitivity of this novel imaging method in relapsing MTC patients, in comparison to conventional imaging and ^{18}F -DOPA PET/CT.

MATERIALS AND METHODS

Population

The inclusion and exclusion criteria have been reported previously (18). Briefly, all eligible adult patients had a histologic diagnosis of MTC treated by complete surgery and presenting a calcitonin serum level of 150 pg/mL or more with at least 1 lesion 10 mm or greater on conventional imaging. In the 4 wk preceding immuno-PET, a staging workup that included a complete history, physical examination, CEA and calcitonin serum level measurements, and ^{18}F -DOPA PET/CT was performed for each patient. Conventional imaging, including contrast-enhanced CT of the neck, chest, abdomen, and pelvis, as well as bone and liver MRI, was performed. The iPET-MTC trial, sponsored by Nantes University Hospital, was approved by the responsible ethics committee (comité de protection des personnes) and registered at ClinicalTrials.gov (NCT01730638), and all patients gave written informed consent.

Investigational Agents and Study Design

Radiopharmaceutical manufacturing and premedication protocols have been previously reported (18). For pharmacokinetics optimization, the first 16 immuno-PET studies were performed under 5 different pretargeting conditions (molar doses of BsmAb and peptide, and delay); 3 patients were included per cohort from cohorts 1 to 5 (18). One patient included in the third cohort did not receive the full hapten dose and was excluded and replaced in the optimization phase of the study. This patient was reintegrated in this part of the study evaluating the performance of immuno-PET. The last 9 immuno-PET studies were performed with the cohort 2 scheme considered as optimal after the optimization phase (Table 1).

Safety was assessed by monitoring vital signs, physical examination findings, and adverse events. Human antihuman antibody titers were measured by Immunomedics at 3 or 6 mo, using an enzyme-linked immunosorbent assay (abnormal when ≥ 50 ng/mL).

PET Acquisition

Immuno-PET and ^{18}F -DOPA PET/CT were performed using a 4-ring Siemens Biograph mCT system and reconstructed using 3-dimensional ordinary Poisson ordered-subsets expectation maximization with point-spread-function correction and time-of-flight mode (3 iterations, 21 subsets, gaussian postfiltering of 2 mm in full width at half maximum, voxel size of $4 \times 4 \times 2$ mm). Whole-body acquisitions were performed under normal tidal respiration for 2.5 min per bed position. CT was performed using a variable mAs, 120 kVp, and a pitch of 1 without contrast enhancement. Acquisitions were performed from the top of the head to the mid thigh (6–8 steps per patient). Immuno-PET was performed 60 and 120 min after a 150-MBq injection of ^{68}Ga -IMP288, and ^{18}F -DOPA PET/CT was performed 60 min after a 3 MBq/kg injection of ^{18}F -DOPA.

Conventional Imaging Acquisition

Patients were scanned with multidetector CT. A contrast-enhanced series was acquired after intravenous injection of nonionic iodinated contrast medium (350 mL, 1.5 mL/kg, rate of 3 mL/s using a power injector), visualizing the body from the neck to the pelvis. MRI was conducted using a 1.5-T whole-body MRI system. The liver was imaged in the axial plane using T2-weighted, MR diffusion-weighted sequences and transverse breath-hold 3-dimensional T1-weighted fat-suppressed spoiled gradient-recalled-echo sequences before and after administration of gadolinium chelate. The standard MR sequences for spine and pelvis included T1-weighted turbo spin-echo, T2-weighted short-T1 inversion recovery with fat suppression, and contrast-enhanced T1-weighted turbo spin-echo with fat suppression. The whole spine was explored in sagittal views with or without complementary axial views and the pelvis in coronal and axial views.

Image Analysis

Abnormal uptake on immuno-PET was defined as a focal increase visually higher than the surrounding background level. Attenuation-correction CT data were used in addition to PET data for interpretation of the immuno-PET and ^{18}F -DOPA PET/CT findings. Tumor SUV_{max} was determined on the most intense focus confirmed as MTC in the whole-body scan. ^{18}F -DOPA PET/CT and immuno-PET were interpreted separately by 2 nuclear medicine physicians who did not know the other diagnostic results and had expertise in immunotargeting and PET.

Conventional imaging findings were interpreted by a consensus of radiologists with expertise in endocrine tumors, who were unaware of the ^{18}F -DOPA PET/CT and immuno-PET results but could consider the results of previous conventional imaging. At initial conventional imaging, lesions were considered metastatic in any of the following 5

TABLE 1
Scheme of Cohorts

Cohort	Patients (n)	TF2 dose (nmol)	Delay (h)	^{68}Ga -IMP288 dose and activity (nmol)	MBq	TF2/IMP288 molar dose ratio
I	3	120	24	6	150	20
II	3 + 9*	120	30	6	150	20
III	3 + 1†	120	42	6	150	20
IV	3	120	30	3	150	40
V	3	60	30	3	150	20

*Three patients in optimization phase of study and 9 in validation phase.

†Patient 8 did not receive full hapten dose and was excluded and replaced for optimization phase study but was reintegrated for sensitivity study.

cases: first, if there were pulmonary nodules on chest CT; second, if there were focal hepatic lesions (hyperintense at a high b value on diffusion-weighted MRI, moderately to strongly hyperintense on T2-weighted MRI [less than the signal intensity of liquid], or hypervascular or peripherally enhanced after contrast injection on MRI or CT); third, if there was hyperintensity on T2- and diffusion-weighted MRI, hypointensity on T2- and T1-weighted MRI, or mixed heterogeneous intensity on MRI; fourth, if there was a short-axis (>1 cm) or hypervascular pattern of lymph nodes; and fifth, if there were soft-tissue tumors. The appearance of new lesions during the course of the disease and an increase in size during follow-up were also considered.

For both ethical and practical reasons, not every suspected lesion was evaluated by histology. If necessary, complementary imaging was performed to assess the most important lesions suspected by immuno-PET and not detected by the initial work-up. For this study, the gold standard was determined on the basis of histology, by confirmation of a lesion by one other imaging method, or by imaging follow-up. Indeed, an imaging assessment with contrast-enhanced CT of the neck, chest, abdomen, and pelvis or bone MRI, liver MRI, or ¹⁸F-DOPA PET/CT was performed 3 mo after immuno-PET, decided by a panel of experts involving endocrinologists, radiologists, and nuclear physicians. CEA and calcitonin serum levels were also measured. The same panel of experts could propose a second biomarker and imaging evaluation at 6 mo after immuno-PET. RECIST or the criteria of the European Organization for Research and Treatment of Cancer were used for conventional imaging follow-up (19,20).

A lesion detected by an imaging method was considered related to MTC (true-positive) when confirmed by one other imaging method, by histopathology, or by follow-up. A lesion visualized by one imaging method and progressing during follow-up using RECIST or the criteria of the European Organization for Research and Treatment of Cancer was considered true-positive. A negative finding on an imaging method was considered false-negative if positive by one other imaging method plus histopathology or by one other imaging method plus follow-up. Sensitivity [(true-positive/true-positive + false-negative) × 100] per lesion was calculated for each imaging modality. A positive finding on an imaging method was considered unconfirmed if not confirmed either by one other imaging method or by follow-up or histopathology. A positive finding on an imaging method was considered false-positive if not confirmed as positive by histopathology.

The Wilcoxon rank sum test was used to compare median tumor SUV_{max} and median tumor SUV_{max}-to-mediastinal blood pool ratio at 60 or 120 min, and the Spearman test was used to evaluate whether SUV_{max} was associated with CEA or calcitonin levels.

RESULTS

Patient Characteristics and Adverse Events

The characteristics of the 22 included patients are presented in Table 2. Three patients underwent a second immuno-PET study at least 12 mo after the first procedure, coupled with conventional imaging or DOPA PET/CT, accounting for a total of 25 immuno-PET, conventional imaging, or DOPA PET/CT studies in the 22 patients. Pathologic lesions were histopathologically analyzed in 6 patients (2 noncontributory biopsies, 3 biopsies confirming MTC metastases, and 1 biopsy diagnosing another disease).

No patient experienced an anaphylactic reaction during or after the TF2 infusion. One patient experienced a grade 3 reaction starting immediately after the hapten infusion, with malaise, bronchospasm, tachycardia, and hypertension, requiring hospitalization. Therefore, the protocol was amended, and a premedication with antihistamine and corticosteroid before both TF2 and IMP288

TABLE 2
Patient Characteristics

Characteristic	Data
Total patients	22
Age (y)	62 (28–75)
Sex	
Male	15
Female	7
Time from diagnosis (y)	5.5 (0.5–31)
Calcitonin concentration (pg/mL)	488 (154–39,000)
CEA concentration (ng/mL)	18 (3–1,443)
Location of disease	
Lymph node	19
Lung	8
Liver	13
Bone	13
Other	4

Qualitative data are number; continuous data are median and range.

injections was given thereafter to all patients. No further allergic reactions occurred afterward.

Human antihuman antibody was analyzed in 19 patients (at 3 and 6 mo in 14 patients and only at 3 mo in 5 patients). Three patients had abnormal human antihuman antibody. In 2 of those patients, the level was abnormal at 3 mo (52 and 152 ng/mL) but had normalized by 6 mo. In the third patient, the level was normal at 3 mo but abnormal at 6 mo (244 ng/mL).

Imaging Results and Sensitivity

All patients had abnormalities detected by immuno-PET, conventional imaging, or ¹⁸F-DOPA PET/CT (Table 3). In total, 190 lesions were confirmed according to the definition of the gold standard: 89 in lymph nodes, 14 in the lungs, 46 in the liver, 37 in bone or bone marrow, and 4 at other sites (subcutaneous tissue, heart, brain, and pancreas). Among these 190 lesions validated by the gold standard, 174 were confirmed by another imaging method, 13 by follow-up, and 3 by histology. Immuno-PET detected a total of 210 abnormal foci (1–22 per patient). Among these, 174 (83%) were confirmed as true-positive according to the gold standard (167 by another imaging method, 4 by follow-up, and 3 by histology). Sixteen lesions were missed (false-negative lesions): 10 in the lungs, 3 in bone, 2 in lymph nodes, and 1 in the liver (Table 3). All immuno-PET lesions were seen at both 60 and 120 min. Tumor SUV_{max} at 60 min ranged from 1.2 to 59.0, with intra- and interpatient variability (Fig. 1). There was no significant difference between median tumor SUV_{max} and median tumor SUV_{max}-to-mediastinal blood pool ratio at 60 or 120 min (19.54 [range, 4.09–94.14] vs. 21.31 [range, 5.14–100.2] [*P* = 0.84] and 8.14 [range, 1.39–34.1] vs. 8.5 [range, 2.7–49.6] [*P* = 0.75], respectively). SUV_{max} was not associated with CEA or calcitonin serum levels (Spearman *P* = 0.71 and 0.73, respectively).

CT, ¹⁸F-DOPA PET/CT, liver MRI, and bone marrow MRI detected 130, 124, 41, and 33 true-positive lesions, respectively, and

TABLE 3
Sensitivity of Immuno-PET, ¹⁸F-DOPA PET/CT, and Conventional Imaging

Location	Immuno-PET	¹⁸ F-DOPA PET/CT	CT	Liver MRI	Bone marrow MRI
Nodes	87/89 (98%)	64/89 (72%)	73/89 (82)%	NA	NA
Lung	4/14 (29%)	2/14 (14%)	14/14 (100%)	NA	NA
Liver	45/46 (98%)	30/46 (65%)	39/46 (87%)	41/46 (89%)	NA
Bone marrow	34/37 (92%)	25/37 (68%)	NA	NA	33/37 (89%)
Other	4/4 (100%)	3/4 (75%)	4/4 (100%)	NA	NA
Global	174/190 (92%)	124/190 (65%)	130/153 (85%)	NA	NA

NA = not applicable.

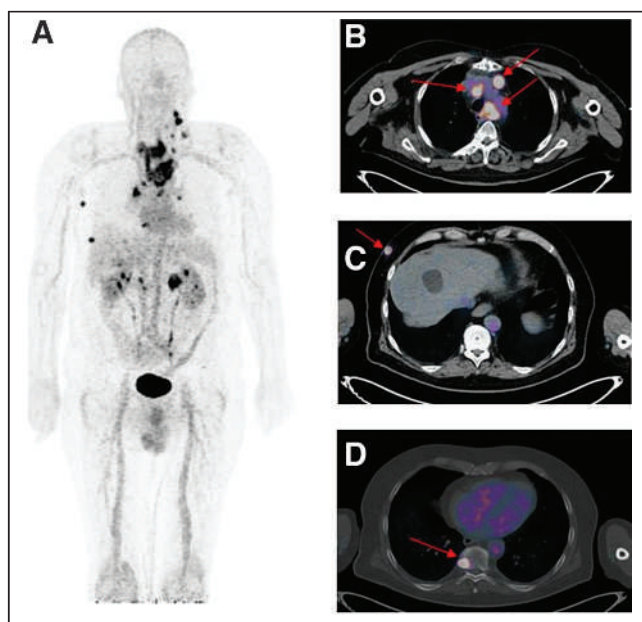


FIGURE 1. Immuno-PET/CT with anti-CEA BsmAb and ⁶⁶Ga-IMP288 peptide showing pathological lesions with heterogeneous SUV_{max} ranging from 3.0 to 20.1. Maximum-intensity-projection (MIP) image (A) showed several pathological lesions. On the fusion axial images, arrows located mediastinal nodes (B), subcutaneous lesions (C), and bone metastasis (D).

missed 23, 66, 5, and 4 lesions (Table 3). Subcutaneous, pancreatic, and heart lesions were detected by immuno-PET, conventional imaging, and ¹⁸F-DOPA PET/CT, whereas a brain lesion was depicted by immuno-PET and confirmed by brain MRI but not detected by ¹⁸F-DOPA PET/CT (Fig. 2). No lesion was considered false-positive by immuno-PET, but 36 lesions remained not confirmed. For ¹⁸F-DOPA PET/CT, 7 lesions remained not confirmed and 1 was false-positive: a diffuse area of pathologic bone marrow uptake was described on ¹⁸F-DOPA PET/CT, whereas Vaquez polycythemia was diagnosed without MTC metastases on bone marrow biopsy. Bone MRI was also false-positive in this patient, whereas immuno-PET was negative. For CT, 7 lesions were not confirmed (1 peritoneal nodule and 6 lung micronodules). Supplemental Table 1 summarizes the per-patient performance of immuno-PET, ¹⁸F-DOPA PET/CT, CT, liver MRI, and bone MRI (supplemental materials are available at <http://jnm.snmjournals.org>).

Immuno-PET showed a higher overall sensitivity (92%) than ¹⁸F-DOPA PET/CT (65%) (Table 3). The sensitivity of immuno-PET was also 92% (79/86) considering only the 13 exams performed with the suboptimal scheme. Regarding the different metastatic sites, immuno-PET had a higher sensitivity than CT or ¹⁸F-DOPA PET/CT for lymph nodes (98% vs. 82% and 72%, respectively) (Fig. 3) and liver (98% vs. 87% and 65%, respectively) (Fig. 4), whereas sensitivity was lower for lung metastases (29% vs. 100% and 14%, respectively). Immuno-PET had a slightly higher sensitivity for bone evaluation than MRI or ¹⁸F-DOPA PET/CT (92% vs. 89% and 68%, respectively).

DISCUSSION

Currently, surgery remains the only treatment for cure of MTC patients. Once the disease is metastatic, the therapeutic options are limited. MTC cells do not concentrate radioiodine, and the efficacy of chemotherapeutic agents is limited (4). In the last decade, tyrosine kinase inhibitors have been evaluated in patients with progressive metastatic disease, with benefits on progression-free survival for both vandetanib and cabozantinib (21). Locally advanced or relapsing MTC requires a careful work-up, including a work-up of calcitonin and CEA serum level measurements and determination of their doubling time, as well as comprehensive imaging to determine the extent of the disease, its aggressiveness, and whether therapy is needed. Calcitonin is the most sensitive and specific tumor biomarker, and CEA represents a prognostic biomarker because an increased CEA serum level suggests an advanced state and tumor dedifferentiation (22). Serum calcitonin and CEA doubling times are prognostic of survival (21,23). Morphologic imaging is often negative or doubtful in the presence of rising levels of calcitonin (3–5). Therefore, functional PET/CT imaging using different radiopharmaceuticals is recommended. ¹⁸F-DOPA seems to be the most useful tracer to detect recurrent MTC based on rising biomarker levels, whereas ¹⁸F-FDG may be complementary in patients with an aggressive tumor phenotype (3,5,8,11,24).

The present study found a high imaging performance for anti-CEA TF2 BsmAb and ⁶⁸Ga-IMP288 in patients who have metastatic MTC, with immuno-PET achieving a 92% overall sensitivity—somewhat better than the sensitivity of conventional imaging and ¹⁸F-DOPA PET/CT for lymph node, liver, and bone or bone marrow examinations. However, as in a previous study on breast cancer patients, immuno-PET was less effective than CT for lung metastasis detection (25). The sensitivity of ¹⁸F-DOPA PET/CT also was low for lung lesion detection in this population. Spontaneous breathing during the PET/CT acquisition and the large positron range of ⁶⁸Ga may affect

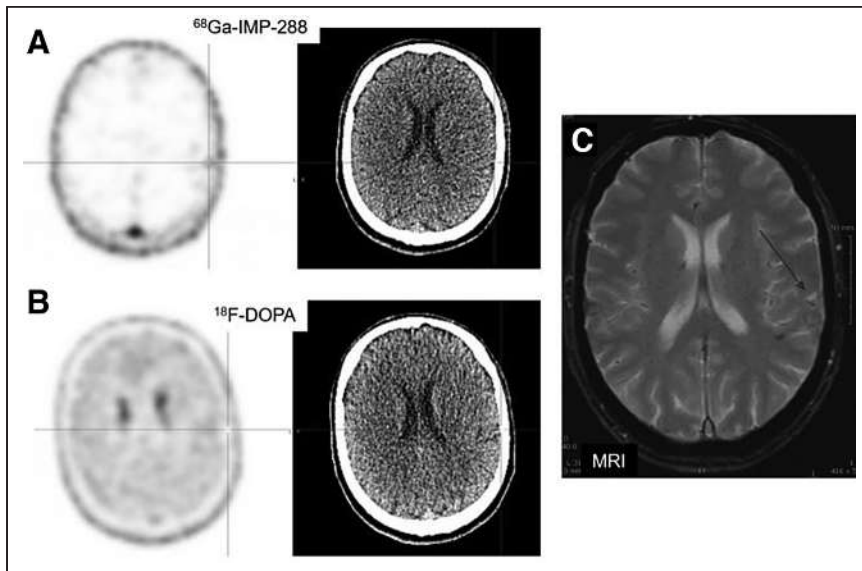


FIGURE 2. (A) Immuno-PET images with anti-CEA BsmAb and ^{68}Ga -IMP288 showing temporoparietal uptake in brain. CT of the PET/CT was negative. (B) PET/CT with ^{18}F -DOPA PET/CT was negative. (C) Brain MRI (guided by immuno-PET) confirmed pathologic temporoparietal lesion (arrow).

the ability of PET to detect small lung lesions. Indeed, the sensitivity of immuno-PET was better than that of ^{18}F -DOPA PET/CT both overall and for metastatic sites, suggesting that this novel functional whole-body imaging method may be of interest for MTC staging and therapeutic evaluation. Excluding lung lesions only 6 lesions (3 in bone, 2 in lymph nodes, and 1 in liver) in 4 patients were false-negative on immuno-PET when all other MTC metastases were positive on immuno-PET. Two of these 6 lesions (1 bone lesion and 1 node lesion) were

significantly upregulated in neuroendocrine tumors, including MTC. In a metaanalysis including 8 studies and 146 patients, the detection rates of ^{18}F -DOPA PET and PET/CT, by per-patient and per-lesion analyses, were 66% and 71%, respectively, with performance increasing in patients with a serum calcitonin level of at least 1,000 ng/L and a calcitonin doubling time of less than 24 mo (26).

^{18}F -FDG is a glucose metabolism tracer, with increased uptake in MTCs undergoing dedifferentiation and becoming more aggressive

positive using ^{18}F -DOPA. The small size of these lesions, in addition to the spontaneous breathing during the PET/CT acquisition, may affect PET performance because of the partial-volume effect. A heterogeneous expression of CEA on some metastatic lesions might also explain these false-negative immuno-PET results. The ^{18}F -DOPA PET/CT results—with a higher number of false-negative lesions (16 for immuno-PET vs. 66 for ^{18}F -DOPA PET/CT)—had no impact on patient staging in this study, suggesting that immuno-PET could potentially replace ^{18}F -DOPA PET/CT in patients with metastatic MTC if the technique were available in clinical practice.

In clinical practice, ^{18}F -DOPA, ^{18}F -FDG, and somatostatin analogs labeled with ^{68}Ga are available to explore MTC patients with an increasing calcitonin serum level. ^{18}F -DOPA penetrates into tumor cells through transmembrane amino acid transporters that are significantly

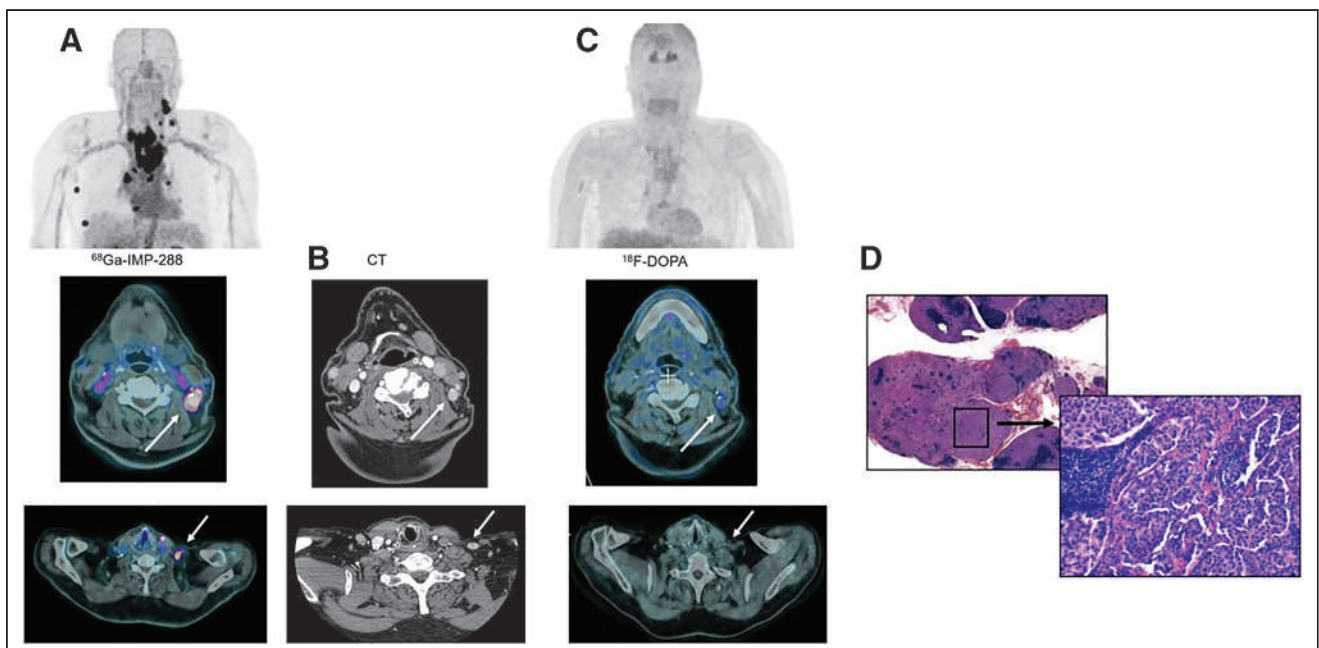


FIGURE 3. (A) Immuno-PET/CT with anti-CEA BsmAb and ^{68}Ga -IMP288 maximum-intensity-projection (MIP) showing multiple pathologic lesions confirmed to be cervical and mediastinal nodes on the fusion axial images (arrows). (B) Pathological nodes were confirmed on contrast-enhanced CT (arrows) but not visualized by MIP or fusion axial ^{18}F -DOPA PET/CT images (C). (D) Metastatic MTC involvement was confirmed by histologic analysis (hematoxylin/eosin/saffron staining, $\times 12.5$ and $\times 200$).

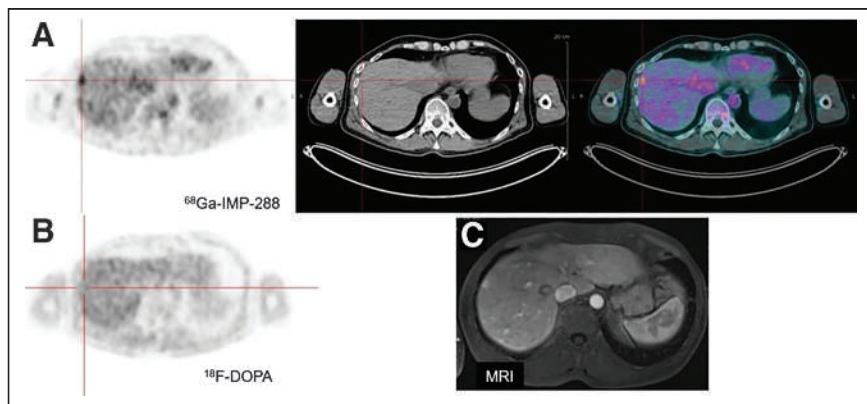


FIGURE 4. (A) Immuno-PET/CT with anti-CEA BsmAb and ^{68}Ga -IMP288 axial PET, CT, and fusion images showing multiple liver lesions (arrows), whereas ^{18}F -DOPA PET was negative (B). (C) MRI-confirmed lesion.

(5). A metaanalysis based on 24 studies comprising 538 patients with suspected recurrent MTC found, using a per-patient-based analysis, that ^{18}F -FDG PET or PET/CT had a detection rate of 59%, with performance increasing when serum calcitonin was at least 1,000 ng/L, CEA at least 5 ng/mL, calcitonin doubling time less than 12 mo, and CEA doubling time less than 24 mo (26). Neuroendocrine tumors usually overexpress somatostatin receptors, and somatostatin analogs labeled with ^{68}Ga are useful for their assessment. A recent prospective study evaluating ^{68}Ga -DOTATATE PET/CT in 30 MTC patients showed that it was inferior to conventional imaging, except for bone scans (27), in patients with metastatic disease. The sensitivity of ^{68}Ga -DOTATATE PET/CT was 56%, 57%, and 9% for detecting neck lymph nodes, lung metastases, and liver metastases, respectively, and 100% for bone metastases.

Even if no comparative studies have been done on homogeneous populations, our results suggest that, except for lung metastasis detection, anti-CEA pretargeted immuno-PET may have a higher performance than other available PET/CT methods and conventional imaging to detect recurrence in MTC patients with rising serum biomarkers. Our previous studies showed that CEA expression seemed to be almost constant in MTC and that high-sensitivity PET imaging using CEA as a target would detect the disease independently of the prognosis (9,28–30).

Despite the excellent sensitivity of pretargeted immuno-PET, our study had some limitations. Only a small number of patients were included. This limited number is explained on the one hand by the relative rarity of the tumor concerned and on the other hand by our intention to test this new pretargeting system in parallel in MTC and breast cancer patients (24). Moreover, we evaluated the performance of immuno-PET in the whole population and not only for the 12 examinations performed under the optimal pretargeting conditions defined by the optimization study. This bias could penalize us because 13 procedures were performed under suboptimal conditions; however, the sensitivity of immuno-PET was the same in this subgroup as in the overall population (92%). The absence of a systematic early acquisition time for ^{18}F -DOPA PET/CT—although ^{18}F -DOPA clearance can sometimes be fast in this tumor—could also represent a bias and explain why the global sensitivity of ^{18}F -DOPA PET/CT was slightly lower than usually reported in the literature (12).

Finally, and this bias is recurrent in many imaging studies, 36 lesions detected by immuno-PET remained unconfirmed by the gold standard during the follow-up period. Although the gold

standard had a relatively extensive definition, not all lesions could be confirmed. Indeed, immuno-PET visualized more lesions than the other modalities—lesions that were often very small, not confirmed by conventional assessment, and inaccessible to histologic analysis. Only 6 biopsies were performed in our study, 2 being non-contributory, 3 confirming the MTC metastases, and 1 diagnosing another disease. This lack of confirmation does not allow an accurate assessment of the positive predictive value and specificity of this new imaging technique.

Pretargeted immuno-PET could also be a theranostic procedure for qualitative and quantitative whole-body tumor biomarker cartography to

select candidates for antibody-based therapy. Our team reported promising results for radionuclide therapy using a previous generation of pretargeting reagents (anti-CEA \times anti-diethylentriaminepentacetic acid [DTPA] BsmAb hMN-14 \times m734 and ^{131}I -di-DTPA-indium hapten) (28–31). In 42 patients with metastatic, progressing MTC included in a phase II study, a 76.2% disease control rate (durable stabilization plus objective response) was observed (2). Using the new-generation IMP288 peptide, the feasibility and safety of theranostics using TF2 and $^{111}\text{In}/^{177}\text{Lu}$ -IMP288 have been reported in metastatic colorectal and lung cancer patients (32,33). Moreover, anti-CEA antibody–drug conjugates are under preclinical and clinical development, and immuno-PET using ^{68}Ga -IMP288 might be able to select patients for these therapeutic strategies (34,35).

CONCLUSION

This post hoc analysis demonstrated that anti-CEA immuno-PET using the trivalent BsmAb TF2 and the ^{68}Ga -IMP288 peptide is a safe and effective procedure for detecting metastatic MTC lesions. Immuno-PET targeting CEA showed a higher overall sensitivity than ^{18}F -DOPA PET/CT for disclosing metastases, including dissemination to the bone marrow and brain. However, CT remains the most effective imaging method for lung examination. Moreover, in the era of precision medicine, immuno-PET represents a potential theranostic molecular imaging technique to select patients for antibody-based therapy.

DISCLOSURE

This work was supported in part by grants in 2010 from the French DHOS INCA (i.e., the French National Agency for Research) (“Investissements d’Avenir” IRON Labex no. ANR-11-LABX-0018-01 and ArronaxPlus Equipex no. ANR-11-EQPX-0004) and by a grant from SIRIC ILIAD (INCa-DGOS-Inserm_12558). The proprietary TF2 and IMP288 reagents were provided by Immunomedics, Inc., and IBC Pharmaceuticals, Inc. David Goldenberg and Robert Sharkey own Immunomedics stock or stock options, and David Goldenberg has royalty-bearing patented inventions. David Goldenberg is the founder and retired Chairman and Chief Scientific Officer of Immunomedics, Inc., and the founder and retired Chairman of IBC Pharmaceuticals, Inc. Robert Sharkey was Senior Director of Scientific and Regulatory Affairs,

and then a consultant, to Immunomedics, Inc. No other potential conflict of interest relevant to this article was reported.

KEY POINTS

QUESTION: What is the sensitivity of anti-CEA immuno-PET using the trivalent BsmAb TF2 and the ^{68}Ga -IMP288 peptide in relapsing MTC patients?

PERTINENT FINDINGS: The overall sensitivity of immuno-PET was 92%, higher than that of ^{18}F -DOPA PET/CT (65%), for disclosing metastases, including dissemination to the bone marrow and brain. CT remains the most effective imaging method for lung examination.

IMPLICATIONS FOR PATIENT CARE: Anti-CEA immuno-PET is an effective procedure for detecting metastatic MTC lesions and represents a potential theranostic molecular imaging technique for selecting patients to receive antibody-based therapy.

REFERENCES

- Roy M, Chen H, Sippel RS. Current understanding and management of medullary thyroid cancer. *Oncologist*. 2013;18:1093–1100.
- Roman S, Lin R, Sosa JA. Prognosis of medullary thyroid carcinoma: demographic, clinical, and pathologic predictors of survival in 1252 cases. *Cancer*. 2006;107:2134–2142.
- Kushchayev SV, Kushchayeva YS, Tella SH, Glushko T, Pacak K, Teytelboym OM. Medullary thyroid carcinoma: an update on imaging. *J Thyroid Res*. 2019;2019:1893047.
- Wells SA, Asa SL, Dralle H, et al. Revised American Thyroid Association guidelines for the management of medullary thyroid carcinoma. *Thyroid*. 2015;25:567–610.
- Filetti S, Durante C, Hartl D, et al. Thyroid cancer: ESMO clinical practice guidelines for diagnosis, treatment and follow-up. *Ann Oncol*. 2019;30:1856–1883.
- Treglia G, Rufini V, Salvatori M, Giordano A, Giovanella L. PET imaging in recurrent medullary thyroid carcinoma. *Int J Mol Imaging*. 2012;2012:324686.
- Luster M, Karges W, Zeich K, et al. Clinical value of ^{18}F -fluorine-fluorodihydroxyphenylalanine positron emission tomography/computed tomography in the follow-up of medullary thyroid carcinoma. *Thyroid*. 2010;20:527–533.
- Kauhanen S, Schalin-Jäntti C, Seppänen M, et al. Complementary roles of ^{18}F -DOPA PET/CT and ^{18}F -FDG PET/CT in medullary thyroid cancer. *J Nucl Med*. 2011;52:1855–1863.
- Oudoux A, Salaun P-Y, Bourmaud C, et al. Sensitivity and prognostic value of positron emission tomography with ^{18}F -fluorodeoxyglucose and sensitivity of immunoscintigraphy in patients with medullary thyroid carcinoma treated with anticarcinoembryonic antigen-targeted radioimmunotherapy. *J Clin Endocrinol Metab*. 2007;92:4590–4597.
- Verbeek HHG, Plukker JTM, Koopmans KP, et al. Clinical relevance of ^{18}F -FDG PET and ^{18}F -DOPA PET in recurrent medullary thyroid carcinoma. *J Nucl Med*. 2012;53:1863–1871.
- Romero-Lluch AR, Cuenca-Cuenca JJ, Guerrero-Vázquez R, et al. Diagnostic utility of PET/CT with ^{18}F -DOPA and ^{18}F -FDG in persistent or recurrent medullary thyroid carcinoma: the importance of calcitonin and carcinoembryonic antigen cut-off. *Eur J Nucl Med Mol Imaging*. 2017;44:2004–2013.
- Giovanella L, Treglia G, Iakovou I, Mihailovic J, Verburg FA, Luster M. EANM practice guideline for PET/CT imaging in medullary thyroid carcinoma. *Eur J Nucl Med Mol Imaging*. 2020;47:61–77.
- Bailly C, Cléry P-F, Faivre-Chauvet A, et al. Immuno-PET for clinical theranostic approaches. *Int J Mol Sci*. 2016;18:57.
- Rossi EA, Goldenberg DM, Cardillo TM, McBride WJ, Sharkey RM, Chang C-H. Stably tethered multifunctional structures of defined composition made by the dock and lock method for use in cancer targeting. *Proc Natl Acad Sci USA*. 2006;103:6841–6846.
- Kraeber-Bodéré F, Rousseau C, Bodet-Milin C, et al. A pretargeting system for tumor PET imaging and radioimmunotherapy. *Front Pharmacol*. 2015;6:54.
- McBride WJ, Sharkey RM, Karacay H, et al. A novel method of ^{18}F radiolabeling for PET. *J Nucl Med*. 2009;50:991–998.
- Schoffelen R, Sharkey RM, Goldenberg DM, et al. Pretargeted immuno-positron emission tomography imaging of carcinoembryonic antigen-expressing tumors with a bispecific antibody and a ^{68}Ga - and ^{18}F -labeled hapten peptide in mice with human tumor xenografts. *Mol Cancer Ther*. 2010;9:1019–1027.
- Bodet-Milin C, Faivre-Chauvet A, Carlier T, et al. Immuno-PET using anticarcinoembryonic antigen bispecific antibody and ^{68}Ga -labeled peptide in metastatic medullary thyroid carcinoma: clinical optimization of the pretargeting parameters in a first-in-human trial. *J Nucl Med*. 2016;57:1505–1511.
- Young H, Baum R, Cremerius U, et al. Measurement of clinical and subclinical tumor response using [^{18}F]fluorodeoxyglucose and positron emission tomography: review and 1999 EORTC recommendations. European Organization for Research and Treatment of Cancer (EORTC) PET Study Group. *Eur J Cancer*. 1999;35:1773–1782.
- Schwartz LH, Litière S, de Vries E, et al. RECIST 1.1: update and clarification—from the RECIST Committee. *Eur J Cancer*. 2016;62:132–137.
- Hadoux J, Schlumberger M. Chemotherapy and tyrosine-kinase inhibitors for medullary thyroid cancer. *Best Pract Res Clin Endocrinol Metab*. 2017;31:335–347.
- Saad MF, Fritsche HA, Samaan NA. Diagnostic and prognostic values of carcinoembryonic antigen in medullary carcinoma of the thyroid. *J Clin Endocrinol Metab*. 1984;58:889–894.
- Barbet J, Campion L, Kraeber-Bodéré F, Chatal J-F, GTE study group. Prognostic impact of serum calcitonin and carcinoembryonic antigen doubling-times in patients with medullary thyroid carcinoma. *J Clin Endocrinol Metab*. 2005;90:6077–6084.
- Lee S-W, Shim SR, Jeong SY, Kim S-J. Comparison of 5 different PET radiopharmaceuticals for the detection of recurrent medullary thyroid carcinoma: a network meta-analysis. *Clin Nucl Med*. 2020;45:341–348.
- Rousseau C, Goldenberg DM, Colombie M, et al. Initial clinical results of a novel immuno-PET theranostic probe in HER2-negative breast cancer. *J Nucl Med*. 2020;61:1205–1211.
- Treglia G, Cocciolillo F, Di Nardo F, et al. Detection rate of recurrent medullary thyroid carcinoma using fluorine-18 dihydroxyphenylalanine positron emission tomography: a meta-analysis. *Acad Radiol*. 2012;19:1290–1299.
- Castroneves LA, Coura Filho G, de Freitas RMC, et al. Comparison of ^{68}Ga PET/CT to other imaging studies in medullary thyroid cancer: superiority in detecting bone metastases. *J Clin Endocrinol Metab*. 2018;103:3250–3259.
- Salaun P-Y, Campion L, Bourmaud C, et al. Phase II trial of anticarcinoembryonic antigen pretargeted radioimmunotherapy in progressive metastatic medullary thyroid carcinoma: biomarker response and survival improvement. *J Nucl Med*. 2012;53:1185–1192.
- Peltier P, Curtet C, Chatal JF, et al. Radioimmunodetection of medullary thyroid cancer using a bispecific anti-CEA/anti-indium-DTPA antibody and an indium-111-labeled DTPA dimer. *J Nucl Med*. 1993;34:1267–1273.
- Barbet J, Peltier P, Bardet S, et al. Radioimmunodetection of medullary thyroid carcinoma using indium-111 bivalent hapten and anti-CEA \times anti-DTPA-indium bispecific antibody. *J Nucl Med*. 1998;39:1172–1178.
- Chatal J-F, Campion L, Kraeber-Bodéré F, et al. Survival improvement in patients with medullary thyroid carcinoma who undergo pretargeted anti-carcinoembryonic-antigen radioimmunotherapy: a collaborative study with the French Endocrine Tumor Group. *J Clin Oncol*. 2006;24:1705–1711.
- Bodet-Milin C, Ferrer L, Rauscher A, et al. Pharmacokinetics and dosimetry studies for optimization of pretargeted radioimmunotherapy in CEA-expressing advanced lung cancer patients. *Front Med (Lausanne)*. 2015;2:84.
- Schoffelen R, Woliner-van der Weg W, Visser EP, et al. Predictive patient-specific dosimetry and individualized dosing of pretargeted radioimmunotherapy in patients with advanced colorectal cancer. *Eur J Nucl Med Mol Imaging*. 2014;41:1593–1602.
- Shinmi D, Nakano R, Mitamura K, et al. Novel anticarcinoembryonic antigen antibody-drug conjugate has antitumor activity in the existence of soluble antigen. *Cancer Med*. 2017;6:798–808.
- Dotan E, Cohen SJ, Starodub AN, et al. Phase I/II trial of labezumab govitecan (anti-CEACAM5/SN-38 antibody-drug conjugate) in patients with refractory or relapsing metastatic colorectal cancer. *J Clin Oncol*. 2017;35:3338–3346.

Synthesis and Preclinical Evaluation of a ^{68}Ga -Labeled Adnectin, ^{68}Ga -BMS-986192, as a PET Agent for Imaging PD-L1 Expression

Stephanie Robu¹, Antonia Richter*¹, Dario Gosmann*², Christof Seidl¹, David Leung³, Wendy Hayes³, Daniel Cohen³, Paul Morin³, David J. Donnelly³, Daša Lipovšek³, Samuel J. Bonacorsi³, Adam Smith³, Katja Steiger^{4,5}, Christina Aulehner², Angela M. Krackhardt^{2,5}, Wolfgang A. Weber^{1,5,6}

¹Department of Nuclear Medicine, Klinikum rechts der Isar, Technical University of Munich, Munich, Germany; ²School of Medicine, Clinic and Policlinic for Internal Medicine III, Klinikum rechts der Isar, Technical University of Munich, Munich, Germany; ³Bristol-Myers Squibb Research and Development, Princeton, New Jersey; ⁴Institute of Pathology, School of Medicine, Technical University of Munich, Munich, Germany; ⁵German Cancer Consortium, Munich, Germany, and German Cancer Research Center, Heidelberg, Germany; and ⁶TranslaTUM (Zentralinstitut für translationale Krebsforschung der Technischen Universität München), Munich, Germany

Blocking the interaction of the immune checkpoint molecule programmed cell death protein-1 and its ligand, PD-L1, using specific antibodies has been a major breakthrough for immune oncology. Whole-body PD-L1 expression PET imaging may potentially allow for a better prediction of response to programmed cell death protein-1-targeted therapies. Imaging of PD-L1 expression is feasible by PET with the adnectin protein ^{18}F -BMS-986192. However, radiofluorination of proteins such as BMS-986192 remains complex and labeling yields are low. The goal of this study was therefore the development and preclinical evaluation of a ^{68}Ga -labeled adnectin protein (^{68}Ga -BMS-986192) to facilitate clinical trials. **Methods:** ^{68}Ga labeling of DOTA-conjugated adnectin (BXA-206362) was performed in NaOAc-buffer at pH 5.5 (50°C, 15 min). In vitro stability in human serum at 37°C was analyzed using radio-thin layer chromatography and radio-high-performance liquid chromatography. PD-L1 binding assays were performed using the transduced PD-L1-expressing lymphoma cell line U-698-M and wild-type U-698-M cells as a negative control. Immunohistochemical staining studies, biodistribution studies, and small-animal PET studies of ^{68}Ga -BMS-986192 were performed using PD-L1-positive and PD-L1-negative U-698-M-bearing NSG mice. **Results:** ^{68}Ga -BMS-986192 was obtained with quantitative radiochemical yields of more than 97% and with high radiochemical purity. In vitro stability in human serum was at least 95% after 4 h of incubation. High and specific binding of ^{68}Ga -BMS-986192 to human PD-L1-expressing cancer cells was confirmed, which closely correlates with the respective PD-L1 expression level determined by flow cytometry and immunohistochemistry staining. In vivo, ^{68}Ga -BMS-986192 uptake was high at 1 h after injection in PD-L1-positive tumors (9.0 ± 2.1 percentage injected dose [%ID]/g) and kidneys (56.9 ± 9.2 %ID/g), with negligible uptake in other tissues. PD-L1-negative tumors demonstrated only background uptake of radioactivity (0.6 ± 0.1 %ID/g). Coinjection of an excess of unlabeled adnectin reduced tumor uptake of PD-L1 by more than 80%. **Conclusion:** ^{68}Ga -BMS-986192 enables easy radiosynthesis and shows excellent in vitro and in vivo PD-L1-targeting characteristics. The high tumor uptake combined with low background accumulation at early imaging time points demonstrates the feasibility of ^{68}Ga -BMS-

986192 for imaging of PD-L1 expression in tumors and is encouraging for further clinical applications of PD-L1 ligands.

Key Words: PD-1/PD-L1 checkpoint inhibitors; PD-L1 PET imaging; ^{68}Ga -adnectin; ^{68}Ga -BMS-986192; ^{18}F -BMS-986192

J Nucl Med 2021; 62:1228–1234
DOI: 10.2967/jnumed.120.258384

The immune system is in principle capable of recognizing and destroying cancer cells even in the presence of larger tumor masses and multiple metastases (1). However, cells of the innate and adaptive immune systems are frequently inhibited by molecular pathways that suppress their activation and effector functions and allow tumor cells to escape immune recognition and attack (2). One major checkpoint that is exploited by cancer cells to evade the immune system is the programmed death protein-1 (PD-1) pathway. The negative costimulatory receptor PD-1 is expressed on the surface of activated T cells (3,4). Its ligand, the programmed death protein ligand-1 (PD-L1), a surface protein, is expressed on both antigen-presenting cells and tumor cells of a variety of human cancers (5–7). PD-1/PD-L1 interaction induces downregulation of T-cell activation and allows tumor cells to evade immune recognition and elimination (8).

Inhibition of the PD-1/PD-L1 interaction by antibodies has been a breakthrough for the treatment of several common malignancies such as melanoma, non-small cell lung cancer, renal cell carcinoma, and urothelial cancer (9–12). However, only a subgroup of patients responds to this immune checkpoint inhibitor treatment, and the underlying reasons are not well understood (13–16). Several studies demonstrated that response to PD-1/PD-L1-targeted immunotherapy correlates with PD-L1 expression levels on tumor tissue of diverse malignancies as determined by immunohistochemistry (17). However, the quantitative analysis of PD-L1 expression in tumor tissue is challenging because of the heterogeneous and dynamic expression of such immune checkpoint molecules (18–21). Prediction of response to PD-1-targeted therapy by immunohistochemistry is therefore limited, and in several tumor types, patients benefit from PD-1-targeted therapies in the absence of significant PD-L1 expression in the tumor tissue (17,22,23).

Received Oct. 12, 2020; revision accepted Jan. 3, 2021.
For correspondence or reprints, contact Stephanie Robu (stephanie.robu@tum.de).

*Contributed equally to this work.

Published online January 30, 2021.

COPYRIGHT © 2021 by the Society of Nuclear Medicine and Molecular Imaging.

Imaging of PD-L1 expression can overcome several of the fundamental limitations of PD-L1 immunohistochemistry. First, imaging can provide a 3-dimensional measure of the overall PD-L1 expression of a tumor, whereas only a very small fraction of the tumor tissues can be routinely studied by immunohistochemistry. Second, imaging can assess PD-L1 expression at the whole-body level and therefore allows for studies of the heterogeneity of PD-L1 expression across multiple metastases in an individual patient. Third, imaging is noninvasive and therefore not only can provide information on PD-L1 status before the start of PD-L1 treatment but also monitor changes in PD-L1 expression at multiple times during treatment. Thus, PD-L1 imaging enables new approaches for studying PD1/PD-L1 pathophysiology in patients and may potentially allow for a better prediction of response to PD-1–targeted therapies than immunohistochemistry (24).

It is feasible to image and quantify PD-L1 expression within the tumor in patients with radiolabeled antibodies (25,26). However, antibody-based imaging has several disadvantages such as the long circulatory half-life of antibodies and their slow penetration in the tumor tissue, which necessitates imaging several days after injection. This requires the use of long-lived radioisotopes for radiolabeling, which cause the radiation exposure of antibody PET to be severalfold higher than that of PET with ^{18}F -FDG.

Adnectins are a family of engineered, target-binding proteins with a size of about 10 kDa, derived from the tenth type III domain of human fibronectin (27). Donnelly et al. synthesized and evaluated an ^{18}F -labeled anti-PD-L1 adnectin (^{18}F -BMS-986192) for PET imaging of the PD-L1 expression in vivo (28). ^{18}F -BMS-986192 showed high in vivo stability and excellent anti-PD-L1–targeting characteristics combined with fast renal clearance, resulting in high-contrast imaging of PD-L1–positive lesions up to hours after injection (28). A first-in-humans study with ^{18}F -BMS-986192 in advanced non–small cell lung carcinoma demonstrated a correlation of ^{18}F -adnectin tumor uptake with PD-L1 expression confirmed by immunohistochemistry and response to nivolumab treatment on a lesional basis. The authors illustrated that ^{18}F -BMS-986192 SUV_{peak} was higher for responding lesions than nonresponding, indicating a correlation of ^{18}F -BMS-986192 PD-L1 PET signal with PD-L1 expression and tumor-level response (29).

However, the multistep synthesis of ^{18}F -BMS-986192 with only moderate radiochemical yields is challenging and time-consuming (28,30). To facilitate a broader clinical application of anti-PD-L1 PET imaging, the development of a corresponding ^{68}Ga -labeled analog based on the adnectin scaffold seemed the conclusive next step, because of the commercial availability of Food and Drug Administration–approved $^{68}\text{Ga}/^{68}\text{Ga}$ -generators, the possibility of large-scale cyclotron production of ^{68}Ga , and the fast and robust ^{68}Ga -labeling technique. Herein, we report the synthesis and preclinical evaluation of ^{68}Ga -BMS-986192 in terms of PD-L1–affinity, metabolic stability, micro-PET imaging, and in vivo biodistribution in PD-L1–positive and PD-L1–negative xenografts to investigate the feasibility of this tracer for in vivo imaging of PD-L1 expression in tumors.

MATERIALS AND METHODS

Materials

All reagents were obtained from Sigma Aldrich unless otherwise stated. The DOTA-conjugated anti-PD-L1 adnectin (BXA-206362) was kindly provided by Bristol-Myers-Squibb Pharmaceutical Research Institute, formulated in phosphate-buffered saline (PBS) buffer (0.9 mg/

mL, pH 7.4), and tested to be endotoxin-free (1.5 EU/mg). ^{68}Ga was obtained from a $^{68}\text{Ge}/^{68}\text{Ga}$ generator (Galliapharm; Eckert and Ziegler AG).

Synthesis of ^{68}Ga -BMS-986192 and Quality Control

The generator was eluted in 1-mL fractions with 0.05 M aqueous HCl (4 mL) containing 170–250 MBq of $^{68}\text{GaCl}_3$. To this eluate, 1 M NaOAc (100 μL , pH 5.5) and 200 μg of DOTA-adnectin (222 μL in PBS) were added, resulting in a labeling solution at pH 5.5. The solution was mixed briefly and incubated for 15 min at 50°C. ^{68}Ga -BMS-986192 was purified by gel filtration on a PD-10 column (GE Healthcare). Radiochemical yield and radiochemical purity was analyzed by radio-thin-layer chromatography (radio-TLC) and radio-high-performance liquid chromatography. Radio-TLC was performed using Varian silica impregnated instant TLC paper (Varian Inc.) and 0.1 M aqueous sodium citrate buffer (pH 5.5) as the mobile phase. TLC strips were analyzed on a B-FC-3600 TLC Scanner (Bioscan). Analytic radio-size-exclusion chromatography of ^{68}Ga -BMS-986192 was performed using a bioZen SEC-2 (300 \times 4.6 mm) column (Phenomenex LTD.) on a Shimadzu high-performance liquid chromatography system (0.1 M phosphate buffer; pH 6.8; flow, 0.35 mL/min) equipped with a NaI(Tl) scintillation detector (5 \times 5 cm [2 \times 2 in]) and a SPD M20A diode array ultraviolet/visible-light detector.

In Vitro Stability of ^{68}Ga -BMS-986192 in Human Serum

An in vitro stability study was performed by adding ^{68}Ga -BMS-986192 (~18 MBq) to freshly prepared human serum (1/8, v/v; Seronorm Human; IGZ Instruments AG), followed by incubation at 37°C for up to 4 h. To investigate the stability of ^{68}Ga -BMS-986192 in human serum, radio-high-performance liquid chromatography and radio-TLC were performed at 0, 1, 2, 3, and 4 h.

Cell Culture

The PD-L1–negative B-cell lymphoma cell line U-698-M was purchased from ATCC. Cultures were maintained in RPMI medium supplemented with 10% fetal bovine serum and penicillin/streptomycin (100 IU/mL). Cells were grown at 37°C in a humidified atmosphere of 5% CO₂. To stably express PD-L1, the U-698-M cells were retrovirally transduced with a construct containing genes for human PD-L1 and green fluorescent protein, as previously described (31). Quantification of PD-L1 expression on transduced and wild-type U-698-M cells was determined by fluorescence-activated cell sorting (FACS) analysis using an antihuman CD274 antibody (Clone MIH1; BD Bioscience) as previously described (32).

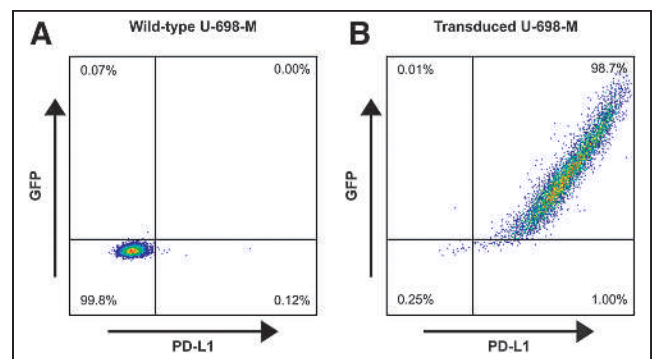


FIGURE 1. Representative dot-plots of expression of green fluorescent protein and PD-L1 in wild-type U-698-M cells (A) and in U-698-M cells transduced by retroviral vector MP71 containing PD-L1 and green fluorescent protein (GFP) separated by P2A element (B).

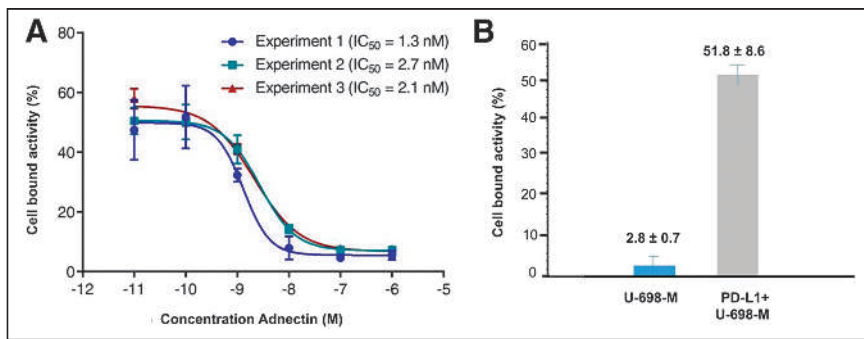


FIGURE 2. Binding affinity and specificity of ^{68}Ga -BMS-986192 toward PD-L1 in competitive radioligand binding assays. (A) Cell-bound activity in presence of increasing concentrations of cold ligand (BXA-206362). (B) Cell-bound activity in presence of cold ligand (0.1 nM) on PD-L1-positive (gray bar) and PD-L1-negative (blue bar) U-698-M cells. IC_{50} = half-maximal inhibitory concentration.

Assessment of PD-L1 Binding Affinity and Specificity

The binding affinity of ^{68}Ga -BMS-986192 toward human PD-L1 was determined in a competitive binding experiment using stable transduced U-698-M PD-L1 cells with elevated PD-L1 expression. Briefly, a solution containing a mixture of ^{68}Ga -labeled (25 μL) and unlabeled DOTA-conjugated antiPD-L1 adnectin (25 μL , competitor) with increasing concentrations (10^{-10} – 10^{-6} M) was added to the cells (400,000 cells per vial). After 1 h of incubation at 37°C, the cells were centrifuged at 600g (1,200 rpm; Biofuge 15) for 5 min, the supernatant of each vial was removed, and the cells were thoroughly washed 2 times with 250

Vet_02–15–216). The transduced U-698-M PD-L1-positive and U-698-M wild-type cell lines were detached from the surface of the culture flask using trypsin/ethylenediaminetetraacetic acid (0.05% and 0.02% in PBS, centrifuged, and resuspended in PBS. Approximately 1×10^7 cells/200 μL of the U-698-M PD-L1-positive cell line were inoculated subcutaneously on the right flank, and U-698-M wild-type cells on the left flank, of 6- to 8-wk-old male NSG mice (Charles River WIGA GmbH). Tumors were grown for 2–3 wk to reach 0.6–1 cm in diameter.

Small-Animal PET Imaging

The mice were anesthetized with isoflurane and intravenously injected via the tail vein with approximately 5–7 MBq (~ 4.5 – 5.5 μg) of ^{68}Ga -BMS-986192. In vivo imaging studies were performed using a Siemens Inveon small-animal PET/CT scanner. Static images were recorded at 1 h and 2 h after injection with an acquisition time of 20 min. For blocking studies, unlabeled BXA-206362 (9 mg/kg) was coinjecting with ^{68}Ga -BMS-986192. Dynamic imaging was performed after on-bed injection for 1.5 h under isoflurane anesthesia. Reconstruction of the images was performed using a 3-dimensional ordered-subsets expectation maximum algorithm with scanner and attenuation correction. Data analysis was performed using Inveon Workplace software (Siemens). Regions of interest were drawn around areas with increased uptake in transaxial slices for calculation of the average tracer concentration as percentage injected dose (%ID)/g.

Ex Vivo Histology and Immunohistochemistry

Tumor tissues were fixed in 10% neutral-buffered formalin solution for at least 48 h, dehydrated under standard conditions (Leica ASP300S), and embedded in paraffin. Serial 2- μm -thick sections prepared with a rotary microtome (HM355S; Thermo Fisher Scientific) were collected and subjected to histologic and immunohistochemical analysis. Hematoxylin–eosin staining was performed on deparaffinized sections with eosin and

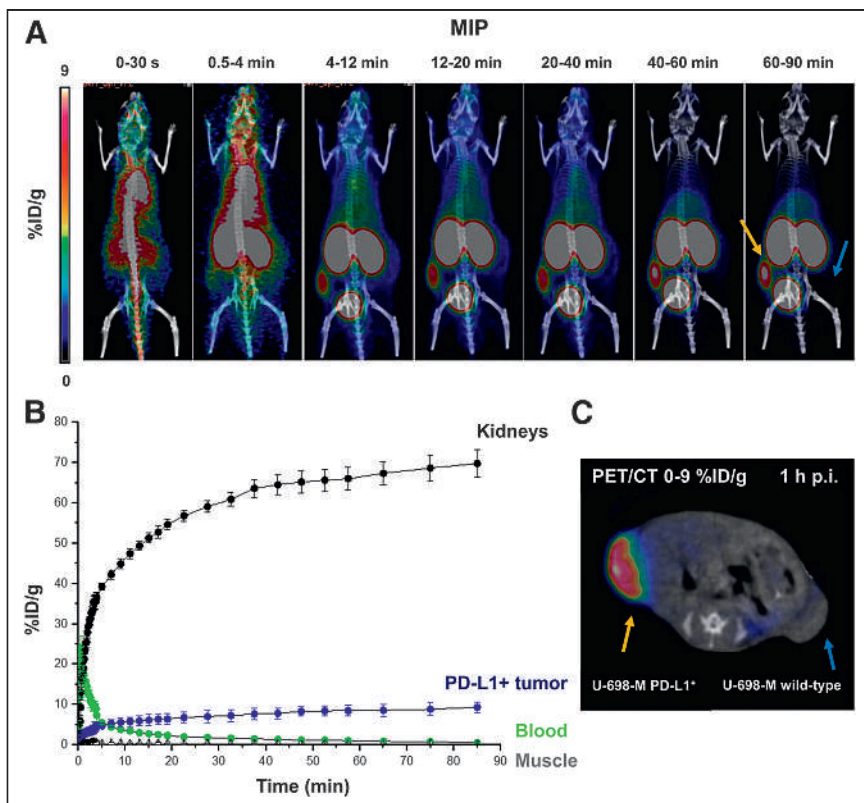


FIGURE 3. Dynamic ^{68}Ga -BMS-986192 PET/CT imaging in anesthetized PD-L1-positive and wild-type U-698-M xenograft-bearing NSG mice. (A) Summation maximum-intensity projections (MIP) of different time frames during 90-min acquisition. (B) Time–activity curves for blood pool (heart), kidneys, muscle, and PD-L1-positive tumor derived from dynamic data. (C) Axial PET/CT scan at 1 h after injection (p.i.).

Mayer hematoxylin according to a standard protocol.

Immunohistochemistry was performed using a Bond RXm system (Leica) with primary antibodies against human PD-L1 (clone 28–8, ab205921, 1:500).

Ex Vivo Biodistribution

About 5–7 MBq of ^{68}Ga -BMS-986192 (4.5–5.5 μg) were injected into the tail vein of the U-698-M-PD-L1–positive and U-698-M wild-type tumor-bearing NSG mice under isoflurane anesthesia. The animals were sacrificed at 1 h after injection ($n = 4$) or 2 h after injection ($n = 4$), the organs of interest were dissected, and the activity in the weighed tissues samples was quantified using a γ -counter.

RESULTS

^{68}Ga Labeling and In Vitro Stability of ^{68}Ga -BMS-986192 in Human Serum

High labeling efficiencies with quantitative radiochemical yields of more than 97% were obtained after 15 min. After purification, moderate specific activities of 11–16 GBq/ μmol and radiochemical purity of more than 98% was achieved.

Radio-high-performance liquid chromatography of ^{68}Ga -BMS-986192 at various time points after mixing with human serum revealed monomeric elution profiles with a minimal radioactive impurity of higher molecular weight (8.97 min), which slightly increased up to 5% after 4 h. Radio-TLC analysis revealed moderate transmetallation (5%) for ^{68}Ga -BMS-986192 within 4 h (Supplemental Fig. 1; supplemental materials are available at <http://jnm.snmjournals.org>).

Characterization of PD-L1 Expression in Transduced U-698-M Cells

Quantification of PD-L1 expression on transduced and wild-type U-698-M cells was determined by FACS analysis. A low PD-L1 expression of approximately 4,000 molecules per cell was observed for wild-type U-698-M cells (Fig. 1). PD-L1 expression was significantly increased by stable transduction of U-698-M cells, with approximately 155,000 PD-L1 molecules per cell.

Competitive Binding Assay of ^{68}Ga -BMS-986192 to PD-L1

Binding affinity of ^{68}Ga -BMS-986192 to human PD-L1 was determined in a competitive radioligand binding experiment using PD-L1–positive and wild-type U-698-M cells. ^{68}Ga -BMS-986192 showed high affinity toward human PD-L1 with a half-maximal inhibitory concentration of 2.0 ± 0.6 nM (Fig. 2A). Specific binding was confirmed using nontransduced U-698-M cells as a negative control (Fig. 2B).

PET/CT Imaging

^{68}Ga -BMS-986192 showed a rapid clearance from the blood pool and from nontarget tissues, with continuously increasing accumulation in the kidneys over time (Figs. 3A and 3B). ^{68}Ga -BMS-986192 uptake in PD-L1–positive tumor was fast within 4 min after injection, and tracer accumulation in PD-L1–expressing tumor tissue increased within 60 min, with high retention over 90 min after injection (Figs. 3A and 3C). No uptake in the PD-L1–negative U-698-M tumor was observed.

Additional static small-animal PET scans were performed with ^{68}Ga -BMS-986192 in PD-L1–positive and PD-L1 wild-type tumor-bearing NSG mice at 1 and 2 h after injection (Fig. 4A). ^{68}Ga -BMS-986192 showed comparably high tumor uptake in PD-L1–positive tumors after 1 and 2 h after injection. As shown in Figure 4A, in contrast to the high uptake of ^{68}Ga -BMS-986192

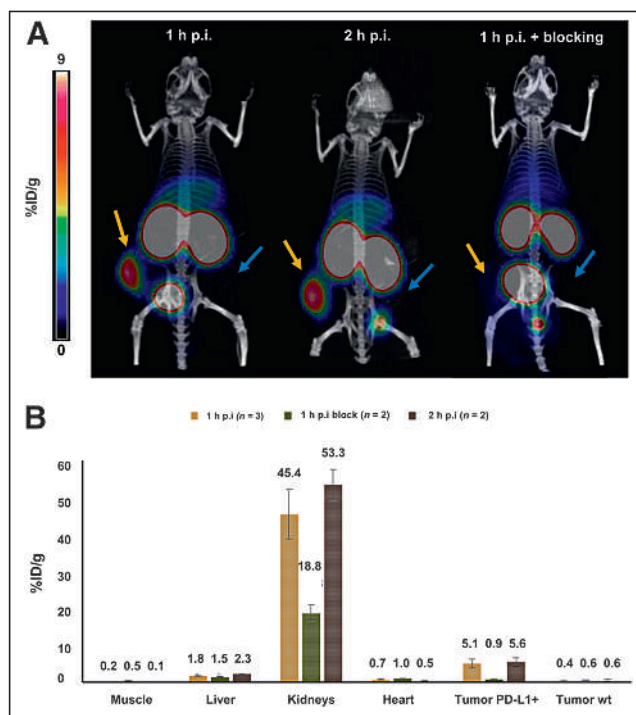


FIGURE 4. (A) Static ^{68}Ga -BMS-986192 PET imaging examples in PD-L1–positive (yellow arrows) and wild-type (blue arrows) U-698-M xenograft-bearing NSG mice. Images are maximum-intensity projections (5–6 MBq, 4.5–5.5 μg) obtained at 1 and 2 h after injection (p.i.). Mouse at far right received ^{68}Ga -BMS-986192 plus blocking with unlabeled adnectin, 9 mg/kg. (B) ROI quantification of static PET scans (mean %ID/g).

in PD-L1–positive U-698-M tumors, no accumulation was observed in U-698-M wild-type xenografts, confirming PD-L1 specific binding of ^{68}Ga -BMS-986192. Additionally, blocking experiments with an excess of unlabeled adnectin (9 mg/kg) demonstrated that ^{68}Ga -BMS-986192 uptake is specific and mediated by PD-L1 (Fig. 4B).

Ex Vivo FACS Analysis, Histology, and Immunohistochemistry

Ex vivo FACS analysis of dissected tumors confirmed the correlation of ^{68}Ga -BMS-986192 uptake with PD-L1 expression levels in tumor tissue (Figs. 5A and 5B). PD-L1 expression levels in transduced U-698-M tumors was highly increased in comparison to nontransduced U-698-M wild-type xenografts, confirming the generation of a stable PD-L1–expressing tumor cell line in vivo and PD-L1–mediated uptake of ^{68}Ga -BMS-986192.

Ex vivo histology and immunohistochemistry of the xenograft tissues also revealed high and homogeneous PD-L1 expression in U-698-M PD-L1–positive tumors, whereas no PD-L1 expression was found in U-698-M wild-type tissues (Fig. 5C). These results confirm the PD-L1–specific uptake of ^{68}Ga -BMS-986192 in small-animal PET imaging in vivo and correlate with ex vivo flow cytometry analysis.

Biodistribution

The biodistribution data of ^{68}Ga -BMS-986192 in PD-L1–positive-U-698-M and U-698-M wild-type tumor-bearing mice (1 and 2 h after injection) are shown in Figure 6 and Supplemental Table 1. The data reflect the results of small-animal PET/CT imaging. ^{68}Ga -BMS-986192 exhibited predominant renal clearance, with only slight uptake in the liver and nontargeted tissues. The significant uptake of ^{68}Ga -BMS-986192 in PD-L1–positive tumor

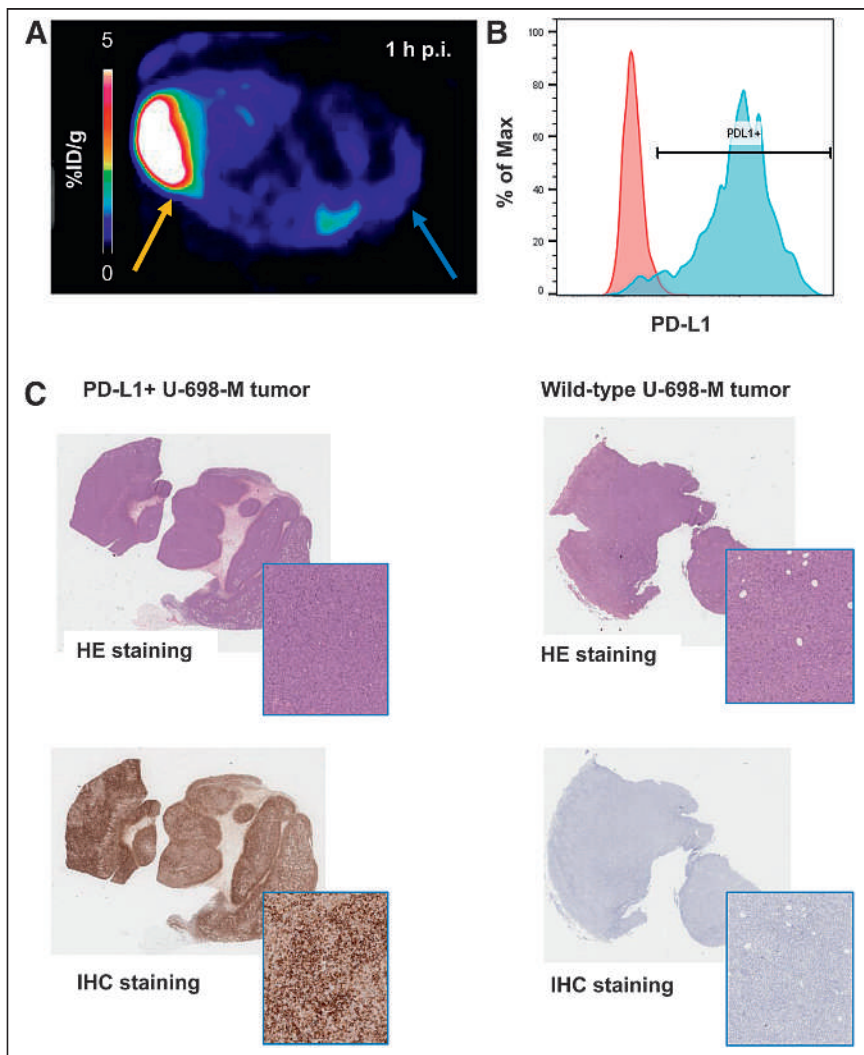


FIGURE 5. (A) Axial ^{68}Ga -BMS-986192 PET scan at 1 h after injection in PD-L1-positive (yellow arrow) and wild-type (blue arrow) U-698-M xenograft-bearing NSG mouse. (B) Ex vivo FACS analysis of PD-L1 expression on wild-type (red) and PD-L1 transduced (blue) tumor cells. (C) Ex vivo hematoxylin-eosin (HE) and anti-PD-L1 immunohistochemistry (IHC) staining of PD-L1-positive and wild-type xenograft tissues.

xenografts is highly specific, as accumulation in PD-L1-negative tumors was less than blood-pool activity (Supplemental Table 1).

DISCUSSION

This study revealed that the high-affinity PD-L1-binding adnectin protein BMS-986192, conjugated at the C terminal position with DOTA via maleimide linkage (BXA-206362), can be labeled with ^{68}Ga while retaining high target binding affinity (half-maximal inhibitory concentration, 2.0 ± 0.6 nM determined in a competitive radioligand binding assay using PD-L1-positive U-698-M cells). The DOTA-maleimide moiety was conjugated to the cysteine residue engineered into the C terminus of the adnectin (28,30). The same position within the adnectin scaffold has been used previously for site-specific conjugation of the ^{18}F -labeled prosthetic group of ^{18}F -BMS-986192 without a significant effect on binding affinity (28). ^{19}F -BMS-986192, an unmodified and DOTA-conjugated adnectin, has displayed picomolar dissociation constants against human PD-L1 determined by surface plasmon

resonance (28). This indicates that conjugation of small molecules to the C terminus of adnectin is well tolerated, without observable effects on human PD-L1 binding. The ease of tracer preparation and the quantitative radiochemical yields with high radiochemical purity make the synthesis of ^{68}Ga -BMS-986192 fully compatible with the everyday workflow in a clinical radiopharmacy and are well suited for automated radiosynthesis via a module or a kit formulation. Furthermore, the pharmacokinetics of ^{68}Ga -BMS-986192 match very well the 68-min physical half-life of ^{68}Ga , as peak tumor uptake reached a plateau within 60 min after injection. Collectively, these characteristics are highly encouraging for using ^{68}Ga -BMS-986192 to image PD-L1 expression in humans.

Small-animal PET and ex vivo biodistribution studies demonstrated excellent targeting of PD-L1-expressing xenografts, whereas tracer uptake was low in tumors without PD-L1 expression on immunohistochemistry (Figs. 4 and 5). The specificity of tracer binding was further confirmed by coinjection of an excess of unlabeled BMS-986192, which decreased tumor uptake of ^{68}Ga -BMS-986192 by 80% (Fig. 6). As expected for a 10-kDa protein, ^{68}Ga -BMS-986192 showed fast renal clearance from the blood. As observed for other small proteins, peptides and peptide-like molecules, ^{68}Ga -BMS-986192 showed significant retention of activity in the kidneys at 1 and 2 h after injection. However, the activity concentration was similar to that of clinically used PET imaging agents such as prostate-specific membrane ligands (33,34). Therefore, we do not expect renal uptake of ^{68}Ga -BMS-986192 to limit its clinical use. Injection of an excess of unlabeled adnectin significantly decreased renal uptake of ^{68}Ga -BMS-986192. This is unlikely to be due to blocking of PD-L1 binding since BMS986192 has only low affinity for murine PD-L1 (28). Nevertheless, it indicates that renal uptake of radioactivity is a partially saturable process that could potentially be reduced by injection of proteins or peptides that do not interfere with the binding of ^{68}Ga -BMS-986192 to its target. The activity concentration in the kidneys increased from 1 to 2 h after injection, probably reflecting redistribution of the ligand from other tissues to the bloodstream (Fig. 6).

A comparison of the preclinical results obtained for ^{18}F -BMS986192 and ^{68}Ga -BMS-986192 revealed similar specific activities and similar in vitro and in vivo behavior for both tracers (28). Although comparable protein and activity doses of ^{18}F -BMS986192 and ^{68}Ga -BMS-986192 were administered to mice, a direct comparison of the tumor uptake of both radiolabeled ligands is not feasible as different cell lines were used in the 2 studies, but both tracers showed similar pharmacokinetics, with fast renal

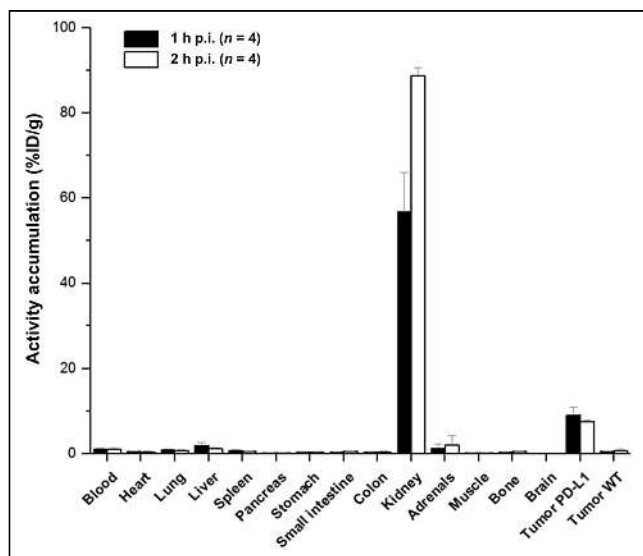


FIGURE 6. Biodistribution data for ^{68}Ga -BMS-986192 in PD-L1-positive and wild-type (WT) U-698-M xenograft-bearing mice at 1 and 3 h after injection (p.i.). Data are %ID/g (mean \pm SD).

clearance and similarly low background activity in all other organs. This is encouraging for the clinical translation of ^{68}Ga -BMS-986192 because PET imaging of PD-L1 expression with ^{18}F -BMS-986192 has already been shown to be feasible in human pilot studies (29,35).

The following limitation of the study should be noted. ^{68}Ga -BMS-986192 exclusively binds to human PD-L1, with no relevant affinity toward its murine counterpart (28). Tumor-to-normal organ uptake rates may therefore be lower in humans than in our mouse model. Furthermore, we used a PD-L1 transduced cell line to study the binding of ^{68}Ga -BMS-986192. The advantages of this approach are that the parent cell line can be used as a negative control to assess the specificity of ligand binding. Furthermore, the stable expression of PD-L1 improves the reproducibility of these results to ensure having a tool for measurement PD-L1 expression of cancer cells, as endogenous cancer cell PD-L1 expression is known to vary significantly over time (36). However, PD-L1 expression levels may be higher in PD-L1 transduced U698-M cells than in human tumors.

CONCLUSION

The novel PD-L1 imaging agent ^{68}Ga -BMS-986192 shows similar PD-L1-targeting characteristics and pharmacokinetic properties to ^{18}F -BMS-986192, which has already been successfully used to image PD-L1 expression in cancer patients. In contrast to ^{18}F -BMS-986192, which requires a 2-step synthesis with low radiochemical yields, radiolabeling of BMS-986192 with ^{68}Ga is a straightforward 1-step process that is easy to automate. ^{68}Ga -BMS-986192 therefore has the potential to significantly facilitate preclinical and clinical imaging of PD-L1 expression.

DISCLOSURE

The current study was financially supported by the Deutsche Forschungsgemeinschaft (SFB824; subprojects C10, Z1, and Z2). David Leung, Wendy Hayes, Paul Morin, Adam Smith, David Donnelly, Daša Lipovšek, Sam Bonacorsi, and Daniel Cohen are employed by Bristol-Myers Squibb Co. ^{18}F -BMS-986192 and ^{68}Ga -BMS-986192 are the subject of patent applications

WO2016086021A1, WO2016086036A2, WO2017/210302, and WO2017/210335. No other potential conflict of interest relevant to this article was reported.

ACKNOWLEDGMENTS

We thank Sybille Reder, Markus Mittelhäuser, and Hannes Rolbiesky for small-animal PET imaging and Olga Seelbach and Marion Mielke for hematoxylin-eosin and immunohistochemistry staining.

KEY POINTS

QUESTION: Can adnectins be efficiently radiolabeled with ^{68}Ga to allow the in vivo assessment and quantification of PD-L1 expression levels on tumor tissue with PET?

PERTINENT FINDINGS: The expansion of the adnectin-based concept for PD-L1 expression PET imaging to the requirements of ^{68}Ga chemistry enables fast and efficient radiolabeling. ^{68}Ga -BMS-986192 showed comparable in vitro and in vivo PD-L1-targeting characteristics to its counterpart, ^{18}F -BMS986192. Both tracers showed favorable pharmacokinetics, with fast renal clearance and similarly low background activity in nontargeted tissues.

IMPLICATIONS FOR PATIENT CARE: The preclinical results are encouraging for the clinical translation of ^{68}Ga -BMS-986192 because PET imaging of PD-L1 expression with ^{18}F -BMS-986192 has already been shown to be feasible in human pilot studies.

REFERENCES

- Gonzalez H, Hagerling C, Werb Z. Roles of the immune system in cancer: from tumor initiation to metastatic progression. *Genes Dev.* 2018;32:1267–1284.
- Topalian SL, Drake CG, Pardoll DM. Immune checkpoint blockade: a common denominator approach to cancer therapy. *Cancer Cell.* 2015;27:450–461.
- Riella LV, Paterson AM, Sharpe AH, Chandraker A. Role of the PD-1 pathway in the immune response. *Am J Transplant.* 2012;12:2575–2587.
- Keir ME, Butte MJ, Freeman GJ, Sharpe AH. PD-1 and its ligands in tolerance and immunity. *Annu Rev Immunol.* 2008;26:677–704.
- Konishi J, Yamazaki K, Azuma M, Kinoshita I, Dosaka-Akita H, Nishimura M. B7-H1 expression on non-small cell lung cancer cells and its relationship with tumor-infiltrating lymphocytes and their PD-1 expression. *Clin Cancer Res.* 2004;10:5094–5100.
- Thompson RH, Gillett MD, Cheville JC, et al. Costimulatory B7-H1 in renal cell carcinoma patients: indicator of tumor aggressiveness and potential therapeutic target. *Proc Natl Acad Sci USA.* 2004;101:17174–17179.
- Hino R, Kabashima K, Kato Y, et al. Tumor cell expression of programmed cell death-1 ligand 1 is a prognostic factor for malignant melanoma. *Cancer.* 2010;116:1757–1766.
- Freeman GJ, Long AJ, Iwai Y, et al. Engagement of the PD-1 immunoinhibitory receptor by a novel B7 family member leads to negative regulation of lymphocyte activation. *J Exp Med.* 2000;192:1027–1034.
- Herbst RS, Baas P, Kim DW, et al. Pembrolizumab versus docetaxel for previously treated, PD-L1-positive, advanced non-small-cell lung cancer: a randomised controlled trial. *Lancet.* 2016;387:1540–1550.
- Weinstock M, McDermott D. Targeting PD-1/PD-L1 in the treatment of metastatic renal cell carcinoma. *Ther Adv Urol.* 2015;7:365–377.
- Simeone E, Ascierto PA. Anti-PD-1 and PD-L1 antibodies in metastatic melanoma. *Melanoma Manag.* 2017;4:175–178.
- Stenhejm DD, Tran D, Nkrumah MA, Gupta S. PD1/PDL1 inhibitors for the treatment of advanced urothelial bladder cancer. *Onco Targets Ther.* 2018;11:5973–5989.
- Alsaab HO, Sau S, Alzhrani R, et al. PD-1 and PD-L1 checkpoint signaling inhibition for cancer immunotherapy: mechanism, combinations, and clinical outcome. *Front Pharmacol.* 2017;8:561.
- Chen L, Han X. Anti-PD-1/PD-L1 therapy of human cancer: past, present, and future. *J Clin Invest.* 2015;125:3384–3391.
- Cottrell TR, Taube JM. PD-L1 and emerging biomarkers in immune checkpoint blockade. *Cancer J.* 2018;24:41–46.

16. Zou W, Wolchok JD, Chen L. PD-L1 (B7-H1) and PD-1 pathway blockade for cancer therapy: mechanisms, response biomarkers, and combinations. *Sci Transl Med*. 2016; 8:328rv4.
17. Chakravarti N, Prieto VG. Predictive factors of activity of anti-programmed death-1/programmed death ligand-1 drugs: immunohistochemistry analysis. *Transl Lung Cancer Res*. 2015;4:743–751.
18. Klotten V, Lampignano R, Krahn T, Schlange T. Circulating tumor cell PD-L1 expression as biomarker for therapeutic efficacy of immune checkpoint inhibition in NSCLC. *Cells*. 2019;8:809.
19. Yue C, Jiang Y, Li P, et al. Dynamic change of PD-L1 expression on circulating tumor cells in advanced solid tumor patients undergoing PD-1 blockade therapy. *Oncol Immunology*. 2018;7:e1438111.
20. Madore J, Vilain RE, Menzies AM, et al. PD-L1 expression in melanoma shows marked heterogeneity within and between patients: implications for anti-PD-1/PD-L1 clinical trials. *Pigment Cell Melanoma Res*. 2015;28:245–253.
21. Niemeijer AN, Leung D, Huisman M, et al. Whole body PD-1 and PD-L1 positron emission tomography in patients with non-small-cell lung cancer. *Nat Commun*. 2018;9:4664.
22. Ribas A, Hu-Lieskovan S. What does PD-L1 positive or negative mean? *J Exp Med*. 2016;213:2835–2840.
23. Abdel-Rahman O. Correlation between PD-L1 expression and outcome of NSCLC patients treated with anti-PD-1/PD-L1 agents: a meta-analysis. *Crit Rev Oncol Hematol*. 2016;101:75–85.
24. Broos K, Lecocq Q, Raes G, Devoogdt N, Keyaerts M, Breckpot K. Noninvasive imaging of the PD-1:PD-L1 immune checkpoint: embracing nuclear medicine for the benefit of personalized immunotherapy. *Theranostics*. 2018;8:3559–3570.
25. Heskamp S, Hobo W, Molkenboer-Kuenen JD, et al. Noninvasive imaging of tumor PD-L1 expression using radiolabeled anti-PD-L1 antibodies. *Cancer Res*. 2015;75:2928–2936.
26. Truillet C, Oh HLJ, Yeo SP, et al. Imaging PD-L1 expression with immunoPET. *Bioconjug Chem*. 2018;29:96–103.
27. Lipovšek D. Adnectins: engineered target-binding protein therapeutics. *Protein Eng Des Sel*. 2011;24:3–9.
28. Donnelly DJ, Smith RA, Morin P, et al. Synthesis and biological evaluation of a novel ¹⁸F-labeled adnectin as a PET radioligand for imaging PD-L1 expression. *J Nucl Med*. 2018;59:529–535.
29. Niemeijer AN, Leung D, Huisman MC, et al. Whole body PD-1 and PD-L1 positron emission tomography in patients with non-small-cell lung cancer. *Nat Commun*. 2018;9:4664.
30. Morin PE, Donnelly D, Lipovsek D, inventors; Bristol-Myers Squibb Company, USA, assignee. Novel PD-L1-binding polypeptides for imaging. U.S. patent WO2016086021A1. 2016.
31. Audehm S, Glaser M, Pecoraro M, et al. Key features relevant to select antigens and TCR from the MHC-mismatched repertoire to treat cancer. *Front Immunol*. 2019;10:1485.
32. Mayer KE, Mall S, Yusufi N, et al. T-cell functionality testing is highly relevant to developing novel immuno-tracers monitoring T cells in the context of immunotherapies and revealed CD7 as an attractive target. *Theranostics*. 2018;8:6070–6087.
33. Weineisen M, Schottelius M, Simecek J, et al. ⁶⁸Ga- and ¹⁷⁷Lu-labeled PSMA I&T: optimization of a PSMA-targeted theranostic concept and first proof-of-concept human studies. *J Nucl Med*. 2015;56:1169–1176.
34. Robu S, Schmidt A, Eiber M, et al. Synthesis and preclinical evaluation of novel ¹⁸F-labeled Glu-urea-Glu-based PSMA inhibitors for prostate cancer imaging: a comparison with ¹⁸F-DCFPyl and ¹⁸F-PSMA-1007. *EJNMMI Res*. 2018;8:30.
35. Huisman MC, Niemeijer AL, Windhorst B, et al. Quantification of PD-L1 expression with [¹⁸F]BMS-986192 PET/CT in patients with advanced stage non-small-cell lung cancer. *J Nucl Med*. 2020;61:1455–1460.
36. Yue C, Jiang Y, Li P, et al. Dynamic change of PD-L1 expression on circulating tumor cells in advanced solid tumor patients undergoing PD-1 blockade therapy. *Oncol Immunology*. 2018;7:e1438111.

⁶⁸Ga-PSMA-11 PET/CT Improves Tumor Detection and Impacts Management in Patients with Hepatocellular Carcinoma

Nader Hirmas¹, Catherine Leyh², Miriam Sraieb¹, Francesco Barbato¹, Benedikt M. Schaarschmidt³, Lale Umutlu³, Michael Nader¹, Heiner Wedemeyer², Justin Ferdinandus¹, Christoph Rischpler¹, Ken Herrmann¹, Pedro Fragoso Costa¹, Christian M. Lange², Manuel Weber^{*1}, and Wolfgang P. Fendler^{*1}

¹Department of Nuclear Medicine, University of Duisburg–Essen and German Cancer Consortium–University Hospital Essen, Essen, Germany; ²Department of Gastroenterology and Hepatology, University Hospital Essen, University of Duisburg–Essen, Essen, Germany; and ³Institute of Diagnostic and Interventional Radiology and Neuroradiology, University Hospital Essen, University of Duisburg–Essen, Essen, Germany

Hepatocellular carcinoma (HCC) is the sixth most prevalent cancer and the third most frequent cause of cancer-related death. A growing number of local and systemic therapies are available, and accurate staging is critical for management decisions. We assessed the impact of neovasculature imaging by ⁶⁸Ga-PSMA-11 PET/CT on disease staging, prognostic groups, and management of patients with HCC compared with staging with CT. **Methods:** Forty patients who received imaging with ⁶⁸Ga-PSMA-11 PET/CT for HCC staging between September 2018 and September 2019 were retrospectively included. Management before and after PET scanning was assessed by standardized surveys. The presence of HCC was evaluated by 3 masked readers on a per-patient and per-region basis for PET/CT (PET criteria) and multiphase contrast-enhanced CT (CT criteria) in separate sessions. Lesions were validated by follow-up imaging or histopathology, and progression-free survival was recorded. Endpoints were detection rate and positive predictive value for ⁶⁸Ga-PSMA-11 PET versus CT, interreader reproducibility, and changes in stage, prognostic groups, and management plans. **Results:** Median age was 65 y (range, 37–81 y), and median Child–Pugh score was 5 (range, 5–9). Most patients were treatment-naïve (27/40, 67.5%). The sensitivity of PET versus CT to identify liver lesions for patients with lesion validation was 31 of 32 (97%) for both modalities, whereas it was 6 of 6 (100%) versus 4 of 6 (67%), respectively, for extrahepatic lesions. PET and CT each had a positive predictive value of 100% at the liver level. PET versus CT stage was congruent in 30 of 40 (75%) patients; upstaging was seen in 8 of 40 patients (20%), whereas 2 of 40 (5%) had downstaging by PET. Intended management changed in 19 of 40 patients (47.5%); 9 of 19 of these patients were found to have detectable distant metastases (47.4%) and assigned stage 4 disease, most of whom were shifted to systemic therapy (8/9, 89%). Two patients underwent ¹⁷⁷Lu-PSMA-617 radioligand therapy. Median progression-free survival was 5.2 mo for the entire cohort; 5.3 mo for PET M0, and 4.7 mo for PET M1 patients, respectively. **Conclusion:** ⁶⁸Ga-PSMA-11 PET demonstrated higher accuracy than CT in the detection of HCC metastases and was associated with a management change in about half the patient cohort.

Key Words: hepatocellular carcinoma; PSMA; PET; staging; theranostic

J Nucl Med 2021; 62:1235–1241
DOI: 10.2967/jnumed.120.257915

Hepatocellular carcinoma (HCC) is the sixth most prevalent cancer and the third most frequent cause of cancer-related death worldwide (1).

Early-stage HCC is often treated with surgical resection, transplantation, or ablation, whereas systemic therapy, transarterial chemoembolization (TACE), and radioembolization (also known as selective internal radiation therapy [SIRT]) are reserved for intermediate to advanced HCC, with SIRT being most often used after progression under sorafenib (2,3). The treatment landscape for HCC changed considerably with the availability of life-prolonging systemic therapy. Despite recent therapy approvals, patient survival remains short, and accurate staging is critically needed for early identification of candidates for the various local and systemic therapies. The European Society for Medical Oncology guidelines recommend CT, MRI, or ultrasound for diagnosis of HCC in patients with cirrhosis (4). However, small HCC lesions may be hard to detect, especially with concomitant cirrhosis.

⁶⁸Ga-PSMA-11 is a novel PET tracer that has been developed for imaging patients with prostate cancer (5,6). Prostate-specific membrane antigen (PSMA) was also found to be expressed on the neovasculature of other tumor entities (7,8), with immunohistochemistry revealing PSMA expression on HCC neovasculature and canalicular membranes, with significantly increased uptake in hepatic and extrahepatic disease (9,10). A recent prospective study on 15 patients with HCC reported improved lesion detection with ⁶⁸Ga-PSMA-11 PET/CT compared with conventional imaging and a subsequent impact on treatment strategies (11).

In light of increasing local and systemic treatment options, ⁶⁸Ga-PSMA-11 PET/CT may demonstrate value for staging and management of patients with initial HCC. In this study, we aimed to assess the accuracy of ⁶⁸Ga-PSMA-11 PET/CT along with interreader agreement and impact on staging, management, and prognostic groups in patients with initial HCC.

Received Oct. 2, 2020; revision accepted Dec. 28, 2020.
For correspondence or reprints, contact Wolfgang P. Fendler (wolfgang.fendler@uk-essen.de).

*Contributed equally to this work.

Published online January 28, 2021.

COPYRIGHT © 2021 by the Society of Nuclear Medicine and Molecular Imaging.

MATERIALS AND METHODS

Study Design and Participants

Patients undergoing ^{68}Ga -PSMA-11 PET/CT for HCC between September 2018 and September 2019 at the Essen University Hospital were retrospectively included in the study. The primary endpoint was detection rate and positive predictive value for ^{68}Ga -PSMA-11 PET versus CT. Secondary endpoints were interreader reproducibility and changes in stage, prognostic group, and management plans. All patients gave written consent to undergo clinical ^{68}Ga -PSMA-11 PET/CT. The retrospective study was approved by the ethics committee at the University Duisburg–Essen (approval 19-8892-BO), and the need for study-specific consent was waived. Anonymized study data were collected retrospectively and managed using the Research Electronic Data Capture (REDCap) electronic data capture tools hosted at the University Hospital Essen (12,13). Patients' records were accessed to retrieve demographic and clinical data, pathology and lab investigations, and imaging studies performed before or after ^{68}Ga -PSMA-11 PET/CT.

Imaging Procedures

^{68}Ga -PSMA-11 (Glu-NH-CO-NH-Lys-(Ahx)-[^{68}Ga (HBED-CC)]) was labeled in accordance with the joint procedure guideline of the European Association of Nuclear Medicine and the Society of Nuclear Medicine and Molecular Imaging (14). PET was performed in accordance with the international guidelines as part of a PET/CT scan and with a field of view from the skull base to the mid thigh. Patients received a median of 112.5 MBq (range, 79–344 MBq) of ^{68}Ga -PSMA-11. Image acquisition was started at a median of 78 min after injection (range, 50–135 min; with an interquartile range of 31.5).

All 40 examinations were performed with radiographic contrast enhancement in the arterial and portal venous phases; contrast-enhanced CT was performed before the PET acquisition. Images were acquired using a Siemens Biograph 128 mCT device in 29 of 40 cases (72.5%) and a Siemens Biograph Vision in 11 of 40 cases (27.5%); both devices are cross-calibrated based on EANM Research Ltd. accreditation standards. PET images were reconstructed by ordered-subset expectation maximization–based algorithms. Data from CT scans were used for attenuation correction and anatomic correlation.

Image Interpretation

Three nuclear medicine physicians masked to all clinical and imaging data interpreted the images separately—first, the attenuation-corrected ^{68}Ga -PSMA-11 PET and CT images using PET criteria, and 2 wk later, CT images only using CT criteria. OsiriX MD (Pixmeo SARL) was used for the readings.

The presence of HCC lesions was recorded separately for ^{68}Ga -PSMA-11 PET and CT across 5 regions (positive/negative): liver segments, abdominal and extraabdominal lymph nodes, peritoneal/visceral lesions, and bone lesions.

For PET interpretation only, a 4-point scale was used to visually rate focal radioligand uptake (from 0 to 3) (15,16), with the corresponding CT scans used for anatomic correlation. Focal uptake was considered positive if the score was at least 1 (extrahepatic lesions) or at least 2 (hepatic lesions). Differentiating between HCC lesions and dysplastic nodules on CT scans (or MRI scans in cases of follow-up imaging) followed the criteria outlined in Supplemental Table 1 (supplemental materials are available at <http://jnm.snmjournals.org>) (17,18).

Readers recorded the SUV_{max} for the lesions with the highest uptake and diameter of the largest lesions (short axis for lymph nodes, long axis for all other lesions) at a given region. Readers determined the TNM staging separately for ^{68}Ga -PSMA-11 PET and CT in accordance with the criteria of the American Joint Committee on Cancer, eighth edition (19).

Consensus (positive vs. negative) was determined by a statistic majority vote among the 3 readers, with average values taken for quantitative values (SUV_{max} and lesion size). Consensus findings for the ^{68}Ga -PSMA-11 PET and CT scans for each patient were compared to determine concordance.

Lesion Validation and Change in Management

Patient files were reviewed for correlative and follow-up information acquired during routine clinical follow-up. CT, MRI, bone scans, and ^{68}Ga -PSMA-11 PET scans performed as preimaging and on follow-up were included in this analysis.

The most valuable comparator, with the following priority order (highest to lowest), was used to assign true or false positivity and negativity to detected lesions: histopathology from biopsies or surgical excision took priority over imaging validation; lesions were also confirmed by presence on the initial and follow-up scans, as well as their change in size, disappearance, or appearance on follow-up imaging during treatment, using modified RECIST (20). Any lesion that could not be verified on the basis of those criteria was excluded from the accuracy analyses. The local investigators interpreted the composite reference standard after reviewing follow-up information.

The management plan before PET was local therapy, including SIRT, radiofrequency ablation, or TACE, as documented by the interdisciplinary tumor board. The implemented management after PET was recorded by the referring physician using a standardized survey.

Statistical Analysis

Descriptive statistics were calculated. Interobserver agreement was determined by the Fleiss κ and interpreted by the criteria of Landis and Koch (21). The positive predictive value, negative predictive value, sensitivity, and specificity of ^{68}Ga -PSMA-11 PET on a per-patient and per-region basis for detection of tumor location, as confirmed by histopathology or biopsy, clinical follow-up, and conventional imaging follow-up, were calculated via standard 2×2 tables. PET progression-free survival was calculated from the date of the ^{68}Ga -PSMA-11 PET scan until progression, death, or last follow-up. κ analysis was performed using R statistics (version 3.4.1).

RESULTS

Patient Characteristics

Forty patients were included; their characteristics are outlined in Table 1. The median age was 65 y (range, 37–81 y). Twenty patients (50%) had histopathologic confirmation of HCC; the other half had imaging findings consistent with HCC. Liver cirrhosis was present in 28 of 40 patients (70%). The most frequent underlying liver disease was chronic hepatitis B or C, in 18 of 40 patients (45%). In addition, portal vein thrombosis or invasion was seen in 9 of 40 patients (22.5%). Eleven patients (27.5%) had ascites. Twenty-seven patients (67.5%) did not receive treatment before their ^{68}Ga -PSMA-11 PET scan.

Detection Accuracy and Lesion Validation

In total, 142 lesions from 36 patients were validated as true-positive, false-positive, or false-negative at the levels of the hepatic segments (1 through 8) and extrahepatic metastases. Lesions from 8 patients (20%) were validated by histopathology, 26 of 40 (65%) by baseline and follow-up imaging correlation and 10 of 40 (25%) by baseline imaging correlation only. All patients with histopathologic verification had follow-up imaging performed.

^{68}Ga -PSMA-11 PET versus CT accuracy for the liver lobes and distant metastases is reported in Table 2. Consensus interpretation on a whole-liver level for the entire cohort and for patients with cirrhosis (28/40, 70%) resulted in an accuracy of 97% for both

TABLE 1
Patient Characteristics (*n* = 40)

Characteristic	Data
M:F ratio	5.7:1
Age at diagnosis (y)	65 (37–81)
Primary diagnostic investigations	
Histopathology	20 (50)
Imaging	31 (77.5)
α-fetoprotein level	19 (47.5)
Comorbidities	
Cirrhosis	28 (70)
Hepatitis B or C	18 (45)
Diabetes	11 (27.5)
Nonalcoholic steatohepatitis/steatosis	5 (12.5)
Portal vein thrombosis or invasion	9 (22.5)
Ascites	
None	29 (72.5)
Controlled	10 (25)
Refractory	1 (2.5)
Baseline investigations	
Body mass index (kg/m ²)	27.4 (20.2–38.5)
α-fetoprotein (ng/mL)	36.1 (1–19,078)
Total bilirubin (μmol/L)	0.8 (0.2–6.7)
Albumin (g/L)	4.1 (2.6–5)
International normalized ratio	1.1 (1–1.6)
Alkaline phosphatase (IU/L)	127 (33–937)
Child–Pugh score	5 (5–9)
Class A	33 (82.5)
Class B	7 (17.5)
Treatment received before PSMA PET/CT	
None	27 (67.5)
Systemic treatment	2 (5)
Surgery	6 (15)
TACE or radiofrequency ablation	14 (35)
SIRT	4 (10)

Qualitative data are number and percentage; continuous data are median and range.

⁶⁸Ga-PSMA-11 PET and CT (sensitivity of 97%, specificity and positive predictive value of 100%, and negative predictive value of 80%). Liver segment–level data for detection rate and accuracy are given in Supplemental Table 2.

⁶⁸Ga-PSMA-11 PET versus CT detected 13 versus 9 distant metastatic lesions in 11 versus 8 patients, respectively (Table 3). Extrahepatic lesions were validated in 6 patients on further follow-up: sensitivity for ⁶⁸Ga-PSMA-11 PET versus CT was 100% versus 67%, respectively, and the negative predictive value was 100% versus 93%, respectively (Table 2).

Of the cases with congruence in ⁶⁸Ga-PSMA-11 PET and CT, 1 patient had disseminated bone metastases on preimaging that were confirmed on ⁶⁸Ga-PSMA-11 PET and CT (Supplemental Fig. 1);

another patient had mediastinal lymph node metastases on ⁶⁸Ga-PSMA-11 PET and CT that were subsequently verified as positive by histopathology after lymph node resection (Supplemental Fig. 2); and a third patient had pathologic lymph nodes in the cardiophrenic angle that were confirmed on follow-up scans (Supplemental Fig. 3).

Among the cases in which ⁶⁸Ga-PSMA-11 PET outperformed CT, one patient had positive PSMA uptake in the right femur on ⁶⁸Ga-PSMA-11 PET that was missed on CT (Supplemental Fig. 4), and follow-up CT scans for that patient confirmed development of an osseous lesion. Another patient, with positive PSMA uptake in the right fourth rib seen on ⁶⁸Ga-PSMA-11 PET but not on CT (Supplemental Fig. 5), had subsequent scans confirming resolution of the lesion after local treatment to the metastatic spot. A third patient had metastatic lesions in mediastinal lymph nodes and lumbar vertebra that were not deemed pathologic on CT (Supplemental Figs. 6-I and 6-II) and was offered systemic treatment as a result. In the remaining patients with lesion validation, distant metastases were ruled out by both ⁶⁸Ga-PSMA-11 PET and CT and were subsequently confirmed as negative on follow-up imaging.

Interobserver Agreement

According to the Fleiss κ , agreement among the 3 independent readers for PET versus CT at the liver level was 0.43 (95% CIs, 0.25–0.61) versus 0.56 (95% CIs, 0.38–0.74), respectively, indicating moderate agreement according to the Landis and Koch criteria. At the extrahepatic level (lymph nodes and osseous metastases), agreement for PET versus CT was 0.83 (95% CIs, 0.65–1.01) versus 0.75 (95% CIs, 0.56–0.93), respectively. This corresponds to almost perfect agreement for PET and substantial agreement for CT, according to the same criteria.

Staging Concordance and Migration

Comparison of staging between ⁶⁸Ga-PSMA-11 PET and CT is shown in Tables 3 and 4. Concordance between ⁶⁸Ga-PSMA-11 PET and CT findings was seen in 30 of 40 patients (75%), whereas 8 of 40 patients (20%) experienced upstaging and 2 of 40 (5%) had downstaging by ⁶⁸Ga-PSMA-11 PET (Supplemental Table 3).

With regard to upstaged patients, 1 patient (2.5%) with no disease on CT was upstaged to post-PET stage 2. In this patient, a single lesion in liver segment 5 was found by ⁶⁸Ga-PSMA-11 PET and missed by CT, as confirmed by histopathology (Supplemental Fig. 7). In addition, 6 of 40 patients (15%) with CT stage 2 were upstaged to post-PET stage 3 (*n* = 4, 10%) and stage 4 (*n* = 2, 5%), and 1 patient (2.5%) with CT stage 3 was upstaged to post-PET stage 4.

In total, there were 3 of 40 patients (7.5%) in whom ⁶⁸Ga-PSMA-11 PET detected distant disease that was not detected by CT. The cases were detailed previously above and in Supplemental Figures 4, 5, and 7.

Downstaging by ⁶⁸Ga-PSMA-11 PET occurred in 2 patients: 1 had CT stage 2 (lesion diameter, 3.4 cm), but ⁶⁸Ga-PSMA-11 PET did not detect any hepatic disease. Follow-up MRI showed a lesion in segment V (diameter, 2.9 cm); hence, the ⁶⁸Ga-PSMA-11 PET result was deemed false-negative. The other patient had a CT stage 3B (T4N0M0) but a PET stage 3A (T3N0M0), with no implications on management in this case.

A summary of concordant and discordant staging between ⁶⁸Ga-PSMA-11 PET and CT is shown in Table 4. Mean lesion

TABLE 2

Accuracy, Sensitivity, Specificity, Positive Predictive Value, and Negative Predictive Value Between PSMA PET and CT

Parameter	Whole-liver analysis		Right lobe (segments 1 and 4–8)		Left lobe (segments 2 and 3)		Distant metastases	
	PSMA PET	CT	PSMA PET	CT	PSMA PET	CT	PSMA PET	CT
Accuracy (%)	97	97	97	94	86	91	100	94
Sensitivity (%)	97	97	97	94	77	85	100	67
Specificity (%)	100	100	100	100	91	95	100	100
Positive predictive value (%)	100	100	100	100	83	92	100	100
Negative predictive value (%)	80	80	83	67	87	91	100	93

size on CT and mean SUV_{max} on ^{68}Ga -PSMA-11 in different stages are summarized in Supplemental Table 4.

Management Follow-up

Figure 1 illustrates changes in management after ^{68}Ga -PSMA-11 PET for different stage groups. Overall, pre- to post-PET/CT treatment plans changed in 19 of 40 patients (47.5%).

^{68}Ga -PSMA-11 PET detected no correlate of disease in 4 of 40 patients (10%). Among these, 1 of 4 patient (25%) experienced a change in management, that is, a switch from SIRT to TACE. This change was based on the original unmasked imaging report, which had reported tumor foci in the liver; such findings were not reported in the consensus readings by the masked readers and were thus considered negative.

TABLE 3

Comparison of Staging Between PSMA PET and CT Scans

Stage	PSMA PET	CT
Stage 0 (T0N0M0)	4 (10)	4 (10)
Stage 2 (T2N0M0)	5 (12.5)	11 (27.5)
Stage 3	20 (50)	17 (42.5)
3A: T3N0M0	17 (42.5)	13 (32.5)
3B: T4N0M0	3 (7.5)	4 (10)
Stage 4B	11 (27.5)	8 (20)
T0N0M1 (bone)	1 (2.5)	—
T2N0M1	4 (10)	4 (10)
Bone	2 (5)	1 (2.5)
Mediastinal LN	1 (2.5)	2 (5)
Mediastinal LN + bone	1 (2.5)	1 (2.5)
T3N0M1	5 (12.5)	2 (5)
Bone	2 (5)	1 (2.5)
Mediastinal LN	1 (2.5)	—
Mediastinal LN + bone	1 (2.5)	—
Cardiophrenic recess	1 (2.5)	1 (2.5)
T4N0M1 (bone)	1 (2.5)	2 (5)

LN = lymph node.

Data are number followed by percentage in parentheses.

^{68}Ga -PSMA-11 PET detected stage 2 disease in 5 of 40 patients (12.5%). Among these, 2 of 5 patients (40%) experienced a change in management as follows: one was shifted from SIRT to systemic therapy, and the other was shifted to TACE from active surveillance.

Twenty patients (50%) were classified as stage 3 by ^{68}Ga -PSMA-11 PET, 7 of whom (35%) had a shift in management as follows: 6 were switched to systemic therapy because of evident portal vein or mesenteric vein thrombosis ($n = 3$), a proven high risk for a hepatopulmonary shunt ($n = 1$), or being deemed not suitable for SIRT treatment ($n = 2$); the remaining patient was switched to best supportive care.

Eleven patients (27.5%) were classified as stage 4 by ^{68}Ga -PSMA-11 PET. The highest rate of change in management occurred in patients with stage 4B, recorded in 9 of 11 (82%), 8 of whom (89%) were shifted to systemic therapy on detection of distant metastases on ^{68}Ga -PSMA-11 PET scan; TACE was performed in the remaining patient (Supplemental Fig. 5). Details of management changes before and after ^{68}Ga -PSMA-11 PET are highlighted in Supplemental Table 5.

Two patients had liver lesions with high uptake on ^{68}Ga -PSMA-11 PET; those patients had no other local or systemic treatment options, and they were deemed eligible for and proceeded with ^{177}Lu -PSMA-617 radioligand therapy. However, as revealed by intratherapeutic SPECT/CT-based dosimetry, the tumor radiation dose by radioligand therapy was at least 10-fold lower than typically achieved by 1 cycle of external-beam radiation therapy for HCC, and as such, this treatment modality was not as effective as anticipated. Radioligand therapy was discontinued after 1 cycle for both patients. Radioligand therapy and dosimetry findings are summarized in Supplemental Figures 8 and 9.

Progression-Free Survival Outcomes

The median observation period was 8.3 mo (range, 0.2 to 18.1 mo) from ^{68}Ga -PSMA-11 PET/CT. Patients with observation periods of less than 6 mo were either deceased ($n = 9/40$, 22.5%) or lost to follow-up ($n = 4/40$, 10%). During the observation period, disease progression after initial ^{68}Ga -PSMA-11 PET was noted for 26 of 40 patients (65%) as follows: 13 of 40 by follow-up imaging (32.5%) and 13 of 40 by death (32.5%). For the remaining patients, 4 of 40 (10%) were lost to follow-up, and 10 of 40 (25%) are still on regular follow-up at our institution.

Median progression-free survival was 5.2 mo. Patients with PET M0 versus M1 disease had a median progression-free survival of 5.3 mo versus 4.7, respectively ($P = 0.865$).

TABLE 4
Stage Migration Through PSMA PET and CT

CT	PSMA PET				
	No disease	Stage 2	Stage 3A	Stage 3B	Stage 4B
No disease	3 (7.5)	1 (2.5)*	0	0	0
Stage 2	1 (2.5) [†]	4 (10)	4 (10)*	0	2 (5)*
Stage 3A	0	0	12 (30)	0	1 (2.5)*
Stage 3B	0	0	1 (2.5) [†]	3 (7.5)	0
Stage 4B	0	0	0	0	8 (20)

*PET upstaging.

[†]PET downstaging.

Data are number followed by percentage in parentheses.

DISCUSSION

We compared ⁶⁸Ga-PSMA-11 PET and CT accuracy for HCC lesion detection and assessed the impact of PET on management and prognostic groups. Our results demonstrate comparable accuracy between ⁶⁸Ga-PSMA-11 PET and CT for staging at the liver level, with superior performance for ⁶⁸Ga-PSMA-11 PET at the extrahepatic level (almost perfect agreement among the independent readers). PET/CT accuracy was associated with a management change,

particularly in patients with advanced disease, leading to a shift toward systemic therapy. PET detection of extrahepatic disease was not associated with shorter progression-free survival.

HCC treatment decisions depend on a multidisciplinary approach that takes into account several factors, including size, extent of tumor burden, and functional status of the liver (22). For intermediate- and advanced-stage disease, the standard of care includes radiofrequency ablation, TACE, SIRT, or systemic therapy, whereas patients with end-stage disease often receive palliative care only (2,23–25). Most patients with HCC present with advanced disease and a poor prognosis (26,27). Imaging is critical to accurately assess local and distant disease extent at baseline and follow-up, thereby refining identification of candidates for systemic treatment.

Currently, international treatment guidelines place sorafenib as the standard first-line systemic therapy for patients with advanced HCC or earlier-stage tumors progressing on or unsuitable for locoregional therapies (2,23–25). Current Food and Drug Administration–approved first-line treatments for advanced or progressive HCC are sorafenib or lenvatinib, which are associated with prolonged survival in patients with advanced tumors (28–30). New options include bevacizumab in combination with atezolizumab as first-line therapy, as well as regorafenib, cabozantinib, and ramucirumab, in addition to immunotherapy agents such as nivolumab and pembrolizumab, as second-line therapies (31). PSMA-directed systemic treatments such as mipsagargin have also been recently studied, with preliminary results showing prolonged disease stabilization in patients with HCC who progressed on or after sorafenib or were intolerant to it (32).

⁶⁸Ga-PSMA-11 PET identified distant disease earlier and led to a change toward systemic treatment in our study. In this non-randomized observational setting, progression-free survival was not significantly different for PET M0 versus M1 patients. PET may contribute to an improved outcome for metastatic HCC through earlier identification of candidates for systemic therapy. However, assessment in a prospective trial is needed, as our retrospective observation is limited to the assessment of stage migration with reported impact on management.

A systematic review and metaanalysis summarized the existing evidence on multiphasic CT versus MRI accuracy for the diagnosis of HCC in patients with underlying cirrhosis (33). A pooled analysis of the 19 studies comparing both modalities showed

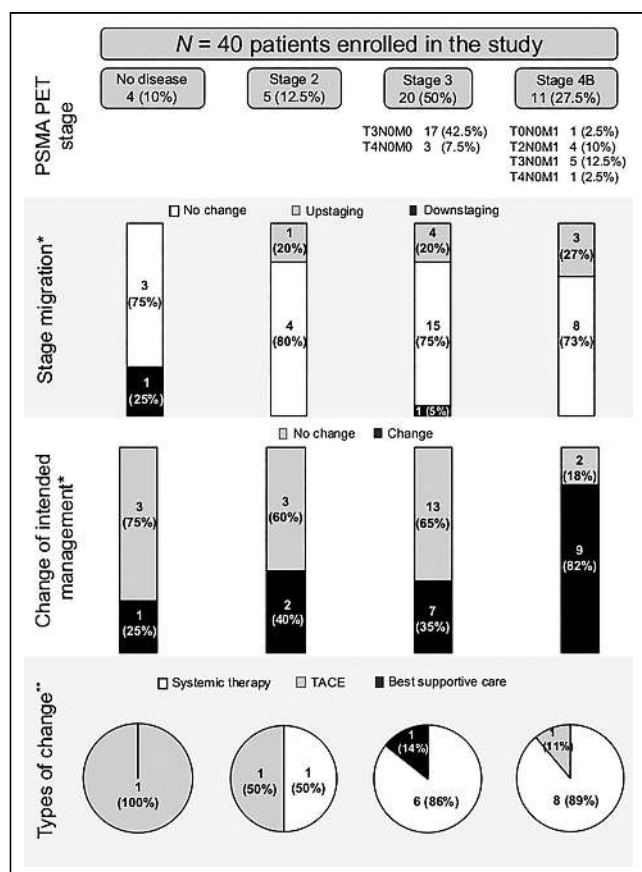


FIGURE 1. PSMA PET stage and change in management. *% from PSMA PET stage. **% from changed management.

significantly higher sensitivity (0.82 vs. 0.66) and a lower negative likelihood ratio (0.20 vs. 0.37) for MRI than for CT. In our study, ^{68}Ga -PSMA-11 PET and CT had a similar detection rate and accuracy at the liver level for both the entire cohort and the subset of patients with cirrhosis. Thus, PET will not replace MRI for accurate liver staging. Underlying cirrhosis did not affect lesion PSMA uptake (median SUV_{max} for patients with cirrhosis and for those without cirrhosis was 14.1).

HCC diagnosis is based more often on imaging than on biopsy (2); therefore, histopathologic information pertaining to tumor grade and aggressiveness is often missing. ^{18}F -labeled choline derivatives, such as ^{18}F -fluoroethylcholine and ^{18}F -fluorocholine, have demonstrated value in identifying differentiated, less aggressive HCC, whereas ^{18}F -FDG is useful in identifying less differentiated, more aggressive tumor forms (34). In 1 study, dual-tracer PET/CT (using ^{18}F -fluorocholine and ^{18}F -FDG) enabled stage upgrading in 11% of patients and treatment modification in 14% (35). With documented expression of PSMA in tumor neovasculature and canalicular membranes of HCC, ^{68}Ga -PSMA-11 PET is a new diagnostic modality; however, correlation with tumor differentiation and aggressiveness requires further assessment.

Our study was limited by its retrospective design and the small number of patients included. Histopathology was available for only a small group of patients, as tissue sampling is not routinely performed and biopsy of extrahepatic lesions is difficult because of their small size or remote location. Thus, most lesion follow-up was based on correlative or follow-up imaging with known intrinsic limitations. In addition, MRI or PET/MRI was not systematically performed for comparison in the included patients. Finally, 18 of 40 (45%) patients had an uptake time outside the range of 50 to 100 min recommended by the European Association of Nuclear Medicine and the Society of Nuclear Medicine and Molecular Imaging (14), which may have impacted image interpretation.

CONCLUSION

Using masked reads and independent lesion validation, we established the accuracy of ^{68}Ga -PSMA-11 PET for HCC staging, which was comparable to the accuracy of CT for hepatic disease detection and more accurate for extrahepatic disease detection. ^{68}Ga -PSMA-11 PET induced stage migration by detection of distant metastases in 11 of 40 patients (27.5%), and this migration was associated with a shift from local to systemic therapy in 8 of 11 (73%) of these patients. ^{68}Ga -PSMA-11 PET may prove valuable for early identification of candidates for systemic therapy.

DISCLOSURE

Ken Herrmann reports personal fees from Bayer, SIRTEX, Adacap, Curium, Endocyte, IPSEN, Siemens Healthineers, GE Healthcare, Amgen, Novartis, and ymabs, as well as personal and other fees from Sofie Biosciences, nonfinancial support from ABX, and grants and personal fees from BTG, all of which are outside the submitted work. Christian M. Lange has received speaker and consultancy fees from Abbvie, MSD, Roche, Eisai, Behring, Falk, Novartis, and Norgine, all of which are outside the submitted work. Manuel Weber is on the Speakers Bureau for Boston Scientific. Wolfgang P. Fendler is a consultant for Endocyte and BTG, and he received personal fees from RadioMedix, Bayer, and Parxel, as well as financial support from Mercator Research Center Ruhr (MERCUR, An-2019-0001), IFORES (D/107-81260, D/107-30240), Doktor Robert Pflieger-Stiftung, and Wiedenfeld-Stiftung/

Stiftung Krebsforschung Duisburg, all of which are outside the submitted work. No other potential conflict of interest relevant to this article was reported.

KEY POINTS

QUESTION: Does ^{68}Ga -PSMA-11 PET/CT improve tumor detection and impact the clinical management of patients with HCC?

PERTINENT FINDINGS: The staging accuracy of ^{68}Ga -PSMA-11 PET was comparable to that of CT for hepatic staging and more accurate for extrahepatic staging, inducing stage migration by detection of distant metastases in 11 of 40 patients (27.5%), with a shift from local to systemic therapy in 8 of 11 (73%) of these patients. ^{68}Ga -PSMA-11 PET may prove valuable for early identification of candidates for systemic therapy.

IMPLICATIONS FOR PATIENT CARE: ^{68}Ga -PSMA-11 PET demonstrated higher accuracy than CT in the detection of HCC metastases and was associated with a management change in about half the patient cohort.

REFERENCES

1. Fomer A, Llovet JM, Bruix J. Hepatocellular carcinoma. *Lancet*. 2012;379:1245–1255.
2. Bruix J, Sherman M. Management of hepatocellular carcinoma: an update. *Hepatology*. 2011;53:1020–1022.
3. Lencioni R, Chen XP, Dagher L, Venook AP. Treatment of intermediate/advanced hepatocellular carcinoma in the clinic: how can outcomes be improved? *Oncologist*. 2010;15(suppl 4):42–52.
4. Vogel A, Cervantes A, Chau I, et al. Hepatocellular carcinoma: ESMO clinical practice guidelines for diagnosis, treatment and follow-up. *Ann Oncol*. 2018;29:iv238–iv255.
5. Perera M, Papa N, Roberts M, et al. Gallium-68 prostate-specific membrane antigen positron emission tomography in advanced prostate cancer: updated diagnostic utility, sensitivity, specificity, and distribution of prostate-specific membrane antigen-avid lesions—a systematic review and meta-analysis. *Eur Urol*. 2020;77:403–417.
6. Perera M, Papa N, Christidis D, et al. Sensitivity, specificity, and predictors of positive ^{68}Ga -prostate-specific membrane antigen positron emission tomography in advanced prostate cancer: a systematic review and meta-analysis. *Eur Urol*. 2016;70:926–937.
7. Chang SS, O'Keefe DS, Bacich DJ, Reuter VE, Heston WDW, Gaudin PB. Prostate-specific membrane antigen is produced in tumor-associated neovasculature. *Clin Cancer Res*. 1999;5:2674–2681.
8. Chang SS, Reuter VE, Heston WD, Bander NH, Grauer LS, Gaudin PB. Five different anti-prostate-specific membrane antigen (PSMA) antibodies confirm PSMA expression in tumor-associated neovasculature. *Cancer Res*. 1999;59:3192–3198.
9. Kesler M, Levine C, Hershkovitz D, et al. ^{68}Ga -PSMA is a novel PET-CT tracer for imaging of hepatocellular carcinoma: a prospective pilot study. *J Nucl Med*. 2019;60:185–191.
10. Tolkach Y, Goltz D, Kremer A, et al. Prostate-specific membrane antigen expression in hepatocellular carcinoma: potential use for prognosis and diagnostic imaging. *Oncotarget*. 2019;10:4149–4160.
11. Kunikowska J, Cieslak B, Gierej B, et al. [^{68}Ga]Ga-prostate-specific membrane antigen PET/CT: a novel method for imaging patients with hepatocellular carcinoma. *Eur J Nucl Med Mol Imaging*. 2021;48:883–892.
12. Harris PA, Taylor R, Minor BL, et al. The REDCap consortium: building an international community of software platform partners. *J Biomed Inform*. 2019;95:103208.
13. Harris PA, Taylor R, Thielke R, Payne J, Gonzalez N, Conde JG. Research electronic data capture (REDCap): a metadata-driven methodology and workflow process for providing translational research informatics support. *J Biomed Inform*. 2009;42:377–381.
14. Fendler WP, Eiber M, Beheshti M, et al. ^{68}Ga -PSMA PET/CT: joint EANM and SNMMI procedure guideline for prostate cancer imaging: version 1.0. *Eur J Nucl Med Mol Imaging*. 2017;44:1014–1024.

15. Eiber M, Herrmann K, Calais J, et al. Prostate cancer molecular imaging standardized evaluation (PROMISE): proposed miTNM classification for the interpretation of PSMA-ligand PET/CT. *J Nucl Med*. 2018;59:469–478.
16. Fendler WP, Calais J, Eiber M, et al. Assessment of ⁶⁸Ga-PSMA-11 PET accuracy in localizing recurrent prostate cancer: a prospective single-arm clinical trial. *JAMA Oncol*. 2019;5:856–863.
17. Willatt J, Ruma JA, Azar SF, Dasika NL, Syed F. Imaging of hepatocellular carcinoma and image guided therapies: how we do it. *Cancer Imaging*. 2017;17:9.
18. Choi JY, Lee JM, Sirlin CB. CT and MR imaging diagnosis and staging of hepatocellular carcinoma: part I. Development, growth, and spread: key pathologic and imaging aspects. *Radiology*. 2014;272:635–654.
19. Amin MB, Edge S, Greene F, et al. *AJCC Cancer Staging Manual*. 8th ed. Springer International Publishing; 2017:287–294.
20. Lencioni R, Llovet JM. Modified RECIST (mRECIST) assessment for hepatocellular carcinoma. *Semin Liver Dis*. 2010;30:52–60.
21. Landis JR, Koch GG. The measurement of observer agreement for categorical data. *Biometrics*. 1977;33:159–174.
22. Clark T, Maximin S, Meier J, Pokharel S, Bhargava P. Hepatocellular carcinoma: review of epidemiology, screening, imaging diagnosis, response assessment, and treatment. *Curr Probl Diagn Radiol*. 2015;44:479–486.
23. European Association for the Study of the Liver. EASL clinical practice guidelines: management of hepatocellular carcinoma. *J Hepatol*. 2018;69:182–236.
24. Heimbach JK, Kulik LM, Finn RS, et al. AASLD guidelines for the treatment of hepatocellular carcinoma. *Hepatology*. 2018;67:358–380.
25. Verslype C, Rosmorduc O, Rougier P, Group EGW. Hepatocellular carcinoma: ESMO-ESDO clinical practice guidelines for diagnosis, treatment and follow-up. *Ann Oncol*. 2012;23(suppl 7):vii41–vii48.
26. Boland P, Wu J. Systemic therapy for hepatocellular carcinoma: beyond sorafenib. *Chin Clin Oncol*. 2018;7:50.
27. Ingle PV, Samsudin SZ, Chan PQ, et al. Development and novel therapeutics in hepatocellular carcinoma: a review. *Ther Clin Risk Manag*. 2016;12:445–455.
28. Llovet JM, Ricci S, Mazzaferro V, et al. Sorafenib in advanced hepatocellular carcinoma. *N Engl J Med*. 2008;359:378–390.
29. Kudo M, Finn RS, Qin S, et al. Lenvatinib versus sorafenib in first-line treatment of patients with unresectable hepatocellular carcinoma: a randomised phase 3 non-inferiority trial. *Lancet*. 2018;391:1163–1173.
30. Cheng A-L, Kang Y-K, Chen Z, et al. Efficacy and safety of sorafenib in patients in the Asia-Pacific region with advanced hepatocellular carcinoma: a phase III randomised, double-blind, placebo-controlled trial. *Lancet Oncol*. 2009;10:25–34.
31. Li D, Sedano S, Allen R, Gong J, Cho M, Sharma S. Current treatment landscape for advanced hepatocellular carcinoma: patient outcomes and the impact on quality of life. *Cancers (Basel)*. 2019;11:841.
32. Mahalingam D, Peguero J, Cen P, et al. A phase II, multicenter, single-arm study of mipsagargin (G-202) as a second-line therapy following sorafenib for adult patients with progressive advanced hepatocellular carcinoma. *Cancers (Basel)*. 2019;11:833.
33. Roberts LR, Sirlin CB, Zaiem F, et al. Imaging for the diagnosis of hepatocellular carcinoma: a systematic review and meta-analysis. *Hepatology*. 2018;67:401–421.
34. Filippi L, Schillaci O, Bagni O. Recent advances in PET probes for hepatocellular carcinoma characterization. *Expert Rev Med Devices*. 2019;16:341–350.
35. Chalaye J, Costentin CE, Luciani A, et al. Positron emission tomography/computed tomography with ¹⁸F-fluorocholine improve tumor staging and treatment allocation in patients with hepatocellular carcinoma. *J Hepatol*. 2018;69:336–344.

PSMA Theranostics: Is the Time Ripe to Pave the Way to Further Tumor Entities?

Winfried Brenner^{1,2}, Joachim Strobel³, and Vikas Prasad^{2,3}

¹Department of Nuclear Medicine, Charité–Universitätsmedizin Berlin, Berlin, Germany; ²German Cancer Consortium (DKTK), Campus Berlin, Berlin, Germany; and ³Department of Nuclear Medicine Universität Ulm, Ulm, Germany

Success of precision oncology is based on increasingly better and individualized tumor characterization. State-of-the-art personalized treatment options are still primarily directed by site of tumor origin and tumor entity rather than by the tumor molecular signature (e.g., the novel treatment approach with neurotrophic tyrosine receptor kinase [NTRK] inhibitors in the case of NTRK gene fusion-positive tumors) irrespective of their origin. Molecular imaging using metabolic tracers and radiolabeled peptides and antibodies offer a unique possibility for noninvasive in vivo tumor characterization, also based on molecular paradigms rather than tumor type. One such radiopharmaceutical, the prostate-specific membrane antigen (PSMA), is currently set to become a blockbuster for both PET diagnostics and radionuclide therapy in prostate cancer. Germany, specifically the University of Heidelberg team, has pioneered the rejuvenation of PSMA and its use in nuclear medicine. The evidence level from initial retrospective German studies was substantiated by subsequent prospective clinical trials in Australia.

The proPSMA diagnostic trial reported that “PSMA PET/CT is a suitable replacement for conventional imaging, providing superior accuracy to the combined findings of CT and bone scanning” in treatment-naïve patients with high-risk prostate cancer with respect to detection of both pelvic nodal and distant metastases (1,2). Similarly, PSMA PET/CT proved also superior in detecting local recurrences, lymph node, or distant metastases in patients with early biochemical relapse and rising prostate-specific antigen levels as low as 0.2 ng/mL (3). These findings support recent U.S. Food and Drug Administration (FDA) approval of 2 new drug applications for PSMA PET imaging at the Universities of California San Francisco and Los Angeles for both primary staging in high-risk prostate cancer patients and patients with biochemical recurrent disease. The findings also reinforce the recommendation for PSMA PET imaging in the setting of biochemical recurrence in the recently updated national German S3 guideline on prostate cancer (4) and reimbursement of this procedure within the framework of *Ambulante Spezialärztliche Versorgung* in Germany. Most recently, the PSMA tracer ¹⁸F-piflufolastat from Lantheus was approved by the FDA (5).

Additionally, major progress in the realm of PSMA treatment in patients with prostate cancer has been made. The results of the

international, prospective, open label, multicenter, randomized phase 3 study of ¹⁷⁷Lu-PSMA-617 in the treatment of patients with progressive PSMA-positive metastatic castration-resistant prostate cancer (VISION trial) showed that ¹⁷⁷Lu-PSMA-617 significantly increased overall survival and radiographic progression-free survival in these patients (6). PSMA-based theranostics, therefore, very soon will increasingly become a clinical standard in prostate cancer patients—as long as these tumors express PSMA.

But PSMA is by far not as prostate-specific as suggested by its name. It is a type II transmembrane zinc metallopeptidase with enzymatic activity that hydrolyzes poly- γ -glutamated folates to folate, which can be taken up by nearby tumor cells (7). The enzyme is also known as glutamate carboxypeptidase II, folate hydrolase 1, folypoly- γ -glutamate carboxypeptidase, and *N*-acetylated- α -linked acidic dipeptidase I. PSMA is physiologically expressed in astrocytes and Schwann cells of the nervous system, prostate, proximal renal tubule of the kidney, salivary glands, and the duodenal brush border (8) as can be seen and quantified on PET images of cancer patients (9).

In malignant tumors, however, PSMA expression is not only documented for prostate cancer cells but also found in the tumor-associated neovasculature of almost all solid tumors though not in normal vasculature. Interestingly, PSMA expression often correlates with the aggressiveness of tumors, as has been shown for prostate cancer as well as other tumor entities, for example, sarcomas in which PSMA expression was higher in more malignant tumors (10).

A comprehensive review on PSMA PET imaging of nonprostatic diseases has been recently compiled by de Galiza Barbosa et al., in which a variety of different tumors, including almost all relevant carcinomas as well as brain and nerve-derived tumors, lymphomas, and soft- and bone tissue sarcomas, were shown to be PSMA-positive, usually related to endothelial expression in the associated neovasculature. The authors therefore concluded that “these unintentional findings have paved the way for the application of PSMA PET imaging as an additional diagnostic tool” (11).

These “unintentional” findings of PET-detectable PSMA expression in many different malignant tumors imply potential use not only for imaging but also for therapy: it may open up a universal theranostic approach of tumor treatment in many tumors, and, thus, should be followed in more detail for different tumor entities, especially in tumors with a high medical need for therapy improvement.

Among all the nonprostatic PSMA-expressing tumors, aggressive brain tumor glioblastoma multiforme (GBM) holds special mention as treatment results in this tumor type, despite extensive research, are still very poor with no curative options thus far. Initial results in 16

Received Jun. 13, 2021; revision accepted Jun. 29, 2021.
For correspondence or reprints, contact Winfried Brenner (winfried.brenner@charite.de).
Published online July 16, 2021.
COPYRIGHT © 2021 by the Society of Nuclear Medicine and Molecular Imaging.
DOI: 10.2967/jnumed.121.262737

patients with histopathologically documented GBM showed PSMA expression, albeit highly heterogeneous, on both tumor-associated vessels and in nonendothelial cells (12). Similarly, further case reports and case series have also demonstrated mild to intense PSMA expression on PET/CT in GBM patients (13–18).

At first instance, these results appear promising, however, using a PSMA-based theranostic concept in glioblastoma may face several challenges based on these first reports. First, PSMA as the binding target is primarily expressed on neovascular rather than tumor cells in GBM, thus irradiating tumor cells only in the immediate vicinity of the vascular cells, depending on the range of the respective radionuclide. Second, the often low and diffusely distributed tumor volume in GBM recurrences with their infiltrating tumor cell clusters in comparison to, for example, solid metastatic prostate cancer lesions, may further reduce the therapeutic index. In this setting, the β -emitting radionuclide ^{177}Lu , with a maximum pathlength of approximately 2 mm, may release significant amounts of radiation to peritumoral brain parenchyma and nerves rather than to the infiltrating tumor cells, which in turn results in higher treatment toxicity. Finally, low to moderate PSMA expression in GBM may not allow sufficient tumor radiation doses if PSMA endoradiotherapy is used as a stand-alone treatment.

However, these limitations may be overcome. We first should perform clinical studies on PSMA PET/CT in correlation to conventional imaging, contrast-enhanced MRI, and ^{18}F -fluoroethyltyrosine or ^{11}C -methionine PET, as well as tumor panel analysis for characterizing GBM lesions in terms of PSMA expression and the respective genotype. Second, we should use PSMA therapy with ^{177}Lu in the case of sufficient PSMA tumor uptake. Thorough state-of-the-art dosimetry in these patients in combination with meticulous tumor response assessment will allow evaluation of the clinical value of this treatment option as a stand-alone therapy and help define sufficient tumor uptake. On the basis of our above-mentioned caveats, combination treatments with stereotactic radiation therapy, sequentially or alternatively, or tyrosine kinase inhibitors should be evaluated early on in these highly treatment-resistant tumors. Furthermore, more effective therapeutic radionuclides, for example, ^{161}Tb or the α -emitter ^{225}Ac (very short pathlength!), have to be tested in comparison to ^{177}Lu for assessing both treatment efficacy and toxicity, and thus, their therapeutic index. Experience from radiation therapy suggests that apart from inherent radiation sensitivity of GBM cells, several other factors such as immune cell infiltration, radiation dose, duration of radiation therapy, and the like play a role in determining the treatment outcome. Radiolabeled PSMA binding to the neovasculature of GBM is expected to deliver relatively moderate radiation doses for inducing double-strand breaks in tumor cell DNA but at the same time modulate the tumor microenvironment to enhance tumor immunity as well as induce apoptosis through metabolic pathways. The radiobiology of PSMA endoradiotherapy of GBM needs to be properly investigated in appropriate preclinical and mathematic models.

It is most evident but imperative to state that such studies in GBM patients, either as prospective studies or under compassionate-use programs, have to be performed in interdisciplinary settings and close collaboration with neurosurgeons and radiation oncologists. Considering the extremely poor outcome of GBM patients, in terms of both survival and quality of life, the potential of PSMA radionuclide therapy should be explored for the benefit of these patients. Let us pave the way for PSMA theranostics to GBM and further tumor entities!

DISCLOSURE

No potential conflict of interest relevant to this article was reported.

REFERENCES

- Hofman MS, Lawrentschuk N, Francis RJ, et al. Prostate-specific membrane antigen PET-CT in patients with high-risk prostate cancer before curative-intent surgery or radiotherapy (proPSMA): a prospective, randomised, multicentre study. *Lancet*. 2020;395:1208–1216.
- Hofman MS, Murphy DG, Williams SG, et al. A prospective randomized multicentre study of the impact of gallium-68 prostate-specific membrane antigen (PSMA) PET/CT imaging for staging high-risk prostate cancer prior to curative-intent surgery or radiotherapy (proPSMA study): clinical trial protocol. *BJU Int*. 2018;122:783–793.
- Radzina M, Tirane M, Roznere L, et al. Accuracy of ^{68}Ga -PSMA-11 PET/CT and multiparametric MRI for the detection of local tumor and lymph node metastases in early biochemical recurrence of prostate cancer. *Am J Nucl Med Mol Imaging*. 2020;10:106–118.
- S3-Leitlinie Prostatakarzinom (version 6) (Guideline Prostate Cancer). Program Oncology c/o Deutsche Krebsgesellschaft e.V website. <https://www.leitlinienprogramm-onkologie.de/leitlinien/prostatakarzinom/>. Updated March 2021. Accessed July 23, 2021.
- Lantheus Receives U.S. FDA approval of PYLARIFY® (piflutofolastat F 18) injection, the first and only commercially available PSMA PET imaging agent for prostate cancer. Business Wire website. <https://www.businesswire.com/news/home/20210527005291/en/Lantheus-Receives-U.S.-FDA-Approval-of-PYLARIFY%C2%AE-piflutofolastat-F-18-Injection-the-First-and-Only-Commercially-Available-PSMA-PET-Imaging-Agent-for-Prostate-Cancer>. Published online May 27, 2021. Accessed August 4, 2021.
- Morris MJ, De Bono JS, Chi KN, et al. Phase 3 study of lutetium-177-PSMA-617 in patients with metastatic castration-resistant prostate cancer (VISION). *J Clin Oncol*. 2021;39(suppl 15):LBA4.
- O'Keefe DS, Bacich DJ, Huang SS, Heston WDW. A perspective on the evolving story of PSMA biology, PSMA-based imaging, and endoradiotherapeutic strategies. *J Nucl Med*. 2018;59:1007–1013.
- Vornov JJ, Peters D, Nedelcovych M, Hollinger K, Rais R, Slusher BS. Looking for drugs in all the wrong places: use of GCPII inhibitors outside the brain. *Neurochem Res*. 2020;45:1256–1267.
- Prasad V, Steffen IG, Diederichs G, Makowski MR, Wust P, Brenner W. Biodistribution of ^{68}Ga PSMA-HBED-CC in patients with prostate cancer: characterization of uptake in normal organs and tumour lesions. *Mol Imaging Biol*. 2016;18:428–436.
- Heitkötter B, Trautmann M, Grünewald I, et al. Expression of PSMA in tumor neovasculature of high grade sarcomas including synovial sarcoma, rhabdomyosarcoma, undifferentiated sarcoma and MPNST. *Oncotarget*. 2017;8:4268–4276.
- de Galiza Barbosa F, Queiroz MA, Nunes RF, et al. Nonprostatic diseases on PSMA PET imaging: a spectrum of benign and malignant findings. *Cancer Imaging*. 2020;20:23.
- Holzgreve A, Biczok A, Ruf VC, et al. PSMA expression in glioblastoma as a basis for theranostic approaches: a retrospective, correlational panel study including immunohistochemistry, clinical parameters and PET imaging. *Front Oncol*. 2021;11:646387.
- Unterrainer M, Niyazi M, Ruf V, Bartenstein P, Albert NL. The endothelial prostate-specific membrane antigen is highly expressed in gliosarcoma and visualized by ^{68}Ga -PSMA-11 PET: a theranostic outlook for brain tumor patients? *Neuro-oncol*. 2017;19:1698–1699.
- Salas Fragomeni RA, Pienta KJ, Pomper MG, Gorin MA, Rowe SP. Uptake of prostate-specific membrane antigen-targeted ^{18}F -DCFPyL in cerebral radionecrosis: implications for diagnostic imaging of high-grade gliomas. *Clin Nucl Med*. 2018;43:e419–e421.
- Matsuda M, Ishikawa E, Yamamoto T, et al. Potential use of prostate specific membrane antigen (PSMA) for detecting the tumor neovasculature of brain tumors by PET imaging with ^{89}Zr -Df-IAB2M anti-PSMA minibody. *J Neurooncol*. 2018;138:581–589.
- Salas Fragomeni RA, Menke JR, Holdhoff M, et al. Prostate-specific membrane antigen-targeted imaging with ^{18}F DFCFPyL in high-grade gliomas. *Clin Nucl Med*. 2017;42:e433–e435.
- Sasikumar A, Kashyap R, Joy A, et al. Utility of ^{68}Ga -PSMA-11 PET/CT in imaging of glioma—a pilot study. *Clin Nucl Med*. 2018;43:e304–e309.
- Marafi F, Sasikumar A, Fathallah W, Esmail A. ^{18}F -PSMA 1007 brain PET/CT imaging in glioma recurrence. *Clin Nucl Med*. 2020;45:e61–e62.

The Impact of Monosodium Glutamate on ⁶⁸Ga-PSMA-11 Biodistribution in Men with Prostate Cancer: A Prospective Randomized, Controlled Imaging Study

Wesley R. Armstrong*¹, Andrei Gafita*¹, Shaojun Zhu¹, Pan Thin¹, Kathleen Nguyen¹, Rejah Alano¹, Stephanie Lira¹, Kiara Booker¹, Linda Gardner¹, Tristan Grogan², David Elashoff², Martin Allen-Auerbach^{1,3,4}, Magnus Dahlbom^{1,5}, Johannes Czernin^{1,3-5}, and Jeremie Calais^{1,3-5}

¹Ahmanson Translational Theranostics Division, Department of Molecular and Medical Pharmacology, UCLA, Los Angeles, California; ²Department of Medicine Statistics Core, David Geffen School of Medicine, UCLA, Los Angeles, California; ³Institute of Urologic Oncology, UCLA, Los Angeles, California; ⁴Jonsson Comprehensive Cancer Center, UCLA, Los Angeles, California; and ⁵Physics and Biology in Medicine Interdepartmental Graduate Program, David Geffen School of Medicine, UCLA, Los Angeles, California

The prostate-specific membrane antigen (PSMA) has been targeted for PET imaging and radioligand therapy (RLT) in patients with prostate cancer. Xerostomia is a common side effect of RLT because of the high salivary gland uptake of PSMA radioligands. Here, we aimed to determine the impact of monosodium glutamate (MSG) administration on PSMA-radioligand biodistribution within healthy organs and tumor lesions by using ⁶⁸Ga-PSMA-11 PET imaging. **Methods:** Sixteen men with prostate cancer were randomized (1:1) into oral ingestion and oral topical application (“swishing”) arms. Each subject underwent 2 ⁶⁸Ga-PSMA-11 PET/CT scans within 14 d under baseline and MSG conditions. The salivary glands and whole-body tumor lesions were segmented using qPSMA software. We quantified tracer uptake via SUV_{mean} and SUV_{max} and compared parameters within each patient. **Results:** For the oral ingestion arm, salivary gland SUV_{mean} and SUV_{max} decreased on average from the control scan to the MSG scan by 45% ± 15% (*P* = 0.004) and 53% ± 11% (*P* < 0.001), respectively. Tumor lesion SUV_{mean} and SUV_{max} also decreased by 38% (interquartile range, −67% to −33%) and −52% (interquartile range, −70% to −49%), respectively (*P* = 0.018). Swishing had no significant effect on ⁶⁸Ga-PSMA-11 accumulation in normal organs or tumor lesions. **Conclusion:** Oral ingestion but not topical application of MSG reduced ⁶⁸Ga-PSMA-11 uptake in salivary glands. Tumor uptake also declined; therefore, the clinical application of MSG is unlikely to be useful in the framework of RLT.

Key Words: monosodium glutamate; PSMA; PET/CT; xerostomia; salivary glands;

J Nucl Med 2021; 62:1244–1251
DOI: 10.2967/jnumed.120.257931

Prostate-specific membrane antigen (PSMA) is a transmembrane glycoprotein highly overexpressed by prostate cancer (PCa) cells (1). In recent years, PSMA has become an attractive target for both diagnosis and treatment of PCa (2). After their

introduction for whole-body imaging with PET/CT, small-molecule PSMA ligands with a DOTA chelator, such as PSMA I&T or PSMA-617, were labeled with β-emitting (¹⁷⁷Lu) or α-emitting (²²⁵Ac) isotopes for therapeutic purposes. PSMA-targeted radioligand therapy (RLT) with ¹⁷⁷Lu demonstrated significant reductions in serum prostate-specific antigen (PSA) levels in phase 2 trials of metastatic castration-resistant PCa (3) and is currently being investigated in a phase 3 trial (VISION: NCT03511664). PSMA RLT with ²²⁵Ac, an α-emitter with a high energy deposition, may have enhanced therapeutic efficacy but has a less favorable toxicity profile (4, 5). The most concerning side effects include xerostomia, long-term nephrotoxicity, and myelosuppression (6–8). In particular, ²²⁵Ac-PSMA is associated with grade 2 or higher xerostomia, which often led to treatment cessation despite an initially favorable PSA response (4, 5, 9, 10). After the preliminary effects of ²²⁵Ac-PSMA on serum PSA levels, multiple efforts have failed to apply protective measures against salivary gland and kidney toxicity (11–14).

The salivary gland binding and uptake mechanism of PSMA radioligands remain unclear. There appears to be limited target expression by the salivary glands (low or intermediate immunohistochemistry PSMA staining intensity; patchy and focal expression, limited in extent [5% of salivary gland tissue]), whereas radioligand uptake is very high (15). In contrast, PSMA-targeted radioantibodies, such as ¹¹¹In-J591 and ¹⁷⁷Lu-J591, do not accumulate in the salivary glands or accumulate only at low levels (16). The high accumulation of the PSMA radioligands in the salivary glands may thus represent an off-target effect (i.e., related not to the PSMA target expression but to the radioligand molecules).

PSMA (also known as glutamate carboxypeptidase II) is targeted by small molecules via interaction of the glutamate moiety of the radioligands (among other features) with its enzymatic region, which has high glutamate affinity (17–19). Therefore, it was hypothesized that the administration of monosodium glutamate (MSG), a well-known food additive, could act as a competitor by blocking the binding of the PSMA-targeting radioligands. In a pre-clinical model, MSG reduced ⁶⁸Ga-PSMA-11 salivary gland and renal uptake, whereas tumor accumulation was unaffected, in LNCap-bearing mice (20). Moreover, MSG stimulates salivary flow as shown in a controlled study, with up to a 1 mL/min mean salivary flow compared with 0.25 mL/min at baseline (21). We

Received Oct. 1, 2020; revision accepted Dec. 29, 2020.
For correspondence or reprints, contact Jeremie Calais (jcalais@mednet.ucla.edu).
Guest Editor: Todd E. Peterson, Vanderbilt University.
*Contributed equally to this work.
Published online January 28, 2021.
COPYRIGHT © 2021 by the Society of Nuclear Medicine and Molecular Imaging.

also hypothesized that MSG could be used as an oral salivary flow stimulant to remove accumulated radioligands from the salivary glands.

^{68}Ga -PSMA-11 PET imaging is a rapid, noninvasive, and safe technique that provides reliable estimates of the biodistribution of therapeutic PSMA ligands.

In this imaging-controlled study on men with PCa, we determined the impact of MSG administration on PSMA-radioligand biodistribution in normal organs and tumors by using ^{68}Ga -PSMA-11 PET/CT with and without MSG administration. We tested 2 administration methods: “swishing” (i.e., oral topical, to increase the salivary flow) and oral ingestion (for competitive binding).

MATERIALS AND METHODS

Study Design and Patient Population

This was a prospective single-center, open-label, randomized, controlled imaging study conducted at UCLA using 16 paired PSMA PET/CT studies with (MSG scan) and without (control scan) MSG administration, with less than 14 d between the 2 scans. The study was investigator-initiated, self-funded, conducted under an investigational new drug application (application 130649), approved by the local institutional review board (approval 18-001776), and registered on clinicaltrials.gov (NCT04282824).

Patients with histopathologically proven PCa who volunteered to undergo 2 PSMA PET/CT scans within 14 d and without any treatment change between the 2 scans were eligible. Patients with prior salivary gland surgery or radiation therapy, a history of salivary gland disease, severe uncontrolled hypertension, or a known allergic responses to MSG or who were unable to comply with the study procedures were excluded (Supplemental Table 1; supplemental materials are available at <http://jnm.snmjournals.org>). We obtained oral and written informed consent from all patients.

To preclude the potential confounding factor of stimulus effect, patients were initially randomized into 2 arms based on the type of MSG administration: oral ingestion ($n = 8$) and swishing ($n = 8$). A second

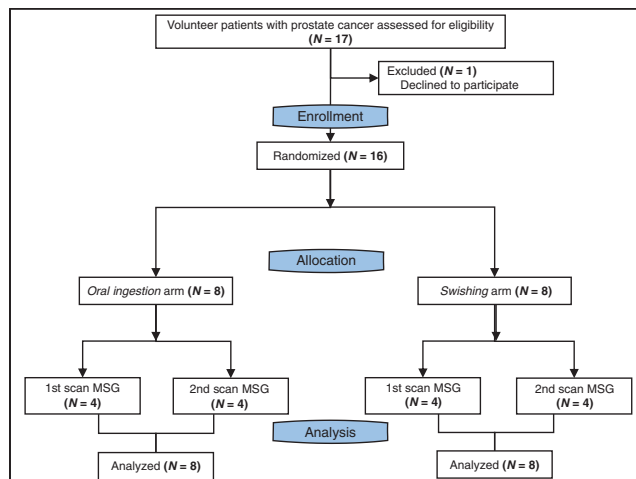


FIGURE 1. Study flowchart.

randomization process subdivided the patients into receiving the control or MSG scan first. Figure 1 depicts the study flowchart.

Procedures

MSG Administration. We obtained food-grade MSG as a sealed salt powder (Ajinomoto). The U.S. Food and Drug Administration has designated MSG to be generally recognized as safe. Patients randomized to oral ingestion received a 150 mg/kg dose of food-grade MSG dissolved in 300 mL of drinking-grade water 30 min before ^{68}Ga -PSMA-11 injection. Patients randomized to swishing received 0.5 M MSG, which they swished within the mouth for 30 s before removing the solution without swallowing. The swishing procedure was repeated at 0, 30, and 45 min after ^{68}Ga -PSMA-11 injection.

Image Acquisition. ^{68}Ga -PSMA-11 (Glu-NH-CO-NH-Lys-(Ahx)-[^{68}Ga (HBED-CC)]) was used as the PSMA ligand and was obtained from the Biomedical Cyclotron Facility at UCLA. ^{68}Ga -PSMA-11 PET/CT imaging was performed according to international guidelines (22). The target injected activity dose was 185 MBq (allowed range, 111–259

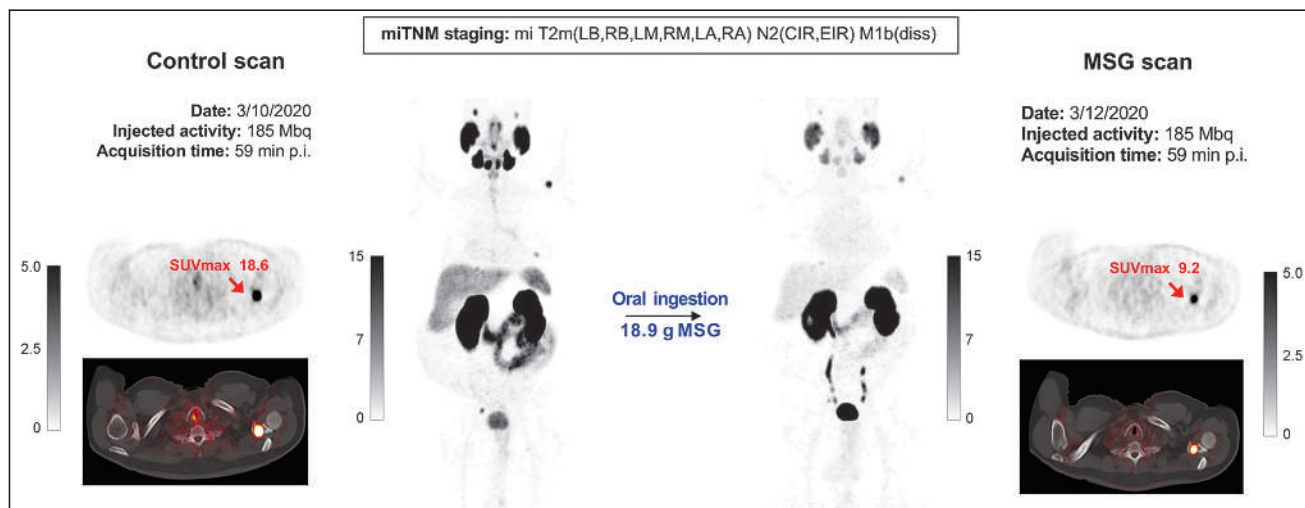


FIGURE 2. Set of images of 73-year-old patient after radiation therapy (initial PSA, 16 ng/mL; biopsy Gleason score, 8; pT2c) and concurrent androgen hormone treatment, currently presenting for rising PSA value (6.27 ng/mL). After enrollment, patient was randomized to oral ingestion arm and received 18.9 g of MSG before second ^{68}Ga -PSMA-11 injection. PSMA PET/CT images revealed multifocal prostate involvement, common iliac right and external iliac right pelvic lymph nodes, and multiple bone lesions. Maximum-intensity-projection images show overall decline in ^{68}Ga -PSMA-11 accumulation within normal organs as well as tumor lesions on MSG scan relative to control scan. Axial view images display relevant case example of bone lesion with significant PSMA decrease after MSG administration (SUV_{max} from 18.6 to 9.2). p.i. = after injection.

TABLE 1
Patient Characteristics

Characteristic	Data
Age (y)	72 (56–81)
Time since diagnosis of PCa (y)	7 (0.6–21)
PSA at diagnosis (ng/mL)	36 (2.5–308)
Gleason score at diagnosis*	
<8	7 (44%)
≥8	8 (50%)
T stage at diagnosis*	
T1	1 (6%)
T2	11 (66%)
T3	3 (18%)
M status at diagnosis [†]	
M0	15 (94%)
M1	1 (6%)
Primary treatment [‡]	
Prostatectomy ± lymphadenectomy	7 (49%)
Local radiotherapy	6 (42%)
Systemic treatment	1 (7%)
Salvage treatment	
None	9 (56%)
Radiotherapy	3 (19%)
Systemic treatment	4 (25%)
Indication for scan	
Primary staging	2 (12%)
Biochemical recurrence	7 (42%)
Metastatic restaging	7 (42%)
PSA at time of PSMA (ng/mL)	6.2 (0.2–53.7)

*Data missing for 1 patient.

[†]M1 was defined as metastatic disease (distant metastases).

[‡]Data missing for 2 patients.

Qualitative data are number and percentage (total $n = 16$); continuous data are median and range.

MBq). The target uptake period was 60 min (allowed range, 50–100 min). We applied oral but no intravenous CT contrast medium for the control and MSG scans. We acquired images using a 64-detector PET/CT scanner (2007 Biograph 64 Truepoint or 2010 Biograph mCT 64; Siemens). The same scanner was used for both visits. A diagnostic CT scan (200–240 mAs, 120 kV) with a 5-mm slice thickness was obtained. PET images were acquired in 3-dimensional mode from mid thigh to vertex (whole-body scan) with a time of 2–4 min per bed position using a weight-based protocol (22). All PET images were reconstructed using corrections for attenuation, dead time, random events, and scatter. PET images were reconstructed with an iterative algorithm (ordered-subset expectation maximization) in an axial 168 × 168 matrix on the Biograph 64 Truepoint (2-dimensional, 2 iterations, 8 subsets, 5.0-mm gaussian filter) and in a 200 × 200 matrix on the Biograph mCT 64 (3-dimensional, 2 iterations, 24 subsets, 5.0-mm gaussian filter).

Image Analyses. Board-certified nuclear medicine physicians and radiologists used a PSMA PET/CT–based TNM staging system (PROMISE) to generate clinical reports of the control scans by consensus (23).

Two nuclear medicine physicians, who did not know the study condition (control vs. MSG administration and type of MSG application), used qPSMA software to interpret the research MSG and control PSMA PET/CT scans by consensus (24). They segmented all detected tumor lesions and normal organs manually. Normal organs included the lacrimal glands, parotid glands, submandibular glands, liver, spleen, kidneys, and urinary bladder. Output parameters included SUV_{mean} and SUV_{max} for both tumor lesions and normal organs.

Measurements of Salivary Radioactivity. To assess the effect of MSG on radioligand excretion, we collected saliva from all patients at 5 time points after ^{68}Ga -PSMA-11 injection at 0 min (range, 0–7 min), 10 min (range, 9–17 min), 30 min (range, 28–39 min), 45 min (range, 44–54 min), and 100 min (range, 88–126 min). We transferred saliva collected in disposable medication cups to disposable borosilicate test tubes. Samples were weighed and radioactivity was measured in a γ -well counter (Capintec CAPRAC-t; Mirion Technologies). Background was measured before each patient injection. We assayed ^{68}Ga decay within a range of 10–1,200 keV and recorded the time of radioactivity collection and measurement to adjust for tracer decay. We corrected tracer uptake in saliva for background and radioactive decay.

Safety. We monitored safety before/after injection of the radiotracer, before/after the MSG administration, and before/after the scan procedure. We recorded blood pressure and heart rate before injection of ^{68}Ga -PSMA-11 and directly after completion of the scan. We communicated with all patients within 72 h after the scan and asked whether they had any untoward side effects or symptoms. Adverse events were documented and evaluated according to the Common Terminology Criteria for Adverse Events, version 5.0.

Outcomes

The primary objective of this trial was to compare the degree of ^{68}Ga -PSMA-11 uptake in the salivary glands with and without MSG administration. A 2-fold reduction after MSG administration was a priori defined as a successful reduction in salivary gland PSMA uptake (25). The secondary objectives were to determine the impact of MSG administration on ^{68}Ga -PSMA-11 uptake in normal organs and tumor lesions, to measure whether MSG stimulates ^{68}Ga -PSMA-11 excretion in the saliva, and to assess the safety of oral MSG ingestion and salivary flow stimulation at the proposed doses.

Statistical Analyses

Radiation doses to the salivary glands from 1 cycle of ^{225}Ac -PSMA or ^{177}Lu -PSMA were estimated at 17 and 10 Gy, respectively (9, 10, 26, 27). The commonly applied safe upper limit for external-beam salivary gland radiation therapy is 32 Gy, which can be reached after 2 cycles of ^{225}Ac -PSMA (28). On the basis of these numbers, we aimed to achieve a 2-fold reduction in the ^{68}Ga -PSMA-11 accumulation in the salivary glands after MSG administration. The primary endpoint measure was the mean difference in SUV_{max} and SUV_{mean} in all assessable salivary glands with and without the administration of MSG interventions. Patients were randomized (1:1) using a computer-generated randomization list. The randomization plan used a permuted block design with 2 blocks of $n = 8$ (arms A and B, Supplemental Table 2).

We report descriptive values as mean ± SD or median and interquartile range (if data were not normally distributed according to the Shapiro–Wilk test). Because individual patients served as their own control, paired t tests were performed. Differences between paired data that were not normally distributed were determined using the Wilcoxon signed-rank test. The independent t test was used to compare the means between unrelated groups. In each analysis, a P value of less than 0.05 was considered statistically significant. We conducted

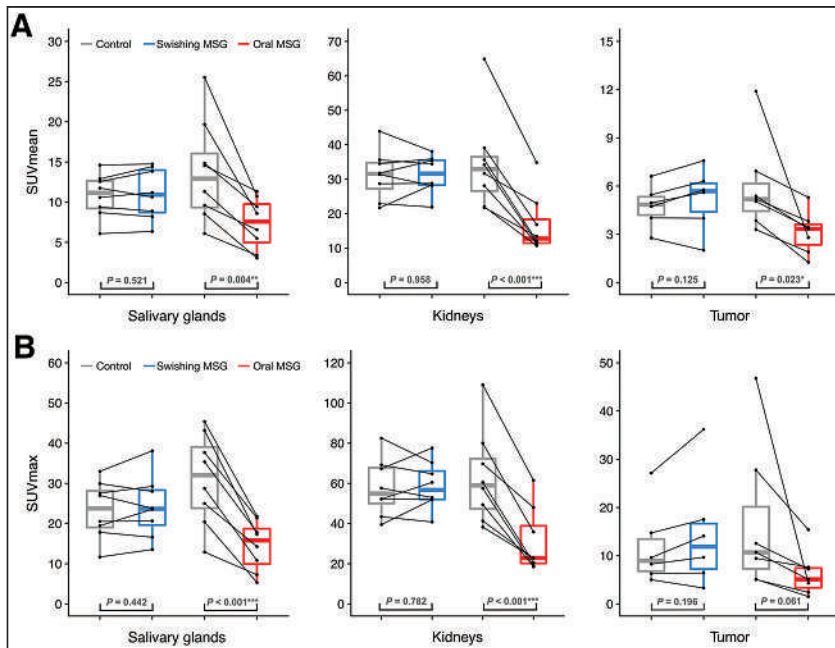


FIGURE 3. SUV_{mean} (A) and SUV_{max} (B) of salivary glands, kidneys, and tumor lesions in control and MSG studies in oral ingestion and swishing arms.

all analyses using SPSS Statistics, version 26.0 (IBM Corp.), and R Studio, version 3.6.1 (R Foundation for Statistical Computing).

RESULTS

A summary image of each of the 16 patients, with all measurements, is provided in the supplemental materials (Supplemental Fig. 1). One patient example (patient 012) is displayed in Figure 2.

Patient Population

Between December 20, 2019, and April 4, 2020, 17 patients were screened to identify 16 patients who met the eligibility criteria (Fig. 1). One patient declined to participate. The demographics and clinical characteristics of the study population are presented in Table 1. Two of 16 (16%) patients underwent the PSMA PET/CT scan for initial staging of PCa, 7 of 16 (42%) for localization of biochemical recurrence, and 7 of 16 (42%) for restaging of metastatic disease.

PSMA PET/CT Images

In the oral ingestion arm, the mean injected activity was 184 ± 1 and 183 ± 2 MBq for the MSG and control scans, respectively ($P = 0.18$). Image acquisition commenced at 61 ± 8 and 61 ± 7 min, respectively, after tracer injection ($P = 0.87$).

In the swishing arm, the mean injected activity was 184 ± 1 and 184 ± 1 MBq for the MSG and control scans, respectively ($P = 0.40$). Image acquisition commenced at 67 ± 15 and 66 ± 14 min, respectively, after tracer injection ($P = 0.87$).

Table 2 summarizes the scan findings and PSMA PET-based staging. Three patients had no visible PCa lesions (1 in the oral ingestion arm and 2 in the swishing arm). There was no change in stage between the control and MSG scans.

⁶⁸Ga-PSMA-11 Uptake in Normal Organs

In the oral ingestion arm, MSG administration was associated with a significant decrease in ⁶⁸Ga-PSMA-11 accumulation in all

TABLE 2
PSMA PET Findings

Study arm	Swishing		Oral ingestion	
	Control	MSG	Control	MSG
⁶⁸Ga-PSMA-11 PET/CT+				
Prostate/prostate bed (T+)	4 (50%)	4 (50%)	5 (63%)	5 (63%)
Pelvic LN (N1)	1 (13%)	1 (13%)	2 (25%)	2 (25%)
Extrapelvic LN (M1a)	1 (13%)	1 (13%)	1 (13%)	1 (13%)
Bone (M1b)	2 (25%)	1 (13%)	3 (38%)	3 (38%)
Visceral (M1c)	0	0	0	0
⁶⁸Ga-PSMA-11 TNM pattern				
PSMA T0 N0 M0	2 (25%)	2 (25%)	1 (13%)	1 (13%)
PSMA T+ N0 M0	3 (38%)	3 (38%)	2 (25%)	2 (25%)
PSMA T0 N1 M0	0	0	0	0
PSMA T+ N1 M0	1 (13%)	1 (13%)	1 (13%)	1 (13%)
PSMA T+ N0 M1	0	0	1 (13%)	1 (13%)
PSMA T0 N0 M1	2 (25%)	2 (25%)	2 (25%)	2 (25%)
PSMA T0 N1 M1	0	0	0	0
PSMA T+ N1 M1	0	0	1 (13%)	1 (13%)

Data are number and percentage.

TABLE 3
Comparison of ⁶⁸Ga-PSMA11 Uptake in Normal Organs in Control and MSG Scans

Site	SUV _{mean}				SUV _{max}			
	Control	MSG	Change	P	Control	MSG	Change	P
Oral ingestion (n = 8)								
Lacrimal glands	5.5 ± 2.3	2.6 ± 0.9	-50.9% ± 6.5%	0.001	9.9 ± 4.7	4.3 ± 1.6	-55.5% ± 6.1%	0.002
Parotid glands	10.9 ± 4.1	6.9 ± 3.3	-32.9% ± 22.6%	0.002	19.0 ± 6.6	13.2 ± 6.2	-34.1% ± 21.7%	0.020
Submandibular glands	15.9 ± 5.7	6.6 ± 2.5	-58.9% ± 8.9%	<0.001	29.0 ± 10.5	10.4 ± 3.7	-63.2% ± 9.9%	<0.001
Salivary glands	12.1 ± 4.6	6.8 ± 3.1	-45.5% ± 14.6%	0.004	29.0 ± 10.5	13.5 ± 5.9	-53.4% ± 11.1%	<0.001
Liver	4.6 ± 0.5	2.1 ± 0.3	-54.2% ± 5.3%	<0.001	10.7 ± 1.3	5.5 ± 0.4	-50.1% ± 8.3%	<0.001
Spleen	8.1 ± 2.0	3.0 ± 0.9	-62.8% ± 6.9%	<0.001	13.7 ± 3.5	5.3 ± 1.5	-61.5% ± 8.6%	<0.001
Kidney	34.5 ± 14.8	17.4 ± 8.8	-51.5% ± 13.7%	<0.001	63.6 ± 25.0	32.7 ± 16.6	-51.3% ± 13.3%	<0.001
Urinary bladder	16.0 ± 8.7	69.1 ± 34.3	+371.6% ± 300.2%	0.004	33.7 ± 23.9	184.2 ± 97.5	+593.2% ± 659.5%	0.003
Total tumor lesions	6.6 ± 3.5	3.5 ± 2.1	-45.0% ± 19.0%	0.023	21.5 ± 19.8	8.2 ± 8.7	-55.7% ± 22.0%	0.061
Swishing (n = 8)								
Lacrimal glands	6.5 ± 1.6	6.0 ± 2.5	+4.9% ± 22.0%	0.625	12.3 ± 3.2	11.1 ± 4.6	-5.2% ± 25.0%	0.556
Parotid glands	11.7 ± 2.2	12.0 ± 2.7	+0.1% ± 8.4%	0.917	22.2 ± 6.1	22.5 ± 6.0	+1.9% ± 10.4%	0.792
Submandibular glands	12.8 ± 3.5	13.4 ± 3.6	+5.6% ± 6.8%	0.061	21.3 ± 7.0	22.6 ± 7.3	+7.7% ± 11.6%	0.188
Salivary glands	11.5 ± 2.3	11.9 ± 2.9	+1.6% ± 7.8%	0.521	25.8 ± 6.0	26.6 ± 7.2	+4.3% ± 12.3%	0.442
Liver	4.1 ± 0.8	4.3 ± 0.9	+5.7% ± 17.3%	0.317	9.8 ± 1.3	10.4 ± 3.0	+5.3% ± 15.7%	0.321
Spleen	6.1 ± 2.0	6.3 ± 1.7	+6.2% ± 18.6%	0.458	10.8 ± 3.9	10.1 ± 2.6	-0.3% ± 15.2%	0.622
Kidney	30.1 ± 8.0	30.1 ± 5.8	+ 1.9% ± 13.9%	0.958	57.1 ± 15.9	57.6 ± 13.6	+3.4% ± 15.8%	0.782
Urinary bladder	20.2 ± 13.5	24.2 ± 8.3	+36.5% ± 41.4%	0.357	50.6 ± 42.4	56.4 ± 20.2	+52.0% ± 70.0%	0.651
Total tumor lesions	4.9 ± 1.1	5.4 ± 1.6	7.8% ± 13.8%	0.125	12.5 ± 7.7	15.0 ± 11.3	12.6% ± 27.8%	0.196

Data are average ± SD.

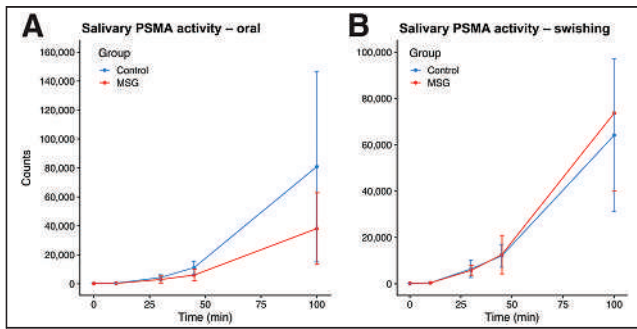


FIGURE 4. Median changes in ^{68}Ga -PSMA11 activity in saliva between control and MSG groups at 0, 10, 30, 45, and 100 min after tracer injection for oral ingestion arm (A) and swishing arm (B).

normal organs ($P < 0.05$) and a large increase in bladder activity (mean difference, $+372\%$ SUV_{mean} and $+593\%$ SUV_{max} ; Table 3). ^{68}Ga -PSMA-11 uptake decreased by more than 50% in the salivary glands (mean difference, -46% SUV_{mean} and -53% SUV_{max}), with a more prominent effect on the submandibular glands (mean difference, -59% SUV_{mean} and -63% SUV_{max}) than on the parotid glands (mean difference, -33% SUV_{mean} and -34% SUV_{max}).

In the swishing arm, no statistically significant difference in ^{68}Ga -PSMA-11 accumulation measured by either SUV_{mean} and SUV_{max} was observed in normal organs after MSG administration ($P > 0.05$) (Table 3).

^{68}Ga -PSMA-11 Uptake in Tumor Lesions

In the oral ingestion arm, MSG administration was associated with a significant decline in ^{68}Ga -PSMA-11 accumulation in tumor lesions (median difference, -38% SUV_{mean} and -52% SUV_{max} ; Table 4). One pelvic bone lesion showed a dramatic decrease in SUV_{max} (from 46.8 to 4.3) after MSG administration (case MSG05 in the supplemental materials).

In the swishing arm, no significant difference in tumor accumulation of ^{68}Ga -PSMA-11 as measured by SUV_{mean} and SUV_{max} was observed between the 2 PET scans ($P = 0.11$ and $P = 0.17$, respectively) (Table 4).

A comparison of pooled SUV_{mean} and SUV_{max} between the control and MSG studies for each arm is depicted in Figure 3.

Saliva Radioactivity Measurements

Salivary radioactivity increased over time, demonstrating ^{68}Ga -PSMA-11 salivary excretion. The median activity counts after

tracer injection for both arms are provided in Supplemental Table 3. Figure 4 shows the median saliva counts over time.

In the oral ingestion arm, a significant decrease in salivary activity counts was observed at 45 and 100 min, with median reductions of -42% and -53% , respectively. In the swishing arm, no significant difference in salivary activity was observed at any time point ($P > 0.05$).

Adverse Events

Grade 1 nausea after administration was recorded in 1 (6%) of 16 patients after oral ingestion of MSG. Five non-study-related events were recorded (diarrhea [$n = 2$ in each arm] and abdominal discomfort [$n = 1$ in the swishing arm]; Supplemental Table 4).

DISCUSSION

This prospective randomized imaging study revealed that oral ingestion of MSG, a food additive, is associated with a significant decrease in ^{68}Ga -PSMA-11 accumulation within normal organs and tumor lesions, whereas topical oral application of MSG has no impact on ^{68}Ga -PSMA-11 biodistribution. The primary endpoint of at least a 50% decrease in ^{68}Ga -PSMA-11 accumulation in the salivary glands was met when expressed as change in SUV_{max} (53%). However, oral administration of MSG also significantly diminished ^{68}Ga -PSMA-11 uptake in tumor lesions (52% and 39% decline in SUV_{max} and SUV_{mean} , respectively) and all other organs. A 3-fold increase in ^{68}Ga -PSMA-11 signal in the urinary bladder highlighted rapidly increased urinary excretion after oral MSG administration. Previous work found a repeatability coefficient of 33%–38% for SUV measurements in PSMA PET/CT, indicating that the reduction in tumor uptake in our patients ($>45\%$) is related to MSG administration (29). The application of MSG to reduce salivary gland toxicity (xerostomia) induced by PSMA RLT is therefore unlikely to be a successful clinical strategy.

Various direct attempts to reduce the salivary gland toxicity of ^{225}Ac -PSMA have been reported: salivary gland duct dilation and clearance via sialendoscopy (30), vasoconstriction of parotid gland blood vessels through external cooling with ice packs (11, 13), and local injection of botulinum toxin A to suppress saliva formation metabolically (31). Indirect attempts to alter the biochemical mechanism of off-target binding by competition included PSMA inhibitors such as 2-(phosphonomethyl) pentanedioic acid or serum glutamate-elevating approaches (20, 32–35). Dosimetry data showed that coadministration of oral polyglutamate administration

TABLE 4
Comparison of SUV_{mean} and SUV_{max} Derived from Control and MSG Scans

Parameter	Control	MSG	Change (%)	<i>P</i>
Oral ingestion (<i>n</i> = 7)				
SUV_{mean}	5.4 (3.9, 11.4)	3.3 (1.9, 3.8)	-37.8 (-67.3 , -32.5)	0.018
SUV_{max}	10.7 (6.5, 46.8)	5.1 (2.6, 9.7)	-52.3 (-70.0 , -48.5)	0.018
Swishing (<i>n</i> = 6)				
SUV_{mean}	4.9 (4.2, 5.5)	5.7 (4.1, 6.3)	13.8 (-4.0 , 15.4)	0.116
SUV_{max}	9.0 (7.8, 14.8)	11.9 (6.7, 17.5)	17.9 (-14.0 , 33.3)	0.173

Data are median and interquartile range for total tumor lesions.

may reduce salivary gland ligand uptake. However, the impact on tumor uptake has not yet been determined (36).

Application of MSG in murine models reduced salivary PSMA radioligand uptake in a dose-dependent manner without affecting tumor uptake (20). In contrast, oral MSG administration in humans led to significant decreases in tumor uptake. Consistent with our findings, a significant decrease in ^{18}F -DCFPyL accumulation in normal organs and tumor lesions after oral administration of MSG was also observed by others (32). Harsini et al. (32) applied a fix dose of 12.7 g, whereas our patients received a 150 mg/kg dose of MSG, which led to higher average dose of 15.1 g. This difference might explain the higher impact of MSG on tracer biodistribution observed in our study, a finding that suggests a dose-dependent effect of MSG. Although the MSG dosages were 10-fold higher than the MSG concentration in a normal meal (37), intake of food containing glutamate (e.g., MSG, umami, tomatoes, cheese, and mushrooms) may impact the biodistribution of PSMA radioligands, and a potential impact on diagnostic or therapy efficacy cannot be formally excluded. Further studies investigating the impact of food containing glutamate on imaging-and-therapy PSMA radioligands may be warranted.

^{68}Ga -PSMA-11 is excreted in the saliva, as shown by our measurements. Oral ingestion of MSG led to diminished salivary excretion of ^{68}Ga -PSMA-11. This finding suggests that its off-target accumulation in the salivary glands interacts with saliva formation, potentially impacting ductal cell transporters within the glands (15, 38). Alternatively, the macromolecular composition of saliva itself may be interacting with PSMA and glutamate, trapping or binding to the molecules and causing an accumulation in the salivary glands within saliva.

Our study had limitations. First, both the dosing and the timing of MSG administration were chosen empirically on the basis of studies largely concerned with safe dosing of MSG rather than application as a blood glutamate-modulating tool (39). Second, although not evaluated in this study, tumor burden may play a role in the efficacy of MSG's impact on radioligand distribution. Although PSMA RLT is currently offered in heavily metastasized patients with late-stage metastatic castration-resistant PCa, our patients were mainly in earlier disease stages that have a low tumor burden. Nevertheless, considering the tumor sink effect, we expect a higher impact of MSG administration on tumor uptake in patients with a high tumor burden (40).

CONCLUSION

Oral administration of MSG successfully decreased ^{68}Ga -PSMA-11 uptake in normal organs, including the salivary glands and kidneys, in human subjects but also reduced tumor uptake significantly. This result suggests that MSG strategies reducing the salivary gland toxicity of PSMA RLT will negatively impact tumor PSMA uptake. Thus, clinical applicability is unlikely. Future investigations evaluating different doses and timings of MSG administration are warranted, considering the possibility that a lower dose may show differential preference for tumor or normal tissue.

DISCLOSURE

No potential conflict of interest relevant to this article was reported.

KEY POINTS

QUESTION: What is the impact of MSG administration on ^{68}Ga -PSMA11 biodistribution?

PERTINENT FINDINGS: This prospective single-center, randomized imaging study, which included 16 men with PCa, met its primary endpoint, defined as a 50% reduction in ^{68}Ga -PSMA11 accumulation in the salivary glands when MSG was administered orally (-53.4% SUV_{max}, $P < 0.001$). However, the radiotracer reduction in normal organs was accompanied by a significant reduction within tumor lesions (-55.7% SUV_{max}, $P = 0.061$).

IMPLICATIONS FOR PATIENT CARE: MSG is capable of modulating ^{68}Ga -PSMA-11 biodistribution, including tumor uptake, which limits its clinical application in the setting of PSMA RLT.

REFERENCES

1. Silver DA, Pellicer I, Fair WR, Heston WD, Cordon-Cardo C. Prostate-specific membrane antigen expression in normal and malignant human tissues. *Clin Cancer Res.* 1997;3:81–85.
2. Eiber M, Fendler WP, Rowe SP, et al. Prostate-specific membrane antigen ligands for imaging and therapy. *J Nucl Med.* 2017;58(suppl):67S–76S.
3. Hofman MS, Violet J, Hicks RJ, et al. [^{177}Lu]-PSMA-617 radionuclide treatment in patients with metastatic castration-resistant prostate cancer (LuPSMA trial): a single-centre, single-arm, phase 2 study. *Lancet Oncol.* 2018;19:825–833.
4. Kratochwil C, Bruchertseifer F, Rathke H, et al. Targeted alpha-therapy of metastatic castration-resistant prostate cancer with ^{225}Ac -PSMA-617: swimmer-plot analysis suggests efficacy regarding duration of tumor control. *J Nucl Med.* 2018;59:795–802.
5. Sathekge M, Bruchertseifer F, Knoesen O, et al. ^{225}Ac -PSMA-617 in chemotherapy-naïve patients with advanced prostate cancer: a pilot study. *Eur J Nucl Med Mol Imaging.* 2019;46:129–138.
6. Okamoto S, Thieme A, Allmann J, et al. Radiation dosimetry for ^{177}Lu -PSMA I&T in metastatic castration-resistant prostate cancer: absorbed dose in normal organs and tumor lesions. *J Nucl Med.* 2017;58:445–450.
7. Fendler WP, Reinhardt S, Ilhan H, et al. Preliminary experience with dosimetry, response and patient reported outcome after ^{177}Lu -PSMA-617 therapy for metastatic castration-resistant prostate cancer. *Oncotarget.* 2017;8:3581–3590.
8. Baum RP, Kulkarni HR, Schuchardt C, et al. ^{177}Lu -labeled prostate-specific membrane antigen radioligand therapy of metastatic castration-resistant prostate cancer: safety and efficacy. *J Nucl Med.* 2016;57:1006–1013.
9. Kratochwil C, Bruchertseifer F, Rathke H, et al. Targeted alpha-therapy of metastatic castration-resistant prostate cancer with ^{225}Ac -PSMA-617: dosimetry estimate and empiric dose finding. *J Nucl Med.* 2017;58:1624–1631.
10. Kratochwil C, Bruchertseifer F, Giesel FL, et al. ^{225}Ac -PSMA-617 for PSMA-targeted alpha-radiation therapy of metastatic castration-resistant prostate cancer. *J Nucl Med.* 2016;57:1941–1944.
11. van Kalmthout LWM, Lam M, de Keizer B, et al. Impact of external cooling with icepacks on ^{68}Ga -PSMA uptake in salivary glands. *EJNMMI Res.* 2018;8:56.
12. Langbein T, Chausse G, Baum RP. Salivary gland toxicity of PSMA radioligand therapy: relevance and preventive strategies. *J Nucl Med.* 2018;59:1172–1173.
13. Yilmaz B, Nisli S, Ergul N, Gursu RU, Acikgoz O, Cermik TF. Effect of external cooling on ^{177}Lu -PSMA uptake by the parotid glands. *J Nucl Med.* 2019;60:1388–1393.
14. Bander NH, Milowsky MI, Nanus DM, Kostakoglu L, Vallabhajosula S, Goldsmith SJ. Phase I trial of ^{177}Lu -labeled J591, a monoclonal antibody to prostate-specific membrane antigen, in patients with androgen-independent prostate cancer. *J Clin Oncol.* 2005;23:4591–4601.
15. Rupp NJ, Umbricht CA, Pizzuto DA, et al. First clinicopathologic evidence of a non-PSMA-related uptake mechanism for ^{68}Ga -PSMA-11 in salivary glands. *J Nucl Med.* 2019;60:1270–1276.
16. Tagawa ST, Vallabhajosula S, Christos PJ, et al. Phase 1/2 study of fractionated dose lutetium-177-labeled anti-prostate-specific membrane antigen monoclonal antibody J591 (^{177}Lu -J591) for metastatic castration-resistant prostate cancer. *Cancer.* 2019;125:2561–2569.
17. Wang H, Byun Y, Barinka C, et al. Bioisosterism of urea-based GCPII inhibitors: synthesis and structure-activity relationship studies. *Bioorg Med Chem Lett.* 2010;20:392–397.
18. Eder M, Schafer M, Bauder-Wust U, et al. ^{68}Ga -complex lipophilicity and the targeting property of a urea-based PSMA inhibitor for PET imaging. *Bioconjug Chem.* 2012;23:688–697.

19. Navrátil M, Ptacek J, Sacha P, et al. Structural and biochemical characterization of the foylyl-poly-gamma-l-glutamate hydrolyzing activity of human glutamate carboxypeptidase II. *FEBS J*. 2014;281:3228–3242.
20. Rousseau E, Lau J, Kuo HT, et al. Monosodium glutamate reduces ⁶⁸Ga-PSMA-11 uptake in salivary glands and kidneys in a preclinical prostate cancer model. *J Nucl Med*. 2018;59:1865–1868.
21. Hodson NA, Linden RW. The effect of monosodium glutamate on parotid salivary flow in comparison to the response to representatives of the other four basic tastes. *Physiol Behav*. 2006;89:711–717.
22. Fendler WP, Eiber M, Beheshti M, et al. ⁶⁸Ga-PSMA PET/CT: joint EANM and SNMMI procedure guideline for prostate cancer imaging: version 1.0. *Eur J Nucl Med Mol Imaging*. 2017;44:1014–1024.
23. Eiber M, Herrmann K, Calais J, et al. Prostate Cancer Molecular Imaging Standardized Evaluation (PROMISE): proposed miTNM classification for the interpretation of PSMA-ligand PET/CT. *J Nucl Med*. 2018;59:469–478.
24. Gafita A, Bieth M, Krönke M, et al. qPSMA: semiautomatic software for whole-body tumor burden assessment in prostate cancer using ⁶⁸Ga-PSMA11 PET/CT. *J Nucl Med*. 2019;60:1–1283.
25. Kratochwil C, Fendler WP, Eiber M, et al. EANM procedure guidelines for radionuclide therapy with ¹⁷⁷Lu-labelled PSMA-ligands (¹⁷⁷Lu-PSMA-RLT). *Eur J Nucl Med Mol Imaging*. 2019;46:2536–2544.
26. Delker A, Fendler WP, Kratochwil C, et al. Dosimetry for ¹⁷⁷Lu-DKFZ-PSMA-617: a new radiopharmaceutical for the treatment of metastatic prostate cancer. *Eur J Nucl Med Mol Imaging*. 2016;43:42–51.
27. Yadav MP, Ballal S, Tripathi M, et al. Post-therapeutic dosimetry of ¹⁷⁷Lu-DKFZ-PSMA-617 in the treatment of patients with metastatic castration-resistant prostate cancer. *Nucl Med Commun*. 2017;38:91–98.
28. Emami B, Lyman J, Brown A, et al. Tolerance of normal tissue to therapeutic irradiation. *Int J Radiat Oncol Biol Phys*. 1991;21:109–122.
29. Pollard JH, Raman C, Zakharia Y, et al. Quantitative test-retest measurement of ⁶⁸Ga-PSMA-HBED-CC in tumor and normal tissue. *J Nucl Med*. 2020;61:1145–1152.
30. Rathke H, Kratochwil C, Hohenberger R, et al. Initial clinical experience performing sialendoscopy for salivary gland protection in patients undergoing ²²⁵Ac-PSMA-617 RLT. *Eur J Nucl Med Mol Imaging*. 2019;46:139–147.
31. Baum RP, Langbein T, Singh A, et al. Injection of botulinum toxin for preventing salivary gland toxicity after PSMA radioligand therapy: an empirical proof of a promising concept. *Nucl Med Mol Imaging*. 2018;52:80–81.
32. Harsini S, Sapruff H, Alden T, Mohammadi B, Wilson D, Bénard F. The effects of monosodium glutamate on PSMA radiotracer uptake in men with recurrent prostate cancer: a prospective, randomized, double-blind, placebo-controlled intraindividual imaging study. *J Nucl Med*. 2021;62:81–87.
33. Paganelli G, Sarnelli A, Severi S, et al. Dosimetry and safety of ¹⁷⁷Lu PSMA-617 along with polyglutamate parotid gland protector: preliminary results in metastatic castration-resistant prostate cancer patients. *Eur J Nucl Med Mol Imaging*. 2020;47:3008–3017.
34. Majer P, Jancarik A, Krecmerova M, et al. Discovery of orally available prodrugs of the glutamate carboxypeptidase II (GCPII) inhibitor 2-phosphonomethylpentanedioic acid (2-PMPA). *J Med Chem*. 2016;59:2810–2819.
35. Kratochwil C, Giesel FL, Leotta K, et al. PMPA for nephroprotection in PSMA-targeted radionuclide therapy of prostate cancer. *J Nucl Med*. 2015;56:293–298.
36. Sarnelli A, Belli ML, Di Iorio V, et al. Dosimetry of ¹⁷⁷Lu-PSMA-617 after mannitol infusion and glutamate tablet administration: preliminary results of EUDRACT/RSO 2016-002732-32 IRST protocol. *Molecules*. 2019;24:621.
37. He K, Du S, Xun P, et al. Consumption of monosodium glutamate in relation to incidence of overweight in Chinese adults: China Health and Nutrition Survey (CHNS). *Am J Clin Nutr*. 2011;93:1328–1336.
38. Sunavala-Dossabhoy G. Radioactive iodine: an unappreciated threat to salivary gland function. *Oral Dis*. 2018;24:198–201.
39. Fernstrom JD, Cameron JL, Fernstrom MH, McConaha C, Weltzin TE, Kaye WH. Short-term neuroendocrine effects of a large oral dose of monosodium glutamate in fasting male subjects. *J Clin Endocrinol Metab*. 1996;81:184–191.
40. Gaertner FC, Halabi K, Ahmadzadehfar H, et al. Uptake of PSMA-ligands in normal tissues is dependent on tumor load in patients with prostate cancer. *Oncotarget*. 2017;8:55094–55103.

Combination of Forced Diuresis with Additional Late Imaging in ^{68}Ga -PSMA-11 PET/CT: Effects on Lesion Visibility and Radiotracer Uptake

Ian Alberts¹, Jan Niklas-Hünemann¹, Christos Sachpekidis¹, Helle Damgaard Zacho², Clemens Mingels¹, Lotte Dijkstra¹, Karl Peter Bohn¹, Tilman Lappchen¹, Eleni Gourni¹, Axel Rominger¹, and Ali Afshar-Oromieh¹

¹Department of Nuclear Medicine, Inselspital, Bern University Hospital, University of Bern, Bern, Switzerland; and ²Aalborg University Hospital, Universitetshospital, Aalborg, Denmark

Renal excretion of some prostate-specific membrane antigen (PSMA) ligands and consequently increased bladder activity can obscure locally relapsing prostate cancer lesions in PSMA PET/CT. Furthermore, additional late imaging in PSMA PET/CT provides a useful method to clarify uncertain findings. The aim of this retrospective study was to investigate a modified imaging protocol combining late additional imaging with hydration and forced diuresis in individuals undergoing additional late scanning for uncertain lesions or low prostate-specific antigen. **Methods:** We compared an older protocol with a newer one. In the old protocol, patients undergoing ^{68}Ga -PSMA-11 PET/CT were examined at 90 min after injection, with 1 L of oral hydration beginning at 30 min after injection and 20 mg of furosemide given intravenously at 1 h after injection, followed by additional late imaging at 2.5 h after injection without further preparation. In the new protocol, a second group received the same procedure as before, with an additional 0.5 L of oral hydration and 10 mg of furosemide intravenously 30 min before the late imaging. We examined 132 patients (76 with the old protocol and 56 with the new one) with respect to urinary bladder activity (SUV_{mean}), prostate cancer lesion uptake (SUV_{max}), and lesion contrast (ratio of tumor SUV_{max} to bladder SUV_{mean} for local relapses and ratio of tumor SUV_{max} to gluteal-muscle SUV_{mean} for nonlocal prostate cancer lesions). **Results:** Bladder activity was significantly greater for the old protocol in the late scans than for the new protocol (ratio of bladder activity at 2.5 h to bladder activity at 1.5 h, 2.33 ± 1.17 vs. 1.37 ± 0.50 , $P < 0.0001$). Increased tumor SUV_{max} and contrast were seen at 2.5 h compared with 1.5 h ($P < 0.0001$ for old protocol; $P = 0.02$ for new protocol). Increased bladder activity for the old protocol resulted in decreased lesion-to-bladder contrast, which was not the case for the new protocol. Tumor-to-background ratios increased at late imaging for both protocols, but the increase was significantly lower for the new protocol. For the old protocol, comparing the 1.5-h to the 2.5-h acquisitions, 4 lesions in 4 patients (4/76 = 5.2% of the cohort) were visible at the postdiuresis 1.5-h acquisition but not at 2.5 h, having been obscured as a result of the higher bladder activity. In the new protocol, 2 of 56 (3.6%) patients had lesions visible only at late imaging, and 2 patients had lesions that could be better discriminated at late imaging. **Conclusion:** Although the combination of diuretics and hydration can be a useful method to increase the visualization and detectability of locally recurrent prostate cancer in standard ^{68}Ga -PSMA-11 PET/CT, their effects do not sufficiently continue into additional late imaging. Additional diuresis and hydration are

recommended to improve the visibility, detection, and diagnostic certainty of local recurrences.

Key Words: PSMA; furosemide; diuresis; dual-time point; hydration

J Nucl Med 2021; 62:1252–1257

DOI: 10.2967/jnumed.120.257741

For recurrent prostate cancer, ^{68}Ga -PSMA-11 PET/CT has become the examination of choice, with excellent tumor-to-background contrast and high sensitivity (1). However, ^{68}Ga -PSMA-11, in common with other prostate-specific membrane antigen (PSMA) radioligands such as ^{18}F -DCFPyl, undergoes predominantly renal excretion (2,3). Activity in the urinary bladder can obscure locally recurrent lesions, which are at risk of being missed (4). PET/MRI and PET/CT are vulnerable to the halo artifact with large activity concentrations in the urinary bladder (5,6), although this can be minimized by adequate scatter correction. Novel radiotracers that undergo biliary excretion have been introduced, which when labeled with ^{18}F combine the advantages of cyclotron production of the radiotracer and improved availability, longer half-life, and reduced bladder activity (7,8).

Despite nearly a decade of routine use, the optimal examination protocol for PSMA radiotracers remains elusive, with only generic guidance available (9). PET/CT with ^{68}Ga -PSMA-11 is commonly performed at 1 h after injection. However, several publications show an increase in tracer uptake for most prostate cancer lesions over time (2,10–13). Later acquisition of images or additional late imaging can improve lesion visibility and aid in the discrimination of tracer uptake not related to prostate cancer (12).

Several publications report the utility of forced diuresis as a means of mitigating urinary bladder activity and improving diagnostic certainty for lesions near the bladder and ureters (14). The extant guidelines recommend application of furosemide either shortly before or after administration of ^{68}Ga -PSMA-11 (9), although early coapplication of radiotracer and diuretic is associated with degraded image quality at delayed imaging (15). Instead, later application is associated with improved lesion detection and reduced bladder activity (16). In cases of uncertain findings, later imaging may better discriminate between pathologic and nonpathologic causes of tracer uptake; most tumor lesions exhibit increasing PSMA ligand uptake, whereas ganglia or inflammatory lymph nodes usually do not (17,18). Whereas previous studies

Received Oct. 5, 2020; revision accepted Dec. 28, 2020.

For correspondence or reprints, contact Ali Afshar-Oromieh (ali.afshar@insel.ch).

Published online February 5, 2021.

COPYRIGHT © 2021 by the Society of Nuclear Medicine and Molecular Imaging.

examined the optimal imaging time point for ^{68}Ga -PSMA-11 (19), with increased lesion detection when combining later imaging (at 90 min vs. 60 min after injection) with diuresis (20), no publications, to our knowledge, have systematically addressed the issue of dual-time-point imaging and forced diuresis. Furthermore, we know of no studies that have reported the influence of diuresis on tumor uptake, which this study aimed to address.

MATERIALS AND METHODS

In this retrospective analysis, we investigated 132 individuals who, having been referred to our center for biochemically recurrent prostate cancer between October 2018 and October 2019, underwent ^{68}Ga -PSMA-11 PET/CT including additional late imaging. The cantonal ethics committee approved this retrospective study (KEK number 2020-00162), and the requirement to obtain informed consent was waived. The study was performed in accordance with the declaration of Helsinki. Starting in 2018, our institutional protocol was to perform PET/CT with ^{68}Ga -PSMA-11 at 90 min after injection, with 20 mg of intravenous furosemide given at 60 min after injection and 1 L of water taken by mouth beginning at 30 min after injection. Additional late scans were acquired at 2.5 h after injection in cases of low prostate-specific antigen (<2.0 ng/mL) or when uncertain lesions were identified on the whole-body PET images, as previously published (10). In the old, 2018, protocol, this late imaging was performed without any further preparation and was as previously published (20). Noting increased bladder activity at late imaging compared with the regular scans, our protocol changed in April 2019 to a new one that includes additional furosemide (10 mg intravenously) at 2 h after injection and 0.5 L of water by mouth before late imaging at 2.5 h after injection. The 2 examination protocols are as outlined in Figure 1. Our analysis

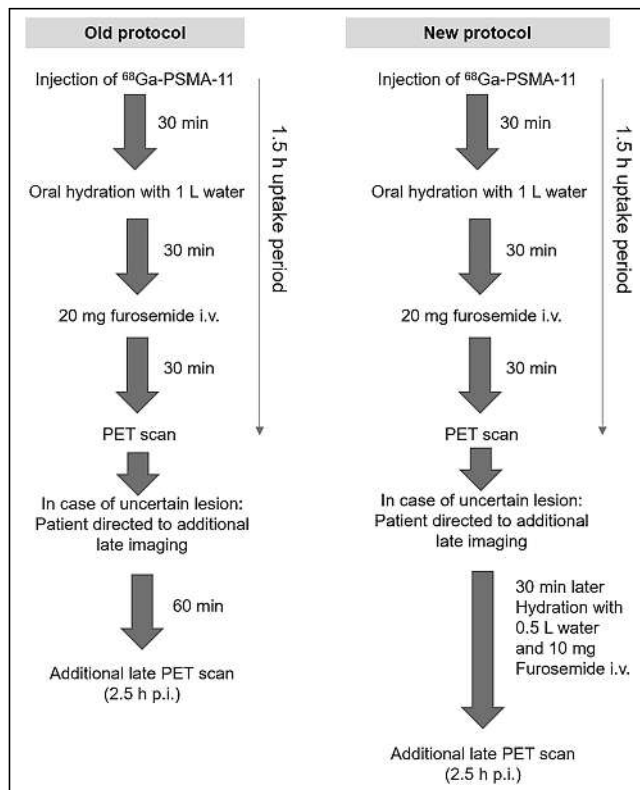


FIGURE 1. Comparison of old and new protocols. p.i. = after injection; i.v. = intravenously.

compared 76 consecutive patients who were imaged according to the old protocol with 56 consecutive patients who were imaged according to the new protocol (until October 2019, when we switched to the routine use of a ^{18}F -PSMA tracer). Patient details, including prior treatments for both cohorts, Gleason score, and prostate-specific antigen level, are outlined in Table 1.

Radiotracer

^{68}Ga -PSMA-11 was produced as previously described (21,22) and given as an intravenous bolus injection with a standard body weight-adjusted dose of 2–3 MBq/kg.

Imaging

All patients received regular whole-body PET scans (from head to thighs) at 1.5 h after injection. Additional late imaging was performed at 2.5 h after injection. Hydration and forced diuresis for both groups were as outlined in Figure 1. Patients were asked to void the bladder immediately before all imaging. Both the 1.5-h and the 2.5-h scans were analyzed for pathologic lesions characteristic of prostate cancer and for the activity concentration in the urinary bladder. Our PET and CT protocol parameters were as previously published (23).

Image Evaluation

Images were analyzed using an appropriate workstation and software (SyngoVia; Siemens). Two experienced physicians read each dataset in consensus. Clinical details and demographics were available. The readers noted the presence of pathologic lesions (including local recurrence, lymph nodes, and bone or organ metastases) on the whole-body scan and whether these lesions were not visible on either early or late imaging. To calculate tracer uptake for locally recurring lesions, circular regions of interest were drawn around areas of focally increased uptake on transaxial slices of the prostatic fossa and were automatically adapted to a 3-dimensional volume of interest at a 40% isocontour as previously described (21). Care was taken to check that the volume of interest in transverse, coronal, and sagittal slices did not include the bladder. Likewise, a volume of interest was drawn around the bladder using the same method, with care to include only the anatomic bladder as seen on CT imaging. Background uptake was measured in the standard way, using a 1 cm³ volume of interest in the left gluteal muscle as previously published (18).

Statistical Analysis

Bladder (and background gluteal) tracer activity was measured by obtaining the SUV_{mean} (the variable with the lowest coefficient of variation (2)). Lesion activity was determined by convention as SUV_{max}. Uptake for the bladder, gluteal musculature, and prostate cancer lesions was compared at 1.5 and 2.5 h by means of the paired Student *t* test; a 2-tailed *P* value of less than 0.05 was considered statistically significant. Protocols were compared for changes in bladder activity using the unpaired Welch *t* test (for unequal sample sizes). The binomial test was used to determine the statistical significance of detection frequency at standard and late imaging. Statistical analyses were performed using SPSS (version 25; IBM) and R (version 4.0.2).

Clinical Follow-up

Rating of lesions as pathologic or benign was confirmed by a composite reference standard as previously published (histology when available, correlative MRI, or a fall in prostate-specific antigen after targeted salvage radiotherapy (23)).

RESULTS

Patient Tolerability

All patients were questioned—according to the institutional standard—by a physician before the examination to exclude

TABLE 1
Patient Characteristics

Parameter	Old protocol	New protocol
Age (y)	67.9 ± 6.7	69.2 ± 6.3
Tracer (MBq)	216.9 ± 35.7	243.7 ± 39.5
Gleason score	7 (6–10)	7 (6–9)
Prostate-specific antigen	1.1 ± 32.7 (mean, 11.5)	0.5 ± 45.6 (mean, 7.6)
TNM*	T (1–4) N (0, 0–1) M (0, 0–1)	T (1–4) N (0, 0–1) M (0, 0–1)

*Classification of the Union for International Cancer Control, eighth edition.
Data are median ± SD followed by range in parentheses, unless otherwise noted.

contraindications to forced diuresis by furosemide (e.g., sulfonamide allergy). Patients tolerated both protocols equally well, and no examples of scanner contamination through urinary incontinence were encountered. We found the application of furosemide and oral hydration to be a simple maneuver that was easily integrated into clinical routine.

Changes in Bladder Activity

Greater urinary activity at 2.5 h was seen in the old protocol (7.01 ± 9.03 SUV at 1.5 h vs. 13.42 ± 9.38 SUV at 2.5 h) than in the new protocol (11.04 ± 12.5 SUV at 1.5 h vs. 12.39 ± 13.36 SUV at 2.5 h), as shown in Figure 2. The ratio of bladder activity at 2.5 h to bladder activity at 1.5 h was significantly higher ($P < 0.0001$) for the old protocol (2.33 ± 1.17) than for the new protocol (1.37 ± 0.50).

Changes in Lesion Activity and Tumor-to-Background Ratio (TBR)

For both the old and the new protocols, a significant increase in SUV_{max} for all pathologic lesions was noted from 1.5 to 2.5 h after injection (from 5.98 to 7.78 for the old protocol and from 4.27 to 4.98 for the new protocol, $P < 0.0001$ and $P = 0.02$, respectively). Similarly, TBR for all pathologic lesions (with respect to the gluteal musculature) increased from 1.5 h to 2.5 h (from 55.80 to 91.39 for the old protocol and from 41.88 to 55.96 for the new protocol; $P < 0.0001$ for both; Fig. 3). Comparing the ratio of the TBR at 2.5 h to the TBR at 1.5 h after injection, the mean increase

for the old protocol was higher than for the new protocol (1.72 ± 0.56 vs. 1.49 ± 0.62, $P = 0.013$; Fig. 4).

Lesion Detectability

Overall, 71% of patients in the new protocol and 70% in the old protocol had a positive scan (at least 1 pathologic lesion). Comparing the 1.5-h and 2.5-h acquisitions, for the old protocol, 4 patients (4/76 = 5.2% of the patient cohort) had 4 lesions that were visible at the postdiuresis 1.5-h acquisition but not at 2.5 h, having been obscured as a result of the higher bladder activity. Example images are shown in Figure 5. Furthermore, for the old protocol, the lesion SUV_{max} at 2.5 h in 2 cases corresponded almost exactly to the urinary bladder activity. As confirmation, follow-up with the composite standard revealed that 2 of the patients had a subsequent fall in prostate-specific antigen after directed radiotherapy, 1 had correlative MRI findings, and 1 had a prostate-specific antigen fall after systemic therapy.

For the new protocol, 2 patients had additional locally recurrent lesions that could be visualized only at 2.5 h because of increasing tracer uptake. Correlative imaging (the composite standard) was available as confirmation of these 2 lesions. A further 2 patients had lesions that were more clearly visualized at late imaging, delivering greater diagnostic certainty (an example patient image is shown in Supplemental Fig. 1; supplemental materials are available at <http://jnm.snmjournals.org>).

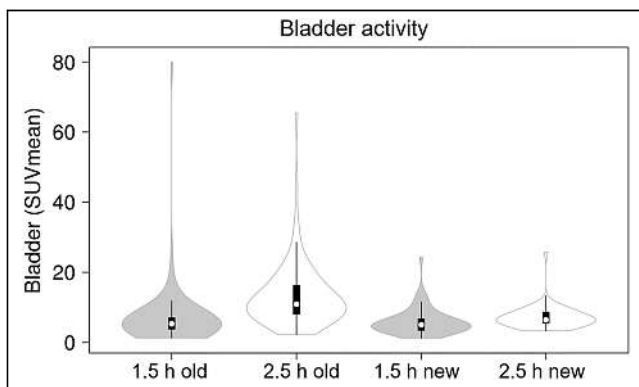


FIGURE 2. Violin plots showing urinary bladder SUV for old and new protocols. Whereas increase in bladder SUV_{mean} is seen for old protocol, this is not the case in new protocol.

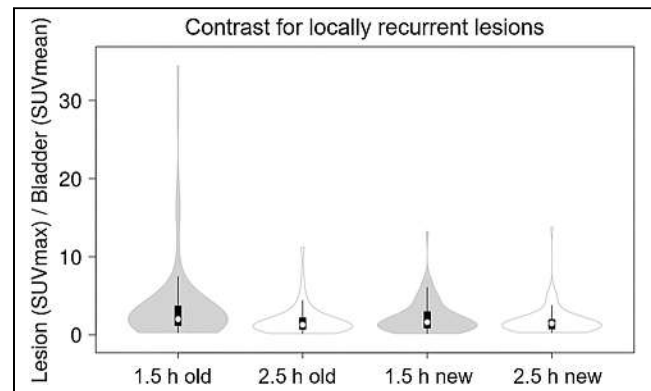


FIGURE 3. Violin plots showing change in locally recurrent lesion SUV_{max} (prostatic fossa/seminal vesicle) vs. bladder SUV_{mean}, that is, lesion-to-bladder contrast. Whereas a decrease in tumor-to-bladder ratio (i.e., lesion visibility) is seen at 2.5 h in old protocol, this was not the case in new protocol.

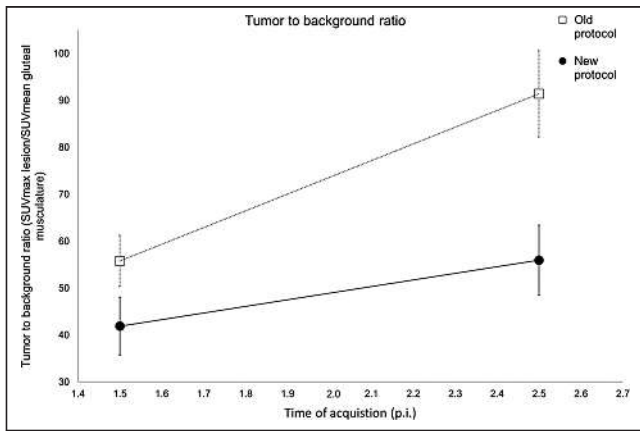


FIGURE 4. TBR change at 1.5 and 2.5 h. Points show mean TBR \pm SE. Increase in TBR was lower for new protocol than for old protocol. p.i. = after injection.

DISCUSSION

In this study, we compared two examination protocols that seek to mitigate increased bladder activity through a combination of forced diuresis and additional late imaging. We found that forced diuresis before acquisition of images at 1.5 h after injection gave good results, with resultant low bladder activities and high lesion TBR. Concordant with numerous studies reporting improved lesion detection and visibility at additional late imaging (2,10–13), we also found an improved pathologic lesion TBR, with a higher SUV_{max} for most pathologic lesions at additional late imaging. In 2 patients, additional later imaging combined with repeated diuresis revealed 2 lesions that were not visible at early imaging. In 2 patients, 2 lesions were revealed with greater clarity.

Although furosemide produces a prompt onset of diuresis, its biologic half-life is as long as 2 h (24). However, our data show that the duration of this residual effect is not sufficient to allow for

additional late imaging. In keeping with previous work suggesting that locally recurrent lesions are at risk of being missed because of high bladder activity (25), we found that in the old protocol, 4 of 76 patients (5.3%) had lesions that were obscured by increased bladder activity at additional late imaging. Comparing locally recurrent tumor uptake with the local bladder activity confirmed this finding, with lower lesion-to-bladder contrast at late imaging for the old protocol. In contrast, for the new protocol, which includes additional furosemide at late imaging, no reduction in lesion-to-bladder contrast was observed, with all prostate cancer lesions clearly visible at both early and late imaging.

Numerous publications have reported the utility of forced diuresis to mitigate accumulation of bladder activity (26). Alternatives, such as the application of intravenous mannitol, have been less well studied (27). The current guidelines for PSMA imaging endorse application of furosemide to mitigate activity in the ureters on ^{68}Ga -PSMA-11 PET/CT images (9), although application “shortly before or after administration” of the radiopharmaceutical is recommended. Judicious timing of diuresis is essential: Derlin et al. compared 2 protocols with early (concomitant application with radiotracer) and late (100 min after injection) diuresis. Whereas the early protocol resulted in reduced image quality and increased bladder activity, this was not the case for late application (15). Likewise, Wondergem et al. advocated application of diuretic shortly before imaging with ^{18}F -DCFPyL (6). Piron et al. published results for an optimized protocol for ^{18}F -PSMA-11 with furosemide application 30 min after injection (28). The wide variation in protocols and recommendations serves to highlight that the issue remains far from settled and a myriad of protocols advocate both early and dynamic imaging (29–32).

We find no publications reporting the influence of forced diuresis on radiotracer uptake: noting the pharmacodynamics of PSMA radioligands, which show increasing radiotracer uptake over time, we posit that forced diuresis might reduce the amount of radiotracer available during this uptake phase; this pharmacokinetic consideration would favor later application over early diuresis (10,19). In

keeping with this hypothesis, Derlin et al. found reduced image quality after early application of diuretic, although no data for lesion radiotracer uptake were reported (15). Early application of the diuretic could result in rapid elimination of the radiotracer during the uptake phase, resulting in reduced lesion uptake. Indeed, our findings suggest that additional diuresis before late imaging results in a lower increase in TBR than was observed in the old protocol. Any protocol must therefore find the optimal balance between improved TBR at later imaging and the short physical half-life of the radiotracer, accumulation of bladder activity, and the ease with which any protocol can be integrated into a busy clinic. Similarly, furosemide should be given when its prompt onset of diuresis has maximum effect; application shortly before or after the radiopharmaceutical is not commensurate with its well-known pharmacodynamics, as is exemplified by our finding that its diuretic effects do not continue into additional late imaging. Application of furosemide

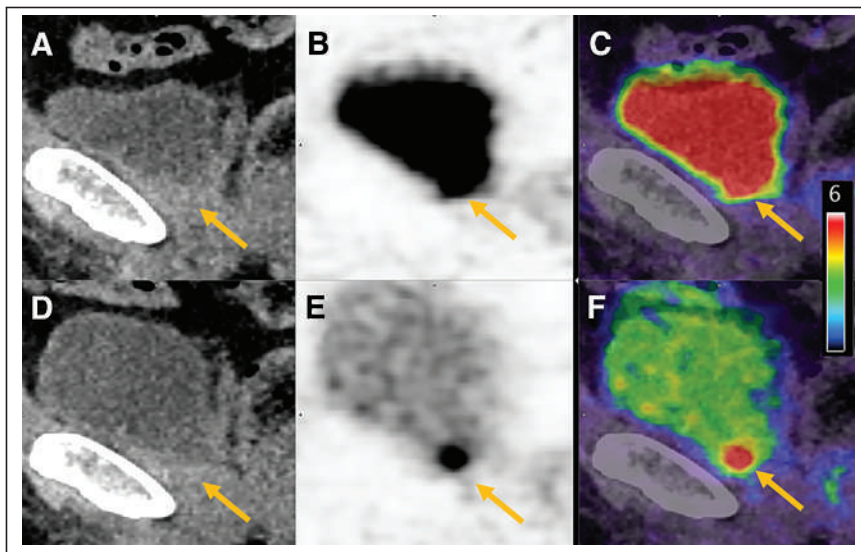


FIGURE 5. Example patient scan showing locally recurrent lesions (arrows) obscured by high bladder activity in old protocol at late imaging. Shown are low-dose CT (A and D), PET (B and E), and fusion of PET and low-dose CT (C and F) images 2.5 h after injection (A–C) and 1.5 h after injection (D–F).

with or shortly after the radiotracer, as recommended by the guidelines (9), is therefore unlikely to result in a satisfactory reduction in bladder activity if imaging is performed at 1 h after injection.

Instead, we find our new protocol be a reasonable balance between these myriad competing demands. A larger dose of furosemide (i.e., 20 mg before additional late imaging) is unlikely to be of additional benefit, and Uprimny et al. found no benefit from 40 mg of furosemide compared with 20 mg for imaging 60 min after injection (33).

Our results may also find application in PET/MRI (34). Because of the halo artifact (35,36), optimal reduction of urinary activity is necessary, although the longer examination times encountered in pelvic MRI may necessitate placement of a urinary catheter if forced diuresis shortly before image acquisition is used. Our findings also place new radiotracers into an important context. Recently, PSMA radioligands undergoing biliary or hepatic excretion have been introduced, such as ^{18}F -PSMA-1007 and ^{18}F -rh-PSMA-7 (8,37). These cyclotron-produced radiotracers have improved availability and simplify logistic supply chains because of a longer half-life. Other theoretical advantages include a lower positron energy, which may improve imaging resolution (7,37). However, the principal clinical advantage of such radiotracers is their low rate of urinary excretion in the first 2 h after injection, with a consequent reduction in bladder activity (38). Nevertheless, our data provide insight into the magnitude of any effect size that can be anticipated because of this reportedly favorable pharmacokinetic property. Only a small number of lesions directly contiguous with the bladder or ureter are likely to be obscured, and large patient cohorts would be required to demonstrate this small effect size with adequate power. Neither a matched-pair comparison nor a head-to-head study found any increased detection rate for these new radiotracers (39,40), although lower specificity has been observed for ^{18}F -PSMA-1007 (39). In contrast, we find that furosemide offers a low-cost, well-tolerated, and easily performed maneuver to reduce urinary activity. Ideally, such protocols would be integrated into any studies comparing tracers undergoing renal extraction and would afford a fair comparison with respect to bladder activity, and consideration must be given to the timing of diuresis when reporting semiquantitative parameters such as lesion SUV.

We note several weaknesses with our study. First, our data were collected retrospectively, and prospective trials are required to confirm the optimum protocol. In keeping with previously published studies (20), we sought to establish the utility of our protocol and its effects on urinary bladder activity and lesion uptake. Therefore, the two patient cohorts do not need to be similar with regard to clinical data since these data do not influence the urinary excretion of the tracer. Applied activity was given according to the same weight-adapted dose regime. Despite a slightly greater mean absolute dose of radiopharmaceutical applied in the new protocol, lower bladder activities were seen than with the old protocol (Fig. 2), meaning that the applied activity did not act as a confounder. Lesions classified as pathologic and where discrepancy between the late and early images was noted were confirmed at follow-up by the composite standard. TBR was slightly higher for the old protocol than for the new one on both early and late imaging, reflecting possible underlying differences in patients between these two nonmatched cohorts.

CONCLUSION

Performing ^{68}Ga -PSMA-11 PET/CT at 1.5 h after injection with application of 20 mg of furosemide half an hour before

imaging yields good results with excellent TBR and low bladder activity. However, the effect of furosemide does not sufficiently last into additional late imaging, where increased bladder activity, due to diminishing furosemide efficacy, can obscure locally recurrent lesions. To overcome this limitation of the additional late scans, additional furosemide before late imaging provides a useful method to increase the contrast of tumor lesions adjacent to the urinary bladder, allowing for better discrimination of lesions and, in a small number of cases, revealing lesions that were not visible at early imaging. However, additional diuresis for late scans can result in lower increases in tumor radiotracer uptake at late imaging, suggesting that the dose and timing of diuresis can influence the radiotracer's pharmacodynamics.

DISCLOSURE

No potential conflict of interest relevant to this article was reported.

KEY POINTS

QUESTION: Does additional late imaging combined with hydration and diuresis improve local-recurrence visibility in ^{68}Ga -PSMA-11 PET/CT?

PERTINENT FINDINGS: Additional late imaging without furosemide is associated with high bladder activity that obscures locally recurrent lesions. The addition of furosemide and hydration results in lower bladder activity, allowing better discrimination of lesions. In 2 cases, late imaging revealed lesions that were not visible at early imaging.

IMPLICATIONS FOR PATIENT CARE: Later application of furosemide 30 min before imaging is recommended. Additional late imaging should be performed with additional diuresis and hydration.

REFERENCES

1. Afshar-Oromieh A, Holland-Letz T, Giesel FL, et al. Diagnostic performance of ^{68}Ga -PSMA-11 (HBED-CC) PET/CT in patients with recurrent prostate cancer: evaluation in 1007 patients. *Eur J Nucl Med Mol Imaging*. 2017;44:1258–1268.
2. Afshar-Oromieh A, Malcher A, Eder M, et al. PET imaging with a [^{68}Ga]gallium-labelled PSMA ligand for the diagnosis of prostate cancer: biodistribution in humans and first evaluation of tumour lesions. *Eur J Nucl Med Mol Imaging*. 2013;40:486–495.
3. Wondergem M, van der Zant FM, Knol RJJ, Lazarenko SV, Pruijm J, de Jong IJ. ^{18}F -DCFPyL PET/CT in the detection of prostate cancer at 60 and 120 minutes: detection rate, image quality, activity kinetics, and biodistribution. *J Nucl Med*. 2017;58:1797–1804.
4. Freitag MT, Radtke JP, Afshar-Oromieh A, et al. Local recurrence of prostate cancer after radical prostatectomy is at risk to be missed in ^{68}Ga -PSMA-11-PET of PET/CT and PET/MRI: comparison with mpMRI integrated in simultaneous PET/MRI. *Eur J Nucl Med Mol Imaging*. 2017;44:776–787.
5. Heusser T, Mann P, Rank CM, et al. Investigation of the halo-artifact in ^{68}Ga -PSMA-11-PET/MRI. *PLoS One*. 2017;12:e0183329.
6. Wondergem M, van der Zant FM, Rafimanesht-Sadr L, Knol RJJ. Effect of forced diuresis during ^{18}F -DCFPyL PET/CT in patients with prostate cancer: activity in ureters, kidneys and bladder and occurrence of halo artefacts around kidneys and bladder. *Nucl Med Commun*. 2019;40:652–656.
7. Rahbar K, Afshar-Oromieh A, Bogemann M, et al. ^{18}F -PSMA-1007 PET/CT at 60 and 120 minutes in patients with prostate cancer: biodistribution, tumour detection and activity kinetics. *Eur J Nucl Med Mol Imaging*. 2018;45:1329–1334.
8. Eiber M, Kroenke M, Wurzer A, et al. ^{18}F -rhPSMA-7 PET for the detection of biochemical recurrence of prostate cancer after radical prostatectomy. *J Nucl Med*. 2020;61:696–701.

9. Fendler WP, Eiber M, Beheshti M, et al. ^{68}Ga -PSMA PET/CT: joint EANM and SNMMI procedure guideline for prostate cancer imaging—version 1.0. *Eur J Nucl Med Mol Imaging*. 2017;44:1014–1024.
10. Afshar-Oromieh A, Sattler LP, Mier W, et al. The clinical impact of additional late PET/CT imaging with ^{68}Ga -PSMA-11 (HBED-CC) in the diagnosis of prostate cancer. *J Nucl Med*. 2017;58:750–755.
11. Sahlmann C-O, Meller B, Bouter C, et al. Biphasic ^{68}Ga -PSMA-HBED-CC-PET/CT in patients with recurrent and high-risk prostate carcinoma. *Eur J Nucl Med Mol Imaging*. 2016;43:898–905.
12. Afshar-Oromieh A, Sattler LP, Steiger K, et al. Tracer uptake in mediastinal and paraaortic thoracic lymph nodes as a potential pitfall in image interpretation of PSMA ligand PET/CT. *Eur J Nucl Med Mol Imaging*. 2018;45:1179–1187.
13. Hohberg M, Kobe C, Täger P, et al. Combined early and late [^{68}Ga]PSMA-HBED-CC PET scans improve lesion detectability in biochemical recurrence of prostate cancer with low PSA levels. *Mol Imaging Biol*. 2019;21:558–566.
14. Fennessy N, Lee J, Shin J, et al. Frusemide aids diagnostic interpretation of ^{68}Ga -PSMA positron emission tomography/CT in men with prostate cancer. *J Med Imaging Radiat Oncol*. 2017;61:739–744.
15. Derlin T, Weiberg D, von Klot C, et al. ^{68}Ga -PSMA I&T PET/CT for assessment of prostate cancer: evaluation of image quality after forced diuresis and delayed imaging. *Eur Radiol*. 2016;26:4345–4353.
16. Schmuck S, Nordlohne S, von Klot CA, et al. Comparison of standard and delayed imaging to improve the detection rate of [^{68}Ga]PSMA I&T PET/CT in patients with biochemical recurrence or prostate-specific antigen persistence after primary therapy for prostate cancer. *Eur J Nucl Med Mol Imaging*. 2017;44:960–968.
17. Alberts I, Sachpekidis C, Gourni E, et al. Dynamic patterns of [^{68}Ga]PSMA-11 uptake in recurrent prostate cancer lesions. *Eur J Nucl Med Mol Imaging*. 2020;47:160–167.
18. Alberts I, Sachpekidis C, Dijkstra L, et al. The role of additional late PSMA-ligand PET/CT in the differentiation between lymph node metastases and ganglia. *Eur J Nucl Med Mol Imaging*. 2020;47:642–651.
19. Afshar-Oromieh A, Hetzheim H, Kubler W, et al. Radiation dosimetry of ^{68}Ga -PSMA-11 (HBED-CC) and preliminary evaluation of optimal imaging timing. *Eur J Nucl Med Mol Imaging*. 2016;43:1611–1620.
20. Haupt F, Dijkstra L, Alberts I, et al. ^{68}Ga -PSMA-11 PET/CT in patients with recurrent prostate cancer: a modified protocol compared with the common protocol. *Eur J Nucl Med Mol Imaging*. 2020;47:624–631.
21. Afshar-Oromieh A, Avtzi E, Giesel FL, et al. The diagnostic value of PET/CT imaging with the ^{68}Ga -labelled PSMA ligand HBED-CC in the diagnosis of recurrent prostate cancer. *Eur J Nucl Med Mol Imaging*. 2015;42:197–209.
22. Eder M, Neels O, Muller M, et al. Novel preclinical and radiopharmaceutical aspects of [^{68}Ga]PSMA-HBED-CC: a new PET tracer for imaging of prostate cancer. *Pharmaceuticals (Basel)*. 2014;7:779–796.
23. Alberts I, Prenosil G, Sachpekidis C, et al. Digital versus analogue PET in [^{68}Ga]PSMA-11 PET/CT for recurrent prostate cancer: a matched-pair comparison. *Eur J Nucl Med Mol Imaging*. 2020;47:614–623.
24. Ponto LL, Schoenwald RD. Furosemide (frusemide): a pharmacokinetic/pharmacodynamic review (part I). *Clin Pharmacokinet*. 1990;18:381–408.
25. Freitag MT, Radtke JP, Afshar-Oromieh A, et al. Local recurrence of prostate cancer after radical prostatectomy is at risk to be missed in ^{68}Ga -PSMA-11-PET of PET/CT and PET/MRI: comparison with mpMRI integrated in simultaneous PET/MRI. *Eur J Nucl Med Mol Imaging*. 2017;44:776–787.
26. Sheikhbahaei S, Afshar-Oromieh A, Eiber M, et al. Pearls and pitfalls in clinical interpretation of prostate-specific membrane antigen (PSMA)-targeted PET imaging. *Eur J Nucl Med Mol Imaging*. 2017;44:2117–2136.
27. Matteucci F, Mezzenga E, Caroli P, et al. Reduction of ^{68}Ga -PSMA renal uptake with mannitol infusion: preliminary results. *Eur J Nucl Med Mol Imaging*. 2017;44:2189–2194.
28. Piron S, De Man K, Schelfhout V, et al. Optimization of PET protocol and interrater reliability of ^{18}F -PSMA-11 imaging of prostate cancer. *EJNMMI Res*. 2020;10:14.
29. Sachpekidis C, Kopka K, Eder M, et al. ^{68}Ga -PSMA-11 dynamic PET/CT imaging in primary prostate cancer. *Clin Nucl Med*. 2016;41:e473–e479.
30. Uprimny C, Kroiss AS, Decristoforo C, et al. Early dynamic imaging in ^{68}Ga -PSMA-11 PET/CT allows discrimination of urinary bladder activity and prostate cancer lesions. *Eur J Nucl Med Mol Imaging*. 2017;44:765–775.
31. Varasteh Z, Mohanta S, Robu S, et al. Molecular imaging of fibroblast activity after myocardial infarction using a ^{68}Ga -labeled fibroblast activation protein inhibitor, FAPI-04. *J Nucl Med*. 2019;60:1743–1749.
32. Beheshti M, Paymani Z, Brilhante J, et al. Optimal time-point for ^{68}Ga -PSMA-11 PET/CT imaging in assessment of prostate cancer: feasibility of sterile cold-kit tracer preparation? *Eur J Nucl Med Mol Imaging*. 2018;45:1188–1196.
33. Uprimny C, Bayerschmidt S, Kroiss AS, et al. Impact of forced diuresis with furosemide and hydration on the halo artefact and intensity of tracer accumulation in the urinary bladder and kidneys on [^{68}Ga]PSMA-11-PET/CT in the evaluation of prostate cancer patients. *Eur J Nucl Med Mol Imaging*. 2021;48:123–133.
34. Li M, Huang Z, Yu H, Wang Y, Zhang Y, Song B. Comparison of PET/MRI with multiparametric MRI in diagnosis of primary prostate cancer: a meta-analysis. *Eur J Radiol*. 2019;113:225–231.
35. Afshar-Oromieh A, Haberkorn U, Schlemmer HP, et al. Comparison of PET/CT and PET/MRI hybrid systems using a ^{68}Ga -labelled PSMA ligand for the diagnosis of recurrent prostate cancer: initial experience. *Eur J Nucl Med Mol Imaging*. 2014;41:887–897.
36. Afshar-Oromieh A, Wolf M, Haberkorn U, et al. Effects of arm truncation on the appearance of the halo artifact in ^{68}Ga -PSMA-11 (HBED-CC) PET/MRI. *Eur J Nucl Med Mol Imaging*. 2017;44:1636–1646.
37. Rahbar K, Afshar-Oromieh A, Seifert R, et al. Diagnostic performance of ^{18}F -PSMA-1007 PET/CT in patients with biochemical recurrent prostate cancer. *Eur J Nucl Med Mol Imaging*. 2018;45:2055–2061.
38. Rahbar K, Weckesser M, Ahmadzadehfah H, Schafers M, Stegger L, Bogemann M. Advantage of ^{18}F -PSMA-1007 over ^{68}Ga -PSMA-11 PET imaging for differentiation of local recurrence vs. urinary tracer excretion. *Eur J Nucl Med Mol Imaging*. 2018;45:1076–1077.
39. Rauscher I, Krönke M, König M, et al. Matched-pair comparison of ^{68}Ga -PSMA-11 PET/CT and ^{18}F -PSMA-1007 PET/CT: frequency of pitfalls and detection efficacy in biochemical recurrence after radical prostatectomy. *J Nucl Med*. 2020;61:51–57.
40. Kuten J, Fahoum I, Savin Z, Shamni O, et al. Head-to-head comparison of ^{68}Ga -PSMA-11 with ^{18}F -PSMA-1007 PET/CT in staging prostate cancer using histopathology and immunohistochemical analysis as a reference standard. *J Nucl Med*. 2020;61:527–532.

Head-to-Head Comparison of ⁶⁸Ga-Prostate-Specific Membrane Antigen PET/CT and Ferumoxtran-10–Enhanced MRI for the Diagnosis of Lymph Node Metastases in Prostate Cancer Patients

Melline G.M. Schilham^{*1}, Patrik Zamecnik^{*1}, Bastiaan M. Privé¹, Bas Israël¹, Mark Rijpkema¹, Tom Scheenen¹, Jelle O. Barentsz¹, James Nagarajah^{†1,2}, and Martin Gotthardt^{†1}

¹Department of Medical Imaging, Nuclear Medicine, Radboud University Medical Centre, Nijmegen, The Netherlands; and

²Department of Nuclear Medicine, Technical University Munich, Klinikum rechts der Isar, Munich, Germany

Accurate assessment of lymph node (LN) metastases in prostate cancer (PCa) patients is critical for prognosis and patient management. Both prostate-specific membrane antigen (PSMA) PET/CT and ferumoxtran-10 nanoparticle–enhanced MRI (nano-MRI) are imaging modalities with high potential to identify LN metastases in PCa patients. The aim of this study was to compare the results of these imaging technologies in terms of characteristics and anatomic localization of suspicious LNs in order to assess the feasibility of their complementary use for imaging in PCa patients. **Methods:** In total, 45 patients with either primary PCa ($n = 8$) or recurrence ($n = 36$) were included in this retrospective study. All patients underwent both ⁶⁸Ga-PSMA PET/CT and nano-MRI between October 2015 and July 2017 within 3 wk. Both scans were performed at the same institution according to local clinical protocols. All scans were analyzed independently by experienced nuclear medicine physicians and radiologists. The size, anatomic location, and level of suspicion were determined for all visible LNs. Subsequently, the findings from ⁶⁸Ga-PSMA PET/CT and nano-MRI were compared without respect to a reference standard. **Results:** In total, 179 suspicious LNs were identified. Significantly more suspicious LNs per patient were detected by nano-MRI ($P < 0.001$): 160 were identified in 33 patients by nano-MRI, versus 71 in 25 patients by ⁶⁸Ga-PSMA PET/CT. Of all suspicious LNs, 108 were identified only by nano-MRI (60%), 19 (11%) only by ⁶⁸Ga-PSMA PET/CT, and 52 (29%) by both methods. The mean size of the suspicious LNs as identified by nano-MRI was significantly smaller (5.3 mm) than that by ⁶⁸Ga-PSMA PET/CT (6.0 mm; $P = 0.006$). The median level of suspicion did not differ significantly. Both modalities identified suspicious LNs in all anatomic regions of the pelvis. **Conclusion:** Both modalities identified suspicious LNs that were missed by the other. Both modalities identified suspicious LNs in all anatomic regions of the pelvis; however, nano-MRI appeared to be superior in detecting smaller suspicious LNs. These findings suggest that nano-MRI has a potential role as a complement to PSMA PET/CT. However, since the clinical implications of the different results are not well established yet, further investigation of this complementary use is encouraged.

Key Words: prostate cancer; lymph node; prostate specific membrane antigen; ⁶⁸Ga-PSMA PET/CT; ferumoxtran-10

J Nucl Med 2021; 62:1258–1263

DOI: 10.2967/jnumed.120.258541

Detecting lymph node (LN) metastases in prostate cancer (PCa) patients is critical for prognosis and patient management. The current gold standard to assess the LN status is extended pelvic LN dissection (PLND). However, this procedure is invasive and associated with considerable morbidity (1). Previous research demonstrated that in a substantial number of patients (60%–85%), LN metastases were located outside the extended PLND template (2–4), illustrating the demand and increasing role for noninvasive imaging techniques to detect LN metastases in PCa patients.

Since conventional imaging techniques—that is, CT and MRI—use only morphologic criteria for LN assessment, and in PCa more than 60% of LN metastases are present in normal-sized LNs (<8 mm), these techniques are of limited value in LN staging (5,6), leading to the development of advanced functional and molecular imaging techniques. Recently, prostate-specific membrane antigen (PSMA)–based PET/CT was introduced. PSMA is a cell-surface glycoprotein that is overexpressed on more than 90% of PCa cells (7). Small molecules with high binding affinity to PSMA are labeled with positron emitters to enable whole-body tumor detection using PET/CT. Whereas data on accuracy were based predominantly on retrospective research (8), a large prospective study by Hofman et al. recently demonstrated sensitivity and specificity of 0.85 and 0.98, respectively, for both LN and distant metastases (9). The rapid implementation of this technique in several PCa guidelines affirmed the demand for accurate staging methods (10,11).

Another potential imaging modality for LN staging is MR lymphography or nanoparticle-enhanced MRI (nano-MRI). In nano-MRI, ultra-small superparamagnetic iron oxide particles (ferumoxtran-10 [Ferrotan; SPL Medical BV]) are used as a contrast agent. Through accumulation of these particles in normal lymphatic tissue after intravenous drip infusion, nano-MRI allows differentiation of metastatic LNs from benign LNs, irrespective of nodal size (5,12). The reported sensitivity and specificity in the detection of LN metastases in PCa patients are 82% and 93%, respectively

Received Oct. 13, 2020; revision accepted Jan. 3, 2021.

For correspondence or reprints, contact Melline G.M. Schilham (melline.schilham@radboudumc.nl).

*Contributed equally to this work.

†Contributed equally to this work.

Published online January 30, 2021.

Immediate Open Access: Creative Commons Attribution 4.0 International License (CC BY) allows users to share and adapt with attribution, excluding materials credited to previous publications. License: <https://creativecommons.org/licenses/by/4.0/>. Details: <http://jnm.snmjournals.org/site/misc/permission.xhtml>.

COPYRIGHT © 2021 by the Society of Nuclear Medicine and Molecular Imaging.

(12). A metaanalysis reported sensitivities of up to 90% and specificities of up to 96% for various cancers, including PCa (13).

Published data suggest that PSMA PET/CT and nano-MRI are the imaging modalities with the highest reported accuracy to detect LN metastases (9,14,15). Since both modalities rely on different technical and biologic features, it was hypothesized that a combined use could even improve LN detection. Therefore, the goal of this study was to investigate the feasibility of a potential complementary role for these imaging modalities by comparing their results in the same patient and identifying differences and similarities in detected LN characteristics without respect to a reference standard.

MATERIALS AND METHODS

Patient Population

Forty-five patients were enrolled in this retrospective study. Before the database creation, the institutional review board approved this study and the requirement to obtain informed consent was waived (CMO2019.5810). The study included all patients with either primary PCa ($n = 8$) or recurrent disease ($n = 36$) who underwent both nano-MRI and ^{68}Ga -PSMA PET/CT in our center between October 2015 and July 2017. The 2 scans needed to be performed within 3 wk of each other for inclusion. Patient characteristics were retrospectively collected from medical files.

^{68}Ga -PSMA-HBED-CC PET/CT

^{68}Ga -PSMA PET/CT was performed using an integrated PET/CT system (Biograph mCT 4-ring, 40-slice time-of-flight PET/CT scanner; Siemens Healthcare). For all patients, ^{68}Ga -PSMA-HBED-CC was manufactured by the Radboud Translational Medicine Facility. The PET acquisition was 4 min per bed position for the pelvic area and 3 min for the rest of the body. A low-dose CT scan (slice thickness, 5.0 mm) was acquired for attenuation correction and image coregistration. PET/CT images were reconstructed in 3 orientations (axial, coronal, and sagittal). The administered dose of the tracer was 2 MBq/kg of body weight, and imaging was initiated after an approximately 60-min incubation time.

Nano-MRI

All patients received ferumoxtran-10 intravenously in a weight-adapted dose of 2.6 mg/kg of body weight 24–36 h before the MRI scan. Ferumoxtran-10 was diluted in 100 mL of 0.9% NaCl solution and administered via drip infusion using a 0.22- μm -pore filter (Minisart NML syringe filter, catalog no. 16534-k; Sartorius AG). The infusion was performed at a slow rate of 1 mL/min at the start, increasing to 4 mL/min. The infusion duration was approximately 45 min and supervised by radiologists. MRI was performed using a 3-T MRI scanner (Magnetom Skyra or Trio; Siemens Healthineers). The imaging area included the pelvis from the pubic bone to the aortic bifurcation. The MRI protocol consisted of an isotropic 3-dimensional T1-weighted gradient-echo sequence (repetition time, 6.5 ms; echo time, 2.5 ms; flip angle, 10°; and spatial resolution, 0.9-mm isotropic) and an isotropic 3-dimensional iron-sensitive T2*-weighted gradient-echo sequence with fat saturation (multiple-echo data image combination, with repetition time, 21 ms; echo time, 12 ms; 3 combined echoes; flip angle, 10°; and spatial resolution, 0.85-mm isotropic).

Image Analysis

All ^{68}Ga -PSMA PET/CT exams were retrospectively reviewed by 2 certified nuclear physicians in consensus, and the nano-MR images were independently reviewed by 1 experienced radiologist. For both modalities, the number, anatomic location, and size of detected LNs were reported. The location was described according to preconfigured

anatomic locations in the pelvis, consistent with clinical practice in our department. LN size was measured (mm) for the smallest axis. Additionally, all detectable LNs were classified with a level of suspicion (LoS) for both nano-MRI and ^{68}Ga -PSMA PET/CT. This classification is a 5-point likelihood scale for potential malignancy that is used by nuclear physicians and radiologists in our center. For nano-MRI, LoS was based on the signal intensity in the iron-sensitive T2*-weighted MRI sequence and its distribution within the LN based on the diagnostic description proposed by Anzai et al. (16). LoS for ^{68}Ga -PSMA PET/CT was based on the proposed criteria of the ^{68}Ga -PSMA reporting and data system by Rowe et al. (17). This evaluation comprised a combination of tracer uptake, location, and size. In more detail, LNs with no tracer uptake were given an LoS of 1, defined as a high probability of being benign. LNs with equivocal tracer uptake at sites atypical of PCa involvement (e.g., axillary or hilar) were given a LoS of 2 (probably benign). A LoS of 3 (equivocal), was given to LNs with equivocal tracer uptake at sites typical of PCa involvement, LNs with intense uptake at sites highly atypical of PCa (i.e., the likelihood of nonprostatic malignancies or other [benign] origins is high), or LNs without tracer uptake but with pathologic aspects suspicious of malignancy on anatomic imaging. LNs with clearly increased tracer uptake at sites typical of PCa involvement but lacking definitive findings on anatomic imaging were given an LoS of 4, or probably malignant. A LoS of 5, defined as a high probability of being malignant, was given to LNs with intense tracer uptake at sites typical of PCa and with corresponding pathologic findings on anatomic imaging. For both modalities, LNs with a LoS of 3 or higher were considered suspicious and taken for statistical evaluation.

Outcome Measurements and Statistical Analysis

Statistical analyses were performed using SPSS software, version 25. Descriptive statistical methods were used to characterize the patient cohort. For continuous data, mean and SD were reported. For categorical data, median and interquartile range were described. Only nonparametric statistical tests (Mann-Whitney U test and Wilcoxon signed-rank test) were performed since all data were nonnormally distributed. A P value of less than 0.05 was considered statistically significant.

RESULTS

Forty-five patients underwent nano-MRI and ^{68}Ga -PSMA PET/CT within a mean of 3 d (range, 1–18 d) between October 2015 and July 2017. The mean age of the patients was 64 y (range, 48–82 y). For the total cohort, the mean prostate-specific antigen (PSA) level at the time of scanning was 9.9 ng/mL (range, 0.1–150 ng/mL). For the subgroup of patients who underwent imaging for primary staging ($n = 8$), the mean PSA level was 28.9 ng/mL (range, 5.6–150 ng/mL). The mean PSA level in patients with recurrent disease ($n = 33$) was 5.0 ng/mL (range, 0.1–46 ng/mL). Detailed patient characteristics are described in Table 1. The median administered dose of ^{68}Ga -PSMA-HBED-CC was 158 MBq (interquartile range, 133–180 MBq).

A cumulative total of 179 suspected LNs (LoS ≥ 3) was identified in 33 patients. Examples of suspicious LNs as identified by nano-MRI, ^{68}Ga -PSMA PET/CT, or both are shown in Figure 1. The characteristics of the nano-MRI and ^{68}Ga -PSMA PET/CT results are shown in Table 2. In total, 179 suspicious LNs were identified. A significantly greater number of suspicious LNs were detected by nano-MRI ($P < 0.001$): 160 were identified in 33 patients by nano-MRI, versus 71 in 25 patients by ^{68}Ga -PSMA PET/CT. Thus, per patient, nano-MRI identified a significantly greater number of suspicious LNs (mean, 3.6; range, 0–15) than

TABLE 1
Patient Characteristics

Characteristic	Data
Patients	45 (100%)
Age (y)	64 (48–82)
Serum PSA level (ng/mL)*	
Overall, <i>n</i> = 42	9.9 (0.0–150)
Primary setting, <i>n</i> = 8	28.9 (5.6–150)
Recurrence setting, <i>n</i> = 33	5.0 (0.0–46)
Time between diagnosis and scans (mo) [†]	50 (1–202)
Time between scans (d)	3.0 (1–18)
Before imaging	
Any PCa treatment	
Yes	36 (80%)
No	8 (18%)
Unknown	1 (2%)
PLND	
Yes	22 (49%)
No	19 (42%)
Unknown	4 (9%)
Clinical ISUP grade	
1	5 (11%)
2	6 (13%)
3	7 (16%)
4	13 (29%)
5	8 (18%)
Unknown	6 (13%)

*No data available for 3 patients.

[†]No data available for 1 patient.

ISUP = International Society of Urological Pathology.

Qualitative data are number and percentage; continuous data are mean and range.

⁶⁸Ga-PSMA PET/CT (mean, 1.6; range, 0–12) (*P* < 0.001). The difference in the size of the detected suspicious LNs between the 2 modalities is shown in Figure 2. The mean size of the suspicious LNs identified by nano-MRI (5.2 mm; range, 2–16) was significantly smaller than that identified by ⁶⁸Ga-PSMA PET/CT (6.0 mm; range, 3–16 mm) (*P* = 0.006).

Table 3 shows which LNs were identified by both modalities and which by only one. Most of the suspicious LNs were identified by nano-MRI alone (*n* = 108, 60%). Almost a third (*n* = 52, 29%) were identified by both modalities, and 19 (11%) were identified by ⁶⁸Ga-PSMA PET/CT alone. Not surprisingly, LNs identified by both modalities were larger (mean size, 6.5 mm; range, 4–16 mm) than those identified by either of the modalities alone. In line with this finding is the higher LoS of LNs identified by both modalities than of LNs identified by one of the techniques alone.

An overview of the anatomic localization of the suspicious LNs is depicted in Figure 3 (para-aortal and paravesical LNs are left out). Both modalities identified LNs across all anatomic locations,

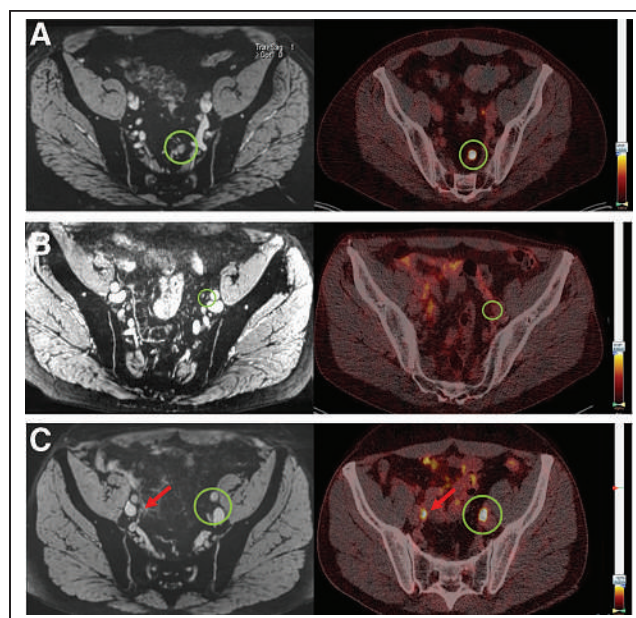


FIGURE 1. Examples of iron-sensitive T2*-weighted fat-saturated nano-MRI images (left) and PSMA PET/CT images (right). (A) Seven-millimeter-diameter LN in left pararectal region that is positive on both nano-MRI and PSMA PET/CT. (B) Four-millimeter-diameter LN in region of left external iliac artery that is positive on nano-MRI but negative on PSMA PET/CT. (C) Suspicious LN dorsal to left external iliac artery that is negative on nano-MRI (nano-MRI also shows no left ureter in this area) but positive on PSMA PET/CT. LNs are encircled; arrows indicate right ureter.

either left- or right-sided. Remarkably, 43% (*n* = 77) of all detected suspicious LNs were outside the standard extended PLND resection field (included in this field were the obturator, internal iliac, and external iliac regions).

DISCUSSION

The aim of this study was to evaluate the feasibility of complementary use of 2 high-precision imaging techniques for the detection of metastatic LNs in PCa patients. We hypothesized that complementary use might even improve LN detection. Therefore, we aimed to identify differences in the number, size, LoS, and location of suspicious LNs in order to determine when this complementary role would be most pronounced. In this direct comparative study, 3 important results were achieved. First, nano-MRI identified a significantly greater number of suspicious LNs per patient than ⁶⁸Ga-PSMA PET/CT (*P* < 0.001). Second, the LNs identified by nano-MRI were significantly smaller (*P* = 0.006) than those identified by ⁶⁸Ga-PSMA PET/CT. Third, both modalities identified LNs throughout the pelvis in all anatomic regions, with, however, a significant number of suspicious LNs (43%) outside the standard extended PLND templates.

To the best of our knowledge, this was the first study directly comparing these specific imaging techniques. In 2005–2006, Fortuin et al. conducted comparable research comparing nano-MRI with ¹¹C-choline-PET/CT. They showed that small suspicious LNs were detected at a higher rate by nano-MRI than by ¹¹C-choline PET/CT (18), a finding consistent with our results. In recent years, however, MRI has continued to develop and improve, and new technologies (PSMA PET/CT) have emerged. To be more precise, technologic improvements compared with the MRI

TABLE 2
Node Detection and Characteristics for Nano-MRI and PSMA PET/CT

Characteristic	Total	Nano-MRI	PSMA PET/CT	<i>P</i>
Total scans	90 (100%)	45 (100%)	45 (100%)	
Total positive scans	58 (64%)	33 (73%)	25 (56%)	
Total suspicious LNs	179 (100%)	160 (89%)	71 (40%)	
Suspicious LNs per patient	4.0 (range, 0–6)	3.6 (range, 0–15)	1.6 (range, 0–12)	<0.001*
Suspicious LN size (mm)	5.2 (range, 2–16)	5.3 (range, 2–16)	6.0 (range, 3–16)	0.006†
LoS	4 (IQR, 4–5)	4 (IQR, 4–5)	5 (IQR, 4–5)	

*Positive scan defined as at least 1 LN with LoS \geq 3.
†Wilcoxon signed-rank test.
‡Mann–Whitney *U* test.
IQR = interquartile range.
Qualitative data are number and percentage; continuous data are mean and range or IQR.

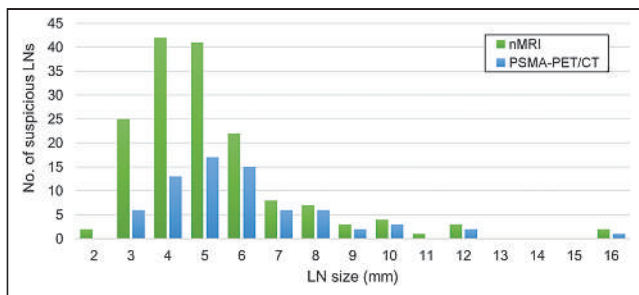


FIGURE 2. Size distribution of suspicious LNs as detected by nano-MRI (nMRI) and PSMA PET/CT.

technique used by Fortuin et al. have led to an even higher spatial resolution (2 mm compared with 4 mm) in MRI. Additionally, PSMA-based PET/CT has already proven to be more sensitive than ^{18}F -choline-based PET/CT (19). Consequently, reevaluation of these 2 imaging methods was considered valuable and led to the implementation of the current study.

The validation studies that have already been conducted for both imaging modalities showed promising sensitivity and specificity, and as technologic possibilities continue to evolve, accuracy is expected to improve further (9,12). Although there was no reference standard in this study, the main results provide insight into the complementary performance of the 2 modalities by identifying areas where they agree and disagree. Such results allow the definition of future areas of research that need to be addressed in order to define the optimal imaging strategy for PCa patients.

Our results show a potentially higher detection rate for nano-MRI than for ^{68}Ga -PSMA PET/CT. As Figure 2 shows, disagreement was most pronounced on LNs smaller than 6 mm, suggesting size to be the most likely explanation for this difference. Recent research demonstrated large differences in the median histologic size of metastatic LNs that were detected—compared with those that were undetected—by ^{68}Ga -PSMA PET/CT, suggesting a size-related sensitivity for LN metastasis detection by ^{68}Ga -PSMA PET/CT (20,21). Possible explanations for this finding might be the biologic properties of PSMA expression on tumor tissue, as larger lesions are likely to have more PSMA receptors and thus

higher tracer uptake. Yet, ^{68}Ga -PSMA PET/CT was able to detect the smallest PSMA-positive lesions (below the spatial resolution of the scanner) when PSMA expression was highly concentrated but sometimes missed a larger lesion when PSMA expression was too dispersed (20). Furthermore, it has been demonstrated that PSMA expression correlates with International Society of Urological Pathology tumor grade and serum PSA level (22,23). Additionally, about 5%–10% of PCa lesions do not express PSMA (7). Since the iron-sensitive MRI sequence of nano-MRI has a higher spatial resolution (isotropic resolution of 0.85 mm) than PET/CT (6 mm), the resolution of nano-MRI enables detection of LNs down to a 2 mm³ voxel size. Thus, in contrast to nano-MRI, the performance of LN detection by PSMA PET/CT is largely dependent on tumor biology (24). Therefore, it could be anticipated that there is a potential advantage of nano-MRI in PCa patients with a lower International Society of Urological Pathology grade and PSA value. To draw solid conclusions from this disagreement on small suspicious LNs, more research is needed on the clinical significance of these small, potentially metastatic LNs and the biology of PSMA expression.

The difference in pathophysiologic targets between the 2 modalities (PSMA expression vs. lymphatic invasion of tumor tissue) could also partly explain our finding that nano-MRI identified suspicious LNs in 8 patients (8/45, 18%) who had no suspicious LNs on ^{68}Ga -PSMA PET/CT. This finding suggests false-positive LNs for nano-MRI, a false-negative rate for ^{68}Ga -PSMA PET/CT, or, most likely, a combination of both. In view of the different pathophysiologic targets, there are multiple explanations. Since about 5%–10% of tumor lesions do not show PSMA expression, these lesions will be missed by PSMA PET/CT (7). The fact that the sensitivity of ^{68}Ga -PSMA PET/CT depends, in essence, on PSMA expression could explain the failure to detect lesions whose PSMA expression is too low. On the other hand, nano-MRI relies on the lymphotropic affinity to ferumoxtran-10 of macrophages, which accumulate the contrast agent in healthy LNs. Thus, when accumulation in nonmetastatic tissue is disturbed, such as by fibrosis, the discriminative ability between metastatic and nonmetastatic tissue in nano-MRI could be impaired. Ideally, a reference standard should be used to evaluate such results, and such research is strongly encouraged but surpassed the scope of the current study.

TABLE 3
Conformity of Nano-MRI and PSMA PET/CT

Characteristic	Suspicious LNs as detected by ...		
	Both nano-MRI and PSMA PET/CT	Nano-MRI only	PSMA PET/CT only
No. of patients	20	30	14
Total suspicious LNs	52 (29%)	108 (60%)	19 (11%)
Suspicious LNs per patient	1.2 (range, 0–10)	2.4 (range, 0–8)	0.4 (range, 0–3)
LN size (mm)	6.5 (range, 4–16)	4.7 (range, 2–16)	4.4 (range, 3–8)
LoS	5 (IQR, 4–5)	4 (IQR, 4–5)	3 (IQR, 3–4)

IQR = interquartile range.

Qualitative data are number and percentage; continuous data are mean and range or IQR.

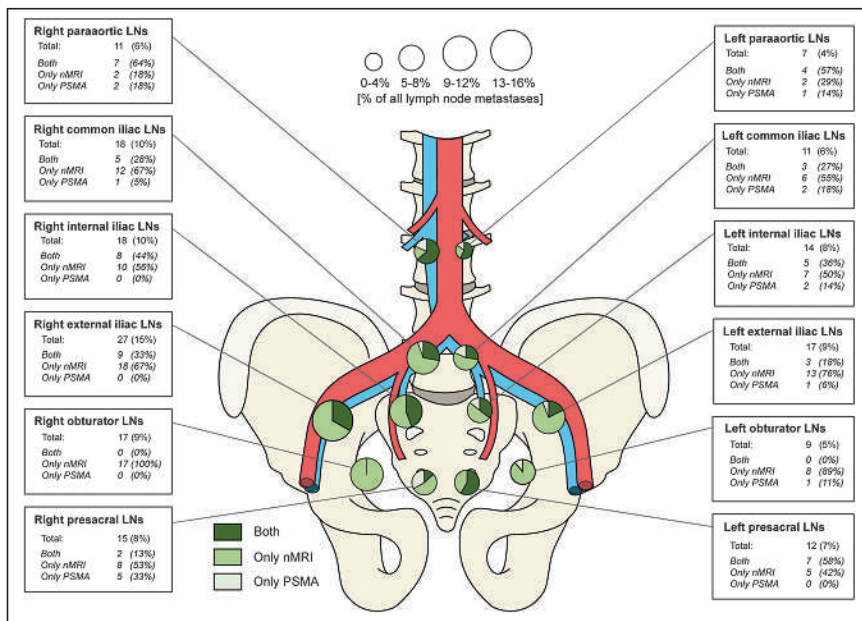


FIGURE 3. Anatomic distribution of identified suspicious LNs as detected by nano-MRI (nMRI) and PSMA PET/CT.

Contrary to the disagreement on size-related detection rates, another important finding was the agreement on anatomic localization; there were no anatomic regions in which either modality could not detect suspicious LNs (Fig. 3). In addition, both modalities identified a substantial number of suspicious LNs outside the extended PLND template (77/179, 43%). This finding was also described in recent research (12,25,26) and has a major impact on clinical care, as it challenges the diagnostic and therapeutic value of extended PLND (27), thus emphasizing the importance of accurate imaging modalities and explaining the current rapidly changing of clinical guidelines since the introduction of PSMA PET/CT (9,28).

This study was not without limitations. An important limitation of the study was its retrospective nature. Also, the studied population was relatively small and heterogeneous, as it consisted of both patients in the primary setting and patients in the biochemically recurrent setting. However, this limitation was due to the small

number of patients who underwent both scans within a sufficiently tight time frame. Although the number of patients was limited, the population was unique and allowed us to compare the diagnostic performance of these imaging techniques without the disruptive effect of anatomic discordances. A final limitation was the lack of histopathologic confirmation of the identified suspicious LNs. Unfortunately, histologic or clinical confirmation of the positive LNs was impossible because most of our patient group was from abroad. Yet, the aim of this study was to compare the findings of both imaging modalities and discuss the potential clinical and scientific value (feasibility) of complementary use rather than to validate their findings.

CONCLUSION

The findings of this comparison study imply potential benefit from complementary use of ⁶⁸Ga-PSMA PET/CT and nano-MRI, most pronounced in small LNs. To make clinical recommendations

for such complementary use, more profound prospective research on the competitive results is warranted and should focus on size-related issues and tumor biology (PSMA). Nevertheless, the results of this study underline the importance of understanding both the technical capabilities of imaging techniques and the tumor biology in order to interpret the imaging results appropriately.

DISCLOSURE

Patrik Zamecnik is a scientific advisor to SPL Medical B.V. and has options in SPL Medical B.V. Jelle Barentsz is a scientific advisor to SPL Medical B.V. No other potential conflict of interest relevant to this article was reported.

ACKNOWLEDGMENT

We thank Robin Merckx, MD, for drawing Figure 3.

KEY POINTS

QUESTION: How do the imaging results of ^{68}Ga -PSMA PET/CT and nano-MRI compare in the same patients?

PERTINENT FINDINGS: In this retrospective head-to-head comparison study comprising 45 patients, nano-MRI identified a significantly greater number of suspicious LNs per patient (mean, 3.6) than did ^{68}Ga -PSMA PET/CT (mean, 1.6), and the mean size of LNs detected by nano-MRI (mean, 5.3 mm) was significantly smaller than that detected by ^{68}Ga -PSMA PET/CT (mean, 6.0 mm). Both modalities identified suspicious LNs in all anatomic pelvic regions.

IMPLICATIONS FOR PATIENT CARE: The present study of 2 highly promising imaging modalities in PCa patients provided insight into their comparability that may contribute to improved interpretation of results.

REFERENCES

1. Fossati N, Willemsse PM, Van den Broeck T, et al. The benefits and harms of different extents of lymph node dissection during radical prostatectomy for prostate cancer: a systematic review. *Eur Urol*. 2017;72:84–109.
2. Joniau S, Van den Bergh L, Lerut E, et al. Mapping of pelvic lymph node metastases in prostate cancer. *Eur Urol*. 2013;63:450–458.
3. Heesakkers RA, Jager GJ, Hövels AM, et al. Prostate cancer: detection of lymph node metastases outside the routine surgical area with ferumoxtran-10-enhanced MR imaging. *Radiology*. 2009;251:408–414.
4. Larbi A, Dallaudière B, Pasoglou V, et al. Whole body MRI (WB-MRI) assessment of metastatic spread in prostate cancer: therapeutic perspectives on targeted management of oligometastatic disease. *Prostate*. 2016;76:1024–1033.
5. Harisinghani MG, Barentsz J, Hahn PF, et al. Noninvasive detection of clinically occult lymph-node metastases in prostate cancer. *N Engl J Med*. 2003;348:2491–2499.
6. Hövels AM, Heesakkers RA, Adang EM, et al. The diagnostic accuracy of CT and MRI in the staging of pelvic lymph nodes in patients with prostate cancer: a meta-analysis. *Clin Radiol*. 2008;63:387–395.
7. Silver DA, Pellicer I, Fair WR, Heston WD, Cordon-Cardo C. Prostate-specific membrane antigen expression in normal and malignant human tissues. *Clin Cancer Res*. 1997;3:81–85.
8. Perera M, Papa N, Roberts M, et al. Gallium-68 prostate-specific membrane antigen positron emission tomography in advanced prostate cancer: updated diagnostic utility, sensitivity, specificity, and distribution of prostate-specific membrane antigen-avid lesions—a systematic review and meta-analysis. *Eur Urol*. 2020;77:403–417.
9. Hofman MS, Lawrentschuk N, Francis RJ, et al. Prostate-specific membrane antigen PET-CT in patients with high-risk prostate cancer before curative-intent surgery or radiotherapy (proPSMA): a prospective, randomised, multicentre study. *Lancet*. 2020;395:1208–1216.
10. Maurer T, Eiber M, Schwaiger M, Gschwend JE. Current use of PSMA-PET in prostate cancer management. *Nat Rev Urol*. 2016;13:226–235.
11. Maurer T, Murphy DG, Hofman MS, Eiber M. PSMA-PET for lymph node detection in recurrent prostate cancer: how do we use the magic bullet? *Theranostics*. 2017;7:2046–2047.
12. Heesakkers RA, Hovels AM, Jager GJ, et al. MRI with a lymph-node-specific contrast agent as an alternative to CT scan and lymph-node dissection in patients with prostate cancer: a prospective multicohort study. *Lancet Oncol*. 2008;9:850–856.
13. Wu L, Cao Y, Liao C, Huang J, Gao F. Diagnostic performance of USPIO-enhanced MRI for lymph-node metastases in different body regions: a meta-analysis. *Eur J Radiol*. 2011;80:582–589.
14. Pfister D, Porres D, Heidenreich A, et al. Detection of recurrent prostate cancer lesions before salvage lymphadenectomy is more accurate with ^{68}Ga -PSMA-HBED-CC than with ^{18}F -fluoroethylcholine PET/CT. *Eur J Nucl Med Mol Imaging*. 2016;43:1410–1417.
15. Fortuin A, Rooij M, Zamecnik P, Haberkorn U, Barentsz J. Molecular and functional imaging for detection of lymph node metastases in prostate cancer. *Int J Mol Sci*. 2013;14:13842–13875.
16. Anzai Y, Piccoli CW, Outwater EK, et al. Evaluation of neck and body metastases to nodes with ferumoxtran 10-enhanced MR imaging: phase III safety and efficacy study. *Radiology*. 2003;228:777–788.
17. Rowe SP, Pienta KJ, Pomper MG, Gorin MA. Proposal for a structured reporting system for prostate-specific membrane antigen-targeted PET imaging: PSMA-RADS version 1.0. *J Nucl Med*. 2018;59:479–485.
18. Fortuin AS, Deserno WM, Meijer HJ, et al. Value of PET/CT and MR lymphography in treatment of prostate cancer patients with lymph node metastases. *Int J Radiat Oncol Biol Phys*. 2012;84:712–718.
19. Afshar-Oromieh A, Zechmann CM, Malcher A, et al. Comparison of PET imaging with a ^{68}Ga -labelled PSMA ligand and ^{18}F -choline-based PET/CT for the diagnosis of recurrent prostate cancer. *Eur J Nucl Med Mol Imaging*. 2014;41:11–20.
20. Jilg CA, Drendel V, Rischke HC, et al. Detection rate of ^{18}F -choline PET/CT and ^{68}Ga -PSMA-HBED-CC PET/CT for prostate cancer lymph node metastases with direct link from PET to histopathology: dependence on the size of tumor deposits in lymph nodes. *J Nucl Med*. 2019;60:971–977.
21. Klíngenberg S, Jochumsen MR, Ulhøi BP, et al. ^{68}Ga -PSMA PET/CT for primary lymph node and distant metastasis NM staging of high-risk prostate cancer. *J Nucl Med*. 2021;62:214–220.
22. Afshar-Oromieh A, Avtzi E, Giesel FL, et al. The diagnostic value of PET/CT imaging with the ^{68}Ga -labelled PSMA ligand HBED-CC in the diagnosis of recurrent prostate cancer. *Eur J Nucl Med Mol Imaging*. 2015;42:197–209.
23. Privé BM, Israël B, Schilham MGM, et al. Evaluating F-18-PSMA-1007-PET in primary prostate cancer and comparing it to multi-parametric MRI and histopathology. *Prostate Cancer Prostatic Dis*. September 30, 2020 [Epub ahead of print].
24. Perera M, Papa N, Christidis D, et al. Sensitivity, specificity, and predictors of positive ^{68}Ga -prostate-specific membrane antigen positron emission tomography in advanced prostate cancer: a systematic review and meta-analysis. *Eur Urol*. 2016;70:926–937.
25. Koerber SA, Stach G, Kratochwil C, et al. Lymph node involvement in treatment-naïve prostate cancer patients: correlation of PSMA PET/CT imaging and Roach formula in 280 men in radiotherapeutic management. *J Nucl Med*. 2020;61:46–50.
26. Meijer HJ, Fortuin AS, van Lin EN, et al. Geographical distribution of lymph node metastases on MR lymphography in prostate cancer patients. *Radiother Oncol*. 2013;106:59–63.
27. Bravi CA, Fossati N, Gandaglia G, et al. Long-term outcomes of salvage lymph node dissection for nodal recurrence of prostate cancer after radical prostatectomy: not as good as previously thought. *Eur Urol*. 2020;78:661–669.
28. Fendler WP, Eiber M, Beheshti M, et al. ^{68}Ga -PSMA PET/CT: joint EANM and SNMMI procedure guideline for prostate cancer imaging—version 1.0. *Eur J Nucl Med Mol Imaging*. 2017;44:1014–1024.

SUVs Are Adequate Measures of Lesional ^{18}F -DCFPyL Uptake in Patients with Low Prostate Cancer Disease Burden

Yves J.L. Bodar¹⁻³, Berend P.F. Koene¹, Bernard H.E. Jansen¹⁻³, Matthijs C.F. Cysouw², Dennie Meijer¹⁻³, N. Harry Hendrikse^{2,4}, André N. Vis^{1,3}, Ronald Boellaard², and Daniela E. Oprea-Lager²

¹Department of Urology, Amsterdam University Medical Centers, VU University, Amsterdam, The Netherlands; ²Department of Radiology and Nuclear Medicine, Amsterdam University Medical Centers, VU University, Amsterdam, The Netherlands; ³Prostate Cancer Network, Noord Holland, The Netherlands; and ⁴Department of Clinical Pharmacology and Pharmacy, Amsterdam University Medical Centers, VU University, Amsterdam, The Netherlands

In prostate cancer (PCa) patients, the tumor-to-blood ratio (TBR) has been validated as the preferred simplified method for lesional ^{18}F -DCFPyL (a radiolabeled prostate-specific membrane antigen ligand) uptake quantification on PET. In contrast to SUVs, the TBR accounts for variability in arterial input functions caused by differences in total tumor burden between patients (the sink effect). However, TBR depends strongly on tracer uptake interval and has worse repeatability and is less applicable in clinical practice than SUVs. We investigated whether SUV could provide adequate quantification of ^{18}F -DCFPyL uptake on PET/CT in a patient cohort with low PCa burden. **Methods:** In total, 116 patients with PCa undergoing ^{18}F -DCFPyL PET/CT imaging were retrospectively included. All ^{18}F -DCFPyL-avid lesions suspected of being PCa were semiautomatically delineated. SUV_{peak} was plotted against TBR for the most intense lesion of each patient. The correlation of SUV_{peak} and TBR was evaluated using linear regression and was stratified for patients undergoing PET/CT for primary staging, patients undergoing restaging at biochemical recurrence, and patients with metastatic castration-resistant PCa. Moreover, the correlation was evaluated as a function of tracer uptake time, prostate-specific antigen level, and PET-positive tumor volume. **Results:** In total, 436 lesions were delineated (median, 1 per patient; range, 1–66). SUV_{peak} correlated well with TBR in patients with PCa and a total tumor volume of less than 200 cm^3 ($R^2 = 0.931$). The correlation between SUV and TBR was not affected by disease setting, prostate-specific antigen level, or tumor volume. SUV_{peak} depended less on tracer uptake time than did TBR. **Conclusion:** For ^{18}F -DCFPyL PET/CT, SUV_{peak} correlates strongly with TBR. Therefore, it is a valuable simplified, semiquantitative measurement in patients with low-volume PCa ($<200\text{ cm}^3$). SUV_{peak} can therefore be applied in ^{18}F -DCFPyL PET assessment as an imaging biomarker to characterize tumors and to monitor treatment outcomes.

Key Words: ^{18}F -DCFPyL; PSMA; prostate cancer; SUVs; tumor-to-blood ratio

J Nucl Med 2021; 62:1264–1269
DOI: 10.2967/jnumed.120.260232

Received Nov. 12, 2020; revision accepted Jan. 3, 2021.
For correspondence or reprints, contact Yves J.L. Bodar (y.j.bodar@amsterdamumc.nl).
Published online January 28, 2021.
COPYRIGHT © 2021 by the Society of Nuclear Medicine and Molecular Imaging.

Prostate cancer (PCa) is the second most prevalent type of cancer in men worldwide (1). Conventional imaging studies such as CT, bone scintigraphy, and MRI have moderate sensitivity for the detection of PCa metastases (2,3). The recent prostate-specific membrane antigen (PSMA) PET/CT scans are showing more promising results in detecting metastases and in primary staging but especially in the recurrent stage of the disease (4,5). In addition, PSMA tracers are most commonly labeled with ^{68}Ga (i.e., ^{68}Ga -PSMA-11) or ^{18}F (^{18}F -DCFPyL or ^{18}F -PSMA-1007) (6).

Recent studies demonstrated a benefit from using semiquantitative measures of radiolabeled PSMA ligand uptake on PET for prognostication, as an imaging biomarker to characterize tumors and monitor treatment outcomes (7,8). A requisite for reliable clinical use of semiquantitative PET uptake parameters is that they correlate with the underlying tracer kinetics in vivo (9). For ^{18}F -DCFPyL uptake, our group recently validated the tumor-to-blood ratio (TBR) as the preferred simplified method, demonstrating a strong correlation with the reference pharmacokinetic parameter based on Patlak analyses (10,11). We observed that for ^{18}F -DCFPyL, high tumor volumes ($1,000$ – $2,000\text{ cm}^3$) had an effect on the tracer plasma input functions. This effect renders SUV invalid for such patients, as it assumes that plasma input functions between patients are similar. In contrast to SUV, using TBR can correct for differences in plasma input functions between patients. Unfortunately, TBR poses some disadvantages (Table 1), as it depends more on uptake interval, has worse repeatability, and is more labor-intensive than SUV (12–14).

The extraordinarily high tumor volumes that affected ^{18}F -DCFPyL kinetics in previous studies are relatively rare and seen only in end-stage disease (15,16). Even in patients with metastasized castration-resistant PCa (mCRPC), only 6.2% have a tumor volume of 500 cm^3 or higher (17). In clinical practice, most patients with PCa who undergo PSMA PET/CT scan in both the primary-PCa and the recurrent-PCa setting have relatively low-volume disease (18–20). We hypothesized that SUV might be a valid alternative to TBR for lesional ^{18}F -DCFPyL quantification in most PCa patients with a low disease burden, defined as 200 cm^3 or less. The aim of this study was to validate SUV against TBR in PCa patients with commonly seen low tumor burdens and potentially define a tumor volume threshold below which SUV remains a valid parameter for ^{18}F -DCFPyL uptake quantification. Second, we illustrated the influence of uptake interval on SUV versus TBR based on the hypothesis that SUV will be less dependent than TBR on uptake intervals.

TABLE 1
Advantages and Disadvantages of SUV vs. TBR

SUV		TBR	
Pro	Con	Pro	Con
Is single measurement without additional data acquisition and evaluation (i.e., no assessment of blood activity is needed) (16,31)	Is susceptible to errors in scanner and dose calibration, correlates insufficiently between systemic distribution volume and body weight, and causes interstudy variability of arterial input function (12)	Is validated surrogate of metabolic uptake rate K_i (16,31)	Needs second region of interest to derive blood activity concentration and is more dependent than SUV on uptake time (12)
Has less variability, given radiotracer clearance (13), therefore providing better repeatability and better response assessment when analyzing effect of PSMA-targeted radioligand therapies (14)	Has no reproducible relationship with K_i (16)	Is SUV normalized to radiotracer concentration in blood plasma available for influx in tissue (32); this immediately poses con because blood plasma should be normal tissue with constant and stable radiotracer volume (12)	Has worse repeatability than SUV, potentially hampering response assessment; image reconstruction via point-spread function worsens this repeatability significantly, whereas SUV _{peak} is not affected (14)

MATERIALS AND METHODS

Patients

A retrospective analysis was performed on 124 patients with histologically proven PCa treated at the Amsterdam University Medical Centers (location VUmc) [Vrije Universiteit Medical center]). As an inclusion criterion, all patients who underwent a ¹⁸F-DCFPyL PET/CT scan within variable stages of disease were eligible. We performed a secondary analysis of data pooled from 4 studies conducted from November 2017 and August 2019 that encompassed patients with primary PCa, recurrent PCa, and mCRPC (5,14,16,21). All 4 studies were approved by the local medical ethical committee (review numbers 2017.543 and 2017.565 [combined for 2 studies] and 2018.453). The main analysis included 116 patients, with 81 patients receiving a ¹⁸F-DCFPyL PET/CT scan for primary PCa, 25 patients having a ¹⁸F-DCFPyL PET/CT scan in the recurrent setting, and 10 patients with mCRPC. The 81 patients who received a ¹⁸F-DCFPyL PET/CT scan in the primary-staging setting were patients who underwent ¹⁸F-DCFPyL PET/CT before surgery, so it is assumed that these patients had low-volume disease. Additionally, dynamic PET acquisitions from 8 patients with end-stage, metastasized CRPC were available and used for time-dependent analyses. All subjects gave written informed consent when enrolling in the original studies, which were approved by the institutional review board of VUmc, explicitly allowing (by both the patients and the review board) secondary analysis of their study data.

Image Acquisition

¹⁸F-DCFPyL was synthesized under good-manufacturing-practice conditions at the on-site cyclotron (22,23). Images were acquired using an Ingenuity TF PET/CT system (Philips Healthcare). The scan trajectory included mid thigh to skull base (static scans), with 4 min per bed position. All PET scans were combined with a low-dose or high-dose CT scan without intravenous contrast medium (30–110 mAs, 110–130 kV). Images were corrected for decay, scatter, random coincidences, and photon attenuation. Images were reconstructed with a binary-large-object-based ordered-subsets expectation maximization algorithm (3 iterations; 33 subsets).

Scan Assessment

The PET/CT scans of the primary cohort of 116 patients were analyzed, and all tumor deposits were delineated according to the

available clinical reports. All local tumors, lymph node metastases, and bone or visceral metastases were delineated individually as a volume of interest. An automatically generated SUV_{peak} isocontour of 50% with correction for background uptake was used to create the volume of interest in the tissues suspected of malignancy (24). Per volume of interest, tumor volume (in cm³) and SUV_{peak} were calculated. SUV_{peak} was chosen because it is less variable and has less inherent inpatient bias than SUV_{max} and does not require exact tumor borders as compared with SUV_{mean} (25,26). Per patient, total tumor volume (TTV) and total lesion uptake were calculated. TTV was defined as the sum of the delineated tumor volumes within 1 patient, and total lesion uptake was defined as the lesional mean uptake multiplied by the lesion volume, as a percentage of injected dose. Additionally, a 3 × 3 volume of interest was placed in the ascending aorta on 5 consecutive slices of the CT scan (27), yielding the blood-pool activity used for the calculation of TBR. TBR was determined by dividing the SUV_{peak} of the lesions by the SUV_{peak} of the aortic blood pool. Delineation was performed using the in-house-developed ACCURATE tool (28).

Effect of Uptake Interval on SUV Versus TBR

In a subanalysis, 8 patients with mCRPC who were dynamically scanned with ¹⁸F-DCFPyL PET/CT were reinvestigated to define their correlation of SUV_{peak} versus TBR over time (16). These patients received a low-dose CT scan (30 mAs, 120 kV) followed by a dynamic PET scan from 0 to 120 min after injection of ¹⁸F-DCFPyL (median dose, 313 MBq; range, 292–314 MBq), with a 30-min break in acquisitions, for patient comfort, 60 min after the first dynamic scan. Similarly to the scans of the main cohort, data were corrected for decay, dead time, scatter, and random coincidences; photon-attenuation correction was performed using the low-dose CT scans. Patient demographic data can be found in the primary publication (16).

Statistical Analysis

Numeric variables were summarized with medians and interquartile ranges; categorical variables were summarized with proportions and percentages. Data were assessed for normality using histograms. The most intense lesion with the highest SUV_{peak} within each patient was compared with the corresponding TBR by linear regression analysis (R^2) using the Pearson correlation coefficient and the Spearman rank

correlation coefficient. To assess whether uptake time (time from injection to scan start) affected the correlation between SUV and TBR, 3 uptake-interval groups were identified: less than 110 min, 110–130 min, and more than 130 min. The significance level was set at a *P* value of less than 0.05. Statistical analysis was performed using SPSS Statistics (version 26; IBM) for Windows (Microsoft) and Prism (version 8.0.0; GraphPad Software) for Windows.

RESULTS

Patient Characteristics

In total, 116 patients were included in the main analysis of this study. Patients had a median age of 68.0 y (range, 49.0–84.0 y). The ¹⁸F-DCFPyL PET/CT scans from 81 primary-PCa patients, 25 recurrent-PCa patients, and 10 patients with mCRPC were analyzed. Therapy before ¹⁸F-DCFPyL PET/CT was given to 35 of 116 (30.1%) patients: in the recurrent-PCa group, 14 of 25 (56.0%) patients received radical prostatectomy, 3 of 25 (12.0%) received androgen deprivation therapy combined with chemotherapy, and 8 of 25 (28.0%) received radiotherapy. In the mCRPC group, 7 of 10 (70.0%) patients received androgen deprivation therapy alone, 3 of 10 (30.0%) received androgen deprivation therapy and chemotherapy, and in 1 patient prior therapy was unknown. Further details of the study population are provided in Table 2. Demographics per disease setting are presented in Supplemental Table 1 (supplemental materials are available at <http://jnm.snmjournals.org>).

PET Imaging Results

The median uptake time was 120.2 min (range, 103.1–163.7 min), with a median injected dose of 314.0 MBq (range, 250.4–330.9 MBq). In total, 436 lesions were delineated (median, 1 per patient; range, 1–66). Sixty-nine of 116 (59.4%) patients had a total of 1 lesion, 35 of 116 (30.1%) had 2–5 lesions, and 11 of 116 (9.4%) had more than 5 lesions. Of the 436 lesions, 105 (24.1%) were intraprostatic, 189 (43.3%) bone, 141 (32.3%) lymph node, and 1 (0.2%) pulmonary. Median TTV was 8.1 cm³ (range, 1.4–79.2 cm³), 24.4 cm³ (range, 2.9–173.4 cm³), and 21.5 cm³ (range, 5.4–473.1 cm³), respectively, for the primary-disease, recurrent-PCa and mCRPC groups. Characteristics stratified per disease setting are detailed in Table 3.

TABLE 2
Baseline Patient Characteristics

Characteristic	Data
<i>n</i>	116
Age (y)	68.0 (49.0–84.0)
Weight (kg)	82.5 (50.0–122.0)
Height (cm)	180.0 (155.0–198.0)
PSA level (ng/mL)	9.7 (0.5–2,790.0)
Gleason score (cumulative)	7 (6–9)
Scan indication	81/116 (69.8%)
Staging	
Recurrent PCa	25/116 (21.6%)
mCRPC	10/116 (8.6%)
Therapy before PET	34/116 (29.3%)

Qualitative data are number and percentage; continuous data are median and range.

Aortic SUV_{peak} as Function of TTV and PSA

On a patient level, there was no correlation between the blood-pool (aorta) SUV_{peak} and the TTV ($R^2 = 0.001$). The blood-pool SUV_{peak} remained stable around increasing TTVs (Fig. 1A). Similarly, no correlation was noted between blood-pool SUV_{peak} and serum PSA (as a potential surrogate marker for disease load) at the time of the scan ($R^2 = 0.007$; Fig. 1B).

Correlative Analysis Between SUV_{peak} and TBR

Overall, SUV_{peak} correlated with TBR with an R^2 of 0.931 (most intense lesion per patient, all patients included; Fig. 2). When plotted separately, SUV_{peak} still correlated with TBR, with an R^2 of 0.950, 0.902, and 0.957, respectively, for the primary, recurrent, and mCRPC groups (Fig. 3). Linear regression slopes were 1.10, 0.90, and 1.26, respectively, for the primary, recurrent, and mCRPC groups. PSA versus SUV_{peak} (most intense lesion) and PSA versus TBR per patient did not correlate ($r = 0.13$, $P = 0.18$, and $r = 0.14$, $P = 0.13$, respectively).

SUV_{peak} Versus TBR over Injection Time

Three patient groups were generated to stratify postinjection scan time in minutes, with the first group being less than 110 min, the second 110–130 min, and the third more than 130 min after radiotracer injection. Figure 4 shows the linear regression analysis; all 3 groups showed a strong correlation on Spearman testing, with an R^2 of 0.907, 0.925, and 0.955 for the first, second, and third groups, respectively. The slopes of these groups were 1.299, 1.053, and 0.9823, respectively. For the subanalysis of 8 mCRPC patients who received a dynamic scan spanning 120 min, Figure 5 shows the development of SUV_{peak} versus TBR over time. In these 8 patients, the SUV_{peak} of the maximally intense lesion showed a stable development after 20 min, whereas TBR showed a gradual increase until 120 min.

DISCUSSION

In this study, we assessed the use of SUV_{peak} as a simplified method for quantification of tumor PSMA expression on ¹⁸F-DCFPyL PSMA PET/CT scans in a combined cohort of PCa patients from primary-staging, recurrent-PCa, and mCRPC settings. A high correlation between SUV_{peak} and TBR was found for each group in the cohort, as well as a high correlation between SUV and TBR in the pooled data. The correlation between SUV_{peak} and TBR in the present study thus implicates SUV_{peak} as a suitable, simplified method to quantify ¹⁸F-DCFPyL PSMA PET/CT in patients with a TTV below 200 cm³, based on the earlier findings that TBR correlates with parameters from full kinetic modeling (16).

When the patient cohort was stratified for tracer uptake time, all subgroups showed a correlation between SUV_{peak} and TBR. Nonetheless, intergroup evaluation showed more favorable slopes (i.e., a slope closest to 1) for uptake times above 110 min. This finding is in line with that of Wondergem et al., who found that a scan time of 120 min was optimal for visualizing an increased number of lesions (29). The weaker correlation for the lower uptake times can be explained by the results from our subanalysis of 8 additional mCRPC patients, which showed that SUV_{peak} increased rapidly after injection and stabilized earlier than TBR. When one is visually interpreting the curve in Figure 5, SUV_{peak} seems to be less dependent on uptake interval. In addition, SUV_{peak} has better repeatability than TBR, especially in lesions with a small volume (defined as <4.2 cm³), as reported by Jansen et al. (14). Therefore, SUV_{peak} may be a more suitable measure for clinical practice than

TABLE 3
Baseline Scan Characteristics

Characteristic	Primary	Recurrent PCa	mCRPC
Administered radiotracer (MBq)	314.1 (250.4–329.3)	311.4 (289.6–328.2)	314.9 (280.0–330.9)
Net time between injection and scan start (min)	118.5 (57.1–163.7)	119.6 (75.8–149.4)	119.9 (118.0–141.2)
Maximal SUV _{peak} per patient	6.7 (2.0–58.7)	11.8 (1.8–62.3)	17.4 (2.8–53.7)
TTV (cm ³)	8.1 (1.4–79.2)	24.4 (2.9–173.4)	21.5 (5.4–473.1)
Total lesion uptake (percentage injected dose)			
Prostate	0.042 (0.004–0.695)	0.026 (0.003–0.457)	0.069 (0.015–0.288)
Whole body	0.042 (0.004–0.704)	0.108 (0.007–1.268)	0.123 (0.011–0.549)

Data are median and range.

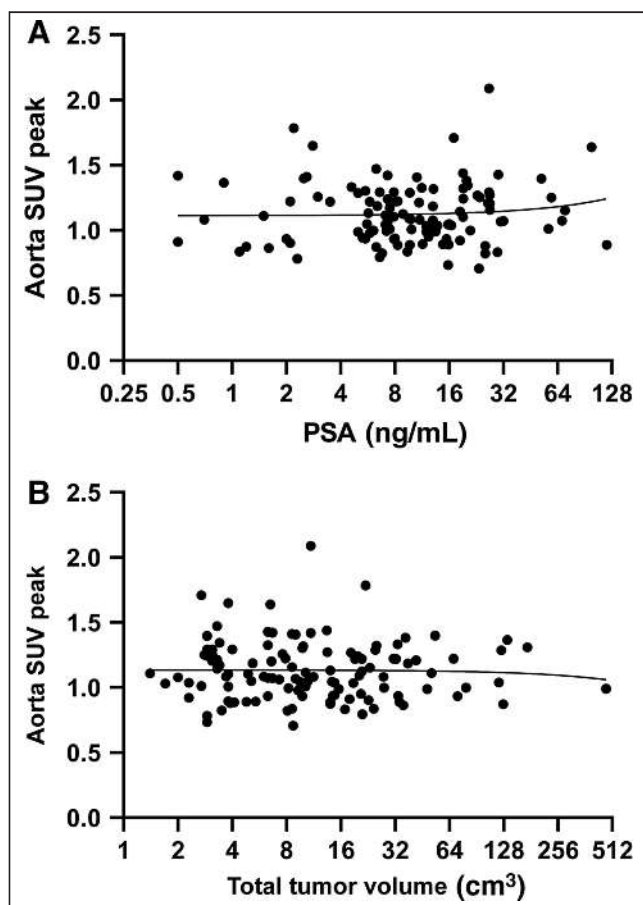


FIGURE 1. (A) Linear regression of aortic SUV_{peak} vs. PSA with exclusion of the PSA outlier on log₂-scaled *x*-axis. Slightly positive slope of 0.001 is visible, with $R^2 = 0.007$. With aortic SUV_{peak} of 0.994, outlier with PSA of 2,790.0 ng/mL did not alter results and was therefore excluded from graph. (B) Linear regression of aortic SUV_{peak} vs. TTV on log₂-scaled *x*-axis. Both R^2 and correlation coefficient r were highly insignificant ($R^2 = 0.001$; $r = 0.038$).

TBR, given the heterogeneity of scan protocols across hospitals. Nevertheless, TBR stands as a reliable method of semiquantification for the whole spectrum of TTVs, but only when adhering to strict uptake timing protocols (16).

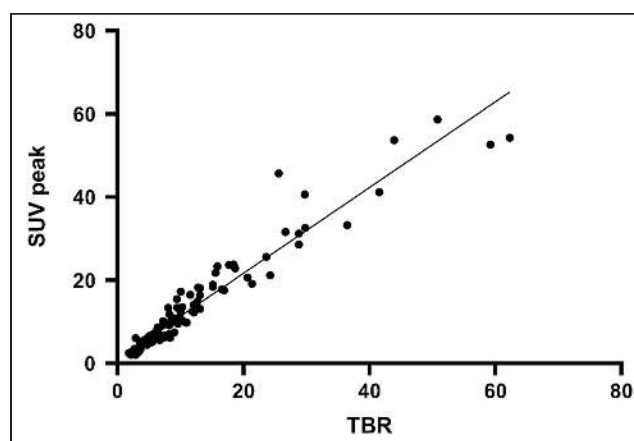


FIGURE 2. Linear regression of maximal SUV_{peak} vs. TBR for most intense lesion suspected of being PCa on ¹⁸F-DCFPyL PET/CT in 114 patients. R^2 measured 0.931, and slope of regression was 1.032.

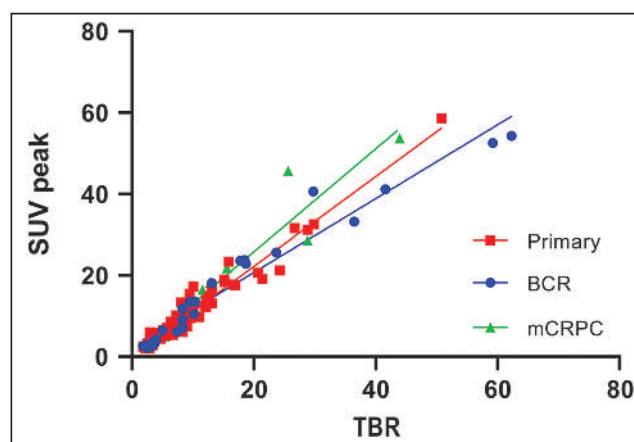


FIGURE 3. Linear regression of SUV_{peak} vs. TBR for most intense lesion suspected of being PCa on ¹⁸F-DCFPyL PET/CT, with stratification for different groups: primary PCa, biochemically recurrent PCa (BCR), and mCRPC. This plot emphasizes high correlation for primary-PCa group ($R^2 = 0.957$) and recurrent-PCa group ($R^2 = 0.950$) and somewhat lower correlation for mCRPC group ($R^2 = 0.902$), as individuals.

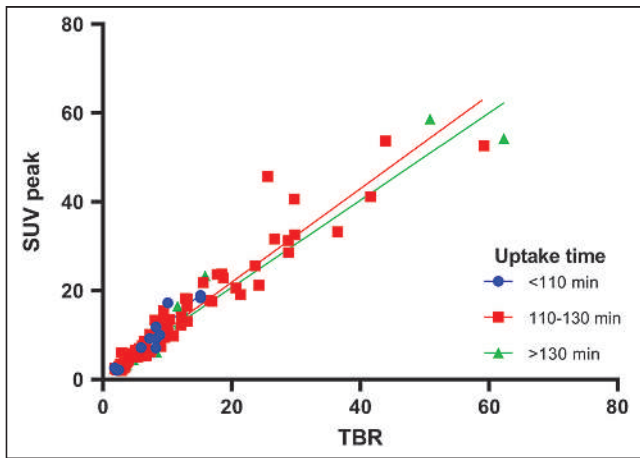


FIGURE 4. Linear regression of SUV_{peak} vs. TBR for most intense lesion suspected of being PCa on ^{18}F -DCFPyL PET/CT, stratified for injection time. R^2 in ascending order for uptake time was 0.907, 0.925, and 0.955.

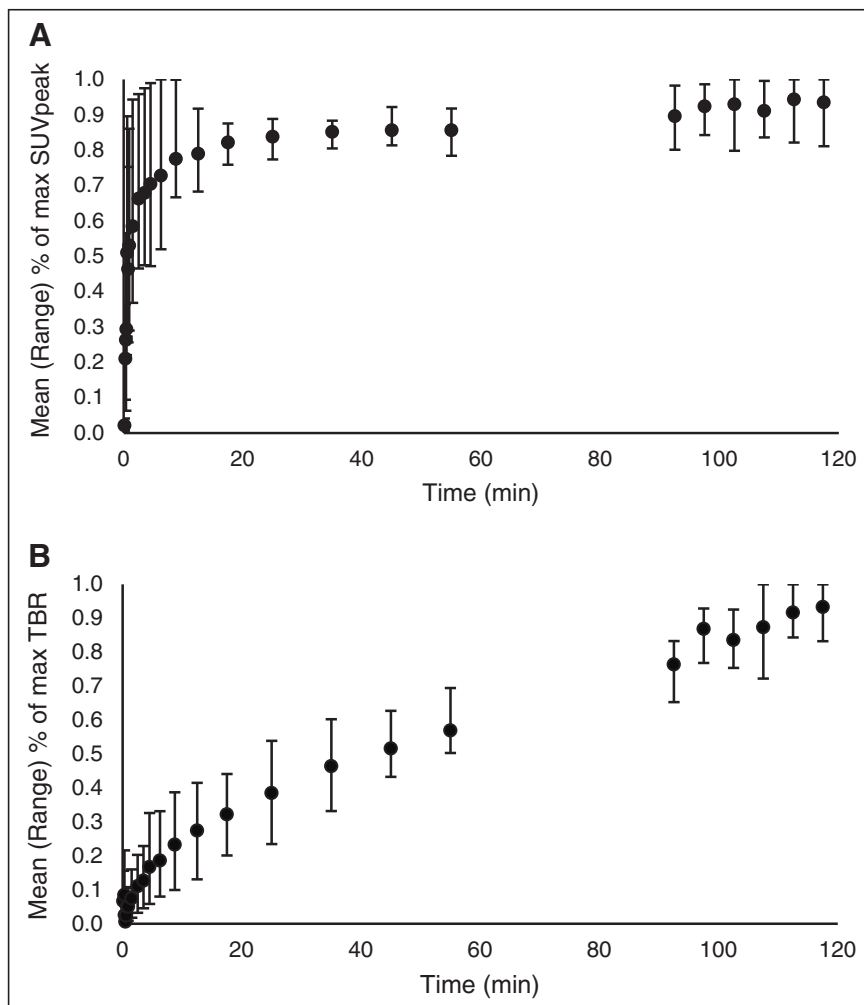


FIGURE 5. Development of mean and range for SUV_{peak} and TBR for most intense lesions as function of uptake interval in 8 mCRPC patients. SUV and TBR are presented as percentage of maximum value measured per respective patient.

The sink effect, as described by Jansen et al. and Gaertner et al. (16,30), was observed only in mCRPC patients with extreme TTVs ranging up to 1,000 or 2,000 cm^3 scanned in a research setting. Following the sink effect hypothesis, the aortic SUV_{peak} is expected to decrease with increasing tumor load (TTV), as was observed in the aforementioned studies. In another study, from Werner et al., conducted on patients with lower PCa TTVs (median, 4.8 cm^3 ; range, 0.3–98.4 cm^3), the absence of a sink effect was noted after analyzing 50 ^{18}F -DCFPyL PET/CT scans (20). Like our study, this cohort included a variety of indications to perform a PSMA PET/CT scan, but no patient presented with a TTV higher than 100 cm^3 . As in the study by Werner et al., a clear cutoff for a sink effect was not established in the present paper, since no measurable effect on ^{18}F -DCFPyL input functions was noticed (Fig. 1B), possibly because only 1 patient with a high TTV (>200 cm^3) was included. Still, a very small slope was observed in both linear regressions. In particular, the trend observed in aortic SUV_{peak} versus TTV may implicate a minor sink effect in larger PCa metastatic volumes caused by increased TTVs that decrease blood-pool activity, as described by Cysouw et al. (15). Since most included patients had either primary PCa or a lower TTV, the nonsignificant correlations can strengthen the argument that

SUV is an applicable semiquantitative measure for most clinical PSMA scans. Still, the validity of TBR has previously been demonstrated (19).

This study carried the limitations inherent in a retrospective study, including a potential selection bias. We tried to overcome this selection bias by including a heterogeneous group of indications for ^{18}F -DCFPyL PSMA PET/CT scans. Second, a pharmacokinetic study (with arterial and venous blood samples) should ideally be performed on the entire cohort to verify our results. Such a study would validate SUV_{peak} versus actual pharmacodynamics but would be very labor intensive for the number of patients we included.

Our findings imply that SUV_{peak} is a valid, simplified method to quantify ^{18}F -DCFPyL PSMA PET/CT scans in patients with PCa and a TTV below 200 cm^3 . Unfortunately, a cutoff for the sink effect could not be identified because of the low number of patients with high TTVs. Therefore further research to find a sink effect is needed in patients with a broad range of TTVs, with at least a reasonable number of TTVs that have a volume above 200 cm^3 , possibly even above 500 cm^3 . Therefore, we recommend use of SUV_{peak} when tumor volumes are less than 200 cm^3 , as was proven accurate in this study. In current clinical practice, this TTV encompasses most patients receiving PSMA PET scans (14,19). Still, TBR remains a reliable, simplified quantification method in the full spectrum of TTVs, provided that injection-to-scan intervals are above 110 min.

CONCLUSION

For ^{18}F -DCFPyL PET/CT, SUV is a valuable simplified, semi-quantitative measurement in patients with low-volume PCa ($<200\text{ cm}^3$) and correlates strongly with TBR. SUV_{peak} can therefore be potentially applied to improve the precision of ^{18}F -DCFPyL PSMA PET/CT scans, as an imaging biomarker to characterize tumors and monitor treatment outcomes. Although the presence of a sink effect has been demonstrated for ^{18}F -DCFPyL PET/CT previously, we could not identify the threshold TTV for this effect within our real-life clinical cohort.

DISCLOSURE

Ronald Boellaard received a grant from Philips Healthcare, outside the submitted work. No other potential conflict of interest relevant to this article was reported.

ACKNOWLEDGMENTS

We gratefully acknowledge the patients for their participation in this study.

KEY POINTS

QUESTION: In clinical practice, do TBRs correlate with SUVs in quantitative evaluation of ^{18}F -DCFPyL PET/CT for patients with a low PCa volume?

PERTINENT FINDINGS: In ^{18}F -DCFPyL PET/CT, TBRs correlate strongly with SUVs. Therefore, TBR is a valuable simplified, semi-quantitative measurement for patients with low-volume PCa ($<200\text{ cm}^3$).

IMPLICATIONS FOR PATIENT CARE: TBRs and SUVs can be used as simplified methods for quantitative assessment of ^{18}F -DCFPyL PET/CT, enabling reliable interpretation of PET/CT scans and use of tracer uptake as an imaging biomarker.

REFERENCES

- Bray F, Ferlay J, Soerjomataram I, Siegel RL, Torre LA, Jemal A. Global cancer statistics 2018: GLOBOCAN estimates of incidence and mortality worldwide for 36 cancers in 185 countries. *CA Cancer J Clin*. 2018;68:394–424.
- Hövels AM, Heesakkers RA, Adang EM, et al. The diagnostic accuracy of CT and MRI in the staging of pelvic lymph nodes in patients with prostate cancer: a meta-analysis. *Clin Radiol*. 2008;63:387–395.
- Shen G, Deng H, Hu S, Jia Z. Comparison of choline-PET/CT, MRI, SPECT, and bone scintigraphy in the diagnosis of bone metastases in patients with prostate cancer: a meta-analysis. *Skeletal Radiol*. 2014;43:1503–1513.
- Perera M, Papa N, Roberts M, et al. Gallium-68 prostate-specific membrane antigen positron emission tomography in advanced prostate cancer: updated diagnostic utility, sensitivity, specificity, and distribution of prostate-specific membrane antigen-avid lesions—a systematic review and meta-analysis. *Eur Urol*. 2020;77:403–417.
- Jansen BHE, Bodar YJL, Zwezerijnen GJC, et al. Pelvic lymph-node staging with ^{18}F -DCFPyL PET/CT prior to extended pelvic lymph-node dissection in primary prostate cancer: the SALT trial. *Eur J Nucl Med Mol Imaging*. 2021;48:509–520.
- Ahmadzadehfar H, Essler M. Prostate-specific membrane antigen imaging: a game changer in prostate cancer diagnosis and therapy planning. *Eur Urol*. 2020;77:418–419.
- Roberts MJ, Morton A, Donato P, et al. ^{68}Ga -PSMA PET/CT tumour intensity pre-operatively predicts adverse pathological outcomes and progression-free survival in localised prostate cancer. *Eur J Nucl Med Mol Imaging*. 2021;48:477–482.
- Uprimny C, Kroiss AS, Decristoforo C, et al. ^{68}Ga -PSMA-11 PET/CT in primary staging of prostate cancer: PSA and Gleason score predict the intensity of tracer accumulation in the primary tumour. *Eur J Nucl Med Mol Imaging*. 2017;44:941–949.
- Prasad V, Steffen IG, Diederichs G, Makowski MR, Wust P, Brenner W. Biodistribution of [^{68}Ga]PSMA-HBED-CC in patients with prostate cancer: characterization of uptake in normal organs and tumour lesions. *Mol Imaging Biol*. 2016;18:428–436.
- Jansen BHE, Yaqub M, Cysouw MCF, et al. Reply: Quantification of ^{18}F -DCFPyL uptake: TBR versus Patlak's analysis. *J Nucl Med*. 2019;60:1834–1835.
- Patlak CS, Blasberg RG. Graphical evaluation of blood-to-brain transfer constants from multiple-time uptake data: generalizations. *J Cereb Blood Flow Metab*. 1985;5:584–590.
- Hoekstra CJ, Paglianiti I, Hoekstra OS, et al. Monitoring response to therapy in cancer using [^{18}F]-2-fluoro-2-deoxy-D-glucose and positron emission tomography: an overview of different analytical methods. *Eur J Nucl Med*. 2000;27:731–743.
- Chen W, Dilisizian V. PET assessment of vascular inflammation and atherosclerotic plaques: SUV or TBR? *J Nucl Med*. 2015;56:503–504.
- Jansen BHE, Cysouw MCF, Vis AN, et al. Repeatability of quantitative ^{18}F -DCFPyL PET/CT measurements in metastatic prostate cancer. *J Nucl Med*. 2020;61:1320–1325.
- Cysouw MCF, Jansen BHE, Yaqub M, et al. Letter to the editor re: semiquantitative parameters in PSMA-targeted PET imaging with [^{18}F]DCFPyL: impact of tumor burden on normal organ uptake. *Mol Imaging Biol*. 2020;22:15–17.
- Jansen BHE, Yaqub M, Voortman J, et al. Simplified methods for quantification of ^{18}F -DCFPyL uptake in patients with prostate cancer. *J Nucl Med*. 2019;60:1730–1735.
- Seifert R, Kessel K, Schlack K, et al. PSMA PET total tumor volume predicts outcome of patients with advanced prostate cancer receiving [^{177}Lu]Lu-PSMA-617 radioligand therapy in a bicentric analysis. *Eur J Nucl Med Mol Imaging*. 2021;48:1200–1210.
- Mottet N, van den Bergh RCN, Briers E, et al. EAU-EANM-ESTRO-ESUR-SIOG guidelines on prostate cancer: 2020 update. Part 1: screening, diagnosis, and local treatment with curative intent. *Eur Urol*. 2021;79:243–262.
- von Klot CJ, Merseburger AS, Boker A, et al. ^{68}Ga -PSMA PET/CT imaging predicting intraprostatic tumor extent, extracapsular extension and seminal vesicle invasion prior to radical prostatectomy in patients with prostate cancer. *Nucl Med Mol Imaging*. 2017;51:314–322.
- Werner RA, Bundschuh RA, Bundschuh L, et al. Semiquantitative parameters in PSMA-targeted PET imaging with [^{18}F]DCFPyL: impact of tumor burden on normal organ uptake. *Mol Imaging Biol*. 2020;22:190–197.
- Jansen BHE, Jansen RW, Wondergem M, et al. Lesion detection and interobserver agreement with advanced image reconstruction for ^{18}F -DCFPyL PET/CT in patients with biochemically recurrent prostate cancer. *J Nucl Med*. 2020;61:210–216.
- Bouvet V, Wuest M, Jans HS, et al. Automated synthesis of [^{18}F]DCFPyL via direct radiofluorination and validation in preclinical prostate cancer models. *EJNMMI Res*. 2016;6:40.
- Ravert HT, Holt DP, Chen Y, et al. An improved synthesis of the radiolabeled prostate-specific membrane antigen inhibitor, [^{18}F]DCFPyL. *J Labelled Comp Radiopharm*. 2016;59:439–450.
- Frings V, van Velden FHP, Velasquez LM, et al. Repeatability of metabolically active tumor volume measurements with FDG PET/CT in advanced gastrointestinal malignancies: a multicenter study. *Radiology*. 2014;273:539–548.
- Akamatsu G, Ikari Y, Nishida H, et al. Influence of statistical fluctuation on reproducibility and accuracy of SUVmax and SUVpeak: a phantom study. *J Nucl Med Technol*. 2015;43:222–226.
- Lodge MA, Chaudhry MA, Wahl RL. Noise considerations for PET quantification using maximum and peak standardized uptake value. *J Nucl Med*. 2012;53:1041–1047.
- Jansen BHE, Kramer GM, Cysouw MCF, et al. Healthy tissue uptake of ^{68}Ga -prostate-specific membrane antigen, ^{18}F -DCFPyL, ^{18}F -fluoromethylcholine, and ^{18}F -dihydrotestosterone. *J Nucl Med*. 2019;60:1111–1117.
- Boellaard R. Quantitative oncology molecular analysis suite: ACCURATE [abstract]. *J Nucl Med*. 2018;59(suppl 1):1753.
- Wondergem M, van der Zant FM, Knol RJJ, Lazarenko SV, Pruim J, de Jong IJ. ^{18}F -DCFPyL PET/CT in the detection of prostate cancer at 60 and 120 minutes: detection rate, image quality, activity kinetics, and biodistribution. *J Nucl Med*. 2017;58:1797–1804.
- Gaertner FC, Halabi K, Ahmadzadehfar H, et al. Uptake of PSMA-ligands in normal tissues is dependent on tumor load in patients with prostate cancer. *Oncotarget*. 2017;8:55094–55103.
- Hofheinz F, Hoff J, Steffen IG, et al. Comparative evaluation of SUV, tumor-to-blood standard uptake ratio (SUR), and dual time point measurements for assessment of the metabolic uptake rate in FDG PET. *EJNMMI Res*. 2016;6:53.
- van den Hoff J, Oehme L, Schramm G, et al. The PET-derived tumor-to-blood standard uptake ratio (SUR) is superior to tumor SUV as a surrogate parameter of the metabolic rate of FDG. *EJNMMI Res*. 2013;3:77.

Detection of Early Progression with ^{18}F -DCFPyL PET/CT in Men with Metastatic Castration-Resistant Prostate Cancer Receiving Bipolar Androgen Therapy

Mark C. Markowski¹, Pedro Isaacsson Velho^{1,2}, Mario A. Eisenberger¹, Martin G. Pomper^{1,3}, Kenneth J. Pienta⁴, Michael A. Gorin⁴, Emmanuel S. Antonarakis¹, Samuel R. Denmeade¹, and Steven P. Rowe^{1,3}

¹Department of Oncology, Sidney Kimmel Comprehensive Cancer Center at Johns Hopkins, Baltimore, Maryland; ²Department of Medical Oncology, Hospital Moinhos de Vento, Porto Alegre, Brazil; ³Russel H. Morgan Department of Radiology and Radiological Science, Johns Hopkins University School of Medicine, Baltimore, Maryland; and ⁴James Buchanan Brady Urological Institute and Department of Urology, Johns Hopkins University School of Medicine, Baltimore, Maryland

Bipolar androgen therapy (BAT) is an emerging treatment for metastatic castration-resistant prostate cancer (mCRPC). ^{18}F -DCFPyL is a small-molecule PET radiotracer targeting prostate-specific membrane antigen (PSMA). We analyzed the utility of ^{18}F -DCFPyL PET/CT in determining clinical response to BAT. **Methods:** Six men with mCRPC receiving BAT were imaged with ^{18}F -DCFPyL PET/CT at baseline and after 3 mo of treatment. Progression by PSMA-targeted PET/CT was defined as the appearance of any new ^{18}F -DCFPyL-avid lesion. **Results:** Three of 6 (50%) patients had progression on ^{18}F -DCFPyL PET/CT. All 3 had stable disease or better on contemporaneous conventional imaging. Radiographic progression on CT or bone scanning was observed within 3 mo of progression on ^{18}F -DCFPyL PET/CT. For the 3 patients who did not have progression on ^{18}F -DCFPyL PET/CT, radiographic progression was not observed for at least 6 mo. **Conclusion:** New radiotracer-avid lesions on ^{18}F -DCFPyL PET/CT in men with mCRPC undergoing BAT can indicate early progression.

Key Words: PSMA; testosterone; early progression

J Nucl Med 2021; 62:1270–1273
DOI: 10.2967/jnumed.120.259226

The imaging of prostate cancer in many parts of the world has recently been revolutionized by the introduction of small-molecule PET radiotracers that bind to prostate-specific membrane antigen (PSMA) (1). PSMA is a transmembrane glycoprotein that is expressed in most prostate cancers (2). Those agents, which include both ^{68}Ga -labeled (e.g., ^{68}Ga -PSMA-11 (3)) and ^{18}F -labeled (e.g., ^{18}F -DCFPyL (4)) compounds, have been shown to have high rates of detection of sites of prostate cancer in a variety of disease states (5).

There is an interplay between androgen signaling and PSMA expression in which blockade of the androgen-signaling pathway leads to upregulation of PSMA (6). Varying responses to androgen-axis-targeted therapies have been observed on serial PSMA-targeted PET studies (7), making it difficult to assess response to

such therapies. To date, changes in serial PSMA-targeted PET have not been described in the context of bipolar androgen therapy (BAT).

BAT is being tested as a novel treatment for men with metastatic castration-resistant prostate cancer (mCRPC). Testosterone is administered to supraphysiologic circulating levels, which subsequently decrease over a 28-d cycle back to near-castrate levels (8). All men are maintained on androgen deprivation to suppress endogenous testosterone production from the testes. Several studies have demonstrated the efficacy of BAT as a treatment option for mCRPC patients (9–11). Measuring the clinical benefit of BAT using changes in prostate-specific antigen (PSA) is difficult because radiographic regression of disease has been observed, with stable or rising PSA values (10,11).

A novel imaging strategy to determine patients at high risk of progression on BAT is needed. In this pilot study, we examined changes in ^{18}F -DCFPyL PET imaging after treatment with BAT in men with mCRPC.

MATERIALS AND METHODS

^{18}F -DCFPyL PET/CT imaging was obtained as part of an Institutional Review Board–approved prospective substudy on 2 clinical trials for men initiating treatment with BAT (ClinicalTrials.gov identifiers NCT02286921 and NCT03554317). Written informed consent was obtained from all participants. All participants had mCRPC and prior treatment with at least 1 novel androgen receptor–targeted therapy. PET/CT images were acquired on either a Biograph mCT 128-slice scanner (Siemens Healthineers) or a Discovery RX 64-slice scanner (GE Healthcare) using 3D emission mode with CT-based attenuation correction. Scans were initiated 60 min after the intravenous infusion of 333 MBq (9 mCi) of ^{18}F -DCFPyL with a field of view from the mid thighs through the skull vertex. Images were reconstructed with standard ordered-subset expectation maximization.

All ^{18}F -DCFPyL PET/CT scans were interpreted by a single radiologist who was masked to the details of the patient's disease status while on BAT. Radiotracer uptake outside the normal biodistribution of ^{18}F -DCFPyL was categorized according to the PSMA Reporting and Data System, version 1.0, interpretive framework, and lesions that were category 3A/3B/4/5 were considered positive for prostate cancer (12). SUV_{max} was recorded for all lesions on baseline and follow-up scans (Supplemental Table 1; supplemental materials are available at <http://jnm.snmjournals.org>). According to the study protocol, patients underwent ^{18}F -DCFPyL PET/CT imaging before starting BAT and

Received Oct. 24, 2020; revision accepted Jan. 3, 2021.
For correspondence or reprints, contact Mark C. Markowski (mmarko12@jhmi.edu).

Published online January 15, 2021.

COPYRIGHT © 2021 by the Society of Nuclear Medicine and Molecular Imaging.

TABLE 1
Best Biochemical, Radiographic, and ¹⁸F-DCFPyL
Response After 3 Months of BAT

Patient	PSA change	Tumor change	PSMA result
1	93%	Not evaluable	No progression
2	-98%	-44%	No progression
3	-93%	-23%	No progression
4	1%	-11%	Progression
5	-55%	-2%	Progression
6	-63%	-25%	Progression

again after 3 cycles. Clinicians were masked to the results of ¹⁸F-DCFPyL PET/CT imaging, and those results were not used in clinical management.

Comparisons were made between the pretreatment and on-treatment PSMA-targeted PET/CT imaging to determine progression. PSMA progression was defined as having one or more new lesions deemed by the interpreting radiologist to be consistent with radiotracer-avid prostate cancer. Radiographic progression on conventional imaging was defined by RECIST, version 1.1 (soft-tissue lesions), and by Prostate Cancer Clinical Trials Working Group 3 guidelines (clinical and bone lesions), and objective response was defined using RECIST (13,14).

RESULTS

Six patients were enrolled. Five of the 6 (83.3%) began BAT on the same day as their baseline ¹⁸F-DCFPyL PET scan, and the final patient started BAT the following day. The interval from initiation of therapy to follow-up PET was a median of 84 d

(interquartile range, 83.25–87.75). At the time of the follow-up PET, repeat imaging was obtained with CT and bone scanning.

The best PSA and change in tumor response are listed for each patient in Table 1. Four of the 6 (66.7%) patients had a PSA₅₀ (decrease in PSA level by 50% from baseline) response, and 1 patient achieved an objective response on conventional imaging. We assessed each patient for progression on PSMA-targeted imaging. Three of the 6 (50.0%) patients had progression on ¹⁸F-DCFPyL PET/CT. A description of each ¹⁸F-DCFPyL PET/CT lesion is provided in Supplemental Table 1. None of the patients had evidence of radiographic progression on conventional imaging at the time of the follow-up ¹⁸F-DCFPyL PET/CT. Two patients, who achieved a PSA₉₀ response with stable disease on CT and bone scanning, had new lesions seen on ¹⁸F-DCFPyL PET. Neither patient with a PSA₉₀ (decrease in PSA level by 90% from baseline) response had progression on ¹⁸F-DCFPyL PET/CT. Maximum-intensity projections of the ¹⁸F-DCFPyL PET/CT for patients before and during treatment are shown in Figure 1. Many radiotracer-avid lesions became less intense after BAT. For instance, patient 1 had a complete PSMA response to BAT (i.e., 100% reduction in SUV_{max} across all PSMA-avid lesions) in the clinical context of a rising PSA on therapy. Patients 4–6 had at least 1 new PSMA-avid lesion that developed on BAT. In all 3 cases of progression on PET/CT, most ¹⁸F-DCFPyL-avid lesions became less intense.

We next explored the relationship between ¹⁸F-DCFPyL PET/CT findings and radiographic progression on conventional imaging. In the 3 patients who did not have progression on ¹⁸F-DCFPyL PET/CT, radiographic progression on BAT was not observed until 6–9 mo after the second PET/CT scan (Fig. 2). In contrast, all patients with progression on PET/CT had evidence of progression on conventional imaging by 3 mo. In all instances of early progression, the sites of progression on CT or bone scanning correlated with the PSMA-targeted PET findings.

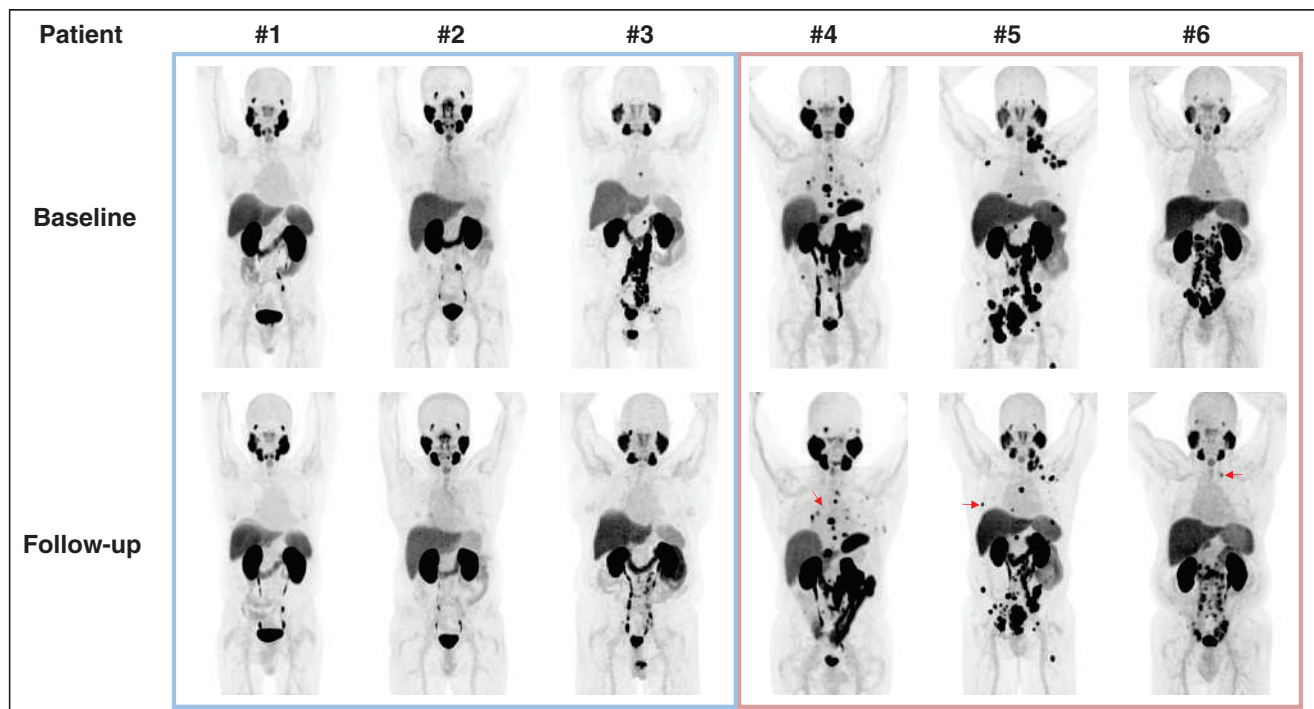


FIGURE 1. Changes in ¹⁸F-DCFPyL PET/CT imaging after 3 mo of BAT. Baseline and follow-up maximum-intensity-projection whole-body images are shown for each patient included in study. For patients 4–6, representative new lesions or sites of progression are demarcated with arrows. Additional new lesions may be hidden by normal uptake or other sites of disease.

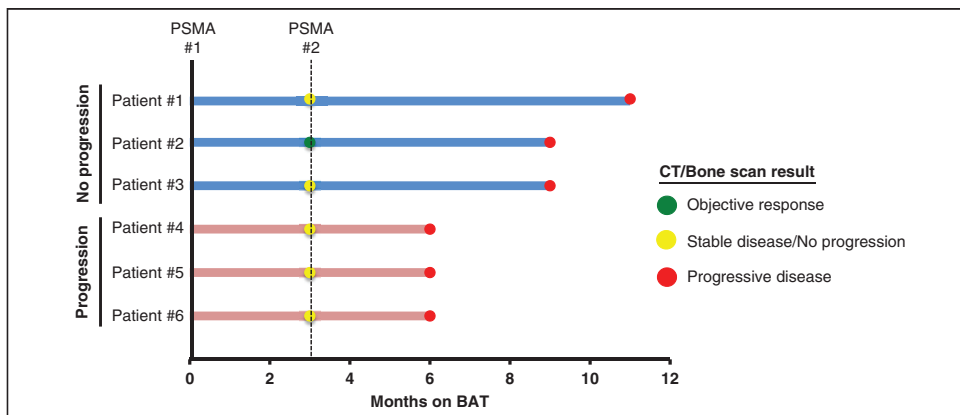


FIGURE 2. Swimmer plot showing radiographic response/progression on BAT. All patients were followed until radiographic progression. ^{18}F -DCFPyL PET/CT imaging was performed before start of BAT and after 3 mo of treatment. Patients 1–3 had no progression noted with ^{18}F -DCFPyL. Patients 4–6 had new ^{18}F -DCFPyL-avid lesions. These data suggest that disease progression on PSMA-targeted PET imaging precedes detection on conventional imaging.

DISCUSSION

BAT and PSMA-targeted imaging both remain under clinical investigation for patients with prostate cancer. When testosterone binds to androgen receptor, it induces PSA expression, meaning there is an urgent need for the development of a biomarker that can identify early disease progression because rising PSA is unreliable.

We performed a pilot imaging study assessing the effect of BAT on ^{18}F -DCFPyL PET/CT imaging. After initiation of treatment, most sites of radiotracer uptake had a decrease in SUV_{max} at the 3-mo time point. There are several possible explanations for this finding. One is that BAT induced regression of disease across multiple sites, as is consistent with the lack of radiographic progression after 3 mo of therapy. However, given the degree of change in SUV_{max} , one would expect to see more objective responses at that time point. A second explanation is that BAT inhibits the expression of PSMA protein. Prior studies have shown that androgen receptor inhibition increases PSMA expression and may cause a flare on PSMA-targeted PET (6,15). It is plausible that reengagement of androgen receptor via exogenous testosterone may downregulate PSMA expression while maintaining tumor viability. This artifact would result in a false-negative scan result. Alternatively, BAT may downregulate PSMA protein as an early event in apoptosis. It has been shown that PSMA may direct cellular growth through phosphatidylinositol-3'-kinase/protein kinase B signaling (16). Thus, decreasing PSMA expression may result in tumor regression. True radiographic progression did not occur for 9–12 mo after the ^{18}F -DCFPyL PET scan, which would support the possibility that these findings indicate an early clinical response. Arguing against transcriptional inhibition of PSMA expression are the findings of new or worsening ^{18}F -DCFPyL-avid lesions. That phenomenon was observed only in patients who experienced radiographic progression at their next restaging scan.

The utility of ^{18}F -DCFPyL PET/CT imaging may be in identifying those patients at highest risk of progressing on BAT. Patients who demonstrate new ^{18}F -DCFPyL-avid lesions all had early radiographic progression.

This study was limited by the small number of patients and the use of only 2 imaging time points. In addition, the fact that all

scans were read by a single radiologist (although masked) could bias the results of the study. A larger prospective study is under way to confirm these findings (NCT04424654).

CONCLUSION

Treatment with BAT induced radiographic changes on ^{18}F -DCFPyL PET/CT imaging. New radiotracer-avid lesions on ^{18}F -DCFPyL PET/CT in men with mCRPC undergoing BAT can indicate early progression.

DISCLOSURE

This project was supported by the Sidney Kimmel Comprehensive Cancer Center at Johns Hopkins; by NIH grants P30 CA006973 and R01 CA184012;

and by the Patrick C. Walsh, PCF Challenge, and Young Investigator Awards. The content is solely the responsibility of the authors and does not necessarily represent the official views of the National Cancer Institute or the National Institutes of Health. Martin Pomper is a coinventor on a U.S. patent covering ^{18}F -DCFPyL and as such is entitled to a portion of any licensing fees and royalties generated by this technology. This arrangement has been reviewed and approved by the Johns Hopkins University in accordance with its conflict-of-interest policies. Steven Rowe is a consultant to Progenics Pharmaceuticals, the licensee of ^{18}F -DCFPyL. Michael Gorin has served as a consultant to Progenics Pharmaceuticals. Martin Pomper, Kenneth Pienta, Michael Gorin, and Steven Rowe receive research funding from Progenics Pharmaceuticals. No other potential conflict of interest relevant to this article was reported.

KEY POINTS

QUESTION: Early progression on BAT is difficult to detect given the effect of testosterone on PSA expression and the limitations of conventional imaging.

PERTINENT FINDINGS: New radiotracer-avid lesions on ^{18}F -DCFPyL PET/CT imaging were observed in mCRPC patients on BAT who experienced early progression on conventional radiography.

IMPLICATIONS FOR PATIENT CARE: PSMA-targeted PET/CT may identify mCRPC patients at risk of early progression on BAT.

REFERENCES

- Rowe SP, Gorin MA, Pomper MG. Imaging of prostate-specific membrane antigen with small-molecule PET radiotracers: from the bench to advanced clinical applications. *Annu Rev Med.* 2019;70:461–477.
- Wright GL Jr, Haley C, Beckett ML, Schellhammer PF. Expression of prostate-specific membrane antigen in normal, benign, and malignant prostate tissues. *Urol Oncol.* 1995;1:18–28.
- Afshar-Oromieh A, Malcher A, Eder M, et al. PET imaging with a [^{68}Ga]gallium-labelled PSMA ligand for the diagnosis of prostate cancer: biodistribution in

- humans and first evaluation of tumour lesions. *Eur J Nucl Med Mol Imaging*. 2013;40:486–495.
4. Szabo Z, Mena E, Rowe SP, et al. Initial evaluation of [¹⁸F]DCFPyL for prostate-specific membrane antigen (PSMA)-targeted PET imaging of prostate cancer. *Mol Imaging Biol*. 2015;17:565–574.
 5. Perera M, Papa N, Christidis D, et al. Sensitivity, specificity, and predictors of positive ⁶⁸Ga-prostate-specific membrane antigen positron emission tomography in advanced prostate cancer: a systematic review and meta-analysis. *Eur Urol*. 2016;70:926–937.
 6. Evans MJ, Smith-Jones PM, Wongvipat J, et al. Noninvasive measurement of androgen receptor signaling with a positron-emitting radiopharmaceutical that targets prostate-specific membrane antigen. *Proc Natl Acad Sci USA*. 2011;108:9578–9582.
 7. Aggarwal R, Wei X, Kim W, et al. Heterogeneous flare in prostate-specific membrane antigen positron emission tomography tracer uptake with initiation of androgen pathway blockade in metastatic prostate cancer. *Eur Urol Oncol*. 2018;1:78–82.
 8. Denmeade SR, Isaacs JT. Bipolar androgen therapy: the rationale for rapid cycling of supraphysiologic androgen/ablation in men with castration resistant prostate cancer. *Prostate*. 2010;70:1600–1607.
 9. Schweizer MT, Wang H, Lubner B, et al. Bipolar androgen therapy for men with androgen ablation naïve prostate cancer: results from the phase II BATMAN study. *Prostate*. 2016;76:1218–1226.
 10. Teplý BA, Wang H, Lubner B, et al. Bipolar androgen therapy in men with metastatic castration-resistant prostate cancer after progression on enzalutamide: an open-label, phase 2, multicohort study. *Lancet Oncol*. 2018;19:76–86.
 11. Markowski MC, Wang H, Sullivan R, et al. A multicohort open-label phase II trial of bipolar androgen therapy in men with metastatic castration-resistant prostate cancer (RESTORE): a comparison of post-abiraterone versus post-enzalutamide cohorts. *Eur Urol*. July 2, 2020 [Epub ahead of print].
 12. Rowe SP, Pienta KJ, Pomper MG, Gorin MA. PSMA-RADS version 1.0: a step towards standardizing the interpretation and reporting of PSMA-targeted PET imaging studies. *Eur Urol*. 2018;73:485–487.
 13. Eisenhauer EA, Therasse P, Bogaerts J, et al. New response evaluation criteria in solid tumours: revised RECIST guideline (version 1.1). *Eur J Cancer*. 2009;45:228–247.
 14. Scher HI, Morris MJ, Stadler WM, et al. Trial design and objectives for castration-resistant prostate cancer: updated recommendations from the Prostate Cancer Clinical Trials Working Group 3. *J Clin Oncol*. 2016;34:1402–1418.
 15. Hope TA, Truillet C, Ehman EC, et al. ⁶⁸Ga-PSMA-11 PET imaging of response to androgen receptor inhibition: first human experience. *J Nucl Med*. 2017;58:81–84.
 16. Caromile LA, Shapiro LH. PSMA redirects MAPK to PI3K-AKT signaling to promote prostate cancer progression. *Mol Cell Oncol*. 2017;4:e1321168.

Addition of ^{131}I -MIBG to PRRT (^{90}Y -DOTATOC) for Personalized Treatment of Selected Patients with Neuroendocrine Tumors

David L. Bushnell^{1,2}, Kellie L. Bodeker^{1,3}, Thomas M. O'Dorisio⁴, Mark T. Madsen¹, Yusuf Menda¹⁻³, Stephen Graves^{1,3}, Gideon K.D. Zamba⁵, and M. Sue O'Dorisio⁶

¹Division of Nuclear Medicine, Department of Radiology, University of Iowa Hospital and Clinics, Iowa City, Iowa; ²Iowa City Virginia Healthcare System, Iowa City, Iowa; ³Department of Radiation Oncology, University of Iowa Hospital and Clinics, Iowa City, Iowa; ⁴Division of Endocrinology, Department of Internal Medicine, University of Iowa Hospital and Clinics, Iowa City, Iowa; ⁵Department of Biostatistics, University of Iowa Hospital and Clinics, Iowa City, Iowa; and ⁶Department of Pediatrics, University of Iowa Hospital and Clinics, Iowa City, Iowa

Peptide receptor radionuclide therapy (PRRT) is an effective treatment for metastatic neuroendocrine tumors. Delivering a sufficient tumor radiation dose remains challenging because of critical-organ dose limitations. Adding ^{131}I -metaiodobenzylguanidine (^{131}I -MIBG) to PRRT may be advantageous in this regard. **Methods:** A phase 1 clinical trial was initiated for patients with nonoperable progressive neuroendocrine tumors using a combination of ^{90}Y -DOTATOC plus ^{131}I -MIBG. Treatment cohorts were defined by radiation dose limits to the kidneys and the bone marrow. Subject-specific dosimetry was used to determine the administered activity levels. **Results:** The first cohort treated subjects to a dose limit of 1,900 cGy to the kidneys and 150 cGy to the marrow. No dose-limiting toxicities were observed. Tumor dosimetry estimates demonstrated an expected dose increase of 34%–83% using combination therapy as opposed to ^{90}Y -DOTATOC PRRT alone. **Conclusion:** These findings demonstrate the feasibility of using organ dose for a phase 1 escalation design and suggest the safety of using ^{90}Y -DOTATOC and ^{131}I -MIBG.

Key Words: personalized dosimetry; MIBG; PRRT; DOTATOC

J Nucl Med 2021; 62:1274–1277

DOI: 10.2967/jnumed.120.254987

Peptide receptor radionuclide therapy (PRRT), either as ^{177}Lu -DOTATATE (Lutathera; Advanced Accelerator Applications) or as ^{90}Y -DOTATOC, is well established as an effective form of treatment for patients with metastatic neuroendocrine tumors (1–3). Delivering a tumor radiation dose sufficient to result in a high percentage of overall response rates remains challenging because of limits imposed on administered activity levels by radiation-induced normal-organ toxicity (4). For ^{90}Y -DOTATOC, the critical organ that limits the amount of deliverable administered activity is typically the kidney (5,6). Targeted radionuclide therapy with ^{131}I -metaiodobenzylguanidine (^{131}I -MIBG) has also

demonstrated promise in some patients with advanced-stage neuroendocrine tumors (7,8). ^{131}I -MIBG targets tumor sites in over 50% of patients with midgut neuroendocrine tumors through a mechanism distinctly different from that of PRRT agents (9). The amount of administered activity that can safely be delivered is limited primarily by radiation to the bone marrow as opposed to the kidneys (10). We have previously demonstrated that this difference enables the combination of large fractions of each agent (relative to amounts that can be delivered safely alone or individually) into a single treatment regimen that results in higher total tumor radiation doses without exceeding dose limits for either the marrow or the kidneys (11). Moreover, known differences in tumor distribution of ^{131}I -MIBG and radiolabeled octreopeptides may prove to be advantages for combined therapy.

Traditionally, cancer trials on targeted radionuclide therapy have relied on a “one size fits all” approach to treating patients in terms of prescribed levels of administered activity. This approach to radionuclide-based therapy is considered by many to be less desirable than using personalized patient-specific dosimetry to guide treatment (12,13). We initiated a phase 1 clinical trial in which the escalation design was based on increasing the radiation dose limits to critical organs between cohorts as opposed to using cohorts defined by specific escalated levels of administered activity. Within this trial framework, we applied the technique previously described for addition of ^{131}I -MIBG to PRRT using patient-specific dosimetry (14). We report here the results from this trial before a redesign wherein ^{90}Y -DOTATOC is being replaced by ^{177}Lu -DOTATATE and low-specific-activity ^{131}I -MIBG is being replaced by high-specific-activity ^{131}I -MIBG.

MATERIALS AND METHODS

The study was approved by the University of Iowa Biomedical Institutional Review Board (IRB-01), and all subjects provided written independent consent. Patients with nonoperable (metastatic or local), progressive neuroendocrine tumors of midgut origin with ^{68}Ga -DOTATATE-positive tumors on PET were invited to participate. Combined imaging with ^{111}In -pentetreotide (as a biodistribution surrogate for ^{90}Y -DOTATOC) and ^{131}I -MIBG was performed on each subject for dosimetric analysis and detailed tumor-targeting assessment. To be eligible to proceed to treatment, subjects had to demonstrate at least one of the following based on the results from the combined imaging/biodistribution studies: either one or more ^{131}I -MIBG-positive

Received Aug. 11, 2020; revision accepted Jan. 11, 2021.
For correspondence or reprints, contact David L. Bushnell (david-bushnell@iowa.edu).

Published online January 30, 2021.
COPYRIGHT © 2021 by the Society of Nuclear Medicine and Molecular Imaging.
Immediate Open Access: Creative Commons Attribution 4.0 International License (CC BY) allows users to share and adapt with attribution, excluding materials credited to previous publications. License: <https://creativecommons.org/licenses/by/4.0/>. Details: <http://jnm.snmjournals.org/site/misc/permission.xhtml>.

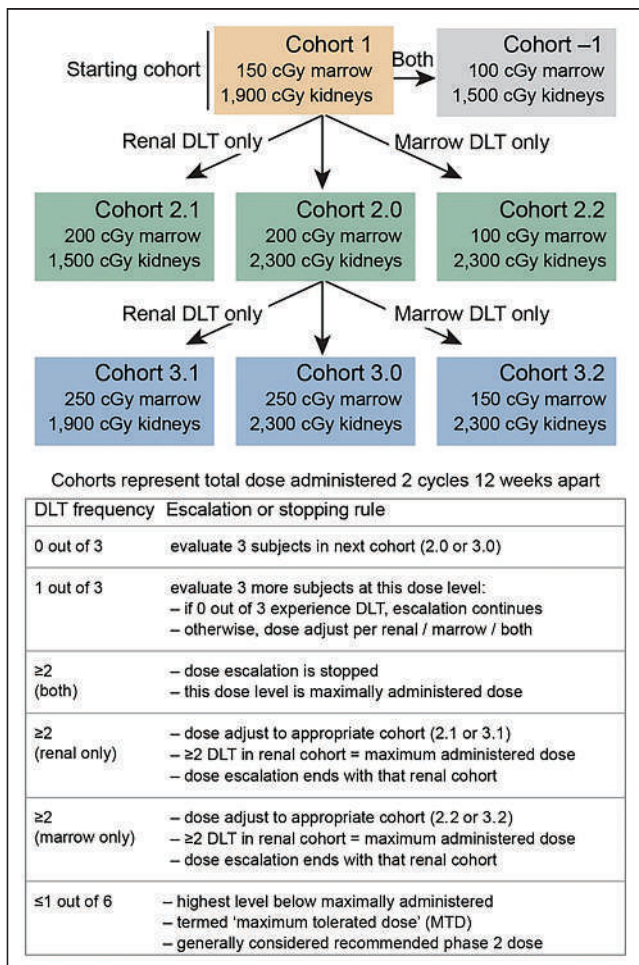


FIGURE 1. Trial design. DLT = dose-limiting toxicities.

and ^{90}Y -DOTATOC–negative tumors, or one or more tumor sites where the expected tumor radiation dose is higher by at least 25% with a combination of ^{90}Y -DOTATOC plus ^{131}I -MIBG than with ^{90}Y -DOTATOC alone.

Imaging and Dosimetry

Imaging and blood sampling were performed at 1, 4, 24, and 48 h after combined administration of 222 MBq of ^{111}In -pentetate plus 74 MBq of ^{131}I -MIBG. Planar and SPECT/CT images were acquired as multiisotope studies with a 20% window on the 364-keV photopeak of ^{131}I and the 247-keV photopeak of ^{111}In . High-energy collimation was used for all simultaneous imaging studies. Scatter correction was performed. Appropriate 1.85-MBq standards of ^{131}I and ^{111}In were placed within the field. Organ and tumor mass were measured from the CT

scan. Dose was determined for the kidneys and bone marrow and for up to 2 soft-tissue tumor sites per organ system. Marrow dosimetry was based on the blood-to-marrow β -contribution and on the organ- or tumor-to-marrow γ -contribution. OLINDA, version 1.1, was used.

Therapy

Cohort 1 subjects were treated with a combination of ^{131}I -MIBG and ^{90}Y -DOTATOC. The administered activity was an amount calculated to deliver a total expected cumulative renal radiation dose of 1,900 cGy and a bone marrow dose of 150 cGy (delivered over 2 equal treatment cycles separated by 10–12 wk). The concept and methods to accomplish these administered activity calculations have been described previously (11,15). The trial escalation paradigm is depicted in Figure 1.

Each cycle consisted of ^{90}Y -DOTATOC delivered on an outpatient basis (day 1) followed by in-patient ^{131}I -MIBG infusion (day 2). A compounded amino acid solution containing 25 g of lysine and 25 g of arginine was administered with the ^{90}Y -DOTATOC infusion.

Blood counts, serum creatinine, and urinary protein were assessed regularly beginning at baseline and continuing through 6 mo after cycle 2 to evaluate for dose-limiting toxicity. Dose-limiting toxicities were based on the Common Terminology Criteria for Adverse Events, version 4.03.

RESULTS

Six patients consented to the trial; of these, one did not meet the second-phase eligibility criteria, a second had insurance deny clinical trial participation, and a third withdrew for personal reasons. There were 2 men and 1 woman in the cohort presented here, aged 50–68 y. The tumors were located in the liver or abdominal lymph nodes and, in one case, the anterior abdominal wall. The primary tumor (small bowel in all cases) had been excised from each patient. None of the subjects had bone metastases.

In each of the 3 treated subjects, it was determined that over 11,100 MBq (300 mCi) (total) of ^{131}I -MIBG could safely be added to dosimetrically determined levels of ^{90}Y -DOTATOC (Table 1). The pretherapy tumor dosimetry results revealed that the expected tumor-dose increases could be achieved through addition of ^{131}I -MIBG to ^{90}Y -DOTATOC, compared with what would have been the case for ^{90}Y -DOTATOC given in maximum amounts alone. The calculated tumor-dose increases through the addition of ^{131}I -MIBG ranged from 34% to 83% in 5 of the 6 target tumors evaluated. An example of one of these tumors is depicted in Figure 2. The calculated expected tumor-dose increase in the sixth tumor was an outlier, at 362%.

No dose-limiting toxicities were observed during the 6-mo dose-limiting-toxicity window. One subject did register a temporary grade 3 thrombocytopenia after the second cycle, and another developed grade 2 kidney toxicity after therapy completion

TABLE 1
Calculated Administered Activity Levels to Achieve Dose Limit of 1,900 cGy to Kidneys Plus 150 cGy to Bone Marrow

Subject no.	Maximum total activity ^{90}Y -DOTATOC only (GBq)	Maximum total activity ^{90}Y -DOTATOC plus ^{131}I -MIBG (GBq)	
		^{90}Y -DOTATOC	^{131}I -MIBG
1	10.8	8.7	11.4
2	7.8	5.6	18.3
3	5.0	2.8	18.7

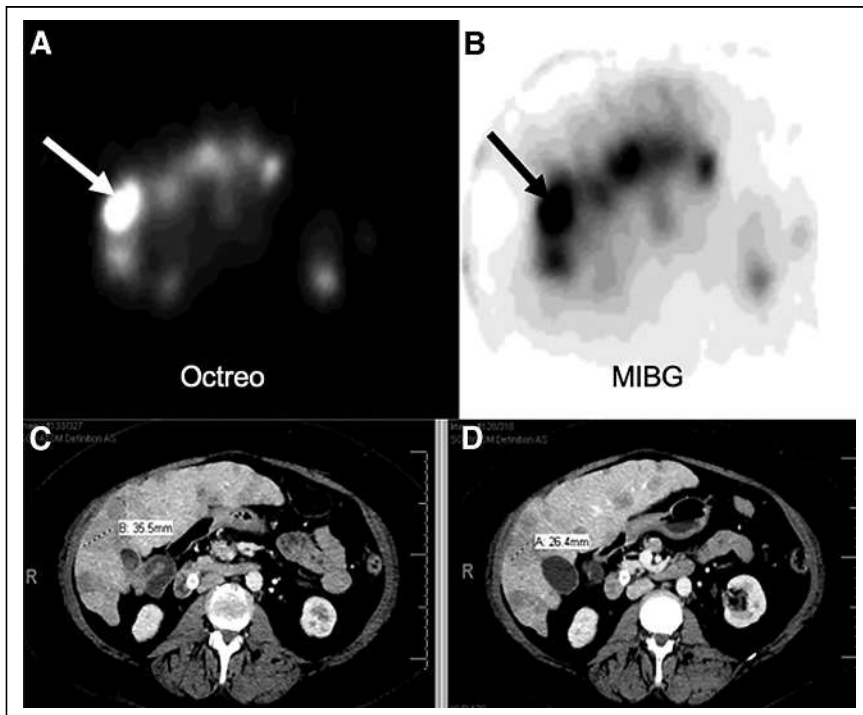


FIGURE 2. Subject 1. (A) ^{111}In -pentetreotide axial SPECT image through mid liver demonstrating multiple octreotide-positive metastases with focal intense uptake in target lesion (arrow). (B) ^{131}I -MIBG SPECT axial slice at same level demonstrating intense uptake in same lesion (arrow). (C) Corresponding baseline venous phase CT scan depicting multiple liver metastases consistent with SPECT findings. Target lesion is 35.5 mm in maximum diameter. (D) Follow-up CT 6-mo after cycle 2 showing measurement of target lesion (maximum diameter, 26.4 mm).

(creatinine level, 1.6 mg/dL), which remained stable at 1 y after treatment. Toxicity data are provided in Table 2. By RECIST, version 1.1, all 3 subjects showed stable disease 6 mo after cycle 2.

DISCUSSION

The opening of the trial was delayed to allow time for review and approval by the Centers for Medicare and Medicaid

surrogate). Moreover, if biodistribution images are obtained after a therapeutic administration, the amino acid effect on renal uptake and radiation dose becomes patient-specific. Finally, high-specific-activity ^{131}I -MIBG (Azedra; Progenics Pharmaceuticals, Inc.) is now an approved agent. High-specific-activity ^{131}I -MIBG may be expected to deliver higher tumor dose levels through improved initial tumor uptake yet with marrow

Services for compliance with billing for clinical trials; as the first study of its kind, the trial created a new billing pathway for radionuclide-based planning dosimetry. Enrollment was later hampered by the Food and Drug Administration (FDA) approval of ^{177}Lu -DOTATATE, which meant potential participants had to choose between an FDA-approved commercial therapy or an experimental phase 1 clinical trial. The trial reported here was designed 6 years ago at a time when the only available cationic amino acid solution in the United States was highly emetogenic. Consequently, we did not wish to subject patients to an additional infusion of amino acids for the dosimetric evaluation phase of our trial. Thus, to partially adjust for this consideration, we applied a fixed 20% reduction to the ^{111}In -pentetreotide-generated residence time for use in estimating the expected ^{90}Y -DOTATOC kidney dose for each subject (16). Because the effect of the lysine/arginine solution on renal octreotide uptake may vary substantially from one individual to another, we have revised the protocol to account for this effect going forward. Subject biodistribution data can be obtained in future cohorts after ^{177}Lu -DOTATATE treatment (eliminating the need for the pretreatment ^{111}In -pentetreotide

TABLE 2
Posttreatment Renal and Bone Marrow Toxicity Assessment

Parameter	Baseline	Cycle 1		Cycle 2		
		1 mo	2 mo	1 mo	2 mo	6 mo
Creatinine (mg/dL)						
Subject 1	1.20	1.1	1.10	1.30	1.10	1.60
Subject 2	1.10	0.86	0.94	0.98	1.13	1.00
Subject 3	1.10	1.14	0.95	1.00	1.07	1.10
Platelet (k/mm^3)						
Subject 1	396	151	215	191	216	165
Subject 2	187	82	128	86	130	189
Subject 3	253	107	150	111	47	173
Absolute neutrophil count (cells/mm^3)						
Subject 1	5,050	6,510	4,310	5,630	4,560	4,100
Subject 2	6,510	4,500	3,800	4,100	4,800	5,180
Subject 3	3,230	3,393	1,575	3,281	1,332	3,520

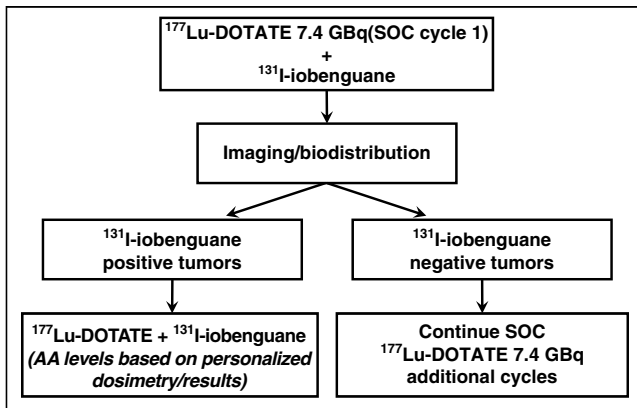


FIGURE 3. Modified trial design. AA = administered activity; DOTATE = DOTATATE; SOC = standard of care.

and renal dosimetry similar to that of low-specific-activity ¹³¹I-MIBG (17). The revised trial design is depicted in Figure 3.

CONCLUSION

These results support the concept that adding ¹³¹I-MIBG to PRRT on the basis of individual patient dosimetry can be performed safely and with the possibility of increasing the delivered tumor dose beyond that achievable with ⁹⁰Y-DOTATOC PRRT alone.

DISCLOSURE

Funding for this trial and support for the investigators was provided by the University of Iowa Department of Radiology, the Holden Comprehensive Cancer Center (3P30CA086862), and the Neuroendocrine SPORE (P50CA174521). No other potential conflict of interest relevant to this article was reported.

KEY POINTS

QUESTION: What are the maximum tolerated critical-organ dose limits for therapy with ¹³¹I-MIBG added to PRRT (⁹⁰Y-DOTATOC)?

PERTINENT FINDINGS: Personalized combination of ¹³¹I-MIBG added to ⁹⁰Y-DOTATOC, calculated to deliver 1,900 cGy to the kidneys and 150 cGy to the bone marrow, demonstrated no clinically significant toxicities. Tumors demonstrated an expected dose increase of 34%–83% (with one outlier of 362%) using combination therapy. ¹⁷⁷Lu-DOTATATE (Lutathera) will replace ⁹⁰Y-DOTATOC, and high-specific-activity ¹³¹I-MIBG (Azedra) will replace low-specific-activity ¹³¹I-MIBG in the next cohort.

IMPLICATIONS FOR PATIENT CARE: Once maximum tolerated organ dose limits for this treatment paradigm are established, a phase 2 trial may safely be initiated.

ACKNOWLEDGMENTS

We are deeply grateful for the important contributions made by the following individuals: Kristin Gamari-Varner, Jeff Murguia, Dan Peterson, Mary Schall, Veronica Howsare, and Phil Danzer, in the Department of Radiology, University of Iowa Hospital and Clinics, as well as Teresa Ruggle in the University of Iowa Design Center. In addition, we sincerely thank the clinical trial participants, their families, and the caregivers for making this trial possible.

REFERENCES

- Strosberg J, El-Haddad G, Wolin E, et al. Phase 3 trial of ¹⁷⁷Lu-dotatate for midgut neuroendocrine tumors. *N Engl J Med*. 2017;376:125–135.
- Hicks RJ, Kwekkeboom DJ, Krenning E, et al. ENETS consensus guidelines for the standards of care in neuroendocrine neoplasms: peptide receptor radionuclide therapy with radiolabelled somatostatin analogues. *Neuroendocrinology*. 2017;105:295–309.
- Hope TA, Bergsland EK, Bozkurt MF, et al. Appropriate use criteria for somatostatin receptor PET imaging in neuroendocrine tumors. *J Nucl Med*. 2018;59:66–74.
- Bodei L, Kidd M, Paganelli G, et al. Long-term tolerability of PRRT in 807 patients with neuroendocrine tumours: the value and limitations of clinical factors. *Eur J Nucl Med Mol Imaging*. 2015;42:5–19.
- Sandström M, Garske-Roman U, Granberg D, et al. Individualized dosimetry of kidney and bone marrow in patients undergoing ¹⁷⁷Lu-DOTA-octreotate treatment. *J Nucl Med*. 2013;54:33–41.
- Barone R, Borsion-Chazot F, Valkema R, et al. Patient specific dosimetry in predicting renal toxicity with ⁹⁰Y-DOTATOC: relevance of kidney volume and dose rate in finding a dose–effect relationship. *J Nucl Med*. 2005;46(suppl):99S-106S.
- Kane A, Thorpe MP, Morse MA, et al. Predictors of survival in 211 patients with stage IV pulmonary and gastroenteropancreatic MIBG-positive neuroendocrine tumors treated with ¹³¹I-MIBG. *J Nucl Med*. 2018;59:1708–1713.
- Ezziddin S, Sabet A, Logvinski T, et al. Long-term outcome and toxicity after dose-intensified treatment with ¹³¹I-MIBG for advanced metastatic carcinoid tumors. *J Nucl Med*. 2013;54:2032–2038.
- Bomanji JB. Treatment of neuroendocrine tumours in adults with ¹³¹I-MIBG therapy. *Clin Oncol (R Coll Radiol)* 2003;15:193–198.
- Pryma DA, Chin BB, Noto RB, et al. Efficacy and safety of high-specific-activity ¹³¹I-MIBG therapy in patients with advanced pheochromocytoma or paraganglioma. *J Nucl Med*. 2019;60:623–630.
- Madsen MT, Bushnell D, Juweid M, et al. Potential increased tumor-dose delivery with combined ¹³¹I-MIBG and ⁹⁰Y-DOTATOC treatment in neuroendocrine tumors: a theoretic model. *J Nucl Med*. 2006;47:660–667.
- Del Prete M, Buteau FA, Arsenault F, et al. Personalized ¹⁷⁷Lu-octreotate peptide receptor radionuclide therapy of neuroendocrine tumours: initial results from the P-PRRT trial. *Eur J Nucl Med Mol Imaging*. 2019;46:728–742.
- Menda Y, Madsen MT, O'Dorisio TM, et al. ⁹⁰Y-DOTATOC dosimetry-based personalized peptide receptor radionuclide therapy. *J Nucl Med*. 2018;59:1692–1698.
- Bushnell DL, Madsen MT, O'Dorisio T, et al. Feasibility and advantage of adding ¹³¹I-MIBG to ⁹⁰Y-DOTATOC for treatment of patients with advanced stage neuroendocrine tumors. *EJNMMI Res*. 2014;4:38–44.
- Besse IM, Madsen M, Bushnell D, Juweid M. Modeling combined radiopharmaceutical therapy: a linear optimization framework. *Technol Cancer Res Treat*. 2009;8:51–60.
- Rolleman EJ, Valkema R, de Jong M, Kooij PP, Krenning EP. Safe and effective inhibition of renal uptake of radiolabelled octreotide by a combination of lysine and arginine. *Eur J Nucl Med Mol Imaging*. 2003;30:9–15.
- Barrett JA, Joyal JL, Hillier SM, et al. Comparison of high-specific-activity ultra-trace ¹²³/¹³¹I-MIBG and carrier-added ¹²³/¹³¹I-MIBG on efficacy, pharmacokinetics, and tissue distribution. *Cancer Biother Radiopharm*. 2010;25:299–308.

Dual PET Imaging in Bronchial Neuroendocrine Neoplasms: The NETPET Score as a Prognostic Biomarker

David L. Chan^{1,2}, Gary A. Ulaner³, David Pattison^{4,5}, David Wyld^{5,6}, Rahul Ladwa^{5,6}, Julian Kirchner³, Bob T. Li⁷, W. Victoria Lai⁷, Nick Pavlakis^{1,2}, Paul J. Roach^{8,9}, and Dale L. Bailey^{8,9,10}

¹Department of Medical Oncology, Royal North Shore Hospital, St. Leonards, New South Wales, Australia; ²Bill Walsh Translational Cancer Research Laboratory, Kolling Institute, University of Sydney, Sydney, New South Wales, Australia; ³Department of Radiology, Memorial Sloan Kettering Cancer Center, New York, New York; ⁴Department of Nuclear Medicine, Royal Brisbane and Women's Hospital, Herston, Queensland, Australia; ⁵School of Medicine, University of Queensland, Brisbane, Queensland, Australia; ⁶Department of Medical Oncology, Royal Brisbane and Women's Hospital, Herston, Queensland, Australia; ⁷Department of Thoracic Oncology, Memorial Sloan Kettering Cancer Center, New York, New York; ⁸Department of Nuclear Medicine, Royal North Shore Hospital, St. Leonards, New South Wales, Australia; ⁹Faculty of Medicine and Health, University of Sydney, Sydney, New South Wales, Australia; and ¹⁰Sydney Vital Translational Cancer Research Centre, Sydney, New South Wales, Australia

PET scans using ¹⁸F-FDG and somatostatin receptor imaging agents are both used in imaging of neuroendocrine neoplasms (NENs). We have suggested the "NETPET score," using uptake of both PET tracers, as a prognostic biomarker in NENs. The name NETPET score was suggested previously to capture the score's intent to summarize information from dual PET imaging in neuroendocrine tumors. We previously demonstrated the effectiveness of the NETPET score in gastroenteropancreatic NENs (GEPNENs). Its prognostic relevance in bronchial NENs remains undetermined. **Methods:** This is a retrospective multicenter study (2011–2018) assessing patients who had advanced bronchial NEN and who underwent both ¹⁸F-FDG and ⁶⁸Ga-DOTATATE PET within 60 d of each other. The NETPET score was assigned by experienced nuclear medicine physicians and compared with other clinical data such as World Health Organization grade. The primary outcome was overall survival; NETPET score and other prognostic variables were analyzed using univariate and multivariate analyses by the Cox proportional-hazards model. **Results:** Thirty-eight patients were included for review. The NETPET score and histology were significantly correlated with overall survival in univariate analyses ($P = 0.003$, $P = 0.01$). On multivariate analysis, only the NETPET score remained significant ($P = 0.03$). The NETPET score was significantly associated with histologic grade ($P = 0.006$, χ^2 test). **Conclusion:** The NETPET score is a prognostic biomarker in bronchial NENs as well as GEPNENs. Although it needs to be validated in prospective studies, it holds significant promise as a biomarker for a wide range of NENs.

Key Words: neuroendocrine tumor; FDG PET; DOTATATE PET; NETPET; biomarker

J Nucl Med 2021; 62:1278–1284

DOI: 10.2967/jnumed.120.257659

Neuroendocrine neoplasms (NENs) are a heterogeneous group of tumors that may secrete bioactive peptides. Although uncommon, they are increasing in incidence (1,2). They can arise in

different parts of the body, most commonly in the gastrointestinal tract, pancreas, and lung. Although they vary considerably in biologic behavior, surgical resection is the only cure, and patients with high-grade metastatic NEN have a very guarded prognosis (3). Tumors in the gastrointestinal tract and pancreas are known collectively as gastroenteropancreatic NENs (GEPNENs). Bronchial NENs are often considered separately and have a different classification system from GEPNENs (4,5). Bronchial NENs have a differing genetic basis from GEPNENs and may also exhibit different clinical behavior, with a median overall survival comparable to pancreatic NENs but inferior to that of small-bowel NENs (6–8). Treatment for patients with advanced bronchial NENs tends to be extrapolated from GEPNENs because of a lack of prospective trials in this subgroup. For instance, the only systemic treatment for bronchial NENs supported by phase III trial evidence is everolimus (9), whereas such evidence exists in various GEPNENs for somatostatin analogs, everolimus, sunitinib, and peptide receptor radionuclide therapy (PRRT) (10–13).

Clinicians find it challenging to predict prognosis and select optimal systemic therapies in metastatic NEN because of the widely variant biologic aggressiveness of different NENs. Although histologic grade can predict disease behavior to some extent, grade may be inaccurately measured in small biopsies, may vary in different metastatic sites, and may also evolve over time. Tissue- and blood-based biomarkers have been suggested, but few have been validated prospectively (14). PET imaging has been increasingly used to image NENs and even to guide the optimal choice of systemic therapies. It is recognized that somatostatin receptor-based radiotracers (such as ⁶⁸Ga-DOTATATE PET) highlight well-differentiated NEN cells that express the somatostatin receptor. Conversely, avidity on ¹⁸F-FDG PET as well as high metabolic tumor volume predicts aggressive tumor biology and poorer prognosis (15–18). The distribution and intensity of somatostatin receptor expression measured by ⁶⁸Ga-DOTATATE PET, together with the absence of sites of discordant ¹⁸F-FDG-avid disease, also provides a theranostic role by confirming suitability for treatment with PRRT. In a similar fashion to NEN treatment, much of the data regarding PET imaging in NENs has been extrapolated from publications concerning GEPNENs.

Given the different roles of these 2 scans, we proposed a system to interpret the complementary findings of the 2 scans—the

Received Oct. 18, 2020; revision accepted Jan. 3, 2021.
For correspondence or reprints, contact David L. Chan (david.chan@sydney.edu.au).

Published online February 12, 2021.

COPYRIGHT © 2021 by the Society of Nuclear Medicine and Molecular Imaging.

“NETPET score” (19). This name was suggested in the original study to capture the score's intent to summarize information from dual PET imaging in neuroendocrine tumors. This score was investigated in a group of predominantly GEPNEN patients, showed prognostic significance independent of histologic grade, and was subsequently validated in 2 other patient cohorts (20,21). As the prognostic impact of the NETPET score had not been formally investigated in bronchial NENs, we aimed to measure this impact in a retrospective study.

MATERIALS AND METHODS

This was a multicenter retrospective study conducted in Australia (Royal North Shore Hospital, Sydney, and Royal Brisbane and Women's Hospital, Brisbane) and the United States (Memorial Sloan Kettering Cancer Center, New York, New York). Subjects aged 18 y or above with histologically confirmed, advanced (unresectable or metastatic) NENs originating from the lung were eligible. All NEN histologies (typical carcinoid, atypical carcinoid, large cell and small cell neuroendocrine carcinoma) were included. Other pathologies (e.g., adenocarcinoma and squamous cell carcinoma) were excluded.

Searches of each site's nuclear medicine database were conducted. All patients fulfilling the above criteria who underwent ⁶⁸Ga-DOTATATE and ¹⁸F-FDG PET imaging within 60 d of each other with no local or systemic therapy between the 2 scans were included. In the case of multiple pairs of eligible scans in the same individual, the earliest pair acquired after diagnosis of advanced disease was chosen.

Imaging

Image data were acquired on PET/CT scanners at each institution. All image data were acquired on current-generation PET/CT scanners with time-of-flight, scatter correction, and point-spread function resolution recovery (UltraHD) capabilities (Royal North Shore Hospital: Biograph mCT.S/64 PET/CT scanner [Siemens Healthcare]; Royal Brisbane and Women's Hospital: Biograph mCT.S/128 PET/CT scanner [Siemens Healthcare]; Memorial Sloan Kettering Cancer Center: 690 or 710 PET/CT scanner [GE Healthcare]). Data were typically acquired as whole-body scans (top of skull to mid thigh), usually requiring 6–8 bed positions in step-and-shoot mode.

For the ⁶⁸Ga-DOTATATE PET scans, the patients were injected with 120–200 MBq of ⁶⁸Ga-DOTA-(Tyr3)-octreotate; imaging commenced approximately 45–60 min after injection, with whole-body low-dose CT followed by the PET acquisition of 120–180 s/bed position. Subjects were advised to cease somatostatin analogs 4 wk before the scan.

For the ¹⁸F-FDG scans, the patients were required to fast for at least 6 h before the scan, and blood glucose levels were checked to ensure they were within the range of 4–11 mmol/L. Subjects were administered ¹⁸F-FDG in the range of 250–450 MBq according to standard institutional protocols (Royal North Shore Hospital: 250 MBq if patient weight under 90 kg and 300 MBq if over 90 kg; Royal Brisbane and Women's Hospital: 4.5 MBq/kg up to a maximum of 350 MBq; Memorial Sloan Kettering Cancer Center: 444 MBq [$\pm 10\%$]). At approximately 60 min after injection of the ¹⁸F-FDG, scanning commenced with whole-body low-dose CT followed by the PET acquisition of 120–150 s/bed position.

Image Analysis

Scans were graded subjectively by visual interpretation on dedicated nuclear medicine reporting workstations. Interpretation was undertaken by experienced nuclear medicine physicians at each site. Both scans were displayed simultaneously in transverse, coronal, and sagittal planes accompanied by a maximal-intensity projection of the PET data, with both image sets anatomically coregistered. The scans were

initially windowed with preset SUVs of 0–15 for ⁶⁸Ga-DOTATATE PET and 0–7 for ¹⁸F-FDG PET, as these were the values used for reporting in clinical practice. The readers had full access to all software tools in the reporting software. Positivity on ¹⁸F-FDG and ⁶⁸Ga-DOTATATE scans was defined as uptake greater than that regarded as physiologic for the organ or tissue in question on the respective scan.

All readers underwent initial training with a standardized dataset of 10 NEN cases (taken from the initial NETPET study (19)) before commencing grading. According to our prior study, scoring was focused on the most discordant lesion on dual PET (Fig. 1). A score of P5 was assigned if there was significant disease that was ¹⁸F-FDG-avid but not ⁶⁸Ga-DOTATATE-avid. A score of P2–P4 corresponded to the presence of ¹⁸F-FDG-avid, ⁶⁸Ga-DOTATATE-avid disease in any of the lesions, with the exact score dependent on the relative avidity on ¹⁸F-FDG and ⁶⁸Ga-DOTATATE PET. P1 denoted ⁶⁸Ga-DOTATATE but not ¹⁸F-FDG avidity in all lesions; P0 denoted neither ⁶⁸Ga-DOTATATE nor ¹⁸F-FDG avidity (Table 1).

Clinicopathologic Data

The included patients' charts were reviewed to extract demographic and prognostic data (including primary site and histologic grade). Outcomes included overall survival (OS) and progression-free survival (PFS), defined as a composite of RECIST-defined radiologic progression, commencement of another systemic therapy after the index scan, and death (22). The primary outcome was OS, measured in days from the latter of the 2 paired PET scans to the date of death or last follow-up.

Statistical Analysis

Patient demographics are presented descriptively. For survival analysis, the included patients were separated into 3 cohorts—P1, P2–P4, and P5—in the same fashion as the original NETPET study (19). Patients with P2, P3, and P4 findings were grouped together as there is no consensus on the exact quantitative cutoffs to separate patients who have lesions exhibiting more ⁶⁸Ga-DOTATATE than ¹⁸F-FDG avidity from those with more ¹⁸F-FDG than ⁶⁸Ga-DOTATATE avidity. Patients with P0 disease were noted but excluded from this analysis (the authors considered that this was an uncommon finding from their clinical experience). Survival outcomes in the different cohorts were compared using the log-rank test. Univariate and multivariate regression was performed using the Cox proportional-hazards model with the following variables: age, presence or absence of distant extrahepatic disease, histologic grade, and NETPET score. Histologic grade was divided into 3 groups: typical carcinoid, atypical carcinoid, and large cell/small cell neuroendocrine carcinoma. Other potential prognostic markers (most pertinently the mitotic count and Ki-67 index) were not included in multivariate analysis because of the potential for introducing collinear factors into multivariate analysis. We conducted sensitivity analyses to determine the value of replacing histologic grade by the Ki-67 index for OS analyses. Finally, the correlation between NETPET score and histologic grade (as well as NETPET score and Ki-67 index) was analyzed using the χ^2 test.

Ethics Approval

This study was approved by the Northern Sydney Local Health District Human Research Ethics Committee, 2019/ETH09817, and relevant local ethics committees for each participating site. The requirement to obtain informed consent for this retrospective study was waived.

RESULTS

Thirty-eight patients were included in this study from 3 sites. Female patients comprised 61% of the cohort, and the median age was 66 y (Table 2). The median time from histologic diagnosis to PET imaging was 13 mo (range, 1–151 mo). Treatments before PET imaging included SSAs (18% of patients), chemotherapy

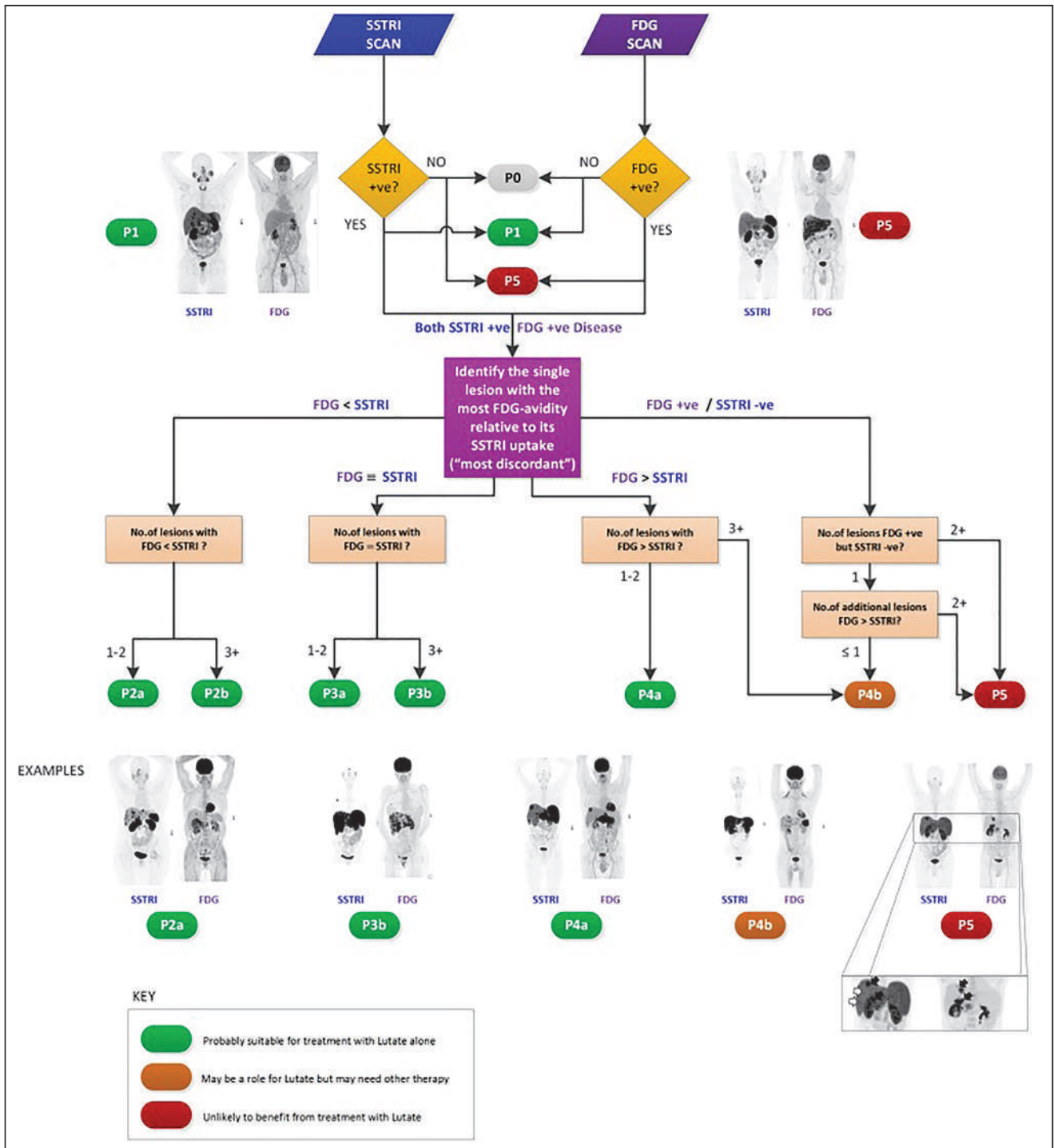


FIGURE 1. Original NETPET schema. SSTR1 = somatostatin receptor imaging. (Reproduced from (19).)

(26%), and PRRT (5%). Treatment after PET imaging included SSAs (24%), chemotherapy (45%), and PRRT (37%). The median follow-up for patients was 18.5 mo.

When the NETPET scoring system was applied to the included patients, more than half the patients (61%) had disease that was both ⁶⁸Ga-DOTATATE-avid and ¹⁸F-FDG-avid (Table 3). The distribution of scores did not significantly differ among the participating institutions (χ^2 test, $P = 0.27$). Eight percent of patients

had a NETPET score of P1 (denoting purely ⁶⁸Ga-DOTATATE-avid disease), and 26% of patients had a score of 5, denoting the presence of significant ¹⁸F-FDG-avid, ⁶⁸Ga-DOTATATE-negative discordant disease. Two patients (5%) had disease that was scored as P0 (i.e., all lesions were negative on both ⁶⁸Ga-DOTATATE and ¹⁸F-FDG PET). In all, 16 of the 38 included patients (42%) underwent PRRT at some point of their disease journey (14/16 after the dual PET scans). These patients had NETPET

TABLE 1
Simplified Schematic of Relationship Between NETPET Score and Dual PET Avidity

NETPET grade	⁶⁸ Ga-DOTATATE result	¹⁸ F-FDG result
0	—	—
1	++	—
2	++	+
3	++	++
4	+	++
5	—	++

scoring as follows: P1, 1/16 (6%); P2–P4, 13/16 (81%); and P5, 2/16 (13%).

OS

Death had occurred in 10 of the 38 patients (26%) at the time of censoring. The median OS was not reached but was estimated at 53 mo. An increasing NETPET score was associated with poorer median OS (P1, not reached; P2–P4, 49.1 mo; P5, 14.5 mo [$P = 0.003$, log-rank test]) (Fig. 2). On univariate analysis, OS was associated with NETPET score ($P = 0.003$) and histology ($P = 0.01$). On multivariate analysis, only NETPET score remained significant as a prognostic factor ($P = 0.03$), with histology no longer significant ($P = 0.39$) (Table 4).

PFS

Of the included patients, 29 of 38 (76%) had progressed at the time of censoring, with a median PFS of 12.9 mo. Median PFS was not reached in patients grouped as P1. In those grouped as P2–P4, it was 14.1 mo, and in those grouped as P5, it was 4.8 mo ($P < 0.0001$, log-rank test) (Fig. 3).

On univariate analysis, PFS was significantly associated with NETPET score ($P < 0.00001$) and histologic grade ($P = 0.04$) but not age ($P = 0.88$) or the presence of extrahepatic disease ($P = 0.68$). On multivariate analysis, only NETPET score remained a significant predictor of PFS ($P < 0.00001$) (Table 5). Finally, NETPET score was significantly associated with histologic grade ($P = 0.006$, χ^2 test).

Sensitivity Analyses

We performed sensitivity analyses to investigate the impact of substituting histologic grade with Ki-67 index. On univariate analysis, Ki-67 index was also associated with OS ($P = 0.004$, log-rank test). This association remained significant on multivariate analysis ($P = 0.034$). The NETPET classification was not significantly associated with OS after adjustment for Ki-67 index ($P = 0.08$). Finally, the NETPET score was associated with the Ki-67 index ($P = 0.01$ by ANOVA).

DISCUSSION

The current project and indeed the NETPET score proposal arose from the hypothesis that ⁶⁸Ga-DOTATATE and ¹⁸F-FDG PET provide complementary information about tumor biology. ⁶⁸Ga-DOTATATE assesses the presence and extent of somatostatin receptors, whereas ¹⁸F-FDG uptake reflects glucose metabolism, with avidity typically highest in more aggressive and less well differentiated tumors. The NETPET score divides patients into 3 main groups: those who only had ⁶⁸Ga-DOTATATE avidity

TABLE 2
Demographics of Study Cohort ($n = 38$)

Characteristic	Parameter	<i>n</i>	%
Total		38	100
Sex	Male	15	39
	Female	23	61
Age (y)	Median	66	
	Range	28–81	
Primary site	Lung	38	100
Grade for bronchial NEN	Typical carcinoid	9	24
	Atypical carcinoid	22	58
	LCNEC	3	8
	SCNEC	1	3
	Unknown*	3	8
Mitotic count	Median	3.5	
	Range	0–50	
Ki-67 index	Median	15	
	Range	1–80	
Necrosis	Yes	16	42
	No	11	29
	Unknown	11	39
Site of metastasis	Lungs	19	50
	Lymph nodes	19	50
	Liver	21	55
	Bone	23	61
	Brain	4	11
	Other [†]	11	32
Extrahepatic disease	Yes	36	95
	No	2	5
Received PRRT	Yes	19	50
	No	19	50

*Of these 3 cases, 2 were well-differentiated NEN without specific comment on histologic report as to whether this represented typical or atypical carcinoid. One was mixed high-grade and low-grade NEN.

[†]Other sites of disease included peritoneum (4 patients), pancreas (3 patients), adrenal glands (2 patients), pericardium (1 patient), and ovary (1 patient).

LCNEC = large cell neuroendocrine carcinoma; SCNEC = small cell neuroendocrine carcinoma.

on dual PET (favorable), those with ¹⁸F-FDG-avid, ⁶⁸Ga-DOTATATE-negative discordant disease (unfavorable), and those with at least one ¹⁸F-FDG-avid, ⁶⁸Ga-DOTATATE-avid lesion on dual PET without any discordance (intermediate). This NETPET score was a significant prognostic biomarker in the original study, which mainly investigated GEPNENs (19). This multicenter study demonstrated that the NETPET scoring system has a similar prognostic ability in bronchial NENs.

In the current study, we extended the findings of the original study of NETPET score to patients with bronchial NENs. Previously suggested factors such as histologic grade, age, and presence

TABLE 3
Distribution of NETPET Scores

NETPET score	n
0	2 (5%)
1	3 (8%)
2A/2B	7 (18%)
3A/3B	4 (11%)
4A/4B	12 (32%)
5	10 (26%)

or absence of extrahepatic disease had less prognostic value in the current study. Although histologic grade and the NETPET score were associated with OS and PFS in univariate analyses, the NETPET score was the only predictor for both OS and PFS in multivariate analyses. The fact that histologic grade is a recognized predictor of outcome further highlights the potential of the NETPET score (23). The lack of OS difference between typical and atypical carcinoids in the current study (compared with the cited reference) may be due to the smaller size of our cohort. However, this lack of difference only serves to show the ability of the NETPET score to reflect the most aggressive lesion on dual PET, particularly relevant in the presence of metastatic heterogeneity. In contrast, histology samples only one unselected site of known disease and is also affected by sample size (needle biopsies may underestimate grade because of the paucity of tumor tissue). These data support a potential role for dual PET in addition to biopsy to determine tumor aggressiveness and optimal therapy in a patient with bronchial NEN. In addition, as PET is a noninvasive modality, the NETPET score may also highlight changes in disease biology over time without the risks incurred with repeated tissue biopsies.

To our knowledge, our findings confirm the prognostic value of the NETPET score in bronchial NENs for the first time, extending the findings from previous GEPNEN studies (20,21). Although a similar analysis in bronchial NENs has recently been published and demonstrated a significant proportion of patients with discordant lesions, a different scoring system was used, and the impact of dual PET scoring on OS was not reported (24). This study suggests that patients with no avidity on PET with either tracer (analogous to P0) and patients with significant disease that is ^{18}F -FDG-avid but not ^{68}Ga -DOTATATE-avid (analogous to P5) should not receive PRRT, as is concordant with our clinical experience. Further investigations into a molecular imaging-led paradigm for treatment selection may impact care for patients with bronchial NEN (e.g., a

TABLE 4
Univariate and Multivariate Analyses for OS

Variable	Univariate P	Multivariate P
NETPET score	0.003*	0.03*
Histology	0.010*	0.39
Presence of extrahepatic disease	0.474	0.09
Age > 65 y	0.429	0.46

*Significant.

score of P1 leading to the use of somatostatin analogs, and a score of P5 arguing more for the use of systemic chemotherapy).

We acknowledge limitations in the current study. The relatively small numbers in this study reflect the uncommon nature of bronchial NENs. As such, the study should be regarded as hypothesis-generating at this point while awaiting additional confirmatory data. Because dual PET for bronchial NENs is not routinely practiced (because of the paucity of data regarding its utility to date), there is also a possibility of selection bias, as clinicians may order both PET examinations for patients with more aggressive disease, as reflected in the high proportion of patients with atypical carcinoids rather than typical carcinoids. This bias may also explain the relatively small number of patients with P1 grading. The retrospective nature of this study meant that the PET scans were not performed on the same day, raising the possibility that there may have been changes in tumor size or characteristics between the time of the 2 PET scans. We restricted inclusion to patients whose scans were done within 60 d of each other to minimize this potential issue. The current findings (particularly the interplay between Ki-67, NETPET score, and prognosis) should ideally be confirmed by a prospective study. Finally, we note that we included bronchial NENs of all histologies (from typical carcinoid to small cell neuroendocrine carcinoma), as opposed to a recent study that enrolled only patients with typical and atypical carcinoid (24). This inclusion allowed us to demonstrate the value of dual PET imaging and its correlation to high-grade histologies; our results remained significant for NETPET score alone on restriction of the cohort to typical and atypical carcinoid histologies (data not shown).

Future research from this study might include investigation of dual PET as a predictive biomarker for PRRT (i.e., one that predicts for differential efficacy from PRRT as opposed to just predicting for poorer prognosis per se). However, ideally this needs

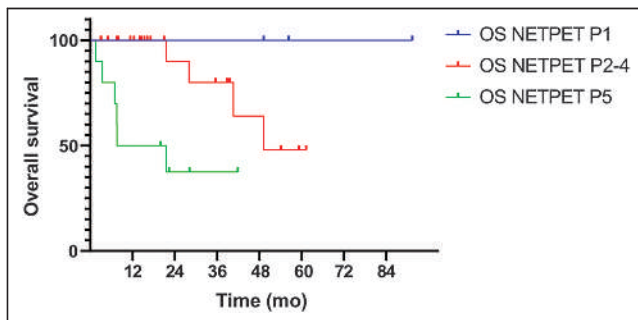


FIGURE 2. OS by NETPET score.

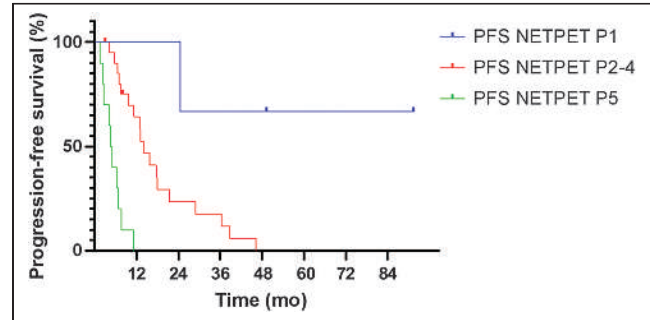


FIGURE 3. PFS by NETPET score.

TABLE 5
Univariate and Multivariate Analyses for PFS

Variable	Univariate <i>P</i>	Multivariate <i>P</i>
NETPET score	<0.00001*	<0.00001*
Histology	0.04*	0.871
Presence of extrahepatic disease	0.68	0.998
Age > 65 y	0.88	0.78

*Significant.

to be done in the context of a prospective clinical trial. The best systemic therapy for each NETPET score and the relative importance of this compared with histologic grade need to be determined. The current study treats the P2–P4 group (patients with lesions that are both ⁶⁸Ga-DOTATATE-avid and ¹⁸F-FDG-avid) as a single group, meaning that subtle differences in relative ⁶⁸Ga-DOTATATE and ¹⁸F-FDG avidity have not been shown to be of significance to date; the P2/P3/P4 classes may be refined into separate prognostic subgroups with larger studies and quantitative evaluation of ⁶⁸Ga-DOTATATE and ¹⁸F-FDG metrics. Further research may show a link between different dual PET imaging phenotypes and molecular changes in bronchial NENs (25). Finally, the etiology and significance of disease that is nonavid on both ⁶⁸Ga-DOTATATE and ¹⁸F-FDG PET remain to be determined (24).

This study also raises some intriguing possibilities for further preclinical investigation. Relatively little is known about the interplay between the molecular bases of NENs and PET findings. Recent studies investigating gene expression profiles of bronchial NENs have implicated multiple abnormalities involving the NF-κB (nuclear factor-κB) and ERK/MAPK (extracellular-signal-regulated kinase/mitogen-activated protein kinase) pathways and also demonstrated significant differences between small cell lung cancer and typical or atypical carcinoids (26,27). The upregulation of these pathways may lead to metabolic reprogramming in favor of increased glycolytic rates and more aggressive behavior. Further understanding of these molecular pathways may shed light on the dual PET findings observed in the current study and also lead to the development of new imaging tracers to better define disease biology.

CONCLUSION

Dual PET divides patients into 4 groups: purely ⁶⁸Ga-DOTATATE-avid disease (P1); dual ⁶⁸Ga-DOTATATE and ¹⁸F-FDG avidity (P2–P4); ¹⁸F-FDG-avid, ⁶⁸Ga-DOTATATE-negative disease (P5); and dual negative disease (P0). The NETPET score predicts OS in patients with metastatic bronchial NEN, even after adjustment for known prognostic variables such as histologic grade. If confirmed by prospective studies, this finding would confirm the role of the NETPET score as a prognostic biomarker above that of histologic grade alone in predicting disease aggressiveness and guiding best care.

DISCLOSURE

David Chan has received a National Health and Medical Research Council investigator grant to fund this research in part (APP1175788). Dale Bailey is supported in part by Sydney Vital,

which receives its funding from a Translational Cancer Research Centre program grant from the Cancer Institute of New South Wales. No other potential conflict of interest relevant to this article was reported.

ACKNOWLEDGMENT

We acknowledge Dr. Elizabeth Bernard (Royal North Shore Hospital) for her assistance in image analysis.

KEY POINTS

QUESTION: What is the prognostic significance of the proposed NETPET scoring system for dual ¹⁸F-FDG and ⁶⁸Ga-DOTATATE PET imaging in patients with metastatic bronchial NEN?

PERTINENT FINDINGS: In a multicenter retrospective study of 38 patients, increasing NETPET score (signifying ¹⁸F-FDG avidity and loss of ⁶⁸Ga-DOTATATE avidity) was associated with worsened OS on univariate and multivariate analysis.

IMPLICATIONS FOR PATIENT CARE: The NETPET score holds significant promise as a biomarker in patients with advanced bronchial NENs.

REFERENCES

- Hallet J, Law CHL, Cukier M, Saskin R, Liu N, Singh S. Exploring the rising incidence of neuroendocrine tumors: a population-based analysis of epidemiology, metastatic presentation, and outcomes. *Cancer*. 2015;121:589–597.
- Dasari A, Shen C, Halperin D, et al. Trends in the incidence, prevalence, and survival outcomes in patients with neuroendocrine tumors in the United States. *JAMA Oncol*. 2017;3:1335–1342.
- Sorbye H, Welin S, Langer SW, et al. Predictive and prognostic factors for treatment and survival in 305 patients with advanced gastrointestinal neuroendocrine carcinoma (WHO G3): the NORDIC NEC study. *Ann Oncol*. 2013;24:152–160.
- Travis WD, Brambilla E, Nicholson AG, et al. The 2015 World Health Organization classification of lung tumors: impact of genetic, clinical and radiologic advances since the 2004 classification. *J Thorac Oncol*. 2015;10:1243–1260.
- Bosman FT, Carneiro F, Hruban RH, Theise ND, eds. *WHO Classification of Tumours of the Digestive System*. 4th ed. International Agency for Research on Cancer; 2010.
- Yao JC, Hassan M, Phan A, et al. One hundred years after “carcinoid”: epidemiology of and prognostic factors for neuroendocrine tumors in 35,825 cases in the United States. *J Clin Oncol*. 2008;26:3063–3072.
- Li X, Hou Y, Shi T, et al. Clinicopathological characteristics and genetic analysis of pulmonary carcinoid tumors: a single-center retrospective cohort study and literature review. *Oncol Lett*. 2020;19:2446–2456.
- Scarpa A, Chang DK, Nones K, et al. Whole-genome landscape of pancreatic neuroendocrine tumours. *Nature*. 2017;543:65–71.
- Yao JC, Fazio N, Singh S, et al. Everolimus for the treatment of advanced, non-functional neuroendocrine tumours of the lung or gastrointestinal tract (RADIANT-4): a randomised, placebo-controlled, phase 3 study. *Lancet*. 2016;387:968–977.
- Rinke A, Muller HH, Schade-Brittinger C, et al. Placebo-controlled, double-blind, prospective, randomized study on the effect of octreotide LAR in the control of tumor growth in patients with metastatic neuroendocrine midgut tumors: a report from the PROMID study group. *J Clin Oncol*. 2009;27:4656–4663.
- Caplin ME, Pavel M, Cwikla JB, et al. Lanreotide in metastatic enteropancreatic neuroendocrine tumors. *N Engl J Med*. 2014;371:224–233.
- Yao JC, Shah MH, Ito T, et al. Everolimus for advanced pancreatic neuroendocrine tumors. *N Engl J Med*. 2011;364:514–523.
- Strosberg J, El-Haddad G, Wolin E, et al. Phase 3 trial of ¹⁷⁷Lu-dotatate for midgut neuroendocrine tumors. *N Engl J Med*. 2017;376:125–135.
- Chan DL, Clarke SJ, Diakos CI, et al. Prognostic and predictive biomarkers in neuroendocrine tumours. *Crit Rev Oncol Hematol*. 2017;113:268–282.
- Binderup T, Knigge U, Loft A, Federspiel B, Kjaer A. ¹⁸F-fluorodeoxyglucose positron emission tomography predicts survival of patients with neuroendocrine tumors. *Clin Cancer Res*. 2010;16:978–985.

16. Chan DL, Bernard EJ, Schembri G, et al. High metabolic tumour volume on 18-fluorodeoxyglucose positron emission tomography predicts poor survival from neuroendocrine neoplasms. *Neuroendocrinology*. 2020;110:950–958.
17. Zhang J, Liu Q, Singh A, Schuchardt C, Kulkarni HR, Baum RP. Prognostic value of 18F-FDG PET/CT in a large cohort of patients with advanced metastatic neuroendocrine neoplasms treated with peptide receptor radionuclide therapy. *J Nucl Med*. 2020;61:1560–1569.
18. Johnbeck CB, Knigge U, Langer SW, et al. Prognostic value of ¹⁸F-FLT PET in patients with neuroendocrine neoplasms: a prospective head-to-head comparison with ¹⁸F-FDG PET and Ki-67 in 100 patients. *J Nucl Med*. 2016;57:1851–1857.
19. Chan DL, Pavlakis N, Schembri GP, et al. Dual somatostatin receptor/FDG PET/CT imaging in metastatic neuroendocrine tumours: proposal for a novel grading scheme with prognostic significance. *Theranostics*. 2017;7:1149–1158.
20. Karfis I, Marin G, Levillain H, et al. Prognostic value of a three-scale grading system based on combining molecular imaging with ⁶⁸Ga-DOTATATE and ¹⁸F-FDG PET/CT in patients with metastatic gastroenteropancreatic neuroendocrine neoplasms. *Oncotarget*. 2020;11:589–599.
21. Furtado O'Mahony L. Combination of ⁶⁸Ga-DOTATATE and ¹⁸F-FDG PET/CT in advanced gastroenteropancreatic neuroendocrine tumours (GEPNET): clinical and prognostic implications [abstract]. *Neuroendocrinology*. 2019;108(suppl 1):D20.
22. Eisenhauer EA, Therasse P, Bogaerts J, et al. New response evaluation criteria in solid tumours: revised RECIST guideline (version 1.1). *Eur J Cancer Oxf Engl*. 2009;45:228–47.
23. Ramirez RA, Beyer DT, Diebold AE, et al. Prognostic factors in typical and atypical pulmonary carcinoids. *Ochsner J*. 2017;17:335–340.
24. Zidan L, Iravani A, Kong G, Akhurst T, Michael M, Hicks RJ. Theranostic implications of molecular imaging phenotype of well-differentiated pulmonary carcinoid based on ⁶⁸Ga-DOTATATE PET/CT and ¹⁸F-FDG PET/CT. *Eur J Nucl Med Mol Imaging*. 2021;48:204–216.
25. Pelosi G, Sonzogni A, Harari S, et al. Classification of pulmonary neuroendocrine tumors: new insights. *Transl Lung Cancer Res*. 2017;6:513–529.
26. Voortman J, Lee J-H, Killian JK, et al. Array comparative genomic hybridization-based characterization of genetic alterations in pulmonary neuroendocrine tumors. *Proc Natl Acad Sci USA*. 2010;107:13040–13045.
27. Asiedu MK, Thomas CF, Dong J, et al. Pathways impacted by genomic alterations in pulmonary carcinoid tumors. *Clin Cancer Res*. 2018;24:1691–1704.

Assessment and Comparison of ^{18}F -Fluorocholine PET and $^{99\text{m}}\text{Tc}$ -Sestamibi Scans in Identifying Parathyroid Adenomas: A Metaanalysis

Julia Whitman¹, Isabel E. Allen², Emily K. Bergsland^{1,3}, Insoo Suh⁴, and Thomas A. Hope^{3,5,6}

¹Division of Hematology/Oncology, Department of Medicine, University of California San Francisco, San Francisco, California; ²Department of Epidemiology and Biostatistics, University of California San Francisco, San Francisco, California; ³Helen Diller Family Comprehensive Cancer Center, University of California San Francisco, San Francisco, California; ⁴Department of Surgery, University of California San Francisco, San Francisco, California; ⁵Department of Radiology and Biomedical Imaging, University of California San Francisco, San Francisco, California; and ⁶Department of Radiology, San Francisco VA Medical Center, San Francisco, California

Hyperparathyroidism is an endocrine disorder caused by one or more hyperfunctioning parathyroid glands. Current imaging consisting of ultrasound and $^{99\text{m}}\text{Tc}$ -sestamibi is imprecise, making localization difficult. ^{18}F -fluorocholine (^{18}F -FCH) PET has recently shown promise in presurgical localization of parathyroid adenomas. The primary aim of this study was to summarize the sensitivities and specificities of studies using ^{18}F -FCH PET to localize hyperparathyroidism. A secondary aim was to summarize a subset of studies in which $^{99\text{m}}\text{Tc}$ -sestamibi scans were also used and to compare the performance of the 2 modalities. **Methods:** We searched the MEDLINE and EMBASE databases following the PRISMA (Preferred Reporting Items for Systematic Review and Metaanalysis) statement. Quality was assessed using the QUADAS-2 tool (Quality Assessment of Diagnostic Accuracy Studies). Twenty studies were included for quantitative assessment in our metaanalysis. A random-effects model and a hierarchic summary receiver-operating-characteristic model was used to summarize the sensitivity of ^{18}F -FCH PET in detecting abnormal parathyroid adenomas. We used the same methodology to assess sensitivity of $^{99\text{m}}\text{Tc}$ -sestamibi, as a comparison to ^{18}F -FCH PET. **Results:** ^{18}F -FCH PET had a high sensitivity, 0.97 (range, 0.96–0.98), for the detection of abnormal parathyroid adenomas. In the subpopulation for which both ^{18}F -FCH and $^{99\text{m}}\text{Tc}$ -sestamibi were reported, ^{18}F -FCH also had a higher sensitivity, 0.96 (0.94–0.98), than the 0.54 (0.29–0.79) reported for $^{99\text{m}}\text{Tc}$ -sestamibi ($P < 0.001$). **Conclusion:** ^{18}F -FCH PET demonstrates high localization accuracy in patients with hyperparathyroidism. This metaanalysis supports the use of ^{18}F -FCH over $^{99\text{m}}\text{Tc}$ -sestamibi in patients with hyperparathyroidism.

Key Words: fluorocholine; hyperparathyroidism; adenoma; PET; $^{99\text{m}}\text{Tc}$ -sestamibi

J Nucl Med 2021; 62:1285–1291
DOI: 10.2967/jnumed.120.257303

Hyperparathyroidism is a common endocrine disorder in which one or more of the parathyroid glands become autonomously

hyperfunctional, causing excessive secretion of parathyroid hormone into the bloodstream (1,2). It is a common endocrine disorder, with an estimated incidence of between 0.4 and 82 cases per 100,000 in the general population (3–6). The etiology is usually a benign overgrowth of parathyroid tissue in at least 1 of the 4 parathyroid glands. This occurs in a single gland in approximately 80% of cases and less frequently (15%–20% of cases) in multiple glands (7). Hyperparathyroidism is diagnosed biochemically and is associated with hypercalcemia and elevated parathyroid hormone (7); in turn, hypercalcemia, if left untreated, can cause significant morbidities ranging from skeletal complications to renal impairment, as well as complications such as nephrocalcinosis, polyuria, and polydipsia.

Surgical removal of the hyperfunctioning gland (i.e., a parathyroidectomy) remains the only curative treatment for hyperparathyroidism (8). Preoperative localization of the hyperfunctioning gland is necessary for a minimally invasive parathyroidectomy, which is associated with a reduced risk of complications and disability after surgery as compared with conventional bilateral cervical exploration (9). Preoperative localization is complex, and imaging recommendations vary considerably. Cervical ultrasonography and $^{99\text{m}}\text{Tc}$ -sestamibi SPECT are the most commonly used methods. However, their accuracy varies considerably depending on the location of the affected glands, the size of the adenoma, and the skill of individual sonographers (10,11).

Given the inconsistencies of currently approved imaging modalities, new approaches are actively being evaluated. Several studies support the utility of ^{18}F -fluorocholine (^{18}F -FCH) PET, and results from the literature are encouraging (12,13). For nearly 20 years, ^{18}F -FCH has been used to detect metastatic prostate cancer. Choline is a precursor for the synthesis of phospholipids in the cell membrane and choline kinase, which results in the elevated phosphocholine that is overexpressed in prostate cancer (14). However, data on the utility of ^{18}F -FCH in localizing hyperparathyroidism remain relatively sparse, and comparison of ^{18}F -FCH PET to traditional tools is limited to single-center studies.

The primary aim of this study was to summarize studies that have used ^{18}F -FCH PET to localize hyperparathyroidism and to assess their sensitivity and specificity after pathologic confirmation. A second aim was to analyze a subset of studies in which a $^{99\text{m}}\text{Tc}$ -sestamibi scan was also used and to compare the sensitivity and specificity with those of ^{18}F -FCH PET imaging.

Received Sep. 26, 2020; revision accepted Jan. 3, 2021.
For correspondence or reprints, contact Thomas A. Hope (thomas.hope@ucsf.edu).
Published online January 15, 2021.
COPYRIGHT © 2021 by the Society of Nuclear Medicine and Molecular Imaging.

MATERIALS AND METHODS

Correct identification of hyperparathyroidism was defined on a per-patient level. The protocol for this metaanalysis was registered with PROSPERO (the International Prospective Register of Systematic Reviews).

Search Strategy

Two of us conducted independent literature reviews for article inclusion in the study. This review included electronic databases, as well as reference lists of relevant articles. The search was applied to the PubMed/MEDLINE and EMBASE databases and was last updated on August 25, 2020. We used a combination of the following terms: choline, fluorocholine, F-choline, FCH; PET, positron emission tomography; and parathyroid, hyperparathyroidism.

Eligibility Criteria

Two reviewers independently assessed article eligibility for inclusion in this study. Disagreements were resolved by consensus. Articles that met the following inclusion criteria were considered for the meta-analysis: studies evaluating the diagnostic accuracy of ^{18}F -FCH PET in patients with hyperparathyroidism, and studies that used pathologic confirmation of hyperparathyroidism as the reference standard. No year or location restrictions were imposed on the studies. Articles were excluded if they risked overlap with other studies (including systematic reviews and other metaanalyses); were not available in English; were on unpublished studies; were on case reports; had fewer than 10 cases; did not use pathology as the reference standard for diagnosing hyperparathyroidism; or did not have data on the diagnosis of hyperparathyroidism at the per-patient level. We also subsequently performed the analysis by removing articles for which cases of secondary and tertiary hyperparathyroidism could not be separated from primary hyperparathyroidism.

Data Collection

The characteristics of the eligible studies are summarized in Table 1. Data were extracted, when available, from each eligible article on the following variables: National Clinical Trial number, prospective versus retrospective, consent performed, number of patients imaged with ^{18}F -FCH, imaging modality (PET/CT or PET/MRI), number of patients with a pathologic correlate, number of imaging readers, whether the readers knew the results of patients' pathology or clinical data, injected dose and range, uptake time, and details on any adverse event reporting.

Quantitative data points were then extracted from eligible studies. These included number of true-positive, false-positive, true-negative, and false-negative diagnoses of hyperparathyroidism based on ^{18}F -FCH imaging as compared with a pathologic correlate on a per-patient basis. If available, the same results were collected for studies in which patients were also imaged with $^{99\text{m}}\text{Tc}$ -sestamibi. One reviewer extracted the data points from eligible studies, and the second reviewer reviewed the extracted data for quality assurance. For each study included in the analysis, bias was assessed qualitatively by 2 reviewers using the Quality Assessment of Diagnostic Accuracy Studies (QUADAS-2) tool (15).

Metaanalytic Methods

For this metaanalysis, we used a random-effects model and a hierarchic summary receiver-operating-characteristic model using Stata, version 12.0 (StataCorp). Sensitivity and specificity are summarized for ^{18}F -FCH imaging accuracy in detecting hyperparathyroidism on a per-patient level using the pathologic correlate as the reference standard. We also assessed sensitivity and specificity for a subset of studies that additionally imaged patients with $^{99\text{m}}\text{Tc}$ -sestamibi. To include all the studies in the metaanalysis, a small number was added to the zero cells

for this subset of studies. All point estimates of sensitivity and specificity from the metaanalysis are reported as the effect size and 95% CIs.

RESULTS

Eligible Studies

An electronic search of the PubMed and EMBASE libraries returned a total of 776 articles (Fig. 1). Twenty studies were deemed eligible for the metaanalysis and are summarized in Table 1. The number of patients assessed ranged from 10 to 151 in our selected studies. All 20 papers were used to evaluate the sensitivity and specificity of ^{18}F -FCH PET in detecting hyperparathyroidism, and 10 studies included data on the results of $^{99\text{m}}\text{Tc}$ -sestamibi to use for comparison. The risk of bias and the applicability of each study to our current research were assessed using the QUADAS-2 tool (Supplemental Table 1; supplemental materials are available at <http://jnm.snmjournals.org>). In several cases, the risk of bias of the index test and the flow and timing of the imaging protocol could not be determined from the information provided in the text. Bias concerned the retrospective nature of many studies included in this analysis, as well as the uncertain time between imaging and parathyroidectomy in several cases. For the purposes of this analysis, a time of less than 4 wk between imaging and surgery was considered to have a low risk of bias.

Performance of ^{18}F -FCH PET in Detecting Hyperparathyroidism

All 20 studies used ^{18}F -FCH imaging (either by PET/CT, $n = 18$, or by PET/MRI, $n = 4$) to identify hyperparathyroidism (Table 2). The included studies were both retrospective ($n = 8$) and prospective ($n = 12$), consent was obtained for research participation in most cases ($n = 17$), and 1 study was registered with ClinicalTrials.gov before conducting research procedures. The average injected ^{18}F -FCH dose ranged from 0.1 MBq/kg to a 325.1-MBq flat dose. The uptake time ranged from 0 min for dynamic imaging to 90 min for static imaging. The most common injected dose was 100 MBq, and the most common uptake time was 60 min. Across the 20 studies, including a total of 796 patients, the results of the random-effects metaanalysis of the sensitivity and specificity was 0.97 (range, 0.96–0.98) and 0.23 (range, 0.11–0.35), respectively (Fig. 2). The positive predictive value of ^{18}F -FCH PET, compared with pathology, was 0.94 (range, 0.92–0.96). In studies that included only patients with primary hyperparathyroidism ($n = 16$), sensitivity and specificity were 0.94 (range, 0.92–0.97) and 0.14 (range, 0–0.36), respectively (Supplemental Fig. 1).

Comparison of ^{18}F -FCH PET and $^{99\text{m}}\text{Tc}$ -Sestamibi in Detecting Hyperparathyroidism

As a secondary analysis, we compared the performance of ^{18}F -FCH PET and $^{99\text{m}}\text{Tc}$ -sestamibi in detecting cases of hyperparathyroidism before surgery. Ten studies, which included 301 patients, had these data available and were used in the comparison (Table 3; Supplemental Fig. 2). ^{18}F -FCH PET had a superior sensitivity of 0.96 (range, 0.94–0.98), compared with 0.54 (range, 0.29–0.79) for $^{99\text{m}}\text{Tc}$ -sestamibi ($P < 0.001$) (Figs. 3 and 4). In studies limited to patients with primary hyperparathyroidism, ^{18}F -FCH PET had a superior sensitivity of 0.97 (range, 0.94–1.00), compared with 0.55 (range, 0.32–0.78) for $^{99\text{m}}\text{Tc}$ -sestamibi.

TABLE 1
Characteristics of Studies Included in Metaanalysis (23–44)

First author	Year	Prospective or retrospective?	NCT number	Consent obtained	Patients with ¹⁸ F-FCH imaging	Patients with parathyroidectomy	Masked readers	Readers	Pathology correlation	PET/CT or PET/MRI?	Injected dose range (MBq)	Injected dose average (MBq)	Uptake time (min)	Primary HPT only?
Alharbi	2018	Retrospective	No	Yes	66	52	No	2	Yes	Both	NR	150	2 & 50	Yes
Amadou	2019	Retrospective	No	No	41	23	No	NR	Yes	PET/CT	NR	231	60	Yes
Bossert	2019	Prospective	No	Yes	34	17	Unclear	2	Yes	PET/CT	NR	3–3.5/kg	9 & 60	Yes
Broos	2019	Prospective	No	Yes	271	139	Yes	3	Yes	PET/CT	NR	150	5 & 60	Yes
Christakis	2019	Prospective	No	Yes	12	12	Yes	1	Yes	PET/CT	NR	300	60 & 90	Yes
Fischli	2017	Retrospective	No	Yes	39	23	No	1	Yes	PET/CT	IQR 180–149	160	45	Yes
Grimaldi	2018	Prospective	No	No	27	21	Unclear	NR	Yes	PET/CT	77–230	100	30	Yes
Hocevar	2017	Retrospective	No	No	151	151	No	NR	Yes	PET/CT	NR	100	5 & 60	Yes
Huber	2018	Retrospective	No	Yes	26	26	Unclear	NR	Yes	Both	NR	151	45	No
Khaff	2019	Prospective	No	Yes	19	19	No	2	Yes	PET/MRI	NR	93.75	16	Yes
Kluijfhout	2017	Prospective	No	Yes	10	10	Yes	2	Yes	PET/MRI	188 ± 26	188	0*	Yes
Kluijfhout	2016	Retrospective	No	Yes	33	33	Unclear	NR	Yes	PET/CT	NR	2/kg	30	No
Lezaic	2014	Prospective	No	Yes	24	24	Unclear	2	Yes	PET/CT	NR	100	5 & 60	Yes
López-Mora	2020	Prospective	No	Yes	33	33	Unclear	3	Yes	PET/CT: digital vs. analog	NR	0.1/kg	Unclear	Yes
Michaud	2014	Prospective	No	Yes	12	12	No	1	Yes	PET/CT	NR	3/kg	0†	No
Piccardo	2019	Prospective	No	Yes	44	31	Unclear	2	Yes	PET/CT	NR	100	10	Yes
Quak	2018	Prospective	NCT02432599	Yes	25	24	Yes	NR	Yes	PET/CT	NR	1.5/kg	60	Yes
Thanseer	2017	Prospective	No	Yes	54	54	Unclear	NR	Yes	PET/CT	150–185	150–185	10–15 & 60	Yes
Uslu-Besli	2020	Retrospective	No	Yes	105	81	No	2	Yes	PET/CT	325.1 ± 86.7	325.1	15 & 45	No
Zajčková	2018	Retrospective	No	Yes	13	13	Unclear	2	Yes	PET/CT	NR	180	30	Yes

*Dynamic imaging for 40 min.

†Dynamic imaging for 10 min followed by static acquisition.

NR = National Clinical Trial; HPT = hyperparathyroidism; NR = not reported; IQR = interquartile range.

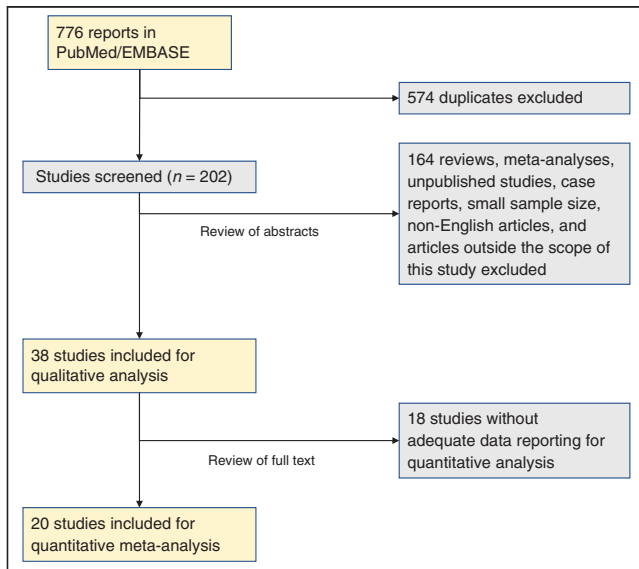


FIGURE 1. PRISMA (Preferred Reporting Items for Systematic Review and Metaanalysis) flow diagram depicting process for selecting papers included in this metaanalysis.

TABLE 2

Overview of Studies Comparing Performance of ^{18}F -FCH PET with Pathology in 20 Studies Reporting Total of 796 Patients

First author	Year	Patients	TP	FP	TN	FN
Alharbi	2018	52	52	0	0	0
Amadou	2019	23	21	1	0	1
Bossert	2019	17	15	0	0	2
Broos	2019	139	131	0	2	6
Christakis	2019	12	7	5	0	0
Fischli	2017	23	21	1	NA	1
Grimaldi	2018	21	17	1	NA	3
Hocevar	2017	151	144	4	1	2
Huber	2018	26	25	0	0	1
Khafif	2019	19	19	0	0	0
Kluijfhout	2017	10	9	0	NA	1
Kluijfhout	2016	33	30	1	NA	2
Lezaic	2014	24	23	0	NA	1
López-Mora	2020	33	29	1	0	3
Michaud	2014	12	11	0	NA	1
Piccardo	2019	31	25	0	0	6
Quak	2018	24	19	3	NA	2
Thanseer	2017	54	52	2	NA	0
Uslu-Bešli	2020	79	76	NA	NA	3
Zajčková	2018	13	12	0	0	1
Total		796	738	19	3	33

TP = true positive; FP = false positive; TN = true negative; FN = false negative; NA = not applicable.

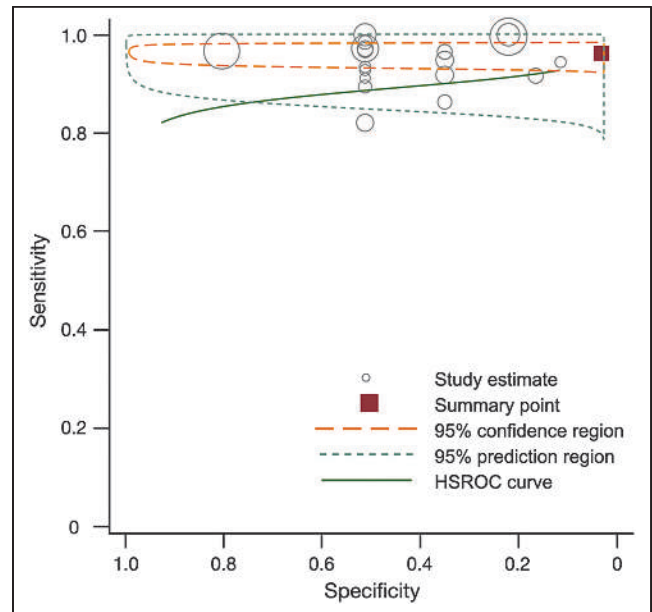


FIGURE 2. Summary of sensitivity, specificity, and hierarchic summary receiver-operating-characteristic (HSROC) plot of sensitivity and specificity for ^{18}F -FCH vs. pathology overall. Effect sizes for sensitivity and specificity were 0.97 (95% CI, 0.96–0.98) and 0.23 (95% CI, 0.11–0.35), respectively. Size of circles represents size of individual studies.

DISCUSSION

Several individual cohort studies have reported ^{18}F -FCH PET to be superior to traditional imaging modalities such as ultrasonography and $^{99\text{m}}\text{Tc}$ -sestamibi in detecting hyperparathyroidism in patients before parathyroidectomy. Individual studies are difficult to interpret because of their small sample sizes and variability between studies. In this metaanalysis, we pool the results of studies using ^{18}F -FCH PET to localize abnormal parathyroid adenomas and using pathology as a reference standard. To acknowledge individual study bias, we assessed each paper using the QUADAS-2 tool and used a random-effects model to account for between-study variability in our quantitative analysis. Overall, the results of this metaanalysis lend further evidence to support the use of ^{18}F -FCH PET as a superior imaging technique over $^{99\text{m}}\text{Tc}$ -sestamibi in the localization of hyperparathyroidism before parathyroidectomy.

To avoid loss of power and incorporate more studies into our analysis, we included studies using both PET/CT and PET/MRI. Diagnostic differences between these modalities for this indication have not been studied in previous literature, but we acknowledge that inclusion of PET/MRI may further bias this analysis. Our study did not consider results on a per-lesion basis, considering only whether imaging localized an overactive parathyroid gland on a per-patient basis. This approach may overestimate the accuracy of ^{18}F -FCH PET as a presurgical tool in avoiding invasive open parathyroidectomies.

As with any metaanalysis, our approach is limited by the underlying data in the articles included. As reported, there was a wide range in acquisition parameters used. Most concerning was that masking of readers to the results of parathyroidectomies before image interpretation was not done or was unclear in most cases,

TABLE 3
Overview of Studies Comparing Performance of ^{99m}Tc-Sestamibi with Pathology

First author	Year	Patients with pathology	^{99m} Tc-sestamibi compared with pathology			
			TP	FP	TN	FN
Amadou	2019	23	9	1	0	13
Bossert	2019	17	3	0	0	14
Huber	2018	26	2	0	0	24
Khaffif	2019	19	17	0	0	2
Kluijfhout	2017	33	8	0	0	21
Lezaic	2014	24	14	0	0	10
Michaud	2014	12	8	2	0	2
Thanseer	2017	54	42	1	1	10
Uslu-Bešli	2020	80	39	1	NA	NA
Zajčková	2018	13	4	2	0	7
Total		301	146	7	1	103

TP = true positive; FP = false positive; TN = true negative; FN = false negative; NA = not applicable.

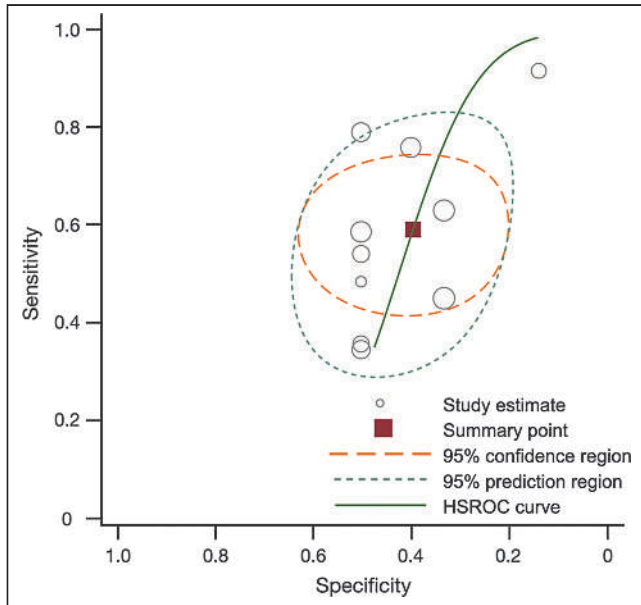


FIGURE 3. Summary of sensitivity, specificity, and hierarchic summary receiver-operating-characteristic (HSROC) plot of sensitivity and specificity for ^{99m}Tc-sestamibi vs. pathology overall. Effect sizes for sensitivity and specificity were 0.54 (0.29–0.79) and 0.43 (0.30–0.57), respectively. Size of circles represents size of individual studies.

and most studies were retrospective. This likely biased individual study results and may have skewed results in favor of ¹⁸F-FCH PET. Furthermore, several studies included patients with a history of thyroid or parathyroid surgery; it is unclear what effect this may have had on the accuracy of either ¹⁸F-FCH PET or ^{99m}Tc-sestamibi in detecting the affected parathyroid glands and may limit the applicability of these results to patients being imaged at baseline.

One other issue is the heterogeneity of the technique used for ^{99m}Tc-sestamibi imaging in our analysis, as each approach has

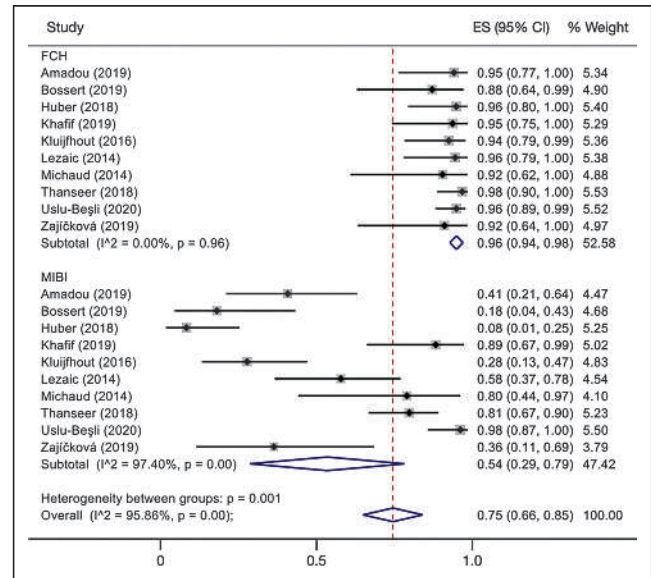


FIGURE 4. Comparison of diagnostic sensitivities of ¹⁸F-FCH and ^{99m}Tc-sestamibi. Overall effect sizes (ES) were 0.96 (95% CI, 0.94–0.98) for ¹⁸F-FCH PET and 0.54 (95% CI, 0.29–0.79) for ^{99m}Tc-sestamibi. Size of squares represents size of individual studies. Reference numbers are in Supplemental Table 2.

varying sensitivities that can lead to inconsistencies across the articles used in the comparison analysis. Of the 10 studies included for comparison with ^{99m}Tc-sestamibi, 6 (including 41% of the analyzed patients) used dual-phase, dual-tracer ^{99m}Tc-sestamibi imaging with SPECT/CT. Three articles used SPECT, 2 of which used ^{99m}Tc-sestamibi alone, and 1 article did not describe the ^{99m}Tc-sestamibi imaging.

Despite these weaknesses, we believe this study is important in a setting that has seen little change in practice over many years. Furthermore, there are features of this study that we feel distinguish it from prior metaanalyses on this topic. We have taken care

to define strict study eligibility criteria, including a minimum cohort size to limit patient selection bias, the requirement of a histopathologic correlate for all cases in the analysis, and a focus on ^{18}F -FCH PET only, excluding studies that incorporate other choline tracers (13). Perhaps most notably, our study included 2 important subanalyses: a comparison of ^{18}F -FCH PET to the standard-of-care $^{99\text{m}}\text{Tc}$ -sestamibi scan, making a strong clinical case for the adoption of this more novel technique; and a further study limited to cases with primary hyperparathyroidism. To our knowledge, it is also the largest study of this kind (12,16).

Beyond $^{99\text{m}}\text{Tc}$ -sestamibi, there are other imaging techniques being evaluated for the localization of abnormal parathyroids, such as 4-dimensional (4D) CT and ^{11}C -choline PET. Both have also demonstrated utility in preoperative localization of parathyroid glands in patients with hyperparathyroidism. Literature on the use of 4D CT, with or without ultrasonography, has reported high but varying sensitivities in localizing adenomas (17,18). There are insufficient data at this time to compare ^{18}F -FCH with 4D CT to perform a metaanalysis. However, there are several theoretic advantages of ^{18}F -FCH over 4D CT, including obviation of intravenous iodinated contrast, as well as the lower total doses of radiation (19). ^{11}C -choline PET, a similar radiotracer to ^{18}F -FCH, received Food and Drug Administration approval in 2012 for use in prostate cancer (20) and has recently been used in preoperative localization for hyperparathyroidism. Because ^{11}C -choline has a half-life of approximately 20 min, compared with 120 min for ^{18}F (21), PET acquisition must occur very shortly after injection. The longer half-life of ^{18}F -FCH allows for more flexible image acquisition and makes for more practical and favorable clinical use (22).

CONCLUSION

In patients with hyperparathyroidism, ^{18}F -FCH PET demonstrates a high sensitivity (0.97) for parathyroid adenomas in patients with hyperparathyroidism. ^{18}F -FCH PET also outperformed $^{99\text{m}}\text{Tc}$ -sestamibi, with a sensitivity of 0.96 for the former compared with 0.54 for the latter. This metaanalysis supports the use of ^{18}F -FCH over $^{99\text{m}}\text{Tc}$ -sestamibi in patients with hyperparathyroidism.

DISCLOSURE

Thomas Hope receives grant support from the National Institutes of Health (R01CA212148). Isabel Allen is supported by the National Institute on Aging (R43AG066230). No other potential conflict of interest relevant to this article was reported.

KEY POINTS

QUESTION: Does ^{18}F -FCH PET aid in the localization of parathyroid adenomas in patients with hyperparathyroidism?

PERTINENT FINDINGS: In this metaanalysis, ^{18}F -FCH PET had a high sensitivity for parathyroid adenomas and increased the sensitivity from 0.54 for $^{99\text{m}}\text{Tc}$ -sestamibi imaging to 0.96 for ^{18}F -FCH PET.

IMPLICATIONS FOR PATIENT CARE: ^{18}F -FCH PET is useful for localizing parathyroid adenomas and should be used when available.

REFERENCES

- Khan AA, Hanley DA, Rizzoli R, Bollerslev J, Young JEM. Primary hyperparathyroidism: review and recommendations on evaluation, diagnosis, and management—a Canadian and international consensus. *Osteoporos Int*. 2017;28:1–19.
- El-Hajj Fuleihan G, Silverberg S. Patient education: primary hyperparathyroidism (beyond the basics). UpToDate website. <https://www.uptodate.com/contents/primary-hyperparathyroidism-beyond-the-basics>. Updated November 5, 2019. Accessed April 22, 2021.
- Yeh MW, Ituarte PHG, Zhou HC, et al. Incidence and prevalence of primary hyperparathyroidism in a racially mixed population. *J Clin Endocrinol Metab*. 2013;98:1122–1129.
- Wermers RA, Khosla S, Atkinson EJ, et al. Incidence of primary hyperparathyroidism in Rochester, Minnesota, 1993–2001: an update on the changing epidemiology of the disease. *J Bone Miner Res*. 2006;21:171–177.
- Press DM, Siperstein AE, Berber E, et al. The prevalence of undiagnosed and unrecognized primary hyperparathyroidism: a population-based analysis from the electronic medical record. *Surgery*. 2013;154:1232–1237.
- Walker MD, Silverberg SJ. Primary hyperparathyroidism. *Nat Rev Endocrinol*. 2018;14:115–125.
- Bilezikian JP, Bandeira L, Khan A, Cusano NE. Hyperparathyroidism. *Lancet*. 2018;391:168–178.
- Imperiale A, Taieb D, Hindie E. ^{18}F -fluorocholine PET/CT as a second line nuclear imaging technique before surgery for primary hyperparathyroidism. *Eur J Nucl Med Mol Imaging*. 2018;45:654–657.
- Udelsman R, Lin Z, Donovan P. The superiority of minimally invasive parathyroidectomy based on 1650 consecutive patients with primary hyperparathyroidism. *Ann Surg*. 2011;253:585–591.
- Ruda JM, Hollenbeck CS, Stack BCJ. A systematic review of the diagnosis and treatment of primary hyperparathyroidism from 1995 to 2003. *Otolaryngol Head Neck Surg*. 2005;132:359–372.
- Kobylecka M, Plazinska MT, Chudzinski W, et al. Comparison of scintigraphy and ultrasound imaging in patients with primary, secondary and tertiary hyperparathyroidism: own experience. *J Ultrason*. 2017;17:17–22.
- Kim S-JJ, Lee S-WW, Jeong SY, et al. Diagnostic performance of F-18 fluorocholine PET/CT for parathyroid localization in hyperparathyroidism: a systematic review and meta-analysis. *Horm Cancer*. 2018;9:440–447.
- Treglia G, Piccardo A, Imperiale A, et al. Diagnostic performance of choline PET for detection of hyperfunctioning parathyroid glands in hyperparathyroidism: a systematic review and meta-analysis. *Eur J Nucl Med Mol Imaging*. 2019;46:751–765.
- Vali R, Loidl W, Pirich C, Langesteger W, Beheshti M. Imaging of prostate cancer with PET/CT using ^{18}F -fluorocholine. *Am J Nucl Med Mol Imaging*. 2015;5:96–108.
- Whiting PF, Rutjes AWS, Westwood ME, et al.; QUADAS-2 Group. QUADAS-2: a revised tool for the quality assessment of diagnostic accuracy studies. *Ann Intern Med*. 2011;154:253–260.
- Pardal-Refoyo JL, Tamayo-Alonso P, Ferreira-Cendon S, Martin-Gomez E. Pathological uptake with 18-fluorocholine versus $^{99\text{m}}\text{Tc}$ -MIBI in the location of the parathyroid glands in hyperparathyroidism: systematic review and meta-analysis. medRxiv website. <https://www.medrxiv.org/content/10.1101/2020.07.25.20161927v1>. Published July 27, 2020. Accessed April 22, 2021.
- Yeh R, Tay Y-KD, Tabacco G, et al. Diagnostic performance of 4D CT and $^{99\text{m}}\text{Tc}$ -sestamibi SPECT/CT in localizing parathyroid adenomas in primary hyperparathyroidism. *Radiology*. 2019;291:469–476.
- Bann DV, Zacharia T, Goldenberg D, Goyal N. Parathyroid localization using 4D-computed tomography. *Ear Nose Throat J*. 2015;94:E55–E57.
- Mahajan A, Starker LF, Ghita M, Udelsman R, Brink JA, Carling T. Parathyroid four-dimensional computed tomography: evaluation of radiation dose exposure during preoperative localization of parathyroid tumors in primary hyperparathyroidism. *World J Surg*. 2012;36:1335–1339.
- FDA approves ^{11}C -choline for PET in prostate cancer. *J Nucl Med*. 2012;53(12):11N–11N.
- Grassi I, Nanni C, Allegri V, et al. The clinical use of PET with ^{11}C -acetate. *Am J Nucl Med Mol Imaging*. 2012;2:33–47.
- Massaro A, Ferretti A, Secchiero C, et al. Optimising ^{18}F -choline PET/CT acquisition protocol in prostate cancer patients. *N Am J Med Sci*. 2012;4:416–420.
- Alharbi AA, Alshehri FM, Albatly AA, et al. [^{18}F]fluorocholine uptake of parathyroid adenoma is correlated with parathyroid hormone level. *Mol Imaging Biol*. 2018;20:857–867.
- Amadou C, Bera G, Ezziane M, et al. ^{18}F -fluorocholine PET/CT and parathyroid 4D computed tomography for primary hyperparathyroidism: the challenge of reoperative patients. *World J Surg*. 2019;43:1232–1242.
- Kluijfhout WP, Pasternak JD, Gosnell JE, et al. ^{18}F fluorocholine PET/MR imaging in patients with primary hyperparathyroidism and inconclusive conventional imaging: a prospective pilot study. *Radiology*. 2017;284:460–467.
- Lezaic L, Rep S, Sever MJ, Kocjan T, Hocevar M, Fettich J. ^{18}F -fluorocholine PET/CT for localization of hyperfunctioning parathyroid tissue in primary hyperparathyroidism: a pilot study. *Eur J Nucl Med Mol Imaging*. 2014;41:2083–2089.

27. Michaud L, Burgess A, Huchet V, et al. Is ^{18}F -fluorocholine-positron emission tomography/computerized tomography a new imaging tool for detecting hyperfunctioning parathyroid glands in primary or secondary hyperparathyroidism? *J Clin Endocrinol Metab.* 2014;99:4531–4536.
28. Piccardo A, Trimboli P, Rutigliani M, et al. Additional value of integrated ^{18}F -choline PET/4D contrast-enhanced CT in the localization of hyperfunctioning parathyroid glands and correlation with molecular profile. *Eur J Nucl Med Mol Imaging.* 2019;46:766–775.
29. Thanseer N, Bhadada SK, Sood A, et al. Comparative effectiveness of ultrasonography, $^{99\text{m}}\text{Tc}$ -sestamibi, and ^{18}F -fluorocholine PET/CT in detecting parathyroid adenomas in patients with primary hyperparathyroidism. *Clin Nucl Med.* 2017;42:e491–e497.
30. Zajíčková K, Zogala D, Kubinyi J, et al. Parathyroid imaging by ^{18}F -fluorocholine PET/CT in patients with primary hyperparathyroidism and inconclusive conventional methods: clinico-pathological correlations. *Physiol Res.* 2018;67(suppl):S551–S557.
31. Quak E, Blanchard D, Houdu B, et al. F18-choline PET/CT guided surgery in primary hyperparathyroidism when ultrasound and MIBI SPECT/CT are negative or inconclusive: the APACH1 study. *Eur J Nucl Med Mol Imaging.* 2018;45:658–666.
32. Khafif A, Masalha M, Landsberg R, et al. The role of F18-fluorocholine positron emission tomography/magnetic resonance imaging in localizing parathyroid adenomas. *Eur Arch Otorhinolaryngol.* 2019;276:1509–1516.
33. López-Mora DA, Sizova M, Estorch M, et al. Superior performance of ^{18}F -fluorocholine digital PET/CT in the detection of parathyroid adenomas. *Eur J Nucl Med Mol Imaging.* 2020;47:572–578.
34. Romano R, Manzo N, Montefusco I, Romano A, Santini A. Liquid carbon dioxide use in the extraction of extra virgin olive oil from olive paste. *J Food Res.* 2014;3:119–128.
35. Beheshti M, Hehenwarter L, Paymani Z, et al. ^{18}F -fluorocholine PET/CT in the assessment of primary hyperparathyroidism compared with $^{99\text{m}}\text{Tc}$ -MIBI or $^{99\text{m}}\text{Tc}$ -tefrosmin SPECT/CT: a prospective dual-centre study in 100 patients. *Eur J Nucl Med Mol Imaging.* 2018;45:1762–1771.
36. Huber GF, Hüllner M, Schmid C, et al. Benefit of ^{18}F -fluorocholine PET imaging in parathyroid surgery. *Eur Radiol.* 2018;28:2700–2707.
37. Uslu-Besli L, Sonmezoglu K, Teksoz S, et al. Performance of F-18 fluorocholine PET/CT for detection of hyperfunctioning parathyroid tissue in patients with elevated parathyroid hormone levels and negative or discrepant results in conventional imaging. *Korean J Radiol.* 2020;21:236–247.
38. Bossert I, Chytiris S, Hodolic M, et al. PET/CT with ^{18}F -choline localizes hyperfunctioning parathyroid adenomas equally well in normocalcemic hyperparathyroidism as in overt hyperparathyroidism. *J Endocrinol Invest.* 2019;42:419–426.
39. Broos WAMM, Wondergem M, Knol RJJJ, et al. Parathyroid imaging with ^{18}F -fluorocholine PET/CT as a first-line imaging modality in primary hyperparathyroidism: a retrospective cohort study. *EJNMMI Res.* 2019;9:72.
40. Christakis I, Khan S, Sadler GP, Gleeson FV, Bradley KM, Mihai R. ^{18}F Fluorocholine PET/CT scanning with arterial phase-enhanced CT is useful for persistent/recurrent primary hyperparathyroidism: first UK case series results. *Ann R Coll Surg Engl.* 2019;101:501–507.
41. Fischli S, Suter-Widmer I, Nguyen BT, et al. The significance of ^{18}F -fluorocholine-PET/CT as localizing imaging technique in patients with primary hyperparathyroidism and negative conventional imaging. *Front Endocrinol (Lausanne).* 2018;8:380.
42. Grimaldi S, Young J, Kamenicky P, et al. Challenging pre-surgical localization of hyperfunctioning parathyroid glands in primary hyperparathyroidism: the added value of ^{18}F -fluorocholine PET/CT. *Eur J Nucl Med Mol Imaging.* 2018;45:1772–1780.
43. Hocevar M, Lezaic L, Rep S, et al. Focused parathyroidectomy without intraoperative parathormone testing is safe after pre-operative localization with ^{18}F -fluorocholine PET/CT. *Eur J Surg Oncol.* 2017;43:133–137.
44. Kluijfhout WP, Vorselaars WMCM, van den Berk SAM, et al. Fluorine-18 fluorocholine PET-CT localizes hyperparathyroidism in patients with inconclusive conventional imaging: a multicenter study from the Netherlands. *Nucl Med Commun.* 2016;37:1246–1252.

Tau^{IQ}: A Canonical Image Based Algorithm to Quantify Tau PET Scans

Alex Whittington¹ and Roger N. Gunn^{1,2} for the Alzheimer's Disease Neuroimaging Initiative

¹Inivcro LLC, London, United Kingdom; and ²Department of Brain Sciences, Imperial College London, Hammersmith Hospital Campus, London, United Kingdom

Recently, Amyloid^{IQ} was introduced as a new canonical image-based algorithm to quantify amyloid PET scans and demonstrated increased power over traditional SUV ratio (SUVR) approaches when assessed in cross-sectional and longitudinal analyses. We build further on this mathematical framework to develop a Tau^{IQ} algorithm for the quantitative analysis of the more complex spatial distribution displayed by tau PET radiotracers. **Methods:** Cross-sectional ($n = 615$) and longitudinal ($n = 149$) ¹⁸F-flortaucipir data were obtained from the Alzheimer's Disease Neuroimaging Initiative along with necessary adjunct amyloid PET and T1-weighted structural MRI data. A subset of these data were used to derive a chronological tau dataset, using Amyloid^{IQ} analysis of associated amyloid PET data to calculate the subject's temporal position in the canonical AD disease process, from which canonical images for the nonspecific and specific binding components of ¹⁸F-flortaucipir in AD were calculated. These 2 canonical images were incorporated into the Tau^{IQ} algorithm that enables the quantification of both global and local tau outcome measures using an image-based regression and statistical parametric analysis of the initial residual image. Performance of the Tau^{IQ} algorithm was compared with SUVR approaches for cross-sectional analyses, longitudinal analyses, and correlation with clinical measures (Alzheimer Disease Assessment Scale–Cognitive Subscale [ADAS-Cog], Clinical Dementia Rating scale–sum of boxes [CDR-SB], and Mini-Mental State Examination [MMSE]). **Results:** Tau^{IQ} successfully calculated global tau load (Tau_L) in all 791 scans analyzed (range, -3.5% to 185.2% ; mean \pm SD, $23\% \pm 20.5\%$) with a nonzero additional local tau component being required in 31% of all scans (cognitively normal [CN], 22%; mild cognitive impairment [MCI], 35%; dementia, 72%). Tau^{IQ} was compared with the best SUVR approach in the cross-sectional analysis (Tau_L increase in effect size: CN– vs. CN+, +45%; CN– vs. MCI+, -5.6% ; CN– vs. dementia+, $+2.3\%$) (+/– indicates amyloid-positive or -negative) and correlation with clinical scores (Tau_L increase in r^2 : CDR-SB+, 7%; MMSE+, 38%; ADAS-Cog+, 0%). Tau^{IQ} substantially outperformed SUVR approaches in the longitudinal analysis (Tau^{IQ} increase in power: CN+, >3.2 -fold; MCI+, >2.2 -fold; dementia+, >2.9 -fold). **Conclusion:** Tau_L as calculated by Tau^{IQ} provides a superior approach for the quantification of tau PET data. In particular, it provides a substantial improvement in power for longitudinal analyses and the early detection of tau deposition and thus should have significant value for clinical imaging trials in AD that are investigating the attenuation of tau deposition with novel therapies.

Key Words: statistical analysis; canonical images; flortaucipir; IQ platform; power in clinical trials; tau PET

J Nucl Med 2021; 62:1292–1300

DOI: 10.2967/jnumed.120.258962

Tau and amyloid- β (A β) are the 2 pathologic hallmarks of Alzheimer disease and consequently represent 2 key targets for both drug and biomarker development. The development of A β PET biomarkers and their associated analytics is well advanced, with established Food and Drug Administration–approved ¹⁸F radiotracers (¹⁸F-florbetapir, ¹⁸F-florbetaben, and ¹⁸F-flutemetamol) available after the pioneering work with ¹¹C-Pittsburgh compound B that originated in 2004 (1). In parallel, analytic approaches for A β agents have advanced from historical SUV ratio (SUVR) methods to the development of centiloids, which allow for conversion of different amyloid agents onto a common scale facilitating their combined use in multicenter imaging trials (2). Further, our previous work using spatiotemporal modeling of A β accumulation in AD (3) deduced that amyloid accumulation is a global process that can be characterized by a single parameter (A β _L) and opened the door for the canonical image based quantification used by Amyloid^{IQ}, which has shown increased power over SUVR-based methods in both cross-sectional and longitudinal analyses (4).

The development of tau imaging agents faced increased challenges due to lower target density, selectivity issues over off-target species, and the existence of different isomeric forms of tau (3R,4R) and gained traction in the following decade only with the introduction of ¹⁸F-flortaucipir in 2013 (5). After this breakthrough, other tau imaging agents have been developed that demonstrate the ability to measure tau deposition in human subjects, including ¹⁸F-MK-6240 (6), ¹⁸F-GTP-1 (7), ¹⁸F-RO-948 (8), ¹⁸F-PI-2620 (9), and ¹⁸F-APN-1607 (10), and in May 2020 ¹⁸F-flortaucipir was Food and Drug Administration–approved as a radioactive diagnostic agent for adults with cognitive impairment who are being evaluated for Alzheimer disease (11,12).

To date, analytic approaches for static tau PET imaging have focused on SUVR approaches, with tau-relevant regions of interest (ROIs) being used to quantify the level of tau deposition in regions corresponding to the different stages of tau accumulation described in the postmortem work of Braak and Braak (13). This includes the use of regions that correspond to Braak stages I–VI and meta-ROIs that consider the initial or strongest areas of deposition (the transentorhinal cortex and other temporal regions (13)), such as the temporal meta-ROI of Jack et al. (14). These SUVR methods have been applied to cross-sectional (15–18) and longitudinal (14,19–21) data to show an increase in tau signals associated with disease progression in AD.

Received Oct. 20, 2020; revision accepted Jan. 13, 2021.
For correspondence or reprints, contact Alex Whittington (alexander.whittington@inivcro.co.uk).
Published online January 30, 2021.
COPYRIGHT © 2021 by the Society of Nuclear Medicine and Molecular Imaging.

The present work extends the prior analytic concepts of Amyloid^{IQ} further to account for the more complex spatiotemporal distribution of tau to develop an algorithm for the quantification of tau PET scans (Tau^{IQ}). Initial investigations of tau PET scans found that the accumulation in many subjects was more complex, with evidence of additional hot spots of local tau deposition. This finding led to the development of an algorithm that can accurately quantify both the global tau accumulation pattern (as with amyloid) and any additional subject-specific localized deposits sitting on top of this pattern. The current work first describes the development of the Tau^{IQ} algorithm and then compares its performance with SUVR approaches for cross-sectional analyses, longitudinal analyses, and correlation with clinical measures using ¹⁸F-flortaucipir data obtained from the Alzheimer's Disease Neuroimaging Initiative (ADNI).

MATERIALS AND METHODS

Imaging Data

Imaging data were obtained from the ADNI database (22). ADNI was launched in 2003 as a public-private partnership, led by Principal Investigator Michael W. Weiner. The primary goal of ADNI has been to test whether serial MRI, PET, other biologic markers, and clinical and neuropsychologic assessment can be combined to measure the progression of mild cognitive impairment (MCI) and early AD. Up-to-date information is available at www.adni-info.org.

Data for Development of Tau^{IQ} Canonical Images

Baseline ¹⁸F-flortaucipir PET, ¹⁸F-florbetapir PET, and structural T1-weighted MRI scans were obtained for 233 subjects (127 cognitively normal [CN], 82 with MCI, and 24 with dementia; 118 men and 114 women; mean age \pm SD, 76.4 y [range, 61.3–94.4 y]; Clinical Dementia Rating scale-sum-of-boxes [CDR-SB] score, 0.88 ± 1.12 [range, 0–5.5]; Mini-Mental State Examination [MMSE] score, 26.7 ± 1.7 [range, 20–30]; Alzheimer Disease Assessment Scale-Cognitive Subscale (ADAS-Cog) score, 16.4 ± 8.7 [range, 2–52.0]).

Cross-Sectional Testing Data

To create a more comprehensive dataset for testing, 382 additional ADNI subjects were added to the development dataset, for a total of 615 subjects (382 CN, 175 with MCI, and 58 with dementia; 290 men and 325 women; age, 74.1 ± 7.7 y [range, 56.0–94.4 y], CDR-SB score, 0.77 ± 1.28 [range, 0–8]; MMSE score, 28.5 ± 2.0 [range, 17–30]; ADAS-Cog score, 16.0 ± 8.1 [range, 2–52]). For these additional subjects, a ¹⁸F-flortaucipir scan, a static amyloid PET scan (¹⁸F-florbetapir or ¹⁸F-florbetaben), and a structural T1-weighted MRI scan were obtained.

Longitudinal Testing Data

From the cross-sectional dataset, 149 subjects (88 CN, 43 with MCI, and 18 with dementia; 76 men and 72 women; age, 74.5 ± 7.4 y [range, 56.3–92.2 y]; CDR-SB score, 0.89 ± 1.42 [range, 0–8]; MMSE score, 28.2 ± 2.3 [range, 17–30]; ADAS-Cog score, 16.5 ± 8.5 [range, 5.3–44.7] at baseline) also had sequential ¹⁸F-flortaucipir PET scans (1 or 2 follow-up visits: 121 subjects had 1 follow-up visit and 27 had 2 follow-up visits) between 4 mo and 2.5 y after baseline, which were used for the longitudinal analysis.

Image Acquisition and Preprocessing

All human PET data were acquired in accordance with the standardized ADNI protocol (23). ¹⁸F-flortaucipir PET scans consisted of emission data from a 30-min (six 5-min frames) acquisition at 75 min after injection, with an injected dose of $370 \text{ MBq} \pm 10\%$. ¹⁸F-florbetapir data consisted of emission data from a 20-min (four 5-min frames)

acquisition collected 50 min after injection, with an injected dose of $370 \text{ MBq} \pm 10\%$. ¹⁸F-florbetaben data consisted of emission data from a 20-min (four 5-min frames) acquisition collected 90 min after injection, with an injected dose of $300 \text{ MBq} \pm 10\%$. Three image-preprocessing steps were applied to the data before entry into the ADNI imaging database (full details are described at <http://adni.loni.usc.edu/methods/pet-analysis/preprocessing>). Briefly, the frames were coregistered and averaged. The resulting image was converted to a $160 \times 160 \times 96$ voxel static image with voxel dimensions of $1.5 \times 1.5 \times 1.5$ mm. Finally, a gaussian filter (of ≤ 6 mm) was applied to harmonize the image resolution with the lowest-resolution scanner used in the study. All subjects also underwent T1-weighted structural MRI. These primary PET and MRI data were downloaded from the ADNI database and used in the subsequent analyses.

Image Processing

Registration of Images into Stereotactic Space. ¹⁸F-flortaucipir, ¹⁸F-florbetapir, and ¹⁸F-florbetaben data were nonlinearly registered into Montreal Neurological Institute template 152 (MNI152) space (24) using the subjects' T1-weighted MRI scan as part of a diffeomorphic nonlinear registration (Diffeomorphic Anatomical Registration using Exponentiated Lie algebra [DARTEL]) (25). Initially, the structural MR images were segmented into gray matter and white matter using SPM, version 12. DARTEL then uses these tissue probability maps to create flow fields that provide the parameters required to spatially normalize any images that are coregistered to the MR image into MNI152 space. Each PET image is registered to the corresponding MRI scan using a rigid-body registration, and the individuals' DARTEL flow-field is applied without modulation, resulting in ¹⁸F-flortaucipir, ¹⁸F-florbetapir, and ¹⁸F-florbetaben images in MNI152 space. The normalized maps are spatially smoothed (gaussian kernel of 8 mm in full width at half maximum).

Generation of SUVR Images. SUVR images for ¹⁸F-flortaucipir were generated using the ventrolateral cerebellum of the CIC atlas (26) as the reference region by dividing all intensities in the image by the mean uptake value for the ventrolateral cerebellum ROI.

Development of Tau^{IQ} Algorithm

Creation of Chronological ¹⁸F-Flortaucipir Dataset and Derivation of Canonical Images. For each subject in the development dataset, Amyloid^{IQ} was performed on the subject's ¹⁸F-florbetapir scan to obtain the subject's amyloid load ($A\beta_L$). Using a previously published functional form, F , describing the temporal accumulation of $A\beta_L$ in AD (27), it was possible to derive the time, T , through the amyloid accumulation process as $T = F^{-1}(A\beta_L)$, which lies in the interval of 0–30 y. This process was repeated for all subjects to produce an estimated time for each of them in the amyloid accumulation process. These times were subsequently associated with each subject's corresponding ¹⁸F-flortaucipir tau PET scan (Fig. 1A).

Next, a linear regression was fitted at the voxel level to the chronological ¹⁸F-flortaucipir PET dataset to estimate the canonical images \mathbf{K} and \mathbf{NS} . The intercept of the linear regression is the nonspecific (\mathbf{NS}) value for that voxel, and the carrying capacity (\mathbf{K}) is 30 multiplied by the gradient so that a scan with 100% global tau load (Tau_L) will correspond to a subject with the expected level of tau observed at the 30-y time point in the amyloid accumulation process (Fig. 1B). In a final step, the carrying-capacity image was made symmetric by averaging the intensities in the left and right hemispheres.

Tau^{IQ} Algorithm. The Tau^{IQ} algorithm decomposes a tau PET scan into nonspecific Tau_L , local tau load ($L\text{Tau}_L$), and noise using \mathbf{NS} and \mathbf{K} and a statistical parametric analysis of an initial residual image (Fig. 2). This process is performed in 2 steps. First, an image-based regression of the tau PET scan with the 2 canonical images is performed in MNI152 space, using QR decomposition in MATLAB,

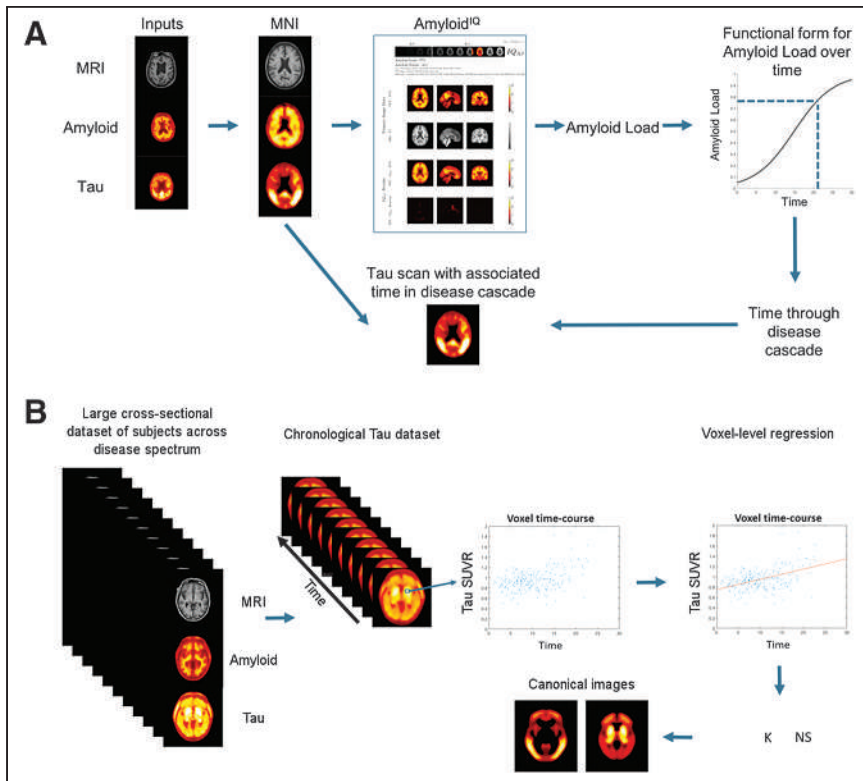


FIGURE 1. Methodology for creating ¹⁸F-flortaucipir canonical images. (A) Creation of chronological ¹⁸F-flortaucipir dataset using associated ¹⁸F-florbetapir data. (B) Generation of ¹⁸F-flortaucipir **K** and **NS** canonical images from voxelwise modeling of chronological dataset.

to estimate the Tau_L , the nonspecific scaling factor (ns), and a residual image:

$$SUVr = ns \cdot NS + Tau_L \cdot K. \quad (1)$$

This step is equivalent to Amyloid^{IQ} (4) and uses DARTEL (25) in the same way to align images into MNI152 space.

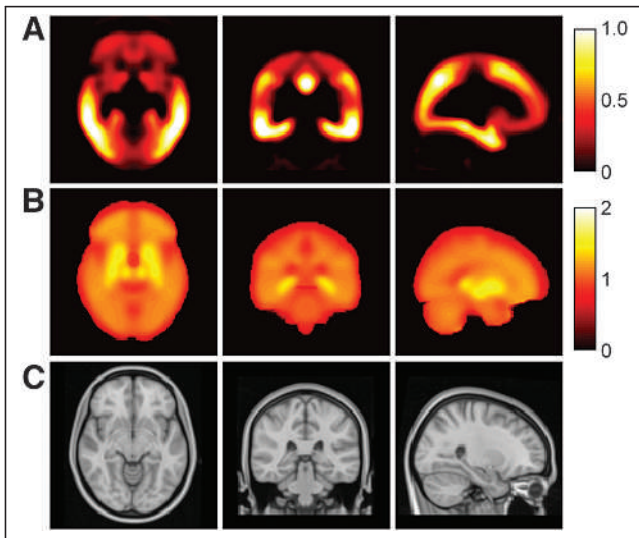


FIGURE 2. Canonical images for ¹⁸F-flortaucipir PET derived from spatiotemporal modeling of chronological AD data in MNI152 space: tau canonical image (**K**) (A), nonspecific canonical image (**NS**) (B), and reference structural T1-weighted MR image (C).

Second, the derived residual image is processed via a statistical parametric analysis to estimate an image representing the local tau signal (i.e., signal that is over and above the level of noise expected in the residual image). This statistical parametric analysis uses data derived from a set of amyloid-negative healthy control ¹⁸F-flortaucipir scans ($n = 65$), where it is assumed that there is negligible tau, to derive mean and SD images from this set of residual images in order to characterize the noise distribution. These mean and SD images allow for the conversion of a residual image calculated by the first step of Tau^{IQ} to a z score image. This z score image is then processed with the SPM gaussian random fields algorithm (28) to estimate clusters of voxels that are significantly greater than zero using a conservative threshold of $P < 0.01$. The $LTau_L$ parameter is then calculated as the 3-dimensional integral of the signal in the local tau image and so is a function of both the intensity and the extent of the local tau signal and has the units $SUVr \cdot cm^3$.

Thus, the overall Tau^{IQ} algorithm (Fig. 3) takes as its input a 3-dimensional tau PET image and corresponding structural MRI scan to produce 3 main outputs: the Tau_L , which is the scaling factor for the carrying capacity image (**K**); the local tau image, which shows the local tau signal across the

brain; and the $LTau_L$, which is a summary measure of this local signal accounting for both extent and intensity.

Comparison of Tau^{IQ} and SUVR Quantification

The Tau^{IQ} outcome measure Tau_L was compared with SUVR in a cross-sectional analysis, in a longitudinal analysis, and in terms of its relationship with clinical scores (CDR-SB, MMSE, and ADAS-Cog). For all ¹⁸F-flortaucipir scans, spatially normalized SUVR images were used to calculate mean regional SUVRs for 4 regions through the application of Jack meta, Braak I/II, Braak III/IV, and Braak V/VI ROIs defined in MNI152 space (Supplemental Fig. 1; supplemental materials are available at <http://jnm.snmjournals.org>). Amyloid^{IQ} was used to classify each subject as $A\beta+$ or $A\beta-$ (positive is defined as an $A\beta_L$ greater than 33% (29)) to enable subsequent cross-sectional and longitudinal analyses that were stratified for amyloid positivity.

Cross-Sectional Analyses. The Hedges g effect sizes were calculated and compared for group comparisons of $CN+$ versus $CN-$, $MCI+$ versus $CN-$, and $dementia+$ versus $CN-$ (+/- indicates amyloid-positive or -negative) using Tau_L and SUVR outcome measures. A 95% CI on the calculated Hedges g was estimated using 10,000 bootstrap replicates of the sample, which was also used to calculate the probability that the outcome measure with the highest effect size in each comparison was superior to all others.

Longitudinal Analyses. A linear regression was performed on the change from baseline of the different outcome measures for each subject, with the intercept constrained to zero. The gradient of this linear regression provides the change per year, and this was recorded for every subject and all analysis approaches. The distributions of the changes per year for the different clinical groups were plotted, and the mean, SD, and effect size (mean divided by SD) were calculated. A 95% CI on the calculated effect size was estimated using 10,000 bootstrap replicates of

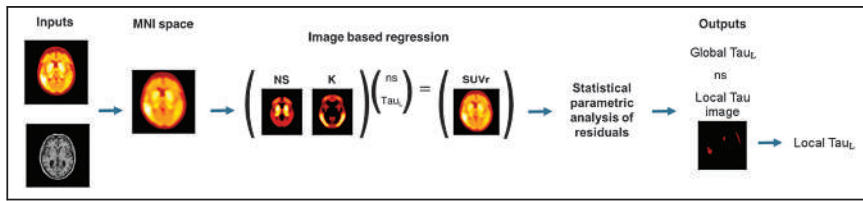


FIGURE 3. Tau^{IQ} algorithm that estimates global and local tau outcome measures.

the sample, which was also used to calculate the probability that the outcome measure with the highest effect size in each clinical group was superior to all others. Finally, the calculated effect size was also used to estimate the sample size required for a clinical trial with an active and placebo arm designed to detect a 25% reduction in tau accumulation in the active arm over 1 y (power = 80%, $\alpha = 0.05$).

Relationship to Clinical Scores. To assess the relationship of the outcome measures Tau_L and SUVR to clinical scores of disease severity, all derived at baseline, correlation analysis (Pearson correlation) was performed with 3 clinical measures: CDR-SB ($n = 615$), MMSE ($n = 615$), and ADAS-Cog ($n = 607$).

RESULTS

Canonical Images

The process of fitting a linear regression at the voxel level to the chronological dataset was performed successfully and produced 2 ¹⁸F-flortaucipir canonical images: the tau carrying-capacity image **K** and the nonspecific-binding image **NS** (Fig. 3). The carrying-capacity image exhibited the highest intensities in the temporal and parietal lobe, and the nonspecific-binding image showed the highest intensities in the striatum, which is consistent with some known off-target binding for ¹⁸F-flortaucipir in this region (30,31).

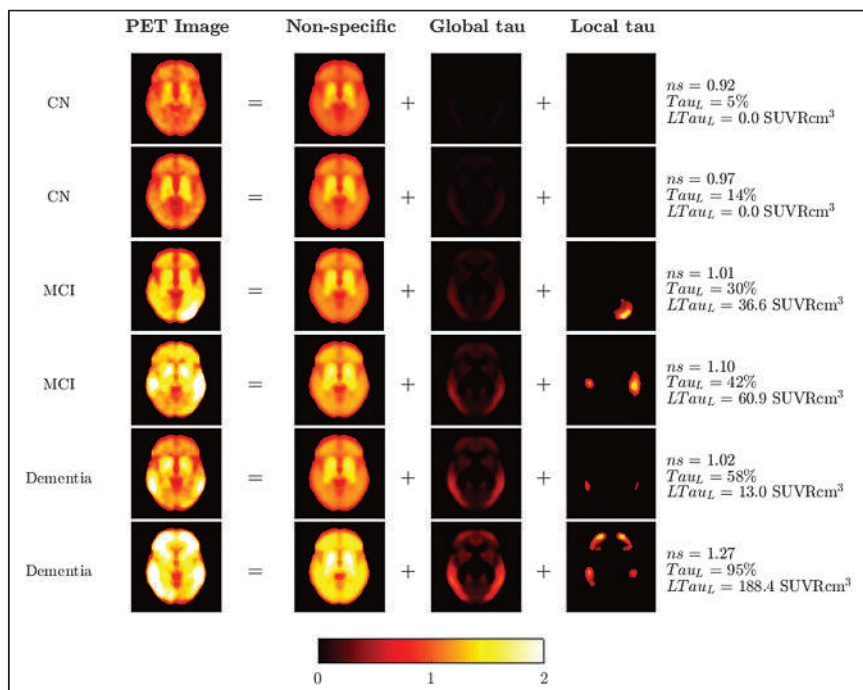


FIGURE 4. Examples of Tau^{IQ} decomposition of ¹⁸F-flortaucipir data into nonspecific, global, and local tau signals.

Tau^{IQ}

The Tau^{IQ} algorithm was successfully applied to 791 tau PET scans (488 CN, 226 MCI, and 77 dementia) from cross-sectional and longitudinal datasets and was able to decompose the scans into 3 key components: nonspecific binding, global tau, and local tau. The ¹⁸F-flortaucipir signal was well characterized, with the final residual images reflecting noise

as expected (representative examples are shown in Fig. 4). Tau_L values estimated across all scans ranged between -3.5% and 185.2% (mean, 21.9% ± 20.4%), and a local tau component was required in 31% of all scans (CN, 22%; MCI, 35%; dementia, 72%).

Cross-Sectional Analysis

Tau_L had the highest effect size for comparison of the CN- and CN+ groups ($P < 0.10$) and an effect size similar to the best SUVR approach for comparison of the CN- and MCI+ groups ($P < 0.64$) and the CN- and dementia+ groups ($P < 0.44$) (Tau_L increase in effect size: CN- vs. CN+, +45%; CN- vs. MCI+, -5.6%; CN- vs. dementia+, +2.3%; Table 1; Fig. 5). Effect sizes among all groups can be found in Supplemental Table 1.

Longitudinal Analysis

The effect size for Tau^{IQ} was greater than that for SUVR in all 6 clinical groups investigated, with the largest value observed in the MCI+ group (Table 2). For Tau^{IQ}, the greatest mean increases per year were also seen in the MCI+ group (3.61%/y), followed by the dementia+ group (2.52%/y) and the CN+ group (2.01%/y). This translated to the MCI+ group's having the lowest clinical trial sample size ($n = 213$ per arm) required to show a 25% attenuation in the accumulation of tau deposition over a 1-y period (power = 80%, $\alpha = 0.05$). Fewer subjects showed a reduction in tau signal over time with Tau^{IQ} than with any of the SUVR measures (34 for Tau_L, 61 for SUVR Jack meta-ROI, 68 for SUVR Braak I/II, 57 for SUVR Braak III/IV, 62 for SUVR Braak V/VI; Fig. 6).

Correlation with Clinical Outcome Measures

Analysis of the relationship between the clinical outcome measures (CDR-SB, MMSE, and ADAS-Cog) with both Tau^{IQ} and SUVR outcome measures demonstrated that Tau_L had the strongest relationship with CDR-SB and MMSE (Fig. 7). For ADAS-Cog, the Jack meta-ROI and Tau_L equaled each other in exhibiting the highest correlation ($r^2 = 0.34$).

DISCUSSION

This work extends to tau PET imaging the canonical image-based quantification recently developed for A β (Amyloid^{IQ}) (7), which has shown increased performance over existing SUVR-based

TABLE 1
Cross-Sectional Analysis*

Outcome measure	CN- vs. CN+	CN- vs. MCI+	CN- vs. dementia+
Tau ^{IQ} Tau _L	1.00 (0.69–1.35), P < 0.10	1.53 (1.21–1.88)	2.70 (2.28–3.26), P < 0.44
SUVR Jack meta-ROI	0.69 (0.39–1.03)	1.58 (1.21–2.01)	2.64 (2.16–3.27)
SUVR Braak I/II	0.55 (0.26–0.85)	1.62 (1.24–2.04), P < 0.64	2.46 (1.98–3.03)
SUVR Braak III/IV	0.57 (0.28–0.88)	1.34 (0.99–1.72)	2.37 (1.93–2.92)
SUVR Braak V/VI	0.49 (0.19–0.80)	0.97 (0.63–1.32)	1.90 (1.48–2.40)

*Effect sizes with CIs for ¹⁸F-flortaucipir Tau_L and SUVR outcome measures derived from group comparisons. Best-performing method in terms of effect size is highlighted in bold along with probability it is best method.

approaches. The more complex deposition of tau, as compared with Aβ, in AD subjects necessitates the incorporation of a local tau component in the algorithm (with 31% of subjects analyzed in this study requiring the addition of this local tau component).

¹⁸F-flortaucipir canonical images characterizing the nonspecific background signal and the global spatial distribution for tau in AD were successfully calculated from a chronological dataset. The nonspecific image, NS, is consistent with ¹⁸F-flortaucipir images observed in Aβ- healthy controls, from whom tau is absent, demonstrating a homogeneous signal throughout the brain apart from increased uptake in the striatum consistent with known off-target binding of the tracer, which has been linked to monoamine oxidases (32). The carrying-capacity image, K, is consistent with postmortem maps of tau from AD subjects that show increased deposition in line with Braak staging (13,33), with the areas of the temporal lobe that have the highest signal being consistent with the earliest deposition of tau in that region. The Tau^{IQ} algorithm presented here uses these canonical images to determine an estimate of Tau_L (the scaling factor associated with the canonical tau image) and an estimate of LTau_L (any additional tau signal that sits on top of the global tau component).

The performance of the primary Tau^{IQ} outcome parameter (Tau_L) was assessed against current SUVR approaches using common composite ROIs in cross-sectional analysis, longitudinal

analysis, and correlation with clinical scores. For the cross-sectional analyses and correlation with clinical outcome measures, Tau^{IQ} typically yielded numerically higher performance metrics than did the best SUVR approach (frequently the Jack meta-ROI). In the longitudinal analysis, Tau^{IQ} provided a substantial increase in power over all SUVR approaches. Tau^{IQ} also demonstrated a more plausible annual change (CN+, 2.0%/y; MCI+, 3.6%/y; dementia+, 2.5%/y) that is consistent with increasing deposition. The clinical trial power calculations demonstrated that Tau^{IQ} would be powered to detect a 25% reduction in tau accumulation with a 2-arm study involving 213 subjects per arm and that a 50% reduction could be detected with 54 subjects per arm. This has significant implications for the use of Tau^{IQ} in clinical trials where tau imaging is being deployed as a pharmacodynamic endpoint to assess the impact of novel therapies. Further, Tau^{IQ} was significantly superior in detecting early tau deposition as evidenced by the increase in effect size for the cross-sectional comparison of the CN- and CN+ groups (+45%) and the longitudinal data from the CN+ (+324%) and MCI- (+205%) groups, which indicate that Tau^{IQ} could play an important role in the stratification of early AD populations for trial entry.

Although Tau_L has been the primary Tau^{IQ} outcome explored in this work, the algorithm also calculates a LTau_L parameter if additional local deposition of tau is present. In this study, 31% of all scans had a nonzero LTau_L, and the percentage was higher as disease progressed (CN, 22%; MCI, 35%; dementia, 72%). This parameter will be investigated further in future work but could have value in stratifying subjects into subgroups for clinical trial analysis, and it will be interesting to explore whether these deposits relate more directly to individual clinical deficits of patients.

One limitation of this work is that longitudinal changes in atrophy and their impact on the PET measures were not considered; however, the magnitude of atrophy effects is lower than the changes observed for Tau_L, and these effects are present for both Tau^{IQ} and SUVR. Partial-volume correction methods could theoretically be applied to both SUVR and Tau^{IQ} approaches, and further work

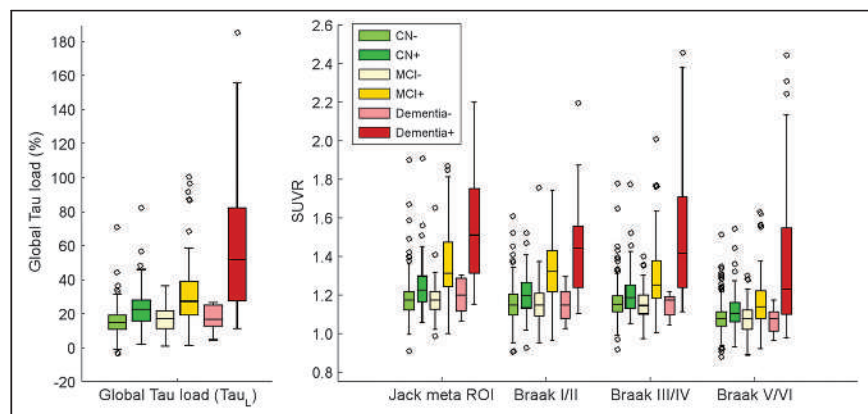


FIGURE 5. Cross-sectional analysis shown as box plots of distributions of ¹⁸F-flortaucipir Tau_L and SUVR outcome measures by clinical group.

TABLE 2
Longitudinal Analysis*

Parameter	Tau ^{IQ} Tau _L	SUVr Jack meta-ROI	SUVr Braak I/II	SUVr Braak III/IV	SUVr Braak V/VI
CN-					
Mean and SD	1.20 (2.31)	0.003 (0.037)	0.001 (0.037)	0.003 (0.036)	-0.001 (0.037)
Effect size and CI	0.52 (0.28 to 0.79), P < 0.016	0.09 (-0.18 to 0.37)	0.02 (-0.25 to 0.30)	0.08 (-0.19 to 0.37)	-0.02 (-0.30 to 0.24)
<i>n</i>	940	33,812	557,745	37,422	847,562
CN+					
Mean and SD	2.01 (2.97)	0.009 (0.044)	0.007 (0.039)	0.007 (0.041)	0.007 (0.039)
Effect size and CI	0.68 (0.43 to 0.98), P < 0.022	0.21 (-0.12 to 0.55)	0.19 (-0.15 to 0.52)	0.18 (-0.16 to 0.55)	0.17 (-0.16 to 0.55)
<i>n</i>	546	5,726	6,699	8,170	9,019
MCI-					
Mean and SD	1.87 (2.28)	0.008 (0.032)	-0.002 (0.040)	0.004 (0.031)	0.010 (0.025)
Effect size and CI	0.82 (0.57 to 1.58), P < 0.13	0.24 (-0.22 to 0.82)	-0.04 (-0.49 to 0.53)	0.13 (-0.31 to 0.79)	0.40 (-0.05 to 0.94)
<i>n</i>	377	4,458	190,970	14,512	1,610
MCI+					
Mean and SD	3.61 (3.31)	0.023 (0.049)	0.008 (0.052)	0.023 (0.047)	0.017 (0.044)
Effect size and CI	1.09 (0.79 to 1.54), P < 0.020	0.47 (0.12 to 0.85)	0.16 (-0.24 to 0.57)	0.49 (0.13 to 0.93)	0.39 (0.00 to 0.89)
<i>n</i>	213	1,130	10,229	1,063	1,655
Dementia-					
Mean and SD	1.53 (2.43)	-0.001 (0.032)	-0.007 (0.019)	0.002 (0.024)	0.002 (0.024)
Effect size and CI	0.63 (-0.13 to 2.14), P < 0.28	-0.04 (-1.55 to 0.76)	-0.34 (-1.32 to 0.76)	0.09 (-1.18 to 1.01)	0.06 (-1.52 to 1.01)
<i>n</i>	640	147,860	2,080	29,595	63,426
Dementia+					
Mean and SD	2.52 (6.64)	0.004 (0.085)	-0.011 (0.079)	0.002 (0.080)	-0.005 (0.078)
Effect size and CI	0.38 (-0.17 to 1.42), P < 0.27	0.05 (-0.44 to 0.83)	-0.13 (-0.58 to 0.71)	0.02 (-0.56 to 0.76)	-0.06 (-0.64 to 0.71)
<i>n</i>	1,741	99,385	13,985	32,2607	67,106

*Change in ¹⁸F-flortaucipir Tau_L and SUVr outcome measures per year for each clinical group. Best-performing method in terms of effect size (mean/SD) is highlighted in bold along with probability that it is the best method. *n* is number of subjects, in both active and placebo arms of simulated clinical trial, required to show 25% reduction in tau accumulation in active arm over period of 1 y (power = 80%, α = 0.05).

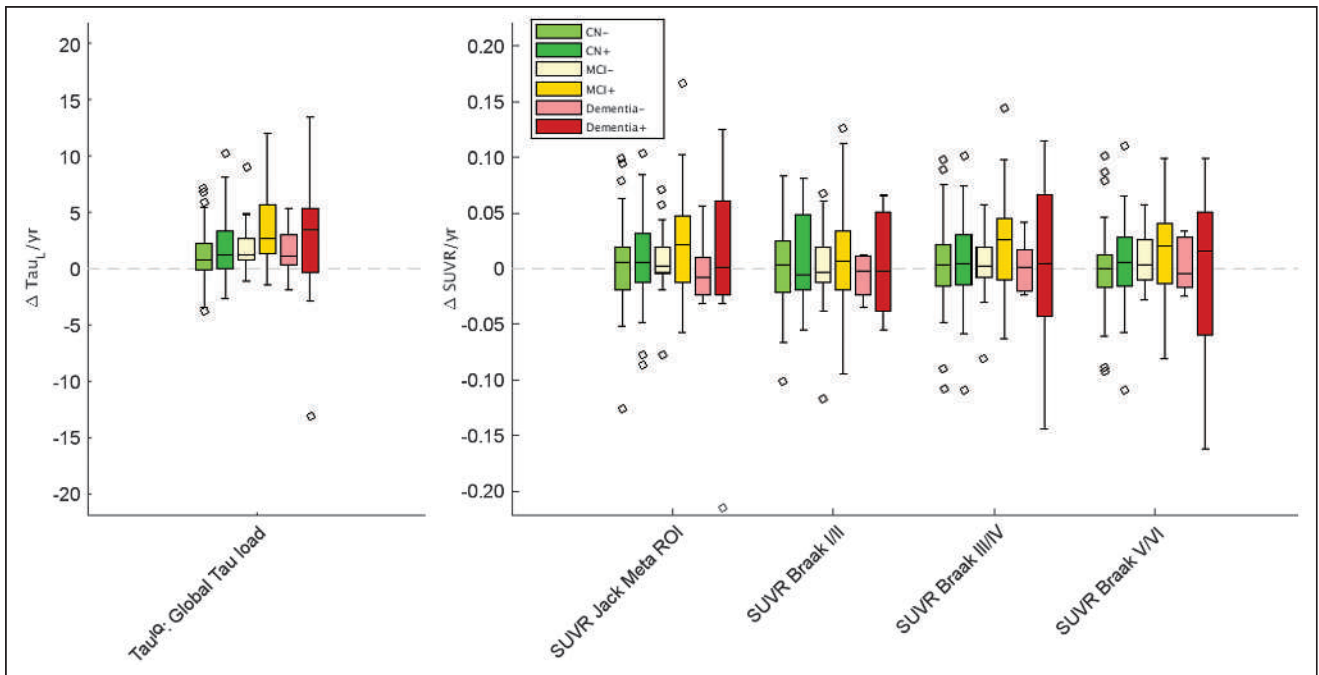


FIGURE 6. Longitudinal analysis shown as box plots of distributions of change in ^{18}F -flortaucipir Tau_L and SUVR outcome measures.

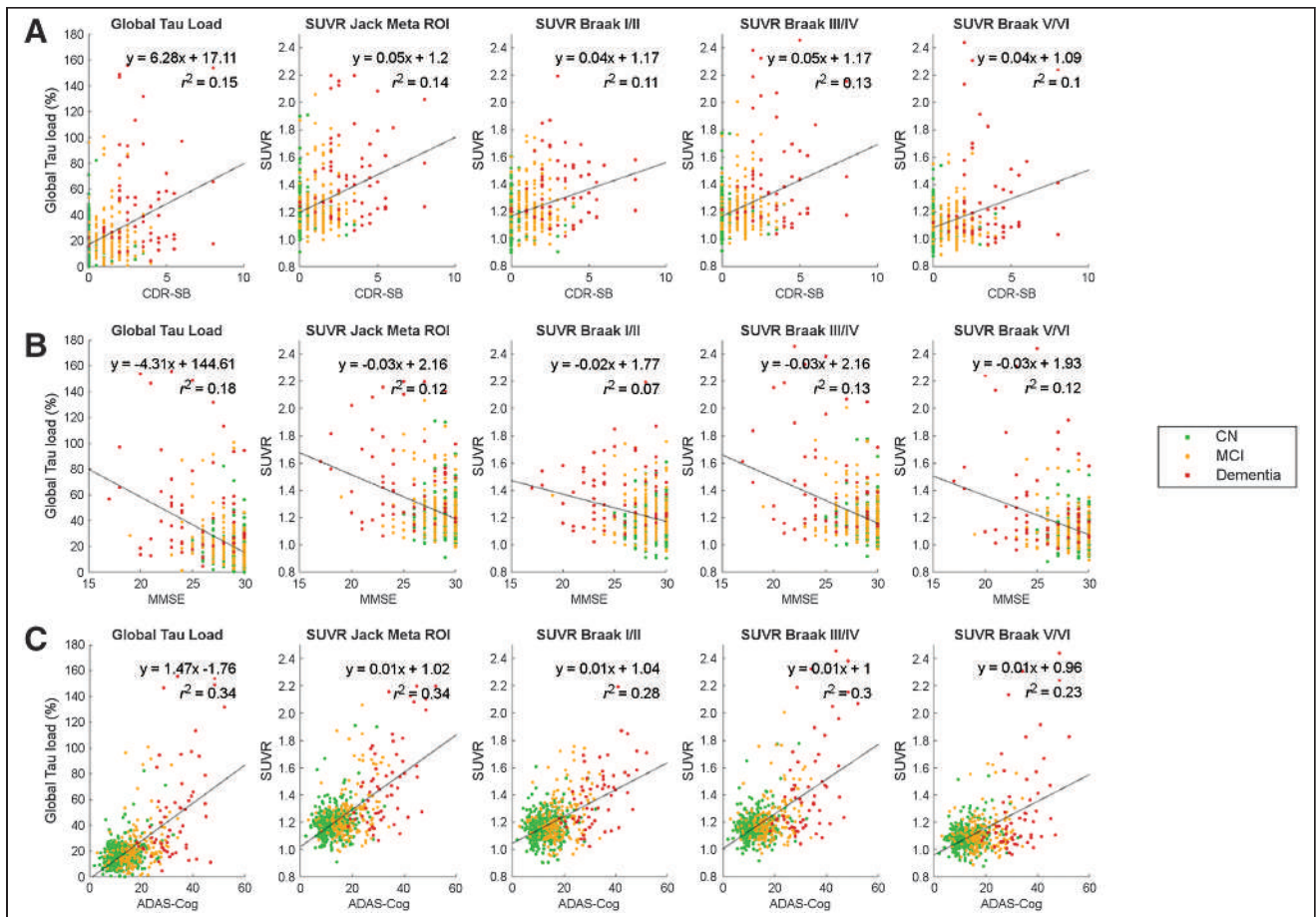


FIGURE 7. Correlations between clinical scores (CDR-SB, MMSE, and ADAS-Cog) and tau imaging outcome measures.

will investigate this possibility. Also, the current analysis used spatially normalized and smoothed images as part of the analytic pipeline. It is possible that further advantages could be obtained through processing of unsmoothed images in native space for both SUVR and Tau^{IQ}.

Although the current work used the tau tracer ¹⁸F-flortaucipir, the algorithm is equally applicable to other tau tracers given the appropriate generation of tracer-specific canonical images. Work with the tracer ¹⁸F-GTP-1 has also been presented and demonstrated increased performance over SUVR approaches (34).

CONCLUSION

Tau^{IQ} is a canonical image-based algorithm for the quantification of tau PET scans and accounts for the more complex deposition of tau than of amyloid. Tau_L as estimated by Tau^{IQ} provides a substantial improvement in power for longitudinal analyses and for early detection of tau deposition over SUVR approaches and should have significant value for clinical imaging trials in AD that are investigating the attenuation of tau deposition with novel therapies.

DISCLOSURE

Data collection and sharing for this project were funded by the ADNI (National Institutes of Health grant U01 AG024904) and DOD ADNI (Department of Defense award W81XWH-12-2-0012). ADNI is funded by the National Institute on Aging, by the National Institute of Biomedical Imaging and Bioengineering, and through generous contributions from the following: AbbVie, Alzheimer's Association; Alzheimer's Drug Discovery Foundation; Araclon Biotech; BioClinica, Inc.; Biogen; Bristol-Myers Squibb Company; CereSpir, Inc.; Cogstate; Eisai Inc.; Elan Pharmaceuticals, Inc.; Eli Lilly and Company; EuroImmun; F. Hoffmann-La Roche Ltd. and its affiliated company Genentech, Inc.; Fujirebio; GE Healthcare; IXICO Ltd.; Janssen Alzheimer Immunotherapy Research & Development, LLC; Johnson & Johnson Pharmaceutical Research & Development LLC; Lumosity; Lundbeck; Merck & Co., Inc.; Meso Scale Diagnostics, LLC; NeuroRx Research; Neurotrack Technologies; Novartis Pharmaceuticals Corporation; Pfizer Inc.; Piramal Imaging; Servier; Takeda Pharmaceutical Company; and Transition Therapeutics. The Canadian Institutes of Health Research provides funds to support ADNI clinical sites in Canada. Private-sector contributions are facilitated by the Foundation for the National Institutes of Health (www.fnih.org). The grantee organization is the Northern California Institute for Research and Education, and the study is coordinated by the Alzheimer's Therapeutic Research Institute at the University of Southern California. ADNI data are disseminated by the Laboratory for Neuro Imaging at the University of Southern California. Alex Whittington is an employee of Invicro. Roger Gunn is an employee of Invicro and a consultant for Abbvie, Biogen, and Cerveau. No other potential conflict of interest relevant to this article was reported.

ACKNOWLEDGMENTS

We thank Jacob Hesterman, John Seibyl, Ken Marek, and Mark Mintun for valuable discussions during this work. Data used in preparation of this article were obtained from the Alzheimer Disease Neuroimaging Initiative (ADNI) database (<http://adni.loni.usc.edu>). As such, the investigators within the ADNI contributed to the design and implementation of ADNI or

provided data but did not participate in analysis or writing of this report. A complete listing of ADNI investigators can be found at https://adni.loni.usc.edu/wp-content/uploads/how_to_apply/ADNI_Acknowledgement_List.pdf.

KEY POINTS

QUESTION: What is the best way of quantifying tau PET images?

PERTINENT FINDINGS: The Tau^{IQ} algorithm introduced in this work shows increased performance over standard SUVR approaches. This quantification approach will provide increased performance when using tau imaging as a biomarker in clinical trials, leading to either studies with fewer subjects or increased signals.

IMPLICATIONS FOR PATIENT CARE: This algorithm might provide data for important clinical decision making when AD therapies become approved.

REFERENCES

1. Klunk WE, Engler H, Nordberg A, et al. Imaging brain amyloid in Alzheimer's disease with Pittsburgh compound-B. *Ann Neurol*. 2004;55:306–319.
2. Klunk WE, Koeppe RA, Price JC, et al. The centiloid project: standardizing quantitative amyloid plaque estimation by PET. *Alzheimers Dement*. 2015;11:1–15.e1.
3. Whittington A, Sharp DJ, Gunn RN. Spatiotemporal distribution of β -amyloid in Alzheimer disease is the result of heterogeneous regional carrying capacities. *J Nucl Med*. 2018;59:822–827.
4. Whittington A, Gunn RN; Alzheimer's Disease Neuroimaging Initiative. Amyloid load: a more sensitive biomarker for amyloid imaging. *J Nucl Med*. 2019;60:536–540.
5. Chien DT, Bahri S, Szardenings AK, et al. Early clinical PET imaging results with the novel PHF-tau radioligand [¹⁸F]-T807. *J Alzheimers Dis*. 2013;34:457–468.
6. Lohith TG, Bennacef I, Vandenberghe R, et al. Brain imaging of Alzheimer dementia patients and elderly controls with ¹⁸F-MK-6240, a PET tracer targeting neurofibrillary tangles. *J Nucl Med*. 2019;60:107–114.
7. Sanabria Bohórquez S, Marik J, Ogasawara A, et al. [¹⁸F]GTP1 (Genentech Tau Probe 1), a radioligand for detecting neurofibrillary tangle tau pathology in Alzheimer's disease. *Eur J Nucl Med Mol Imaging*. 2019;46:2077–2089.
8. Wong DF, Comley RA, Kuwabara H, et al. Characterization of 3 novel tau radiopharmaceuticals, ¹¹C-RO-963, ¹¹C-RO-643, and ¹⁸F-RO-948, in healthy controls and in Alzheimer subjects. *J Nucl Med*. 2018;59:1869–1876.
9. Mueller A, Bullich S, Barret O, et al. Tau PET imaging with ¹⁸F-PI-2620 in patients with Alzheimer disease and healthy controls: a first-in-humans study. *J Nucl Med*. 2020;61:911–919.
10. Hsu J-L, Lin K-J, Hsiao I-T, et al. The imaging features and clinical associations of a novel tau PET tracer—¹⁸F-APN1607 in Alzheimer disease. *Clin Nucl Med*. 2020;45:747–756.
11. Barthel H. First tau PET tracer approved: toward accurate in vivo diagnosis of Alzheimer disease. *J Nucl Med*. 2020;61:1409–1410.
12. Mattay VS, Fotenos AF, Ganley CJ, Marzella L. Brain tau imaging: Food and Drug Administration approval of ¹⁸F-flortaucipir injection. *J Nucl Med*. 2020;61:1411–1412.
13. Braak H, Braak E. Neuropathological staging of Alzheimer-related changes. *Acta Neuropathol (Berl)*. 1991;82:239–259.
14. Jack CR Jr, Wiste HJ, Schwarz CG, et al. Longitudinal tau PET in ageing and Alzheimer's disease. *Brain*. 2018;141:1517–1528.
15. Johnson KA, Schultz A, Betensky RA, et al. Tau positron emission tomographic imaging in aging and early Alzheimer disease. *Ann Neurol*. 2016;79:110–119.
16. Villemagne VL, Fodero-Tavoletti MT, Masters CL, Rowe CC. Tau imaging: early progress and future directions. *Lancet Neurol*. 2015;14:114–124.
17. Schöll M, Lockhart SN, Schonhaut DR, et al. PET imaging of tau deposition in the aging human brain. *Neuron*. 2016;89:971–982.
18. Ossenkoppele R, Schonhaut DR, Schöll M, et al. Tau PET patterns mirror clinical and neuroanatomical variability in Alzheimer's disease. *Brain*. 2016;139:1551–1567.

19. Pontecorvo MJ, Devous MD, Kennedy I, et al. A multicentre longitudinal study of flortaucipir (¹⁸F) in normal ageing, mild cognitive impairment and Alzheimer's disease dementia. *Brain*. 2019;142:1723–1735.
20. Sintini I, Martin PR, Graff-Radford J, et al. Longitudinal tau-PET uptake and atrophy in atypical Alzheimer's disease. *Neuroimage Clin*. 2019;23:101823.
21. Harrison TM, La Joie R, Maass A, et al. Longitudinal tau accumulation and atrophy in aging and Alzheimer disease. *Ann Neurol*. 2019;85:229–240.
22. Mueller SG, Weiner MW, Thal LJ, et al. Ways toward an early diagnosis in Alzheimer's disease: the Alzheimer's Disease Neuroimaging Initiative (ADNI). *Alzheimers Dement*. 2005;1:55–66.
23. Jagust WJ, Landau SM, Koeppe RA, et al. The Alzheimer's Disease Neuroimaging Initiative 2 PET Core: 2015. *Alzheimers Dement*. 2015;11:757–771.
24. Mazziotta J, Toga A, Evans A, et al. A probabilistic atlas and reference system for the human brain: International Consortium for Brain Mapping (ICBM). *Philos Trans R Soc Lond B Biol Sci*. 2001;356:1293–1322.
25. Ashburner J. A fast diffeomorphic image registration algorithm. *Neuroimage*. 2007;38:95–113.
26. Tziortzi AC, Searle GE, Tzimopoulou S, et al. Imaging dopamine receptors in humans with [¹¹C]-(+)-PHNO: dissection of D3 signal and anatomy. *Neuroimage*. 2011;54:264–277.
27. Jack CR, Wiste HJ, Lesnick TG, et al. Brain β -amyloid load approaches a plateau. *Neurology*. 2013;80:890–896.
28. Friston KJ, Worsley KJ, Frackowiak RS, Mazziotta JC, Evans AC. Assessing the significance of focal activations using their spatial extent. *Hum Brain Mapp*. 1994;1:210–220.
29. Whittington A, Seibyl J, Gunn RN. Calculation of A β L with the IQA β algorithm enables automatic and reproducible classification of [¹⁸F]-florbetapir scans [abstract]. *Alzheimers Dement*. 2018;14:P503–P504.
30. Lowe VJ, Curran G, Fang P, et al. An autoradiographic evaluation of AV-1451 tau PET in dementia. *Acta Neuropathol Commun*. 2016;4:58.
31. Marquié M, Normandin MD, Vanderburg CR, et al. Validating novel tau positron emission tomography tracer [F-18]-AV-1451 (T807) on postmortem brain tissue. *Ann Neurol*. 2015;78:787–800.
32. Vermeiren C, Motte P, Viot D, et al. The tau positron-emission tomography tracer AV-1451 binds with similar affinities to tau fibrils and monoamine oxidases. *Mov Disord*. 2018;33:273–281.
33. Braak H, Thal DR, Ghebremedhin E, Del Tredici K. Stages of the pathologic process in Alzheimer disease: age categories from 1 to 100 years. *J Neuropathol Exp Neurol*. 2011;70:960–969.
34. Gunn R. TauIQ demonstrates increased power for cross-sectional and longitudinal analysis of tau tracers as evidenced by [18F]flortaucipir and [18F]GTP1. Presented at: Human Amyloid Imaging Conference; January 15, 2020; Miami, FL.

Hypermetabolism on Pediatric PET Scans of Brain Glucose Metabolism: What Does It Signify?

Harry T. Chugani

Department of Neurology, NYU Langone School of Medicine, New York, New York

When one is interpreting clinical ^{18}F -FDG PET scans of the brain (excluding tumors) in children, the typical abnormality seen is hypometabolism of various brain regions. Focal areas of hypermetabolism are noted occasionally, and the usual interpretation is that the hypermetabolic region represents a seizure focus. In this review, I discuss and illustrate the multiple causes of hypermetabolism on ^{18}F -FDG PET studies that should not be interpreted as seizure activity, as such an interpretation could potentially be incorrect. Various conditions in which focal hypermetabolism can be encountered on ^{18}F -FDG PET studies include interictal hypermetabolism, Sturge-Weber syndrome, changes associated with brain plasticity after injury, Rett syndrome, hypoxic-ischemic brain injury, various inborn errors of metabolism, and autoimmune encephalitis. The radiologist or nuclear medicine physician interpreting clinical ^{18}F -FDG PET studies should be aware of these circumstances to accurately assess the findings.

Key Words: ^{18}F -FDG PET; brain; hypermetabolism; epilepsy

J Nucl Med 2021; 62:1301–1306

DOI: 10.2967/jnumed.120.256081

PET scans of glucose metabolism using the radiotracer ^{18}F -FDG have been performed for over 3 decades and have been incorporated into clinical practice, particularly in oncology. In adults, brain ^{18}F -FDG PET scans are approved for the evaluation of dementia and intractable epilepsy and for differentiation between recurrent brain tumor and radiation necrosis. In children, however, brain ^{18}F -FDG PET scans are approved for the evaluation of intractable epilepsy before potential epilepsy surgery and for brain tumors. I recently presented data and argued that ^{18}F -FDG PET scans are also clinically valuable in the management of children with neurodegenerative disorders, and I recommended that approval be extended to include this population as well (1).

In the interpretation of ^{18}F -FDG PET scans of the brain, the typical abnormality seen is hypometabolism of various brain regions. For clinical studies, hypometabolic brain regions are determined on visual inspection by comparison with adjacent regions and with the contralateral hemisphere. Various semiquantitative objective methods are also used in some centers to augment visual interpretation. However, brain regions showing hypermetabolism are occasionally noted, and the interpretation of such images can be challenging. The usual conclusion is that the hypermetabolic region

represents an epileptic focus (if small) or an epileptogenic region (if large). Although this interpretation may be correct in most patients with epilepsy, it may be incorrect in many cases and lead to erroneous interpretation of the findings. In addition, the semiquantitative objective methods designed to aid in visual analysis have been validated only for the detection of hypometabolism, not for hypermetabolism. In this article, which is based on a review of the literature and focuses mainly on children, I discuss and illustrate the multiple causes of hypermetabolism that can be encountered in ^{18}F -FDG PET studies. A discussion of the hypermetabolism seen in malignant brain tumors is not within the scope of this review. Since this is a review of previously published studies, institutional review board approval was not required. It should be noted that the figures in this article are from several decades ago, and image resolution has since improved considerably. Unless otherwise stated, the images are from the author's personal dataset. Intensity scales/side bars are not shown because they are not available, but are less relevant for these black-and-white qualitative images.

^{18}F -FDG PET HYPERMETABOLISM IN EPILEPSY

Unlike SPECT, for which ictal scans can be planned, scheduling of ictal PET scans is not practical because of the short half-life of ^{18}F (~110 min). Patients (particularly children) with frequent seizures may occasionally experience a seizure during the approximately 30-min ^{18}F -FDG uptake period, thus yielding an ictal PET scan. In some institutions, patients with frequent seizures are monitored with an electroencephalogram during the tracer uptake period, and if a clinical or subclinical seizure occurs, its localization, timing, and duration can accurately be analyzed (2). If the seizure occurs early enough (~the first 10 min) during the tracer uptake period and lasts for more than a few minutes, hypermetabolism may be seen on the images and may provide useful localization data (Fig. 1A), both from the PET scan itself and from the concurrent electroencephalogram, if performed. Brief seizures or seizures occurring late in the relatively long ^{18}F -FDG uptake period will usually not show hypermetabolism.

Less well known and often missed is the phenomenon of interictal hypermetabolism (2,3). This occurs when the patient's electroencephalogram shows a focal interictal epileptiform discharge that persists throughout much of the tracer uptake period. No actual seizure is recorded clinically or on the electroencephalogram, yet the PET images show focal hypermetabolism in a cortical region (Fig. 1B) corresponding to the focal discharge seen on the electroencephalogram. This phenomenon is similar to observations from experimental animal models of focal epilepsy induced by electrical or chemical kindling, and ^{14}C -2-deoxyglucose autoradiography reveals hypermetabolism in the spiking focus without an actual clinical seizure recorded on the electroencephalogram or a clinical seizure observed

Received Sep. 2, 2020; revision accepted Dec. 22, 2021.
For correspondence or reprints, contact: Harry T. Chugani (harry.chugani@nyulangone.org).

Published online January 15, 2021.

COPYRIGHT © 2021 by the Society of Nuclear Medicine and Molecular Imaging.

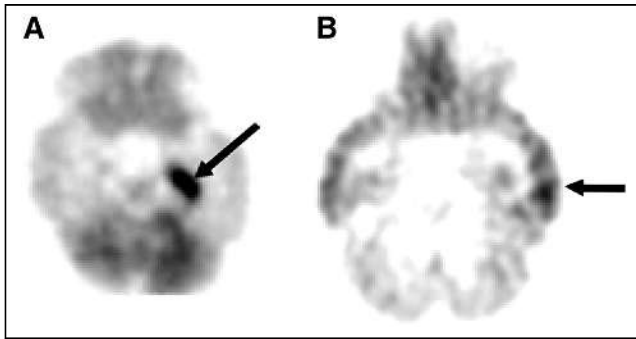


FIGURE 1. (A) Ictal ^{18}F -FDG PET scan of 14-mo-old child with infantile spasms who fortuitously developed convulsive seizure 12 min after administration of ^{18}F -FDG. Intense hypermetabolism (arrow) is seen in left medial temporal lobe. (B) Interictal hypermetabolism in adolescent with left temporal lobe epilepsy who showed spiking on electroencephalogram during entire ^{18}F -FDG uptake period, producing left temporal cortex hypermetabolism (arrow). No actual seizures were witnessed clinically or observed on electroencephalogram. Without electroencephalography, this ^{18}F -FDG PET study could have been interpreted as right temporal cortex hypometabolism, thus falsely lateralizing seizure focus.

in the animal (4). The high energy demand of the persistent epileptic spiking is sufficient to produce observable hypermetabolism in the ^{14}C -2-deoxyglucose experimental model and with ^{18}F -FDG in human PET studies. Therefore, patients who are known to have actively spiking foci and are undergoing an ^{18}F -FDG PET study should be monitored with electroencephalography during the uptake period to allow accurate interpretation of the findings, a practice only rarely followed in clinical PET centers. Interictal hypermetabolism is seen more commonly in children than in adults, presumably

because the electroencephalograms often show more robust epileptiform activity in epileptic children than in adults. When concurrent electroencephalography during PET is not feasible, a review of previous electroencephalograms of the patient may also aid in the accurate interpretation of the ^{18}F -FDG PET results.

HYPERMETABOLISM IN STURGE-WEBER SYNDROME (SWS)

In children with SWS, the typical finding on ^{18}F -FDG PET is hypometabolism in the involved cortex, often with extension to additional areas beyond the vascular abnormality (leptomeningeal angioma) seen on MRI (5,6). However, in the early stages of the evolution in SWS, affected infants may show a paradoxical pattern of hypermetabolism interictally in the cortex underlying the leptomeningeal angioma. As the disease progresses, the hypermetabolic area becomes hypometabolic and atrophied, indicating a dynamic course of brain injury in this disorder (5). Different regions within the affected hemisphere may undergo this process independently (Fig. 2A). Eventually all affected regions become atrophied and hypometabolic. This can occur in unilateral as well as bilateral cases of SWS (Figs. 2B and 2C). Early hypermetabolism seen on the ^{18}F -FDG PET scans of children with SWS is almost never the result of seizure activity unless an actual seizure is witnessed during the tracer uptake period. Moreover, the hypermetabolism in SWS is typically not due to interictal spiking since this is not a common finding in their electroencephalograms, which more typically show focal slowing and background attenuation over the angioma.

The finding of focal glucose hypermetabolism in the early stages of SWS should not be misinterpreted as a seizure focus or an area of ischemia requiring more glucose because it has switched to anaerobic metabolism. Indeed, these considerations were dismissed after findings reported from SPECT studies that showed hyperperfusion in affected regions in babies and infants even before seizure onset (7).

Both the ^{18}F -FDG PET and the SPECT observations are consistent with an earlier study that found accelerated myelination in the affected hemisphere on MRI scans (8).

Glucose hypermetabolism, hyperperfusion, and accelerated myelination in focal brain regions early in the course of SWS are likely interrelated phenomena indicating dynamic changes within these regions leading to eventual tissue damage. A study using MR spectroscopy to address the underlying cause of the hypermetabolism found mean ipsilateral/contralateral glutamate/creatine ratios to be highest in the youngest of the 10 children evaluated, with a strong positive correlation to their seizure frequency scores. All scans were performed in the interictal state as verified by concurrent electroencephalogram monitoring. In 5 children, increased glutamate concentrations in the affected hemisphere were seen in the same areas as those currently or previously manifesting hypermetabolism on ^{18}F -FDG PET (9). The authors suggested that increased glutamate concentrations are common in young children with SWS and likely to be associated with their tissue damage and epilepsy. These findings are also consistent

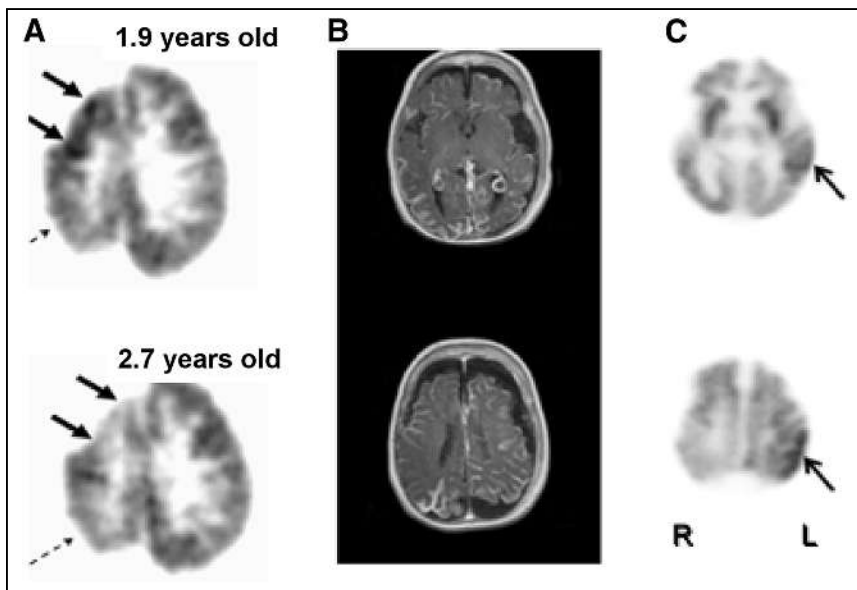


FIGURE 2. (A) Transient focal hypermetabolism evolving to hypometabolism and brain injury in SWS may undergo different temporal course in various regions within affected hemisphere. In this child, ^{18}F -FDG PET scan shows interictal right frontal cortex hypermetabolism at age 1.9 y evolving to hypometabolism at age 2.7 y (solid arrows), whereas right parietal cortex hypometabolism was already present at age 1.9 y and unchanged at 2.7 y (dashed arrows). (B and C) MRI and ^{18}F -FDG PET in child with bilateral brain involvement showing both hypometabolism and hypermetabolism (arrows).

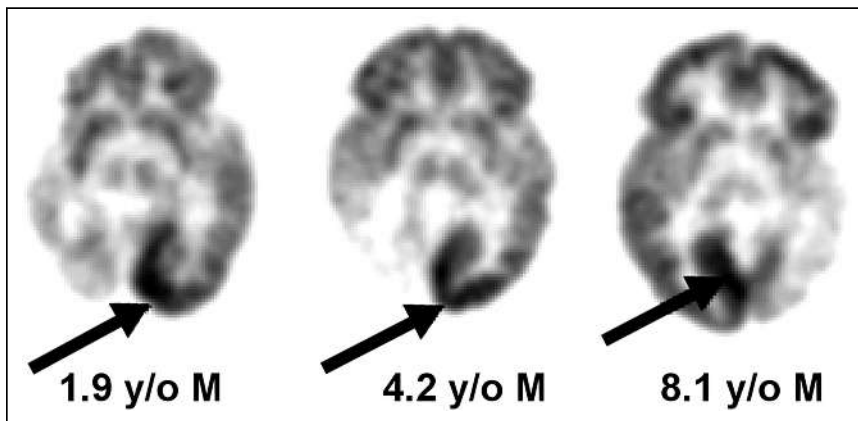


FIGURE 3. ^{18}F -FDG PET scans of 3 children with unilateral leptomenigeal angiomatosis in SWS. Arrows point to normal occipital cortex showing hypermetabolism, as compared with contralateral affected hemisphere, which shows severe hypometabolism and atrophy.

with observations from a previous study suggesting that the early cortical hypermetabolism may be predictive of subsequent severe epilepsy (10).

Another phenomenon displaying focal hypermetabolism in SWS relates to occipital lobe plasticity. When there is significant and early (likely intrauterine) occipital lobe injury resulting in severe hypometabolism and atrophy in the affected occipital lobe, there may be dramatic hypermetabolism in the contralateral intact occipital lobe (Fig. 3), which appears normal on the MRI scan (11). This hypermetabolism seen in the intact hemisphere is not related to epilepsy and should not be misinterpreted as a seizure focus. It is likely due to reorganizational changes (plasticity) in the intact occipital lobe and is not specific to SWS but may also be seen in other conditions, such as focal cortical dysplasia affecting one occipital lobe (12).

RETT SYNDROME

Focal glucose hypermetabolism in interictal ^{18}F -FDG PET studies has been reported in Rett syndrome, which is a neurodevelopmental disorder, affecting primarily girls, that progresses over several stages to severe intellectual and physical disabilities; the disorder results from mutations in the MECP2 gene, as was recently reviewed (13). Neuroimaging studies in Rett syndrome have revealed restriction of brain growth beginning in the first year of

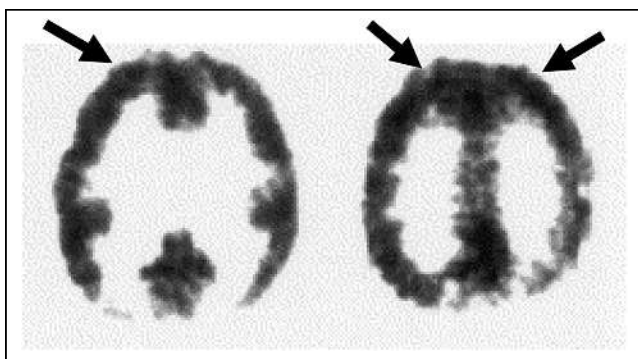


FIGURE 4. Eight-year-old girl with Rett syndrome whose ^{18}F -FDG PET scan shows bilateral frontal cortex hypermetabolism (arrows). (Reprinted with permission from Elsevier (14).)

life; neuropathology examination suggests that axodendritic connections are the most vulnerable in this neurodegenerative process. Naidu et al. (14) studied children with Rett syndrome using various neuroimaging approaches and found the largest changes in the frontal lobes, which showed hypoperfusion, as well as increased choline and reduced *N*-acetylaspartate on MR spectroscopy. However, ^{18}F -FDG PET showed hypermetabolism in the frontal lobes not related to seizure activity (Fig. 4). The authors concluded that the frontal cortex was hypermetabolic (rather than the occipital cortex hypometabolic) based on the SPECT hypoperfusion and MR spectroscopy findings in the frontal lobe of Rett patients. They hypothesized increased glutamate cycling in synapses leading to brain injury as the mechanism of frontal lobe

hypermetabolism. The role of glutamate neurotoxicity in dendritic and synaptic injury is strongly supported by findings from mouse models of Rett syndrome (15). Indeed, the drug trofinetide, which is a glutamate antagonist, is currently undergoing clinical trials in children with Rett syndrome (16) and ^{18}F -FDG PET may potentially serve as an objective biomarker to monitor therapeutic efficacy.

HYPOXIC-ISCHEMIC BRAIN INJURY IN THE NEWBORN

Hypermetabolism in damaged brain regions can be seen in newborns in the acute phase after perinatal hypoxic-ischemic brain injury. Previous ^{18}F -FDG PET studies in this population have not reported this phenomenon, presumably because the babies were scanned in the subacute or chronic state. Instead, various patterns of hypometabolism were reported, extending beyond the affected structural abnormalities shown by CT scanning (17). Subsequent studies in these babies suggested that persistently low quantitative cerebral glucose metabolic rates are associated with delayed development (18). Total cerebral metabolic rates of glucose were found to be inversely correlated with the severity of the brain injury. Thus, neonates with the lowest cerebral metabolic rates of glucose subsequently developed permanent neurologic symptoms and cerebral palsy (19).

A transient hypermetabolism has been observed in the basal ganglia after the near-total type of hypoxic-ischemic injury in the neonatal period, followed by severe hypometabolism in the lenticular nuclei and thalami when the child was restudied several years later (Fig. 5) (20). This type of acute catastrophic injury may be seen in cases of placental abruption, uterine rupture, or umbilical cord prolapse. The selective vulnerability of the basal ganglia in this setting may be related to the transient excess of glutamate receptors seen in the newborn basal ganglia compared with older children and adults (21). This form of injury is associated with the subsequent development of the dystonic (choreoathetoid, extrapyramidal) type of cerebral palsy, as, indeed, was the sequela in this child. It was postulated that the transition from hypermetabolism to hypometabolism indicates the culmination of the brain injury due to excitotoxic mechanisms, which are mediated by glutamatergic neurotransmission (22). Unfortunately, the time course of the transient hypermetabolism is unknown and yet to be defined. Also unknown is whether transient hypermetabolism is seen in the

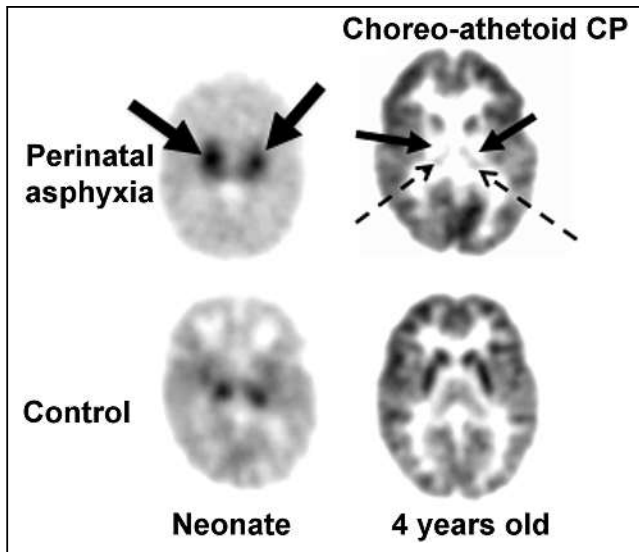


FIGURE 5. ^{18}F -FDG PET scan of child who had hypoxic-ischemic encephalopathy at birth and later developed dystonic/choreoathetoid cerebral palsy. Left image, from newborn period, shows intense hypermetabolism in basal ganglia (solid arrows) compared with control. Right image, at 5 y of age, shows severe hypometabolism in lenticular nuclei (solid arrows) and thalami (dotted arrows). Metabolism is relatively preserved in cerebral cortex.

watershed types of neonatal hypoxic-ischemic brain injury (also referred to as the partial prolonged type of brain injury) sometimes encountered at birth.

INBORN ERRORS OF METABOLISM

Transient hypermetabolism of the basal ganglia seen on ^{18}F -FDG PET scans has been reported in several inborn errors of metabolism. This transient phase is followed by hypometabolism in the same brain region and indicates a selective vulnerability due to the abnormal biochemical state (i.e., metabolic toxins) in the specific disorder.

Propionic acidemia is an organic acidemia associated with diverse neurologic manifestations, including developmental delay, intellectual disability, seizures, optic neuropathy, and strokelike episodes. The disorder is progressive and may also result in cardiac, gastrointestinal, and renal complications. Serial MRI and ^{18}F -FDG PET scans in 5 children with biochemically confirmed propionic acidemia showed normal findings on both ^{18}F -FDG PET and MRI in the early stages of the disorder. As the disease progressed, the ^{18}F -FDG PET scans revealed glucose hypermetabolism in the basal ganglia and thalami with subsequent evolution to hypometabolism in the basal ganglia (Figs. 6A–6C), whereas MRI showed atrophy and an abnormal signal in the caudate and putamen, with normal thalami (23). The investigators suggested that the neurotoxins in this metabolic disorder have a predilection for the basal ganglia, activate glutamatergic mechanisms, and eventually damage or destroy the basal ganglia. This notion is supported by the transient hypermetabolism in the basal ganglia in accordance with the dynamic nature of neurodegeneration during the course of this disorder.

A somewhat similar phenomenon has been reported in ethylmalonic aciduria, which is a severe organic aciduria affecting mitochondria and the vasculature. Ethylmalonic aciduria, in addition to involving the central nervous system, can also lead to changes in the retinal vessels, acrocyanosis, petechiae, and gastrointestinal symptoms. The central nervous system symptoms include hypotonia, physical and intellectual regression, and, as the disease progresses, dystonia and spasticity. Neuroimaging studies in a 6-mo-old boy with ethylmalonic aciduria showed normal MRI findings but bilaterally intense hypermetabolism in the caudate and putamen on ^{18}F -FDG PET (Figs. 6D and 6E). When performed again a year later, ^{18}F -FDG PET showed bilateral hypometabolism in the putamen, caudate head, and frontal cortex, whereas MRI showed atrophy and infarcts in the basal ganglia (24). These findings are again consistent with the selective vulnerability of the basal ganglia in some inborn errors of metabolism.

^{18}F -FDG PET scans have been performed on several other inborn errors of metabolism, often published in case reports. The general finding is hypometabolism, but in some cases, the hypometabolism is specific to, or most prominent in, the basal ganglia. These include glutaric aciduria

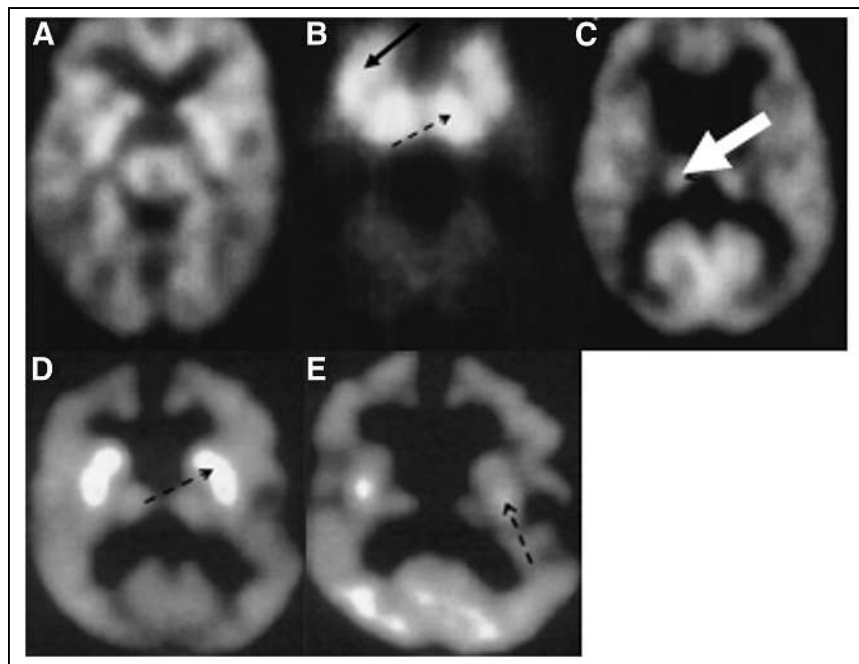


FIGURE 6. (A–C) ^{18}F -FDG PET scans of 3 children with propionic acidemia at different stages of disease: at age 1 mo (A), this baby shows relatively normal pattern of glucose metabolism for age; this 2-mo-old infant (B) shows intense hypermetabolism in basal ganglia (solid arrow) and thalamus (dashed arrow); this 2-y-old child (C) shows relatively normal glucose metabolism in thalamus (dashed arrow), but basal ganglia shows no metabolic activity. (Reprinted with permission from Elsevier (23).) (D and E) ^{18}F -FDG PET images of boy with ethylmalonic aciduria: at 2 y of age (D), intense bilateral hypermetabolism is seen in caudate nucleus and putamen (dashed arrow); when scanned again at age 3 y (E), there has been evolution of hypermetabolism to hypometabolism (dashed arrow). (Reprinted with permission from Elsevier (24).)

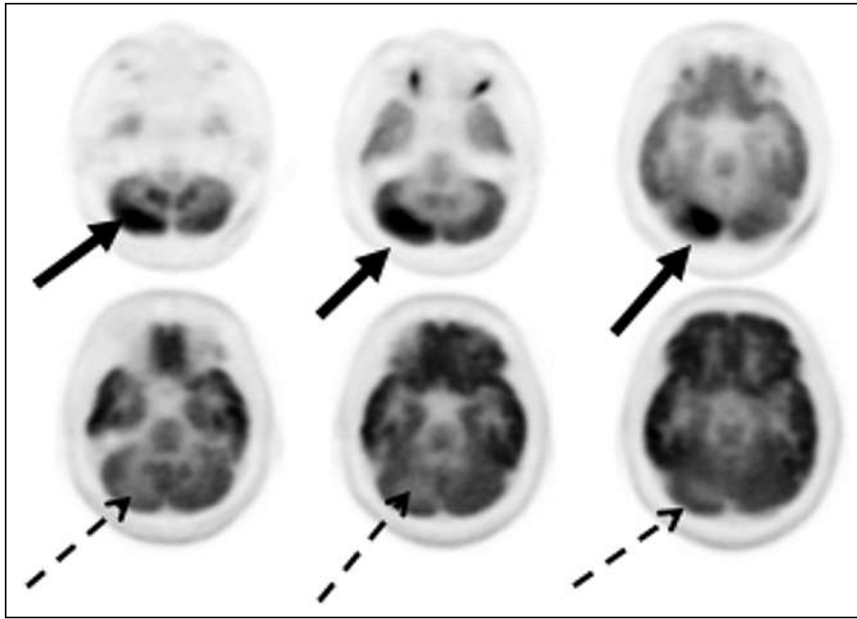


FIGURE 7. ^{18}F -FDG PET scans of 15-y-old boy with anti-*N*-methyl-D-aspartate receptor encephalitis. (Top) Focal intense hypermetabolism in right cerebellar cortex (solid arrows) and diffuse hypometabolism of bilateral cerebral hemispheres. (Bottom) Subsequent focal hypermetabolism in right cerebellar cortex (dashed arrows), corresponding to initially hypermetabolic region. (Reprinted with permission from Sage (29).)

type 1 (25,26) and 3-methylglutaconic aciduria (27). It is unclear at which stage of disease progression these ^{18}F -FDG PET studies were conducted. I postulate that had the ^{18}F -FDG PET studies been performed at an earlier stage of rapid clinical regression in these disorders, the ^{18}F -FDG PET scans might also have shown transient hypermetabolism in the basal ganglia. Furthermore, recently developed hybrid PET/MRI scanners provide a unique opportunity to determine the time course and relationship between structural, glucose metabolism, and MR spectroscopic changes seen in this group of rare disorders.

AUTOIMMUNE ENCEPHALITIS

The autoimmune encephalitides comprise a group of disorders characterized by changes in mental status, seizures, dyskinesias, or memory decline in association with the presence of serum and cerebrospinal fluid autoantibodies against brain proteins (28). MRI scans in these disorders often have normal findings or may show increased fluid-attenuated inversion recovery/T2 signal in various locations, such as in one or both temporal lobes in limbic encephalitis. ^{18}F -FDG PET scans may show focal hypermetabolism in various locations (29,30).

A report of focal hypermetabolism in a case of autoimmune encephalitis involved a 15-y-old boy with anti-*N*-methyl-D-aspartate receptor encephalitis whose brain MRI findings were repeatedly normal (29). On day 26 of admission, ^{18}F -FDG PET showed global hypometabolism with a prominent focally intense hypermetabolic lesion in the right cerebellar cortex (Fig. 7). The patient showed clinical signs of improvement after 2 courses of intravenous immunoglobulin therapy over 4 wk. On day 46, repeat brain ^{18}F -FDG PET showed overall improvement, but in contrast to the previous ^{18}F -FDG PET scan, the right cerebellar cortex showed focal

hypometabolism. Focal hypermetabolism or more commonly hypometabolism in autoimmune encephalitis has been confirmed by other investigators and can be useful in early diagnosis in these disorders (30–32). In particular, some cases of suspected autoimmune encephalitis may be antibody-negative, and ^{18}F -FDG PET may contribute toward establishing a clinical diagnosis.

CONCLUSION

In this review, I have illustrated multiple examples of hypermetabolism that should not be interpreted as seizure activity on ^{18}F -FDG PET scans. The radiologist or nuclear medicine physician interpreting these studies needs to be aware that focal hypermetabolism does not always indicate a seizure focus, and the physician should be familiar with the less common causes of hypermetabolism. Since seizures do not emanate from the basal ganglia, the physician should also be aware that increased glucose metabolism in the basal ganglia may be a clue to an underlying metabolic disorder. In these cases, the timing of the

^{18}F -FDG PET scan in relation to the course of a progressive neurologic disorder should be noted, and if indicated, the study should be repeated to determine progressive changes in brain glucose metabolism.

Finally, it is acknowledged that when interpreting ^{18}F -FDG PET scans of glucose metabolism visually (as in clinical studies), we are looking at relative hypermetabolism since absolute quantification is not available, and interpretation may thus be challenging. Some general rules may be helpful in this regard. For example, if supratentorial cortical metabolism is decreased, thalamic metabolism usually follows; caudate may follow, but not the rest of the basal ganglia or brain stem. Frontal, parietal, and temporal cortex metabolism is usually lower than metabolism in the primary visual cortex (medial occipital cortex, calcarine cortex). Cerebellar metabolism is higher than most supratentorial cortical metabolism in the first few months postnatally, but never after the first year. This rule is particularly useful when deciding between supratentorial cortical hypometabolism and basal ganglia hypermetabolism. Brain stem nuclei metabolism is usually around the same as that of the basal ganglia. Ultimately, the experience of the interpreting physician, as well as knowledge of the patient history, is crucial.

DISCLOSURE

No potential conflict of interest relevant to this article was reported.

REFERENCES

1. Chugani HT. Positron emission tomography in pediatric neurodegenerative disorders. *Pediatr Neurol.* 2019;100:12–25.
2. Schur S, Allen V, White A, et al. Significance of FDG-PET hypermetabolism in children with intractable focal epilepsy. *Pediatr Neurosurg.* 2018;53:153–162.

3. Chugani HT, Shewmon DA, Khanna S, Phelps ME. Interictal and postictal focal hypermetabolism on positron emission tomography. *Pediatr Neurol.* 1993;9:10–15.
4. Ackermann RF, Chugani HT, Handforth A, Moshe S, Caldecott-Hazard S, Engel J. Autoradiographic studies of cerebral metabolism and blood flow in rat amygdala kindling. In: Wada JA, ed. *Kindling 3*. Raven Press; 1986:73–87.
5. Chugani HT, Mazziotta JC, Phelps ME. Sturge-Weber syndrome: a study of cerebral glucose utilization with positron emission tomography. *J Pediatr.* 1989;114:244–253.
6. Juhász C, Batista CE, Chugani DC, Muzik O, Chugani HT. Evolution of cortical metabolic abnormalities and their clinical correlates in Sturge-Weber syndrome. *Eur J Paediatr Neurol.* 2007;11:277–284.
7. Pinton F, Chiron C, Enjolras O, Motte J, Syrota A, Dulac O. Early single photon emission computed tomography in Sturge-Weber syndrome. *J Neurol Neurosurg Psychiatry.* 1997;63:616–621.
8. Jacoby CG, Yuh WT, Afifi AK, Bell WE, Schelper RL, Sato Y. Accelerated myelination in early Sturge-Weber syndrome demonstrated by MR imaging. *J Comput Assist Tomogr.* 1987;11:226–231.
9. Juhász C, Hu J, Xuan Y, Chugani HT. Imaging increased glutamate in children with Sturge-Weber syndrome: association with epilepsy severity. *Epilepsy Res.* 2016;122:66–72.
10. Alkonyi B, Chugani HT, Juhász C. Transient focal cortical increase of interictal glucose metabolism in Sturge-Weber syndrome: implications for epileptogenesis. *Epilepsia.* 2011;52:1265–1272.
11. Batista CE, Juhász C, Muzik O, Chugani DC, Chugani HT. Increased visual cortex glucose metabolism contralateral to angioma in children with Sturge-Weber syndrome. *Dev Med Child Neurol.* 2007;49:567–573.
12. Jeong JW, Tiwari VN, Shin J, Chugani HT, Juhász C. Assessment of brain damage and plasticity in the visual system due to early occipital lesion: comparison of FDG-PET with diffusion MRI tractography. *J Magn Reson Imaging.* 2015;41:431–438.
13. Gold WA, Krishnarajy R, Ellaway C, Christodoulou J. Rett syndrome: a genetic update and clinical review focusing on comorbidities. *ACS Chem Neurosci.* 2018;9:167–176.
14. Naidu S, Kaufmann WE, Abrams MT, et al. Neuroimaging studies in Rett syndrome. *Brain Dev.* 2001;23(suppl 1):S62–S71.
15. Maezawa I, Jin LW. Rett syndrome microglia damage dendrites and synapses by the elevated release of glutamate. *J Neurosci.* 2010;30:5346–5356.
16. Glaze DG, Neul JL, Kaufmann WE, et al. Double-blind, randomized, placebo-controlled study of trofinetide in pediatric Rett syndrome. *Neurology.* 2019;92:e1912–e1925.
17. Doyle LW, Nahmias C, Firnau G, Kenyon DB, Garnett ES, Sinclair JC. Regional cerebral glucose metabolism of newborn infants measured by positron emission tomography. *Dev Med Child Neurol.* 1983;25:143–151.
18. Suhonen-Polvi H, Kero P, Korvenranta H, et al. Repeated fluorodeoxyglucose positron emission tomography of the brain in infants with suspected hypoxic-ischaemic brain injury. *Eur J Nucl Med.* 1993;20:759–765.
19. Thormgren-Jerneck K, Ohlsson T, Sandell A, et al. Cerebral glucose metabolism measured by positron emission tomography in term newborn infants with hypoxic ischaemic encephalopathy. *Pediatr Res.* 2001;49:495–501.
20. Batista CE, Chugani HT, Juhász C, Behen ME, Shankaran S. Transient hypermetabolism of the basal ganglia following perinatal hypoxia. *Pediatr Neurol.* 2007;36:330–333.
21. Greenamyre T, Penney JB, Young AB, Hudson C, Silverstein FS, Johnston MV. Evidence for transient perinatal glutamatergic innervation of globus pallidus. *J Neurosci.* 1987;7:1022–1030.
22. Johnston MV. Excitotoxicity in neonatal hypoxia. *Ment Retard Dev Disabil Res Rev.* 2001;7:229–234.
23. Al-Essa M, Bakheet S, Patay Z, et al. ¹⁸fluoro-2-deoxyglucose (¹⁸FDG) PET scan of the brain in propionic acidemia: clinical and MRI correlations. *Brain Dev.* 1999;21:312–317.
24. al-Essa MA, Al-Shamsan LA, Ozand PT. Clinical and brain ¹⁸fluoro-2-deoxyglucose positron emission tomographic findings in ethylmalonic aciduria, a progressive neurometabolic disease. *Europ J Paediatr Neurol.* 1999;3:125–127.
25. Al-Essa M, Bakheet S, Patay Z, et al. Fluoro-2-deoxyglucose (¹⁸FDG) PET scan of the brain in glutaric aciduria type 1: clinical and MRI correlations. *Brain Dev.* 1998;20:295–301.
26. Awaad Y, Shamoto H, Chugani H. Hemidystonia improved by baclofen and PET scan findings in a patient with glutaric aciduria type I. *J Child Neurol.* 1996;11:167–169.
27. Al-Essa M, Bakheet S, Al-Shamsan L, Patay Z, Powe J, Ozand PT. ¹⁸fluoro-2-deoxyglucose (¹⁸FDG) PET scan of the brain in type IV 3-methylglutaconic aciduria: clinical and MRI correlations. *Brain Dev.* 1999;21:24–29.
28. Graus F, Titulaer MJ, Balu R, et al. A clinical approach to diagnosis of autoimmune encephalitis. *Lancet Neurol.* 2016;15:391–404.
29. Maqbool M, Oleske DA, Huq AH, Salman BA, Khodabakhsh K, Chugani HT. Novel FDG-PET findings in anti-NMDA receptor encephalitis: a case based report. *J Child Neurol.* 2011;26:1325–1328.
30. Newey CR, Sarwal A, Hantus S. [¹⁸F]-fluoro-deoxy-glucose positron emission tomography scan should be obtained early in cases of autoimmune encephalitis. *Autoimmune Dis.* 2016;2016:9450452.
31. Solnes LB, Jones KM, Rowe SP, et al. Diagnostic value of ¹⁸F-FDG PET/CT versus MRI in the setting of antibody-specific autoimmune encephalitis. *J Nucl Med.* 2017;58:1307–1313.
32. Tripathi M, Tripathi M, Roy SG, et al. Metabolic topography of autoimmune non-paraneoplastic encephalitis. *Neuroradiology.* 2018;60:189–198.

Dopamine D₁ Receptor Agonist PET Tracer Development: Assessment in Nonhuman Primates

Olivier Barret^{1,2}, Lei Zhang³, David Alagille^{1,4}, Cristian C. Constantinescu¹, Christine Sandiego¹, Caroline Papin¹, Jenna M. Sullivan¹, Thomas Morley¹, Vincent M. Carroll¹, John Seibyl¹, Jianqing Chen⁵, Chewah Lee³, Anabella Villalobos³, David Gray^{3,6}, Timothy J. McCarthy⁵, Gilles Tamagnan^{1,4}

¹Invivo, LLC, New Haven, Connecticut; ²Université Paris-Saclay, CEA, CNRS, MIRCen, Laboratoire des Maladies Neurodégénératives, Fontenay-aux-Roses, France; ³Medicine Design, Medicinal Chemistry, Pfizer Inc., Cambridge, Massachusetts; ⁴Xing Imaging, New Haven, Connecticut; ⁵Digital Medicine and Imaging, Early Clinical Development, Pfizer Inc., Cambridge, Massachusetts; and ⁶Cerevel Therapeutics, Boston, Massachusetts

Non-catechol-based high-affinity selective dopamine D₁ receptor (D1R) agonists were recently described, and candidate PET ligands were selected on the basis of favorable properties. The objective of this study was to characterize in vivo in nonhuman primates 2 novel D1R agonist PET radiotracers, racemic ¹⁸F-MNI-800 and its more active atropisomeric (–)-enantiomer, ¹⁸F-MNI-968. **Methods:** Ten brain PET experiments were conducted with ¹⁸F-MNI-800 on 2 adult rhesus macaques and 2 adult cynomolgus macaques, and 8 brain PET experiments were conducted with ¹⁸F-MNI-968 on 2 adult rhesus macaques and 2 adult cynomolgus macaques. PET data were analyzed with both plasma-input-based methods and reference-region-based methods. Whole-body PET images were acquired with ¹⁸F-MNI-800 from 2 adult rhesus macaques for radiation dosimetry estimates. **Results:** ¹⁸F-MNI-800 and ¹⁸F-MNI-968 exhibited regional uptake consistent with D1R distribution. Specificity and selectivity were demonstrated by dose-dependent blocking with the D₁ antagonist SCH-23390. ¹⁸F-MNI-968 showed a 30% higher specific signal than ¹⁸F-MNI-800, with a nondisplaceable binding potential of approximately 0.3 in the cortex and approximately 1.1 in the striatum. Dosimetry radiation exposure was favorable, with an effective dose of about 0.023 mSv/MBq. **Conclusion:** ¹⁸F-MNI-968 has significant potential as a D1R agonist PET radiotracer, and further characterization in human subjects is warranted.

Key Words: D₁ receptor; agonist; PET imaging; schizophrenia; Parkinson disease;

J Nucl Med 2021; 62:1307–1313
DOI: 10.2967/jnumed.120.256008

Dopamine D₁ receptors (D1Rs) are the most abundant dopamine receptor subtype in the brain and the primary subtype in the prefrontal cortex (1,2) and are exclusively found postsynaptically on dopamine-receptive neurons (medium spiny neurons in the striatum and pyramidal neurons in the prefrontal cortex). Despite its extensive brain distribution, D1R interest has dropped behind other subtypes, especially D₂ receptors, partly because of the lack of

D1R-selective agents that would facilitate a greater understanding of this target.

Dihydropyridine, the first high-affinity catechol-based selective full D1R agonist, demonstrated the therapeutic potential of D1R-selective ligands in schizophrenia (alleviation of cognitive deficit and negative symptoms (3)) and Parkinson disease (antiparkinsonian action in MPTP-treated primate model (4)). The recent introduction of non-catechol-based high-affinity selective D1R agonists has revived interest in this target (5–9).

The development of in vivo imaging techniques has proven extremely valuable to elucidate disease pathology, disease progression, and advancement of target-specific therapies. Several PET radiotracers for D1R have been developed, mainly the antagonists ¹¹C-NNC-112 (10), ¹¹C-SCH-23390 (11), and ¹¹C-A-69024 (12); the partial agonist ¹¹C-N-methyl-NNC 01-0259 (13); and the agonist ¹¹C-SKF 82957 (14). However, ¹¹C-SCH-23390 and ¹¹C-NNC-112 suffer from selectivity against 5-HT_{2a} (15), and ¹¹C-N-methyl-NNC 01-0259 and ¹¹C-SKF 82957 have brain-penetrating radiometabolites (13,14). Moreover, D1Rs exhibit both high- and low-affinity states, with agonists preferentially binding to the high-affinity active state whereas antagonists do not discriminate between the 2 states. Therefore, development of a full D1R agonist PET tracer could provide important in vivo functional information and be a useful imaging tool to assess D1R agonists.

Two novel D1R agonists from a noncatechol chemotype discovered by Pfizer were selected on the basis of favorable properties as potential PET ligands. The objective of this study was to characterize these 2 D1R agonist PET radiotracers, racemic ¹⁸F-MNI-800 and the atropisomeric (–)-enantiomer ¹⁸F-MNI-968, in vivo in nonhuman primates (NHP). We assessed their brain distribution and kinetic profile, the specificity of the signal in preblocking studies with a D1R antagonist and a partial agonist, test–retest variability, and radiation dosimetry estimates of ¹⁸F-MNI-800.

MATERIALS AND METHODS

In Vitro Pharmacology and PET Properties of Novel Noncatechol D1R Agonists

The identification of a suitable PET ligand was guided by a set of PET properties to find a D1R-selective agonist that resides within favorable physicochemical property space defined by the central nervous system PET multiparameter optimization score (>3) (16) and shows potent binding affinity to D1R ($B_{\max}/K_d > 10$), high passive permeability

Received Sep. 28, 2020; revision accepted Dec. 22, 2020.
For correspondence or reprints, contact Olivier Barret (olivier.barret@cea.fr).
Published online February 12, 2021.
COPYRIGHT © 2021 by the Society of Nuclear Medicine and Molecular Imaging.


 Radiolabeling site MNI-968	In vitro pharmacology	PET properties
	hD1 K_i = 2 nM hD1 EC_{50} = 5 nM (96% E_{max}) rD1 K_i = 8 nM NHP D1 K_i = 2 nM hD2, D3 and D4 binding IC_{50} > 10 μ M	CNS PET MPO = 3.57 LogD = 2.2 RRCK P_{app} AB = 21.6×10^{-6} cm/s MDR1 BA/AB = 1.46 cFu _b = 0.06

FIGURE 1. Profile of D1R agonist PET ligand lead MNI-968. AB = apical to basolateral; BA = basolateral to apical; CNS = central nervous system; cFu_b = fraction unbound in brain; EC_{50} = half-maximal effective concentration; E_{max} = maximal effect; hD1 = human D₁; hD2 = human D₂; IC_{50} = half-maximal inhibitory concentration; K_i = inhibition constant; MDR1 = multi-drug resistance 1; MPO = multiparameter optimization; rD1 = rat D₁; P_{app} = apparent permeability; RRCK = Ralph Russ canine kidney assay.

(RRCK P_{app} AB > 5×10^{-6} cm/s), low p-glycoprotein efflux (Pgp) efflux (MDR1 BA/AB \leq 2.5), and a sufficient fraction unbound in brain (cFu_b > 0.05) for low nonspecific binding.

Initially, racemate MNI-800 (PK-84677) and subsequently its (–)-enantiomer MNI-968 (PF-0110), a noncatechol D1R agonist from a chemotype developed by Pfizer (7), emerged as a promising PET ligand lead with a benzyl fluoride moiety for late-stage ¹⁸F radiolabeling (Fig. 1; Supplemental Scheme 1; supplemental materials are available at <http://jnm.snmjournals.org>).

Indeed, MNI-968 has a potent binding affinity to human D1R (K_i = 2 nM), and minimal species differences in rat (K_i = 8 nM) and NHP (K_i = 2 nM). Given a D1R B_{max} in human and NHP striatum of approximately 52 pmol/g tissue (~52 nM assuming 100 mg of protein/g of tissue) (17), a desired B_{max}/K_d of more than 10 corresponds to a binding affinity of less than 5 nM, indicating that MNI-968 meets this affinity requirement. Moreover, unlike other known D1R antagonist radiotracers (SCH-23390 and NNC-112), MNI-968 is a potent D1R functional agonist with an EC_{50} of 5 nM and 96% E_{max} . Finally, MNI-968 showed selectivity for D1R over other dopamine receptors, with no appreciable binding to human D₂, D₃, and D₄ receptors (IC_{50} > 10 μ M).

In addition to its favorable in vitro pharmacology profile, MNI-968 met all the PET ligand property parameters: high central nervous system PET multiparameter optimization score (3.57), good passive permeability (RRCK P_{app} AB = 21.6×10^{-6} cm/s), low p-glycoprotein efflux (MDR1 BA/AB = 1.46), and a reasonable fraction unbound in brain (cFu_b = 0.06), suggesting a low risk of nonspecific binding.

Details on the synthesis of MNI-968 and MNI-800 are provided in the supplemental materials.

Radiochemistry of ¹⁸F-MNI-800 and ¹⁸F-MNI-968

All ¹⁸F-MNI-800 and ¹⁸F-MNI-968 radiolabeling reactions were performed in a GE Healthcare TRACERlab FX-FN automated synthesis module using the Boc-protected benzyl chloride precursor (Fig. 2, MNI-799 or MNI-969).

For ¹⁸F-MNI-800, the 2-step, 1-pot production with the racemic precursor MNI-799 afforded sufficiently high yields (15%–35%) with high radiochemical purity (>95%), chemical purity (<0.20 μ g/mL), and specific activity (>220 GBq/ μ mol).

For ¹⁸F-MNI-968, it proved too difficult to confidently control the undesired racemization of the enantiopure precursor MNI-969, and the procedure was modified. First, an in-process chiral high-performance liquid chromatography separation step with inclusion of a chiral column before the C18 reverse-phase column provided sequential separation of the desired atropisomer followed by mass purification. Second, the radiolabeling solvent was changed to acetonitrile because dimethyl sulfoxide was not compatible with the chiral stationary phase. Beyond these 2 changes, the ¹⁸F-MNI-968 process was similar to the process for ¹⁸F-MNI-800 and provided the desired product in expected lower yields (5%–15%) and an acceptable chemical profile (radiochemical purity

> 95%, chemical purity < 0.10 μ g/mL, and specific activity > 75 GBq/ μ mol). Atropisomeric purity was assessed to confirm enantiopurities of more than 99% at the end of synthesis, throughout storage in solution, and before injection.

Details on the radiosynthesis of ¹⁸F-MNI-800 and ¹⁸F-MNI-968 are provided in the supplemental materials.

Animals

All experiments were conducted in accordance with the U.S. Public Health Service's Policy on Humane Care and Use of Laboratory Animals and with institutional approval (Yale PET Center and Charles River Laboratories). Adult rhesus macaques (*Macaca mulatta*, 2 females [7.6 \pm 1.4 kg, NHPs A and B] and 1 male [19.6 \pm 3.0 kg, NHP C]) and cynomolgus macaques (*Macaca fascicularis*, 3 males, 5.0 \pm 0.4 kg, NHPs D–F) were studied. The animals were anesthetized with intramuscular ketamine and given glycopyrrolate to reduce secretions, transferred to the camera, and intubated for continuous anesthesia with approximately 2.5% isoflurane. Radiotracer was injected 2 h after administration of anesthetics to allow for stabilization of the animals' physiology. Body temperature was maintained by a heated water blanket and monitored with a rectal thermometer.

Blocking Agent Preparation and Administration

SCH-23390 (R(+)-SCH-23390 hydrochloride; Sigma-Aldrich) and PF-2562 (8,9) are a potent, selective D1R antagonist and a partial agonist, respectively. SCH-23390 was dissolved in normal saline. PF-2562 was dissolved in 5% ethanol, 5% Cremophor (BASF Corp.), and 18.5% sulfolbutylether- β -cyclodextrin in sterile water.

Receptor occupancy experiments were performed with ¹⁸F-MNI-800 and 4 doses of SCH-23390 (0.03, 0.1, 0.2, and 0.5 mg/kg) administered intravenously over a 20-min period beginning 25 min before the radiotracer injection, and with ¹⁸F-MNI-968 and 1 dose of PF-2562 in duplicate (1.2 mg/kg total dose) administered intravenously over a 120-min period beginning 30 min before tracer injection (bolus of 0.121 mg/kg/min for 3 min followed by infusion of 0.007 mg/kg/min for 117 min). Plasma samples were taken at several time points during each PET scan.

Brain PET Studies

PET scans were performed on a Focus 220 microPET camera (Siemens Healthcare Molecular Imaging) after intravenous bolus administration of ¹⁸F-MNI-800 (170.5 \pm 16.5 MBq, 0.28 \pm 0.22 μ g) or ¹⁸F-MNI-968 (158.0 \pm 29.1 MBq, 0.47 \pm 0.22 μ g). Ten scans were done with ¹⁸F-MNI-800, and 8 scans were done with ¹⁸F-MNI-968 (Table 1). Test and retest scans were separated by 2 wk for ¹⁸F-MNI-800 and 4 mo for ¹⁸F-MNI-968. The dynamic series were reconstructed using filtered backprojection with corrections for random, scatter, and attenuation.

Arterial Input Function. After tracer administration, radial artery blood samples were collected over 2 h. Radioactivity in whole blood and plasma was measured in all samples. Radiometabolites were

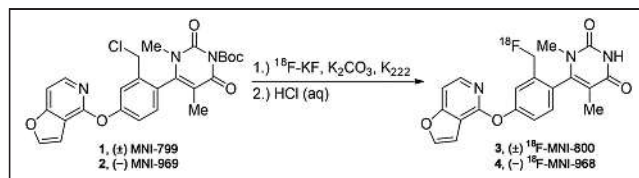


FIGURE 2. Radiosynthesis of ¹⁸F-MNI-800 and ¹⁸F-MNI-968.

TABLE 1
Summary of Scans with ^{18}F -MNI-800 or ^{18}F -MNI-968

Species	NHP no.	^{18}F -MNI-800	^{18}F -MNI-968
Rhesus	A	Test, retest, SCH23390 (0.5 and 0.1 mg/kg)	Test, retest,* PF-2562 (1.2 mg/kg)*
	B	Test, retest, SCH23390 (0.2 and 0.03 mg/kg), dosimetry	Baseline
	C	Dosimetry	Baseline,* PF-2562 (1.2 mg/kg)*
Cynomolgus	D	Baseline	Baseline
	E	Baseline	
	F		Baseline

*90-min scan.
Scans are 120 min unless otherwise indicated.

measured in a subset of samples by reverse-phase high-performance liquid chromatography performed on a Phenomenex Luna C18(2) (10×250 mm, $10 \mu\text{m}$) at a flow rate of 4 mL/min. The mobile phase consisted of a mixture of methanol/water with 0.2% triethylamine in a 65/35 ratio. Plasma samples were processed by acetonitrile denaturation, and the plasma protein binding free fraction (f_p) was measured by ultrafiltration (Centrifree; Millipore).

Image Processing. PET images were analyzed in PMOD, version 3.609 (PMOD Technologies), and were motion-corrected frame by frame when necessary. The initial PET images (15 min) were averaged and aligned onto a rhesus or cynomolgus structural T1-weighted MRI template, and the transformation matrix was applied to the whole PET series. A volume-of-interest atlas (including the caudate, putamen, globus pallidus, nucleus accumbens, thalamus, cortical regions, and cerebellum) was applied to the PET series in MRI rhesus or cynomolgus template space to extract the regional time-activity curves. Curves were expressed in SUV by normalizing the activity concentration by the injected dose and animal body weight.

Kinetic Modeling and Analysis. Time-activity curves were analyzed with 1- and 2-tissue-compartment (2T) models (18) and Logan graphical analysis (LGA) (19) using the arterial plasma input function corrected for radiometabolites to derive the volume of distribution (V_T) and the influx rate constant K_1 in each region. The nondisplaceable binding potential (BP_{ND}) was estimated using the cerebellum as a reference region: $\text{BP}_{\text{ND}} = V_T/V_{\text{ND}} - 1$, V_T and V_{ND} being the distribution volumes in the target region (specific and nondisplaceable binding) and reference region (nondisplaceable binding), respectively (20). In addition, BP_{ND} was directly derived from the simplified reference tissue model (SRTM) (21) and noninvasive LGA (NI-LGA) (19) with the cerebellum as a reference region. All kinetic analyses were performed using PMOD. Test-retest variability for V_T and BP_{ND} was estimated as absolute (test - retest)/average (test + retest).

The D1R occupancy (Occ) produced by SCH-23390 or PF-2562 was determined as the percentage change in BP_{ND} : $\text{Occ} = (\text{BP}_{\text{ND}}^{\text{baseline}} - \text{BP}_{\text{ND}}^{\text{drug}}) / \text{BP}_{\text{ND}}^{\text{baseline}}$. The SCH-23390 plasma-occupancy curves for the striatum (putamen and caudate) were fitted in Prism (version 6.01; GraphPad Software) with a single specific binding site model: $\text{Occ} = \text{Occ}_{\text{max}} \times C / (C + \text{EC}_{50})$, where Occ_{max} is the maximum occupancy; EC_{50} is the half-maximal effective concentration, which represents the SCH-23390 plasma level for 50% occupancy; and C represents the SCH-23390 average plasma level during the scan.

^{18}F -MNI-800 Whole-Body PET Studies

Two adult rhesus monkeys (*Macaca mulatta*), 1 male and 1 female, were used for whole-body PET imaging from head to mid thigh over 4 h on a Biograph mCT PET/CT camera (Siemens Healthcare Molecular

Imaging) after intravenous bolus injection of ^{18}F -MNI-800 to determine the biodistribution and estimate absorbed radiation doses.

PET images were imported into PMOD, and volumes of interest were drawn on source organs. Absorbed radiation dose and effective dose (International Commission on Radiological Protection publication 60) were estimated with OLINDA/EXM software, version 1.0 (22), according to the male or female model. The gastrointestinal model of International Commission on Radiological Protection publication 30 was used with the assumption that activity entered the gastrointestinal tract through the small intestine (fraction of activity entering the intestine was estimated as the highest fraction encountered in the intestinal area).

RESULTS

Plasma Analysis

High-performance liquid chromatography analysis of ^{18}F -MNI-800 and ^{18}F -MNI-968 arterial plasma revealed 1 major radiometabolite and 1 minor metabolite eluting just after the first one (whose contribution remained small throughout the study), with both metabolites more polar than the parent compound. No difference was observed between rhesus and cynomolgus macaques, and the results were pooled across the 2 species. ^{18}F -MNI-800 and ^{18}F -MNI-968 showed similar moderate metabolic profiles, with about 60%–70% and 40%–50% of intact parent remaining at 30 and 120 min after

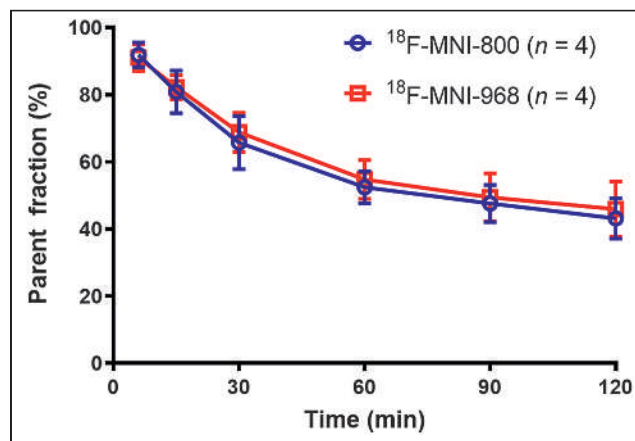


FIGURE 3. Parent fraction profile in arterial plasma after intravenous administration of ^{18}F -MNI-800 (mean \pm SD, $n = 4$) or ^{18}F -MNI-968 (mean \pm SD, $n = 4$).

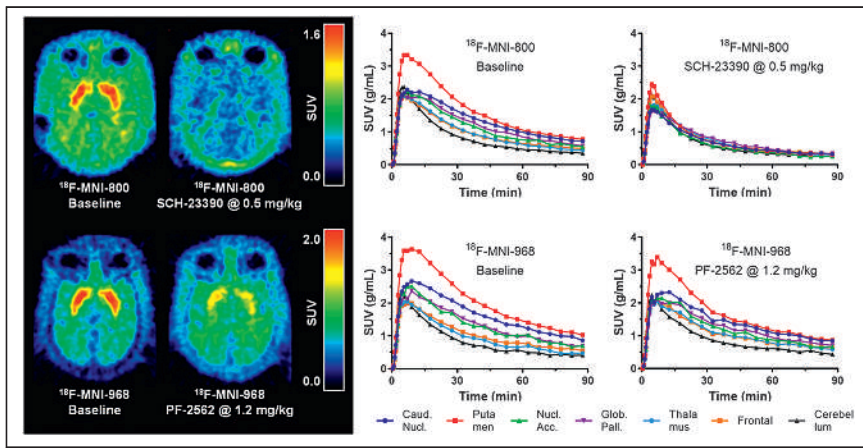


FIGURE 4. (Left) Average PET images from 30 to 90 min after injection for rhesus macaque (NHP A) in transverse plane of ¹⁸F-MNI-800 at baseline and after dosing with SCH-23390 at 0.5 mg/kg (occupancy of ~85%) and of ¹⁸F-MNI-968 at baseline and after dosing with PF-2562 at 1.2 mg/kg (occupancy of ~40%). (Right) Time-activity curves in some brain regions for same rhesus macaque for studies with ¹⁸F-MNI-800 and ¹⁸F-MNI-968. Caud. Nucl. = caudate nucleus; Glob. Pall. = globus pallidus; Nucl. Acc. = nucleus accumbens.

injection, respectively (Fig. 3). Plasma parent f_p measured by ultrafiltration was $13.4\% \pm 1.3\%$ ($n = 4$) for ¹⁸F-MNI-800 and $13.5\% \pm 1.5\%$ ($n = 4$) for ¹⁸F-MNI-968.

Brain Uptake Distribution and Time-Activity Curves

Representative average ¹⁸F-MNI-968 and ¹⁸F-MNI-800 PET images in a rhesus macaque at baseline showed the highest uptake in the striatum, consistent with known D1R distribution (Fig. 4, left). The ¹⁸F-MNI-800 PET image after a SCH-23390 preblock (0.5 mg/kg) demonstrated almost complete saturation. ¹⁸F-MNI-968 and ¹⁸F-MNI-800 time-activity curves at baseline and after a SCH-23390 (0.5 mg/kg) or PF-2562 (1.2 mg/kg) preblock are presented in Figure 4 (right) in the same rhesus macaque. Both ¹⁸F-MNI-968 and ¹⁸F-MNI-800 readily entered the brain, with SUV_{peak} at 5–10 min after injection. The signal was highest in the putamen and caudate nucleus, followed by the globus pallidus and nucleus accumbens, with the lowest uptake consistently found in the cerebellum. Clear blocking of ¹⁸F-MNI-800 or ¹⁸F-MNI-968 uptake was seen after preblocking with SCH-23390 (0.5 mg/kg, occupancy of ~85%) or PF-2562 (1.2 mg/kg, occupancy of ~40%), respectively. Higher uptake was also observed for ¹⁸F-MNI-968 than for ¹⁸F-MNI-800, particularly in the putamen and caudate nucleus, whereas a similar profile was maintained in the cerebellum.

Kinetic Analysis

2T was favored for both ¹⁸F-MNI-800 and ¹⁸F-MNI-968 data over 1 tissue compartment based on the Akaike information criterion. Typical 2T and SRTM fits and Logan plots (LGA with $t^* = 15$ min, and NI-LGA with $t^* = 10$ min) are provided in Figure 5 for a baseline study in a rhesus macaque with ¹⁸F-MNI-968. SRTM determined k'_2 to be $0.17 \pm 0.04 \text{ min}^{-1}$ ($n = 4$) for ¹⁸F-MNI-800 and $0.16 \pm 0.02 \text{ min}^{-1}$ ($n = 5$) for ¹⁸F-MNI-968, and these SRTM estimates of k'_2 were used for the NI-LGA fit.

A within-animal comparison ($n = 2$) between ¹⁸F-MNI-800 and ¹⁸F-MNI-968 V_T estimates (2T model) is shown in Figure 6A and indicates a higher specific signal for ¹⁸F-MNI-968 (negative y-intercept) and the same target/ B_{max} for both tracers (linearity of the relationship) (23). Since the f_p was similar for ¹⁸F-MNI-800 and ¹⁸F-MNI-968, the slope corresponds to the in vivo affinities ratio

and predicts a K_d about 1.3 times higher for ¹⁸F-MNI-800 (23). Furthermore, V_T in the cerebellum was $1.83 \pm 0.06 \text{ mL/cm}^3$ for ¹⁸F-MNI-800, compared with $1.87 \pm 0.01 \text{ mL/cm}^3$ for ¹⁸F-MNI-968, demonstrating a similar nondisplaceable signal for both tracers, with a relationship with BP_{ND} (2T model) for the within-animal studies: BP_{ND} (MNI-968) = $1.29 \times BP_{\text{ND}}$ (MNI-800) + 0.006.

Figures 6B and 6C compare V_T and BP_{ND} across methods for ¹⁸F-MNI-968, demonstrating very good agreement between the different estimates ($R^2 = 0.99$), in particular for BP_{ND} between plasma-based and reference region-based methods, with points aligning almost on the identity line. Similar results were obtained for ¹⁸F-MNI-800 (data not shown). A summary of V_T and BP_{ND} for the different methods is provided for a subset of regions in Table 2 for ¹⁸F-MNI-800

($n = 4$) and in Table 3 for ¹⁸F-MNI-968 ($n = 3$ for 2T and LGA, and $n = 5$ for SRTM and NI-LGA). Additional kinetic parameters for 2T are provided in Supplemental Tables 1 and 2. V_T ranged from approximately $1.9 \pm 0.1 \text{ mL/cm}^3$ in the cerebellum (similar estimates for both tracers) to approximately $3.7 \pm 0.3 \text{ mL/cm}^3$ and $4.3 \pm 0.2 \text{ mL/cm}^3$ in the putamen for ¹⁸F-MNI-800 and ¹⁸F-MNI-968, respectively. BP_{ND} ranged from approximately 0.2 in the cortex to 0.9 in the putamen for ¹⁸F-MNI-800, and from approximately 0.3 in the cortex to 1.1–1.2 in the putamen for ¹⁸F-MNI-968, confirming an average specific signal higher by approximately 30%. K_1 (2T model) was similar across regions, animals, and tracers, with $K_1 = 0.23 \pm 0.03 \text{ mL}\cdot\text{cm}^{-3}\cdot\text{min}^{-1}$ for ¹⁸F-MNI-800 and $K_1 = 0.27 \pm 0.06 \text{ mL}\cdot\text{cm}^{-3}\cdot\text{min}^{-1}$ for ¹⁸F-MNI-968 (Supplemental Tables 1 and 2).

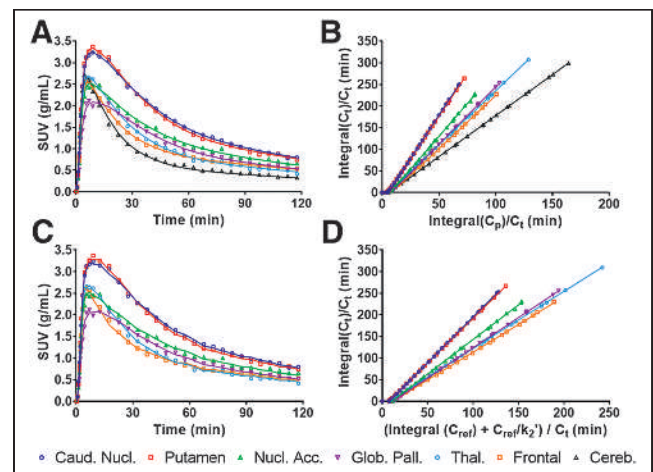


FIGURE 5. (A and C) Representative time-activity curves at baseline for rhesus macaque (NHP B) in some brain regions after bolus injection of ¹⁸F-MNI-968, showing 2T compartment model fits (A) and SRTM fits (C). (B and D) Graphical analysis with LGA with plasma input function ($t^* = 15$ min) (B) and NI-LGA with reference region input function ($t^* = 10$ min) (D). Caud. Nucl. = caudate nucleus; C_p = activity concentration in plasma; C_{ref} = activity concentration in reference region; C_i = activity concentration in region of interest; Glob. Pall. = globus pallidus; Nucl. Acc. = nucleus accumbens; Thal. = thalamus.

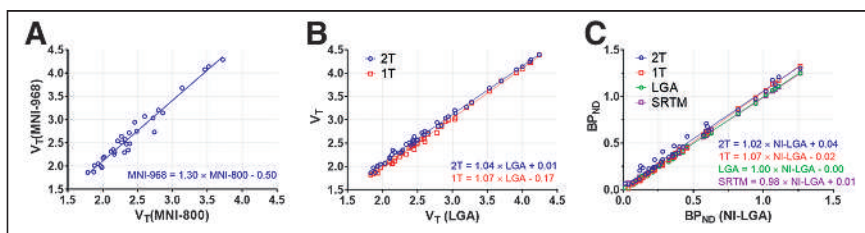


FIGURE 6. (A) Within-animal comparison ($n = 2$) of ^{18}F -MNI-800 and ^{18}F -MNI-968 $2T V_T$ estimates. (B) Comparison of ^{18}F -MNI-968 V_T estimates across models ($n = 3$). (C) Comparison of ^{18}F -MNI-968 BP_{ND} estimates across models ($n = 3$). $1T = 1$ tissue compartment.

Test–retest variability was assessed in a limited number of repeat studies for ^{18}F -MNI-800 ($n = 2$) and ^{18}F -MNI-968 ($n = 1$). The results are summarized in Supplemental Tables 3 and 4 for the different methods. Variability in V_T estimates was low in all regions and both tracers ($<10\%$), whereas that of BP_{ND} in the striatum remained low for ^{18}F -MNI-800 ($<5\%$) and somewhat higher for ^{18}F -MNI-968 ($\sim 15\%$), for which, however, test and retest scans were separated by 4 mo.

SCH-23390 Occupancy Studies

Preblocking with SCH-23390 increased the measured occupancies in a dose-dependent fashion and reduced the ^{18}F -MNI-800 uptake to levels close to those in the cerebellum at the highest dose tested (Fig. 4), supporting the specificity and selectivity of ^{18}F -MNI-800 for D1R, with measured occupancies of approximately 85% and 60% at the 2 highest SCH-23390 doses of 0.5 and 0.2 mg/kg, respectively.

SCH-23390 plasma levels during the preblocking studies are shown in Figure 7A, and the relationship between the measured D1R occupancy and the average plasma levels during the PET imaging (25–145 min after administration of SCH-23390) is shown in Figure 7B for the various analysis methods used, for which the maximum occupancy was constrained to 100%. All methods produced similar occupancy measurements, with slightly lower estimates for 2T at the 2 lowest SCH-23390 doses, with a consistent estimated EC_{50} ranging from 6.0 ± 1.0 ng/mL for NI-LGA to 8.5 ± 1.0 ng/mL for 2T (average, ~ 7 ng/mL).

^{18}F -MNI-800 Dosimetry

Whole-body studies showed that ^{18}F -MNI-800 is eliminated mainly via the hepatobiliary route. The urinary bladder, gallbladder, and liver were determined to be the critical organs with the highest absorbed dose (Supplemental Table 5). The whole-body effective dose (ED) was estimated to be 0.025 mSv/MBq for the female rhesus and 0.021 mSv/MBq for the male rhesus, in line with other ^{18}F -labeled tracers (e.g., 0.019 mSv/MBq for ^{18}F -FDG (24)).

DISCUSSION

Both ^{18}F -MNI-800 and its active atropisomeric (–)-enantiomer ^{18}F -MNI-968 demonstrated high penetration in monkey brain, with uptake distribution in agreement with the known D1R distribution. Blood profiles were highly similar, with an almost identical metabolism rate and f_p ($\sim 13\%$).

SCH-23390 has a 5-HT_{2a} component (15); however, the density of 5-HT_{2a} receptors in the striatum is negligible compared with D1R. Therefore, SCH-23390 preblocking studies confirmed the specificity and selectivity of ^{18}F -MNI-800 for D1R over other targets in

the striatum, as is expected to hold true for ^{18}F -MNI-968 because it is one enantiomer. Absolute selectivity against 5-HT_{2a} receptors could be tested further by a challenge with the selective 5-HT_{2a} antagonist MDL 100907. These studies also confirmed the choice of the cerebellum as a reference region for non-invasive methods, BP_{ND} calculations, and occupancy measurements since the signal in this region was not blocked. This choice is also supported by a V_{ND} estimate from occupancy plots of 2.0 ± 0.1 (25), in very good agreement with a V_T of 1.9 ± 0.1 in the cerebellum (Table 2). Assuming passive diffusion through the blood–brain barrier, the tissue non-displaceable free fraction (f_{ND}) can be calculated from the measured f_p and V_{ND} above (20), giving an f_{ND} of approximately 7%, in close agreement with the unbound fraction of 6% in brain. Finally, the agreement in occupancy estimates between the plasma-based and reference-region–based methods suggests that D1R occupancy can be quantitatively assessed in monkeys using SRTM or NI-LGA, without the need for arterial sampling.

BP_{ND} in humans and NHPs was reported to be approximately 0.4–0.6 in the cortex and 2.0–3.0 in the striatum for ^{11}C -SCH-23390 and approximately 0.6–0.8 in the cortex and 3.0–4.0 in the striatum for ^{11}C -NNC-112 (15,26–28), which are higher than the values reported here for ^{18}F -MNI-968 (~ 0.3 in the cortex and ~ 1.1 in the striatum, Table 3). Also, BP_{ND} variability in humans was reported as approximately 10%–15% in the cortex and 5.0%–10% in the striatum for both ^{11}C -SCH-23390 and ^{11}C -NNC-112 (27,29), marginally better than that reported here (Supplemental Table 3), although we assessed the variability in a limited number of animals. However, both ^{11}C -SCH-23390 and ^{11}C -NNC-112 are antagonist radioligands and therefore cannot provide information on the high- or low-affinity state of D1R, and both suffer from a cortical 5-HT_{2a} signal that represents about 20%–30% of the total signal (15,26). Therefore, further evaluation and characterization of ^{18}F -MNI-968 in human subjects is warranted because the tracer could prove to be a valuable tool in Parkinson disease (9) and in psychiatric disorders such as schizophrenia (8).

CONCLUSION

We report here the evaluation of racemate ^{18}F -MNI-800 and its (–)-enantiomer ^{18}F -MNI-968 in NHPs. Both tracers had regional uptake consistent with D1R distribution. The selectivity and

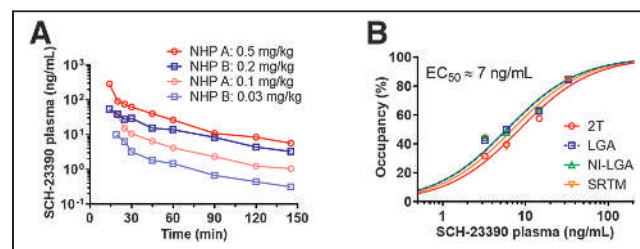


FIGURE 7. (A) SCH-23390 plasma levels for 4 doses, with ^{18}F -MNI-800 injection at 25 min after drug administration. (B) Striatal D1R occupancy against average plasma levels between 25 and 145 min after administration of SCH-23390. EC_{50} = half-maximal effective concentration.

TABLE 2
¹⁸F-MNI-800 V_T and BP_{ND} in Pooled Rhesus and Cynomolgus Macaques

Region	V _T		BP _{ND}			
	2T	LGA	2T	LGA	SRTM	NI-LGA
Striatum	3.6 ± 0.3 (8%)	3.5 ± 0.3 (8%)	0.86 ± 0.10 (11%)	0.83 ± 0.08 (9%)	0.83 ± 0.07 (8%)	0.83 ± 0.07 (8%)
Caudate	3.5 ± 0.4 (11%)	3.4 ± 0.4 (11%)	0.81 ± 0.11 (14%)	0.78 ± 0.10 (12%)	0.78 ± 0.09 (11%)	0.78 ± 0.09 (12%)
Putamen	3.7 ± 0.3 (7%)	3.6 ± 0.3 (7%)	0.91 ± 0.14 (15%)	0.88 ± 0.12 (13%)	0.89 ± 0.11 (12%)	0.89 ± 0.11 (13%)
Nucleus accumbens	2.9 ± 0.2 (7%)	2.8 ± 0.2 (7%)	0.48 ± 0.03 (6%)	0.46 ± 0.02 (5%)	0.45 ± 0.02 (5%)	0.46 ± 0.02 (5%)
Globus pallidus	2.9 ± 0.3 (9%)	2.8 ± 0.3 (9%)	0.50 ± 0.06 (13%)	0.48 ± 0.06 (12%)	0.48 ± 0.06 (12%)	0.48 ± 0.05 (11%)
Thalamus	2.4 ± 0.2 (9%)	2.4 ± 0.2 (8%)	0.25 ± 0.06 (22%)	0.25 ± 0.04 (17%)	0.26 ± 0.04 (16%)	0.26 ± 0.04 (16%)
Frontal cortex	2.3 ± 0.0 (0%)	2.2 ± 0.0 (1%)	0.24 ± 0.04 (18%)	0.20 ± 0.05 (24%)	0.20 ± 0.05 (23%)	0.20 ± 0.05 (25%)
Cerebellum	1.9 ± 0.1 (7%)	1.9 ± 0.1 (6%)				

Data are mean ± SD, followed by coefficient of variation in parentheses (n = 4).

specificity of ¹⁸F-MNI-800 and ¹⁸F-MNI-968 for D1R were demonstrated against SCH-23390 or PF-2562, a selective D1R antagonist and a partial agonist, respectively. Noninvasive quantification of ¹⁸F-MNI-800 and ¹⁸F-MNI-968 with SRTM or LGA using the cerebellum as a reference is possible, particularly for occupancy studies. ¹⁸F-MNI-800 dosimetry, and putatively dosimetry of ¹⁸F-MNI-968, are favorable, with an effective dose consistent with values reported for other PET radiotracers. Therefore, ¹⁸F-MNI-968 has great potential as a D1R agonist PET radiotracer and warrants further characterization in human subjects.

DISCLOSURE

The research reported in this publication was supported by the National Institute of Mental Health of the National Institutes of Health under award U01MH107803. No other potential conflict of interest relevant to this article was reported.

ACKNOWLEDGMENTS

We thank Dr. Richard Carson and the staff at the Yale PET Center for conducting the rhesus monkey experiments.

KEY POINTS

QUESTION: Does the agonist PET tracer ¹⁸F-MNI-968 show suitable properties and specific binding to quantify D₁ dopamine receptor?

PERTINENT FINDINGS: ¹⁸F-MNI-968, the atropisomeric (–)-enantiomer, showed a suitable in vitro pharmacology profile, high brain uptake, favorable kinetics, and specific binding that was blocked by a selective D1R antagonist and a partial agonist.

IMPLICATIONS FOR PATIENT CARE: ¹⁸F-MNI-968 has potential as an agonist PET radioligand to quantify D1Rs in the high-affinity state in human brains, particularly in neurologic and psychiatric disorders.

TABLE 3
¹⁸F-MNI-968 V_T and BP_{ND} in Pooled Rhesus and Cynomolgus Macaques

Region	V _T		BP _{ND}			
	2T	LGA	2T	LGA	SRTM	NI-LGA
Striatum	4.1 ± 0.2 (4%)	4.0 ± 0.2 (4%)	1.14 ± 0.05 (5%)	1.07 ± 0.02 (2%)	1.07 ± 0.03 (2%)	1.08 ± 0.03 (3%)
Caudate	4.0 ± 0.3 (8%)	3.9 ± 0.3 (8%)	1.08 ± 0.12 (11%)	1.02 ± 0.09 (9%)	1.06 ± 0.09 (8%)	1.06 ± 0.08 (8%)
Putamen	4.3 ± 0.2 (4%)	4.1 ± 0.2 (4%)	1.20 ± 0.09 (8%)	1.13 ± 0.10 (9%)	1.11 ± 0.08 (7%)	1.12 ± 0.08 (8%)
Nucleus accumbens	3.2 ± 0.2 (5%)	3.1 ± 0.2 (6%)	0.65 ± 0.02 (4%)	0.61 ± 0.00 (0%)	0.59 ± 0.07 (12%)	0.60 ± 0.07 (12%)
Globus pallidus	3.2 ± 0.6 (18%)	3.1 ± 0.5 (18%)	0.65 ± 0.20 (31%)	0.60 ± 0.21 (35%)	0.58 ± 0.18 (31%)	0.58 ± 0.18 (31%)
Thalamus	2.6 ± 0.2 (9%)	2.6 ± 0.2 (9%)	0.35 ± 0.04 (13%)	0.33 ± 0.04 (13%)	0.29 ± 0.05 (19%)	0.29 ± 0.06 (20%)
Frontal cortex	2.6 ± 0.1 (2%)	2.4 ± 0.1 (2%)	0.33 ± 0.08 (25%)	0.27 ± 0.04 (15%)	0.28 ± 0.05 (17%)	0.28 ± 0.05 (18%)
Cerebellum	1.9 ± 0.1 (6%)	1.9 ± 0.1 (5%)				

Data are mean ± SD, followed by coefficient of variation in parentheses (n = 3 for 2T and LGA, and n = 5 for SRTM and NI-LGA).

REFERENCES

- Hall H, Sedvall G, Magnusson O, Kopp J, Halldin C, Farde L. Distribution of D1- and D2-dopamine receptors, and dopamine and its metabolites in the human brain. *Neuropsychopharmacology*. 1994;11:245–256.
- Meador-Woodruff JH, Damask SP, Wang J, Haroutunian V, Davis KL, Watson SJ. Dopamine receptor mRNA expression in human striatum and neocortex. *Neuropsychopharmacology*. 1996;15:17–29.
- Rosell DR, Zaluda LC, McClure MM, et al. Effects of the D1 dopamine receptor agonist dihydrexidine (DAR-0100A) on working memory in schizotypal personality disorder. *Neuropsychopharmacology*. 2015;40:446–453.
- Schneider JS, Sun ZQ, Roeltgen DP. Effects of dihydrexidine, a full dopamine D-1 receptor agonist, on delayed response performance in chronic low dose MPTP-treated monkeys. *Brain Res*. 1994;663:140–144.
- Kozak R, Kiss T, Dlugolenski K, et al. Characterization of PF-6142, a novel, non-catecholamine dopamine receptor D1 agonist, in murine and nonhuman primate models of dopaminergic activation. *Front Pharmacol*. 2020;11:1005.
- Hall A, Provins L, Valade A. Novel strategies to activate the dopamine D1 receptor: recent advances in orthosteric agonism and positive allosteric modulation. *J Med Chem*. 2019;62:128–140.
- Coe JW, Allen JA, Davoren JE, et al., inventors; Pfizer Inc., assignee. Heteroaromatic compounds and their use as dopamine D1 ligands. International patent WO2014072881 A1. 2014.
- Arce E, Balice-Gordon R, Duvvuri S, et al. A novel approach to evaluate the pharmacodynamics of a selective dopamine D1/D5 receptor partial agonist (PF-06412562) in patients with stable schizophrenia. *J Psychopharmacol*. 2019;33:1237–1247.
- Papapetropoulos S, Liu W, Duvvuri S, Thayer K, Gray DL. Evaluation of D1/D5 partial agonist PF-06412562 in Parkinson's disease following oral administration. *Neurodegener Dis*. 2018;18:262–269.
- Halldin C, Foged C, Chou YH, et al. Carbon-11-NNC 112: a radioligand for PET examination of striatal and neocortical D1-dopamine receptors. *J Nucl Med*. 1998;39:2061–2068.
- Halldin C, Stone-Elander S, Farde L, et al. Preparation of ¹¹C-labelled SCH 23390 for the in vivo study of dopamine D-1 receptors using positron emission tomography. *Int J Rad Appl Instrum [A]*. 1986;37:1039–1043.
- Kassiou M, Scheffel U, Ravert HT, et al. [¹¹C]A-69024: a potent and selective non-benzazepine radiotracer for in vivo studies of dopamine D1 receptors. *Nucl Med Biol*. 1995;22:221–226.
- Finnema SJ, Bang-Andersen B, Jorgensen M, et al. The dopamine D₁ receptor agonist (S)-[¹¹C]N-methyl-NNC 01-0259 is not sensitive to changes in dopamine concentration: a positron emission tomography examination in the monkey brain. *Synapse*. 2013;67:586–595.
- Palner M, McCormick P, Parkes J, Knudsen GM, Wilson AA. Systemic catechol-O-methyl transferase inhibition enables the D1 agonist radiotracer R-[¹¹C]SKF 82957. *Nucl Med Biol*. 2010;37:837–843.
- Ekelund J, Slifstein M, Narendran R, et al. In vivo DA D₁ receptor selectivity of NNC 112 and SCH 23390. *Mol Imaging Biol*. 2007;9:117–125.
- Zhang L, Villalobos A, Beck EM, et al. Design and selection parameters to accelerate the discovery of novel central nervous system positron emission tomography (PET) ligands and their application in the development of a novel phosphodiesterase 2A PET ligand. *J Med Chem*. 2013;56:4568–4579.
- Cumming P. Absolute abundances and affinity states of dopamine receptors in mammalian brain: a review. *Synapse*. 2011;65:892–909.
- Slifstein M, Laruelle M. Models and methods for derivation of in vivo neuroreceptor parameters with PET and SPECT reversible radiotracers. *Nucl Med Biol*. 2001;28:595–608.
- Logan J. A review of graphical methods for tracer studies and strategies to reduce bias. *Nucl Med Biol*. 2003;30:833–844.
- Innis RB, Cunningham VJ, Delforge J, et al. Consensus nomenclature for in vivo imaging of reversibly binding radioligands. *J Cereb Blood Flow Metab*. 2007;27:1533–1539.
- Lammertsma AA, Hume SP. Simplified reference tissue model for PET receptor studies. *Neuroimage*. 1996;4:153–158.
- Stabin MG, Sparks RB, Crowe E. OLINDA/EXM: the second-generation personal computer software for internal dose assessment in nuclear medicine. *J Nucl Med*. 2005;46:1023–1027.
- Guo Q, Owen DR, Rabiner EA, Turkheimer FE, Gunn RN. A graphical method to compare the in vivo binding potential of PET radioligands in the absence of a reference region: application to [¹¹C]PBR28 and [¹⁸F]PBR111 for TSPO imaging. *J Cereb Blood Flow Metab*. 2014;34:1162–1168.
- Delbeke D, Coleman RE, Guiberteau MJ, et al. Procedure guideline for tumor imaging with ¹⁸F-FDG PET/CT 1.0. *J Nucl Med*. 2006;47:885–895.
- Cunningham VJ, Rabiner EA, Slifstein M, Laruelle M, Gunn RN. Measuring drug occupancy in the absence of a reference region: the Lassen plot re-visited. *J Cereb Blood Flow Metab*. 2010;30:46–50.
- Slifstein M, Kegeles LS, Gonzales R, et al. [¹¹C]NNC 112 selectivity for dopamine D1 and serotonin 5-HT(2A) receptors: a PET study in healthy human subjects. *J Cereb Blood Flow Metab*. 2007;27:1733–1741.
- Abi-Dargham A, Martinez D, Mawlawi O, et al. Measurement of striatal and extrastriatal dopamine D1 receptor binding potential with [¹¹C]NNC 112 in humans: validation and reproducibility. *J Cereb Blood Flow Metab*. 2000;20:225–243.
- Kosaka J, Takahashi H, Ito H, et al. Decreased binding of [¹¹C]NNC112 and [¹¹C]SCH23390 in patients with chronic schizophrenia. *Life Sci*. 2010;86:814–818.
- Hirvonen J, Nagren K, Kajander J, Hietala J. Measurement of cortical dopamine D₁ receptor binding with [¹¹C]SCH23390: a test-retest analysis. *J Cereb Blood Flow Metab*. 2001;21:1146–1150.

Optical Navigation of the Drop-In γ -Probe as a Means to Strengthen the Connection Between Robot-Assisted and Radioguided Surgery

Samaneh Azargoshasb¹, Krijn H.M. Houwing¹, Paul R. Roos¹, Sven I. van Leeuwen¹, Michael Boonekamp², Elio Mazzone^{3,4}, Kevin Bauwens⁴, Paolo Dell'Oglio^{1,4-6}, Fijs W.B. van Leeuwen^{1,4,6}, Matthias N. van Oosterom^{1,6}

¹Interventional Molecular Imaging Laboratory, Department of Radiology, Leiden University Medical Center, Leiden, The Netherlands; ²Instrumentele Zaken Ontwikkeling, Facilitair Bedrijf, Leiden University Medical Center, Leiden, The Netherlands; ³Department of Urology and Division of Experimental Oncology, URI, Urological Research Institute IRCCS San Raffaele Scientific Institute, Milan, Italy; ⁴Orsi Academy, Melle, Belgium; ⁵Department of Urology, ASST Grande Ospedale Metropolitano Niguarda, Milan, Italy; and ⁶Department of Urology, Netherlands Cancer Institute–Antoni van Leeuwenhoek Hospital, Amsterdam, The Netherlands

With translation of the Drop-In γ -probe, radioguidance has advanced into laparoscopic robot-assisted surgery. Global-positioning-system-like navigation can further enhance the symbiosis between nuclear medicine and surgery. Therefore, we developed a fluorescence-video-based tracking method that integrates the Drop-In with navigated robotic surgery. **Methods:** Fluorescent markers, integrated into the Drop-In, were automatically detected using a daVinci Firefly laparoscope. Subsequently, a declipseSPECT-navigation platform calculated the Drop-In location within the surgical field. Using a phantom ($n = 3$), we pursued robotic navigation on SPECT/CT, whereas intraoperative feasibility was validated during porcine surgery ($n = 4$). **Results:** Video-based tracking allowed for navigation of the Drop-In toward all lesions detected on SPECT/CT (external iliac and common iliac artery regions). Augmented-reality visualization in the surgical console indicated the distance to these lesions in real time, confirmed by the Drop-In readout. Porcine surgery underlined the feasibility of the concept. **Conclusion:** Optical navigation of the Drop-In probe provides a next step toward connecting nuclear medicine with robotic surgery.

Key Words: radioguided surgery; robot-assisted surgery; optical navigation; image-guided surgery; augmented reality

J Nucl Med 2021; 62:1314–1317
DOI: 10.2967/jnumed.120.259796

In the pursuit of precision surgery, robot-assisted approaches are gaining traction (e.g., prostatectomy and lymphatic dissections). An effective minimally invasive approach requires not only well-engineered (robotic) instruments but also precise target definition. Interventional molecular imaging can help achieve this: radioguided surgery is one of the most used image-guided surgery techniques (1). Unfortunately, the use of laparoscopic γ -probes is cumbersome with the robot (2). To overcome these limitations, tethered drop-in γ - and β -probes have been introduced for sentinel lymph node resection

(2,3) and prostate-specific membrane antigen–targeted resection (4,5). These robot-tailored modalities allow the surgeon to autonomously position the detector to localize lesions during surgery. In areas with great anatomic complexity, road maps provided by preoperative imaging (SPECT/CT or PET/CT) are considered a critical tool to provide insight on the number and location of surgical targets (6). Unfortunately, during robotic procedures, real-time registration of such preoperative imaging information into the surgical view is challenging.

SPECT-based navigation of γ -probes could translate road maps created at nuclear medicine to the surgical theater (7). Unfortunately, traditional tool-tracking technologies cannot be used with a drop-in probe, whose tethered nature prohibits tracking with external optical tracking systems, and the metal parts of the robot setup degrade the accuracy of electromagnetic tracking systems (8,9). Alternatively, video-based tracking concepts have been pursued (8,9). Use of patterned-surface markers, which can be segmented from a laparoscopic video feed using traditional white-light imaging, has been explored for tethered ultrasound and γ -probes (10,11). For such a tracking method, a direct line of sight has to be maintained between the drop-in probe and the laparoscope. However, Wild et al. have proposed use of fluorescence surface markers, with which a direct line of sight is less easily impaired by smoke, water, or blood and which can be used in combination with fluorescence guidance (12). In combination with multicolor fluorescence imaging (13), use of fluorescence markers would also aid the integration of robotic navigation with bimodal tracers (14).

In this study, we exploit real-time fluorescence-based optical tracking for navigation of a drop-in γ -probe during robotic procedures on phantoms and a porcine model. To increase the translational potential of this concept, we used image-guided surgery technologies already available in the clinic (Drop-In [Eurorad S.A.] (2), multicolor fluorescence (13), and declipseSPECT [SurgicEye GmbH]).

MATERIALS AND METHODS

Tracking and Navigation Setup

The SPECT-navigated setup (Fig. 1) consisted of the Drop-In γ -probe (3), a Da Vinci Si robot (Intuitive Inc.) with a Firefly fluorescence laparoscope (Intuitive Inc.), and a declipseSPECT navigation system (SurgicEye GmbH) with near-infrared optical tracking (Northern Digital Inc.),

Received Nov 5, 2020; revision accepted Jan. 3, 2021.
For correspondence or reprints, contact Matthias N. van Oosterom (m.n.van_oosterom@lumc.nl).
Published online January 8, 2021.
COPYRIGHT © 2021 by the Society of Nuclear Medicine and Molecular Imaging.

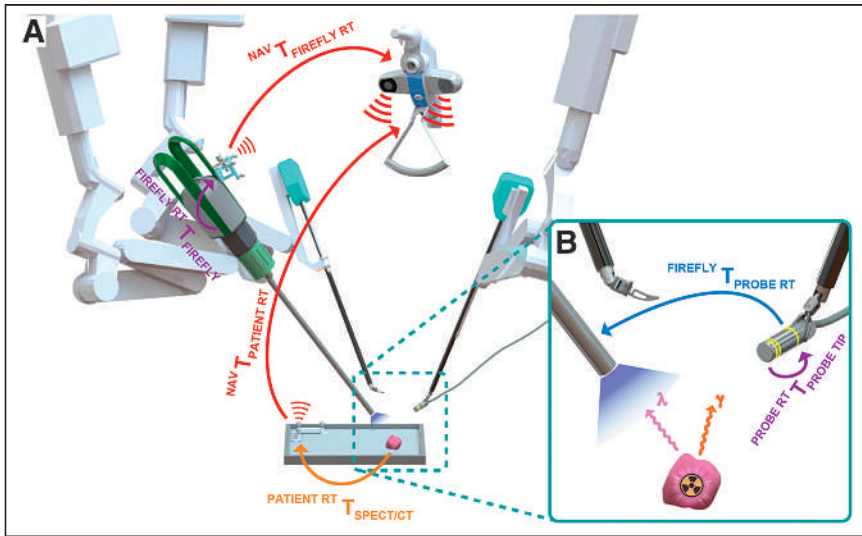


FIGURE 1. Overview of Drop-In tracking-and-navigation setup displaying underlying pose relations with colored arrows, describing the relative positions and orientations of all objects in the navigation workflow. (A) Near-infrared optical tracking determines the pose of Firefly and patient reference targets (red arrows), whereas underlying registrations translate this pose to Firefly camera (purple arrow) and lesions as found on SPECT/CT (orange arrow). (B) Vision-based tracking from Firefly determines the pose of Drop-In markings within surgical field (blue arrow), and these markings are calibrated with Drop-In probe tip (purple arrow). Finally, the Drop-In can be navigated toward SPECT/CT-marked lesions. NAV = navigation system; RT = reference target; T = pose transformation.

running customized tracking software. The Firefly Si laparoscope records the raw fluorescence video feed and allows for simultaneous visualization of fluorescein in yellow, indocyanine green (ICG) in pink, and the anatomic background in blue or in black and white (13). To allow for accurate calculations within the tracking software, the Firefly intrinsic and extrinsic camera properties were calibrated (15).

An asymmetric 3-ring fluorescent-marker pattern was incorporated into the Drop-In housing, fabricated from medical-grade ultraviolet-curable adhesives comprising fluorescein. The fluorescent emissions were automatically detected on the basis of color and shape. Using the known geometric arrangement, the pose of the Drop-In tip could be estimated (5 degrees of freedom) with respect to the Firefly laparoscope (Fig. 1B). With one reference target attached to the Firefly and one to the patient (Fig. 1A), the declipseSPECT was used to determine the pose of the Firefly and the patient within the operating room.

Phantom Evaluation

To study the concept of SPECT/CT-based navigation, we used a laparoscopic torso phantom (15) that contained bones, artery structures, and a radioactive model of pelvic lymph nodes (2 MBq of ^{99m}Tc each). Radioactive nodes were placed at different locations (i.e., right and left external iliac artery and left common iliac artery), and 3 separate SPECT/CT scans were acquired with the navigation reference target fixated at the

phantom's hip, allowing for registration of the scans in the operating room.

Porcine Evaluation

To investigate the Drop-In tracking setup in a real-life surgical setting, 4 pigs underwent robot-assisted laparoscopic surgery. Surgical targets were created by depositing ICG ($\sim 50 \mu\text{L}$, 2.5 mg/mL solution in saline) in the abdominal wall (average of 3 depositions per pig). The tracer deposits were manually set as targets to which the Drop-In probe was navigated. Animal experiments were performed under the approval of the local ethical committee.

RESULTS

Phantom Evaluation

Figure 2 illustrates the concept of performing SPECT-based navigation of the Drop-In in the robot-assisted laparoscopic setting (see also Supplemental Video 1; supplemental materials are available at <http://jnm.snmjournals.org>). A navigation-enriched view of the abdomen was visible in the robotic console, including an augmented-reality overlay of the lesion segmented from SPECT/CT. Maintaining a direct line-of-sight between the Firefly and the Drop-In allowed for real-time calculation of the distance between the targeted lesion and the Drop-In tip in millimeters. The marker geometry allowed for a great range of maneuverability: at a 10-cm distance in line with the laparoscope,

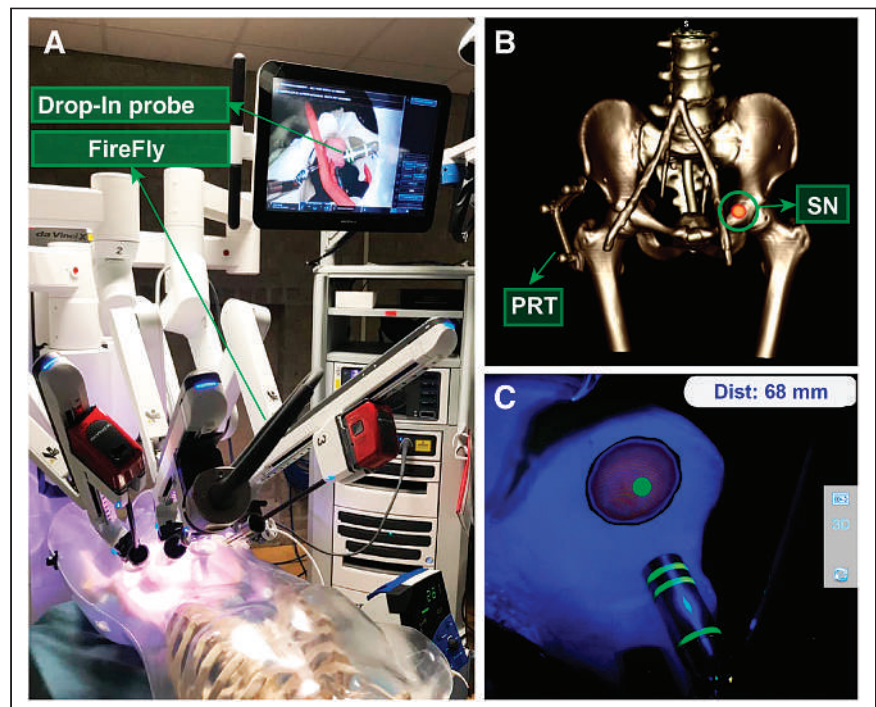


FIGURE 2. Real-time Drop-In tracking and navigation during robot-assisted laparoscopic surgery on phantom. (A) Setup overview. (B) Phantom SPECT/CT example, displaying patient reference target (PRT) and targeted lymph node (SN). (C) Augmented-reality visualization in surgical console, displaying Drop-In navigation toward lymph node (including calculated distance).

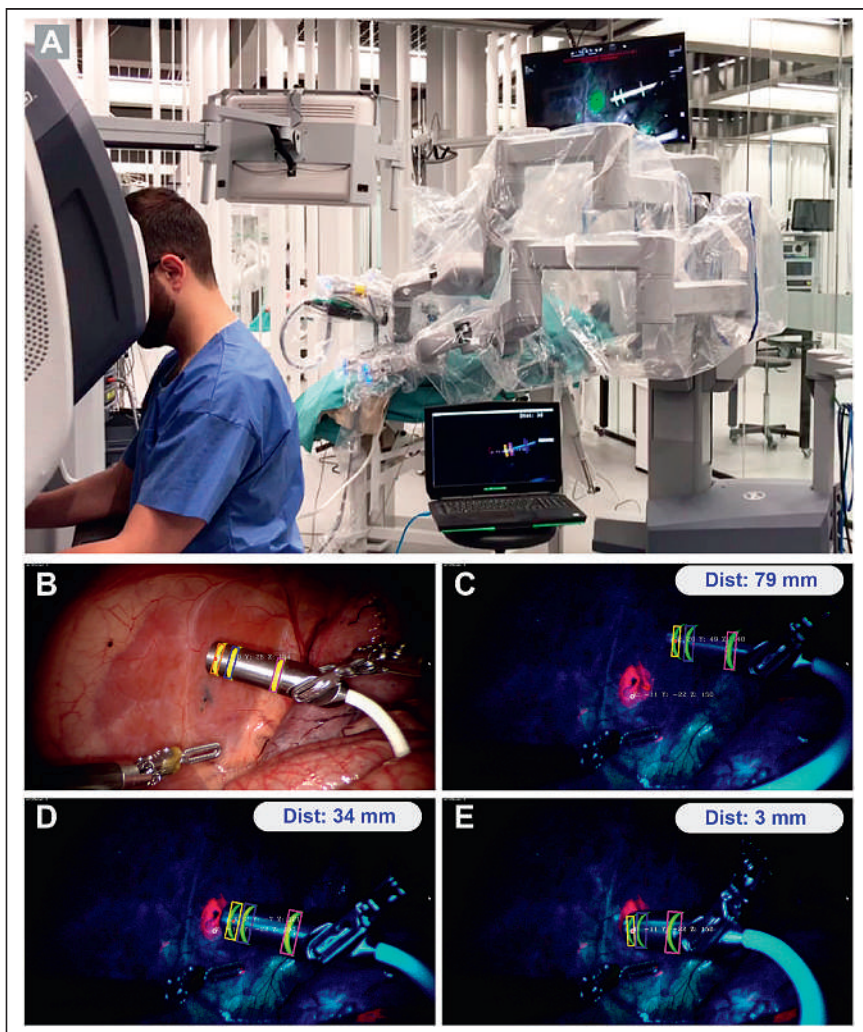


FIGURE 3. Real-time tracking of Drop-In probe with respect to targeted lesions during robot-assisted laparoscopic surgery on pig. (A) Operating room overview. (B) White-light image. (C–E) Tracking of Drop-In probe with respect to targeted lesion (pink) using fluorescence imaging at calculated target distances of 79, 34, and 3 mm.

Drop-In tracking was feasible for 0° – 360° (roll), 0° – 360° (pitch), and 15° – 165° and 195° – 345° (yaw). The location of the lesion targets (i.e., left and right external iliac artery and left common iliac artery) meant that the high maneuverability of the Drop-In was instrumental for intraoperative detection (2). The audible feedback provided by the Drop-In γ -probe confirmed effective navigation.

Porcine Evaluation

Robotic surgery on a porcine model was used to evaluate translation into an actual surgical setting (Fig. 3; Supplemental Video 1). In this real surgical environment, the fluorescein markers on the Drop-In probe remained clearly detectable (in yellow), both in white-light and fluorescence imaging mode. ICG-containing lesions were visible only in fluorescence imaging mode (in pink) and could be detected at the same time as the Drop-In markers (Figs. 3C–E). Uniquely, the fluorescent emissions of fluorescein (maximal λ -emission, 515 nm) and ICG (maximal λ -emission, 820 nm) could be excited simultaneously and could be distinguished by exploring the fluorescence-multiplexing capabilities of the Firefly Si camera (13). The surgeon was thus also able to visually confirm the localized lesions during

navigation. Although the excitation power in the near-infrared region with this Firefly is roughly 100 times higher than in the blue region of the spectrum (13), there was no clear difference in intensity observed between the fluorescein markers and ICG lesions. Bleaching of the fluorescein ring markers was not observed within the approximately 1-h experiments. In addition, problems with blood contamination of the Drop-In markers were not observed, indicating the potential of fluorescence-based markers as discussed previously (12).

DISCUSSION

We investigated the first steps toward optical navigation of the Drop-In γ -probe, a concept that further integrates interventional nuclear medicine during robotic surgery. Visualizing the position of the Drop-In with respect to predefined lesions is likely to help surgeons reduce intraoperative uncertainties about the target location and the γ -probe readout. The translational character of the findings is underscored by the proven utility of the Drop-In concept in prostate-cancer surgery (sentinel node targeting with both the tracer ICG- ^{99m}Tc -nanocolloid and the tracer ^{99m}Tc -nanocolloid (2) and prostate-specific membrane antigen targeting with ^{99m}Tc -PSMA-I&S (5)), the use of medical-grade fluorescent materials as markers, the use of the clinically approved Firefly camera and declipseSPECT navigation system, and a proof of concept in porcine surgery. Obviously, the concept could in the future be disseminated to alternative indications for which ^{125}I -, ^{99m}Tc -, or ^{111}In -based radioguided surgery approaches have been reported (1) or even to alternative multicolor fluorescence approaches (16).

In this study, we evaluated navigation in preoperative SPECT/CT scans, but the same concept could also be expanded using, for example, a drop-in β -probe (or even a drop-in ultrasound probe) in combination with PET/CT scans (4). Unfortunately, the surgical facilities that we used to test the presented technologies did not allow us to evaluate SPECT/CT-based navigation in porcine models. Since to date a facility allowing such an experiment is unavailable, this link has to be further validated in clinical trials, as was done for other γ -probes (7). The current study, however, ensures that follow-up trials can rely on a validated technology, thus limiting the exposure of patients to unnecessary risks.

CONCLUSION

Surgical navigation of the Drop-In probe based on SPECT/CT is promising, providing the next step toward precision radioguided surgery, connecting nuclear medicine with robotic surgery. Studies on humans are in preparation to confirm these findings and evaluate the oncologic benefit of such an image-guided surgery approach.

DISCLOSURE

Financial support was received through NWO-TTW-VICI grant 16141, and hardware support was received from Eurorad S.A. Matthias van Oosterom, Fijs van Leeuwen, and Krijn Houwing have a pending patent on fluorescent-marker tracking. During this research, Elio Mazzone, Kevin Bauwens, Paolo Dell'Oglio, and Fijs van Leeuwen were partially affiliated with Orsi Academy. No other potential conflict of interest relevant to this article was reported.

ACKNOWLEDGMENTS

We acknowledge Danny van Willigen, Tessa Buckle (LUMC, The Netherlands), and the Orsi Academy staff (Belgium) for assistance during surgical evaluations, as well as the Skills-Lab and Petra Dibbets (LUMC) for assistance during phantom evaluations.

KEY POINTS

QUESTION: Is it possible to navigate the Drop-In γ -probe toward preoperatively marked lesions during robotic surgery?

PERTINENT FINDINGS: As evaluated in a robot-assisted phantom setting, fluorescence markers can be used to navigate the Drop-In toward lesions as identified on SPECT/CT. The feasibility of this concept was confirmed during surgery in a porcine model.

IMPLICATIONS FOR PATIENT CARE: Proving its utility in large-animal models, a next step has been taken toward precision radioguided surgery in the human robot-assisted setting.

REFERENCES

1. Van Oosterom MN, Rietbergen DD, Welling MM, et al. Recent advances in nuclear and hybrid detection modalities for image-guided surgery. *Expert Rev Med Devices*. 2019;16:711–734.
2. Dell'Oglio P, Meershoek P, Maurer T, et al. A DROP-IN gamma probe for robot-assisted radioguided surgery of lymph nodes during radical prostatectomy. *Eur Urol*. 2021;79:124–132.
3. van Oosterom MN, Simon H, Mengus L, et al. Revolutionizing (robot-assisted) laparoscopic gamma tracing using a drop-in gamma probe technology. *Am J Nucl Med Mol Imaging*. 2016;6:1–17.
4. Collamati F, van Oosterom MN, De Simoni M, et al. A DROP-IN beta probe for robot-assisted ^{68}Ga -PSMA radioguided surgery: first ex vivo technology evaluation using prostate cancer specimens. *EJNMMI Res*. 2020;10:92.
5. van Leeuwen FW, van Oosterom MN, Meershoek P, et al. Minimal-invasive robot-assisted image-guided resection of prostate-specific membrane antigen-positive lymph nodes in recurrent prostate cancer. *Clin Nucl Med*. 2019;44:580–581.
6. Meershoek P, Buckle T, van Oosterom MN, KleinJan GH, van der Poel HG, van Leeuwen FWB. Can intraoperative fluorescence imaging identify all lesions while the road map created by preoperative nuclear imaging is masked? *J Nucl Med*. 2020;61:834–841.
7. Bowles H, Sánchez N, Tapias A, et al. Radioguided surgery and the GOSTT concept: from pre-operative image and intraoperative navigation to image-assisted excision. *Rev Esp Med Nucl Imagen Mol*. 2017;36:175–184.
8. Bernhardt S, Nicolau SA, Soler L, et al. The status of augmented reality in laparoscopic surgery as of 2016. *Med Image Anal*. 2017;37:66–90.
9. van Oosterom MN, van der Poel HG, Navab N, et al. Computer-assisted surgery: virtual-and augmented-reality displays for navigation during urological interventions. *Curr Opin Urol*. 2018;28:205–213.
10. Fuerst B, Sprung J, Pinto F, et al. First robotic SPECT for minimally invasive sentinel lymph node mapping. *IEEE Trans Med Imaging*. 2016;35:830–838.
11. Huang B, Tsai Y-Y, Cartucho J, et al. Tracking and visualization of the sensing area for a tethered laparoscopic gamma probe. *Int J Comput Assist Radiol Surg*. 2020;15:1389–1397.
12. Wild E, Teber D, Schmid D, et al. Robust augmented reality guidance with fluorescent markers in laparoscopic surgery. *Int J Comput Assist Radiol Surg*. 2016;11:899–907.
13. Meershoek P, KleinJan GH, van Willigen DM, et al. Multi-wavelength fluorescence imaging with a da Vinci Firefly: a technical look behind the scenes. *J Robot Surg*. November 11, 2020 [Epub ahead of print].
14. van Leeuwen FW, Schottelius M, Brouwer OR, et al. Trending: radioactive and fluorescent bimodal/hybrid tracers as multiplexing solutions for surgical guidance. *J Nucl Med*. 2020;61:13–19.
15. van Oosterom MN, Engelen MA, van den Berg NS, et al. Navigation of a robot-integrated fluorescence laparoscope in preoperative SPECT/CT and intraoperative freehand SPECT imaging data: a phantom study. *J Biomed Opt*. 2016;21:86008.
16. van Beurden F, van Willigen DM, Vojnovic B, et al. Multi-wavelength fluorescence in image-guided surgery, clinical feasibility and future perspectives. *Mol Imaging*. 2020;19:1536012120962333.

Distinguishing Primary Lateral Sclerosis from Parkinsonian Syndromes with the Help of Advanced Imaging

Pegah Masrori¹⁻³, Donatienne Van Weehaeghe^{4,5}, Koen Van Laere^{4,5}, and Philip Van Damme¹⁻³

¹Neuromuscular Reference Centre, Department of Neurology, University Hospitals Leuven, Leuven, Belgium; ²Department of Neurosciences, Experimental Neurology, and Leuven Brain Institute, KU Leuven, University of Leuven, Leuven, Belgium; ³Laboratory of Neurobiology, Center for Brain and Disease Research, VIB, Leuven, Belgium; ⁴Division of Nuclear Medicine, University Hospitals Leuven, Leuven, Belgium; and ⁵Nuclear Medicine and Molecular Imaging, Department of Imaging and Pathology, University Hospitals Leuven and KU Leuven, Leuven, Belgium

We describe a unique case of a patient presenting with unilateral mild paresis, slowing of the upper limb, and parkinsonism, who underwent a full imaging work-up including MRI, ¹²³I-FP-CIT PET, ¹⁸F-FE-PE2I PET, and ¹⁸F-FDG PET. This case demonstrates that imaging may aid substantially in the diagnostic work-up of complex neurologic disorders.

Key Words: neurology; PET/CT; PET/MRI; motor neuron disease; neurodegenerative disorders; functional imaging

J Nucl Med 2021; 62:1318–1319

DOI: 10.2967/jnumed.121.261942

PART 1

Case Report

We report the case of a 60-y-old man who initially presented after 6 mo of subacute and slowly progressive symptoms including muscle stiffness, decreased fine motor skills, slowing of movements, and mild muscle weakness in his right hand. The patient was right-handed and experienced writing difficulties—without cramps or dystonia—that affected legibility. He had no complaints of postural symptoms associated with orthostatic hypotension or other autonomic failure. No sleep disturbance, periodic limb movement during sleep, or restless legs syndrome was mentioned.

The patient had a history of a myocardial infarction, diabetes mellitus, and hypercholesterolemia; the latter two were relatively well controlled with medication. His family history was negative for neurodegenerative diseases.

The neurologic examination showed slowness in whole-hand grasping and on tapping tasks, as well as mild paresis of the dorsal interosseous muscles of the right hand. Furthermore, we found an asymmetric mild hypertonia in the lower right limb. A unilateral positive Hoffman sign (right) was noted, but we found no Babinski sign and tendon reflexes were symmetrically brisk. When the patient walked, we observed a reduced arm swing on the right side without postural imbalance or gait disorder. There was no evidence of myoclonus. All sensory modalities were normal. Eye movements, both

saccades and vertical gaze, were normal. Furthermore, detailed language testing and a behavioral assessment showed no abnormalities. Obtaining a diagnosis remained challenging, as it was difficult to distinguish between parkinsonism and a motor neuron disorder.

Hematologic and serum biochemistry tests had normal findings. The electromyography results were strictly normal.

MRI of the brain demonstrated mild white matter lesions normal for his age, without any hyperintensity in the corticospinal tracts. The cervical MR images showed no evidence of myelopathy or radiculopathy. ¹⁸F-FDG brain PET showed asymmetric mild hypometabolism in the left sensorimotor cortex compatible with the right arm symptoms, in favor of a motor neuron disease. To exclude neurodegenerative parkinsonism ¹²³I-*N*- ω -fluoropropyl-2 β -carbomethoxy-3 β -(4-iodophenyl)nortropine (¹²³I-FP-CIT) SPECT was performed 9 mo later and showed normal presynaptic dopaminergic transmission (Fig. 1).

Notably, there was no response to dopaminergic treatment with levodopa and benserazide.

Discussion

The differential diagnosis was broad. After excluding structural, metabolic, inflammatory, and infectious disorders, we were leaning toward diagnosis of a motor neuron disorder. Finally, we found no mutations in the SOD1, TARDBP, FUS, or C9orf72 genes. Whole-exome sequencing was done but showed no mutations related to neurodegenerative disorders.

Besides a slow progression of isolated paresis of the right hand, the patient's condition remained unchanged during a 1-y follow-up period. Repetition of the electromyography showed no signs of lower motor neuron degeneration. We requested a more sensitive ¹⁸F-(*E*)-*N*-(3-iodoprop-2-enyl)-2 β -carbofluoroethoxy-3 β -(4'-methylphenyl) nortropine (¹⁸F-FE-PE2I) PET scan to exclude subtle presynaptic dopaminergic transmission deficits. This imaging showed no abnormalities in the striatum or in the substantia nigra.

PART 2

Final Diagnosis

Together, the clinical picture and ancillary tests were compatible with an asymmetric form of pure upper motor neuron disorder. The imaging allowed diagnosis of primary lateral sclerosis (PLS) by showing on the one hand a hypometabolism of the sensory-motor cortex contralateral to the clinical involvement and on the other hand a presynaptic integrity of the dopaminergic pathways.

Received Jan. 22, 2021; revision accepted Apr. 13, 2021.

For correspondence, contact Philip Van Damme (philip.vandamme@uzleuven.be).

Published online May 20, 2021.

COPYRIGHT © 2021 by the Society of Nuclear Medicine and Molecular Imaging.

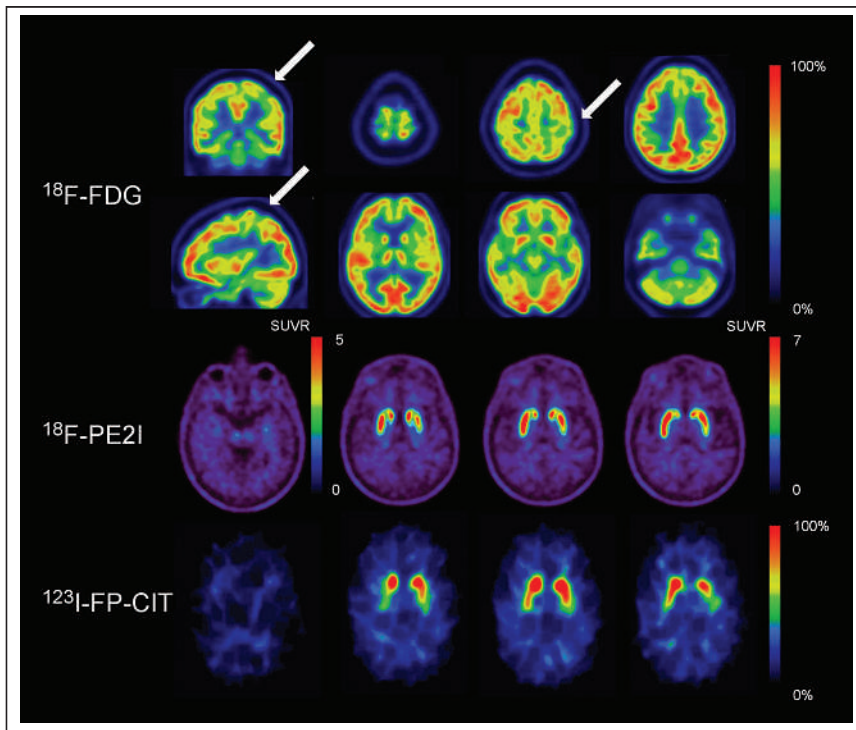


FIGURE 1. (Top) Orthogonal ^{18}F -FDG PET slices showing mild hypometabolism (arrows) in left sensorimotor cortex corresponding to right arm location of cortical homunculus. (Middle and bottom) Transverse slices of dopamine transporter imaging. Both classic ^{123}I -FP-CIT SPECT and high-resolution, selective ^{18}F -PE2I PET showed normal presynaptic dopaminergic uptake. Images are in radiologic orientation. SUVR = SUV ratio.

Conclusion

PLS is a rare neurodegenerative disorder characterized by a slowly progressive upper motor neuron syndrome. Compared with classic variants of amyotrophic lateral sclerosis, PLS has a significantly slower rate of disease progression and longer survival. Diagnosis of PLS is challenging and is based on excluding structural disorders (e.g., cervical spondylotic myelopathy, Arnold–Chiari malformation, spinal arteriovenous fistula, and tumor), hereditary spastic paraparesis, leukodystrophies, metabolic and toxic disorders (e.g., vitamin E deficiency, cerebrotendinous xanthomatosis, and hexosaminidase deficiency), neurodegenerative disorders (e.g., Parkinson disease, multiple systems atrophy, and corticobasal syndrome), inflammatory disorders (e.g., primary progressive multiple sclerosis), and infections (e.g., neurosyphilis, tropical spastic paraparesis, neuroborreliosis, spinal sarcoidosis, and AIDS). Thalamic, hippocampal, and basal ganglia atrophy, as well as subcortical gray matter degeneration, have been demonstrated in imaging studies of PLS (1). Postmortem studies have reported atrophy of the thalamus and striatum, as well as TDP-43 inclusions in the striatum, amygdala, hippocampus, and basal ganglia.

In this case, molecular imaging had a substantial added value to aid in the differential diagnosis between neurodegenerative parkinsonian syndromes and amyotrophic lateral sclerosis. Neurodegenerative parkinsonian syndromes are characterized by a presynaptic dopaminergic deficit. ^{123}I -FP-CIT SPECT is widely used in clinical practice to visualize dopaminergic system integrity at the level of the presynaptic terminals in the striatum (2). ^{18}F -FE-PE2I PET is a novel highly selective and high-resolution DAT imaging technique that allows visualization and quantification of both the striatum and the substantia nigra (3). As both techniques, when repeated after 12 mo of follow-up, had normal results, a presynaptic dopaminergic deficit could be excluded. Although dopaminergic deficits have been described in amyotrophic lateral sclerosis patients, a recent report on PLS patients with atypical signs of parkinsonism did not find any dopaminergic deficits (4), in line with our results.

Moreover, ^{18}F -FDG PET also showed typical signs of a motor neuron disease, as a mild hypometabolism in the left sensorimotor cortex was found corresponding to the right arm location of the homunculus (5,6). Therefore, advanced brain imaging guided the diagnosis.

DISCLOSURE

No potential conflict of interest relevant to this article was reported.

REFERENCES

1. Finegan E, Li Hi Shing S, Chipika RH, et al. Widespread subcortical grey matter degeneration in primary lateral sclerosis: a multimodal imaging study with genetic profiling. *Neuroimage Clin.* 2019;24:102089.
2. Calvo A, Chio A, Pagani M, et al. Parkinsonian traits in amyotrophic lateral sclerosis (ALS): a prospective population-based study. *J Neurol.* 2019;266:1633–1642.
3. Delva A, Van Weehaeghe D, van Aalst J, et al. Quantification and discriminative power of ^{18}F -FE-PE2I PET in patients with Parkinson's disease. *Eur J Nucl Med Mol Imaging.* 2020;47:1913–1926.
4. Norlinah IM, Bhatia KP, Ostergaard K, Howard R, Arabia G, Quinn NP. Primary lateral sclerosis mimicking atypical parkinsonism. *Mov Disord.* 2007;22:2057–2062.
5. Van Laere K, Wilms G, Van Damme P. Neurological picture. FDG-PET findings in three cases of Mills' syndrome. *J Neurol Neurosurg Psychiatry.* 2016;87:222–223.
6. Claassen DO, Josephs KA, Peller PJ. The stripe of primary lateral sclerosis: focal primary motor cortex hypometabolism seen on fluorodeoxyglucose F18 positron emission tomography. *Arch Neurol.* 2010;67:122–125.

Bowel Obstruction as a Complication of Peptide Receptor Radionuclide Therapy

TO THE EDITOR: With great interest, we recently read Strosberg et al.'s publication regarding the risk of bowel obstruction in patients with mesenteric or peritoneal disease who receive peptide receptor radionuclide therapy (PRRT) (1). At the author's institution, 5 patients experienced a bowel obstruction within 3 mo of treatment. The authors hypothesized that the mechanism of the bowel obstruction was inflammation induced by PRRT; this hypothesis was supported by surgical findings of a "frozen abdomen" in 2 of those patients. Before their publication, there had been no known reports highlighting intestinal obstruction as a complication of PRRT.

On the basis of our institution's experience with PRRT (^{177}Lu -DOTATATE) for gastroenteropancreatic neuroendocrine tumors, we would like to provide further evidence supporting Strosberg et al.'s hypothesis by reporting additional cases of bowel obstruction after PRRT. After witnessing several patients presenting with abdominal pain in the days shortly after treatment, we reviewed 80 patients who received PRRT before December 2018 at our institution. We found that 16 patients went to the emergency department or were admitted to the hospital within the first 14 d after a PRRT cycle, 4 of whom were ultimately diagnosed with a bowel obstruction.

Our findings are in contrast to the clinical trial data from NETTER-1. In the supplemental appendix of an article on that trial, there was a report of only 2 hospitalizations among a much larger cohort of patients who received PRRT ($n = 116$) (2). This finding could be explained by significant differences between the study population and our real-world cohorts. In the NETTER-1 trial, only 17 (15%) and 7 (6%) of the patients in the PRRT arm had metastases to the mesentery and peritoneum, respectively. On the other hand, all 4 of our patients who had a bowel obstruction had known peritoneal disease, and in Strosberg et al.'s report, 81 of 159 (51%) of their patients had peritoneal or mesenteric disease, including all 5 who had an obstruction (1).

Although peritoneal disease itself is a risk factor for intestinal obstruction, the fact that the patients at our institution developed obstructive complications within 14 d of PRRT treatment suggests an even stronger temporal cause-effect relationship. The hypothesized inflammation mechanism is even further supported by the radiographic finding of pseudoprogession with neuroendocrine tumors, which has already been commonly observed, as shown by other reports (3).

Existing literature regarding the safety of PRRT has previously focused primarily on long-term complications and laboratory abnormalities, such as hematologic or renal toxicity. For example, the rare but serious complication of secondary myeloid neoplasms has been well documented (4). There are fewer reports of immediate toxicity or short-term complications, but in 1 retrospective review of patients who received PRRT for grade 3 neuroendocrine tumors ($n = 69$), the authors reported that "PRRT was well tolerated by all patients" (5).

Unfortunately, our real-world experience provides additional examples that support Strosberg et al.'s observation that bowel obstruction is a short-term complication of PRRT treatment in

patients with baseline peritoneal and mesenteric disease. To our knowledge, ours is the only other report that highlights this specific complication of PRRT. Clinicians should remain cognizant of the potential for intestinal obstruction when weighing risks and benefits of treatment options until we have more definitive evidence and experience.

REFERENCES

1. Strosberg JR, Al-Toubah T, Pellè E, et al. Risk of bowel obstruction in patients with mesenteric or peritoneal disease receiving peptide receptor radionuclide therapy. *J Nucl Med*. 2021;62:69–72.
2. Strosberg J, El-Haddad G, Wolin E, et al. Phase 3 trial of ^{177}Lu -Dotatate for midgut neuroendocrine tumors. *N Engl J Med*. 2017;376:125–135.
3. Brabander T, Van Der Zwan WA, Teunissen JJM, et al. Pitfalls in the response evaluation after peptide receptor radionuclide therapy with [^{177}Lu -DOTA0,Tyr3] octreotate. *Endocr Relat Cancer*. 2017;24:243–251.
4. Sonbol MB, Halfdanarson TR, Hilal T. Assessment of therapy-related myeloid neoplasms in patients with neuroendocrine tumors after peptide receptor radionuclide therapy: a systematic review. *JAMA Oncol*. 2020;6:1086–1092.
5. Zhang J, Kulkarni HR, Singh A, Niepsch K, Müller D, Baum RP. Peptide receptor radionuclide therapy in grade 3 neuroendocrine neoplasms: safety and survival analysis in 69 patients. *J Nucl Med*. 2019;60:377–385.

Christopher E. Wee
Ayca Dundar
Rachel A. Eiring
Mohamed Badawy
Timothy J. Hobday
A. Tuba Kendi
Annie T. Packard
Thorvardur R. Halfdanarson*

*Mayo Clinic

Rochester, Minnesota

E-mail: halfdanarson.thorvardur@mayo.edu

Published online March 19, 2021.
 DOI: 10.2967/jnumed.121.262048

Reply: Bowel Obstruction as a Complication of Peptide Receptor Radionuclide Therapy

REPLY: Dr. Wee and colleagues reviewed their database of gastroenteropancreatic neuroendocrine tumor patients treated with ^{177}Lu -DOTATATE and observed patterns of bowel obstruction very similar to those described in our study (1). These corroborating data significantly strengthen the evidence of a causal link between ^{177}Lu -DOTATATE and risk of intestinal obstruction among patients with mesenteric or peritoneal disease. Fortunately, the increased use of high-sensitivity somatostatin receptor PET imaging (e.g., ^{68}Ga -DOTATATE and ^{64}Cu -DOTATATE PET) improves the ability of clinicians to identify peritoneal carcinomatosis and screen patients who are at risk for bowel obstruction.

What can be done to mitigate this complication? We have adopted a strategy of classifying mesenteric or peritoneal disease patterns as high or intermediate risk for intestinal obstruction. We define high risk as extensive peritoneal implants, omental caking, or mesenteric masses with significant bowel tethering causing symptoms of intermittent partial bowel obstruction. Intermediate risk is defined as scattered peritoneal or mesenteric metastases (greater than 10 but not innumerable), mesenteric mass with minimal bowel tethering, or implants in the rectovesical or rectouterine pouch.

Patients at high risk of obstruction are advised to pursue other second-line options such as everolimus, cytotoxic drugs, or (in select cases) debulking peritoneal or mesenteric surgery. We prophylactically treat intermediate-risk patients with corticosteroids after each cycle of ^{177}Lu -DOTATATE based on the presumption that radiation-induced inflammation contributes to the obstructive process. The regimen we use generally consists of 8 mg of intravenous dexamethasone after completion of amino acid infusion followed the next day by a 3-wk oral dexamethasone taper starting at 4 mg by mouth daily. We acknowledge that evidence for the prophylactic use of corticosteroids remains theoretic, and that other regimens (such as solumedrol dose pack) may be equally effective or ineffective.

We have not observed any episodes of irreversible bowel obstruction occurring after ^{177}Lu -DOTATATE since adopting these

mitigation strategies. Hopefully, our real-world experience, combined with that of the Mayo Clinic, will help ensure that clinicians are cognizant of this potential complication and will stimulate further research into prevention strategies.

REFERENCE

1. Strosberg JR, Al-Toubah T, Pellè E, et al. Risk of bowel obstruction in patients with mesenteric or peritoneal disease receiving peptide receptor radionuclide therapy. *J Nucl Med.* 2021;62:69–72.

Jonathan R. Strosberg*
Taymeyah Al-Toubah
Ghassan El-Haddad

**H. Lee Moffitt Cancer Center & Research Institute
Tampa, Florida*

E-mail: jonathan.strosberg@moffitt.org

Published online July 8, 2021.
DOI: 10.2967/jnumed.121.262340

What Member Benefits Do You Value?

Basic numbers show your dues **value** but **benefits** of SNMMI membership are more than just a dollar amount! Stay a **member** of your professional **community** and the society **dedicated** to **supporting** you at every stage of your **career**. Join us for another **membership** year—Renew today!

Community Knowledge & Influence

SNMMI's **14,000+** members form a knowledge center of nuclear medicine and molecular imaging professionals, involved in peer-to-peer learning, in-person and virtual networking opportunities, and advocacy efforts for our community.

Continuing Education

Members can earn all the CME/CE credits needed to maintain certification requirements with **FREE** webinars, Journal exams, and other **complimentary** education products.

Publication & Research

Membership comes with a complimentary subscription to *The Journal of Nuclear Medicine (JNM)* and *Journal of Nuclear Medicine Technology (JNMT)*—a **\$770 publication package**.

Awards & Recognition

SNMMI provides more than **\$400,000 annually** through grants, awards, and scholarships along with opportunities to showcase professional expertise as a speaker, presenter, and author to a global audience.

...And exclusive discounts offering up to 40% off event registrations, products, and services

www.snmmi.org/renew

SNMMI Value Initiative
SOCIETY OF NUCLEAR MEDICINE & MOLECULAR IMAGING

SNMMI Nuclear Medicine Review Course

September 11-12, 2021

This two-day course—featuring 14 lectures by world-renowned experts on the most critical topics in clinical nuclear medicine—is the perfect resource to help you prepare for your board exam or use as a great general refresher to enhance your practice!

Saturday, September 11, 2021

11:00 am-5:15 pm ET

- **Welcome**

Erica J. Cohen Major, DO, MPH, FACNM
Ishani Dalal, MD

- **Musculoskeletal**

Justin G. Peacock, MD, PhD

- **Neuroendocrine**

Courtney Lawhn-Heath, MD

- **Pediatrics**

Frederick Grant, MD

- **Renal**

Bital Savir-Baruch, MD

- **Cardiology**

Sharmila Dorbala, MD

- **Parenteral Therapies**

Dave Brandon, MD

- **Physics**

Kenneth Nichols, PhD

Sunday, September 12, 2021

11:00 am-5:15 pm ET

- **Welcome**

Erica J. Cohen Major, DO, MPH, FACNM
Ishani Dalal, MD

- **Neurology**

Katherine Zukotynski, BAsC, MD, PhD, P.Eng

- **Gastrointestinal**

Ishani Dalal, MD

- **Pulmonary**

Shana Elman, MD

- **PET/CT**

Twyla B. Bartel, DO, FACNM, FSNMMI

- **Thyroid and Parathyroid**

Chirayu Shah, MD

- **Infection**

Christopher Palestro, MD

- **NRC**

Darlene Metter, MD, FACNM, FSNMMI

Register to attend: www.snmmi.org/NMRC2021

Continuing Medical Education

The Society for Nuclear Medicine and Medical Imaging, Inc. (SNMMI) is accredited by the Accreditation Council for Continuing Medical Education (ACCME) to provide continuing medical education for physicians.

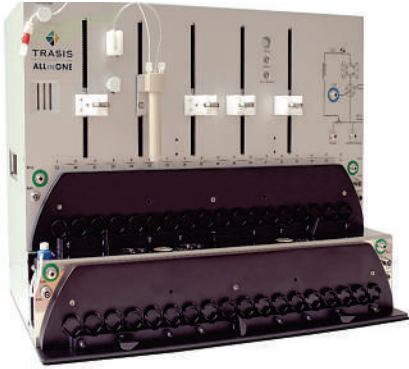
SNMMI designates this enduring material for a maximum of **11.0 AMA PRA Category 1 Credits™**. To receive CE credit, learners must achieve a score of 80% on the post-course assessment and complete the evaluation.



TRASIS

YOUR PARTNER IN RADIOPHARMACY

ALLINONE



ALLINONE mini



EASYONE



**Cutting-edge embedded technology for limitless research
and routine production**

**More than 30 radiotracers commercially available with various radioisotopes
 Lu^{177} , Ga^{68} , F^{18} , C^{11} , Cu^{64} , Ac^{225} , Zr^{89} , and more**

- ✓ International network
- ✓ Fast growth with 900+ synthesizers installed in the world
- ✓ 50+ collaborations both with radiopharmaceutical companies and research centers
- ✓ Developing customized synthetic methods and instruments

Contact us on [trasis.com](https://www.trasis.com)

The Journal of Music Therapy

September 2021

Vol. 62

Pages 177-321